

nature

THE INTERNATIONAL WEEKLY JOURNAL OF SCIENCE



BOTTOM-UP BIOLOGY

How to build a cell from scratch

PAGE 171

PANDEMICS

PATTERNS OF DYSFUNCTION

*Lessons from the front
lines of Ebola*

PAGE 180

QUANTUM PHYSICS

BEYOND EQUILIBRIUM

*Universal dynamics
in ultracold atoms*

PAGES 191, 217, 221 & 225

ARTIFICIAL INTELLIGENCE

SOUND OF THE CROWD

*Nano-oscillators learn to
recognize spoken vowels*

PAGE 230

NATURE.COM

8 November 2018

Vol. 563, No. 7730

THIS WEEK

EDITORIALS

CURRENCY Bank of England should choose female scientist **p.156**

WORLD VIEW How a viral video showed the world my science **p.157**

CONSERVATION Genomics aims to leave no animal behind **p.160**



Biology from the bottom up

Scientists have overturned the conventional approach to studying cells to instead build life's systems from scratch.

Evolution has famously never produced a wheel. Humans famously did — and have spent much of the time since urging each other not to reinvent it. This example illustrates a clear difference between two approaches to problem solving. Nature works with what it has from the bottom up, and eventually finds a solution through an inefficient process of trial and error. Nature has never explicitly asked itself: how can I move this bulk from here to there as quickly and easily as possible? Hence, no wheeled animals, although plenty of legs, wings and other ways of getting about. Humans tend to take the opposite approach: reduce, simplify and break down a complex problem to find the most efficient solution.

This human framing of a problem is often described as top-down analysis, and that's usually how research into cell biology proceeds. Even where the overall intention of the science is simply to expand knowledge (compared with the specific task-focused goal of engineering), the cell is too complex and sophisticated an object to analyse without being broken down conceptually.

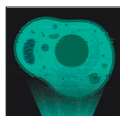
Top down involves a decomposition process. So although a researcher can make a career out of unpicking the workings of a cellular machine such as a ribosome or mitochondrion, the starting point for such projects has always been the role of these structures in existing cells. The work is directed by the context in which it originated and into which it will fold back once complete.

Decomposition and working out from the top down how systems function is a valuable approach, but it might not be the best way to make a cellular process work better — or to produce a different one that does the same thing but more effectively. To do that, researchers must be able to put aside the context, the system that evolution generated, and instead design and construct a system afresh from component parts, the so-called bottom-up approach.

Take the very real challenge of finding a way to copy the natural process of photosynthesis — which could revolutionize energy production. As we discuss in a News Feature on page 172, one approach cell biologists are taking is to mix unusual combinations of enzymes — including some taken from bacteria and the human liver — to make different versions of metabolic pathways involved in photosynthesis and incorporate them into an artificial chloroplast.

That research, and other work in a similar vein, is at the forefront of bottom-up biology. Biologists, physicists and chemists are attempting to reconstruct cellular processes by looking afresh at the constituent parts. In doing so, they argue, bottom-up science can extend the reach of researchers and perhaps offer some novel insight and solutions to long-standing problems.

"It is important for researchers to focus on the benefits of such ambitious projects, not just the intellectual challenges."



BOTTOM-UP BIOLOGY
A *Nature* special issue
go.nature.com/bottomupbiology

In a special issue this week, *Nature* brings together a series of articles that discuss and explore some of the challenges, opportunities and complexity of this emerging field. At its most far-reaching, bottom-up biology could construct a reproducing artificial 'cell' completely from scratch. But it is important for researchers to focus on the benefits of such ambitious projects, not just the intellectual or practical challenges. A Comment piece on page 177 urges bottom-up biologists to set their sights on definite applications, such as artificial blood.

Bottom-up biology is typically seen as different from 'synthetic biology', which usually refers to an emerging branch of biotechnology that aims to assemble some highly derived (synthetic) products by bringing many separate parts together in complex sequences of elementary steps. In pursuing this goal, synthetic biology uses both top-down and bottom-up approaches.

The creation of living systems according to human design throws up some powerful questions — not least who gets given the responsibility to do it and how the work and what results from it can be controlled and regulated. So it's important that scientists, policymakers and the public are kept informed and consulted about where this research could lead. ■

Launch sequence

Life on Earth is to have its DNA analysed in a welcome conservation effort.

An ambitious project launched last week aims to slow the decline in biodiversity by sampling and decoding the DNA of every species of plant and animal on Earth. Called the Earth BioGenome Project, the effort is seeking funding to help it get off the ground. It is asking for US\$4.7 billion to sequence all 1.35 million known eukaryotic species — those with a cell nucleus enclosed by a membrane — over the next 10 years.

Given the colossal scale of the crisis that faces life on the planet, genomics might seem an unlikely saviour. Biology has certainly advanced to a different realm since physicist Ernest Rutherford's famous quip that science was either physics or stamp collecting. But how much — really — can reading the DNA sequences of species save the organisms from the threat of climate change, the destruction of their habitats or human over-exploitation of natural resources through fishing and farming? To someone with a hammer, every problem looks like a nail. Are scientists with DNA-sequencing machines falling for the same logical fallacy? Is this a project that is being done because technology means that it now can, rather

than because the need for conservation says that it must?

The organizers have yet to make their case fully — after all, the project is still on the drawing board — but the early signs suggest that it is worthwhile. Yes, it is likely to be relatively expensive to accomplish fully, but so is much of modern science on a grand scale. In today's money, the Human Genome Project cost \$5 billion, and few people would argue that this was not money well spent. The construction of the Large Hadron Collider, which discovered the Higgs boson, cost about the same amount. (And as Harris Lewin, the organizer of the London launch of the Earth BioGenome Project, provocatively asked: "What has the Higgs boson done for you lately?")

What can genomics do for conservation? Quite a lot, actually, and the vast scope of the project can easily obscure the intensely local insights that might emerge. To point to one small example reported this year, an analysis of 3,095 DNA variations called single nucleotide polymorphisms in the genome of the endangered eastern tiger salamander (*Ambystoma tigrinum*) in Long Island, New York, found that, because roads were restricting the animals' movement between breeding ponds, genetic fragmentation of populations was occurring (E. McCartney-Melsad *et al.* Preprint at bioRxiv <http://doi.org/gdcd5x>; 2018). The finding highlighted the need for conservation efforts to focus on mitigating this development.

But so far, scientists have just scratched the surface in terms of the diversity of organisms sequenced. And sequencing technologies are only now mature enough to generate high-quality (complete) genomes for in-depth studies. Of the 33,000 genomes in the archives of the US National Center for Biotechnology Information (which represent 0.2% of eukaryotic species diversity), only 50% are of high quality.

Arguably, the highest-quality (and the most expensive) genomes are not strictly necessary for conservation efforts to benefit, but they might reveal the route to new biofuels, drug leads and useful agricultural traits. Finding such applications, and so presenting the conservation of biodiversity as a boon to national economies, local cultures and the environment, should further help governments to take biodiversity issues even more seriously.

Certainly, the need is urgent and the statistics alarming: 50% of

current biodiversity could be lost by the end of the century. Earth's sixth great extinction event is firmly under way, and ending this crisis will take much more than DNA sequences. But the Earth BioGenome Project can play a part, and early signs are that it might work.

It is right to seek commitment from participants, by asking them to chip in with money from their own grants. And a good sign is that it's not a top-down monolith. Unlike a typical genome-sequencing project, it has come together as a grass-roots initiative, driven by individuals who study diverse groups of organisms and who are already working to sequence the organisms' DNA. The new project includes ongoing efforts such as i5K (insects), B10K (birds) and the Darwin Tree of Life project, which aims to sequence all of the estimated 66,000 eukaryotic species in the United Kingdom. That suggests the pay-off could come more quickly because many of the genomes are already targeted by research communities keen to process and annotate them.

One looming issue is how easy it will be to transfer samples and genetic data across national borders. A meeting of the United Nations Convention on Biological Diversity (CBD) in Egypt later this month will consider new controls on the sharing of digital genetic data. The proposals would extend the reach of the 2014 Nagoya Protocol, which provides for equitable sharing of the benefits obtained from using genetic resources. If properly implemented, such rules will create greater legal certainty and transparency for the countries that provide such resources and the scientists and companies that use them. They will also help to boost local scientific capacity in the many poorest countries that hold some of the world's richest biodiversity.

Extending the protocol to cover genetic data makes sense, but, if done clumsily, it could create a mess. The CBD has to its credit held extensive consultations with scientists and research institutions likely to be affected. The Earth BioGenome Project could help, by speaking as one voice for researchers. It's better to have one international effort to negotiate solutions for data sharing, instead of a hotchpotch of complex individual and bilateral agreements. And that will help to ensure that the Earth BioGenome Project really does benefit the entire Earth. ■

Note worthy

The Bank of England should put a female scientist on its next £50 note.

What does Marie Curie have in common with the bacteriologist Hideyo Noguchi and the theoretical astrophysicist Victor Ambartsumian? They are among the scientists who have featured on banknotes around the world (respectively, the old 20,000 Polish zloty, the ¥1,000 in Japan and the 100 Armenian dram). Now, the British public has the chance to choose who should join them. Last week, the Bank of England announced that it is looking for an inspirational scientist to appear on the next £50 note. It has invited suggestions and will pass them to a dedicated committee, which will make the final decision and announce it next year.

Scientists and engineers have featured heavily on UK banknotes since the bank started to print historical figures on their reverse sides in 1970. Generations of Britons have been paid with notes depicting Isaac Newton, George Stephenson, Michael Faraday and Florence Nightingale. The designs have not always pleased everyone. The £10 note released in 2000 featured Charles Darwin and his trip on HMS *Beagle*, but also threw in some hummingbirds — which many biologists felt were irrelevant.

Whoever is chosen (the only binding criteria are that they must be

British and dead) will replace the steam-engine pioneers Matthew Boulton and James Watt on the £50 note, the highest denomination in circulation. It has yet to feature a woman, and this has led to suggestions that the Bank of England should choose a female scientist. *Nature* agrees. It's true that this would rule out deserving figures such as Alan Turing and Stephen Hawking (who died this year and who bank officials have said would be allowed, even though the bank usually expects banknote candidates to have been dead for at least 20 years). But here is an opportunity to celebrate the hugely important achievements of a woman in science, and to offer an important and inspiring role model at the same time.

A straw poll of some *Nature* staff highlighted some clear possibilities, none of whom will come as a particular surprise to readers. Mary Anning (1799–1847) was a prolific fossil hunter who changed the way we think about the history of life. Ada Lovelace (1815–1852) is credited with producing the first account of a prototype computer and its possible applications. Rosalind Franklin (1920–1958) was an X-ray crystallographer who played a key part in work to establish the structure of DNA. And Dorothy Hodgkin (1910–1994) remains the only British woman to win a science Nobel prize, for her research to unravel the structures of proteins including insulin.

We intend to determine and submit our choice before the 14 December deadline. We welcome the recommendations of readers everywhere as to who they would choose (e-mail: briefing@nature.com). And we encourage you to submit your own nominations at go.nature.com/2jrkt4y. The launch date of the note itself has not yet been confirmed, but it will not appear in circulation before 2020. ■



What I learnt pulling a straw out of a turtle's nose

When my video went viral, I found that communicating to non-scientists is uncomfortable — and effective, says Christine Figgenger.

Three years ago, I uploaded a video of a sea turtle in distress. While collecting data for my PhD off the coast of Costa Rica, my team decided to remove what looked to be a barnacle encrusted in the nostril of the turtle, which we had captured for a research study. The object turned out to be a 10-centimetre section of a disposable plastic drinking straw. We filmed the process. That upsetting video (see go.nature.com/2qfci6f) has now had more than 33 million views, and became an emblem of the anti-straw movement.

It also thrust me into a world of high-profile advocacy I never expected to enter. I became involved in a documentary project, and community activists who were launching plastic-free campaigns asked for my support; I've gone to schools, conferences and screenings to talk about a subject that is not my main research focus. Last month, to my surprise, *Time* named me a 2018 Next Generation Leader, alongside celebrities such as Ariana Grande and Hasan Minhaj. All this has taught me that communicating beyond academia is worth trying, but it demands constant vigilance and caution.

I always have to remind non-scientists that my video is, of course, not the first documentation of how plastic harms marine wildlife. A legion of scientific articles does exactly that. But, for many, it takes videos such as mine to make these articles less abstract. I'd spent years making videos that I hoped would encourage conservation by showing the beauty of nature. They had little effect compared with my video of a bleeding turtle and a spontaneous anti-straw tirade.

Many scientists shy away from the press — or from uploading videos that show emotion, especially anger and frustration. We fear the simplification and inaccuracies likely to be introduced into accounts of our research, which could cause us to lose credibility with peers and funders. Yet, these routes might be the most effective way of getting information to policymakers and citizens, and so promoting conservation.

This year, companies including Alaska Airlines, Disney and Starbucks announced programmes to phase out plastic straws. Seattle, Washington, and San Francisco, California, among other cities, have moved to ban or limit them. Of course, straws are just a tiny fraction of the plastics in the ocean. (Roughly, they make up less than 0.03% of the more than 8 million tonnes of plastic waste, largely consumer trash and fishing nets, that makes its way to the ocean every year, mainly from middle-income countries.)

I take care to explain that the straw is emblematic of unnecessary plastic items and how human activity harms oceans. The message is getting through. Last week, the European Union moved to prohibit several single-use plastics, including plates and cutlery.

Activists need scientists' input. When you're trying to preserve species effectively and have limited funds, you need to know which

life stages have the highest chance of survival and whether there is enough suitable habitat left for a species to even sustain larger numbers. Sometimes people are eager to undertake intense hands-on work (such as rescuing turtle eggs by digging them up and reburying them) even when less-dramatic efforts (such as establishing protected beach areas) would be sufficient and longer lasting.

Delivering compelling messages is difficult. I am used to obsessing over my data, not over how I look on camera. My research is dirty and smelly, full of long hours and unkempt hair. Conservation campaigns focus more on appearances, marketing and selling.

Thanks to my video, I have acquired a thicker skin and an eclectic set of skills ranging from copyright law, social-media marketing and unconventional ways of fundraising (I started a GoFundMe page for research). I learnt to ignore most rude and ignorant remarks: for instance, claims that I shoved the straw into the turtle's nose for self-promotion. If I respond, I draft an unemotional e-mail debunking accusations point by point with established facts.

What rankles more is when people try to take advantage of me. As in academia, philanthropy and advocacy are full of big egos that sometimes care more about advancing themselves than a cause. They are also less likely to buy into an ideal of citing and crediting others. I have learnt to be careful about how others use my work.

It might seem to other early-career scientists that I won the lottery by publishing a gruesome video rather than hundreds of scientific articles, but I am not even sure whether my modicum of celebrity makes me more or less employable.

My advocacy has taken time away from my

research. I still need to finish my dissertation on the migration patterns of olive ridley sea turtles (*Lepidochelys olivacea*). Yet I am scared that if I turn down speaking engagements or other chances to spread the message about plastics pollution, I'm letting down the creatures I'd hoped to help by studying them.

Although it might never feel entirely comfortable, I intend to keep straddling both academia and advocacy. After the straw-extraction video went viral, my colleague and I decided that we needed a conventionally citable publication, and so we wrote a piece that appeared in *Marine Turtle Newsletter* (N. J. Robinson and C. Figgenger *Mar. Turtle Newsl.* 147, 5–6; 2015). That article exemplifies why doing outreach beyond academia is so important. Maybe a few hundred scientists read the peer-reviewed article, whereas millions of people saw the video. Which had the bigger impact? ■

Christine Figgenger is a PhD student in the ID Marine Biology Program at Texas A&M University in College Station.
e-mail: christine.figgenger@tamu.edu

**I AM SCARED
THAT IF I TURN DOWN
CHANCES TO
SPREAD THE
MESSAGE,
I'M LETTING DOWN
THE CREATURES I'D
HOPED TO HELP.**

SEVEN DAYS

The news in brief

EVENTS

Ebola vaccine

On 2 November, the Uganda Ministry of Health announced that it would give the experimental Ebola vaccine, rVSV-ZEBOV, to around 3,000 people at high risk of infection near the country's border with the Democratic Republic of the Congo (DRC). Uganda has not yet confirmed any Ebola cases, but the outbreak in the DRC is spreading and the World Health Organization (WHO) says there's a high risk of it reaching neighbouring countries. As of 3 November, the DRC had reported 298 cases and 186 deaths, including one in a previously unaffected part of the country. The number of infections has increased by roughly 50% over the past 4 weeks, according to the WHO. In the past week, the neighbouring Republic of the Congo, South Sudan, Uganda and Yemen have reported suspected Ebola cases.

POLICY

Grant-funding test

Australia's government is set to introduce a 'national-interest test' for research projects seeking grant funding from next year. The policy will require researchers to outline how their project will advance the country's interests, said education minister Dan Tehan in a statement on 31 October. The test will apply to applications seeking money from the Australian Research Council (ARC), a major funder of science and humanities research. Research groups and academics have criticized the decision, saying that grant assessments already demand a description of a project's potential benefits. The policy announcement came days after news emerged that the previous education

minister, Simon Birmingham, used his authority to reject 11 grant applications that had been recommended for ARC funding by independent peer-review panels in 2017 and 2018.

Boost for Plan S

Two of the world's largest biomedical research funders have backed a plan to make all papers resulting from work they fund open-access (OA) on publication by 2020. On 5 November, the London-based Wellcome Trust and the Bill and Melinda Gates Foundation in Seattle, Washington, endorsed 'Plan S', adding their weight to the initiative, which is already backed by 13 research funders from across Europe.

Plan S was launched in September and is spearheaded by Robert-Jan Smits, the European Commission's special envoy on OA. The Wellcome Trust, which gave out £1.1 billion (US\$1.4 billion) in grants in 2016–17, is also the first funder to detail how it intends to implement Plan S. It already has an OA policy, but it allows an embargo of up to six months after publication before papers have to be made free to read. It now says that by 2020, it will ban such embargoes. Wellcome-funded work will not be able to appear in subscription journals unless these publications permit papers to be published under OA terms. Wellcome will also

at the Wellcome Sanger Institute in Hinxton, UK, have committed up to £50 million (US\$65 million) over 8 years to sequence the genomes of the eukaryotic species in the United Kingdom, thought to number about 66,000 — among the largest commitments to the effort yet made. At the London meeting, participants thrashed out guidelines for sample collection, sequencing and data curation and sharing.

Bold genome project kicks off

An ambitious effort to sequence the genome of every complex organism on Earth was launched on 1 November in London. The Earth BioGenome Project aims to decode the genomes of the roughly 1.5 million known animal (pictured, composite image of platypus), plant, protozoan and fungal species — the eukaryotes — over the next decade, at an estimated cost of US\$4.7 billion. As part of the effort, scientists



DAVE WATTS/NATURE PICTURE LIBRARY

stop providing OA funds for 'hybrid' journals, but it will not bar publication in them if scientists can pay for it themselves.

Gender protest

More than 1,600 scientists in the United States sent a letter to the US Department of Health and Human Services (HHS) on 2 November, condemning the department's recently revealed proposal to define whether a person is male or female by their genitals at birth. The presidents of three biological societies, which together represent more than 3,000 scientists, sent a similar letter to the HHS last week. The researchers reject

NASA the government's argument that its proposal is based on science. They say that the science linking genetics, anatomy and gender identity is complex and still unclear, and that implementing the policy would erase protections for and identities of millions of people who do not identify with their sex assigned at birth — including those who are transgender or intersex. The proposed change would apply to Title IX, a US civil-rights law that bans discrimination on the basis of sex in education programmes that receive government funds.

FACILITIES

Lost in space

NASA officials pronounced two of the agency's long-running space missions dead after the spacecraft ran out of fuel last month. On 30 October, NASA announced that its Kepler space telescope (pictured) had ceased science operations. Since its 2009 launch, Kepler has discovered more than 2,680 confirmed planets beyond the Solar System, including Kepler-186f, an Earth-sized planet in the habitable zone. The telescope also spotted thousands of other potential worlds that are awaiting confirmation. And on 31 October, when the



Dawn spacecraft failed to make contact with Earth from its orbit around the asteroid Ceres, mission managers concluded that it, too, had stopped functioning. Launched in 2007, Dawn visited two big asteroids — Vesta in 2011 and Ceres in 2015 — the first probe to orbit two objects beyond Earth.

India's neutrino lab

Long-delayed efforts to build a major neutrino observatory in India cleared a legal hurdle on 2 November, when the country's National Green Tribunal upheld environmental clearance for the project. The clearance had been challenged by activists, who say that excavation will affect wildlife and resources. The 15-billion-rupee (US\$206-million) facility, called the India-based Neutrino Observatory, is set to be built under 1.2 kilometres of rock in the southern state of Tamil Nadu. Physicists

hope that the detector will help them to elucidate the relative masses of neutrinos, elusive particles produced when cosmic rays strike the atmosphere. India's government approved funding for the project in 2015, but the experiment has been opposed by environmentalists and local politicians. Before construction can begin, the project must also gain approvals from wildlife and pollution boards.

PEOPLE

'Noteworthy' figure

A scientist will grace Britain's next £50 banknote — and the public has the chance to suggest who it should be. The Bank of England is looking for a UK scientist to replace the industrialists Matthew Boulton and James Watt on the next iteration of the note, which will be printed on a polymer material for the

first time. Nominations can be made through the bank's website until 14 December, and proposed scientists must be dead. An advisory committee — including four scientists — will then whittle down the list to a few names. The bank's governor, Mark Carney, will make the final decision, which will be announced in 2019. See page 156 for more.

Sanger probe

The Wellcome Sanger Institute in Hinxton, UK, has dismissed allegations that its high-profile director, geneticist Mike Stratton, bullied staff, discriminated against them because of their gender and misused funds. On 30 October, the institute, one of the world's top genomics centres, announced that an investigation had cleared Sanger's management, in particular Stratton, of these accusations. Carried out by the barrister Thomas Kibling at Matrix Chambers, London, the investigation did identify "failings in the way in which people have been managed", and a lack of diversity at senior levels of the organization. In a statement, Stratton apologized for "failures in people management that have occurred and have had unintended detrimental effects on individuals."

TREND WATCH

Unpaid research stints are common in sub-Saharan Africa, according to an online survey of 412 academics that spanned 6 countries. Eighty-five per cent of respondents report having had research positions with no pay. Of those, 33% had spent between 1 and 5 years doing research for free, and 4% had spent more than 5 years doing so.

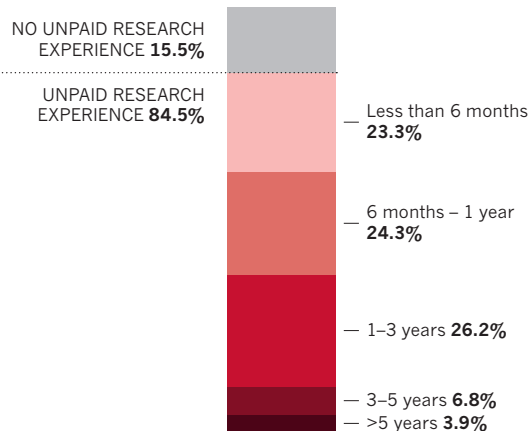
Many researchers on the continent work with organizations out of personal interest or to contribute to a specific cause, says Lem Ngongalah, head of the Collaboration for Research Excellence in Africa in Douala,

Cameroon, which posted the results on 17 October (L. Ngongalah *et al.* Preprint at bioRxiv <http://doi.org/cwr9>; 2018). "In many cases, there is no payment for such work, because the organization itself has no funding for the work it does," she says. "Funding continues to be a significant challenge for research in Africa."

The respondents — who come from Cameroon, Nigeria, Kenya, Uganda, Tanzania and South Africa — also identified other barriers to conducting research in Africa, including a shortage of training facilities and a loss of motivation to continue research.

UNPAID RESEARCH IN AFRICA

Some 85% of 412 academics and students in 6 countries reported having been in research positions with no pay at some point in their career. Academics cite a lack of funds for research as one of the main causes.

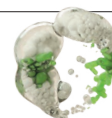


NEWS IN FOCUS

ECOLOGY Cost of South Africa's invasive species laid bare in government report **p.164**

EVOLUTION AI spots natural selection at work in the human genome **p.167**

ASTRONOMY Enthralling 'Cow' supernova divulges its secrets **p.168**



BIOLOGY The quest to create cells from scratch **p.171**

ROBIN LOZNAK/ZUMA WIRE



A group of children and young people (shown here with lawyer Julia Olson) is suing the US government to force stronger action on climate change.

LAW

Historic kids' climate lawsuit gets green light

Young people claim US government has violated their rights by failing to avert warming.

BY EMMA MARRIS

A landmark climate-change lawsuit brought by young people against the US government can proceed, the Supreme Court said on 2 November. The case, *Juliana v. United States*, had been scheduled to begin trial on 29 October in Eugene, Oregon, in a federal district court. But those plans were scrapped last month, after President Donald

Trump's administration asked the Supreme Court to intervene and dismiss the case.

The plaintiffs, who include 21 people ranging in age from 11 to 22, allege that the government has violated their constitutional rights to life, liberty and property by failing to prevent dangerous climate change. They are asking the district court to order the federal government to prepare a plan that will ensure that the level of carbon dioxide in the atmosphere falls below

350 parts per million by 2100, down from an average of 405 parts per million in 2017.

By contrast, the US Department of Justice argues that "there is no right to 'a climate system capable of sustaining human life'" — as the *Juliana* plaintiffs assert.

Although the Supreme Court has now denied the Trump administration's request to dismiss the case, the path ahead is unclear. In its 2 November order, the Supreme Court ►

► suggested that a federal appeals court should consider the administration's arguments before any trial starts in the Oregon district court. Lawyers for the young people said that they would push the district court to reschedule the trial this week.

"The youth of our nation won an important decision today from the Supreme Court that shows even the most powerful government in the world must follow the rules and process of litigation in our democracy," said Julia Olson, co-counsel for the plaintiffs, in a statement.

Although climate change is a global problem, lawyers around the world have brought climate-change-related lawsuits against local and national governments and corporations since the late 1980s. These suits have generally sought to force the sort of aggressive action against climate change that has been tough to achieve through political means.

Many of the cases have failed, but in 2015, a citizen's group called the Urgenda Foundation won a historic victory against the Dutch government. The judge in that case ordered the Netherlands to cut its greenhouse-gas emissions to at least 25% below 1990 levels by 2020, citing the possibility of climate-related damages to "current and future generations of Dutch nationals" and the government's "duty of care ... to prevent hazardous climate change". A Dutch appeals court upheld the verdict last month.

Over the past few years, the Dutch case has emerged as a model for climate lawsuits in other countries, says Gillian Lobo, a lawyer who specializes in climate-change-related cases at ClientEarth in London. More recently, she says, the *Juliana* lawsuit has inspired

its own copycats — some of which have progressed further than *Juliana* itself. "It is a global phenomenon," Lobo says.

One case modelled on the *Juliana* lawsuit has already produced a striking victory. In January, 25 young people sued the Colombian government for their right to a healthy environment, in a case called *Demanda Generaciones Futuras v. Minambiente*.

The Colombian Supreme Court found in the plaintiffs' favour in April. Not only did it order the government to take steps to reduce deforestation and climate change, it also ruled that the Colombian Amazon rainforest is "a subject of rights" that is entitled to "protection, conservation, maintenance and restoration".

The young plaintiffs in the *Juliana* case allege that they have already suffered harm from climate change. Seventeen-year-old Jaime and her family left their home on the Navajo Nation Reservation in Cameron, Arizona, in 2011 because the springs that supplied their water were drying up. Fifteen-year-old Jayden's home in Louisiana was severely damaged by flooding in 2016, and 19-year-old Vic's school in White Plains, New York, closed temporarily in 2012 after Hurricane Sandy hit.

US climate hawks hope that the *Juliana* plaintiffs will ultimately prevail, but President Trump's administration is mounting a multipronged defence. The Justice Department denies that the district court in Oregon has jurisdiction over the broad sweep of federal

policies at issue, and that the rights to life, liberty and property set out in the Constitution translate into the right to a stable climate. In any case, the department argues, no meaningful redress is possible, given that sharp cuts in US emissions might not move the needle on climate change much if other countries' greenhouse-gas output grows.

Andrea Rodgers, co-counsel for the *Juliana* plaintiffs, says that the Trump administration hasn't challenged the fact that humans are changing the climate. "They haven't presented experts to contest what our scientists are saying about ice melt or sea-level rise or terrestrial impacts or how climate change happens or ocean acidification," she says.

To win, Rodgers says, "we have to show that the United States government is liable, but also that there is a remedy that the judge can order". The United States has seen its greenhouse-gas emissions drop in recent years, as the country shifts its energy mix away from coal and towards renewable sources, but as of 2016, it remains the second-largest emitter after China.

James Hansen, a climatologist at Columbia University in New York City and a long-time climate activist, is an expert witness in the case — and a plaintiff, representing "future generations" not yet born. (His 20-year-old granddaughter Sophie Kivlehan is also a plaintiff.)

Hansen has been fighting for action on climate change since he first testified on the subject before the US Senate in 1988. He says that if the *Juliana* plaintiffs lose their case, he will simply try another way. "We need to win as soon as possible," Hansen says, "but if we lose, we don't give up — we come back with a stronger case." ■

"We need to win as soon as possible. But if we lose, we don't give up — we come back with a stronger case."

ECOLOGY

South Africa's invasive species guzzle water and cost US\$450 million a year

The country's first report on its biological invaders is pioneering in scope, and paints a dire picture for resources and biodiversity.

BY SARAH WILD

South Africa is losing its battle against biological invaders, according to the government's first attempt to comprehensively assess the status of the country's alien species.

The invaders, including forest-munching wasps and hardy North American bass, cost the country around 6.5 billion rand (US\$450 million) a year and are responsible for about one-quarter of its biodiversity loss. That's the conclusion of a pioneering report (see go.nature.com/2qmwgag) that the South African National

Biodiversity Institute in Pretoria released on 2 November.

Invasive species also guzzle water, a serious problem in a country suffering from a prolonged and catastrophic drought that is expected to worsen as the climate changes.

The report, which the institute compiled in response to 2014 regulations that mandate a review of invasive species every three years, examines the pathways by which these species enter the country and the effectiveness of interventions. It also weighs the toll they take on the nation's finances and biodiversity.

This achievement constitutes a "significant advance" compared with efforts by most other countries, says Piero Genovesi, who chairs the invasive species specialist group of the International Union for Conservation of Nature in Rome. He says that other reports have looked at the impact of biological invasions, or at measures to address the problem, but have not considered all aspects of invasions.

The report provides "an incredible basis" on which to deal with invasive species in South Africa, says Helen Roy, an ecologist at the Centre for Ecology and Hydrology near Oxford, UK.

ENVIRONMENT

Australia cuts coral research

Reef-science centre set to lose government funding.

BY ADAM MORTON

Ocean researchers around the world are dismayed that an Australian research institute that has become an international authority on the declining health of reef ecosystems will lose most of its government funding after 2021.

Papers by scientists at the Centre of Excellence for Coral Reef Studies, based at James Cook University in Townsville, were cited almost 40,000 times in 2017 — the most citations for any institute in the world doing reef science. But in late October, it emerged that the Australian Research Council (ARC), an independent government agency, had not shortlisted the centre to receive a share of the latest round of funding. The ARC has funded the centre since its inception 13 years ago.

The centre will lose 37% of its current annual budget of about Aus\$12 million (US\$8.7 million), and its title as an ARC centre of excellence. James Cook University says it is committed to delivering world-class coral-reef research into the future, but has not explained how the centre will be supported. The centre's director, Terry Hughes, declined to comment on the decision.

Scientists fear job losses and a reduced research capacity are to come. They say the centre's work is important to people living alongside reefs across the tropics. "It is deeply stupid for Australia not to fund, or even consider funding, its world-leading coral-reef research," says Garry Peterson, an environmental scientist at the Stockholm Resilience Centre.

The coral-reef centre employs about 300 scientists. Its most celebrated work, which established the extent of recent bleaching along the Great Barrier Reef (T. P. Hughes *et al.* *Nature* **543**, 373–377; 2017), involved aerial surveys and 100 divers.

Some researchers link the ARC's decision to the Australian government's failure to adequately address climate change, which is the greatest threat to coral reefs. "A different government with a different outlook would have found a way to support that centre," says physicist Bill Hare, chief executive of the climate-research and policy institute Climate Analytics in Berlin.

But ARC chief executive Sue Thomas says that the decision was based on a standard competitive process. ■



The invasive ant *Linepithema humile* disrupts seed dispersal in indigenous South African plants.

Across the world, invasive species — organisms that have been introduced into ecosystems beyond their natural habitats, and that spread over large distances on their own — are considered a major threat to biodiversity, human health and economies. Climate change is expected to further their global spread, in part by reducing the resilience of native ecosystems.

To create the report, in 2015, 37 researchers from 14 national organizations, led by the National Biodiversity Institute and the Centre of Excellence for Invasion Biology at Stellenbosch University, began collating data from institutions around the country.

MAJOR IMPACTS

The researchers report that 7 new species are introduced into South Africa each year, and that about 775 invasive species have been introduced so far. This contrasts with the 556 invasive species previously reported by the government. Most of the species identified by the latest report are plants, with insects the next most common. (For comparison, the United Kingdom says that it has 184 non-native invasive species.) The report's authors consider 107 of the species in South Africa to have major impacts on biodiversity or human well-being.

Invaders of note include trees in the *Prosopis* genus, such as honey mesquite (*P. glandulosa*), which damages animal grazing areas, outcompetes local plants and, according to a 2017 study in Mali, seems to encourage the growth of populations of the malaria-carrying *Anopheles* mosquito, among other effects (G. C. Muller *et al.* *Malar. J.* **16**, 237; 2017).

Others include the *Sirex* wasp (*Sirex noctilio*), which threatens South Africa's 16-billion-rand forestry industry; the ant

Linepithema humile, from Argentina, which disrupts seed dispersal in indigenous plants; the North American small-mouth bass (*Micropterus dolomieu*), which has outcompeted indigenous fish; and the water hyacinth (*Eichhornia crassipes*), from South America, which chokes the country's waterways.

As well as their cost and toll on biodiversity, the report explores the pressure that invasive species put on the water supply. This year, Cape Town almost became the first major city in the world to run out of water. In May, researchers argued that alien plants, which often use more water than do indigenous ones, consumed more than 100 million litres of water a day — about one-fifth of the city's daily usage — and that water losses due to invasive species could triple by 2050. The report estimates that invasive trees and shrubs, if left unchecked, could threaten up to one-third of the water supply to cities such as Cape Town, and consume up to 5% of the country's mean annual rainfall run-off.

Despite enacting the 2014 regulations and spending at least 1.5 billion rand a year to curb invasive species, the country is not keeping up, says the report. "The most concerning finding was how ineffective we have been," says co-author Brian van Wilgen, an applied ecologist at Stellenbosch University.

But the authors also note that their confidence in almost all their estimates is low, because of poor monitoring and evaluation data — and that more research into impacts and monitoring techniques is needed.

Jasper Slingsby, an ecologist with the South African Environmental Observation Network in Cape Town, agrees. "We need better funding and concerted research effort in this space as a national priority," he says. ■



Towering thunderstorms regularly roll over central Argentina.

ATMOSPHERIC SCIENCE

Inside Argentina's mega-storms

Massive project aims to improve severe-weather predictions in shadow of the Andes mountains.

BY ALEXANDRA WITZE

Some of the worst thunderstorms on the planet are about to give up their secrets. Deadly downpours, grapefruit-sized hail and severe lightning regularly pepper the eastern side of the Andes mountains in Argentina. These storms often flood towns and destroy the vineyards of the region's wine industry, but remain poorly understood. About 160 atmospheric scientists — mostly from the United States, Argentina and Brazil — have descended on central Argentina to change that.

Their ultimate goal is to improve severe-weather warnings, so that people know to avoid areas where flash floods are likely, or to prepare their vineyards for a hailstorm.

The US\$30-million project kicked into high gear on 1 November, as researchers headed to the centre of the country with storm-chasing equipment, including radar scanners mounted on trucks. The atmospheric-sciences experiment, called Remote sensing of Electrification,

Lightning, And Mesoscale/microscale Processes with Adaptive Ground Observations (RELAMPAGO, which is Spanish for lightning), is the biggest of this type ever conducted outside the United States.

"It's the craziest activity I have ever been in in my life," says Paola Salio, an atmospheric scientist at the University of Buenos Aires and the Argentina lead on the project. "But it is also like a dream come true."

From now until mid-December, the scientists hope to chase at least a dozen severe storms to study air temperature, wind speed and direction, rainfall amounts, the number of lightning strikes and other factors. They want to use those data to improve models of how descending air on the eastern side of the Andes triggers towering thunderstorms that

regularly reach 18 kilometres into the atmosphere. Such storms are more powerful than typical thunderstorms elsewhere, which might grow 12 kilometres high.

The lines of thunderstorms that often form along the Andes look very similar to the ones in the central United States that usually produce tornadoes. But the Argentinian storms are larger and, for some reason, don't spawn tornadoes nearly as often as the US storms do.

"That's one of the mysteries we want to answer, why there are so few tornadoes," says Steve Nesbitt, an atmospheric scientist at the University of Illinois at Urbana-Champaign who heads RELAMPAGO.

In addition, the researchers will drive hundreds of kilometres southwest of their base near Córdoba to target systems that produce strong hail in Mendoza province.

A second, related project called CACTI (Cloud, Aerosol, and Complex Terrain Interactions) will focus on how atmospheric particles such as dust or haze influence storm development. Funding for both projects comes from national research agencies and institutions in the United States — such as the National Science Foundation and the Department of Energy — Argentina and Brazil.

The work would not have been possible a few years ago, before Argentina beefed up its national weather radar system. Workers installed the first of the upgraded radars in Córdoba in 2015, says Celeste Saulo, director of Argentina's weather service in Buenos Aires. There are seven other such radars operating around the country, and three more should be up and running by December, she adds.

RELAMPAGO scientists plan to compare the data from the Córdoba radar with those from their truck-based instruments — which can reach more rural areas and capture additional information on how storms grow — to gain a better picture of how severe weather works in central Argentina.

During the project, the weather service will test a type of forecasting system that continually ingests updated weather data to improve forecasts. It's similar to ones used by meteorologists in the United States and Europe. Argentina's weather agency wants to use the system going forward, Saulo says.

RELAMPAGO could even provide a glimpse of the future, says Kristen Rasmussen, an atmospheric scientist at Colorado State University in Fort Collins. As global temperatures rise, the warming atmosphere will provide more energy to feed thunderstorms around the world. Rasmussen's computer simulations show that those changes could result in storms similar to the powerful ones now seen in Argentina (K. L. Rasmussen and R. A. Houze Jr *Mon. Weather Rev.* **144**, 2351–2374; 2016).

"What we're seeing in South America could be more like what we will see in a future climate," she says. This means that other parts of the world could soon get a taste of the storms that Argentina knows so well. ■

MARCOS FURER

GENETICS

Deep learning spots natural selection at work

Scientists use artificial intelligence to hunt for genetic sequences moulded by evolution.

BY AMY MAXMEN

Pinpointing where and how the human genome is evolving can be like hunting for a needle in a haystack. Each person's genome contains three billion building blocks called nucleotides, and researchers must compile data from thousands of people to discover patterns that signal how genes have been shaped by evolutionary pressures.

To find these patterns, a growing number of geneticists are turning to a form of machine learning called deep learning. Proponents of the approach say that deep-learning algorithms incorporate fewer explicit assumptions about what the genetic signatures of natural selection should look like than do conventional statistical methods.

"Machine learning is automating the ability to make evolutionary inferences," says Andrew Kern, a population geneticist at the University of Oregon in Eugene. "There is no question that it is moving things forward."

One deep-learning tool called DeepSweep, developed by researchers at the Broad Institute of MIT and Harvard in Cambridge, Massachusetts, has flagged 20,000 single nucleotides for further study. These simple mutations might have helped humans to survive disease, drought or what Charles Darwin called the "conditions of life", researchers reported last month at the annual meeting of the American Society of Human Genetics in San Diego, California.

Since the 1970s, geneticists have created mathematical models to describe the fingerprint of natural selection in DNA. If a mutation arises that renders a person better able to survive and produce offspring than their neighbours, the percentage of the population with that gene variant will grow over time.

One example is the mutation that gives many adults the ability to drink cow's milk. It enables the body to produce lactase, an enzyme that digests the sugar in milk, into adulthood. By analysing human genomes using statistical methods, researchers discovered that the mutation spread rapidly through Europe thousands of years ago — presumably because nutrients in cow's milk helped people to produce healthy children¹. Today, nearly 80% of people of European descent carry this variant.

Yet geneticists have struggled to identify, and confirm, other specific snippets of the genome that spread throughout populations

because they provided an adaptive edge. Deep learning excels at just this sort of task: discovering subtle patterns in large amounts of data.

But there is a catch. Deep-learning algorithms often learn to classify information after being trained by exposure to real data; Facebook, for example, primes algorithms to recognize faces using pictures that people have already labelled. Because geneticists don't yet know which parts of the genome are being shaped by natural selection, they must train their algorithms on simulated data.

To generate that simulated data, researchers need to imagine what the signature of natural selection looks like, says Sohini Ramachandran, a population geneticist at Brown University in Providence, Rhode Island. "We don't have ground-truth data, so the worry is that we may not be simulating properly."

And because deep-learning algorithms operate as black boxes, it's hard to know what criteria they use to identify patterns in data, says Philipp Messer, a population geneticist at Cornell University in Ithaca, New York. "If the simulation is wrong, it's not clear what the response means," he adds.

Researchers who use deep-learning algorithms do try to peek into the black box. DeepSweep's creators trained the algorithm on signatures of natural selection that they inserted into simulated genomes. When they tried it on real genomes, the algorithm zeroed

in on the mutations that allow adults to drink milk. That bolstered the team's confidence in the tool, says Joseph Vitti, a computational geneticist at the Broad Institute who helped to develop DeepSweep.

The researchers then sifted through data from the 1000 Genomes Project — an initiative that sequenced DNA from 2,504 people around the world — using a statistical method to identify regions that might be under evolutionary pressure. When DeepSweep examined these areas more closely, it delivered a list of 20,000 single mutations to explore.

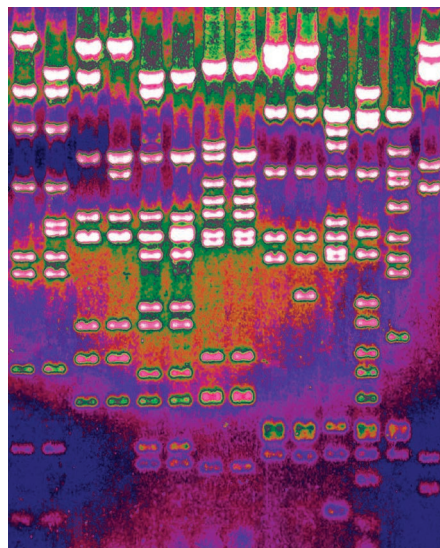
In the coming months, Vitti and his colleagues will investigate what these mutations do by editing them in the DNA of living cells, to compare what happens when the mutations are present with when they are not.

Several other researchers are training deep-learning algorithms to search for signs of adaptation in genomes. A deep-learning model developed by Kern suggests that, at first, most mutations in humans are neither beneficial nor harmful². Rather, they seem to drift along in populations, increasing natural genetic variability, and become more frequent only when a change in the environment gives people with a particular mutation an evolutionary edge.

In February, Ramachandran and her colleagues reported³ on a deep-learning algorithm they developed, called SWIF(r). When they applied it to the genomes of 45 members of the Khomani San ethnic group in southern Africa, it flagged variations near genes associated with metabolism. The researchers speculate that the changes could have occurred thousands of years ago and helped members of the group to store fat when food was scarce.

The effects of the mutations still need to be tested. But, as with the variants spotted by DeepSweep, the candidates singled out by SWIF(r) provide scientists with a place to start.

"These are incredibly powerful methods for looking for the signals of natural selection," says Pardis Sabeti, a computational geneticist at the Broad Institute, and Vitti's PhD supervisor. "Some people didn't think you could pinpoint variants when I started. Some thought it was impossible." ■



DNA fragments separated for analysis.

1. Itan, Y. *et al.* *PLoS Comput. Biol.* **5**, e1000491 (2009).
2. Schrider, D. R. & Kern, A. D. *Mol. Biol. Evol.* **34**, 1863–1877 (2017).
3. Sugden, L. A. *et al.* *Nature Commun.* **9**, 703 (2018).



Mauna Kea, the planned site of the Thirty Meter Telescope, is sacred to many Native Hawaiians.

ASTRONOMY

Embattled telescope scores big win

Hawaii's supreme court rules that the Thirty Meter Telescope's construction permit is valid.

BY ALEXANDRA WITZE

Hawaii's supreme court has ruled in favour of building the Thirty Meter Telescope (TMT) atop the mountain Mauna Kea. The decision removes the last legal hurdle preventing the US\$1.4-billion project from resuming construction.

"This clears the way for the TMT to begin construction," says Doug Simons, executive director of the Canada-France-Hawaii Telescope, which is located on Mauna Kea. "So,

yeah, it's a really big deal."

For years, the next-generation astronomical observatory has been mired in public protests and legal challenges. Some Native Hawaiians say that building the mega-telescope would further desecrate a sacred mountain that is already home to multiple observatories. In April 2015, protesters blocked the road to Mauna Kea's summit as construction of the TMT was set to begin. That December, the state supreme court revoked the project's construction permit, saying that the state

government had granted it before opponents of the telescope could have their full say.

Hawaii's Board of Land and Natural Resources issued a fresh construction permit in September 2017, prompting opponents to appeal. The latest ruling upholds that permit.

A separate legal issue, involving the University of Hawaii's sublease of land on Mauna Kea for the TMT site, was resolved in August. The state supreme court ruled in the project's favour in that case, as well.

TMT opponents have few legal options; they include petitioning the US Supreme Court.

One of the groups opposing the TMT, the environmental advocacy organization KAHEA in Honolulu, said it was "disappointed" by the latest ruling. "Thousands of Hawaiian cultural practitioners have affirmed the sacredness of the entirety of Mauna Kea," the group said in a statement.

TMT officials have been considering an alternative site for the telescope, in Spain's Canary Islands, in case they cannot resolve the obstacles to building in Hawaii. It could take months before project leaders decide whether to go ahead in Hawaii, now that they have the supreme court's backing. Among the issues they face is how to restart construction on Mauna Kea, given the protests that broke out the last time they tried to do so.

"We remain committed to being good stewards on the mountain and inclusive of the Hawaiian community," said Henry Yang, chair of the TMT International Observatory board of governors, in a statement.

In Hawaii, the battle over how Mauna Kea is used may soon shift from the TMT to the University of Hawaii's master lease, which covers all land on the mountain that is used for astronomical observatories. The lease expires in 2033, and Shelley Muneoka, a representative of KAHEA, says that the group is considering a challenge to the lease's renewal. ■

TMT INTERNATIONAL OBSERVATORY

ASTROPHYSICS

Mystery supernova known as 'Cow' spills its secrets

A superbright explosion in a galaxy far, far away has drawn astronomers' full attention.

BY DAVIDE CASTELVECCHI

For many astronomers, 2018 will be remembered as the year of the cow — after the nickname of a spectacular stellar explosion that has kept them busy for months.

The unusual event has offered an unprecedented window on to the collapse of a star, two

teams of researchers suggest in papers submitted to the arXiv preprint server on 25 October^{1,2}. In contrast to the slow ramp-up of a typical supernova, Cow became stupendously bright essentially overnight, leaving astronomers perplexed. "It popped up out of nowhere," says Stephen Smartt, an astronomer at Queen's University Belfast, UK, who discovered the

explosion on 16 June. He named it according to an alphabetical protocol that just happened to spell out the word 'Cow' — technically, it is the event AT2018cow.

Iair Arcavi, an astrophysicist at the University of California, Santa Barbara, says that "pretty much everything about its emission is something we haven't seen before." This is "the

dream” for those who study stellar explosions, adds Raffaella Margutti, an astrophysicist at Northwestern University in Evanston, Illinois, who led one of the teams behind the two papers.

The two groups behind the latest papers arrived independently at the same conclusion: that a ‘central engine’ has kept agitating the exploding star for months, and that the energy must have come from either a newly formed black hole in the process of accreting matter, or the frenetic rotation of a neutron star.

Both black holes and neutron stars are born when massive stars reach the end of their lives. Explosions such as Cow could provide direct evidence of this type of birth, says Mansi Kasliwal, an astronomer at the California Institute of Technology (Caltech) in Pasadena. “I think this is telling us about how to understand the most extreme incarnations of massive-star explosions.” Arcavi is impressed by the quality of the observations and the latest results, but, he says, “there’s still no bottom line as to what this is”. For now, Cow remains a mystery.

After the initial discovery, Smartt traced Cow to a galaxy called CGCG 137-068 known to be around 60 megaparsecs (200 million light years) away. And this was no ordinary supernova: it reached its peak brightness in days, not weeks. “Everybody put down what they were doing up to that point” and started following Cow, says Daniel Perley, an astrophysicist at Liverpool

John Moores University, UK. Perley and his collaborators commanded a robotic telescope on La Palma, one of Spain’s Canary Islands, to observe Cow nearly every night for a month and a half. They also used other telescopes around the globe that belong to a network Kasliwal designed for this kind of follow-up study.

CURIOUSER AND CURIOUSER

The evidence that the team gathered — mostly in the optical spectrum — suggested that an existing black hole is tearing a star apart, an observation they posted online³ in August. But to get the full picture, researchers needed to look at the spectrum of electromagnetic energy, from radio waves to γ -rays.

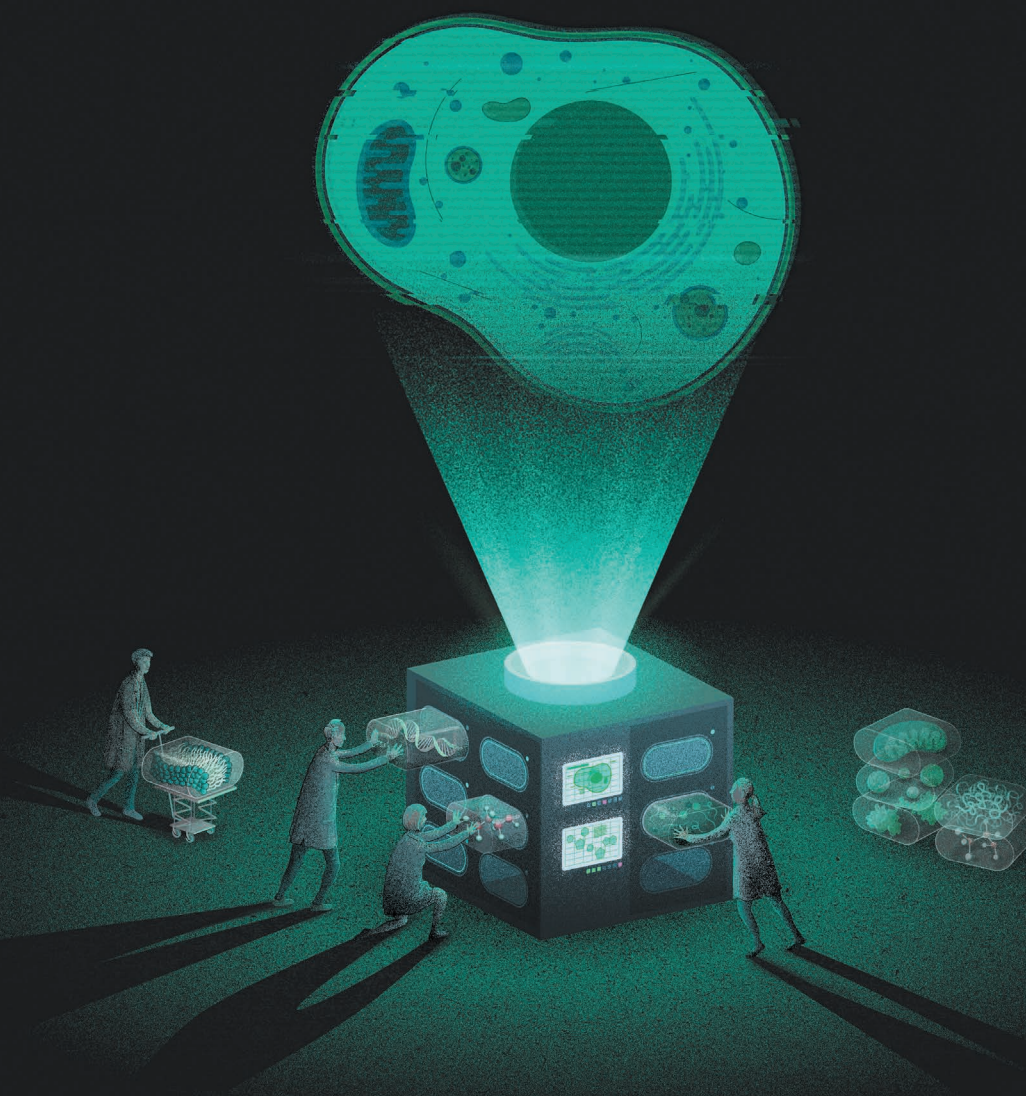
Just days after Smartt’s discovery, Anna Ho, another astronomer at Caltech, moved quickly to observe Cow in the radio spectrum. In a stellar explosion, charged particles emit radio waves as they spiral inside strong magnetic fields, and their wavelengths stretch as the material spreads out. This happens quickly, so astronomers are unlikely to catch events early enough to see short-wavelength emissions. But with Cow, Ho realized that she might have a rare chance to observe wavelengths of one millimetre or less. Early observations in June by her group and others indeed found emissions in the sub-millimetre range, so she submitted an emergency proposal for observing time to the Atacama

Large Millimeter/submillimeter Array (ALMA) in the Chilean Andes.

For weeks, Ho’s team watched the spectrum of the event’s millimetre emissions as it evolved. The researchers found that matter was expanding outward as fast as one-tenth of the speed of light². But, unlike an ordinary supernova, this short-wavelength radiation lasted for weeks, revealing the presence of a central ‘engine’ — a black hole or a spinning neutron star. “We were able to show that it’s not consistent with any of the usual mechanisms,” Ho says.

Margutti and her colleagues, meanwhile, took advantage of a proposal Margutti had made to observe ‘transient’ events using NASA’s NuSTAR X-ray telescope. Observations of Cow on NuSTAR and other telescopes confirmed the event was highly unusual: X-ray spectra showed that it was being reheated from the inside. This, too, points to a black hole or neutron star at the centre — although it’s too soon to conclude which. Margutti hopes that astronomers will observe more of these events and so begin to pin down the conditions that lead to one outcome over another. “The game begins now.” ■

1. Margutti, R. *et al.* Preprint at <https://arxiv.org/abs/1810.10720> (2018).
2. Ho, A. Y. Q. *et al.* Preprint at <https://arxiv.org/abs/1810.10880> (2018).
3. Perley, D. A. *et al.* Preprint at <https://arxiv.org/abs/1808.00969> (2018).



BOTTOM-UP BIOLOGY

Researchers are tearing up the biology rule books by trying to construct cells from scratch. A special issue explores the lessons being learnt about life.

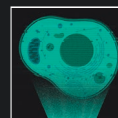
Cells are often called the building blocks of life — but that metaphor fails to capture their complexity. How do the multitudes of different molecules within a lipid envelope come together to carry out the functions required to sustain organisms? The standard approach in biology has been to work from the top down to study how cell components interact in their natural environment. But technical advances now allow researchers to take a different tack: using engineering principles to reconstruct biological processes from the bottom up. This special issue explores the potential and possible limits of bottom-up cell biology.

The ultimate goal for many is to construct an artificial cell from scratch. But there are vigorous debates about how to build it and what functions would be required to constitute life. A News Feature on page 172 explores how researchers are working to develop components such as membranes and metabolic pathways and to piece them together into a whole. And an Editorial on page 155 reminds us to consider the responsibility that comes with creating artificial life.

Before they succeed in creating an artificial cell, researchers might be able to develop cell-like systems engineered for biomedical applications. On page 177, Dan Fletcher, a bioengineer at the University of California, Berkeley, offers a wish list for such ventures that address pressing medical needs, including artificial blood cells and smart delivery vehicles for drugs.

Some groups are extending the bottom-up approach beyond cell construction. On page 203, Xavier Trepat at Spain's Barcelona Institute for Science and Technology and his colleagues report that they have developed a system in which cells stretch and deform themselves *in vitro* in ways that have been seen only in metal alloys. Now we can investigate whether this property helps to shape tissues during development, say Manuel Théry and Atef Asnacios from Paris Diderot University in an accompanying News & Views article, on page 192.

Like all scientific approaches, there are limits to what can be learnt from engineering biology. As a News & Views forum on page 188 highlights, researchers disagree about how useful the approach is for studying biological phenomena that are governed by physical variables. The complexity of cells is precisely what makes it appealing to build one, piece by piece. ■



BOTTOM-UP BIOLOGY

A Nature special issue

go.nature.com/bottomupbiology

BIOLOGY FROM SCRATCH

BUILT FROM THE BOTTOM UP, SYNTHETIC CELLS
COULD REVEAL THE BOUNDARIES OF LIFE.

BY KENDALL POWELL





ILLUSTRATION BY DAVID MCLEOD

here were just eight ingredients: two proteins, three buffering agents, two types of fat molecule and some chemical energy. But that was enough to create a flotilla of bouncing, pulsating blobs — rudimentary cell-like structures with some of the machinery necessary to divide on their own.

To biophysicist Petra Schwille, the dancing creations in her lab represent an important step towards building a synthetic cell from the bottom up, something she has been working towards for the past ten years, most recently at the Max Planck Institute of Biochemistry in Martinsried, Germany.

“I have always been fascinated by this question, ‘What distinguishes life from non-living matter?’” she says. The challenge, according to Schwille, is to determine which components are needed to make a living system. In her perfect synthetic cell, she’d know every single factor that makes it tick.

Researchers have been trying to create artificial cells for more than 20 years — piecing together biomolecules in just the right context to approximate different aspects of life. Although there are many such aspects, they generally fall into three categories: compartmentalization, or the separation of biomolecules in space; metabolism, the biochemistry that sustains life; and informational control, the storage and management of cellular instructions.

The pace of work has been accelerating, thanks in part to recent advances in microfluidic technologies, which allow scientists to coordinate the movements of minuscule cellular components. Research groups have already determined ways of sculpting cell-like blobs into desired shapes; of creating rudimentary versions of cellular metabolism; and of transplanting hand-crafted genomes into living cells. But bringing all these elements together remains a challenge.

The field is, nevertheless, imbued with a new sense of optimism about the quest. In September 2017, researchers from 17 laboratories in the Netherlands formed the group Building a Synthetic Cell (BaSyC), which aims to construct a “cell-like, growing and dividing system” within ten years, according to biophysicist Marileen Dogterom, who directs BaSyC and a laboratory at Delft University of Technology. The project is powered by an €18.8-million (US\$21.3-million) Dutch Gravitation grant.

In September, the US National Science Foundation (NSF) announced its first programme on synthetic cells, funded to the tune of \$10 million. And several European investigators, including Schwille, have proposed building a synthetic cell as one of the European Commission’s Future and Emerging Technologies Flagship schemes, which receive funding of €1 billion.

Bottom-up synthetic biologists predict that the first fully artificial cells could spark to life in little more than a decade. “I’m pretty sure we’ll get there,” says Schwille.

ALL IN THE PACKAGING

Research groups have made big strides recreating several aspects of cell-like life, especially in mimicking the membranes that surround cells and compartmentalize internal components. That’s because organizing molecules is key to getting them to work together at the right time and place. Although you can open up a billion bacteria and pour the contents into a test tube, for example, the biological processes would not continue for long. Some components need to be kept apart, and others brought together.

“To me, it’s about the sociology of molecules,” says Cees Dekker, a biophysicist also at Delft University of Technology.

For the most part, this means organizing biomolecules on or within lipid membranes. Schwille and her team are expert membrane-wranglers. Starting about a decade ago, the team started adding Min proteins, which direct a bacterial cell’s division machinery, to sheets



BOTTOM-UP BIOLOGY

A *Nature* special issue
go.nature.com/bottomupbiology

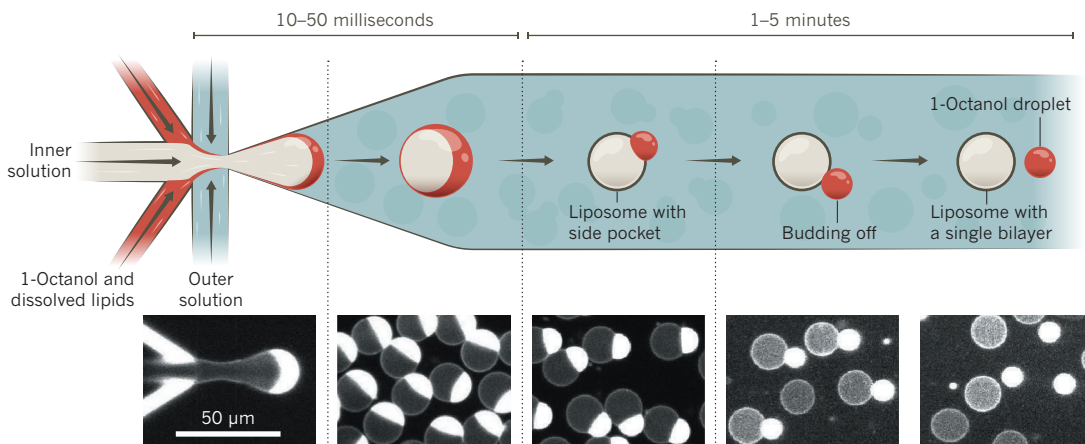
of artificial membrane made of lipids. The Mins, the researchers found, would pop on and off the membranes and make them wave and swirl¹. But when they added the Mins to 3D spheres of lipids, the structures burst like soap bubbles, says Schwille. Her group and others have overcome this problem using microfluidic techniques to construct cell-sized membrane containers, or liposomes, that can tolerate multiple insertions of proteins — either into the membranes themselves or into the interior.

Schwille’s graduate student, Thomas Litschel, and his collaborators dissolved the Min proteins in water and released droplets of the mixture into a rapidly spinning test tube. Centrifugal force pulls the droplets through layers of dense lipids that encapsulate them along the way. They come out at the other end as liposomes measuring 10–20 micrometres across — about the size of an average plant or animal cell. These liposomes, known as giant unilamellar vesicles (GUVs), can be made in different ways, but in Litschel’s hands, the Min proteins caused the GUVs to pulsate, dance around and contract in the middle².

Schwille’s group wants to capitalize on its knowledge of these proteins, which can produce membrane patterns and self-organize. “We understand these molecules really well,” she says. “We’d like to see how far we can get with relatively simple elements like the Mins.” Perhaps, as Litschel’s work hints, the team could use the proteins to mould membranes for division or to gather components at one end of a synthetic cell. Just as some physicists might use duct tape and tinfoil to fine-tune their experiments, Schwille says she hopes that these handy biological molecules will give her the ability to tinker with cell-like structures: “I’m an experimentalist to the bone.”

THE BUBBLE MACHINES

Researchers use microfluidic chips to make lipid bubbles, or liposomes, which are similar to the envelopes that contain cells. One approach features a six-way junction that can fill liposomes with solution and pinch them off. With the fatty alcohol 1-octanol in the mix, a lipid bilayer forms around the inner solution. Over time, excess lipids and 1-octanol pool at one end and spontaneously split off, leaving a fully formed liposome.



ADAPTED FROM REF. 3

Dekker's team members have also filled liposomes with their favourite proteins using a microfluidic chip (see 'The bubble machines'). On the chip, two channels containing lipid molecules converge on a water-filled channel and spit out cell-sized liposomes that can hold various biological molecules, either stuck through the membrane or free-floating inside the container³.

His group has experimented with pressurizing, deforming and reshaping the liposomes to take on non-spherical shapes that mimic cells better. Microfluidic devices give researchers more control to move, sort and manipulate liposomes using micro-channels that operate almost like circuits. This year, the Dekker lab designed a chip that could mechanically split a liposome in two by pushing it up against a sharp point⁴.

"This, of course, is not what we are after — we want to demonstrate division from the inside, but it still tells us interesting information," says Dekker. Examples include the force it takes to divide a cell, and what types of physical manipulation the liposomes can tolerate. Along the same lines, his team has also played around with the shape of living *Escherichia coli* cells — making them wider or square by growing them in nanofabricated silicone chambers. In this way, team members can see how cell shape affects the division machinery, and assess how the Min proteins work in cells of different size and shape⁵.

"We play with nanofabrication techniques and do things a normal cell biologist would never do," he says. "But a strange biophysicist like me can do this."

ADDING ENERGY TO THE SYSTEM

Now that it's possible to add components to the liposome bubbles without popping them, groups can plan how to make molecules work together. Almost anything life-like requires cellular energy, usually in the form of ATP. And although this can be added from the outside to feed a synthetic system, many biologists working on bottom-up approaches argue that a true synthetic cell should have its own power plant, something similar to an animal cell's mitochondrion or a plant's chloroplast, both of which make ATP.

Joachim Spatz's group at the Max Planck Institute for Medical Research in Heidelberg, Germany, has built a rudimentary mitochondrion that can create ATP inside a vesicle.

To do this, his team took advantage of new microfluidic techniques. First, they stabilized GUVs by placing them inside water-in-oil droplets surrounded by a viscous shell of polymers. Then, as these droplet-stabilized GUVs flowed down a microchannel, the team injected big proteins into them, either inside the vesicle or embedded in the membrane's surface (see 'The assembly lines').

They loaded these membranes with an enzyme called ATP synthase, which acts as a kind of molecular waterwheel, creating ATP energy from precursor molecules as protons flow through the membrane. By adding acid to boost protons outside the GUVs, the team drove ATP's production on the inside⁶.

Spatz explains that researchers could cycle the GUVs around the microchannel again for another protein injection, to sequentially add components. For instance, the next step could be to add a component that will automatically set up the proton gradient for the system.

"That's an important module, like you have in real life," says Spatz.

Another Max Planck synthetic-biology group led by biochemist Tobias Erb has been chipping away at other approaches to constructing cellular metabolic pathways. He's particularly interested in pathways that allow photosynthetic microbes to pull carbon dioxide from the environment and make sugars and other cellular building blocks.

Erb, a group leader at the Max Planck Institute for Terrestrial Microbiology in Marburg, Germany, takes a blank-slate approach to synthesizing cellular metabolic pathways. "From an engineering point of view, we think about how to design," he says, "and then we build it in the lab".

His group sketched out a system design that could convert CO₂ into malate, a key metabolite produced during photosynthesis. The team predicted that the pathway would be even more efficient than photosynthesis. Next, Erb and his team searched databases for enzymes that might perform each of the reactions. For a few, they needed to tweak existing enzymes

into designer ones.

In the end, they found 17 enzymes from 9 different organisms, including *E. coli*, an archaeon, the plant *Arabidopsis* and humans. The reaction, perhaps unsurprisingly, was inefficient and slow⁷.

"We put a team of enzymes together that did not play well together," says Erb. After some further enzyme engineering, however, the team has a "version 5.4" that Erb says operates 20% more efficiently than photosynthesis.

Expanding this work, Erb's group has begun constructing a crude version of a synthetic chloroplast. By grinding up spinach in a blender, and adding its photosynthesis machinery to their enzyme system in the test tube, the biologists can drive the production of ATP and the conversion of CO₂ to malate — solely by shining ultraviolet light on it.

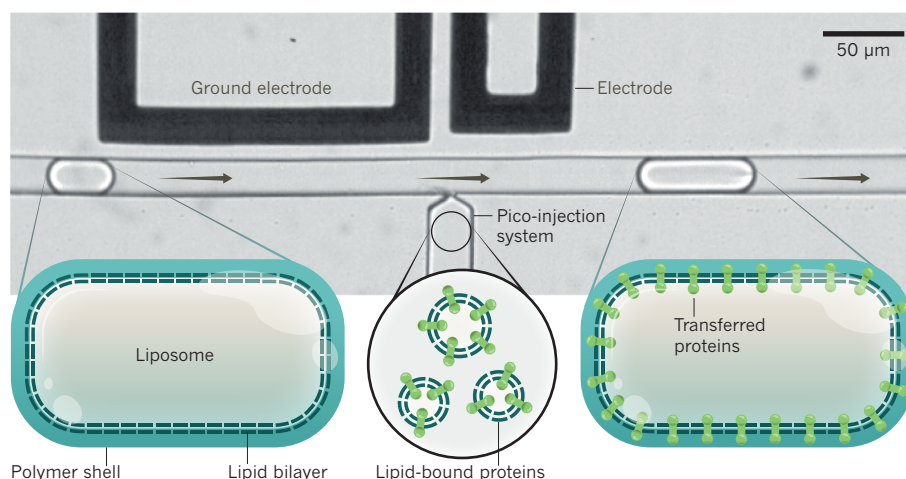
Although everything can work for a brief time in a test tube, says Erb, "at the end, we would like it compartmentalized, like a chloroplast". He's excited to collaborate with synthetic biologists such as Kate Adamala, who can build and control complex compartments.

Adamala's group at the University of Minnesota in Minneapolis is working on ways to build programmable bioreactors, by introducing simple genetic circuits into liposomes and fusing them together to create more-complex bioreactors. She calls them "soap bubbles that make proteins".

Her group builds these bioreactors using a spinning tube system similar to Schwille's, but which produces smaller liposomes. The researchers add circles of DNA called plasmids that they have designed to perform a particular

THE ASSEMBLY LINES

A pico-injection system allows researchers to load cell-membrane-like compartments called liposomes with functional proteins. Liposomes are stabilized by a polymer coating and pushed through a microfluidic channel. As they pass over a pico-injection site, an electrical pulse can trigger the incorporation of internal proteins or membrane-bound proteins (as shown) into the liposomes.



“FOR A CELL TO BE LIVING, IT NEEDS TO DEVELOP NEW FUNCTIONALITY.”

function, along with all the machinery needed to make proteins from DNA.

For instance, her group has made liposome bioreactors that can sense an antibiotic in their environment through membrane pores and can generate a bioluminescent signal in response⁸.

By fusing simple bioreactors together sequentially, the team can construct more-complex genetic circuits. But the systems start to break down as they expand to include ten or so components. This is a major challenge for the field, Adamala says. In a real cell, proteins that might interfere with each other's actions are kept apart by a variety of mechanisms. For much simpler synthetic cells, biologists must find other ways to impose that control. This could be through external gatekeeping, in which the experimenter decides which liposomes get mixed together and when. It might also be accomplished through chemical tags that regulate which liposomes can fuse together, or through a time-release system.

INFORMATIONAL INJECTIONS

Another key to making a cell is getting the software right. Enabling a synthetic cell to follow scientists' instructions and to replicate itself will require some way of storing and retrieving information. For living systems, this is done by genes — from hundreds for some microbes, to tens of thousands for humans.

How many genes a synthetic cell will need to run itself is a matter of healthy debate. Schwillie and others would like to keep it in the neighbourhood of a few dozen. Others, such as Adamala, think that synthetic cells need 200–300 genes.

Some have chosen to start with something living. Synthetic biologist John Glass and his colleagues at the J. Craig Venter Institute (JCVI) in La Jolla, California, took one of the smallest-known microbial genomes on the planet, that of the bacterium *Mycoplasma mycoides*, and systematically disrupted its

genes to identify the essential ones. Once they had that information, they chemically stitched together a minimal genome in the laboratory.

This synthesized genome contained 473 genes — about half of what was in the original organism — and it was transplanted into a related bacterial species, *Mycoplasma capricolum*⁹. In 2016, the team showed that this minimal synthetic genome could 'boot up' a free-living, although slow-growing organism¹⁰. Glass thinks that it will be hard to decrease that number much more: take any gene away, and it either kills the cells or slows their growth to near zero, he says.

He and his JCVI colleagues are compiling a list of 'cellular tasks' based on the latest version of their creation, JCVI-syn3.0a, which could act as a blueprint of a cell's minimal to-do list. But for about 100 of these genes, they can't identify what they do that makes them essential.

As a next step, and supported by an NSF grant of nearly \$1 million, Glass and Adamala will attempt to install the JCVI-syn3.0a genome into a synthetic liposome containing the machinery needed to convert DNA into protein, to see whether it can survive. In that case, both the software and the hardware of the cell would be synthetic from the start.

If it could grow and divide, that would be a tremendous step. But many argue that to truly represent a living system, it would also have to evolve and adapt to its environment. This is the goal with the most unpredictable results and also the biggest challenges, says Schwillie. "A thing that just makes itself all the time is not life — although I would be happy with that!" she says. "For a cell to be living, it needs to develop new functionality."

Glass's team at the JCVI has been doing adaptive laboratory evolution experiments with JCVI-syn3.0a, selecting for organisms that grow faster in a nutrient-rich broth. So far, after about 400 divisions, he and his team have obtained cells that grow about 15% faster than the original organism. And they have

seen a handful of gene-sequence changes popping up. But there's no evidence yet of the microbe developing new cellular functions or increasing its fitness by leaps and bounds.

Erb says that working out how to add evolution to synthetic cells is the only way to make them interesting. That little bit of messiness in biological systems is what allows them to improve their performance. "As engineers, we can't build a perfect synthetic cell. We have to build a self-correcting system that becomes better as it goes," he says.

Synthetic cells could lead to insights about how life might look on other planets. And synthetic bioreactors under a researcher's complete control might offer new solutions to treating cancer, tackling antibiotic resistance or cleaning up toxic sites. Releasing such an organism into the human body or the environment would be risky, but a top-down engineered organism with unknown and unpredictable behaviours might be even riskier.

Dogterom says that synthetic living cells also bring other philosophical and ethical questions: "Will this be a life? Will it be autonomous? Will we control it?" These conversations should take place between scientists and the public, she says. As for concerns that synthetic cells will run amok, Dogterom is less worried. "I'm convinced our first synthetic cell will be a lousy mimic of what already exists." And as the engineers of synthetic life, she and her colleagues can easily incorporate controls or a kill switch that renders the cells harmless.

She and other synthetic biologists will keep pushing ahead exploring the frontiers of life. "The timing is right," says Dogterom. "We have the genomes, the parts list. The minimal cell needs only a few hundred genes to have something that looks sort of alive. Hundreds of parts is a tremendous challenge, but it's not thousands — that's very exciting." ■

Kendall Powell is a freelance science journalist in Lafayette, Colorado.

- Loose, M., Fischer-Friedrich, E., Ries, J., Kruse, K. & Schwillie, P. *Science* **320**, 789–792 (2008).
- Litschel, T., Ramm, B., Maas, R., Heymann, M. & Schwillie, P. *Angew. Chem. Int. Edn* <https://doi.org/10.1002/anie.201808750> (2018).
- Deshpande, S., Caspi, Y., Meijering, A. E. C. & Dekker, C. *Nature Commun.* **7**, 10447 (2016).
- Deshpande, S., Spoelstra, W. K., van Doorn, M., Kersemakers, J. & Dekker, C. *ACS Nano* **12**, 2560–2568 (2018).
- Wu, F., van Schie, B. G., Keymer, J. E. & Dekker, C. *Nature Nanotechnol.* **10**, 719–726 (2015).
- Weiss, M. *et al. Nature Mater.* **17**, 89–96 (2018).
- Schwander, T., von Borzyskowski, L. S., Burgener, S., Cortina, N. S. & Erb, T. J. *Science* **354**, 900–904 (2016).
- Adamala, K. P., Martin-Alarcon, D. A., Guthrie-Honea, K. R. & Boyden, E. S. *Nature Chem.* **9**, 431–439 (2017).
- Gibson, D. G. *et al. Science* **329**, 52–56 (2010).
- Hutchinson, C. A. *et al. Science* **351**, aad6253 (2016).

COMMENT

PUBLIC HEALTH Lessons for next time from the front lines of an Ebola outbreak **p.180**



VISION Reflections of a researcher who threw peas at hoverflies **p.182**

CONSERVATION Dams threaten one of the world's largest inland fisheries **p.184**

OBITUARY Leon Lederman, particle-finding Nobel laureate, remembered **p.185**

NOOR ALAM/ZUMA WIRE



Children receiving blood transfusions in Bangladesh, where maintaining the supply from donors can be more challenging than in wealthy countries.

Which biological systems should be engineered?

To solve real-world problems using emerging abilities in synthetic biology, research must focus on a few ambitious goals, argues **Dan Fletcher**.

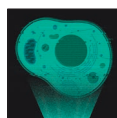
The difference between tweaking and engineering is subtle but important. Scientists have been tweaking cells at the molecular scale for decades. In 1974, two researchers loaded DNA from a frog into a bacterium, prompting the microbe to produce a foreign RNA¹. Twenty years later, scientists used a fluorescent protein from jellyfish to track gene expression in nematode worms, and to tag selected molecules in fruit flies^{2,3}. The fluorescent components lit up under

a microscope — kicking off a new era of watching cell biology in action.

Now, biologists at the Allen Institute for Cell Science in Seattle, Washington, are tweaking the DNA of human stem cells to probe cell organization and function by replacing natural proteins with their

fluorescent counterparts (27 so far; see go.nature.com/2afaka5). Even physicians are getting in on the act, tweaking patients' immune cells to improve the treatment of cancers, often with remarkable success⁴.

In my view, engineering is something different. The ultimate goal of engineering is to construct systems that solve problems, such as a synthetic pancreas for people with diabetes. The systems must be planned in mechanistic detail — to achieve the desired function, and to minimize the risk of ▶



BOTTOM-UP BIOLOGY

A *Nature* special issue
go.nature.com/bottomupbiology

► failure or unintended consequences. That means building systems from the bottom up, with precise knowledge of all the component parts. In other words, engineering begins when design enters the picture.

Tweaking — fine-tuning a system through small changes — will continue to be an essential part of biological discovery and the development of new therapies. Engineering, by contrast, usually requires big teams, big budgets and narrow goals to achieve ambitious objectives through design. It also tends to lay bare how much (or how little) we know about controlling nature.

Never has it been more possible to engineer biology (see ‘Tailor, not tinker’). But solving grand problems requires a switch from demonstrating that something is feasible in a laboratory to homing in on a few ambitious goals. The time has come to decide where to focus this emerging ability to engineer biology — and to commit resources to doing it.

AN ENGINEER'S WISH LIST

So what should those goals be?

In this discussion, I leave aside multicellular engineering projects, such as artificial tissues and organs, simply because it makes sense to start with something simpler. I have narrowed the scope of the projects I propose to those that could feasibly be achieved in the next decade with the right coordination, collaboration and support. And I focus on problems in human health, because this is an area I've thought most about. (Engineering plants to produce crops that are high yield, drought- and pest-resistant and environmentally friendly, including plant-based ‘meat’, deserves its own separate discussion.)

My ‘wish list’ is as follows:

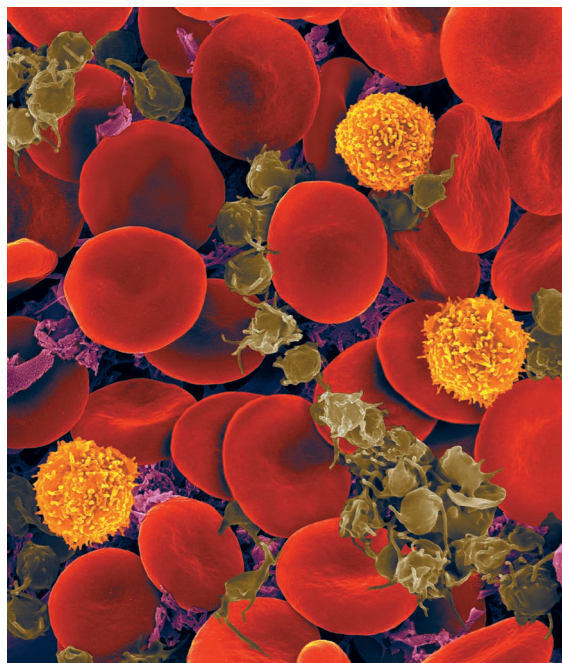
Artificial blood cells. Blood transfusions are crucial in treatments for everything from transplant surgery and cardiovascular procedures to car accidents, pregnancy-related complications and childhood malaria (see go.nature.com/2ozbfwt). In the United States alone, 36,000 units of red blood cells and 7,000 units of platelets are needed every day (see go.nature.com/2ycr2wo).

But maintaining an adequate supply of blood from voluntary donors can be challenging, especially in low- and middle-income countries. To complicate matters, blood from donors must be checked extensively to prevent the spread of infectious diseases, and can be kept for only a limited time — 42 days or 5 days for platelets alone. What if blood cells could be assembled from purified or synthesized components on demand?

In principle, cell-like compartments

could be made that have the oxygen-carrying capacity of red blood cells or the clotting ability of platelets. The compartments would need to be built with molecules on their surfaces to protect the compartments from the immune system, resembling those on a normal blood cell. Other surface molecules would be needed to detect signals and trigger a response.

In the case of artificial platelets, that signal might be the protein collagen, to



Human blood as viewed under a scanning electron microscope.

which circulating platelets are exposed when a blood vessel ruptures⁵. Such compartments would also need to be able to release certain molecules, such as factor V or the von Willebrand clotting factor. This could happen by building in a rudimentary form of exocytosis, for example, whereby a membrane-bound sac containing the molecule would be released by fusing with the compartment's outer membrane.

It is already possible to encapsulate cytoplasmic components from living cells in membrane compartments^{6,7}. Now a major challenge is developing ways to insert desired protein receptors into the lipid membrane⁸, along with reconstituting receptor signalling.

Red blood cells and platelets are good candidates for the first functionally useful synthetic cellular system because they lack nuclei. Complex functions such as nuclear transport, protein synthesis and protein trafficking wouldn't have to be replicated. If successful, we might look back with horror on the current practice of bleeding one person to treat another.

Designer immune cells. Immunotherapy is currently offering new hope for people with cancer by shaping how

the immune system responds to tumours. Cancer cells often turn off the immune response that would otherwise destroy them. The use of therapeutic antibodies to stop this process has drastically increased survival rates for people with multiple cancers, including those of the skin, blood and lung⁹. Similarly successful is the technique of adoptive T-cell transfer. In this, a patient's T cells or those of a donor are engineered to express a receptor that targets

a protein (antigen) on the surface of tumour cells, resulting in the T cells killing the cancerous cells (called CAR-T therapies)¹⁰. All of this has opened the door to cleverly rewiring the downstream signalling that results in the destruction of tumour cells by white blood cells¹¹.

What if researchers went a step further and tried to create synthetic cells capable of moving towards, binding to and eliminating tumour cells?

In principle, untethered from evolutionary pressures, such cells could be designed to accomplish all sorts of tasks — from killing specific tumour cells and pathogens to removing brain amyloid plaques or cholesterol deposits. If mass production of artificial immune cells were possible, it might even lessen the need to tailor treatments to individuals — cutting costs and increasing accessibility.

To ensure that healthy cells are not targeted for destruction, engineers would also need to design complex signal-processing systems and safeguards. The designer immune cells would need to be capable of detecting and moving towards a chemical signal or tumour. (Reconstituting the complex process of cell motility is itself a major challenge, from the delivery of energy-generating ATP molecules to the assembly of actin and myosin motors that enable movement.)

Researchers have already made cell-like compartments that can change shape¹², and have installed signalling circuits within them¹³. These could eventually be used to control movement and mediate responses to external signals.

Smart delivery vehicles. The relative ease of exposing cells in the lab to drugs, as well as introducing new proteins and engineering genomes, belies how hard it is to deliver molecules to specific locations inside living organisms. One of the biggest challenges in most therapies is getting molecules to the right place in the right cell at the right time.

Harnessing the natural proclivity of viruses to deliver DNA and RNA molecules into cells has been successful¹⁴. But virus size limits cargo size, and viruses don't necessarily infect the cell types researchers and clinicians are aiming at. Antibody-targeted

synthetic vesicles have improved the delivery of drugs to some tumours. But getting the drug close to the tumour generally depends on the vesicles leaking from the patient's circulatory system, so results have been mixed.

Could 'smart' delivery vehicles containing therapeutic cargo be designed to sense where they are in the body and move the cargo to where it needs to go, such as across the blood-brain barrier?

This has long been a dream of those in drug delivery. The challenges are similar to those of constructing artificial blood and immune cells: encapsulating defined components in a membrane, incorporating receptors into that membrane, and designing signal-processing systems to control movement and trigger release of the vehicle's contents.

The development of immune-cell 'backpacks' is an exciting step in the right direction. In this, particles containing therapeutic molecules are tethered to immune cells, exploiting the motility and targeting ability of the cells to carry the molecules to particular locations¹⁵.

A minimal chassis for expression. In each of the previous examples, the engineered cell-like system could conceivably be built to function over hours or days, without the need for additional protein production and regulation through gene expression. For many other tasks, however, such as the continuous production of insulin in the body, it will be crucial to have the ability to express proteins, upregulate or downregulate certain genes, and carry out functions for longer periods.

Engineering a 'minimal chassis' that is capable of sustained gene expression and functional homeostasis would be an invaluable starting point for building synthetic cells that produce proteins, form tissues and remain viable for months to years. This would require detailed understanding and incorporation of metabolic pathways, trafficking systems and nuclear import and export — an admittedly tall order.

It is already possible to synthesize DNA in the lab, whether through chemically reacting bases or using biological enzymes or large-scale assembly in a cell¹⁶. But we do not yet know how to 'boot up' DNA and turn a synthetic genome into a functional system in the absence of a live cell.

Since the early 2000s, biologists have achieved gene expression in synthetic compartments loaded with cytoplasmic extract¹⁷. And genetic circuits of increasing complexity (in which the expression of one protein results in the production or degradation of another) are now the subject of extensive research. Still to be accomplished are: long-lived gene expression, basic protein trafficking and energy production reminiscent of live cells.

TAILOR, NOT TINKER

Tools for engineering biological systems are in place

Researchers have established the separation and characterization methods needed to identify almost all the parts of a single cell. They've also made strides in designing some desired functions and putting parts together in new ways.

Thanks to the work of synthetic biologists in the early 2000s, gene circuits can be designed that use AND, OR and NAND logic gates (elementary signalling circuits)¹⁸. They can also be designed to produce proteins that sense and kill

tumours — including photoreceptive elements that act like pixels in a camera and capture photographs¹⁹.

Using genome-editing tools, yeast can be modified to produce biofuels, opiates or plant-free hop flavouring for beer²⁰. Even complete makeovers are possible: in 2016, researchers simplified the entire genome of the bacterium *Mycoplasma mycoides*, and incorporated this 'minimal genome' into cells that proved viable and were able to grow¹⁶. **D.F.**

RISK AND REWARD

In ten years' time, this wish list could seem either ridiculously myopic or foolishly ambitious. That is what makes this era of engineering biology so exciting. Whether or not these goals are reached, the attempt to build systems from known parts will focus our attention on the significant gaps in our understanding of how such systems work.

Already, many of these ideas are being explored by researchers from diverse fields. They are often considered too risky to be

embraced by conventional funding sources, and are thus relegated to a side project.

But risky ideas only get the chance to become real through focused attention and

effort, and that means giving them enough time and money. Some moves to provide this are happening. The Max Planck Research Network in Synthetic Biology, a German collaboration, is funding efforts to identify the minimal building blocks of living systems. And in September, the US National Science Foundation launched a project to foster the engineering of synthetic cells under its Understanding the Rules of Life programme.

More support is needed — specifically, from organizations and foundations with longer time horizons than those typical of industry or federal-grant providers. With sustainable funds and a willingness to embrace or at least accept the role of engineering biology in addressing societal challenges, we could build a world in which we trust artificial cells engineered to detect and treat the early signs of Alzheimer's disease as much as we trust aeroplanes to land safely.

To be clear, there is nothing wrong with tweaking biology. My lab will continue to

tweak, fiddle, futz and tinker as we pursue a deeper understanding of how cells organize their membranes and cytoskeletons. But the time has come to focus, organize and set clear goals to solve big problems. The necessary tools are ready and the issues are pressing. Physicist Richard Feynman famously said: "What I cannot create, I do not understand." For this era of designing biological systems, his quote should have a corollary: "What I cannot engineer, I should not use." ■

Dan Fletcher is a professor of bioengineering and biophysics, and chair of the Department of Bioengineering at the University of California, Berkeley, USA. He is also a Chan Zuckerberg Biohub Investigator.
e-mail: fletch@berkeley.edu

1. Morrow, J. F. *et al. Proc. Natl Acad. Sci. USA* **71**, 1743–1747 (1974).
2. Chalfie, M. *et al. Science* **263**, 802–805 (1994).
3. Wang, S. & Hazelrigg, T. *Nature* **369**, 400–403 (1994).
4. Porter, D. L., Levine, B. L., Kalos, M., Bagg, A. & June, C. H. *N. Engl. J. Med.* **365**, 725–733 (2011).
5. Majumder, S. & Liu, A. P. *Phys. Biol.* **15**, 013001 (2017).
6. Richmond, D. L. *et al. Proc. Natl Acad. Sci. USA* **108**, 9431–9436 (2011).
7. Weiss, M. *et al. Nature Mater.* **17**, 89–96 (2018).
8. Dezi, M., Di Cicco, A., Bassereau, P. & Lévy, D. *Proc. Natl Acad. Sci. USA* **110**, 7276–7281 (2013).
9. Sharma, P. & Allison, J. P. *Science* **348**, 56–61 (2015).
10. June, C. H., O'Connor, R. S., Kawalekar, O. U., Ghassemi, S. & Milone, M. C. *Science* **359**, 1361–1365 (2018).
11. Morsut, L. *et al. Cell* **164**, 780–791 (2016).
12. Abu Shah, E. & Keren, K. *eLife* **3**, e01433 (2014).
13. Weitz, M. *et al. Nature Chem.* **6**, 295–302 (2014).
14. Kotterman, M. A., Chalberg, T. W. & Schaffer, D. V. *Annu. Rev. Biomed. Eng.* **17**, 63–89 (2015).
15. Huang, B. *et al. Sci. Transl. Med.* **7**, 291ra94 (2015).
16. Hutchison, C. A. *et al. Science* **351**, aad6253 (2016).
17. Noireaux, V. & Libchaber, A. *Proc. Natl Acad. Sci. USA* **101**, 17669–17674 (2004).
18. Cameron, D. E., Bashor, C. J. & Collins, J. J. *Nature Rev. Microbiol.* **12**, 381–390 (2014).
19. Levskaya, A. *et al. Nature* **438**, 441–442 (2005).
20. Denby, C. M. *et al. Nature Commun.* **9**, 965 (2018).



Workers prepare to bury the body of someone who died of Ebola in Sierra Leone in 2014.

PUBLIC HEALTH

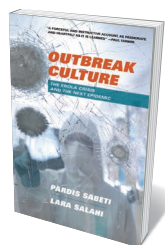
Lessons from the Ebola front lines

Nahid Bhadelia hails an analysis of the fraught campaign to contain the 2013–16 outbreak crisis.

When you work inside a system that you believe in, yet recognize as dysfunctional, it can be hard to offer a balanced critique. And the stakes are high when the system in question is the response to a humanitarian emergency, where public opinion determines crucial funding. *Outbreak Culture*, on the Ebola crisis of 2013–16, strikes this delicate balance expertly.

The central theme of the book, by geneticist Pardis Sabeti and journalist Lara Salahi, is that common threads of dysfunction run through responses to epidemics. These emerge from the underlying architecture of societies (resulting from history, politics and culture), the competition between international organizations and (sometimes) the self-serving motivations of individuals in high-stress situations. We fracture along lines of existing weaknesses.

Sabeti — who was part of the Ebola response effort — and Salahi show that the world is doomed to repeat the same mistakes with every new epidemic unless



Outbreak Culture: The Ebola Crisis and the Next Epidemic
PARDIS SABETI AND LARA SALAH
Harvard University Press (2018)

outbreak response shifts to a “mode that favors collaboration instead of competition, and readiness instead of reaction”. My experience leads me to concur. I was a clinical responder in Sierra Leone during the Ebola epidemic in both 2014 and 2015; I now work in Uganda, across the border from the current outbreak in the Democratic Republic of the Congo. (Full disclosure: I appear briefly in the book.)

Outbreak Culture is based on the cumulative accounts of more than 200 people who worked on the West African response, from clinicians and researchers to public-health workers and administrators. By bringing in these voices, the work distinguishes itself

from recent individual accounts. Yet it maintains a personal tone. It also incorporates the post-epidemic analyses by international organizations and governments, such as the internal and external World Health Organization reviews, and independent reports by the US National Academy of Medicine and other academic collaboratives. And it puts a human face on the challenges by telling the stories of researchers, clinicians and patients, including Sabeti and members of her lab.

Today, every new outbreak demands the re-creation of administrative structures. Negotiations for access and operations are made in real time. Sabeti and Salahi argue that the dearth of dependable administrative structures and oversight in West Africa created a space in which competing incentives and personal ambitions wreaked havoc. They highlight the dark underbelly of on-the-ground interactions that slow down and ultimately stymie the response itself, and which many reports have previously shied away from.

The authors interviewed numerous people and sent out an e-mail survey; 132 people answered. This was anonymous, because otherwise most of us (I took the survey) would have balked at answering the hard questions it featured about competition, corruption and waste. About 27% of respondents said that they had experienced illegal tactics during the epidemic. Another 37% noted that they had experienced intimidation, for instance by personally facing, witnessing, hearing about or perpetuating it.

Sabeti and Salahi share stories of how data and samples that could have helped were hoarded by researchers and organizations, including individuals within several international public-health bodies. They give an unflinching account of how corruption at all levels siphoned resources away from communities in need. For example, the International Federation of Red Cross and Red Crescent Societies confirmed that almost US\$6 million of its Ebola funds were misappropriated in West Africa. The authors also highlight concrete examples of how organizational politics, cultural differences and mistrust led to ineffective communication at crucial points during the epidemic.

Despite these revelations, the book ends on a positive note. It links failures during the epidemic to specific underlying gaps in governance (for example, the ways in which aid is distributed and reported allowed for individuals to siphon off funds). It identifies core processes required for reform. These include streamlining communication systems between outbreak-response partners, and establishing a central research-governance structure composed of experts without conflicts of interest.

It would have been interesting to know what, if any, changes the organizations

named have made in the aftermath of the epidemic. And the authors could have invited the individuals singled out for bad behaviour to give their perspective, even if confidentially.

Indeed, my favourite part of the book was the authors' description of Sierra Leone's Fambul Tok (Krio for 'family talk'), a version of truth and reconciliation committees that operate at the village level. They propose these as a best-practice example of how international organizations can elicit real-time feedback from outbreak responders.

The power of *Outbreak Culture* is its universality. It describes dynamics common at varying levels in every humanitarian emergency. But if this book is in any way about one person, it is about Sheik Humarr Khan. His story is woven through the authors' arguments. Khan was born and grew up in Sierra Leone, and against immense odds

"Where you are born decides whether or not you survive Ebola."

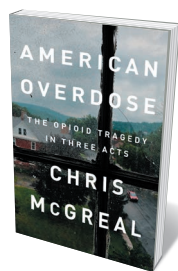
he became a leading researcher in haemorrhagic fevers there. He was one of the first physicians to care for people with Ebola in the

country in the first half of the epidemic. In July 2014, he died of the disease. The book begins with the political and ethical issues surrounding his treatment. Where should he have been treated? Should he have been given experimental therapeutics? What about the failure to evacuate him (or delay in doing so) for more advanced supportive care, even as international responders from the West were offered this opportunity?

My first deployment as physician in an Ebola treatment unit during the epidemic was in Kenema, Sierra Leone. I arrived about three weeks after Khan died; the health-care community there was still reeling from the loss. His story underscores one of the basic truths of the book: where you are born decides whether or not you survive Ebola. From the comfort of a Western lab or clinic, it is easy to forget the differences in quality of treatment (and a million other small injustices) for people in poorer communities. It is much harder to ignore those differences when you are working in the field, shoulder to shoulder with health-care providers who know that they will not be airlifted to better care if they get sick, yet have the unimaginable courage to carry on. *Outbreak Culture* is a much-needed call for greater justice next time. ■

Nahid Bhadelia is an infectious-diseases physician and medical director of the Special Pathogens Unit at Boston Medical Center and the National Emerging Infectious Diseases Laboratories in Boston, e-mail: nbhadelia@bu.edu

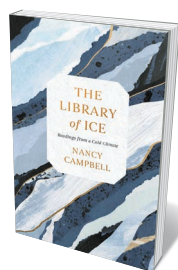
Books in brief



American Overdose: The Opioid Tragedy in Three Acts

Chris McGreal PUBLICAFFAIRS (2018)

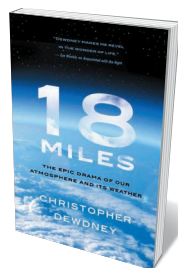
Since 1999, opioids have killed an estimated 350,000 people in the United States. In this powerful encapsulation of that epidemic, which grew nearly unchecked for two decades, journalist Chris McGreal argues that the culprits are three: a profit-driven medical system, pharmaceutical-industry greed and bad science. He traces the unfolding crisis through the emergence of drugs such as oxycodone; 'pill mill' medical clinics that became addiction hotspots; and uneven regulation. As opioid use rises in Britain, parts of Africa and Australia, this is a timely examination of hard-won lessons.



The Library of Ice

Nancy Campbell SCRIBNER (2018)

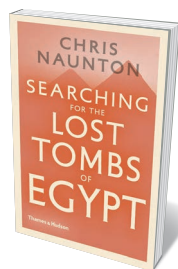
In winter 2010, poet and writer Nancy Campbell journeyed to the night-shrouded Arctic, where a residence at a Greenland museum launched this kaleidoscopic exploration of ice in science and culture. An intellectual omnivore, Campbell examines ice cores as archives in which researchers "read the alphabet of elements and isotopes"; and probes the weird dynamics of hail, proto-chemist Robert Boyle's 1665 *New Experiments and Observations Touching Cold*, curling rinks and the exploits of polar explorers from Knud Rasmussen to George Murray Levick. A marvellously subtle journey by way of flake, frost and berg.



18 Miles: The Epic Drama of Our Atmosphere and Its Weather

Christopher Dewdney ECW (2018)

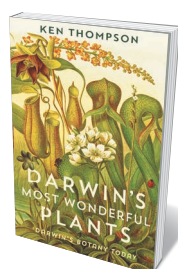
Our atmosphere may be just a few tens of kilometres deep, but in its vast amphitheatre, weather — the greatest show off Earth — struts its stuff. Poet and naturalist Christopher Dewdney's grand tour mingles meteorology, planetary science and literature, taking us from oxygenation 2.5 billion years ago through atmospheric layers, precipitation, the architecture of wind and the work of scientists from Robert FitzRoy to Milutin Milanković. Among many remarkable stories is that of US Marine William Rankin's 1959 parachute drop into the wild, convulsed depths of an active cumulonimbus cloud.



Searching for the Lost Tombs of Egypt

Chris Naunton THAMES & HUDSON (2018)

For all the astounding finds in Egypt over the past two centuries, its storied landscape is still riddled with 'known unknowns' — the lost or undiscovered tombs of ancient luminaries, tantalizingly mentioned in historical accounts. In this gorgeously illustrated study, Egyptologist Chris Naunton builds a case for the probable burial sites of several figures, from the brilliant third-millennium BC architect Imhotep to fourth-century BC empire builder Alexander the Great. Perhaps the most fascinating case is that of Cleopatra, ruler of Egypt from 51 to 30 BC, whose vast mausoleum may rest on the sea bed off Alexandria.



Darwin's Most Wonderful Plants

Ken Thompson PROFILE (2018)

In this quietly riveting study, plant biologist Ken Thompson reveals Charles Darwin as a botanical revolutionary through works such as *On the Movement and Habits of Climbing Plants* (1865), which remains pertinent. Interweaving current research with Darwin's insights, Thompson probes marvels such as "ivy glue", a nanocomposite that functions not unlike a gecko's bristles in sticking stems to surfaces; the astonishing mimicry of the chameleon vine *Boquila trifoliolata*; and the Cook pine *Araucaria columnaris*, which always leans towards the equator. **Barbara Kiser**



Hoverflies' large compound eyes give them a very large field of view.

VISION SCIENCE

An eye on ocular wonders

Todd Oakley enjoys a meander through vision research in myriad organisms.

The many eyes of scallops use reflecting mirrors, something like telescopes. Mantis shrimp have 12 classes of colour receptor to our 3. These findings in vision science are just two of many milestones in neurobiologist Michael Land's meander through topics in the field

— from the optical physics of eye function to the neurobiology of how brains interpret optical phenomena. *Eyes to See* is the journey of a scientist who followed his nose (and eyes) towards what fascinated him.

The book is organized loosely around Land's career. Opening with his 1960s

discovery of scallop eyes' bizarre reflecting mechanism, Land quickly transitions to the evolution of early eyes. Here, he lucidly encapsulates zoologist Dan-Eric Nilsson's functional synthesis, which links demands such as efficiency of light capture to optical innovations such as elaborations of cell

USGS-BIML

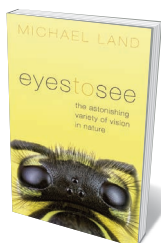
membranes. These innovations underlie four main stages of eye evolution: non-directional, directional, low-resolution and high-resolution vision.

Land dives into history, such as the contributions of late-nineteenth-century scientist Sigmund Exner, along with fun anecdotes and clearly described optical principles. He relates how he and a colleague shot peppercorns, pieces of potato and tethered peas towards male hoverflies, which mistook the objects for females, while another colleague lay on his back to film the flies' pursuit. Land describes the optics of arthropods' compound eyes, which include apposition and superposition eyes, both reflecting (co-discovered by Land) and refracting. Superposition eyes combine light from multiple facets onto a single receptor and are found in many nocturnal insects.

UNDERWATER WONDERERS

To study the eyes of deep-sea animals, Land spent time on research vessels. He writes of camouflage. Silver-sided fishes, for instance, reflect the homogeneous horizontal scenes of the open sea to blend in. Bioluminescence, is often deployed to match downwelling light and avoid casting a shadow. Here in the deep, we also meet some other amazing creatures, including the hyperiid amphipods and the spookfish *Dolichopteryx longipes*, which have peculiar double eyes that look straight up and down to take advantage of the environment's vertically oriented light.

Even the most sophisticated eyes are of no use without a brain with which to interpret and use the information. In examining neurobiology, Land first looks at how animals recognize things. He found, through experimentation with cotton reels and remote-controlled toy cars, that fiddler crabs use simple rules to detect potential mates or predators — anything seen to extend above the horizon is bigger than a crab and therefore a foe. Thus, crabs are easily fooled, even by simple shapes shown to them by experimenters. Land also recounts how, in 1968, he developed an ophthalmoscope for tiny jumping spiders such as *Phidippus johnsoni*, to track their eye movements in an era before video. With this, he discovered something like a program of eye movements that the spiders use to detect potential mates, for example by looking for legs. The spider ophthalmoscope is one of the clearest accounts in the book of Land's scientific ingenuity.



Eyes to See:
The Astonishing
Variety of Vision in
Nature
MICHAEL F. LAND
Oxford University Press
(2018)



The eyes of scallops contain mirrored structures, a little like telescopes.

Leaving invertebrates behind, Land moves on to humans. As he writes, we can communicate about what we see, making some aspects of vision — especially perception — easier to study in humans than in (say) a mantis shrimp. He has used eye-tracking tools to learn where people look when driving around a curve, reading words or music, or striking a cricket ball. This research expands into the realms of psychology — investigating mental images of colour and depth — and beyond, to philosophical territory such as consciousness.

BEHIND THE LENS

I had a few criticisms. First, instances of outdated scholarship pepper the book. One example is Land's discussion of graded-index lenses in aquatic animals, which achieve high power without spherical aberration, using a smooth transition from low to high refractive power. Land suggests that how the proteins of a graded lens are arranged remains a mystery. This omits high-profile work by biophysicist Alison Sweeney and her colleagues on squid lenses, which shows how proteins — duplicated and differently sized — pack to different densities to create a smooth transition in refractive index (A. M. Sweeney

et al. *J. R. Soc. Interface* **22**, 685–698 (2007); J. Cai et al. *Science* **357**, 564–569; 2017).

Land's organization of ideas often seems forced, as if he has tried to shoehorn research driven mainly by curiosity into synthetic constructs. For example, I found his adaptationist summary unsatisfying. He uses geneticist Theodosius Dobzhansky's ubiquitous quote — “nothing in biology makes sense except in the light of evolution” — to contend that evolution makes progress when needed. But evolution has not been the main thrust of Land's research, and a view of it as an optimizing force does little to inform us about how a specific eye works or how a specific brain decodes visual information.

Yet the positives of *Eyes to See* outweigh its negatives. It is enjoyable to get frequent glimpses of Land's career, which has defined many of the most actively studied topics and organisms in visual ecology today. Ultimately, there is a coherence to the book's seemingly stochastic journey through the workings of vision, as we proceed from photon to philosophy. ■

Todd Oakley is a professor of evolutionary biology at the University of California, Santa Barbara.
e-mail: oakley@ucsb.edu

Correspondence

Nobel boost for basic research

At a time when curiosity-driven research struggles for respect, this year's Nobel Prize in Physiology or Medicine provides a visceral example of its value. The prize was won by James Allison and Tasuku Honjo for their discoveries of the potentially immunotherapeutic molecules CTLA-4 and PD-1, respectively (see *Nature* **562**, 20–21; 2018).

In 1990, when Jim suggested that we work on the role of a newly identified member of the immunoglobulin superfamily, called CTLA-4, we agreed simply because it was similar in sequence to another molecule, CD28, on the surface of mouse immune cells (T cells). We were investigating things about which we knew very little, with no inkling that the work would spawn a whole industry of life-saving drugs for tens of thousands of people with cancer.

Within 5 years of my start, we found that antibodies against CTLA-4 could harness T cells to destroy tumours in mice. Although extraordinary levels of current funding for variations on the checkpoint method (new molecules and reagents) and for T-cell therapies in general will yield more cures, the next generation of advances is likely to come from curiosity-based studies. These, too, will need substantial funding.

Matthew Krummel *University of California, San Francisco, USA.*
matthew.krummel@ucsf.edu

Mentorship training will curb bullying

Academic mentorship is not synonymous with supervision. It is the nurturing of researchers' scientific and professional growth. Cultures that explicitly value and reward mentoring make it clear that bullying has no place in research (see also S. Moss *Nature* **560**, 529; 2018).

Crucially, mentorship also promotes constructive scientific

dialogue between mentors and trainees. Just like research and teaching, however, mentoring philosophy and practice cannot be learnt in standalone workshops. It must be continually refined and improved through feedback and institutional support. Proven initiatives at my own institution, for example, include encouraging mentors to exchange experiences and to share best practices.

Susan E. Liao *Johns Hopkins University, Baltimore, Maryland, USA.*
seliao@jhmi.edu

China tracks its progress on SDGs

China's progress in meeting the United Nations Sustainable Development Goals (SDGs) is being successfully monitored using geospatial and statistical information in a pilot scheme running in Deqing county, Zhejiang province.

A team of 20 researchers, led by the National Geomatics Center of China, measured 100 SDG indicators over the 938-square-kilometre county. In line with the UN Global SDG Indicator Framework, multi-scale and multi-type geospatial and statistical data were integrated for comprehensive measurement and evidence-based progress analysis. These data included topographic and land-cover maps, aerial and satellite images, disaggregated socio-economic information and environment statistics, as well as some from social media.

The conclusion is that the county, which has a population of around 430,000, has made significant economic and social advances and maintained a good ecological environment over the past 5 years. Challenges such as inadequate public transport in some regions have been drawn to the attention of policymakers.

An online public information service charts Deqing's progress towards achieving the SDGs. The pilot scheme's findings will be

discussed at the UN's first World Geospatial Information Congress later this month.

Jun Chen *National Geomatics Center of China, Beijing, China.*
Zhilin Li *Hong Kong Polytechnic University, Hung Hom, Hong Kong.*
chenjun@nsdi.gov.cn

Tap into the joy of open-access data

As an underfunded clinical researcher working in Jordan, I am limited to pursuing inexpensive observational studies that are based on patients' records. Happily, open-access data from repositories around the world have enabled me to make a bigger contribution to science.

My best experience was with the Biologic Specimen and Data Repository Information Coordinating Center, which curates data from large studies funded by the National Institutes of Health. I was able to access rigorous, high-quality data from almost 1,200 people with an inflammatory disease known as sarcoidosis, along with a control group. In Jordan, it would take me until I retired to generate this much data first-hand.

Our results will be published in the journal that hosted the original data. We completed two more studies on the same data set within six months (see S. A. AlRyalat *et al. Curr. Respir. Med. Rev.* **13**, 241–246; 2017).
Saif Aldeen AlRyalat *University of Jordan, Amman, Jordan.*
saifryalat@yahoo.com

Don't dismiss Myers–Briggs

In his review of Merve Emre's book *The Personality Brokers: The Strange History of Myers–Briggs and the Birth of Personality Testing*, S. Alexander Haslam repeats the contention that the Myers–Briggs Type Indicator (MBTI) fails to “measure what it purports to measure” and to “elicit consistent responses

across testing contexts” and that it “has low validity” (*Nature* **561**, 176; 2018). As an author of works on this topic, I have presented considerable evidence to the contrary (see, for example, P. Moyle and J. Hackston *J. Pers. Assess.* **100**, 507–517; 2018).

Before dismissing the MBTI as lacking in reliability and validity, evaluators would do well to consult this and other peer-reviewed papers (see, for example, T. Sitzmann *et al. J. Appl. Psychol.* <https://doi.org/10.1037/apl0000352>; 2018). They can then make an informed judgement.

Penny Moyle *Oxford, UK.*
pennymoyle@hotmail.com

Mekong's dams damn fisheries

One of the world's largest inland fisheries is under threat from overfishing, dams and habitat fragmentation. The Tonlé Sap Lake in the Mekong River Basin now yields stable harvests of only very small fish species. Stakeholders, government and developers must put conservation and mitigation measures in place before it's too late.

Hydropower construction is proliferating in the Lower Mekong Basin, disrupting natural seasonal river pulses and blocking the migration routes of riverine fishes. An estimated 60% of the catch in the Lower Mekong Basin is made up of migratory fish (G. Vaidyanathan *Nature* **478**, 305–307; 2011). People who live along the Mekong River and on the floodplain will be particularly affected because the local fish they consume also rely on migratory riverine species for prey.

Without urgent action, the outlook is bleak for this once-sustainable fishery.

Peng Bun Ngor* *Fisheries Administration, Phnom Penh, Cambodia.*

*On behalf of 4 correspondents (see go.nature.com/2shx1kz for full list).
pengbun.ngor@gmail.com

Leon Lederman

(1922–2018)

Physicist who expanded the family tree of fundamental particles.

Leon Max Lederman's stunning discoveries, leadership and advocacy laid the foundations for particle physics today. His discovery of the muon neutrino established that there was more than one type of neutrino. His observation of muon decay knocked down a pillar theory about symmetry in one of the fundamental forces. His discovery of the long-lived neutral kaon meson helped to home in on one of the great mysteries of physics. And his discovery of bottom quarks — subatomic particles that make up neutrons and protons — led researchers to uncover a third family of quarks.

Self-effacing, approachable and imaginative, Lederman was a consummate joke-teller. "Physics is not religion," he used to quip. "If it were, we would have a much easier time raising money." He had good taste in research problems and a gift for recognizing connections and opportunities. He was also a charismatic communicator; in later years, he focused on advancing science education. He died on 3 October in Rexburg, Idaho, aged 96.

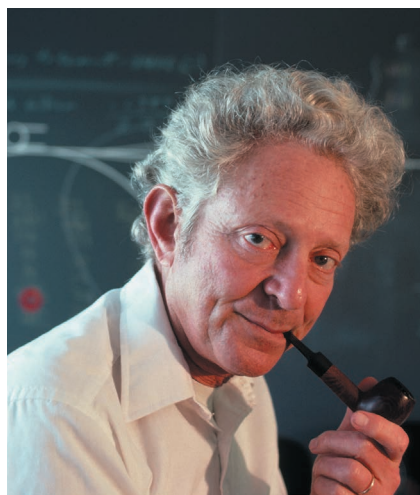
Lederman was born on 15 July 1922 in New York City to Jewish parents who had emigrated from Russia and who were keen on education. Lederman grew up at a time when Jewish scientists were fleeing imminent war in Europe for the United States, and he was attracted to the excitement surrounding the twentieth-century physics revolution of which many scientists were a part.

He did his bachelor's degree in chemistry at the City College of New York in 1943. After three years of US Army service in Europe, he earned his PhD in physics from Columbia University in New York City in 1951.

There, he spent three decades teaching and conducting experimental research as a faculty member. Nature was ripe for discovery, and clever experiments with particles accelerated to the highest energies were expected to yield the biggest discoveries.

From his mentor at Columbia, Nobel-prizewinning physicist Isidor Isaac Rabi, Lederman learnt to distinguish observation (a hint of something new) from measurement (a more precise endeavour). Lederman became the master of both, with the creativity to devise unique experiments and the tenacity to follow through on them.

Lederman's most famous work was done in 1962 at Brookhaven National Laboratory in Long Island, New York, with two of his Columbia University colleagues, Jack Steinberger and Mel Schwartz. In what would



today be called a 'beam dump' experiment, the researchers aimed a powerful proton beam at a target, producing an abundance of every type of known particle. These were absorbed by a wall of dense material.

The experimenters examined the debris to see whether anything interesting emerged. It did: the muon neutrino, the second neutrino family to be discovered. The surprising discovery indicated that fundamental particles come in pairs, and advanced the idea that symmetry is intrinsic to nature's building blocks. For this work, the team shared the 1988 Nobel Prize in Physics.

Lederman conducted experiments at high-energy accelerators around the world, and contributed to the founding of the 200-gigaelectronvolt Fermi National Accelerator Laboratory (now Fermilab) in Batavia, Illinois.

Indeed, Lederman made Fermilab's first major discovery, the bottom quark, in 1977. In an elegant experiment, his team looked for particles so rare that they would result from maybe one in a hundred-trillion collisions between an intense proton beam and a target. Lederman described the new, more-sensitive set-up as being as enlightening as the first telescope. They saw a signal coming from a bottom–antibottom quark pair. They named the signal ψ , after the shape of the decay-particle trajectories, which resembled the Greek letter.

Lederman was the second director of Fermilab from 1979 to 1989. He led the rigorous design and early operation of the Tevatron Collider (1983–2011), which was the highest-energy proton–antiproton collider in the world for nearly three decades.

From 1982, Lederman championed the most ambitious accelerator project ever — the Superconducting Super Collider. But in 1993, with construction already under way, Congress cancelled the project during tight-budget years. The torch was passed to the Large Hadron Collider at CERN, Europe's particle-physics laboratory near Geneva, Switzerland. Here, the Higgs boson was discovered — its popular name in the press, the 'God Particle', was taken from the 1993 popular-science book Lederman co-wrote with Dick Teresi, *The God Particle: If the Universe is the Answer, What is the Question?*

Lederman leaves a lasting educational legacy. As director of Fermilab, he introduced Saturday Morning Physics, a ten-week physics class for high-school students, which is still popular more than three decades on. He started the Friends of Fermilab, a school outreach effort that grew into the Lederman Science Center at Fermilab. He founded the Illinois Mathematics and Science Academy, a residential, state-supported high school, and he championed the 'Physics First' high-school science curriculum, which teaches foundational physics before chemistry and biology.

His scientific legacy continues with ongoing efforts to explore the particles that he discovered. The neutrino, perhaps the most ubiquitous particle in the Universe, is still one of the least understood. Its tiny mass and quirky interactions remain puzzles. Alongside enormous neutrino detectors around the world, Fermilab is leading an ambitious global effort to study muon neutrinos beamed from Chicago to South Dakota, to understand how they oscillate from one flavour to another.

Several nations built dedicated accelerators to explore the bottom quark in detail. This year, Japan commissioned an ambitious new one at the KEK laboratory in Tsukuba, for example. Measurements of rare, bottom-quark decays seem to be harbingers of new physics beyond the standard model.

Lederman, among others, is also credited with merging the sciences of the very small and the very big — particle physics and cosmology. Since Lederman's heyday, the study of subatomic particles has been used to probe the early Universe and its most energetic phenomena. ■

Nigel S. Lockyer is the director of Fermilab in Batavia, Illinois.
e-mail: lockyer@fnal.gov

FORUM Biophysics

Living systems engineered

Engineering approaches allow biological structures and behaviours to be reconstituted *in vitro*. A biologist and a physicist discuss the potential and limitations of this bottom-up philosophy in providing insights into complex biological processes.

THE TOPIC IN BRIEF

- In bottom-up approaches, cellular structures and behaviours are reconstituted from their constituent parts.
- This strategy reduces a complex, living system to a more manageable set of component parts, defined by the researcher.
- Bottom-up experiments have provided insights into processes such as cell division,

chromosome packaging and tissue patterning (Fig. 1).

- Some researchers believe that any cellular behaviour could eventually be modelled from the bottom up.
- Others, however, argue that this strategy is insufficient for understanding more-complex biological functions that bridge scales of complexity — for example, those in which individual cells act collectively.

Understanding by building

MATTHEW GOOD

The complexity of living cells is staggering — their cytoplasm contains tens of thousands of distinct macromolecules and metabolites that must be coordinated to interact in time and space. This intricacy often makes it difficult to interpret results from conventional ‘top-down’ studies, in which individual components are removed or modified. Bottom-up approaches complement investigations of living cells, make it easier to define the rules that govern biological organization, and have provided insights into many previously intractable biological problems.

Biochemical reconstitution has conventionally been used to identify the minimal set of purified factors needed to recapitulate a given cellular activity *in vitro*. Today, spurred on by advances in materials and engineering, we can carry out more-ambitious cellular reconstitutions. These experiments combine biochemical reconstitution with defined spatial boundaries that can be generated in a range of ways, including through micropatterning and microfabrication of surfaces, and through microfluidic techniques that create compartments surrounded by membranes made up of lipid bilayers or monolayers. The boundaries can be set to either mimic or perturb the natural organization of a cell.

Unexpected properties and activities have emerged from the mixing of boundaries and biochemical reactions, leading to new

mechanistic insights and extending our ability to model biological processes. For instance, it has been found that encapsulating the motor protein kinesin with filaments called microtubules produces a force-generating network that can propel the movement of cell-size capsules¹. This experiment acts as a proof of concept that simplified systems can generate force, and motivates researchers to look for analogous systems in nature, rather than assuming that the solution to this problem in living organisms must always be complex.

As another example, changes in the size and shape of encapsulated compartments —

“Bottom-up reconstitution approaches promise to expand our understanding of biology at higher levels.”

manipulations that are easy in micro-fabricated systems, but not in living cells — have revealed roles for these parameters in controlling the oscillatory behaviour of proteins involved in cell division² and the sizes of organelles³. These discoveries act as a potent reminder that experiments carried out in test tubes involve much greater volumes than that of a cell; an absence of boundary conditions might obfuscate underlying biological principles, such as size scaling.

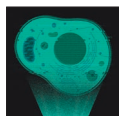
In some cases, biological insight can be gained only by removing boundaries, to simplify the system or enable it to be

expanded — another feat not possible in living cells. For example, cytoplasmic extracts from cells have been used to show that chromosomes can condense in preparation for cell division even in the absence of histone proteins, around which DNA is packaged in cells⁴. Because histones are essential to living cells, such experiments could be performed only *ex vivo*.

The same cytoplasmic-extract system has also been combined with an elongated chamber (many times longer than a cell) to identify a new class of signalling reaction that spatially coordinates the cell cycle and is based on self-propagating ‘trigger waves’⁵. These waves, first postulated by mathematical modelling, could be identified and characterized more easily in a deconstructed system containing defined boundary conditions than by *in vivo* methods.

For bottom-up approaches to further complement and one day even surpass top-down approaches, certain challenges must be addressed. One is deciding which elements of a cell can be removed without limiting the biological relevance of the findings. Another is to identify empirical approaches to validate whether rules derived from *in vitro* experiments are predictive for *in vivo* situations. A third is that we must continue to improve the precision and reliability of engineered boundaries to better mimic those in cells.

Bottom-up reconstitution approaches promise to expand our understanding of biology at higher levels. By continuing to increase the number of components that can be patterned together, it might eventually be possible to reconstruct systems that rival the complexity of living cells and tissues. For example, micropatterning techniques and assembly principles are being used to configure cells in geometries that mimic those found in embryonic development⁶, and to produce designer tissues⁷. In these experiments, complex, controllable 3D tissue shapes can be obtained by defining simple interactions between individual cells, between cells and the structural matrix that surrounds them and between proteins involved in tissue patterning. Given well-characterized building blocks, a preliminary understanding of boundary conditions and a reasonable period of time, it should be realistic to consider reconstituting any complex cell



BOTTOM-UP BIOLOGY

A Nature special issue

go.nature.com/bottomupbiology

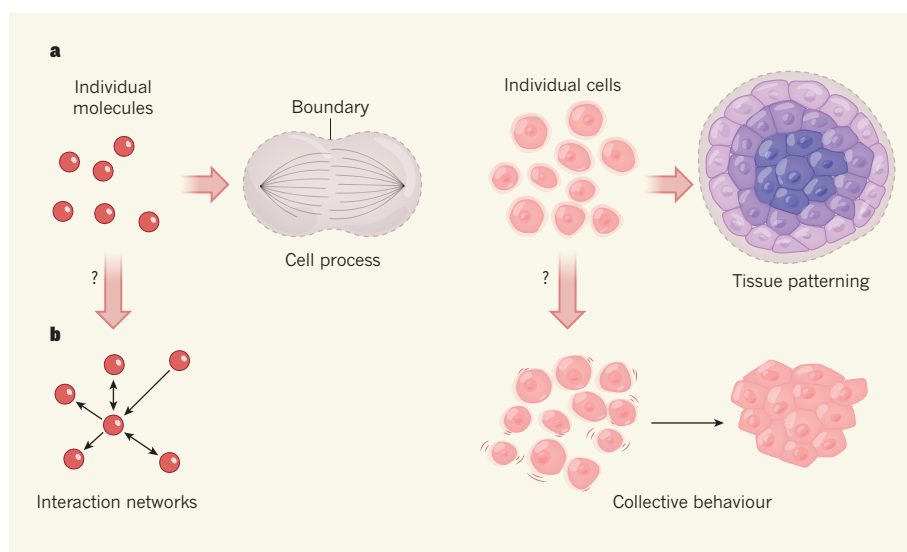


Figure 1 | Increasing levels of complexity modelled from the bottom up. **a**, *In vitro* reconstitution, biological parts and processes can be recreated from a minimal set of components. For example, by enclosing individual molecules within specific boundaries, the minimal set of proteins and interactions needed for the emergence of complex phenomena such as cell division can be defined. Likewise, spatial confinement of cells has provided insights into tissue patterning in embryos. **b**, However, there is debate about whether these bottom-up approaches can provide mechanistic insight into biological processes that bridge scales of complexity — the processes by which thousands of individual molecules interact in cells, for instance, or by which cells act collectively to switch from a fluid-like to a solid-like state.

behaviour. From there, a new understanding of the rules that underlie biological processes can emerge.

Matthew Good is in the Departments of Cell and Developmental Biology and of Bioengineering, University of Pennsylvania, Philadelphia, Pennsylvania 19104, USA. e-mail: mattgood@pennmedicine.upenn.edu

Bottom does not explain top

XAVIER TREPAT

Picture yourself as an engineer in the car industry. You know the role of every bolt, joint and circuit in a car. You have great understanding of the hierarchies and redundancies that ensure smooth functioning of all systems. In a nutshell, you know how to build a car from the bottom up. Now imagine that you are asked to solve the problem of traffic jams during rush hour. Traffic jams are a problem of cars, and you know everything about cars — but this detailed knowledge is irrelevant to understanding why they jam. Similarly, an understanding of how complex biological structures or even whole cells are built can provide only a certain level of understanding about how biological systems function at higher levels of organization.

Much like cars in traffic, cells can jam. At low density, cells grown in culture move and exchange neighbours frequently, like

molecules in a fluid. But at higher densities, cellular movements slow down, rearrangements vanish, and the system jams into a solid-like state⁸. Other variables can also cause cell jamming — when cultured at the same density, epithelial cells obtained from people with asthma move collectively, like a fluid, whereas their healthy counterparts jam⁹. Cell jamming also occurs *in vivo*, and is key to the normal elongation of zebrafish embryos during development¹⁰.

Jamming is a prominent example of a meso-scale phenomenon — a process that operates at a longer scale than do the elementary components of a system — in which ‘bottom’ does not explain ‘top’. It is unlikely that being able to reconstitute the differing protein pathways in healthy and asthmatic cells will explain why one jams more easily than the other. In fact, the most predictive variable for cell jamming is the shape index, a geometric quantity defined as the ratio of the cell’s perimeter to the square root of its area⁹. Similarly, it is also unlikely that the genetic programs that are turned on and off during development will explain why cells jam as the vertebrate body elongates.

Another example of a process in which mechanisms at the bottom cannot explain phenomena at the top is collective gradient sensing, whereby a group can sense and respond to an environmental gradient but individual constitutive elements cannot. Collective gradient sensing has been observed in a variety of groups undergoing directed migration, including shoals of fish moving in response to light¹¹, clusters of leukaemia cells responding to chemical signals¹², and epithelial cells whose migration is guided by a gradient of rigidity¹³.

The reconstitution of each element of these motile groups, no matter how detailed, will never explain why groups move in the direction of the gradient but individual elements do not.

This is not to say, of course, that reconstitution of molecular-scale processes is not useful. Indeed, the engineering of genetic circuits responsible for cell communication is sufficient to control 3D tissue shape¹⁴. However, principles at the molecular scale cannot generally explain functions at a higher level of organization.

Well before its discovery in cells, jamming was proposed to tie together liquid-to-solid transitions in a wide range of inert materials such as foams, emulsions and sand piles¹⁵. The materials differ broadly in composition, but their physical behaviour can be captured by a simple set of physical variables. These variables configure a phase diagram — a graph that plots whether the system is jammed or unjammed as a function of interaction forces, temperature or density. Like jamming in inert¹⁵ and living matter^{9,10}, other biological functions might be explained in terms of phase diagrams. Given the complexity of cells and tissues, the position of a system in those diagrams will be compatible with many different combinations of molecular states, concentrations and interactions.

It is questionable whether trying to understand each of these combinations is an efficient path towards a predictive understanding of complex living systems. Rather, we should aim to identify the mesoscale principles and variables that ultimately determine how these systems work. To do so, we need to develop experimental approaches to probe tissues at multiple length scales and timescales through both mechanical and biochemical manipulation. ■

Xavier Trepap is at the Institute for Bioengineering of Catalonia, Barcelona Institute for Science and Technology, ICREA and CIBER-BBN, 08028 Barcelona, Spain. e-mail: xtrepap@ibecbarcelona.eu

- Sanchez, T., Chen, D. T. N., DeCamp, S. J., Heymann, M. & Dogic, Z. *Nature* **491**, 431–434 (2012).
- Zieske, K. & Schwille, P. *eLife* **3**, e03949 (2014).
- Good, M. C., Vahey, M. D., Skandarajah, A., Fletcher, D. A. & Heald, R. *Science* **342**, 856–860 (2013).
- Shintomi, K. *et al. Science* **356**, 1284–1287 (2017).
- Chang, J. B. & Ferrell, J. E. Jr *Nature* **500**, 603–607 (2013).
- Degincerti, A. *et al. Nature Protoc.* **11**, 2223–2232 (2016).
- Todhunter, M. E. *et al. Nature Methods* **12**, 975–981 (2015).
- Angelini, T. E. *et al. Proc. Natl Acad. Sci. USA* **108**, 4714–4719 (2011).
- Park, J.-A. *et al. Nature Mater.* **14**, 1040–1048 (2015).
- Mongera, A. *et al. Nature* **561**, 401–405 (2018).
- Berdahl, A., Torney, C. J., Ioannou, C. C., Faria, J. J. & Couzin, I. D. *Science* **339**, 574–576 (2013).
- Malet-Engra, G. *et al. Curr. Biol.* **25**, 242–250 (2015).
- Sunyer, R. *et al. Science* **353**, 1157–1161 (2016).
- Toda, S., Blauch, L. R., Tang, S. K. Y., Morsut, L. & Lim, W. A. *Science* **361**, 156–162 (2018).
- Liu, A. J. & Nagel, S. R. *Nature* **396**, 21–22 (1998).

GEOLOGY

Proposed early signs of life not set in stone

Efforts to find early traces of life on Earth often focus on structures in ancient rocks, called stromatolites, that formed by microbial activity. One of the oldest proposed stromatolite discoveries has now been questioned. [SEE LETTER P.241](#)

MARK A. VAN ZUILEN

In 2016, Nutman *et al.*¹ reported the discovery of cone-shaped structures in 3.7-billion-year-old rocks in the Isua Supracrustal Belt, Greenland, that they identified as being stromatolites — structures that arise as a result of the presence of water-dwelling microorganisms. Previously, the earliest known stromatolites were reported to be those in 3.45-billion-year-old rocks in Australia². Being able to accurately date the first signs of the emergence of life has important implications for understanding how life on Earth evolved. However, on page 241, Allwood *et al.*³ now report their own independent analysis of these ancient rocks in Greenland, and argue that, in this particular case, the structures that Nutman and colleagues interpreted to be stromatolites instead arose by non-biological processes. This finding shows that a natural process that does not require any input from a living organism can mimic the formation of a structure that normally counts as a strong indication of previous biological activity.

Stromatolites have a laminated (layered)

structure (Fig. 1a), formed by sediment trapping, binding and mineral deposition within microbial communities⁴. They can form in a range of shapes: conical, columnar or dome-like. Whether microorganisms have a role in the formation of certain types of stromatolite shape is unclear. There are models for how stromatolites can arise without input from a living organism⁵, and various laminated structures that occur naturally without requiring any biological activity can be mistaken for stromatolites, such as silica deposits around geysers⁴ or laminated carbonate crusts that form when water evaporates⁶. In well-preserved stromatolite specimens, a biological contribution to such structures can often be confirmed by the presence of complex branching, intricate laminar textures, cavities or, in some rare instances, preserved microfossils and moulds^{1,7}.

Conical stromatolites are a special case, however, because their shape alone can be sufficient to identify them as arising from biological processes. Their steep laminar slopes cannot arise from non-biological processes such as sedimentation or mineral precipitation. From the analysis of present-day stromatolites and laboratory experiments, it is known that

conical stromatolites are the preserved remains of motile microbial communities that form vertical cones^{1,8}, and that this cone structure can be preserved by the trapping, binding and precipitation of non-biological material.

When stromatolite structures in the early rock record (which often have a centimetre-scale size) are analysed, their intricate laminations, textures and composition have usually already been partially or completely destroyed through a process called metamorphism, in which rock structure is substantially altered and deformed by heat and pressure, often when the rock is buried deep underground. Stromatolite shape therefore becomes the main way to identify signs of biological input in ancient stromatolite-like structures. In the strongly metamorphosed Early Archean rock record (formed around 3.2 billion to 4 billion years ago), the identification of stromatolites arising from biological processes thus becomes particularly difficult.

However, a convincing case was made for the presence of such biologically arising stromatolites in 3.45-billion-year-old rocks in Australia². In addition to conical stromatolites, six other stromatolite shapes were found in the samples there; they all existed in specific parts of what was considered to be an ancient, shallow, marine, carbonate-rich environment. This diversity in stromatolite shape convincingly excluded a uniform non-biological formation process and suggested that ecological controls governed the overall stromatolite growth. Evidence of such a clearly defined ancient environmental setting is difficult to find in any older metamorphosed rock on Earth.

Nutman and colleagues reported the identification of ancient stromatolites in a newly described rock outcrop in Greenland, and also interpreted these structures as

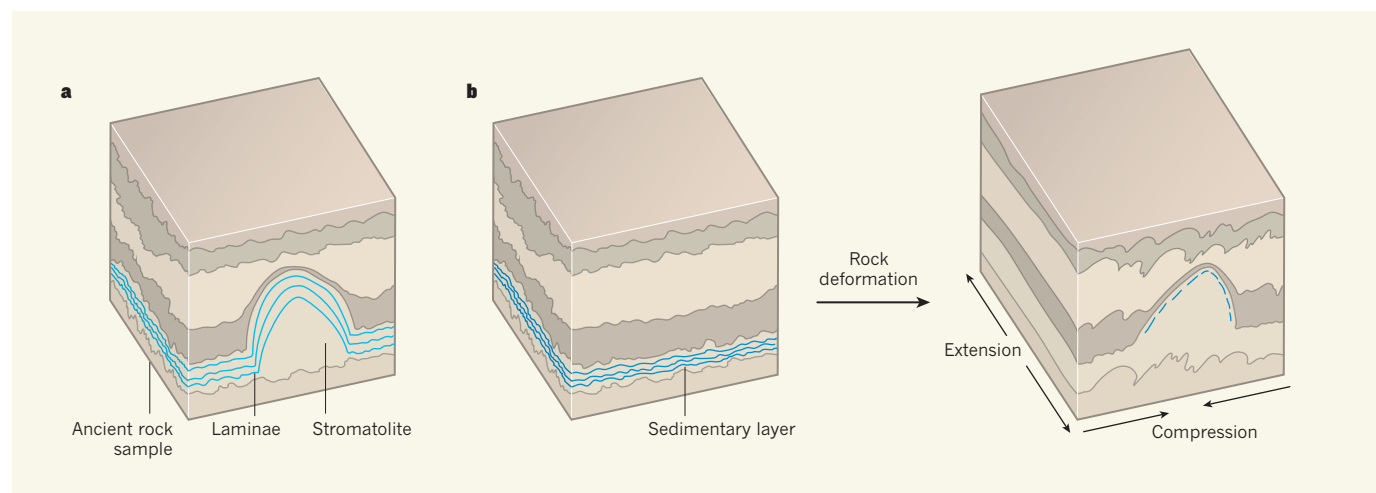


Figure 1 | Layered structures in ancient rocks. **a**, Conical structures that have internal layers (laminae) and are found in ancient rocks have been identified as a type of stromatolite structure — specifically, a stromatolite that forms as the result of the action of water-dwelling microorganisms. Such stromatolites, which typically have a size on a centimetre scale in these ancient rocks, have been cited as providing early evidence of life on Earth. However, the positive identification of stromatolites can be controversial, given that

ancient rocks have been subject to deformations over time. **b**, Processes of rock extension and compression might create cone-like structures that look like stromatolites, and the deformation and replacement of layers of sedimentary rock might generate structures that look similar to stromatolite laminae that arise from biological activity. Allwood *et al.*³ argue that structures previously identified¹ as stromatolites in 3.7-billion-year-old rocks in Greenland might have formed through such processes.

having arisen in an ancient, shallow, marine environment, on the basis of the textures of interlayered sediments and the distribution patterns of rare-earth elements. Such patterns have previously been interpreted to indicate the deposition of carbonate minerals from seawater⁹. The entire region in which these rocks are located was previously found to be metamorphosed rock that had been subjected to high temperature and pressure¹⁰. In the Australian rocks with ancient stromatolites², laminations are clearly visible; in the Greenland samples, however, the proposed laminations are less clear, and the degree of metamorphism is higher than that of the Australian rocks.

The lack of unambiguous, well-preserved laminated structures would preclude the identification of any intricate original textures that might indicate biological input to the structure. However, Nutman *et al.* identified remnant laminations and conical stromatolite-like shapes that they consistently interpreted as being microbially generated structures. Apart from these conical shapes, Nutman and co-workers also identified some dome-like shapes of proposed stromatolites. However, they did not find the diversity of stromatolite forms described in the Australian study. With few specimens, and a complex history of rock metamorphism, this raised the question of whether non-biological processes might have generated the dome-like and conical shapes in these ancient Greenland rocks.

Allwood *et al.* argue that the stromatolite-like shapes observed at the Greenland site arise from rock deformation. When they compared the front and side profiles of rock samples that contained stromatolite-like structures, they noted that one side shows a compressional deformation whereas the other shows an extensional deformation. This indicates that the structures are not stromatolite cones, but elongated ridges (Fig. 1b). Furthermore, the folding direction of the stromatolite ridges is parallel to the orientation of pressure-induced mineral textures on smaller scales in the same rock. These observations provide strong evidence for physical rock deformation and therefore offer a non-biological explanation for the observed structures.

In addition, Allwood and colleagues argue that the rock itself did not form in a shallow marine setting, but instead arose when carbonate minerals crystallized from fluids that circulated through an existing rock. If this is true, the observed dome-like and conical structures are definitely not stromatolites. Allwood *et al.* used a trace-element analysis technique that has high spatial resolution to show that the internal laminations in the conical structures represent the specific replacement of a type of silicate rock by fluid-derived carbonate minerals. The authors found that the rare-earth-element signal associated with the presence of seawater seems to be mainly concentrated in mica minerals in the rock, but is also present in the carbonate areas. Allwood and co-workers

suggest that this is possible if the fluids from which the minerals crystallized during later stages of the rock's existence ultimately derived from seawater as well. So although Nutman *et al.*¹ and Allwood *et al.*² report similar patterns of rare-earth elements in the rocks, they offer diverging interpretations of what these patterns mean. This highlights the complexities in discerning primary chemical signatures in such highly deformed rocks.

The biological input to ancient stromatolites is a long-standing controversy. The rocky outcrop on Greenland has not been discovered for long, and few researchers have studied this rock in relation to its geological surroundings. Future research might lead to a firm understanding of the primary versus secondary processes that shaped this rock. Clearly, the work of both Nutman *et al.* and Allwood *et al.* will form the basis for the interpretation of other possible stromatolites in the ancient rock record. ■

Mark A. van Zuilen is in the Department of Geomicrobiology, Institut de Physique du

Globe de Paris, Sorbonne Paris Cité, Paris Diderot University, UMR 7154 CNRS, Paris 75005, France.

e-mail: vanzuilen@ipggp.fr

1. Nutman, A. P., Bennett, V. C., Friend, C. R. L., Van Kranendonk, M. J. & Chivas, A. R. *Nature* **537**, 535–538 (2016).
2. Allwood, A. C., Walter, M. R., Kamber, B. S., Marshall, C. P. & Burch, I. W. *Nature* **441**, 714–718 (2006).
3. Allwood, A. C., Rosing, M. T., Flannery, D. T., Hurowitz, J. A. & Heirweh, C. M. *Nature* **563**, 241–244 (2018).
4. Walter, M. R. (ed.) *Stromatolites. Developments in Sedimentology* 20 (Elsevier, 1976).
5. Grotzinger, J. P. & Rothman, D. H. *Nature* **383**, 423–425 (1996).
6. Pope, M. C., Grotzinger, J. P. & Schreiber, B. C. *J. Sediment. Res.* **70**, 1139–1151 (2000).
7. Grotzinger, J. P. & Knoll, A. H. *Annu. Rev. Earth Planet. Sci.* **27**, 313–358 (1999).
8. Bosak, T. *et al. Geobiology* **10**, 384–401 (2012).
9. Bolhar, R., Kamber, B. S., Moorbath, S., Fedo, C. M. & Whitehouse, M. J. *Earth Planet. Sci. Lett.* **222**, 43–60 (2004).
10. Boak, J. L. & Dymek, R. F. *Earth Planet. Sci. Lett.* **59**, 155–176 (1982).

This article was published online on 17 October 2018.

QUANTUM PHYSICS

Quenching our thirst for universality

Understanding the dynamics of quantum systems far from equilibrium is one of the most pressing issues in physics. Three experiments based on ultracold atomic systems provide a major step forward. [SEE LETTERS P.217, P.221 & P.225](#)

MICHAEL KOLODRUBETZ

Although we live in a world of constant motion, physicists have focused largely on systems in or near equilibrium. In the past few decades, interest in non-equilibrium systems has increased, spurred by developments that are taking quantum mechanics from fundamental science to practical technology. Physicists are therefore tasked with an important question: what organizing principles do non-equilibrium quantum systems obey? On pages 217, 221 and 225, respectively, Prüfer *et al.*¹, Eigen *et al.*² and Erne *et al.*³ report experiments that provide a partial answer to this question. The studies show, for the first time, that ultracold atomic systems far from equilibrium exhibit universality, in which measurable experimental properties become independent of microscopic details.

The researchers use low-density gases of rubidium^{1,3} or potassium² atoms that are cooled to temperatures close to absolute zero. At sufficiently low temperatures, these atoms begin to show quantum-mechanical behaviour, forming a macroscopic quantum state known as a Bose–Einstein condensate.

Starting from either such a condensate^{1,2} or an uncondensed gas³, the researchers rapidly change experimental parameters — a process known as a quench. Rather like a cartoon character that looks down to discover they have accidentally run off a cliff, the quench initiates far-from-equilibrium dynamics.

Such quenches are relatively easy to realize, but what the researchers see next is surprising. Consider all the variables that can be associated with a given experiment: power fluctuations of lasers, variations in the lab's temperature, microscopic details of atomic interactions, and so on. The researchers find that the dynamics of their experiments, despite involving strongly interacting atoms far from equilibrium, become independent of these variables.

Eigen *et al.* accomplish this universality by carefully eliminating all but two of the variables in their experiment: the density of the atomic gas and the scattering length. The latter describes how closely two atoms can pass without interacting. The authors then go one step further and eliminate the dependence of the scattering length on variables in a clever way.

First, to prepare the initial condensate, the

authors set the scattering length to zero — they ‘turn off’ the interactions — using a magnetic field⁴. Second, they quench the scattering length to infinity, again using the magnetic field. If we consider increasing the density of the gas by, for example, a factor of eight, the spacing between the atoms decreases by a factor of two. Zooming in (rescaling) by this factor of two, the atomic system looks exactly the same as it did before the density was increased, because the scattering lengths of zero and infinity are unchanged.

Eigen and colleagues vary the density of the gas by a factor of about ten, and observe that the experimental dynamics are independent of the density after rescaling both space and time. They also adjust the temperature of the gas and show that universality holds when one more variable is considered — namely, the length scale on which the gas exhibits quantum-mechanical behaviour.

Prüfer *et al.* and Erne *et al.* uncover a different form of universality. On the face of it, the experiments of these two groups are wildly different. Erne and colleagues start with a three-dimensional gas, quench to one dimension, and observe the density of the gas as a function of position and time. Prüfer and colleagues work in one dimension throughout, explore the internal states (spins) of the atoms and carry out a quench that allows these spins to fluctuate. But, after a short time, both groups observe universality, which they argue results from a phenomenon called a non-thermal fixed point.

For systems in equilibrium, the concept of a fixed point comes from one of the great discoveries of twentieth-century physics, known as the renormalization group. This framework studies how a system evolves as we zoom out from the microscopic to the macroscopic scale, and successfully describes the emergence of key phases of matter such as magnetism. Fixed points are states of a system that remain unchanged on zooming out. Non-thermal fixed points occur when non-equilibrium systems approach such a state, with the role of zooming out played by the passage of time⁵.

A classic example of a non-thermal fixed point is wave turbulence, in which the energy of waves is transferred from large to small scales. Prüfer *et al.* and Erne *et al.* demonstrate the first examples of universality caused by non-thermal fixed points in systems dominated by quantum mechanics. Like Eigen and colleagues, the groups show that their results are robust by widely varying the initial conditions of their experiments and observing that the dynamics are effectively unchanged.

Although Prüfer *et al.* and Erne *et al.* use different quenches and measure different properties, their results are remarkably similar. This resemblance provides perhaps the best evidence for the existence of universality in these atomic systems. At a technical level, the experiments do differ in their critical exponents (numbers that describe the properties

of fixed points), which indicates that the two fixed points are different.

Together, these three studies provide a substantial step forward in our understanding of quantum systems far from equilibrium. However, a complete picture of the underlying universality remains to be determined. A notable concern for all of the experiments is that the universality occurs over limited time and length scales. Longer times, in particular, would probably be required to realize non-equilibrium steady states that are useful for practical applications. By analogy with wave turbulence, one possibility for extending the reach of the universality could involve continuously pumping energy into the systems; it is well documented that universality is, at best, transient in the absence of an external drive.

From a fundamental perspective, these experiments pave the way for exploring a wide range of theoretical and experimental questions regarding non-equilibrium universality.

BIOPHYSICS

Cellular stretch reveals superelastic powers

External forces can make cells undergo large, irreversible deformations. It emerges that stretched mammalian cells grown *in vitro* can enter a state called superelasticity, in which large, reversible deformations occur. [SEE ARTICLE P.203](#)

MANUEL THÉRY & ATEF ASNACIOS

In Rudyard Kipling’s classic children’s bedtime story¹, the elephant’s elongated trunk arose because a crocodile grabbed “and pulled, and pulled, and pulled” on the nose of an elephant’s child. The elephant’s child escaped, but waited in vain for its nose to shrink back to normal. This scenario of an irreversible extension mirrors what happens in the laboratory when cells that are subject to external tension undergo major deformation. However, *Nature*, Latorre *et al.*² report on page 203 that mammalian epithelial cells grown *in vitro* can, unexpectedly, demonstrate a mode of reversible, large-scale shape changes — a property termed superelasticity.

When our skin gets cut, it breaks apart at the wound site. This is because the surface of skin, like that of most organs, is subjected to tension. This tension helps to limit the size and sculpt the shape of organs. Moreover, a cell can both generate and resist tension. In the cytoplasm, there are fibre-like elements of the cell’s structural ‘skeleton’, called cytoskeletal filaments, that can transmit force. The type of cytoskeletal filaments that form from the protein actin can be moved by myosin proteins to generate the contractile forces that regulate cell shape. Adhesion

For example, what are the possible classes of non-thermal fixed points? What happens at extremely high or low energy scales, at which the universality breaks down? And under what conditions does universality arise in generic quenched systems? These are challenging questions to answer, but I, for one, hope that these experiments open the door to placing non-equilibrium quantum systems alongside equilibrium ones in the lexicon of modern physics. ■

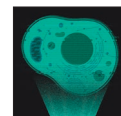
Michael Kolodrubetz is in the Department of Physics, University of Texas at Dallas, Texas 75080, USA.

e-mail: mkolodru@utdallas.edu

1. Prüfer, M. *et al.* *Nature* **563**, 217–220 (2018).
2. Eigen, C. *et al.* *Nature* **563**, 221–224 (2018).
3. Erne, S., Bucker, R., Gasenzer, T., Berges, J. & Schmiedmayer, J. *Nature* **563**, 225–229 (2018).
4. Chin, C., Grimm, R., Julienne, P. & Tiesinga, E. *Rev. Mod. Phys.* **82**, 1225–1286 (2010).
5. Orioli, A. P., Boguslavski, K. & Berges, J. *Phys. Rev. D* **92**, 025041 (2015).

sites that join cells together can relay this force between cells and cause tension to build up throughout an entire tissue³. However, cells under tension do not usually tear apart, because their material properties enable them to resist this tension^{4,5}.

If cells under tension undergo small-scale deformations, the resulting changes are mainly elastic⁶, and a linear relationship exists between an increase in tension and an increase in deformation^{7,8}. But in large-scale deformations, cells can enter a state termed plasticity, in which the breakage of bonds between cytoskeletal filaments leads to irreversible deformations that prevent full cellular recovery, even if the associated stress is released⁹. Latorre and colleagues describe a mechanism whereby cells under tension that undergo large-scale deformations change from being in an elastic state to enter a regime in which the cells elongate without requiring an increase in tension. Moreover, these deformations are reversible, indicating that cells can shift from an elastic state to what is called a superelastic state, and



BOTTOM-UP BIOLOGY
A *Nature* special issue
go.nature.com/bottomupbiology

thus avoid entering a state of irreversible deformation.

Why has superelasticity not been previously detected in living cells, despite decades of investigations into cellular properties? One explanation could be that the timescale matters¹⁰. In previous experiments, external forces have usually been applied for seconds or minutes^{8,11}, whereas Latorre and colleagues studied changes that occurred over several hours. Cells subjected to rapidly increasing tension often rupture, even at low tension levels, in just a few minutes⁸, whereas even if the tension is 100 times higher, it can be resisted if cells stretch at their own rate, such as if they slowly spread out over a surface¹².

Latorre and colleagues grew monolayers of mammalian epithelial cells *in vitro* on a deformable substrate surface that enabled them to estimate the forces acting on the system. The authors exploited the ability of cells to pump water from the upper to the lower side of the cell (Fig. 1). This induced a build-up of water underneath the cells, generating pressure that caused a dome-like bulging of the cell layer under tension. Using microscopy and physical-modelling techniques, Latorre and co-workers precisely measured the tension in these cellular domes.

The regularity of the curvature of the structures indicated constant tension, in which all of the cells experienced the same level of force. However, the uniformity of deformation was lost above a certain deformation threshold, and some cells in the domes became more stretched than others. The reason this occurred in only some cells was probably due to variability in cellular mechanical properties^{6,8}, wherein some cells were more sensitive than others to external tension. The highly stretched cells had entered a state of superelasticity: they were no longer resistant to the tension and instead elongated under this constant force. It is as if the cells had transitioned towards 'fluidization' of their cytoskeletal filaments¹³; in other words, instead of behaving like a coiled spring that resists force, these cells entered a distinct mechanical state akin to the way in which a liquid flows.

How do cells resist the application of force solely until a certain level of deformation is reached, yet after that point, transition to a state of superelasticity? One explanation could be the availability of actin. The pool of cellular actin is limited¹⁴, and each actin-based structure assembles itself at the expense of other potential such structures. When all cellular pools of actin are exhausted, actin-based structures can't form any more.

Latorre *et al.* focused on the cell cortex, a meshwork of actin filaments and myosin that forms a thin layer beneath the cell membrane.

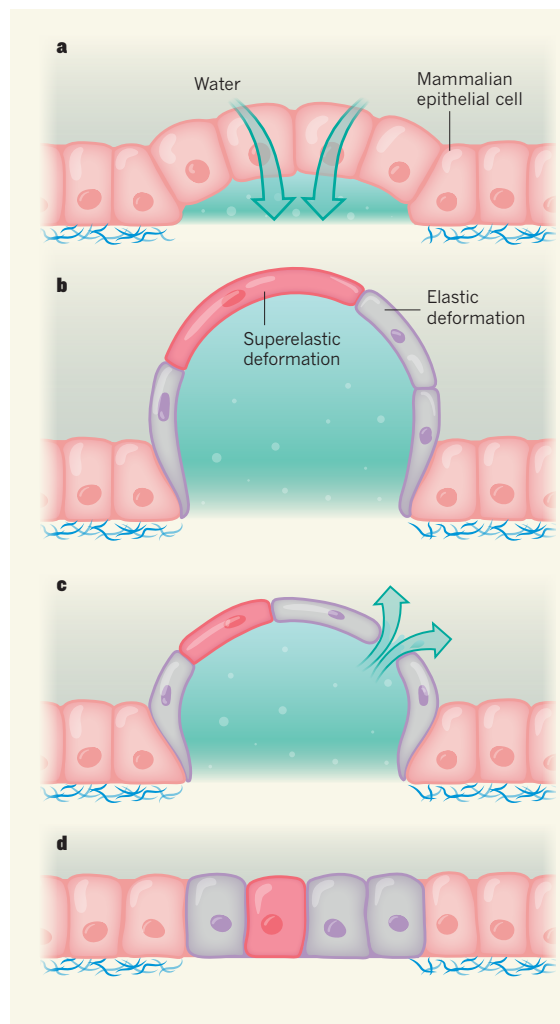


Figure 1 | Cells can exist in a state of superelasticity. **a**, Latorre *et al.*² analysed the stretching of monolayers of mammalian epithelial cells grown *in vitro* on top of a layer of fibronectin protein (blue). These cells can pump water from the upper to the lower side of the cell (green arrows). This resulted in a build-up of water beneath a dome-like layer of cells. The water build-up generates pressure and puts the cells under tension. **b**, The tension caused some stretched cells to undergo small-scale elastic deformations in which there is a linear relationship between the increase in tension and the extent of cellular deformation. The authors unexpectedly discovered that some cells underwent large-scale deformations and entered a state of superelasticity, in which cellular deformation increases without requiring a corresponding increase in tension. **c**, As pressure inside the dome-like layer of cells rose, rupture eventually occurred as a result of the breakage of an adhesive junction between cells; water escaped through this breakage point. **d**, The cellular deformations were fully reversible, and the cells returned to their initial small size.

The authors measured cortex thickness, which is tightly coupled to the tension that the cortex is under¹⁵. Cortex thickness decreased with cellular stretching, suggesting that a sufficiently thick cortex might be required to enable cellular elasticity, and raising the possibility that, below a certain thickness, the cortex stops resisting tension and starts to 'flow'. However, the authors could not identify a clear transition in the structure of the cortex between that found in an elastic or in a superelastic state.

Perhaps finer details of the actin-network

architecture are crucial for understanding the transition to superelasticity. The protein-mediated crosslinking of actin filaments ensures that components of the actin network are connected successfully, and that they function as a whole, rather than as numerous independent units¹⁶. It's possible that, as the cortex thins during cell stretching, a point is reached when this network connectivity is lost, and disconnected parts of the network start separating, or 'flowing apart', under tension. If this is true, the density of actin-filament crosslinking proteins might be a key factor in the transition towards superelasticity. Moreover, the investigation of actin-network density and crosslinking during specific developmental stages might reveal whether superelastic deformations occur as tissues are being shaped during development.

A cellular elongation process that does not require an increase in force for increased deformation will end when rupture occurs. Latorre and colleagues note that when the layer of cells ruptured, holes appeared between adjacent cells. Pressurized water inside the dome escaped through the rupture point, the dome collapsed and the superelastically stretched cells returned to their initial unstretched size. That the adhesive junctions joining cells, rather than the cells themselves, are the points of weakness, is consistent with observations of tissue rupture made using externally stretched cellular monolayers¹¹.

If the adhesive junctions had not ruptured in Latorre and colleagues' experiments, would the individual cells have kept on elongating? Probably not. A type of cytoskeletal structure called an intermediate filament might have an effect in this type of scenario. Intermediate filaments have been under-studied in comparison with actin filaments because of their slow turnover dynamics and the absence of convenient experimental tools, such as drugs, that can disassemble them. However, their importance in cellular mechanics is gaining recognition¹⁷.

Intermediate filaments make a substantial contribution to the elasticity of stretched cells¹⁸ and can support extensive levels of stretching¹⁹. These filaments typically form in a wheel-spoke-like architecture that connects the nucleus to junctions between epithelial cells²⁰. This raised another question: might these filaments have a role in the resistance to tension at high strain that would allow cells to limit their deformation?

Evidence directly supporting this possibility has been lacking. Latorre *et al.* used a laser to cut bundles of intermediate filaments in stretched cells in a state of superelasticity, and found that this induced cellular relaxation — a release

of stress and an elongation that increased the cellular area. This suggests that intermediate filaments might protect superelastic cells from undergoing an unlimited deformation by acting like springs that resist tension at high levels of deformation. In such circumstances, the ability of intermediate filaments to return to their usual length after being stretched might even enable such cells to recover their initial shape when tension is released.

Latorre and colleagues' work has revealed a more complex relationship between cell size and the forces that cells experience than was previously appreciated. Future studies should attempt to unravel the mechanisms that enable cells to enter a state of superelasticity and to recover from high levels of deformation. Now that we know cell shape is not an appropriate proxy for assessing cellular tension, it will be crucial to develop ways to accurately monitor tension

levels in tissues, so as to better understand the factors that influence tissue shape. ■

Manuel Théry is at UMR 1160, Paris Diderot University, Saint-Louis Hospital, CEA, INSERM, AP-HP, 75010 Paris, France, and at UMR5168, University Grenoble-Alpes, BIG/LPCV, CEA, CNRS, INRA, Grenoble, France. **Atef Asnacios** is at UMR7057 CNRS, Paris Diderot University, MSC, 75205 Paris Cedex 13, France.

e-mails: manuel.thery@cea.fr; atef.asnacios@univ-paris-diderot.fr

1. Kipling, R. *Just So Stories* (Macmillan, 1902).
2. Latorre, E. *et al. Nature* **563**, 203–208 (2018).
3. Treppe, X. *et al. Nature Phys.* **5**, 426–430 (2009).
4. Fernández, P., Pullarkat, P. A. & Ott, A. *Biophys. J.* **90**, 3796–3805 (2006).
5. Gardel, M. L. *et al. Proc. Natl. Acad. Sci. USA* **103**, 1762–1767 (2006).
6. Fabry, B. *et al. Phys. Rev. Lett.* **87**, 1–4 (2001).

7. Lenormand, G., Millet, E., Fabry, B., Butler, J. P. & Fredberg, J. J. *J. R. Soc. Interface* **1**, 91–97 (2004).
8. Desprat, N., Richert, A., Simeon, J. & Asnacios, A. *Biophys. J.* **88**, 2224–2233 (2005).
9. Bonakdar, N. *et al. Nature Mater.* **15**, 1090–1094 (2016).
10. Webster, K. D., Ng, W. P. & Fletcher, D. *Biophys. J.* **107**, 146–155 (2014).
11. Harris, A. R. *et al. Proc. Natl. Acad. Sci. USA* **109**, 16449–16454 (2012).
12. Mitrossilis, D. *et al. Proc. Natl. Acad. Sci. USA* **106**, 18243–18248 (2009).
13. Treppe, X. *et al. Nature* **447**, 592–595 (2007).
14. Burke, T. A. *et al. Curr. Biol.* **24**, 579–585 (2014).
15. Chugh, P. *et al. Nature Cell Biol.* **19**, 689–697 (2017).
16. Ennomani, H. *et al. Curr. Biol.* **26**, 616–626 (2016).
17. Quinlan, R. A. *et al. J. Cell Sci.* **130**, 3437–3445 (2017).
18. Mendez, M. G., Restle, D. & Janmey, P. A. *Biophys. J.* **107**, 314–323 (2014).
19. Kreplak, L., Bär, H., Leterrier, J. F., Herrmann, H. & Aebi, U. *J. Mol. Biol.* **354**, 569–577 (2005).
20. Troyanovsky, S. M., Eshkind, L. G., Troyanovsky, R. B., Leube, R. E. & Franke, W. W. *Cell* **72**, 561–574 (1993).

This article was published online on 31 October 2018.

demonstrate that both T cells and another type of immune cell called a B cell from these samples could proliferate when grown *in vitro*. The authors term this type of division auto-proliferation, because it occurs spontaneously *in vitro* without the addition of an antigen.

Jelcic *et al.* found that signalling through a TCR-initiated T-cell proliferation, and that cell proliferation was associated with the production by T cells of a signalling protein called IFN- γ (Fig. 1), which is associated with multiple sclerosis⁵. IFN- γ is a potent activator of a category of immune cells called macrophages, which directly damage the myelin sheath^{6,7} in multiple sclerosis.

The authors implicate B-cell proliferation in driving T-cell autoprolieration, because neither T cells nor B cells divided if the cultured cells were exposed to a drug called ibrutinib. Ibrutinib inhibits the protein BTK, which is essential for signalling downstream of the B-cell antigen receptor that leads to B-cell proliferation⁸. Interestingly, a phase IIb clinical trial (see go.nature.com/2yhfpfu) has reported preliminary evidence that the BTK inhibitor evobrutinib could potentially provide benefit for people with multiple sclerosis (see go.nature.com/2qtqby9).

Each of the multiple-sclerosis treatments currently in use suppresses disease-associated brain inflammation, but in different ways. Jelcic *et al.* took advantage of this to test whether interactions between B cells and T cells are needed for T-cell autoprolieration, and whether this phenomenon might be involved in processes that lead to the symptoms of multiple sclerosis.

The authors analysed blood samples from people with the disease who were receiving different anti-inflammatory treatments, and compared these results with control samples from people with the disease who were not receiving treatment. For those receiving an antibody called natalizumab, which causes an increase in the numbers of T cells and

MEDICAL RESEARCH

Immune–cell crosstalk in multiple sclerosis

Interactions between the B and T cells of the human immune system are implicated in the brain disease multiple sclerosis. It emerges that B cells make a protein that is also made in the brain, and that T cells recognize this protein.

RICHARD M. RANSOHOFF

A hallmark of the disease multiple sclerosis is an inflammatory autoimmune attack¹ on the proteins of the myelin sheath, a structure that wraps around the nerve fibres that project from neurons. The myelin sheath provides protection and nourishment to nerve fibres and enables efficient transmission of nerve impulses. Myelin-sheath injury causes a range of symptoms, depending on the neurons that are affected. Which immune-system cells and protein targets have key roles in the initiation and progression of multiple sclerosis is not fully understood, and such information might aid the development of new treatments. Writing in *Cell*, Jelcic *et al.*² present an analysis of immune-system cells found in people with multiple sclerosis that deepens our understanding of how immune cells might contribute to this disease.

One factor linked^{3,4} to the risk of developing multiple sclerosis is the possession of a particular version of a protein called HLA. HLA proteins enable cells to display antigens — fragments of proteins — on their surfaces. If the receptor for an antigen (the T-cell receptor; TCR) on a T cell recognizes an antigen presented by an HLA protein, the T cell is activated to trigger an immune response against cells that express the antigen.

Variations in the antigen-binding capacity of different HLA proteins and in the antigen-recognition capacity of TCRs enable the body to respond to a wide range of antigens associated with disease-causing microorganisms. However, there is a danger that if an HLA protein efficiently binds an antigen that is normally part of the body, and if a T cell that recognizes the HLA–antigen complex is activated, autoimmunity could develop. Such a mechanism might underlie the fact that the version of HLA called HLA-DR15 is a risk factor for multiple sclerosis³, and is estimated⁴ to contribute 60% of the total genetic risk for developing the condition.

T cells from people with multiple sclerosis are more prone to divide *in vitro* than are T cells from people without the condition³. Such cell division is reminiscent of the division that occurs as the result of normal immune-cell activation by an antigen stimulus, but in this case it does not seem to require the addition of an antigen stimulus to the sample of immune cells³. This suggests either that the normal requirement for antigen recognition is being bypassed, or that these T cells recognize an antigen that is present on other immune cells in the blood sample. Jelcic *et al.* investigated further, analysing in more detail the behaviour of immune cells in blood samples of people with multiple sclerosis. They convincingly

immature B cells in the blood, *in vitro* analysis showed that autoproliiferation of B cells and T cells was increased compared with the controls. Samples from those receiving an antibody called rituximab, which depletes B cells from the bloodstream, had much-reduced T-cell proliferation compared with controls.

This analysis of the effect of anti-inflammatory treatments that affect T cells or B cells provides evidence consistent with the authors' model that clinically relevant interactions between B cells and T cells occur in multiple sclerosis. For many years, it was generally thought that B cells do not have a role in multiple sclerosis, because of results from animal studies⁹. This view changed when striking benefits were observed in clinical trials of B-cell depletion for multiple-sclerosis treatment^{10–12}.

Jelcic and colleagues needed to answer the question of whether the autoproliiferating T cells contribute to the development of multiple sclerosis. To address this tough problem, the authors analysed the cellular descendants of individual proliferating T cells from the blood of people with multiple sclerosis. They looked at the variable portions of the TCRs present in the cells because these variable regions provide a unique pattern, akin to a barcode, that can identify any T cell and its genetically identical descendants — which form a cellular lineage termed a clone.

In rigorous and challenging experiments using material from two people who had multiple sclerosis, the authors analysed T cells found in brain tissue taken at biopsy or post-mortem and compared these with T cells from the same person's blood samples taken before brain-tissue samples were obtained. The authors found that T cells from blood samples that underwent autoproliiferation *in vitro* belonged to an identical cellular lineage that matched T cells found in the brain-tissue samples taken from the same person.

This finding strongly suggests that some proliferating cells in the blood of people with multiple sclerosis could enter their brain. Once there, such T cells might release immune-signalling molecules called cytokines, such as macrophage-stimulating IFN- γ , that could initiate inflammatory tissue injury. Immune cells are always present in the cerebrospinal fluid that bathes the brain and spinal cord, and IFN- γ -producing T cells^{13,14} and proliferating T cells¹⁵ have previously been identified in the cerebrospinal fluid of individuals with multiple sclerosis. Jelcic and colleagues' findings therefore highlight the significance of previous observations and provide additional support for established models of how this disease proceeds.

A final conundrum remains: what are the antigenic target(s) of these T cells? This is a key question because the relevant self-antigens driving multiple sclerosis have not been definitively identified. To try to answer this, the authors analysed a clonal cell population grown *in vitro*, derived from one T cell

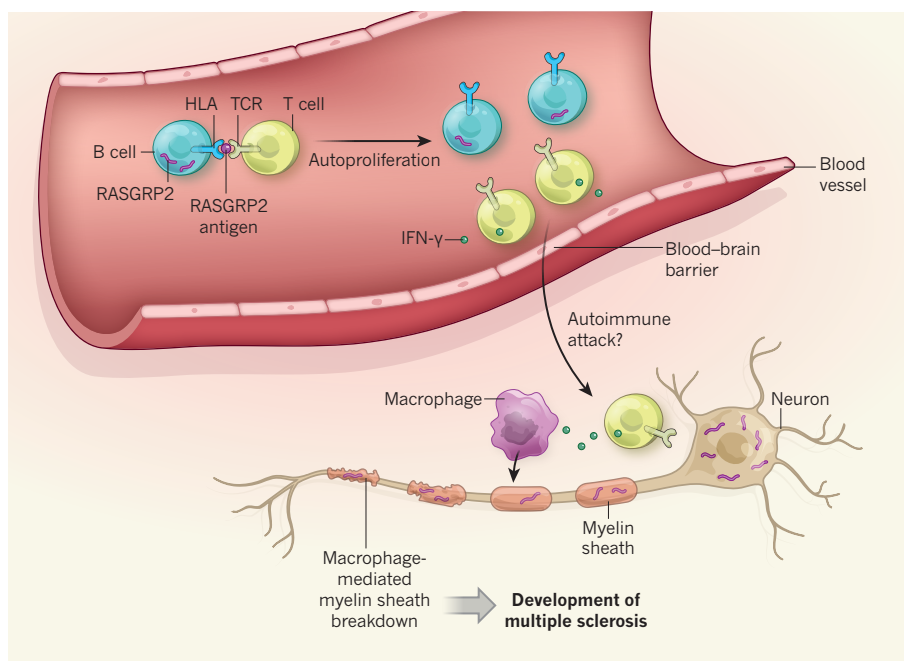


Figure 1 | Immune-cell action associated with multiple sclerosis. Jelcic *et al.*² report that B cells of the immune system present in the bloodstream make a protein called RASGRP2. These cells use a protein called HLA to present a peptide fragment (an antigen) of RASGRP2 on their cell surface. If this antigen is recognized by the T-cell receptor (TCR) of another immune cell called a T cell, this interaction leads to the proliferation of both the T cells and the B cells, a phenomenon that the authors call autoproliiferation. Their evidence indicates that these autoproliiferating T cells can, by an unknown route, cross the blood-brain barrier to enter the brain. RASGRP2 is also found in brain tissue. If neurons or other brain cells express RASGRP2, this might trigger T cells that infiltrate the brain to orchestrate an autoimmune attack by producing inflammatory mediators. For example, the production of IFN- γ proteins by activated T cells could stimulate the macrophages of the immune system, which are known^{6,7} to attack the myelin-sheath structure that protects nerve fibres and supports neuronal function. This in turn could lead to the development of multiple sclerosis.

and its descendants that were present in the blood and the post-mortem brain of a person with multiple sclerosis. Jelcic and colleagues used an innovative approach that relied on computational evaluation of data obtained using standard methods to stimulate T cells. The authors evaluated an almost unimaginably large number of structurally similar but non-identical peptides for their capacity to act as an antigen that would generate a response from this T-cell population. They uncovered an antigen from the protein RASGRP2 as one that probably stimulates the TCR of this T-cell population. RASGRP2 had not previously been linked to processes related to multiple sclerosis. The authors demonstrated that RASGRP2 is expressed both in B cells that elicit T-cell proliferation and in brain tissue.

Jelcic and colleagues' study provides a model for how B-cell and T-cell interactions outside the brain might generate disease-contributing T cells that then enter the brain. Their discovery of an antigen associated with multiple sclerosis might, if other such antigens are identified in the future, reveal how autoimmunity occurs and, perhaps, how it could be remedied. ■

Richard M. Ransohoff is at Third Rock Ventures, Boston, Massachusetts 02116, USA,

and in the Department of Cell Biology, Harvard Medical School, Boston.
e-mail: rransohoff@thirdrockventures.com

1. Wekerle, H. *Acta Neurol. Scand.* **136** (Suppl. 201), 22–25 (2017).
2. Jelcic, I. *et al. Cell* **175**, 85–100 (2018).
3. Mohme, M. *et al. Brain* **136**, 1783–1798 (2013).
4. Oksenberg, J. R., Baranzini, S. E., Sawcer, S. & Hauser, S. L. *Nature Rev. Genet.* **9**, 516–526 (2008).
5. Panitch, H. S., Hirsch, R. L., Haley, A. S. & Johnson, K. P. *Lancet* **329**, 893–895 (1987).
6. Bitsch, A., Schuchardt, J., Bunkowski, S., Kuhlmann, T. & Bruck, W. *Brain* **123**, 1174–1183 (2000).
7. Bruck, W. *et al. Immunobiology* **195**, 588–600 (1996).
8. Hendriks, R. W., Yuvaraj, S. & Kil, L. P. *Nature Rev. Cancer* **14**, 219–232 (2014).
9. Mertin, J. *Proc. R. Soc. Med.* **70**, 871–874 (1977).
10. Greenfield, A. L. & Hauser, S. L. *Ann. Neurol.* **83**, 13–26 (2018).
11. Hauser, S. L. *et al. N. Engl. J. Med.* **358**, 676–688 (2008).
12. Wekerle, H. *Autoimmunity* **50**, 57–60 (2017).
13. Kivisäkk, P. *et al. Clin. Exp. Immunol.* **129**, 510–518 (2002).
14. Restorick, S. M. *et al. Brain Behav. Immun.* **64**, 71–79 (2017).
15. Richert, J. R., McFarlin, D. E., Rose, J. W., McFarland, H. F., Greenstein, J. I. *J. Neuroimmunol.* **5**, 317–324 (1983).

The author declares competing financial interests.
See go.nature.com/2aiyh28 for details

This article was published online on 22 October 2018.

Gene expression variability across cells and species shapes innate immunity

Tzachi Hagai^{1,2*}, Xi Chen¹, Ricardo J. Miragaia^{1,3}, Raghd Rostom^{1,2}, Tomás Gomes¹, Natalia Kunowska¹, Johan Henriksson¹, Jong-Eun Park¹, Valentina Proserpio^{4,5}, Giacomo Donati^{4,6}, Lara Bossini-Castillo¹, Felipe A. Vieira Braga^{1,7}, Guy Naamati², James Fletcher⁸, Emily Stephenson⁸, Peter Vegh⁸, Gosia Trynka¹, Ivana Kondova⁹, Mike Dennis¹⁰, Muzlifah Haniffa^{8,11}, Armita Nourmohammad^{12,13}, Michael Lässig¹⁴ & Sarah A. Teichmann^{1,2,15*}

As the first line of defence against pathogens, cells mount an innate immune response, which varies widely from cell to cell. The response must be potent but carefully controlled to avoid self-damage. How these constraints have shaped the evolution of innate immunity remains poorly understood. Here we characterize the innate immune response's transcriptional divergence between species and variability in expression among cells. Using bulk and single-cell transcriptomics in fibroblasts and mononuclear phagocytes from different species, challenged with immune stimuli, we map the architecture of the innate immune response. Transcriptionally diverging genes, including those that encode cytokines and chemokines, vary across cells and have distinct promoter structures. Conversely, genes that are involved in the regulation of this response, such as those that encode transcription factors and kinases, are conserved between species and display low cell-to-cell variability in expression. We suggest that this expression pattern, which is observed across species and conditions, has evolved as a mechanism for fine-tuned regulation to achieve an effective but balanced response.

The innate immune response is a cell-intrinsic defence program that is rapidly upregulated upon infection in most cell types. It acts to inhibit pathogen replication while signalling the pathogen's presence to other cells. This programme involves the modulation of several cellular pathways, including production of antiviral and inflammatory cytokines, upregulation of genes that restrict pathogens, and induction of cell death^{1,2}.

An important characteristic of the innate immune response is the rapid evolution that many of its genes have undergone along the vertebrate lineage^{3,4}. This rapid evolution is often attributed to pathogen-driven selection^{5–7}.

Another hallmark of this response is its high level of heterogeneity among responding cells: there is extensive cell-to-cell variability in response to pathogen infection^{8,9} or to pathogen-associated molecular patterns (PAMPs)^{10,11}. The functional importance of this variability is unclear.

These two characteristics—rapid divergence in the course of evolution and high cell-to-cell variability—seem to be at odds with the strong regulatory constraints imposed on the host immune response: the need to execute a well-coordinated and carefully balanced programme to avoid tissue damage and pathological immune conditions^{12–15}. How this tight regulation is maintained despite rapid evolutionary divergence and high cell-to-cell variability remains unclear, but it is central to our understanding of the innate immune response and its evolution.

Here, we study the evolution of this programme using two cell types—fibroblasts and mononuclear phagocytes—in different mammalian clades challenged with several immune stimuli (Fig. 1a).

Our main experimental system uses primary dermal fibroblasts, which are commonly used in immunological studies^{8,13}. We compare the response of fibroblasts from primates (human and macaque) and rodents (mouse and rat) to polyinosinic:polycytidylic acid (poly(I:C)), a synthetic double-stranded RNA (dsRNA; Fig. 1a, left). Poly(I:C) is frequently used to mimic viral infection as it rapidly elicits an antiviral response¹⁶.

We comprehensively characterize the transcriptional changes between species and among individual cells in their innate immune response. We use population (bulk) transcriptomics to investigate transcriptional divergence between species, and single-cell transcriptomics to estimate cell-to-cell variability in gene expression. Using promoter sequence analyses along with chromatin immunoprecipitation with sequencing (ChIP-seq), we study how changes in the expression of each gene between species and across cells relate to the architecture of its promoter. Furthermore, we examine the relationship between cross-species divergence in gene coding sequence and expression and constraints imposed by host–pathogen interactions.

Additionally, we use a second system—bone marrow-derived mononuclear phagocytes from mouse, rat, rabbit and pig challenged with lipopolysaccharide (LPS), a commonly used PAMP of bacterial origin (Fig. 1a, right).

Together, these two systems provide insights into the architecture of the immune response across species, cell types and immune challenges.

Transcriptional divergence in immune response

First, we studied the transcriptional response of fibroblasts to stimulation with dsRNA (poly(I:C)) across the four species (human, macaque,

¹Wellcome Sanger Institute, Cambridge, UK. ²EMBL – European Bioinformatics Institute, Cambridge, UK. ³Centre of Biological Engineering, University of Minho, Braga, Portugal. ⁴Department of Life Sciences and Systems Biology, University of Turin, Torino, Italy. ⁵Italian Institute for Genomic Medicine (IIGM), Torino, Italy. ⁶Molecular Biotechnology Center, University of Turin, Torino, Italy. ⁷Open Targets, Wellcome Sanger Institute, Cambridge, UK. ⁸Institute of Cellular Medicine, Newcastle University, Newcastle upon Tyne, UK. ⁹Division of Pathology and Microbiology, Animal Science Department, Biomedical Primate Research Centre, Rijswijk, The Netherlands. ¹⁰Research Department, Public Health England, National Infection Service, Porton Down, UK. ¹¹Department of Dermatology and NIHR Newcastle Biomedical Research Centre, Newcastle Hospitals NHS Foundation Trust, Newcastle upon Tyne, UK. ¹²Max Planck Institute for Dynamics and Self-Organization, Göttingen, Germany. ¹³Department of Physics, University of Washington, Seattle, WA, USA. ¹⁴Institute for Biological Physics, University of Cologne, Cologne, Germany. ¹⁵Theory of Condensed Matter Group, Cavendish Laboratory, University of Cambridge, Cambridge, UK. *e-mail: tzachi@ebi.ac.uk; st9@sanger.ac.uk

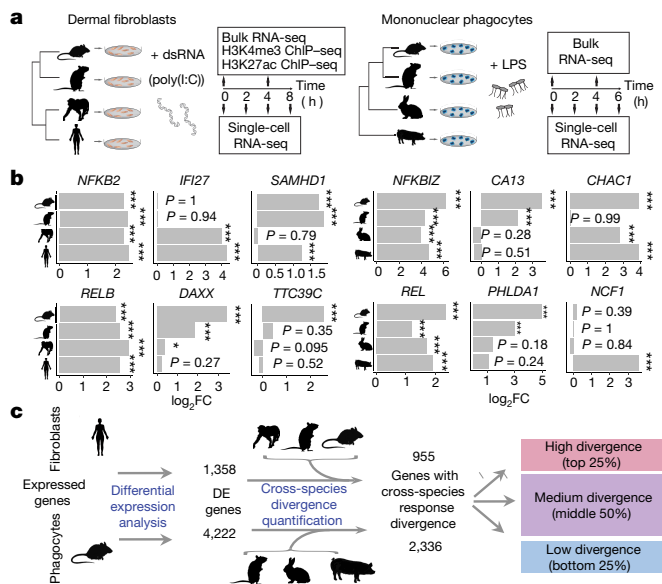


Fig. 1 | Response divergence across species in innate immune response. **a**, Study design. Left, primary dermal fibroblasts from mouse, rat, human and macaque stimulated with dsRNA or controls. Samples were collected for bulk and single-cell RNA-seq and ChIP-seq. Right, primary bone marrow-derived mononuclear phagocytes from mouse, rat, rabbit and pig stimulated with LPS or controls. Samples were collected for bulk and single-cell RNA-seq. **b**, Left, fold-change (FC) in dsRNA stimulation in fibroblasts for sample genes across species (edgeR exact test, based on $n = 6, 5, 3$ and 3 individuals from human, macaque, rat and mouse, respectively). Right, fold-change in LPS stimulation in phagocytes for sample genes across species (Wald test implemented in DESeq2, based on $n = 3$ individuals from each species). False discovery rate (FDR)-corrected P values are shown (** $P < 0.001$, $P < 0.01$, $P < 0.05$). **c**, Top, estimating each gene's level of cross-species divergence in transcriptional response to dsRNA stimulation in fibroblasts. Using differential expression analysis, fold-change in dsRNA response was assessed for each gene in each species. We identified 1,358 human genes as differentially expressed (DE) (FDR-corrected $q < 0.01$), of which 955 had one-to-one orthologues across the four studied species. For each gene with one-to-one orthologues across all species, a response divergence measure was estimated using: $\text{response divergence} = \log[1/4 \times \sum_{i,j} (\log[\text{FC}_{\text{primate}_i}] - [\log(\text{FC}_{\text{rodent}_j})]^2]$. Genes were grouped into low, medium and high divergence according to their response divergence values for subsequent analysis. Bottom, estimating each gene's level of cross-species divergence in LPS response in mononuclear phagocytes. A response divergence measure was estimated using: $\text{response divergence} = \log[1/3 \times \sum_{i,j} (\log[\text{FC}_{\text{pig}}] - \log[\text{FC}_{\text{glire}_j}]^2]$ (where glires are mouse, rat and rabbit).

rat and mouse). We generated bulk RNA-sequencing (RNA-seq) data for each species after 4 h of stimulation, along with respective controls (see Fig. 1a and Methods).

In all species, dsRNA treatment induced rapid upregulation of genes that encode expected antiviral and inflammatory products, including *IFNB*, *TNF*, *IL1A* and *CCL5* (see also Supplementary Table 3). Focusing on one-to-one orthologues, we performed correlation analysis between species and observed a similar transcriptional response (Spearman correlation, $P < 10^{-10}$ in all comparisons; Extended Data Fig. 1), as reported in other immune contexts^{17–19}. Furthermore, the response tended to be more strongly correlated between closely related species than between more distantly related species, as in other expression programmes^{20–24}.

We characterized the differences in response to dsRNA between species for each gene, using these cross-species bulk transcriptomics data. While some genes, such as those encoding the NF- κ B subunits *RELB* and *NFKB2*, respond similarly across species, other genes respond differently in the primate and rodent clades (Fig. 1b, left). For example, *Ifi27* (which encodes a restriction factor against numerous viruses) is strongly upregulated in primates but not in rodents, whereas

Daxx (which encodes an antiviral transcriptional repressor) exhibits the opposite behaviour.

Similarly, in our second experimental system, which consists of lipopolysaccharide (LPS)-stimulated mononuclear phagocytes from mouse, rat, rabbit, and pig (Fig. 1b, right), some genes responded similarly across species (for example, *Nfkb2*), whereas others were highly upregulated only in specific clades (for example, *Phlda1*).

To quantify transcriptional divergence in immune responses between species, we focused on genes that were differentially expressed during the stimulation (see Methods). For simplicity, we refer to these genes as ‘responsive genes’ (Fig. 1c). In this analysis, we study the subset of these genes with one-to-one orthologues across the studied species. There are 955 such responsive genes in dsRNA-stimulated human fibroblasts and 2,336 in LPS-stimulated mouse phagocytes. We define a measure of response divergence by calculating the differences between the fold-change estimates while taking the phylogenetic relationship into account (Methods, Supplementary Figs. 1–7 and Supplementary Table 4).

For subsequent analyses, we split the 955 genes that were responsive in fibroblasts into three groups on the basis of their level of response divergence: (1) high-divergence dsRNA-responsive genes (the top 25% of genes with the highest divergence values in response to dsRNA across the four studied species); (2) low-divergence dsRNA-responsive genes (the bottom 25%); and (3) genes with medium divergence across species (the middle 50%; Fig. 1c). We performed an analogous procedure for the 2,336 LPS-responsive genes in phagocytes.

Promoter architecture of diverging genes

Next, we tested whether divergence in transcriptional responses is reflected in the conservation of promoter function and sequence. Using ChIP-seq, we profiled active histone marks in the fibroblasts of all species. The presence of trimethylation of lysine 4 on histone H3 (H3K4me3) in promoter regions of high-divergence genes was significantly less conserved between humans and rodents than was the presence of H3K4me3 in promoters of low-divergence genes (Extended Data Fig. 2).

We then used the human H3K4me3 ChIP-seq peaks to define active promoter regions of the responsive genes in human fibroblasts. The density of transcription factor binding motifs (TFBMs) was significantly higher in the active promoter regions of high-divergence genes than in low-divergence genes (Fig. 2a). Notably, when comparing the conservation of the core promoter regions in high- versus low-divergence dsRNA-responsive genes, we found that genes that diverge highly in response to dsRNA show higher sequence conservation in this region (Fig. 2b).

This unexpected discordance may be related to the fact that promoters of high- and low-divergence genes have distinctive architectures, associated with different constraints on promoter sequence evolution^{18,25,26}. Notably, promoters containing TATA-box elements tend to have most of their regulatory elements in regions immediately upstream of the transcription start site (TSS). These promoters are thus expected to be more conserved. The opposite is true for CpG island (CGI)^{26,27} promoters. Indeed, we found that TATA-boxes are associated with higher transcriptional divergence, while genes with CGIs diverge more slowly, both in fibroblasts and phagocytes (Fig. 2c; Extended Data Fig. 3). Thus, a promoter architecture enriched in TATA-boxes and depleted of CGIs is associated with higher transcriptional divergence, either entailing higher sequence conservation upstream of these genes^{18,26,27}.

Transcriptional divergence of cytokines

We next investigated whether different functional classes among responsive genes are characterized by varying levels of transcriptional divergence. To this end, we divided responsive genes into categories according to function (such as cytokines, transcriptional factors and kinases) or the processes in which they are known to be involved (such as apoptosis or inflammation).

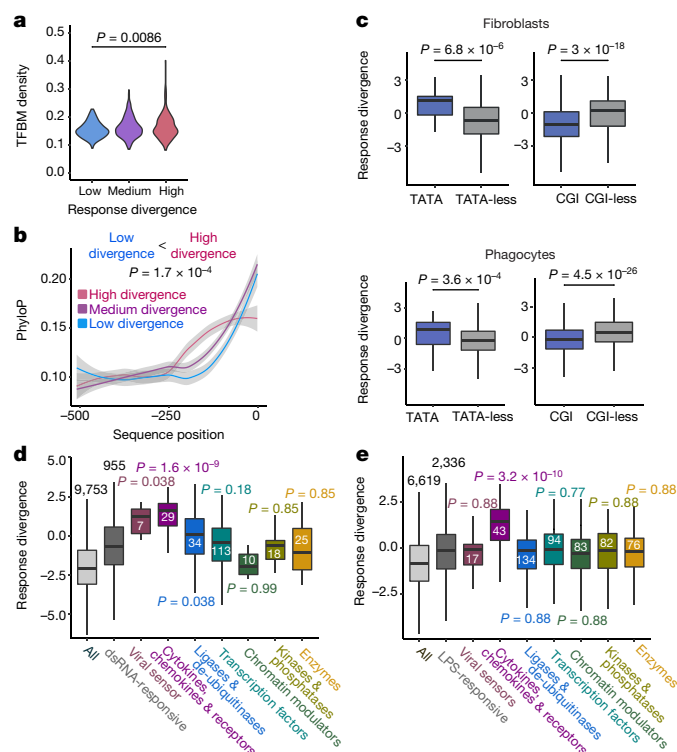


Fig. 2 | Transcriptionally divergent genes have unique functions and promoter architectures. **a**, TFBM density in active promoters and response divergence. For each gene studied in fibroblast dsRNA stimulation, the total number of TFBM matches in its H3K4me3 histone mark was divided by the length of the mark (human marks were used; $n = 879$ differentially expressed genes with ChIP-seq data). High-divergence genes have higher TFBM density than low-divergence genes (one-sided Mann–Whitney test). **b**, Promoter sequence conservation and response divergence in fibroblast dsRNA stimulation. Sequence conservation values are estimated with phyloP7 for 500 base pairs upstream of the transcription start site (TSS) of the human gene. Mean conservation values of each of the 500 base pairs upstream of the TSS are shown for high-, medium- and low-divergence genes ($n = 840$ genes). Genes that are highly divergent have higher sequence conservation (one-sided Kolmogorov–Smirnov test). The 95% confidence interval for predictions from a linear model computed by `geom_loess` function is shown in grey. **c**, Comparison of divergence in response of genes with and without a TATA-box and a CGI in fibroblast dsRNA stimulation and phagocyte LPS stimulation. TATA-box matches and CGI overlaps were computed with respect to the TSS of human genes in fibroblasts ($n = 955$ genes), and to the TSS of mouse genes in phagocytes ($n = 2,336$). **d**, Distributions of divergence values of 9,753 expressed genes in fibroblasts, 955 dsRNA-responsive genes and different functional subsets of the dsRNA-responsive genes (each subset is compared with the set of 955 genes using a one-sided Mann–Whitney test and FDR-corrected P values are shown). **e**, Distributions of divergence values of 6,619 expressed genes in phagocytes, 2,336 LPS-responsive genes and different functional subsets of the LPS-responsive genes (each subset is compared with the set of 2,336 genes using a one-sided Mann–Whitney test and FDR-corrected P values are shown). Violin plots show the kernel probability density of the data. Boxplots represent the median, first quartile and third quartile with lines extending to the furthest value within 1.5 of the interquartile range (IQR).

Genes related to cellular defence and inflammation—most notably cytokines, chemokines and their receptors (hereafter ‘cytokines’)—tended to diverge in response significantly faster than genes involved in apoptosis or immune regulation (chromatin modulators, transcription factors, kinases and ligases) (Fig. 2d, e, Extended Data Fig. 4, Supplementary Fig. 1).

Cytokines also had a higher transcriptional range in response to immune challenge (a higher fold-change). Regressing the fold-change from the divergence estimates resulted in reduction of the relative

divergence of cytokines versus other responsive genes, but the difference still remained (Supplementary Fig. 2). Cytokine promoters are enriched in TATA-boxes (17% versus 2.5%, $P = 1.1 \times 10^{-3}$, Fisher’s exact test) and depleted of CGIs (14% versus 69%, $P = 1.6 \times 10^{-9}$), suggesting that this promoter architecture is associated both with greater differences between species (response divergence) and larger changes between conditions (transcriptional range).

Cell-to-cell variability in immune response

Previous studies have shown that the innate immune response displays high variability across responding cells^{28,29}. However, the relationship between cell-to-cell transcriptional variability and response divergence between species is not well understood.

To study heterogeneity in gene expression across individual cells, we performed single-cell RNA-seq in all species in a time course following immune stimulation. We estimated cell-to-cell variability quantitatively using an established measure for variability: distance to median (DM)³⁰.

We found a clear trend in which genes that were highly divergent in response between species were also more variable in expression across individual cells within a species (Fig. 3a). The relationship between rapid divergence and high cell-to-cell variability held true in both the 955 dsRNA-responsive genes in fibroblasts and the 2,336 LPS-responsive genes in phagocytes. This can be observed across the stimulation time points and in different species (Extended Data Figs. 5, 6). We analysed in depth the relationship between transcriptional divergence and cell-to-cell variability by using additional immune stimulation protocols (Supplementary Figs. 8, 9), and different experimental and computational approaches (Extended Data Fig. 7, Supplementary Figs. 10–13). Notably, the trends we observed are not a result of technical biases due to low expression levels in either the bulk or the single-cell RNA-seq data (Supplementary Figs. 14, 15).

Next, we examined the relationship between the presence of promoter elements (CGIs and TATA-boxes) and a gene’s cell-to-cell variability. Genes that are predicted to have a TATA-box in their promoter had higher transcriptional variability, whereas CGI-containing genes tended to have lower variability (Fig. 3b), in agreement with previous findings³¹. Thus, both transcriptional variability between cells (Fig. 3b) and transcriptional divergence between species (Fig. 2c) are associated with the presence of specific promoter elements.

Transcriptional variability of cytokines

We subsequently compared the response divergence across species with the transcriptional cell-to-cell variability of three groups of responsive genes with different functions: cytokines, transcription factors, and kinases and phosphatases (hereafter ‘kinases’; Fig. 3c, Extended Data Fig. 8). In contrast to kinases and transcription factors, many cytokines display relatively high levels of cell-to-cell variability (Extended Data Fig. 9), being expressed only in a small subset of responding cells (Extended Data Fig. 10). This has previously been reported for several cytokines²⁹. For example, IFNB is expressed in only a small fraction of cells infected with viruses or challenged with various stimuli^{8,11,32}. Here, we find that cells show high levels of variability in expression of cytokines from several families (for example, IFNB, CXCL10 and CCL2).

Cell-to-cell variability of cytokines remains relatively high in comparison to kinases and transcription factors during a time course of 2, 4 and 8 h after dsRNA stimulation of fibroblasts (Extended Data Fig. 9). This pattern is similar across species, and can also be observed in LPS-stimulated phagocytes (Extended Data Fig. 9). Thus, the high variability of cytokines and their expression in a small fraction of stimulated cells across all time points is evolutionarily conserved.

Cytokines tended to be co-expressed in the same cells, raising the possibility that their expression is coordinated (see Supplementary Information and Supplementary Fig. 16). We also identified genes whose expression was correlated with cytokines in human fibroblasts and showed that their orthologues tend to be co-expressed with cytokines in other species. This set is enriched with genes known to be involved in cytokine regulation (Supplementary Table 5).

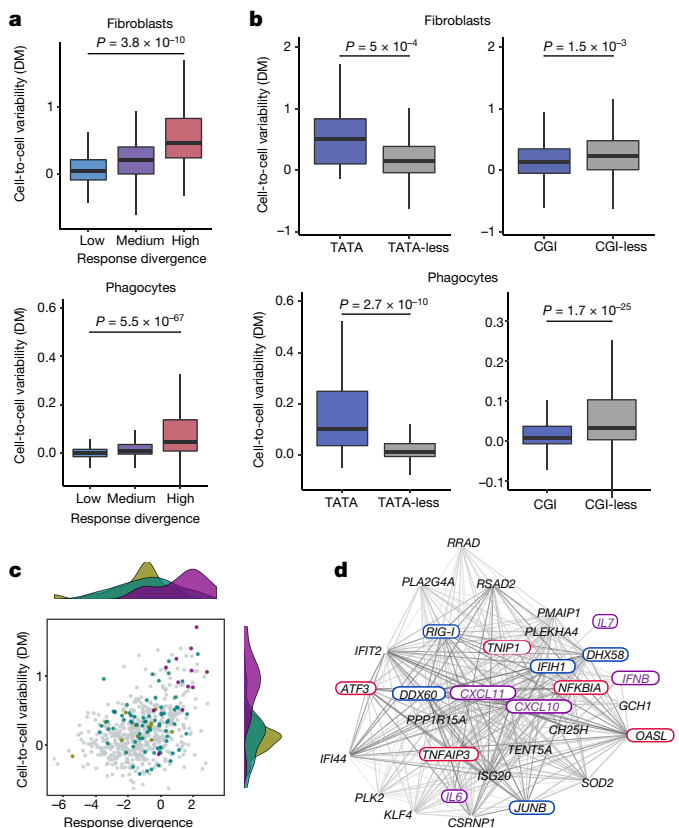


Fig. 3 | Cell-to-cell variability in immune response corresponds to response divergence. **a**, Comparison of divergence in response across species with transcriptional variability between individual cells. Top, fibroblast dsRNA stimulation (variability measured in $n = 55$ human cells, following 4 h dsRNA stimulation). Bottom, phagocyte LPS stimulation (variability measured in $n = 3,293$ mouse cells, following 4 h LPS stimulation). Genes classified as high-, medium- or low-divergence according to level of response divergence. Cell-to-cell variability values of high-divergence genes were compared with those of low-divergence genes (one-sided Mann–Whitney test). **b**, Comparison of cell-to-cell variability of genes with and without a TATA-box and a CGI, in fibroblast dsRNA stimulation and phagocyte LPS stimulation (one-sided Mann–Whitney test). Cell-to-cell variability values are from DM estimations of human fibroblasts stimulated with dsRNA for 4 h ($n = 55$ cells) and from mouse phagocytes stimulated with LPS for 4 h ($n = 3,293$ cells). **c**, Scatter plot showing divergence in response to dsRNA in fibroblasts across species and transcriptional cell-to-cell variability in human cells following 4 h of dsRNA stimulation ($n = 684$ dsRNA-responsive genes). Purple, cytokines; green, transcription factors; beige, kinases. The distributions of divergence and variability values of these groups are shown above and to the right of the scatter plot, respectively. **d**, A network showing genes that correlate positively in expression with the chemokine gene *CXCL10* across cells (Spearman correlation, $\rho > 0.3$), in at least two species (one of which is human), following dsRNA treatment in fibroblasts (based on $n = 146, 74, 175$ and 170 human, macaque, rat and mouse cells, respectively). Purple, cytokines; red, positive regulators of cytokine expression; blue, negative regulators. Colours of lines, from light to dark grey, reflect the number of species in which this pair of genes was correlated. Boxplots represent the median, first quartile and third quartile with lines extending to the furthest value within $1.5 \times \text{IQR}$.

As an example, we focused on the genes whose expression is positively correlated with the chemokine *CXCL10* in at least two species (Fig. 3d). This set includes four cytokines co-expressed with *CXCL10* (in purple), as well as known positive regulators of the innate immune response and cytokine production (in blue), such as the viral sensors *IFIH1* (also known as *MDA5*) and *RIG-I* (also known as *DDX58*). This is in agreement with previous evidence that *IFNB* expression is limited to cells in which important upstream regulators are expressed at sufficiently high levels^{8,11,32}. Here, we show that this phenomenon

of co-expression with upstream regulators applies to a wider set of cytokines and is conserved across species. Notably, cytokines were co-expressed not only with their positive regulators but also with genes that are known to act as negative regulators of cytokine expression or cytokine signalling (in red), suggesting that cytokine expression and function is tightly controlled at the level of individual cells.

The evolutionary landscape of innate immunity

Many immune genes, including several cytokines and their receptors, have been shown to evolve rapidly in coding sequence^{3,33}. However, it is not known how divergence in coding sequence relates to transcriptional divergence in innate immune genes. Using the set of 955 dsRNA-responsive genes in fibroblasts, we assessed coding sequence evolution in the three subsets of low-, medium- and high-divergence genes (as defined in Fig. 1c).

We compared the rate at which genes evolved in their coding sequences with their response divergence by considering the ratio of non-synonymous (dN) to synonymous (dS) nucleotide substitutions. Genes that evolved rapidly in transcriptional response had higher coding sequence divergence (higher dN/dS values) than dsRNA-responsive genes with low response divergence (Fig. 4a).

Rapid gene duplication and gene loss have been observed in several important immune genes^{34–39} and are thought to be a result of pathogen-driven pressure^{40,41}. We therefore tested the relationship between a gene's divergence in response and the rate at which the gene's family has expanded and contracted in the course of vertebrate evolution. We found that transcriptionally divergent dsRNA-responsive genes have higher rates of gene gain and loss (Fig. 4b) and consequently are also evolutionarily younger (Fig. 4c, Supplementary Fig. 17).

Previous reports have suggested that proteins encoded by younger genes tend to have fewer protein–protein interactions (PPIs) within cells⁴². Indeed, we found that rapidly diverging genes tend to have fewer PPIs (Fig. 4d). Together, these results suggest that transcriptionally divergent dsRNA-responsive genes evolve rapidly through various mechanisms, including fast coding sequence evolution and higher rates of gene loss and duplication events, and that their products have fewer interactions with other cellular proteins than those of less divergent genes.

The interaction between pathogens and the host immune system is thought to be an important driving force in the evolution of both sides. We therefore investigated the relationship between transcriptional divergence and interactions with viral proteins by compiling a data set of known host–virus interactions in humans^{6,43,44}. Notably, genes whose products had no known viral interactions showed higher response divergence than genes encoding proteins with viral interactions (Fig. 4e). Furthermore, the transcriptional divergence of genes targeted by viral immunomodulators⁴⁵—viral proteins that subvert the host immune system—was lower still (Fig. 4e). These observations suggest that viruses have evolved to modulate the immune system by interacting with immune proteins that are relatively conserved in their response. Presumably, these genes cannot evolve away from viral interactions, unlike host genes that are less constrained⁴⁶.

The summary of our results in Fig. 4f highlights the differences in both regulatory and evolutionary characteristics between cytokines and other representative dsRNA-responsive genes. Cytokines evolve rapidly through various evolutionary mechanisms and have higher transcriptional variability across cells. By contrast, genes that are involved in immune response regulation, such as transcription factors and kinases, are more conserved and less heterogeneous across cells. These genes encode proteins that have more interactions with other cellular proteins, suggesting that higher constraints are imposed on their evolution. This group of conserved genes is more often targeted by viruses, revealing a relationship between host–pathogen dynamics and the evolutionary landscape of the innate immune response.

Discussion

Here, we have charted the evolutionary architecture of the innate immune response. We show that genes that diverge rapidly between

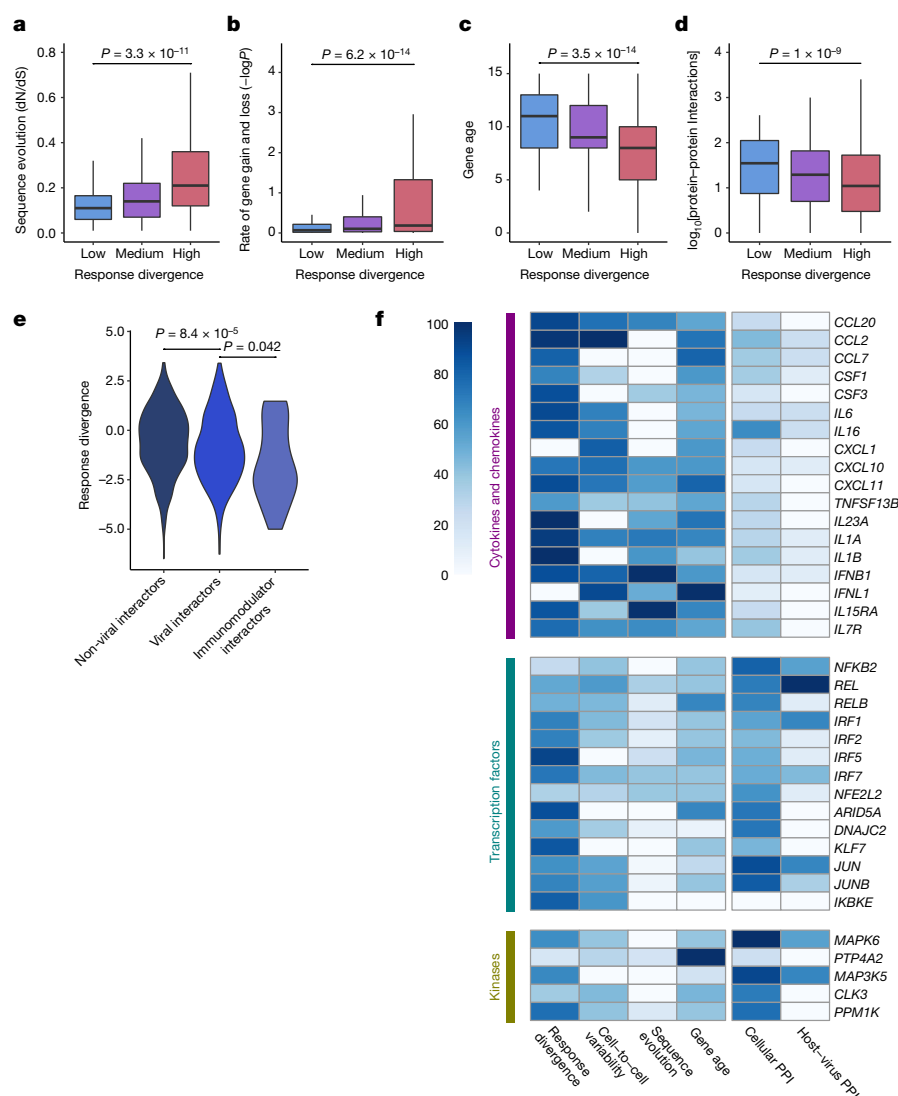


Fig. 4 | Relationship of response divergence and other evolutionary modes. **a–d**, dsRNA-responsive genes in fibroblasts are divided by level of response divergence into three groups, as in Fig. 1c. **a**, Coding sequence divergence, as measured using dN/dS values across 29 mammals. Higher dN/dS values denote faster coding sequence evolution ($n = 567$ genes). **b**, Rate at which genes were gained and lost within the gene family across the vertebrate clade (plotted as $-\log P$). Higher values denote faster gene gain and loss rate ($n = 955$ genes). **c**, Evolutionary age (estimated with Panther7 phylogeny and Wagner reconstruction algorithm). Values denote the branch number with respect to human (distance from human in the phylogenetic tree); higher values indicate greater age ($n = 931$ genes). **d**, Number of known physical interactions with other cellular proteins ($n = 955$ genes). **e**, Distribution of transcriptional response divergence values among dsRNA-responsive genes whose protein products do

not interact with viral proteins, interact with at least one viral protein, or interact with viral immunomodulators ($n = 648$, 307 and 25 genes, respectively). **a–e**, One-sided Mann–Whitney tests. **f**, A scaled heat map showing values of response divergence (as in Fig. 1c), cell-to-cell variability (as in Fig. 3a), coding sequence divergence (dN/dS values, as in **a**), gene age (as in **c**; younger genes have darker colours), number of cellular PPIs (as in **d**) and number of host–virus interactions (as in **e**), for example genes from three functional groups: cytokines, transcription factors, and kinases. Values are shown in a normalized scale between 0 and 100, with the gene with the highest value assigned a score of 100. Missing values are shown in white. Boxplots represent the median, first quartile and third quartile with lines extending to the furthest value within $1.5 \times \text{IQR}$. Violin plots show the kernel probability density of the data.

species show higher levels of variability in their expression across individual cells than genes that diverge more slowly. Both of these characteristics are associated with a similar promoter architecture, enriched in TATA-boxes and depleted of CGIs. Notably, such promoter architecture is also associated with the high transcriptional range of genes during the immune response. Thus, transcriptional changes between conditions (stimulated versus unstimulated), species (transcriptional divergence), and individual cells (cell-to-cell variability) may all be mechanistically related to the same promoter characteristics. In yeast, TATA-boxes are enriched in promoters of stress-related genes, displaying rapid transcriptional divergence between species and high variability in expression^{30,47}. This finding suggests intriguing analogies between the mammalian immune and yeast stress responses—two

systems that have been exposed to continuous changes in external stimuli during evolution.

We have also shown that genes involved in regulation of the immune response—such as transcription factors and kinases—are relatively conserved in their transcriptional responses. These genes might be under stronger functional and regulatory constraints, owing to their roles in multiple contexts and pathways, which would limit their ability to evolve. This limitation could represent an Achilles' heel that is used by pathogens to subvert the immune system. Indeed, we found that viruses interact preferentially with conserved proteins of the innate immune response. Cytokines, on the other hand, diverge rapidly between species, owing to their promoter architecture and because they have fewer constraints imposed by intracellular interactions or additional

non-immune functions. We therefore suggest that cytokines represent a successful host strategy to counteract rapidly evolving pathogens as part of the host–pathogen evolutionary arms race.

Cytokines also display high cell-to-cell variability and tend to be co-expressed with other cytokines and cytokine regulators in a small subset of cells, and this pattern is conserved across species. As prolonged or increased cytokine expression can result in tissue damage^{48–50}, restriction of cytokine production to only a few cells may enable a rapid, but controlled, response across the tissue to avoid long-lasting and potentially damaging effects.

Online content

Any methods, additional references, Nature Research reporting summaries, source data, statements of data availability and associated accession codes are available at <https://doi.org/10.1038/s41586-018-0657-2>.

Received: 24 August 2017; Accepted: 17 August 2018;

Published online 24 October 2018.

- Borden, E. C. et al. Interferons at age 50: past, current and future impact on biomedicine. *Nat. Rev. Drug Discov.* **6**, 975–990 (2007).
- Iwasaki, A. A virological view of innate immune recognition. *Annu. Rev. Microbiol.* **66**, 177–196 (2012).
- Nielsen, R. et al. A scan for positively selected genes in the genomes of humans and chimpanzees. *PLoS Biol.* **3**, e170 (2005).
- Haygood, R., Babbitt, C. C., Fedrigo, O. & Wray, G. A. Contrasts between adaptive coding and noncoding changes during human evolution. *Proc. Natl Acad. Sci. USA* **107**, 7853–7857 (2010).
- Fumagalli, M. et al. Signatures of environmental genetic adaptation pinpoint pathogens as the main selective pressure through human evolution. *PLoS Genet.* **7**, e1002355 (2011).
- Enard, D., Cai, L., Gnennap, C. & Petrov, D. A. Viruses are a dominant driver of protein adaptation in mammals. *eLife* **5**, e12469 (2016).
- Barreiro, L. B. & Quintana-Murci, L. From evolutionary genetics to human immunology: how selection shapes host defence genes. *Nat. Rev. Genet.* **11**, 17–30 (2010).
- Zhao, M., Zhang, J., Phatnani, H., Scheu, S. & Maniatis, T. Stochastic expression of the interferon- β gene. *PLoS Biol.* **10**, e1001249 (2012).
- Avraham, R. et al. Pathogen cell-to-cell variability drives heterogeneity in host immune responses. *Cell* **162**, 1309–1321 (2015).
- Shalek, A. K. et al. Single-cell RNA-seq reveals dynamic paracrine control of cellular variation. *Nature* **510**, 363–369 (2014).
- Hwang, S. Y. et al. Biphasic RLR-IFN- β response controls the balance between antiviral immunity and cell damage. *J. Immunol.* **190**, 1192–1200 (2013).
- Porritt, R. A. & Hertzog, P. J. Dynamic control of type I IFN signalling by an integrated network of negative regulators. *Trends Immunol.* **36**, 150–160 (2015).
- Ivashkiv, L. B. & Donlin, L. T. Regulation of type I interferon responses. *Nat. Rev. Immunol.* **14**, 36–49 (2014).
- Brinkworth, J. F. & Barreiro, L. B. The contribution of natural selection to present-day susceptibility to chronic inflammatory and autoimmune disease. *Curr. Opin. Immunol.* **31**, 66–78 (2014).
- Kobayashi, K. S. & Flavell, R. A. Shielding the double-edged sword: negative regulation of the innate immune system. *J. Leukoc. Biol.* **75**, 428–433 (2004).
- Kumar, H., Kawai, T. & Akira, S. Pathogen recognition by the innate immune system. *Int. Rev. Immunol.* **30**, 16–34 (2011).
- Barreiro, L. B., Marioni, J. C., Blekman, R., Stephens, M. & Gilad, Y. Functional comparison of innate immune signaling pathways in primates. *PLoS Genet.* **6**, e1001249 (2010).
- Schroder, K. et al. Conservation and divergence in Toll-like receptor 4-regulated gene expression in primary human versus mouse macrophages. *Proc. Natl Acad. Sci. USA* **109**, E944–E953 (2012).
- Shay, T. et al. Conservation and divergence in the transcriptional programs of the human and mouse immune systems. *Proc. Natl Acad. Sci. USA* **110**, 2946–2951 (2013).
- Brawand, D. et al. The evolution of gene expression levels in mammalian organs. *Nature* **478**, 343–348 (2011).
- Kalinka, A. T. et al. Gene expression divergence recapitulates the developmental hourglass model. *Nature* **468**, 811–814 (2010).
- Khaitovich, P., Enard, W., Lachmann, M. & Pääbo, S. Evolution of primate gene expression. *Nat. Rev. Genet.* **7**, 693–702 (2006).
- Levin, M. et al. The mid-developmental transition and the evolution of animal body plans. *Nature* **531**, 637–641 (2016).
- Reilly, S. K. & Noonan, J. P. Evolution of gene regulation in humans. *Annu. Rev. Genomics Hum. Genet.* **17**, 45–67 (2016).
- Tirosh, I., Weinberger, A., Carmi, M. & Barkai, N. A genetic signature of interspecies variations in gene expression. *Nat. Genet.* **38**, 830–834 (2006).
- Haberle, V. & Lenhard, B. Promoter architectures and developmental gene regulation. *Semin. Cell Dev. Biol.* **57**, 11–23 (2016).
- Lenhard, B., Sandelin, A. & Carninci, P. Metazoan promoters: emerging characteristics and insights into transcriptional regulation. *Nat. Rev. Genet.* **13**, 233–245 (2012).
- Franz, K. M. & Kagan, J. C. Innate immune receptors as competitive determinants of cell fate. *Mol. Cell* **66**, 750–760 (2017).
- Satija, R. & Shalek, A. K. Heterogeneity in immune responses: from populations to single cells. *Trends Immunol.* **35**, 219–229 (2014).
- Newman, J. R. et al. Single-cell proteomic analysis of *S. cerevisiae* reveals the architecture of biological noise. *Nature* **441**, 840–846 (2006).
- Faure, A. J., Schmiedel, J. M. & Lehner, B. Systematic analysis of the determinants of gene expression noise in embryonic stem cells. *Cell Syst.* **5**, 471–484.e474 (2017).
- Rand, U. et al. Multi-layered stochasticity and paracrine signal propagation shape the type-I interferon response. *Mol. Syst. Biol.* **8**, 584 (2012).
- Fumagalli, M. & Sironi, M. Human genome variability, natural selection and infectious diseases. *Curr. Opin. Immunol.* **30**, 9–16 (2014).
- Johnson, W. E. & Sawyer, S. L. Molecular evolution of the antiretroviral TRIM5 gene. *Immunogenetics* **61**, 163–176 (2009).
- Choo, S. W. et al. Pangolin genomes and the evolution of mammalian scales and immunity. *Genome Res.* **26**, 1312–1322 (2016).
- Braun, B. A., Marcovitz, A., Camp, J. G., Jia, R. & Bejerano, G. Mx1 and Mx2 key antiviral proteins are surprisingly lost in toothed whales. *Proc. Natl Acad. Sci. USA* **112**, 8036–8040 (2015).
- Xu, L. et al. Loss of RIG-I leads to a functional replacement with MDA5 in the Chinese tree shrew. *Proc. Natl Acad. Sci. USA* **113**, 10950–10955 (2016).
- Sackton, T. B., Lazzaro, B. P. & Clark, A. G. Rapid expansion of immune-related gene families in the house fly, *Musca domestica*. *Mol. Biol. Evol.* **34**, 857–872 (2017).
- Brunette, R. L. et al. Extensive evolutionary and functional diversity among mammalian AIM2-like receptors. *J. Exp. Med.* **209**, 1969–1983 (2012).
- Malfavon-Borja, R., Wu, L. I., Emerman, M. & Malik, H. S. Birth, decay, and reconstruction of an ancient TRIMCyp gene fusion in primate genomes. *Proc. Natl Acad. Sci. USA* **110**, E583–E592 (2013).
- Barber, M. F., Lee, E. M., Griffin, H. & Elde, N. C. Rapid evolution of primate type 2 immune response factors linked to asthma susceptibility. *Genome Biol. Evol.* **9**, 1757–1765 (2017).
- Saeed, R. & Deane, C. M. Protein–protein interactions, evolutionary rate, abundance and age. *BMC Bioinformatics* **7**, 128 (2006).
- Calderone, A., Licata, L. & Cesareni, G. VirusMentha: a new resource for virus-host protein interactions. *Nucleic Acids Res.* **43**, D588–D592 (2015).
- Halehalli, R. R. & Nagarajaram, H. A. Molecular principles of human virus protein–protein interactions. *Bioinformatics* **31**, 1025–1033 (2015).
- Pichlmair, A. et al. Viral immune modulators perturb the human molecular network by common and unique strategies. *Nature* **487**, 486–490 (2012).
- Dyer, M. D., Murali, T. M. & Sobral, B. W. The landscape of human proteins interacting with viruses and other pathogens. *PLoS Pathog.* **4**, e32 (2008).
- Tirosh, I. & Barkai, N. Two strategies for gene regulation by promoter nucleosomes. *Genome Res.* **18**, 1084–1091 (2008).
- Crow, Y. J. & Manel, N. Aicardi-Goutières syndrome and the type I interferonopathies. *Nat. Rev. Immunol.* **15**, 429–440 (2015).
- Hall, J. C. & Rosen, A. Type I interferons: crucial participants in disease amplification in autoimmunity. *Nat. Rev. Rheumatol.* **6**, 40–49 (2010).
- Tisoncik, J. R. et al. Into the eye of the cytokine storm. *Microbiol. Mol. Biol. Rev.* **76**, 16–32 (2012).

Acknowledgements We thank N. Eling, M. Fumagalli, Y. Gilad, O. Laufman, A. Marcovitz, J. Marioni, K. Meyer, M. Muffato, D. Odom, O. Stegle, A. Stern, M. Stubbington, V. Svensson and M. Ward for discussions; G. Emerton, A. Jinat, L. Mamanova, K. Polanski, A. Fullgrave, N. George, S. Barnett, R. Boyd, S. Patel and C. Gomez for technical assistance; the HipSci consortium for human fibroblast lines; and members of the Teichmann laboratory for support at various stages. This project was supported by ERC grants (ThDEFINE, ThSWITCH) and an EU FET-OPEN grant (MRG-GRAMMAR No 664918) and Wellcome Sanger core funding (Grant No WT206194). T.H. was supported by an HFSP Long-Term Fellowship and by EMBO Long-Term and Advanced fellowships. V.P. is funded by Fondazione Umberto Veronesi.

Reviewer information Nature thanks L. Barreiro, I. Yanai and the other anonymous reviewer(s) for their contribution to the peer review of this work.

Author contributions T.H. and S.A.T. designed the project; T.H., X.C., R.J.M., R.R., N.K. and J.-E.P. performed experiments with help from V.P., G.D. and F.A.V.B.; T.H., X.C., R.J.M., R.R., T.G. and J.H. analysed the data with help from G.N., L.B.-C., G.T.A.N. and M.L.; J.F., E.S., P.V., I.K., M.D. and M.H. provided samples; S.A.T. supervised the project; T.H., R.R., N.K. and S.A.T. wrote the manuscript with input from all authors.

Competing interests The authors declare no competing interests.

Additional information

Extended data is available for this paper at <https://doi.org/10.1038/s41586-018-0657-2>.

Supplementary information is available for this paper at <https://doi.org/10.1038/s41586-018-0657-2>.

Reprints and permissions information is available at <http://www.nature.com/reprints>.

Correspondence and requests for materials should be addressed to T.H. or S.A.T.

Publisher's note: Springer Nature remains neutral with regard to jurisdictional claims in published maps and institutional affiliations.

METHODS

Ethical compliance. This project was approved by the Wellcome Sanger Institute Animal Welfare and Ethical Review Body, and complied with all relevant ethical regulations regarding animal research and human studies. Human cells were obtained from the HipSci project⁵¹, where they were collected from volunteers recruited from the NIHR Cambridge BioResource (written consent was given). Human skin profiling was performed in accordance with protocols approved by the Newcastle Research Ethics Committee (REC approval 08/H0906/95+5). Macaque skin samples were obtained from animals assigned to unrelated non-infectious studies, provided by Public Health England's National Infection Service in accordance with Home Office (UK) guidelines and approved by the Public Health England Ethical Review Committee under an appropriate UK Home Office project license.

Cross-species dermal fibroblast stimulation with dsRNA and IFN β . *Tissue culture.* We cultured primary dermal fibroblasts from low passage cells (below 10) that originated from females from four different species (human (European ancestry), rhesus macaque, C57BL/6 (black 6) mouse and brown Norway rat). All skin samples were taken from shoulders. Stimulation experiments and library preparations were done in identical conditions across all species and for all genomics techniques. Details on the numbers of individuals used in each technique are listed in each technique's section and in Supplementary Table 1.

Human cells were obtained from the HipSci project⁵¹ (<http://www.hipsci.org/>). Rhesus macaque cells were extracted from skin tissues that were incubated for 2 h with 0.5% collagenase B (Roche; 11088815001) after mechanical processing, and then filtered through 100- μ m strainers before being plated and passaged before cryo-banking. Rodent cells were obtained from PelcoBiotech where they were extracted using a similar protocol. In vitro cultured fibroblasts from all four species resemble a particular in vivo cluster of dermal fibroblasts (see Supplementary Information). Cells were not tested for mycoplasma contamination.

Prior to stimulation, cells were thawed and grown for several days in ATCC fibroblast growth medium (Fibroblast Basal Medium (ATCC, ATCC-PCS-201-030) with Fibroblast Growth Kit-Low serum (ATCC, PCS-201-041) (supplemented with Primocin (Invivogen, ant-pm-1) and penicillin/streptomycin (Life Technologies, 15140122)) - a controlled medium that has proven to provide good growing conditions for fibroblasts from all species, with slightly less than 24 h doubling times. About 18 h before stimulation, cells were trypsinized, counted and seeded into 6-well plates (100,000 cells per well). Cells were stimulated as follows: (1) stimulated with 1 μ g/ml high-molecular mass poly(I:C) (Invivogen, tlr-pic) transfected with 2 μ g/ml Lipofectamin 2,000 (ThermoFisher, 11668027); (2) mock transfected with Lipofectamin 2,000; (3) stimulated with 1,000 IU of IFN β for 8 h (human IFN β : 11410-2 (for human and macaque cells); rat IFN β : 13400-1; mouse IFN β : 12401-1; all IFNs were obtained from PBL, and had activity units based on similar virological assays); or (4) left untreated. Interferon stimulation was used as a control, to study how genes that were upregulated in the secondary wave of the innate immune response diverge between species.

Additional human and mouse samples were stimulated with 1,000 IU of cross-mammalian IFN (CMI, or Universal Type I IFN Alpha, PBL, 11200-1). The latter stimulation was done to assess the effects of species-specific and batch-specific IFN β .

In all of the above-mentioned stimulations, we used a longer time course for single-cell RNA-seq than for bulk RNA-seq, for two main reasons: (1) in the bulk, we chose to focus on one main stimulation time point for simplicity and to obtain an intuitive fold-change between stimulated and unstimulated conditions; (2) in single cells, when studying cell-to-cell variability, we chose to profile, in addition to the main stimulation time point, cells in earlier and later stages of the response. This is important for studying how the dynamics and magnitude of the response affect gene expression variability between responding cells.

The poly(I:C) we used tested negative for the presence of bacterial beta-endotoxin using a coagulation test (PYROGENT Plus, 0.06 EU/ml sensitivity, N283-06).

Bulk RNA-seq: library preparation and sequencing. For bulk transcriptomics analysis, cells from individuals from different species were grown in parallel and stimulated with dsRNA, IFN β (and cross-mammalian IFN) and their respective controls. In total, samples from 6 humans, 6 macaques, 3 mice and 3 rats were used. Total RNA was extracted using the RNeasy Plus Mini kit (Qiagen, 14136), using QIAcube (Qiagen). RNA was then measured using a Bioanalyzer 2100 (Agilent Technologies), and samples with RIN < 9 were excluded from further analysis (one macaque sample stimulated with poly(I:C) and its control).

Libraries were produced using the Kapa Stranded mRNA-seq Kit (Kapa Biosystems, KK8421). The Kapa library construction protocol was modified for automated library preparation by Bravo (Agilent Technologies). cDNA was amplified in 13 PCR cycles, and purified using Ampure XP beads (Beckman Coulter, A63882) (1.8 \times volume) using Zephyr (Perkin Elmer). Pooled samples were sequenced on an Illumina HiSeq 2500 instrument, using paired-end 125-bp reads.

ChIP-seq: library preparation and sequencing. Samples from three individuals from each of the four species were grown and stimulated (with poly(I:C) for 4 h or left untreated, as described above) in parallel to samples collected for bulk RNA-seq. Following stimulation, samples were crosslinked in 1% HCHO (prepared in 1 \times DPBS) at room temperature for 10 min, and HCHO was quenched by the addition of glycine at a final concentration of 0.125 M. Cells were pelleted at 4°C at 2,000g, washed with ice-cold 1 \times DPBS twice, and snap-frozen in liquid nitrogen. Cell pellets were stored at -80°C until further stages were performed. ChIPmentation was performed according to version 1.0 of the published protocol⁵² with a few modifications (see additional details in Supplementary Methods).

Library preparation reactions contained the following reagents: 10 μ l purified DNA (from the above procedure), 2.5 μ l PCR Primer Cocktails (Nextera kit, Illumina, FC-121-1030), 2.5 μ l N5xx (Nextera index kit, Illumina FC-121-1012), 2.5 μ l N7xx (Nextera index kit, Illumina, FC-121-1012), 7.5 μ l NPM PCR Master Mix (Nextera kit, Illumina, FC-121-1030). PCR cycles were as follows: 72°C, 5 min; 98°C, 2 min; [98°C, 10 s, 63°C, 30 s, 72°C, 20 s] \times 12; 10°C hold.

Amplified libraries were purified by double AmpureXP bead purification: first with 0.5 \times bead ratio, keep supernatant, second with 1.4 \times bead ratio, keep bound DNA. Elution was done in 20 μ l Buffer EB (QIAGEN).

One microlitre of library was run on a Bioanalyzer (Agilent Technologies) to verify normal size distribution. Pooled samples were sequenced on an Illumina HiSeq 2000 instrument, using paired-end 75-bp reads.

Flow cytometry for single-cell RNA-seq. For scRNA-seq, we performed two biological replicates, with each replicate having one individual from each of the four studied species. A time course of dsRNA stimulation of 0, 4, and 8 h was used in one replicate (divided into two technical replicates), while the second replicate included a time course of 0, 2, 4, and 8 h. Poly(I:C) transfection was done as described above. In the case of sorting with IFNLUX, we used rhodamine-labelled poly(I:C).

Cells were sorted with either Beckman Coulter MoFlo XDP (first replicate) or Becton Dickinson INFLUX (second replicate) into wells containing 2 μ l lysis buffer (1:20 solution of RNase Inhibitor (Clontech, 2313A) in 0.2% v/v Triton X-100 (Sigma-Aldrich, T9284)), spun down and immediately frozen at -80°C.

When sorting with MoFlo, a pressure of 15 psi was used with a 150- μ m nozzle, using the 'Single' sort purity mode. Dead or late-apoptosis cells were excluded using propidium iodide at 1 μ g/ml (Sigma, Cat Number P4170) and single cells were selected using FSC W versus FSC H. When sorting with INFLUX, a pressure of 3 psi was used with a 200- μ m nozzle, with the 'single' sort mode. Dead or late-apoptosis cells were excluded using 100 ng/ml DAPI (4',6-diamidino-2-phenylindole) (Sigma, D9542). DAPI was detected using the 355-nm laser (50 mW), using a 460/50 nm bandpass filter. Rhodamine was detected using the 561-nm laser (50 mW), using a 585/29 nm bandpass filter. Single cells were collected using FSC W versus FSC H.

Library preparation from full-length RNA from single cells and sequencing. Sorted plates were processed according to the Smart-seq2 protocol⁵³. Oligo-dT primer (IDT), dNTPs (ThermoFisher, 10319879) and ERCC RNA Spike-In Mix (1:25,000,000 final dilution, Ambion, 4456740) were added to each well, and reverse transcription (using 50 U SmartScribe, Clontech, 639538) and PCR were performed following the original protocol with 25 PCR cycles. cDNA libraries were prepared using Nextera XT DNA Sample Preparation Kit (Illumina, FC-131-1096), according to the protocol supplied by Fluidigm (PN 100-5950 B1). Quality Checks on cDNA were done using a Bioanalyzer 2100 (Agilent Technologies). Libraries were quantified using the LightCycler 480 (Roche), pooled and purified using AMPure XP beads (Beckman Coulter) with Hamilton 384 head robot (Hamilton Robotics). Pooled samples were sequenced on an Illumina HiSeq 2500 instrument, using paired-end 125-bp reads.

Read mapping to annotated transcriptome. For bulk RNA-seq samples, adaptor sequences and low-quality score bases were first trimmed using Trim Galore (version 0.4.1) (with the parameters '-paired-quality 20-length 20-e 0.1-adaptor AGATCGGAAGAGC'). Trimmed reads were mapped and gene expression was quantified using Salmon (version 0.6.0)⁵⁴ with the following command: 'salmon quant -i [index_file_directory] -l ISR -p 8-biasCorrect-sensitive-extraSensitive -o [output_directory] -l -g [ENSEMBL_transcript_to_gene_file]-useFSPD-numBootstraps 100'. Each sample was mapped to its respective species' annotated transcriptome (downloaded from ENSEMBL, version 84: GRCh38 for human, MMUL_1 for macaque, GRCm38 for mouse, Rnor_6.0 for rat). We included only the set of coding genes (*.cdna.all.fa files). We removed annotated secondary haplotypes of human genes by removing genes with 'CHR_HSCHR'.

Quantifying differential gene expression in response to dsRNA. To quantify differential gene expression between treatment and control for each species and for each treatment separately, we used edgeR (version 3.12.1)⁵⁵ using the rounded estimated counts from Salmon. This was done only for genes that had a significant level of expression in at least one of the four species (TPM > 3 in at least N - 1 libraries, where N is the number of different individuals we have for this species with libraries that passed quality control, and TPM is transcripts per million). Differential

expression analysis was performed using the edgeR exact test, and *P* values were adjusted for multiple testing by estimating the false discovery rate (FDR).

Conservation and divergence in immune response: fold-change-based analysis. We compared the overall change in response to treatment (dsRNA or IFNB) between pairs of species, by computing the Spearman correlation of the fold-change in response to treatment across all one-to-one orthologues that were expressed in at least one species (Extended Data Fig. 1a–h). Fold-change was calculated with edgeR, as described above. Spearman correlations of all expressed genes appear in grey. Correlations of the subset of differentially expressed genes (genes with FDR-corrected *P* < 0.01 in at least one of the compared species) appear in black.

In Extended Data Fig. 1a–c, we show comparisons in response to dsRNA. In Extended Data Fig. 1d–f, we show comparisons in response to IFNB, which we use here to study the similarity of the secondary immune response between species.

We constructed a tree based on a gene's change in expression in response to dsRNA and to IFNB, using expressed genes that had one-to-one orthologues across all four species and were expressed in at least one species in at least one condition (Extended Data Fig. 1i). We used hierarchical clustering, with the *hclust* command from the stats R package, with the distance between samples computed as $1 - \rho$, where ρ is the pairwise Spearman correlation between each pair of species mentioned above (a greater similarity, reflected in a higher correlation, results in a smaller distance) and 'average' as the clustering method.

The above-mentioned analyses focus on one-to-one orthologues between the compared species. In Supplementary Table 6, we quantify the similarity in response between species (based on Spearman correlations) when adding genes with one-to-many orthologues.

Quantifying gene expression divergence in response to immune challenge. To quantify transcriptional divergence in immune response between species, we focus on genes that have annotated one-to-one orthologues across the studied species (human, macaque, mouse and rat). 9,753 of the expressed genes have annotated one-to-one orthologues in all four species, out of which 955 genes are differentially expressed in human in response to dsRNA treatment (genes with an FDR-corrected *P* < 0.01).

We define a measure of response divergence (based on a previous study⁵⁶) by calculating the differences between the fold-change estimates across the orthologues: response divergence = $\log[1/4 \times \sum_i (\log[\text{FC}_{\text{primate},i}] - \log[\text{FC}_{\text{rodent},i}])^2]$. This measure takes into account the structure of the phylogeny, and gives a relative measure of divergence in response across all genes with one-to-one orthologues.

To consider differences between species, we focus on between-clade differences (primates versus rodents), rather than on within-clade differences. In this way, we map the most significant macro-evolutionary differences along the longest branches of our four-species phylogeny. In addition, averaging within clades acts as a reduction of noise⁵⁶.

We compared this divergence measure to two other measures that use models (and incorporate both between- and within-clade divergence) and found a strong correlation between the divergence estimates across the three approaches (Supplementary Figs. 3, 4).

In most of the subsequent analyses, we focus on the 955 dsRNA-responsive genes: genes that were differentially expressed in response to dsRNA (genes that have an FDR-corrected *P* < 0.01 in human, and have annotated one-to-one orthologues in the other three species). For some of the analyses, we split these 955 genes based on quartiles, into genes with high, medium and low divergence (Fig. 1c).

We also studied how imprecisions in the fold-change estimates affected the response divergence estimates and subsequent analyses (Supplementary Figs. 5, 6). **Comparison of response divergence between different functional groups.** To compare the divergence rates between sets of dsRNA-responsive genes that have different functions in the innate immune response, we split these 955 genes into the following functional groups (all groups are mutually exclusive, and any gene that belongs to two groups was excluded from the latter group; human gene annotations were used).

We first grouped genes by annotated molecular functions: viral sensors (genes that belong to one of the GO categories: GO:0003725 (dsRNA binding), GO:0009597 (detection of virus), and GO:0038187 (pattern recognition receptor activity)); cytokines, chemokines and their receptors (GO:0005125 (cytokine activity), GO:0008009 (chemokine activity), GO:0004896 (cytokine receptor activity), and GO:0004950 (chemokine receptor activity)); transcription factors (taken from the Animal Transcription Factor DataBase (version 2.0)⁵⁷); chromatin modulators (GO:0016568 (chromatin modification), GO:0006338 (chromatin remodelling), GO:0003682 (chromatin binding), and GO:0042393 (histone binding)); kinases and phosphatases (GO:0004672 (protein kinase activity) and GO:0004721 (phosphoprotein phosphatase activity)); ligases and deubiquitinases (GO:0016579 (protein deubiquitination), GO:0004842 (ubiquitin-protein transferase activity) and GO:0016874 (ligase activity)); and other enzymes (mostly involved in metabolism rather than regulation: GO:0003824 (catalytic activity)). The divergence response values of these functional subsets were compared to the entire group of 955 dsRNA-responsive genes (Fig. 2d, e).

Next, we grouped genes by biological processes that are known to be important in the innate immune response: antiviral defence (GO:0051607 (defence response to virus)); inflammation (GO:0006954 (inflammatory response)); apoptosis (GO:0006915 (apoptotic process)); and regulation (GO annotations related to regulation of innate immune response pathways include only few genes. We thus used as the group of genes related to regulation, the merged group of genes that are annotated as transcription factors, chromatin modulators, kinases and phosphatases or ligases and deubiquitinases, since all these groups include many genes that are known to regulate the innate immune response.)

Gene lists belonging to the mentioned GO annotations were downloaded using QuickGo⁵⁸. The distribution of response divergence values for each of the functional groups was compared with the distribution of response divergence of the entire set of dsRNA-responsive genes. Cytokines, chemokines and their receptors are merged in Fig. 2d, e, 3c. Analogous comparisons of functional groups in IFNB response (with 841 IFNB-responsive genes) are shown in Supplementary Fig. 1. See additional analyses in Supplementary Information.

Alignment and peak calling of ChIP-seq reads. ChIP-seq reads were trimmed using trim_galore (version 0.4.1) with '-paired-trim1-nextera' flags. The trimmed reads were aligned to the corresponding reference genome (hg38 for human, rheMac2 for macaque, mm10 for mouse, rn6 for rat; all these genomes correspond to the transcriptomes used for RNA-seq mapping) from the UCSC Genome Browser⁵⁹ using bowtie2 (version 2.2.3) with default settings⁶⁰. In all four species, we removed the Y chromosome. In the case of human, we also removed all alternative haplotype chromosomes. Following alignment, low-confident mapped and improperly paired reads were removed by samtools⁶¹ with '-q 30 -f 2' flags.

Enriched regions (peaks) were called using MACS2 (v.2.1.1)⁶² with a corrected *P* value cutoff of 0.01 with '-f BAMPE -q 0.01 -B-SPMR' flags, using input DNA as control. The genome sizes (the argument for '-g' flag) used were 'hs' for human, 'mm' for mouse, 3.0×10^9 for macaque and 2.5×10^9 for rat. Peaks were considered reproducible when they were identified in at least two of the three biological replicates and overlapped by at least 50% of their length (non-reproducible peaks were excluded from subsequent analyses). Reproducible peaks were then merged to create consensus peaks from overlapping regions of peaks from the three replicates by using mergeBed from the bedtools suite⁶³.

Gene assignment and conservation of active promoters and enhancers. We subsequently linked human peaks with the genes they might be regulating as follows: H3K4me3 consensus peak was considered the promoter region of a given gene if its centre was between 2 kb upstream and 500 bp downstream of the annotated TSS of the most abundantly expressed transcript of that gene.

Similarly, H3K27ac was considered the enhancer region of a given gene if its centre was in a distance above 1 kb and below 1 Mb, and there was no overlap (of 1 bp or more) with any H3K4me3 peak.

In each case where, based on the distance criteria, more than a single peak was linked to a gene (or more than a single gene was linked to a peak), we took only the closest peak–gene pair (ensuring that each peak will have up to one gene and vice versa).

To compare active promoters and enhancers between species, we excluded any human peak that could not be uniquely mapped to the respective region in the other species. This was done by looking for syntenic regions of human peaks in the other three species by using liftOver⁶⁴, and removing peaks that had either unmapped regions or more than one mapped region in the compared species. We considered syntenic regions with at least 70% sequence similarity between the species (minMatch = 0.7, and 0.8 in the case of human–macaque comparison), with a minimal length (minSizeQ and minSizeT) corresponding to the length of the shortest peak (128 bp in H3K4 and 142 bp in H3K27).

We defined an active human promoter or enhancer as conserved if a peak was identified in the corresponding region of the other species (we repeated this analysis by comparing human with each of the other three species separately). We compared the occurrence of conserved promoters and enhancers in genes that are highly divergent in response to dsRNA with low-divergence genes, and used Fisher's exact test to determine the statistical significance of the observed differences between high- and low-divergence genes (Extended Data Fig. 2).

Promoter sequence analysis. To calculate the total number of transcription factor binding motifs in a gene's active promoter region, we downloaded the non-redundant JASPAR core motif matrix (pfm vertebrates.txt) from the JASPAR 2016 server⁶⁵ and searched for significant matches for these motifs using FIMO⁶⁶ in human H3K4me3 peaks. The TFBM density of peaks was calculated by dividing the total number of motif matches in a peak by the peak's length. TFBM density values in human H3K4me3 peaks linked with high- and low-divergence genes were compared (Fig. 2a).

PhyloP7 values were used to assess promoter sequence conservation⁶⁷. Sequence conservation quantification was performed by taking the estimated nucleotide substitution rate for each nucleotide along the promoter sequence (500 bp upstream of the TSS of the relevant human gene). When several annotated transcripts existed,

the TSS of the most abundantly expressed transcript was used (based on bulk RNA data). The substitution rate values from all genes were aligned, based on their TSS position, and a mean for each of the 500 positions was calculated separately for the group of genes with high, medium and low response divergence. The two-sample Kolmogorov–Smirnov test was used to compare the paired distribution of rates between the means of the high-divergence and low-divergence sets of genes. To plot the mean values of the three sets of divergent genes, the *geom_smooth* function from the *ggplot2* R package was used with default parameters (with *loess* as the smoothing method) (Fig. 2b).

Human CGI annotations were downloaded from the UCSC genome table browser (hg38), and CGI genes were defined as those with a CGI overlapping their core promoter (300 bp upstream of the TSS reference position, and 100 bp downstream of it, as suggested previously¹⁸). Genes were defined as having a TATA box if they had a significant match to the Jaspur TATA box matrix (MA0108.1) in the 100 bp upstream of their TSS by FIMO⁶⁶ with default settings (we used a 100 bp window owing to possible inaccuracies in TSS annotations). We note that only 28 out of 955 dsRNA-responsive genes had a matching TATA-box motif in this region. For both TATA and CGI analyses, the promoter sequences of the human orthologues were used.

Read mapping and quality control of scRNA-seq (full-length RNA). Gene expression was quantified in a manner similar to the quantification for bulk transcriptomics libraries described above. Low-quality cells were filtered using quality control criteria (cells with at least 100,000 mapped reads, with at least 2,000 expressed genes with TPM > 3, with ERCC < 10% and MT < 40%, where ERCC and MT refer to reads mapped to synthetic RNA Spike-In genes and mitochondrial genes). This quality control filtering resulted in 240 cells from a first biological replicate, including two technical replicates (with a time course of 0, 4, 8 h). In a second larger biological replicate (with a dsRNA stimulation time course of 0, 2, 4, 8 h), 728 cells passed quality control. Results throughout the manuscript relate to the second cross-species biological replicate in which a higher proportion of cells passed QC, and the lower-quality first replicate data were not considered further.

Cell-to-cell variability analysis. To quantify the biological cell-to-cell variability of genes, we applied the DM (Distance to Median) approach—an established method, which calculates the cell-to-cell variability in gene expression while accounting for confounding factors such as gene expression level³⁰. This is done by first filtering out genes that are expressed at low levels: for Smart-seq2 data we included only genes that had an average expression of at least 10 size-factor normalized reads (except for Extended Data Fig. 9a, in which we reduced the threshold to 5, to allow a larger number of genes to be included in the comparisons). This procedure was done to filter genes that displayed higher levels of technical variability between samples owing to low expression. Second, to account for gene expression level, the observed cell-to-cell variability of each gene was compared with its expected variability, based on its mean expression across all samples and in comparison with a group of genes with similar levels of mean expression. This DM value is also corrected by gene length (in the case of Smart-seq2 data), yielding a value of variability that can be compared across genes regardless of their length and mean expression values⁶⁸. As a second approach, we used BASiCS^{69,70} (see Supplementary Information).

We note that the relationship observed in Fig. 3a between response divergence and cell-to-cell variability is not an artefact, stemming from differences in expression levels: (A) With respect to cell-to-cell variability, a gene's expression level is controlled for by DM calculations, where expression level is regressed by using a running median (Supplementary Fig. 14). (B) Similarly, we can regress the expression level measured in bulk RNA-seq from the quantified response divergence by subtracting the running median of expression from the divergence estimates. When repeating the analysis comparing cell-to-cell variability versus regressed response divergence, the relationship between the two is maintained (Supplementary Fig. 15).

Cytokine co-expression analysis. For the chemokine gene *CXCL10*, we built a network (using CytoScape⁷¹) of genes that correlate with *CXCL10* in dsRNA-stimulated human fibroblasts and in at least one more species, using genes with a Spearman correlation value above 0.3 (see Fig. 3d and Supplementary Information).

Coding sequence evolution analysis. The ratio dN/dS (non-synonymous to synonymous codon substitutions) of human genes across the mammalian clade was obtained from a previous study that used orthologous genes from 29 mammals⁷². Distributions of dN/dS values were computed for each of the three groups of genes with low, medium and high divergence in response to dsRNA, and are plotted in Fig. 4a.

Rate of gene gain and loss analysis. The significance at which a gene's family has experienced a higher rate of gene gain and loss in the course of vertebrate evolution, in comparison with other gene families, was retrieved from ENSEMBL⁷³. The statistics provided by ENSEMBL are calculated using the CAFE method⁷⁴, which estimates the global birth and death rate of gene families and identifies gene

families that have accelerated rates of gain and loss. Distributions of the *P* values from this statistic were computed for each of the three groups of genes with low, medium and high divergence in response to dsRNA and are plotted as the negative logarithm values in Fig. 4b.

Gene age analysis. Gene age estimations were obtained from ProteinHistorian⁷⁵. To ensure that the results were not biased by a particular method of ancestral protein family reconstruction or by specific gene family assignments, we used eleven different estimates for mammalian genes (combining five different databases of protein families with two different reconstruction algorithms for age estimation, as well as an estimate from the phylostratigraphic approach). For each gene, age was defined with respect to the species tree, where a gene's age corresponds to the branch in which its family is estimated to have appeared (thus, larger numbers indicate evolutionarily older genes).

Data for gene age in comparison with divergence in response to dsRNA are shown in Fig. 4c (using Panther7 phylogeny and Wagner reconstruction algorithm) and in Supplementary Fig. 17a (for all 11 combinations of gene family assignments and ancestral family reconstructions). See additional analyses in Supplementary Information.

Cellular protein–protein interaction analysis. Data on the number of experimentally validated PPIs for human genes were obtained from STRING (version 10)⁷⁶. Distributions of PPIs for genes with low, medium and high divergence in response to dsRNA are plotted in Fig. 4d.

Host–virus interaction analysis. Data on host–virus protein–protein interactions were downloaded from the VirusMentha database⁴³, and combined with two additional studies that have annotated host–virus protein–protein interactions^{6,44}. We split the 955 dsRNA-responsive genes into genes with known viral interactions (genes whose protein products were reported to interact with at least one viral protein), and genes with no known viral interactions: ‘viral interactors’ and ‘no viral interactions’, respectively, in Fig. 4e. In addition, we define a subset of genes within the viral interactors set: those known to interact with viral proteins that are immunomodulators (proteins known to target the host immune system and modulate its response⁴⁵).

We note that the results presented in Fig. 4e are in agreement with previous analyses that are based on all human genes and on coding sequence evolution⁴⁶. However, the overlap in the sets of genes between the previous analyses and the one presented here is small (for example, in one published study⁴⁶ there were 535 human genes with known interactions with pathogens, 57 of which overlap with the 955 genes that are the basis of the current analysis).

Additional experiments with human fibroblasts and human skin tissue.

Additional experiments were performed with human dermal fibroblasts and with cells extracted from human skin tissues to study in greater detail the relationship between response divergence across species and cell-to-cell variability. See Supplementary Methods and Supplementary Discussion for details.

Cross-species bone marrow-derived phagocyte stimulation with LPS and dsRNA.

Tissue culture. Primary bone marrow-derived mononuclear phagocytes originating from females of four different species (black 6 mouse, brown Norway rat, rabbit and pig) and cultured with GM-CSF, were obtained from PloBiotech. Twenty-four hours before the start of the stimulation time course, cells were thawed and split into 12-well plates (500,000 cells per well). Cells were stimulated with: (1) 100 ng/ml LPS (Invivogen, tlr-smpls), or with (2) 1 µg/ml high-molecular mass poly(I:C) (Invivogen, tlr-pic) transfected with 2 µl/ml Lipofectamin 2,000 (ThermoFisher, 11668027). LPS stimulation time courses of 0, 2, 4, 6 h were performed for all species. Poly(I:C) stimulations were performed for rodents for 0, 2, 4, 6 h. We also processed cells for bulk RNA-seq for 0 and 4 h stimulation time points. Details on the individuals used in each technique are listed in Supplementary Table 2.

Library preparation for single cells using microfluidic droplet cell capture. Following stimulation, cells were collected using Cell Dissociation Solution Non-enzymatic (Sigma-Aldrich, C5914), washed and resuspended in 1 × PBS with 0.5% (w/v) BSA. Cells were then counted and loaded on the 10x Chromium machine aiming for a targeted cell recovery of 5,000 cells according to the manual. Libraries were prepared following the Chromium Single Cell 3' v2 Reagent Kit Manual⁷⁷. Libraries were sequenced on an Illumina HiSeq 4000 instrument with 26 bp for read 1 and 98 bp for read 2.

Library preparation and sequencing for bulk RNA-seq. Total RNA was extracted and libraries were prepared as described in the fibroblasts section. Pooled samples were sequenced on an Illumina HiSeq 4000 instrument, using paired-end 75-bp reads. **Quantifying gene expression in bulk RNA-seq data.** Adaptor sequences and low-quality score bases were trimmed using Trim Galore (version 0.4.1). Trimmed reads were mapped and gene expression was quantified using Salmon: (version 0.9.1)⁵⁴ with the following command: ‘salmon quant -i [index_file_directory] / -l ISR -p 8 -seqBias -gcBias -posBias -q -o [output_directory] -l -g [ENSEMBL_transcript_to_gene_file] -useVBOpt -numBootstraps 100’. Mouse samples were mapped to mouse transcriptome (ENSEMBL, version 84). We note that we used

the bulk data only for TSS analysis. For differential expression analysis, we used an in silico bulk from the single-cell data (see below).

Quantifying gene expression in microfluidic droplet cell capture data. Microfluidic droplet cell capture data was first quantified using 10x Genomics' Cell Ranger Single-Cell Software Suite (version 2.0, 10x Genomics Inc.)⁷⁷ against the relevant genome (ENSEMBL, version 84). We removed cells with fewer than 200 genes or more than 10% mitochondrial reads. To remove potential doublets, we excluded the top 10% of cells expressing the highest numbers of genes. Genes expressed in less than 0.5% of the cells were excluded from the calculations. We then filtered cells that expressed fewer than 10% of the total number of filtered genes.

Since bone marrow-derived phagocytes may include secondary cell populations, we focused our analysis on the major cell population. We identified clusters within each data set, using the Seurat⁷⁸ functions RunPCA, followed by FindClusters (using 20 dimensions from the PCA, default perplexity and a resolution of 0.1) and have taken the cells belonging to the largest cluster for further analysis, resulting in a less heterogeneous population of cells. A lower resolution of 0.03 was used for rabbit-LPS4, rabbit-LPS2, mouse-PIC2, mouse-PIC4; and 0.01 for rabbit-LPS6.

Quantifying gene expression divergence in response to immune challenge. We created an in silico bulk table by summing up the UMIs of the post-QC single cells belonging to the largest cluster of cells, in each of the samples. We then used the three replicates in unstimulated conditions and in 4 h LPS stimulation to perform a differential expression analysis using DESeq2⁷⁹ Wald test, and *P* values were adjusted for multiple testing by estimating the FDR. A similar procedure was performed with mouse and rat dsRNA stimulation (with 4 h dsRNA stimulation versus unstimulated conditions).

To quantify transcriptional divergence in immune response between species, we focused on genes that have annotated one-to-one orthologues across the studied species.

We define a measure of response divergence by calculating the differences between the fold-change estimates across the orthologues: response divergence = $\log[1/3 \times \sum_i (\log[\text{FC pig}] - \log[\text{FC glire}_i])^2]$. For each gene, the fold-change in the outer group (pig), is subtracted from the fold-change in the orthologues of the three glires (mouse, rat and rabbit), and the average of the square values of these subtractions is taken as the response divergence measure. In most of the analyses, we focus on the 2,336 LPS-responsive genes—genes that are differentially expressed in response to LPS (genes that have an FDR-corrected *P* < 0.01 in mouse, and have annotated one-to-one orthologues in the other three species).

Promoter elements, gene function and cell-to-cell variability analyses. Promoter elements (TATA and CGIs), gene function and cell-to-cell variability analyses were performed as described in the fibroblasts section. Mouse genes were used as the reference for gene function and TSS annotations. For variability analysis, we used one representative replicate out of three.

Statistical analysis and reproducibility. Statistical analyses were done with R version 3.3.2 for Fisher's exact test, two-sample Kolmogorov–Smirnov test and Mann–Whitney test. Data in boxplots represent the median, first quartile and third quartile with lines extending to the furthest value within 1.5 of the interquartile range (as implemented by the R function `geom_boxplot`). Violin plots show the kernel probability density of the data (as implemented by the R function `geom_violin`).

All cross-species bulk RNA-seq replicates were successful, except for one macaque individual in which the treated sample had a low RNA quality and was removed from the analysis (along with the matching control). All cross-species ChIP-seq replicates were successful. Cross-species scRNA-seq of fibroblasts was performed in two biological replicates. Results throughout the manuscript relate to the second cross-species biological replicate, for which a higher proportion of cells passed technical quality control. Three out of three replicates for each species and condition were successful when preparing single-cell libraries for mononuclear phagocytes, except for two libraries that failed at the emulsion preparation stage. Two out of two replicates of single-cell in situ RNA hybridization assay were performed and both are shown.

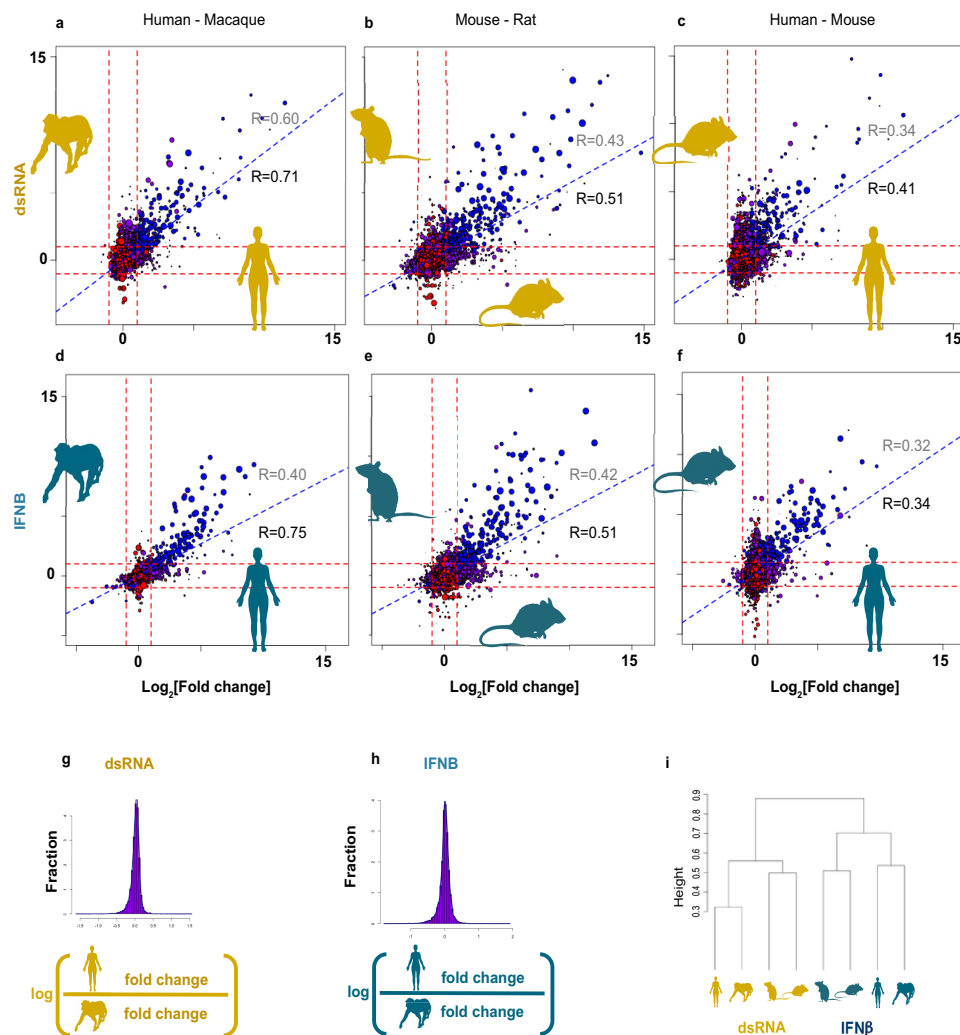
Reporting summary. Further information on research design is available in the Nature Research Reporting Summary linked to this paper.

Code availability. Scripts for major analyses are available at https://github.com/Teichlab/innate_evo.

Data availability

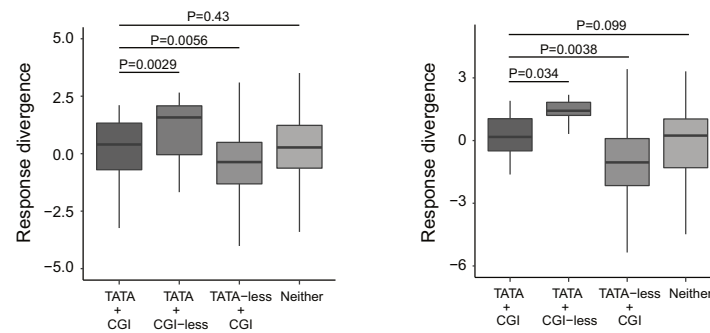
Sequencing data have been deposited in ArrayExpress with the following accessions: E-MTAB-5918, E-MTAB-5919, E-MTAB-5920, E-MTAB-6754, E-MTAB-6773, E-MTAB-5988, E-MTAB-5989, E-MTAB-6831, E-MTAB-6066, E-MTAB-7032, E-MTAB-7037, E-MTAB-7051 and E-MTAB-7052.

- Kilpinen, H. et al. Common genetic variation drives molecular heterogeneity in human iPSCs. *Nature* **546**, 370–375 (2017).
- Schmidl, C., Rendeiro, A. F., Sheffield, N. C. & Bock, C. ChIPmentation: fast, robust, low-input ChIP-seq for histones and transcription factors. *Nat. Methods* **12**, 963–965 (2015).
- Picelli, S. et al. Full-length RNA-seq from single cells using Smart-seq2. *Nat. Protocols* **9**, 171–181 (2014).
- Patro, R., Duggal, G., Love, M. I., Irizarry, R. A. & Kingsford, C. Salmon provides fast and bias-aware quantification of transcript expression. *Nat. Methods* **14**, 417–419 (2017).
- Robinson, M. D., McCarthy, D. J. & Smyth, G. K. edgeR: a Bioconductor package for differential expression analysis of digital gene expression data. *Bioinformatics* **26**, 139–140 (2010).
- Nourmohammad, A. et al. Adaptive evolution of gene expression in *Drosophila*. *Cell Reports* **20**, 1385–1395 (2017).
- Zhang, H. M. et al. AnimalTFDB: a comprehensive animal transcription factor database. *Nucleic Acids Res.* **40**, D144–D149 (2012).
- Binns, D. et al. QuickGO: a web-based tool for Gene Ontology searching. *Bioinformatics* **25**, 3045–3046 (2009).
- Kent, W. J. et al. The human genome browser at UCSC. *Genome Res.* **12**, 996–1006 (2002).
- Langmead, B. & Salzberg, S. L. Fast gapped-read alignment with Bowtie 2. *Nat. Methods* **9**, 357–359 (2012).
- Li, H. et al. The sequence alignment/map format and SAMtools. *Bioinformatics* **25**, 2078–2079 (2009).
- Zhang, Y. et al. Model-based analysis of ChIP-Seq (MACS). *Genome Biol.* **9**, R137 (2008).
- Quinlan, A. R. & Hall, I. M. BEDTools: a flexible suite of utilities for comparing genomic features. *Bioinformatics* **26**, 841–842 (2010).
- Kuhn, R. M. et al. The UCSC genome browser database: update 2007. *Nucleic Acids Res.* **35**, D668–D673 (2007).
- Mathelier, A. et al. JASPAR 2016: a major expansion and update of the open-access database of transcription factor binding profiles. *Nucleic Acids Res.* **44**, D110–D115 (2016).
- Grant, C. E., Bailey, T. L. & Noble, W. S. FIMO: scanning for occurrences of a given motif. *Bioinformatics* **27**, 1017–1018 (2011).
- Pollard, K. S., Hubisz, M. J., Rosenbloom, K. R. & Siepel, A. Detection of nonneutral substitution rates on mammalian phylogenies. *Genome Res.* **20**, 110–121 (2010).
- Kolodziejczyk, A. A. et al. Single cell RNA-sequencing of pluripotent states unlocks modular transcriptional variation. *Cell Stem Cell* **17**, 471–485 (2015).
- Vallejos, C. A., Marioni, J. C. & Richardson, S. BASiCS: Bayesian analysis of single-cell sequencing data. *PLOS Comput. Biol.* **11**, e1004333 (2015).
- Martinez-Jimenez, C. P. et al. Aging increases cell-to-cell transcriptional variability upon immune stimulation. *Science* **355**, 1433–1436 (2017).
- Smoot, M. E., Ono, K., Ruscheinski, J., Wang, P. L. & Ideker, T. Cytoscape 2.8: new features for data integration and network visualization. *Bioinformatics* **27**, 431–432 (2011).
- Lindblad-Toh, K. et al. A high-resolution map of human evolutionary constraint using 29 mammals. *Nature* **478**, 476–482 (2011).
- Herrero, J. et al. Ensembl comparative genomics resources. *Database* **2016**, bav096 (2016).
- De Bie, T., Cristianini, N., Demuth, J. P. & Hahn, M. W. CAFE: a computational tool for the study of gene family evolution. *Bioinformatics* **22**, 1269–1271 (2006).
- Capra, J. A., Williams, A. G. & Pollard, K. S. ProteinHistorian: tools for the comparative analysis of eukaryote protein origin. *PLOS Comput. Biol.* **8**, e1002567 (2012).
- Szklarczyk, D. et al. STRING v10: protein-protein interaction networks, integrated over the tree of life. *Nucleic Acids Res.* **43**, D447–D452 (2015).
- Zheng, G. X. et al. Massively parallel digital transcriptional profiling of single cells. *Nat. Commun.* **8**, 14049 (2017).
- Satija, R., Farrell, J. A., Gennert, D., Schier, A. F. & Regev, A. Spatial reconstruction of single-cell gene expression data. *Nat. Biotechnol.* **33**, 495–502 (2015).
- Love, M. I., Huber, W. & Anders, S. Moderated estimation of fold-change and dispersion for RNA-seq data with DESeq2. *Genome Biol.* **15**, 550 (2014).



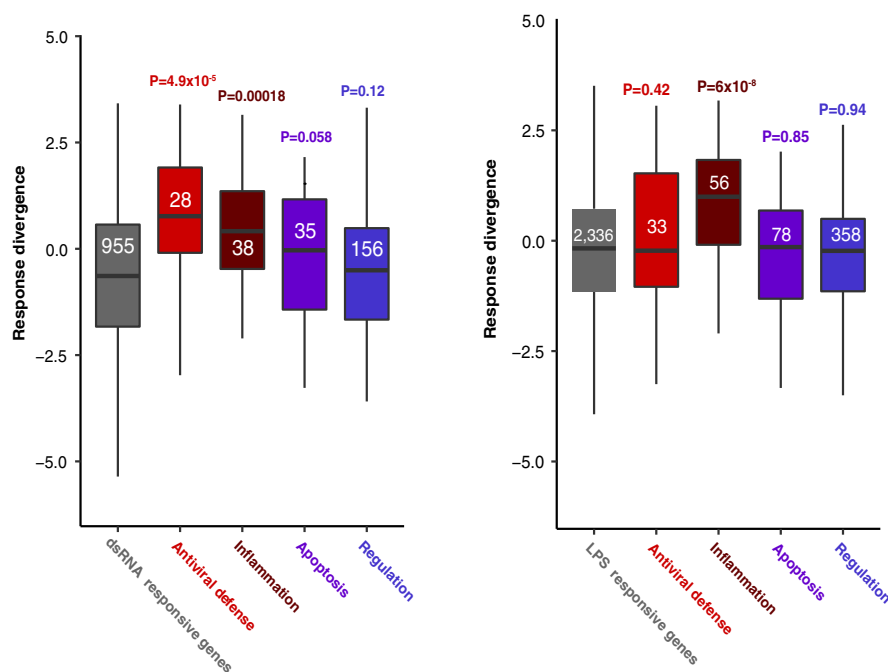
Extended Data Fig. 1 | Fibroblast response to dsRNA and IFNβ across species. To study the similarity in response to treatment across species, we plotted the fold-change values of all expressed genes (with one-to-one orthologues) between pairs of species (human-macaque, mouse-rat and human-mouse) in response to dsRNA (poly(I:C)) (**a-c**). As a control, we performed the same procedure with IFNβ stimulations (**d-f**). Fold-changes were inferred from differential expression analyses, determined by the exact test in the edgeR package⁶ and based on $n = 6, 5, 3$ and 3 individuals from human, macaque, rat and mouse, respectively. Spearman correlations between all expressed one-to-one orthologues are shown in grey, Spearman correlations between the subset of differentially expressed

genes (FDR-corrected $P < 0.01$ in at least one species) appear in black. Number of genes shown is $n = 11,035, 11,005, 11,137, 10,851, 10,826$ and $10,957$ in **a-f**, respectively. Genes are coloured blue if they were differentially expressed (FDR-corrected $P < 0.01$) in both species, purple if they were differentially expressed in only one species, or red if they were not differentially expressed. **g, h**, Density plots of ratio of fold-change in response to dsRNA or to IFNβ. **g**, Comparison between human and macaque orthologues in dsRNA response. **h**, Comparison between human and mouse orthologues in IFNβ response. **i**, Dendrogram based on the fold-change in response to dsRNA or to IFNβ across 9,835 one-to-one orthologues in human, macaque, rat and mouse.



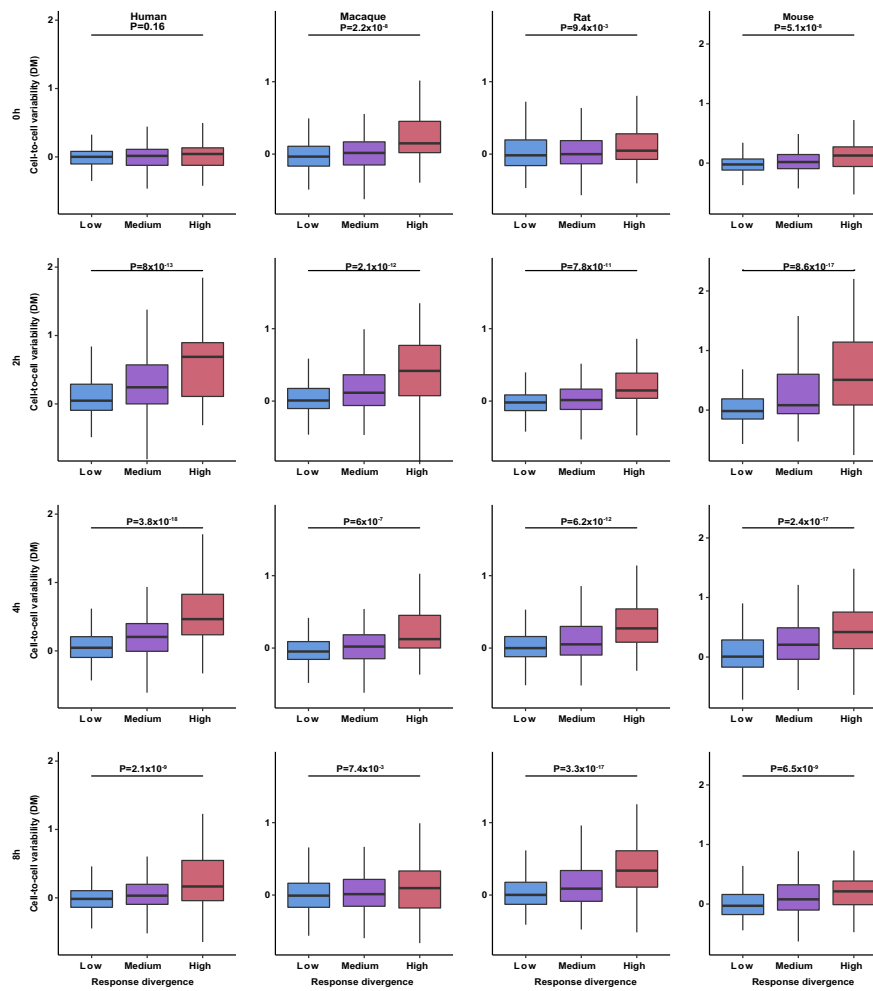
Extended Data Fig. 3 | Comparison of response divergence of genes containing various promoter elements. Comparison of response divergence between genes with and without a TATA-box and a CGI. Left, fibroblasts ($n = 14, 14, 633$ and 294 differentially expressed genes with only TATA-box element, with both CGI and TATA-box elements, with only CGI, and with neither element in their promoters, respectively); right, phagocytes ($n = 13, 29, 1,718$ and 576 differentially expressed genes with only a TATA-box element, with both CGI and TATA-box elements, with

only a CGI, and with neither element in their promoters, respectively). Genes with a TATA-box without a CGI have higher response divergence than genes with both elements. Genes with a CGI but without a TATA-box diverge more slowly than genes with both elements. Genes with both elements do not differ significantly in their divergence from genes lacking both elements (one-sided Mann–Whitney test). Data in boxplots represent the median, first quartile and third quartile with lines extending to the furthest value within 1.5 of the IQR.



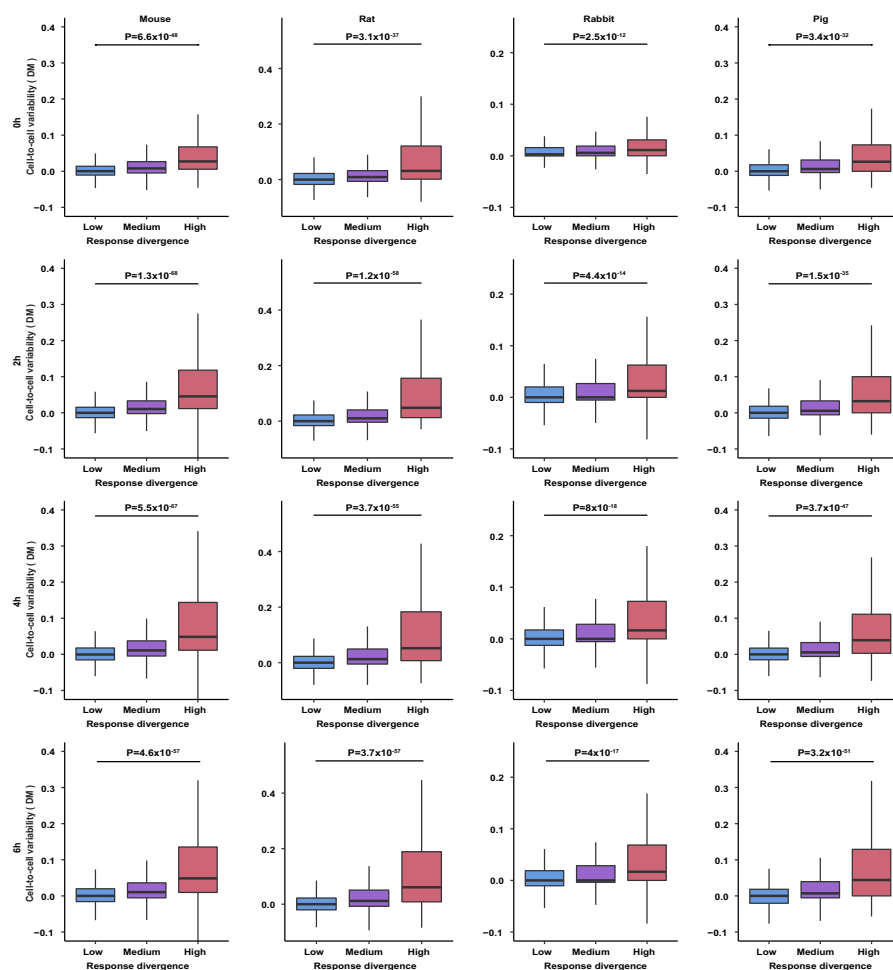
Extended Data Fig. 4 | Response divergence of molecular processes upregulated in immune response. Left, distributions of divergence values of $n = 955$ dsRNA-responsive genes in fibroblasts and subsets of this group belonging to different biological processes. For each functional subset, the distribution of divergence values is compared with the set of 955 dsRNA-responsive genes using a one-sided Mann–Whitney test. FDR-corrected P values are shown above each group and group size is shown inside each box. Right, distributions of divergence values of $n = 2,336$ LPS-responsive

genes in mononuclear phagocytes and subsets of this group belonging to different biological processes. For each functional subset, the distribution of divergence values is compared with the set of 2,336 LPS-responsive genes. FDR-corrected P values (one-sided Mann–Whitney test) are shown above each group and group size is shown inside each box. Data in boxplots represent the median, first quartile and third quartile with lines extending to the furthest value within 1.5 of the IQR.



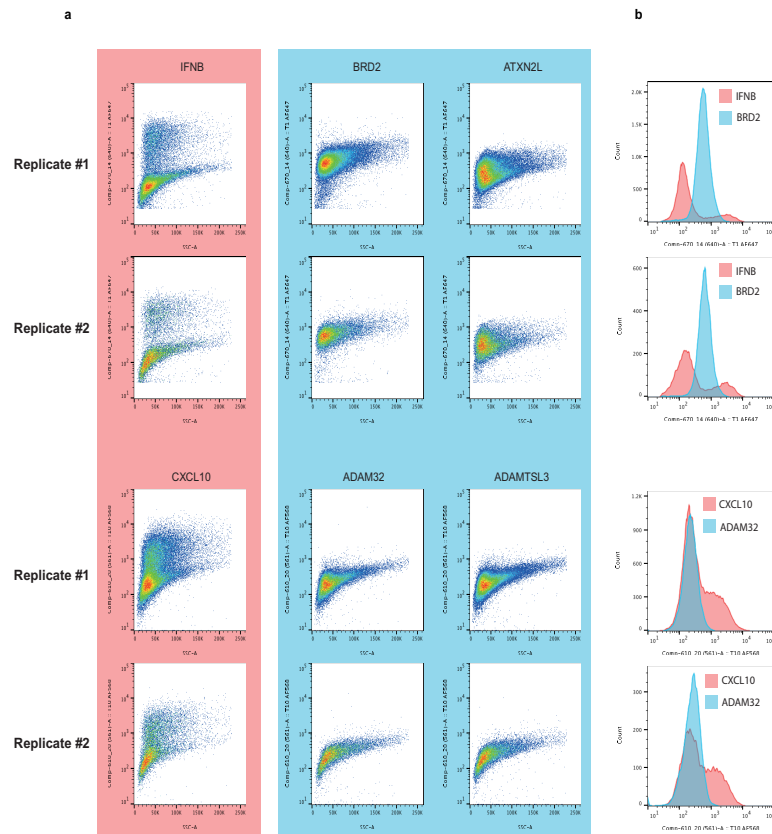
Extended Data Fig. 5 | Cell-to-cell variability versus response divergence across species and conditions in fibroblasts after dsRNA stimulation. Cell-to-cell variability values, as measured with DM across individual cells, compared with response divergence between species (grouped into low, medium and high divergence). Variability values are based on $n = 29, 56, 55, 35$ human cells, $n = 20, 32, 29, 13$ rhesus cells, $n = 33, 70, 65, 40$ rat cells, and $n = 53, 81, 59, 30$ mouse cells, stimulated

with dsRNA for 0, 2, 4 and 8 h, respectively. Rows represent different dsRNA stimulation time points (0, 2, 4 and 8 h), and columns represent different species as shown. High-divergence genes were compared with low-divergence genes using a one-sided Mann–Whitney test. Data in boxplots represent the median, first quartile and third quartile with lines extending to the furthest value within 1.5 of the IQR.



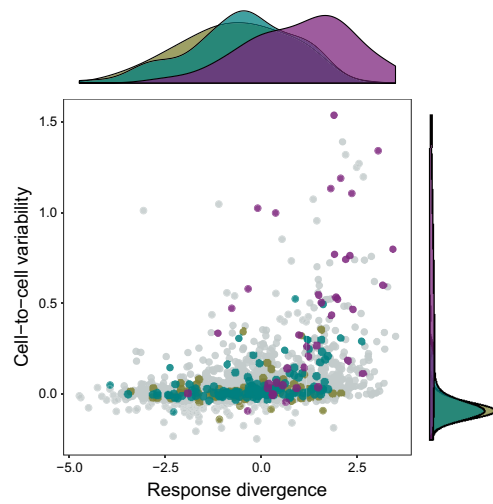
Extended Data Fig. 6 | Cell-to-cell variability versus response divergence across species and conditions in mononuclear phagocytes after LPS stimulation. Cell-to-cell variability values, as measured with DM across cells, compared with response divergence between species (grouped into low, medium and high divergence). Variability values are based on $n = 3,519, 4,321, 3,293, 2,126$ mouse cells, $n = 2,266, 2,839, 1,963, 1,607$ rat cells, $n = 3,275, 1,820, 1,522, 1,660$ rabbit cells, and $n = 1,748,$

1,614, 1,899, 1,381 pig cells, stimulated with LPS for 0, 2, 4 and 6 h, respectively. Rows represent different LPS stimulation time points (0, 2, 4 and 6 h), and columns represent different species as shown. High-divergence genes were compared with low-divergence genes using a one-sided Mann–Whitney test. Data in boxplots represent the median, first quartile and third quartile with lines extending to the furthest value within 1.5 of the IQR.

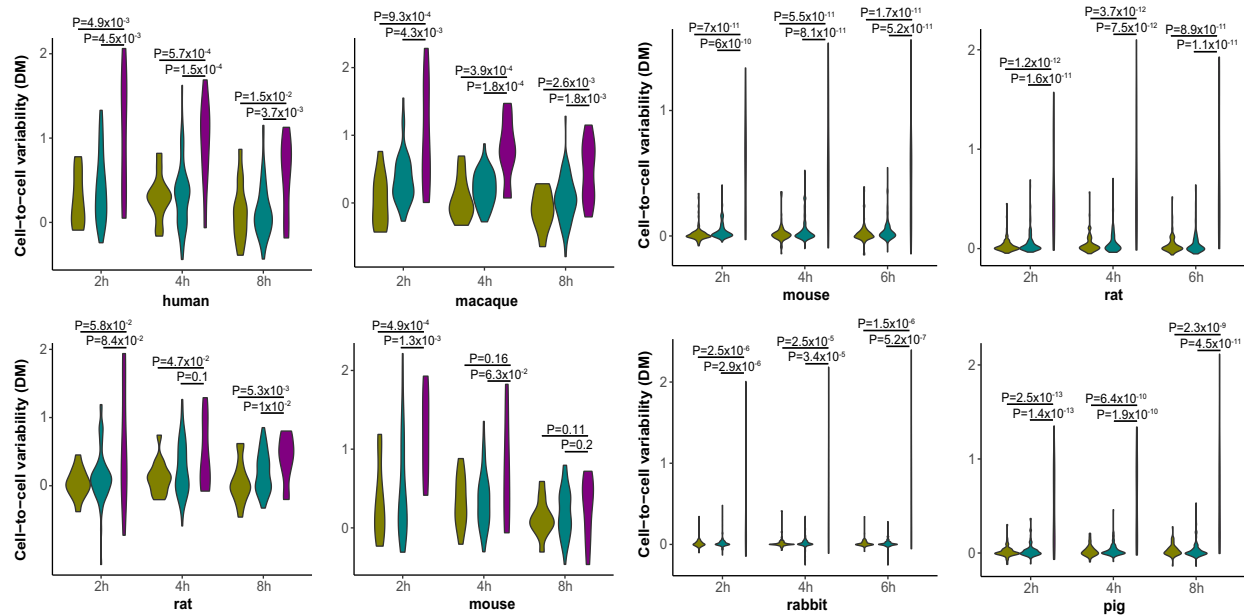


Extended Data Fig. 7 | Cell-to-cell variability of cytokine expression in single cell in situ RNA hybridization assay combined with flow cytometry (PrimeFlow). PrimeFlow measurement of two cytokine genes (*IFNB* and *CXCL10*) that show high cell-to-cell variability in scRNA-seq. As controls, two genes matched on expression levels (*ATXN2L* and *ADAM32*) but that show low cell-to-cell variability in scRNA-seq data are shown. As the expression of cytokines is at the low end of the distribution, we also chose two genes with middle-range expression values (*ADAMTSL3* and *BRD2*) as additional controls. The experiment was performed in $n = 2$ independent replicates, originating from the same individual. Both replicates are shown. **a**, Pseudocolour contour plot for RNA target expression in dsRNA-stimulated human fibroblasts. The x-axis

shows area of side scatter (SSC-A) and the y-axis shows fluorescent signal for target RNA probes. RNA targets detected by the same fluorescent channel are displayed together. Top, *IFNB* and control genes *BRD2* and *ATXN2L*, type 1 probe, Alexa FluorTM 647. Bottom, *CXCL10* and control genes *ADAMTSL3* and *ADAM32*, type 10 probe, Alexa FluorTM 568. The cytokine genes display a broader range of fluorescence signal than the controls. **b**, Histograms comparing fluorescence of cytokine and control pairs (*IFNB*–*BRD2* for type 1 probe and *CXCL10*–*ADAM32* for type 10 probe). The histograms show a bimodal distribution of expression signal for the two cytokine genes (*IFNB* and *CXCL10*, red), but not for controls (blue). This agrees with scRNA-seq data in which *CXCL10* and *IFNB* display high levels of cell-to-cell variability.

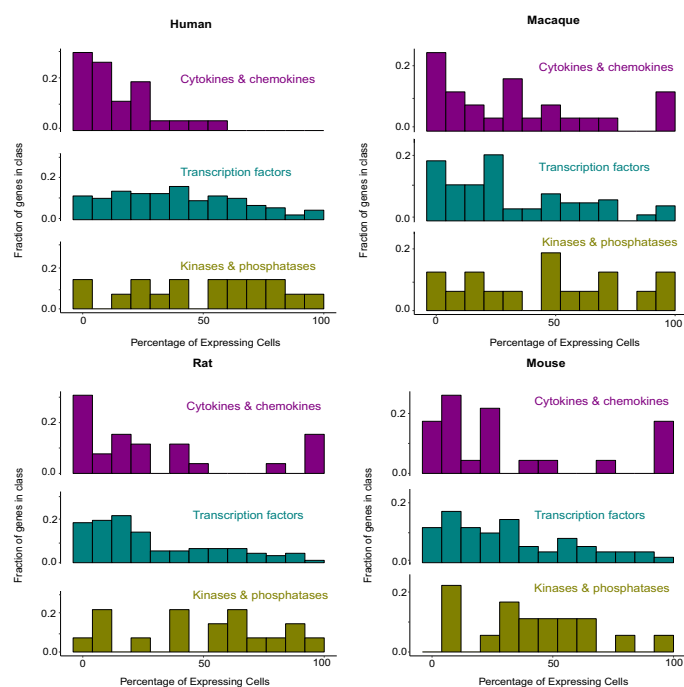


Extended Data Fig. 8 | Cell-to-cell variability levels and response divergence of cytokines, transcription factors and kinases in response to LPS stimulation of phagocytes. A scatter plot showing divergence in response to LPS across species and transcriptional cell-to-cell variability in mouse mononuclear phagocytes following 4 h of LPS treatment, in $n = 2,262$ LPS-responsive genes. Purple, cytokines; green, transcription factors; beige, kinases. The distributions of divergence values and cell-to-cell variability values of each of the three functional groups are shown above and to the right of the scatter plot, respectively.



Extended Data Fig. 9 | Cell-to-cell variability levels in cytokines, transcription factors and kinases across species and stimulation time points. Violin plots showing the distribution of cell-to-cell variability values (DM) of cytokines, transcription factors and kinases during immune stimulation. Left, fibroblast dsRNA stimulation time course. Number of cells used in each species (at 2, 4, 8 h dsRNA, respectively): human, 56, 55, 35; macaque, 32, 29, 13; rat, 70, 65, 40; mouse, 81, 59, 30.

Right, phagocyte LPS stimulation time course. Number of cells used in each species (at 2, 4, 6 h LPS, respectively): mouse, 4,321, 3,293, 2,126; rat, 2,839, 1,963, 1,607; rabbit, 1,820, 1,522, 1,660; pig, 1,614, 1,899, 1,381. For both panels, colours as in Fig. 3c. Comparisons between groups of genes were performed using one-sided Mann–Whitney tests. Violin plots show the kernel probability density of the data.



Extended Data Fig. 10 | Percentage of cells expressing cytokines, transcription factors and kinases. Histograms showing the percentage of fibroblasts expressing cytokines (top), transcription factors (middle) and kinases (bottom) following 4 h dsRNA stimulation, in human, macaque, rat and mouse cells (based on $n = 55, 29, 65$ and 59 cells, respectively).

The percentage of expressing cells is divided into 13 bins (x -axis). The y -axis represents the fraction of genes from this gene class (for example, cytokines) that are expressed in each bin (for example, in human, nearly 30% of the cytokine genes (y -axis) are expressed in the first bin, corresponding to expression in fewer than 8% of cells).

Active superelasticity in three-dimensional epithelia of controlled shape

Ernest Latorre^{1,2}, Sohan Kale², Laura Casares¹, Manuel Gómez-González¹, Marina Uroz¹, Léo Valon¹, Roshna V. Nair³, Elena Garreta¹, Nuria Montserrat^{1,4}, Aránzazu del Campo^{3,5}, Benoit Ladoux^{6,7}, Marino Arroyo^{1,2,*} & Xavier Trepat^{1,4,8,9*}

Fundamental biological processes are carried out by curved epithelial sheets that enclose a pressurized lumen. How these sheets develop and withstand three-dimensional deformations has remained unclear. Here we combine measurements of epithelial tension and shape with theoretical modelling to show that epithelial sheets are active superelastic materials. We produce arrays of epithelial domes with controlled geometry. Quantification of luminal pressure and epithelial tension reveals a tensional plateau over several-fold areal strains. These extreme strains in the tissue are accommodated by highly heterogeneous strains at a cellular level, in seeming contradiction to the measured tensional uniformity. This phenomenon is reminiscent of superelasticity, a behaviour that is generally attributed to microscopic material instabilities in metal alloys. We show that in epithelial cells this instability is triggered by a stretch-induced dilution of the actin cortex, and is rescued by the intermediate filament network. Our study reveals a type of mechanical behaviour—which we term active superelasticity—that enables epithelial sheets to sustain extreme stretching under constant tension.

Epithelial tissues enable key physiological functions, including morphogenesis, transport, secretion and absorption¹. To perform these functions, epithelia often adopt a three-dimensional (3D) architecture that consists of a curved cellular sheet enclosing a pressurized fluid-filled lumen^{2,3}. The loss of this 3D architecture is associated with developmental defects, inflammatory conditions and cancer^{4,5}.

The acquisition of a 3D shape by epithelial sheets requires a tight control of cellular deformation, mechanical stress and luminal pressure. How these mechanical variables are tuned together to sculpt 3D epithelia is unknown, because current techniques to map epithelial mechanics are largely restricted to two-dimensional (2D) layers seeded on a flat substrate^{6,7} or freely standing between cantilevers⁵. Here we report direct measurements of traction, tension, pressure and deformation in 3D epithelial monolayers of controlled size and shape. These measurements establish that epithelial monolayers exhibit active superelasticity, an unanticipated mechanical behaviour that enables extreme deformations at nearly constant tension.

Micropatterned epithelial domes

We used transmural pressure as the morphogenetic driving force to shape epithelial monolayers in 3D. We seeded Madin-Darby canine kidney (MDCK) cells on a soft polydimethylsiloxane (PDMS) substrate that was homogeneously coated with fibronectin except for micropatterned, non-adhesive areas of precise geometry (Fig. 1a). A few hours after seeding, cells covered the adherent regions of the gel, and with time they invaded the non-adherent areas^{8,9}. Because MDCK cells are known to actively pump osmolites in the apico-basal direction^{10,11}, we reasoned that fluid pressure should build up in the interstitial space between cells and the impermeable substrate, which would lead to tissue delamination from the substrate in the non-adherent regions. Consistent with this rationale, we observed the spontaneous formation of multicellular epithelial domes that closely followed micropatterned shapes, such as circles, rectangles and stars (Fig. 1b–e, Extended Data

Fig. 1a–d). In contrast to spontaneous doming by delamination^{10,11}, our control of the dome footprint gave us access to large variations in the dome aspect ratio (Fig. 1c–e).

Measurement of dome mechanics

To measure dome mechanics, we focused on circular patterns and implemented 3D traction microscopy to determine the three components of tractions at the surface of the PDMS substrate (Fig. 2a, b). Traction in adherent regions showed large fluctuations without a clear spatial pattern (Fig. 2b). By contrast, non-adherent areas exhibited systematic normal and nearly uniform negative tractions that indented the substrate. In a narrow annular region at the margin of the dome footprint, the traction vector consistently exhibited a positive normal component that pulled the substrate upward. These observations—along with the morphology of the domes—established that the lumen was in a state of hydrostatic pressure, and that the free-standing part of the monolayer sustained tension to balance this pressure (Fig. 2a).

We then wondered whether we could map the tensional state of the dome, even though constituent cells did not directly generate tractions on the substrate. Epithelial domes followed a spherical cap geometry very closely (Fig. 2b), which implies that their surface tension (σ) was isotropic, uniform and obeyed Laplace's law ($2\sigma = R \times \Delta P$, where ΔP is the transmural pressure and R the radius of curvature of the dome; see Supplementary Note 1). This equation enabled us to measure the epithelial tension of the domes, as the normal traction in the non-adherent regions provides a direct readout of ΔP and R could be measured from confocal stacks. We found tissue tensions in the millinewton per metre range, similar to previous measurements in 2D monolayers^{5,7}.

To test the principle behind our tension measurement, we perturbed the system with the Rho kinase inhibitor Y-27632, which is known to reduce tissue tension. Because the epithelial barrier has finite permeability to water, the enclosed volume—and hence R —cannot change

¹Institute for Bioengineering of Catalonia (IBEC), The Barcelona Institute for Science and Technology (BIST), Barcelona, Spain. ²LaCàN, Universitat Politècnica de Catalunya-BarcelonaTech, Barcelona, Spain. ³INM-Leibniz Institut für Neue Materialien, Saarbrücken, Germany. ⁴Centro de Investigación Biomédica en Red en Bioingeniería, Biomateriales y Nanomedicina, Barcelona, Spain. ⁵Chemistry Department, Saarland University, Saarbrücken, Germany. ⁶CNRS UMR 7592, Institut Jacques Monod (IJM), Université Paris Diderot, Paris, France. ⁷Mechanobiology Institute (MBI), National University of Singapore, Singapore, Singapore. ⁸Unitat de Biofísica i Bioenginyeria, Universitat de Barcelona, Barcelona, Spain. ⁹Institució Catalana de Recerca i Estudis Avançats (ICREA), Barcelona, Spain. *e-mail: marino.arroyo@upc.edu; xtrepat@ibecbarcelona.eu

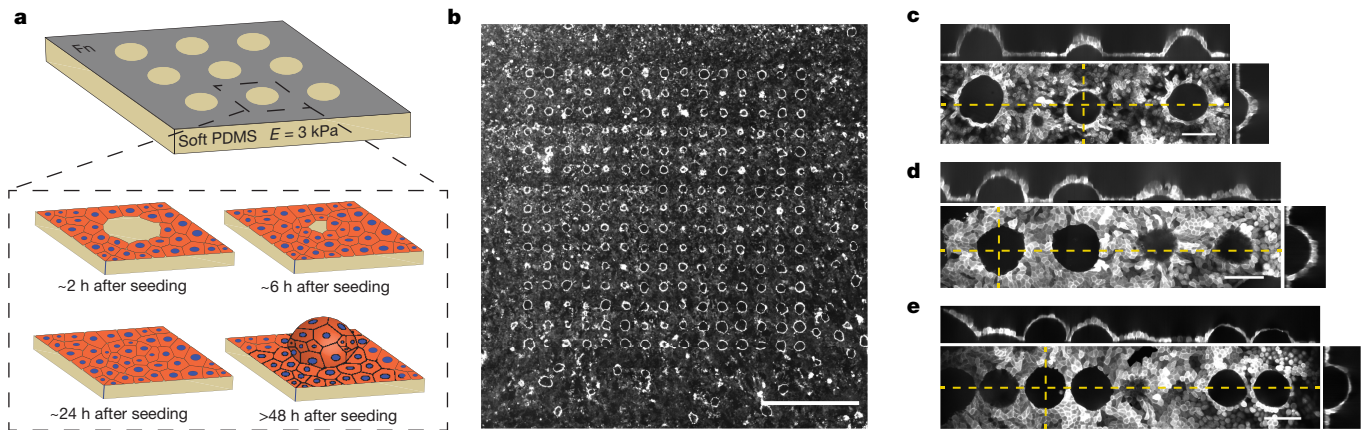


Fig. 1 | Generation of epithelial domes of controlled size and shape.

a, Scheme of the process of dome formation. **b**, Top view of an array of 15×15 epithelial domes ($n = 10$). Scale bar, 1 mm. **c–e**, Confocal x - y , y - z

and x - z sections of MDCK–LifeAct epithelial domes (see ‘Cell culture’ in Methods) with a circular basal shape and varying spacing ($n = 10$). Scale bar, 100 μm .

instantaneously upon this perturbation. Consequently, Laplace’s law requires that tension relaxation be paralleled by a pressure drop. This prediction was confirmed by our measurements (Fig. 2c–g, Extended Data Fig. 2a–c, Supplementary Video 1). We also examined water transport by subjecting domes to hyper-osmotic shocks (Supplementary Note 2). Volume dynamics under osmotic perturbations were consistent with a simple physical picture in which the epithelium behaves in a manner similar to a semi-permeable membrane actively pumping osmolites at nearly constant rate.

Constitutive relation between dome tension and strain

In the absence of pharmacological or osmotic perturbations and over timescales of hours, epithelial domes exhibited large volume fluctuations (Fig. 3a, Supplementary Video 2). These fluctuations involved periods of slow swelling and de-swelling combined with sudden volume drops, often up to total dome collapse and subsequent rebirth. The magnitude of collapse events, presumably caused by localized disruptions of epithelial integrity, and the duration of swelling phases exhibited high variability (Fig. 3a, b, Extended Data Fig. 3). During these spontaneous fluctuations, we tracked luminal pressure and dome geometry, which provided a measurement of epithelial tension at different degrees of swelling (Fig. 3c–e, Supplementary Video 2). To examine these data, we represented tension in the free-standing tissue as a function of nominal areal strain of the dome $\varepsilon_d = (h/a)^2$, which is defined as the difference between the actual area of the dome $\pi(h^2 + a^2)$ and the area of the non-adhesive region πa^2 , normalized by the latter (see Fig. 2b for a definition of h and a). All domes exhibited tensions of about 1 mN m^{-1} at small strains. At moderate strains (below 100%), tension progressively increased according to a highly reproducible law. Beyond this point, tension exhibited larger scatter but reached a plateau at about 2 mN m^{-1} for areal strains up to 300% (Fig. 3e, Extended Data Fig. 4a). The existence of this plateau is notable, as it reveals that epithelial domes maintain tensional homeostasis while undergoing deformations that change their area by up to fourfold. Human epithelial colorectal adenocarcinoma (Caco-2) cells showed a plateau at similar tension but lower strain (Extended Data Fig. 4b, c; see Supplementary Table 1 for a list of cell lines known to form domes).

A number of mechanisms could contribute to such tensional homeostasis, including directed¹² or accelerated¹³ cell division, junctional network rearrangements¹⁴, and cell exchange between domes and the adjacent adhered tissue. Visual examination of the domes showed that cell division and extrusion were rare (Supplementary Videos 3, 4). Moreover, the number of cells in the dome remained constant during the several-fold increases in dome area (Extended Data Fig. 1f).

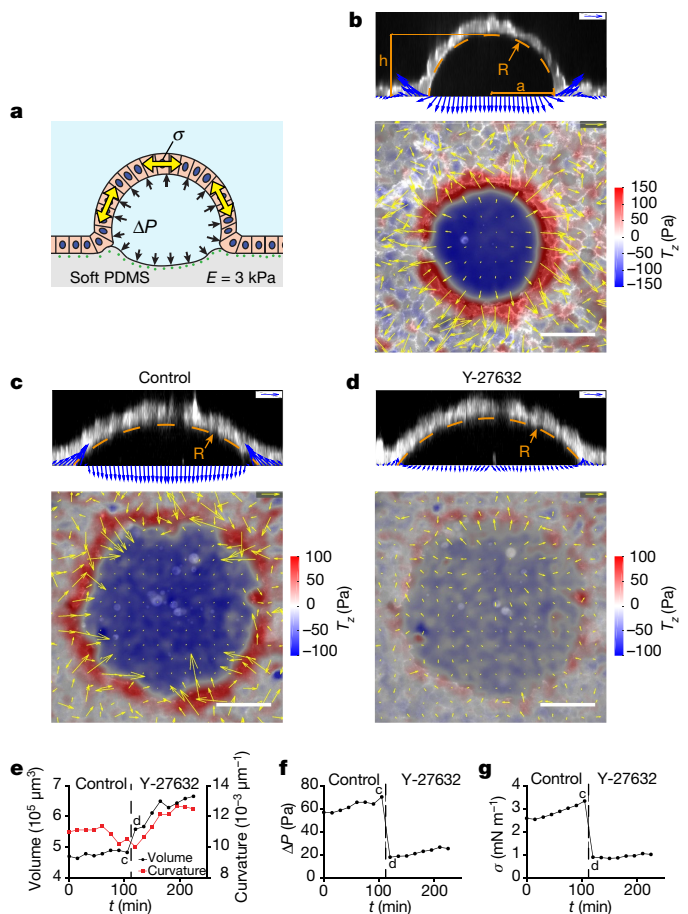


Fig. 2 | Measurement of luminal pressure and dome tension. **a**, Scheme of dome mechanics. The lumen is under uniform pressure ΔP (black arrows) and the free-standing monolayer is under surface tension σ (yellow arrows). **b**, Traction vectors of a dome of MDCK–LifeAct cells. Top, lateral view. Bottom, 3D traction maps overlaid on a top view of the dome. Yellow arrows represent in-plane components and the colour map represents the vertical component. Scale bar, 50 μm . Scale arrows, 150 Pa (representative of $n = 13$ domes). **c**, **d**, Traction vectors exerted by MDCK–LifeAct cells before (control) and after a 5-min incubation with $30 \mu\text{M}$ of Y-27632. Scale bar, 50 μm . Scale arrows, 75 Pa. **e–g**, Time evolution of dome volume and curvature (**e**), pressure (**f**) and tension (**g**) before (control) and after adding Y-27632. The time points corresponding to **c**, **d** are labelled in **e–g** (representative of $n = 3$ domes).

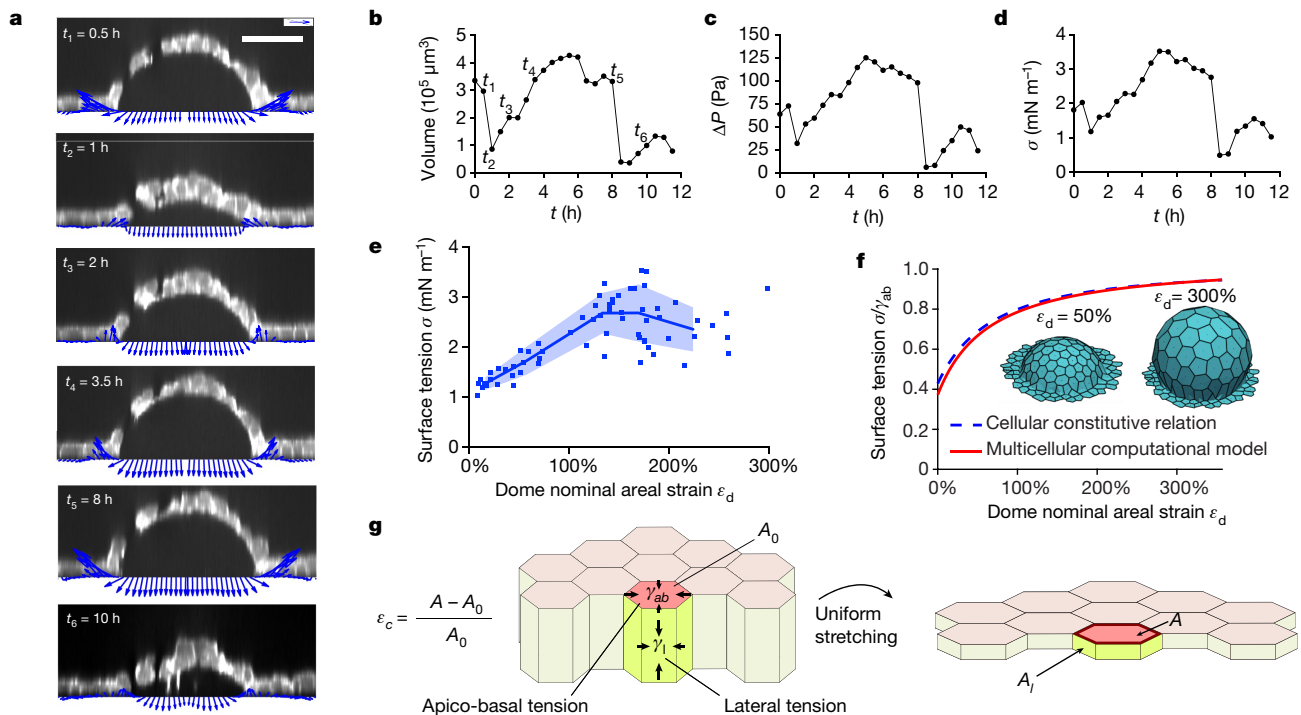


Fig. 3 | Constitutive relation between dome tension and strain.

a, Spontaneous time evolution of tractions in a MDCK–LifeAct dome (y – z section). Scale bar, 50 μm . Scale arrows, 150 Pa. Regions in the dome monolayer that lack fluorescence signal correspond to unlabelled cells, not to gaps. **b–d**, Time evolution of spontaneous fluctuations in dome volume (**b**), pressure ΔP (**c**) and surface tension σ (**d**) (representative of $n = 9$ domes). **e**, Surface tension in the free-standing sheet as a function of nominal areal strain of the dome ε_d ($n = 9$ domes, each sampled over various time points). The solid line and shaded area indicate mean \pm s.d. obtained by binning the data ($n = 14$ points per bin). **f**, Normalized dome

surface tension as a function of areal strain calculated with the vertex model. The dashed blue line represents the cellular constitutive relation in equation (1), based on a sheet of identical hexagonal cells under uniform strain ($\varepsilon_d = \varepsilon_c$). The solid red line is the result of a multicellular computational vertex model for a dome with an initial geometry that was obtained experimentally. Insets show the computed dome shape at 50% (left) and 300% (right) nominal areal strain. **g**, Scheme of an idealized monolayer undergoing uniform equibiaxial stretching, representing model assumptions leading to equation (1).

We thus concluded that the tension–strain response of the tissue had to depend on the mechanics of cell stretching.

To understand the tension–strain relation of the dome monolayer, we developed a theoretical vertex model in 3D^{15,16}. The model is based on the well-established observation that the major determinant of epithelial-cell mechanics is the actin cortex¹⁷. In the timescales of our experiments, this thin cytoskeletal network behaves in a manner similar to a fluid gel, and is capable of developing contractile tension owing to myosin motors¹⁷. In 3D vertex models, these active tensions act along lateral (γ_l) and apico-basal (γ_{ab}) faces of polyhedral cells (Fig. 3g, Supplementary Note 3). Assuming constant cell volume⁵ and idealizing cells as regular hexagonal prisms of uniform thickness under uniform equibiaxial strain, this model predicts that the effective surface tension of the tissue depends on cellular areal strain ε_c as

$$\sigma = \gamma_{ab} - k \frac{\gamma_l}{(1 + \varepsilon_c)^{3/2}} \quad (1)$$

where k is a non-dimensional constant. This active constitutive relation recapitulates the initial increase in tension and the subsequent plateau at larger areal strain that are observed experimentally (Fig. 3e, f). The tendency of tension to plateau at large strains emerges naturally from the fact that the area of lateral faces decreases with cell stretching and, hence, tissue tension converges to apico-basal tension. To theoretically examine tissue stretching by dome swelling, we developed a computational version of the vertex model shown in Fig. 3g (Supplementary Note 3). The tension–strain law evaluated using this computational approach closely matched the analytical constitutive relation in equation (1) (Fig. 3f).

Although this simple theoretical framework captured the tension–strain relationship, it missed a notable experimental feature: during swelling and de-swelling, we systematically observed cells that barely changed area coexisting with cells that reached cellular areal strains of up to 1,000%, which is five times greater than the average dome strain (Fig. 4a, b, Extended Data Fig. 5a–e, Supplementary Videos 5–7). This extreme heterogeneity in strain is reminiscent of that observed in highly stretched epithelia *in vivo*, such as the trophoblast in human and mouse blastocysts^{18,19} (Extended Data Fig. 5f, g). In both epithelial domes and blastocysts, strain heterogeneity would seem to be in contradiction with their spherical shape, which implies tensional uniformity. The heterogeneity of cellular strain increased sharply beyond areal strains of approximately 100% (Fig. 4a, Extended Data Fig. 5). This strain threshold coincides with the onset of the tensional plateau and with the increase in the scatter of tissue tension (Fig. 3e).

Epithelial domes exhibit superelastic behaviour

Taken together, our experiments show that epithelial domes exhibit large reversible deformations and a tensional plateau during which superstretched constitutive elements coexist with barely stretched ones. These uncommon material features are defining hallmarks of superelasticity, a behaviour that is observed in some inert materials such as nickel–titanium alloys²⁰. These materials are able to undergo large and reversible deformations at constant stress by heterogeneously switching between low- and high-strain phases²⁰. The microscopic trigger of superelasticity is a mechanical instability that results from a decreasing branch in the stress–strain relation of the material (strain softening). We reasoned that, by analogy with this behaviour, cell monolayers might behave as superelastic materials by switching from barely stretched to superstretched cellular states at constant tension.

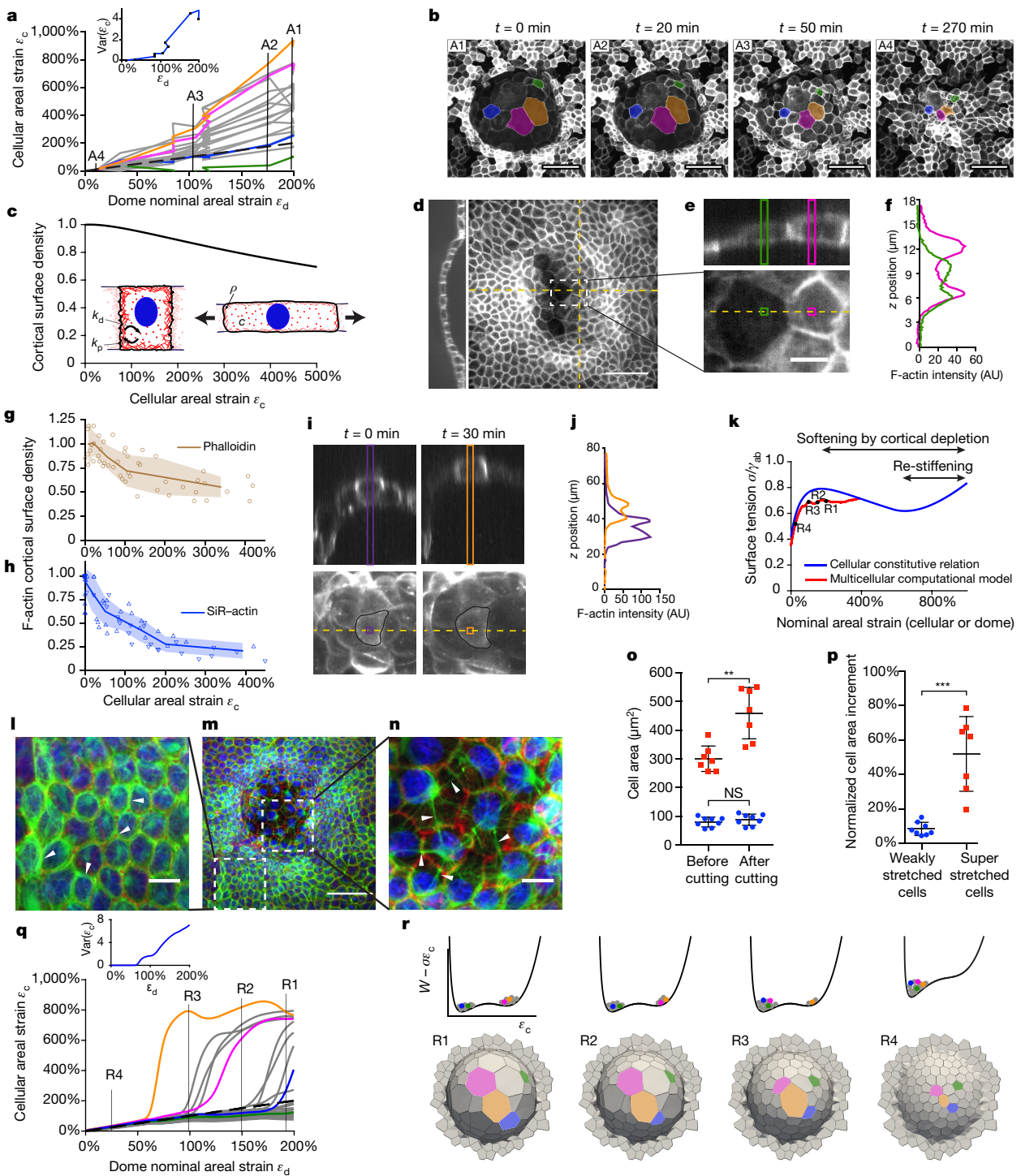


Fig. 4 | Epithelial domes exhibit superelasticity. **a**, Cell strain ϵ_c versus dome strain ϵ_d during a deflation event for a subset of cells. Coloured curves correspond to cells labelled in **b**. Dashed line, $\epsilon_c = \epsilon_d$. Inset shows variance (Var) of ϵ_c versus ϵ_d . **b**, Deflating dome of MDCK-CAAX cells (see 'Cell culture' in Methods). Scale bar, 50 μm . **c**, Model prediction of stretch-induced cortical dilution. **d**, Sum of intensity projection and confocal section of a dome stained with phalloidin for F-actin. Scale bar, 50 μm . **e**, Zoom of representative cells. Scale bar, 10 μm . **f**, F-actin intensity along the bands marked in **e**. AU, arbitrary units. **g**, Normalized density of cortical F-actin (stained with phalloidin) versus cellular strain ($n = 68$ cells from 5 domes). **h**, Normalized density of cortical F-actin (SiR-actin) versus cellular strain during swelling (upward triangles) and de-swelling (downward triangles). $n = 26$ cells from 7 domes. Solid line and shaded area in **g**, **h** indicate mean \pm s.d. **i**, Live imaging of the cortex (SiR-actin) at two instants during swelling. **j**, Intensity profiles along bands shown in **i**. **k**, Non-monotonic cellular constitutive relation predicted by the vertex

model, accounting for softening by cortical depletion and re-stiffening at extreme cellular strains (blue line). Dome tension-strain relationship for the multicellular computational version of the same model (red line). Labels R1 to R4 correspond to panels shown in **q** and **r**. **l–n**, Dome of MDCK cells expressing keratin-18-GFP (green) stained for F-actin (phalloidin, red), and nuclei (Hoechst, blue) ($n = 3$). Scale bar, 10 μm (**l**, **n**), 50 μm (**m**). **o**, **p**, Changes in cell area after laser cuts of keratin bundles for weakly stretched (blue, $n = 8$) and superstretched cells (red, $n = 7$), represented as cell area before and after cuts (**o**) and as normalized cell-area increment (**p**). **q**, ϵ_c versus ϵ_d from the vertex model. Inset, variance of ϵ_c versus ϵ_d . **r**, Bottom, computed geometries during deflation. Top, effective potential energy landscape of active origin. Tilted by tissue tension, this landscape exhibits two wells at sufficiently high tension, corresponding to barely stretched and superstretched cellular states.

To explore this possibility further, we sought a strain-softening mechanism that would explain the mechanical instability that underlies the transition between low- and high-strain phases.

Because cellular deformations increased the surface area of the actin cortex by over threefold, we hypothesized that strain softening arose from the limited availability of cytoskeletal components²¹. Scarcity of cytoskeletal components could lead to stretch-induced cortical dilution, which could impair the ability of the cortex to generate active tension²² (Supplementary Note 3). To test this hypothesis, we incorporated cortical dynamics in the 3D vertex model. We focused on actin as the main cortical component, although cortical depletion could also affect actin cross-linkers, polymerization agents and molecular motors. In our model, cortical thickness—or, equivalently, cortical surface density ρ —is determined by a balance between polymerization at the plasma membrane and depolymerization in the bulk of the actin gel²³. If the availability of cytoskeleton components ready for polymerization is infinite, this model predicts that cortical density ρ , and hence cortical tension γ , are constant and independent of strain, which leads to equation (1). However, if free cytoskeleton components are limited, the model predicts a progressive depletion of cortical density ρ with cellular areal strain—and hence strain softening when the cortex becomes sufficiently thin²² (Fig. 4c). To test this physical mechanism, we measured cortical surface density ρ in cells located at the apex of fixed domes and represented this surface density as a function of cell strain ε_c . These experiments showed that superstretched cells systematically exhibited less-dense cortices (Fig. 4d–g, Extended Data Fig. 6). Moreover, live imaging of cells labelled with SiR-actin showed that the actin cortex became progressively and reversibly diluted with cell stretching (Fig. 4h–j, Supplementary Video 8).

We exogenously interfered with cell–cell junctions and the actin cytoskeleton (Extended Data Figs. 2, 7). Notably, we locally triggered actin depolymerization using a photoactivatable derivative of cytochalasin D. Upon activation, targeted cells increased their area without noticeable changes in the overall shape of the dome (Extended Data Fig. 8, Supplementary Video 9), which indicates that cortical dilution is sufficient to cause large increases in cell area. Taken together, these results are consistent with our hypothesis that cortical dilution underlies cellular superstretching.

Besides strain softening, superelasticity also requires re-stiffening at large strains to confine the high-strain phase. Without such a mechanism, the first cell to reach the softening regime would easily deform further, relaxing neighbouring cells and eventually localizing deformation in an unbounded fashion²⁴ (Supplementary Note 3, Supplementary Video 10). Multiple mechanisms could stiffen cells that are subjected to extreme stretching, including exhaustion of the plasma membrane reservoir²⁵, crowding of adhesion molecules in shrinking cell–cell adhesions²⁶, confinement of the nucleus between tensed cortices or load transfer to the otherwise-relaxed intermediate filament cytoskeleton⁵. Our experiments do not rule out any of these possibilities but do provide support for the last. Indeed, intermediate filaments in superstretched cells appeared unusually straight, which suggests that these filaments are load-bearing (Fig. 4l–n, Extended Data Fig. 9). To further test this mechanism, we laser-ablated keratin-18 filaments. In weakly stretched cells, laser ablation did not induce changes in cell area. By contrast, laser ablation in superstretched cells resulted in a rapid increase in cell area, indicating that intermediate filaments in superstretched cells—but not in relaxed cells—bear tension (Fig. 4o, p, Extended Data Fig. 10). By introducing re-stiffening at large strains into our computational vertex model, we were able to recapitulate our most-salient experimental observations (Supplementary Videos 11, 12). At low levels of dome stretching, tissue tension increased with strain, and heterogeneity in cellular strain was low (Fig. 4k, q, r). By contrast, at high levels of stretching, the domes reached a tensional plateau and heterogeneity in cellular strain rose sharply. Thus, strain softening by stretch-induced depletion of cortical components followed by re-stiffening at extreme stretches configures an effective bistable energy landscape of active origin that explains the emergence of a stable

high-strain phase of superstretched cells under sufficiently large tension (Fig. 4r, Supplementary Note 3).

Active superelasticity provides a mechanism for epithelial tissues to undergo extreme and reversible deformations at nearly constant tension by progressive switching of individual cells to a superstretched state. Our study suggests that, because the underlying subcellular mechanisms are generic, superelasticity may have a broad applicability in vivo. For example, epithelial superelasticity may mediate the spreading of superstretched extra-embryonic tissues and their subsequent rapid compaction²⁷. Active superelasticity may also enable extreme cellular strains in the trophectoderm during the swelling and hatching of mammalian blastocysts^{18,19}. Besides providing a framework to understand epithelial mechanics and morphogenesis in vivo, the material laws established here set the stage for a rational manipulation of cell monolayers in organoids and organ-on-a-chip technologies²⁸.

Online content

Any methods, additional references, Nature Research reporting summaries, source data, statements of data availability and associated accession codes are available at <https://doi.org/10.1038/s41586-018-0671-4>.

Received: 13 November 2017; Accepted: 8 October 2018;
Published online 31 October 2018.

- Alberts, B., Wilson, J. & Hunt, T. *Molecular Biology of the Cell*, 6th edn (Garland Science, New York, 2014).
- Bosveld, F. et al. Mechanical control of morphogenesis by Fat/Dachsous/Four-jointed planar cell polarity pathway. *Science* **336**, 724–727 (2012).
- He, B., Doubrovinski, K., Polyakov, O. & Wieschaus, E. Apical constriction drives tissue-scale hydrodynamic flow to mediate cell elongation. *Nature* **508**, 392–396 (2014).
- Wilson, P. D. Polycystic kidney disease. *N. Engl. J. Med.* **350**, 151–164 (2004).
- Harris, A. R. et al. Characterizing the mechanics of cultured cell monolayers. *Proc. Natl Acad. Sci. USA* **109**, 16449–16454 (2012).
- Tambe, D. T. et al. Collective cell guidance by cooperative intercellular forces. *Nat. Mater.* **10**, 469–475 (2011).
- Vincent, R. et al. Active tensile modulus of an epithelial monolayer. *Phys. Rev. Lett.* **115**, 248103 (2015).
- Vedula, S. R. et al. Mechanics of epithelial closure over non-adherent environments. *Nat. Commun.* **6**, 6111 (2015).
- Nier, V. et al. Tissue fusion over nonadhering surfaces. *Proc. Natl Acad. Sci. USA* **112**, 9546–9551 (2015).
- Leighton, J., Brada, Z., Estes, L. W. & Justh, G. Secretory activity and oncogenicity of a cell line (MDCK) derived from canine kidney. *Science* **163**, 472–473 (1969).
- Tanner, C., Frambach, D. A. & Misfeldt, D. S. Transepithelial transport in cell culture. A theoretical and experimental analysis of the biophysical properties of domes. *Biophys. J.* **43**, 183–190 (1983).
- Wyatt, T. P. et al. Emergence of homeostatic epithelial packing and stress dissipation through divisions oriented along the long cell axis. *Proc. Natl Acad. Sci. USA* **112**, 5726–5731 (2015).
- Gudipaty, S. A. et al. Mechanical stretch triggers rapid epithelial cell division through Piezo1. *Nature* **543**, 118–121 (2017).
- Guillot, C. & Lecuit, T. Mechanics of epithelial tissue homeostasis and morphogenesis. *Science* **340**, 1185–1189 (2013).
- Alt, S., Ganguly, P. & Salbreux, G. Vertex models: from cell mechanics to tissue morphogenesis. *Phil. Trans. R. Soc. Lond. B* **372**, 20150520 (2017).
- Hannezo, E., Prost, J. & Joanny, J. F. Theory of epithelial sheet morphology in three dimensions. *Proc. Natl Acad. Sci. USA* **111**, 27–32 (2014).
- Salbreux, G., Charras, G. & Paluch, E. Actin cortex mechanics and cellular morphogenesis. *Trends Cell Biol.* **22**, 536–545 (2012).
- Hildebrand, S. et al. The E-cadherin/AmotL2 complex organizes actin filaments required for epithelial hexagonal packing and blastocyst hatching. *Sci. Rep.* **7**, 9540 (2017).
- Deglicenti, A. et al. Self-organization of the *in vitro* attached human embryo. *Nature* **533**, 251–254 (2016).
- Otsuka, K. & Wayman, C. M. *Shape Memory Materials* (Cambridge Univ. Press, Cambridge, 1998).
- Suarez, C. & Kovar, D. R. Internetwork competition for monomers governs actin cytoskeleton organization. *Nat. Rev. Mol. Cell Biol.* **17**, 799–810 (2016).
- Chugh, P. et al. Actin cortex architecture regulates cell surface tension. *Nat. Cell Biol.* **19**, 689–697 (2017).
- Turlier, H., Audoly, B., Prost, J. & Joanny, J. F. Furrow constriction in animal cell cytokinesis. *Biophys. J.* **106**, 114–123 (2014).
- Jirásek, M. & Bazant, Z. P. *Inelastic Analysis of Structures* (Wiley, Chichester, 2002).
- Raucher, D. & Sheetz, M. P. Characteristics of a membrane reservoir buffering membrane tension. *Biophys. J.* **77**, 1992–2002 (1999).
- Maître, J. L. & Heisenberg, C. P. Three functions of cadherins in cell adhesion. *Curr. Biol.* **23**, R626–R633 (2013).
- Hilbrant, M., Horn, T., Koelzer, S. & Panfilio, K. A. The beetle amnion and serosa functionally interact as apposed epithelia. *eLife* **5**, e13834 (2016).

28. Clevers, H. Modeling development and disease with organoids. *Cell* **165**, 1586–1597 (2016).

Acknowledgements We thank N. Castro for technical assistance; C. Pérez-González, A. Labernadie, R. Sunyer and A. Torres-Sánchez for discussions and G. Charras for providing cells; J. Colombelli, L. Bardia and A. Lladó (IRB) for assistance with laser ablation and photoactivation; N. Borges from Embryotools S.L. for fixation of mouse blastocysts. This work was supported by the Spanish Ministry of Economy and Competitiveness/FEDER (BFU2015-65074-P to X.T., DPI2015-71789-R to M.A., SAF2017-89782-R to N.M., SAF2015-72617-EXP to N.M., RYC-2014-16242 to N.M.), the Generalitat de Catalunya and CERCA program (2014-SGR-927 to X.T., 2017-FI-B1-00068 to E.L., 2014-SGR-1471 to M.A., 2017 SGR 1306 to N.M., 'ICREA Academia' award to M.A.), the European Research Council (CoG-616480 to X.T., CoG-681434 to M.A., CoG-617233 to B.L., StG-640525 to N.M.), European Commission (project H2020-FETPROACT-01-2016-731957 to M.A., A.d.C. and X.T.), LABAE16006 to N.M., Instituto de Salud Carlos III (CardioCell, TerCel to N.M.), the Deutsche Forschung Gemeinschaft (SFB 1027 to A.d.C.) and Obra Social 'La Caixa'. IBEC is the recipient of a Severo Ochoa Award of Excellence from the MINECO.

Reviewer information *Nature* thanks U. Schwarz, M. Théry and the other anonymous reviewer(s) for their contribution to the peer review of this work.

Author contributions E.L., L.C., M.A. and X.T. conceived the study and designed experiments. E.L. and L.C. performed the experiments with the help of L.V., E.G. and N.M. E.L., M.G.-G. and M.U. developed the 3D traction microscopy algorithm. E.L. and M.G.-G. developed computational analysis tools. E.L. and L.C. processed and analysed the experimental data with the help of M.G.-G. S.K. and M.A. developed the theory and implemented the vertex model. B.L. contributed expertise in the implementation of the micropatterned substrates. R.V.N. and A.d.C. developed the photoactivatable derivative of Cytochalasin D. E.L., M.A. and X.T. wrote the manuscript. All authors helped with the interpretation of the results and commented on the manuscript. M.A. and X.T. supervised the study.

Competing interests The authors declare no competing interests.

Additional information

Extended data is available for this paper at <https://doi.org/10.1038/s41586-018-0671-4>.

Supplementary information is available for this paper at <https://doi.org/10.1038/s41586-018-0671-4>.

Reprints and permissions information is available at <http://www.nature.com/reprints>.

Correspondence and requests for materials should be addressed to M.A. or X.T.
Publisher's note: Springer Nature remains neutral with regard to jurisdictional claims in published maps and institutional affiliations.

METHODS

No statistical methods were used to predetermine sample size. The experiments were not randomized and investigators were not blinded to allocation during experiments and outcome assessment.

Fabrication of soft silicone gels. Soft elastomeric silicone gels were prepared using a protocol based on previous publications^{29–32}. In brief, a silicone elastomer was synthesized by mixing a 1:1 weight ratio of CY52-276A and CY52-276B polydimethylsiloxane (Dow Corning Toray). After degassing for 5 min, the gel was spin-coated on glass-bottom dishes (35-mm, no. 0 coverslip thickness, Mattek) for 90 s at 400 r.p.m. The samples were then cured at 80°C for 1 h. The substrates were kept in a clean, dust-free and dry environment and they were always used within 4 weeks of fabrication.

Coating the soft PDMS substrate with fluorescent beads. After curing, the soft PDMS was treated with (3-aminopropyl)triethoxysilane (APTES, Sigma-Aldrich, cat. no. A3648) diluted at 5% in absolute ethanol for 3 min, rinsed 3 times with ethanol 96%, and dried in the oven for 30 min at 60°C. Samples were incubated for 5 min with a filtered (220 nm) and sonicated solution of 200-nm-diameter red fluorescent carboxylate-modified beads (FluoSpheres, Invitrogen) in sodium tetraborate (3.8 mg/ml, Sigma-Aldrich), boric acid (5 mg/ml, Sigma-Aldrich) and 1-ethyl-3-(3-dimethylaminopropyl)carbodiimide (EDC, 0.1 mg/ml, Sigma-Aldrich), as previously described²⁹. Next, gels were rinsed 3 times with type-1 water and dried in the oven for 15 min at 60°C. Beads were passivated by incubating the samples with tris-buffered saline (TBS, Sigma-Aldrich) solution for 20 min at room temperature. Finally, substrates were rinsed again 3 times with type-1 water and dried in the oven for 15 min at 60°C.

Soft PDMS stiffness measurements. Gel stiffness was measured by indenting the gel with a large metal sphere (diameter, 1,000 µm) of known mass. The indentation caused by the weight of the sphere was determined using confocal microscopy. From the measured indentation and sphere mass, we obtained Young's modulus by applying Hertz theory, corrected for the finite thickness of the gel³³. We found a Young's modulus of 2.9 ± 0.5 kPa (mean \pm s.d., $n = 6$), in good agreement with published data^{29–32,34,35}.

Cell patterning on soft PDMS. PDMS patterning stamps were incubated with a fibronectin solution at 40 µg/ml (fibronectin from human plasma, Sigma-Aldrich) for 1 h. Next, the protein was transferred to poly vinyl alcohol (PVA, Sigma-Aldrich) membranes which were then placed in contact with the gel surface for 1 h. Membranes were dissolved and the surface was passivated at the same time using Pluronic F127 (Sigma-Aldrich) 0.2% w/v overnight at 4°C. Afterwards, the soft silicone gels were washed with phosphate-buffered saline (PBS, Sigma-Aldrich) and incubated with cell culture medium for 30 min. For cell seeding, the culture medium was removed and a 70-µl drop containing ~150,000 cells was placed on the soft PDMS. Fifty minutes after seeding, the unattached cells were washed away using PBS and more medium was added. Cells were seeded at least 48 h before experiments.

PDMS patterning stamps. PDMS (Sylgard, Dow Corning) stamps for micropatterning were fabricated. In brief, SU8-50 masters containing cylinders that were 80 µm or 100 µm in diameter were raised using conventional photolithography. Uncured PDMS was poured on the masters and cured for 2 h at 65°C. PDMS was then peeled off from the master and kept at room temperature in a clean and dust-free environment until use.

Three-dimensional traction microscopy. Three-dimensional traction forces were computed using traction microscopy with finite gel thickness^{36,37}. To account for both geometrical and material nonlinearities, a finite element method (FEM) solution was implemented. Confocal stacks of the fluorescent beads covering the gel surface were taken with z -step = 0.3 µm and total depth of 15 µm. A 3D displacement field of the top layer of the gel between any experimental time point and its relative reference image (obtained after cell trypsinization) were computed using home-made particle imaging velocimetry software based on an iterative algorithm with a dynamic interrogation window size and implementing convergence criteria based on image intensity as described in previous publications³⁸. Results for the normal traction inside the dome were compared to analytical solutions for a liquid droplet over an elastic substrate with finite thickness^{39–42}.

Cell culture. MDCK strain II and Caco-2 cells were used. To visualize specific cell structures, the following stable fluorescent cell lines were used: MDCK expressing LifeAct-GFP (MDCK-LifeAct) to visualize the actin cytoskeleton, MDCK expressing CIBN-GFP-CAAX to visualize the plasma membrane (MDCK-CAAX), MDCK expressing keratin-18-GFP (MDCK-K18) to visualize intermediate filaments. All MDCK lines were cultured in minimum essential medium with Earle's Salts and L-glutamine (Gibco) supplemented with 10% v/v fetal bovine serum (FBS; Gibco), 100 µg/ml penicillin and 100 µg/ml streptomycin. Selection antibiotic geneticin (Thermo Fisher Scientific) was added at 0.5 mg/ml to LifeAct stable cell lines. Cells were maintained at 37°C in a humidified atmosphere with 5% CO₂. Live imaging of F-actin was performed by incubating cells (12 h, 100 nM) using live cell fluorogenic F-actin labelling probe (SiR-actin, Spirochrome). Caco-2 cells

were imaged using BODIPY FL C16 dye (1 µM, 1 h incubation, Thermo Fisher Scientific). MDCK-LifeAct cells were obtained from the laboratory of B. Ladoux. MDCK keratin-18-GFP cells were obtained from the laboratory of G. Charras. MDCK-CAAX cells were obtained by viral infection of CIBN-GFP-CAAX. Caco-2 cells were bought from Sigma Aldrich (86010202). Cell lines tested negative for mycoplasma contamination. All MDCK cell lines were authenticated by the laboratories that provided them. Caco-2 cells were authenticated by the provider (Sigma Aldrich, from the ECACC).

Pharmacological interventions and osmotic shocks. To perturb actomyosin contractility, cells were treated with Rho kinase inhibitor Y-27632 (InSolution Calbiochem, Merck-Millipore, 30 µM, 5-min incubation). To inhibit ARP2/3 complex, cells were treated with CK666 (Sigma Aldrich, 100 µM, 1-h incubation). To perturb the osmolarity, D-mannitol (Sigma-Aldrich, final concentration 100 mM) was added to the medium. To weaken cell-cell junctions, EGTA (Sigma-Aldrich, final concentration 2 mM, 30-min incubation) was added to the medium.

Cell immunofluorescence. MDCK cells were fixed with 4% paraformaldehyde in PBS for 10 min at room temperature and permeabilized using 0.1% Triton X100 (Sigma-Aldrich) in PBS for 10 min at room temperature. Cells were blocked in 1% bovine serum albumin (BSA, Sigma-Aldrich) in PBS for 1 h (at room temperature). Phalloidin (Alexa Fluor 555 phalloidin, Thermo Fisher Scientific) was then added at 1:1,000 dilution in PBS and incubated for 30 min at room temperature. To identify nuclei, cells were then incubated for 10 min in a Hoechst solution (Hoechst 33342, Thermo Fisher Scientific) at 1:2,500 dilution in PBS. Images were acquired with a spinning disk confocal microscope using a Nikon 60 \times oil 1.4 numerical aperture (NA) lens.

Time-lapse microscopy. Multidimensional acquisition for traction force measurements was performed using an inverted Nikon microscope with a spinning disk confocal unit (CSU-W1, Yokogawa), Zyla sCMOS camera (Andor, image size 2,048 \times 2,048 pixels) using a Nikon 40 \times 0.75 NA air lens. The microscope was equipped with temperature control and CO₂ control, using Andor iQ3 or Micro-Manager software⁴³.

Laser ablation. The set-up used has previously been described⁴⁴. In brief, MDCK keratin-18-GFP cells were cultured on thin PDMS micropatterned substrates and allowed to form domes. We then used a sub-nanosecond ultraviolet pulsed laser to ablate individual filament bundles in weakly stretched and superstretched cells. Immediately after ablation we monitored the time evolution of keratin filaments, and we obtained bright-field images of the domes to measure cell area. Experiments were performed at 37°C and 5% CO₂.

Photoactivatable cytochalasin D. We used a phototriggerable derivative of cytochalasin D that includes a nitroveratryloxycarbonyl photoremovable group located at the hydroxyl group at C7 of cytochalasin D. Attachment of the chromophore renders cytochalasin D temporarily inactive. Upon light exposure, cytochalasin D becomes active and causes local depolymerization of the actin cytoskeleton. For experiments, MDCK-CAAX domes were incubated with SiR-actin to visualize the cortical cytoskeleton. Individual cells were illuminated with a 405-nm laser to activate cytochalasin D. After the pulse, the cell area and actin cytoskeleton were visualized using time-lapse microscopy (63 \times oil, Zeiss LSM 880).

Image analysis. Fiji software was used to perform the image analysis⁴⁵. The pairwise stitching plugin was used to create 3D montages, the maximum intensity z -projection and the sum-slices z -projection were used where appropriate. Actual cell areas were computed from z -projections using the methodology described in Supplementary Note 4.

Animals. Animal care and experiments were carried out according to protocols approved by the Ethics Committee on Animal Research of the Science Park of Barcelona (PCB), Spain (Protocol number 7436). Outbred B6CBAF1/JRj mice (male and females of 5–6 weeks of age) were obtained from Janvier Labs. Mice were kept in a 12 h light:dark cycle (lights on 07:00–19:00) with ad libitum access to food and water.

Embryo collection and in vitro culture. For embryo collection, superovulation was induced in B6CBAF1/JRj female mice by intraperitoneal injection of 7.5 I.U. of pregnant mare serum gonadotropin (PMSG), followed—after 48 h—by 7.5 I.U. of human chorionic gonadotropin (hCG). Superovulated females were then paired with male mice, and subsequently euthanized by cervical dislocation 20 h after hCG injection. Then, one-cell stage embryos (zygotes) were collected from the excised oviducts into medium containing 0.1% (w/v) hyaluronidase (Sigma) to remove cumulus cells under a dissection microscope. Recovered zygotes were cultured in micro-droplets of culture medium covered with mineral oil at 37°C and 5% CO₂ until the blastocyst stage. No randomization nor blinding were performed as experiments did not involve comparisons between groups. Experiments were reproduced four times.

Blastocyst immunofluorescence. Blastocysts at different degrees of development were fixed with 4% paraformaldehyde (Aname) for 20 min at room temperature. Then, fixed blastocysts were washed three times with PBS containing 1% bovine

serum albumin (Sigma), 2% goat serum (Sigma) and 0.01% Triton X-100 (Sigma), referred to as blocking buffer. Next, blastocysts were permeabilized with 2.5% Triton X-100 (Sigma) in PBS for 30 min at room temperature and subsequently washed three times with blocking buffer. Blastocysts were incubated overnight at 4°C in anti-E-cadherin primary antibody (610181, BD Biosciences), diluted 1:50 in blocking buffer. The following day, blastocysts were washed three times with blocking buffer and incubated for 90 min at 37°C in Alexa Fluor (A) 488-conjugated secondary antibody (A21202, Thermo Fisher), diluted 1:200 in blocking buffer. Nuclei were counterstained with DAPI (D1306, Life Technologies) for 30 min. Image acquisition was performed in a SP5 Leica microscope or a Zeiss LSM780 confocal microscope using a plan-apochromat 40× oil DIC M27 objective.

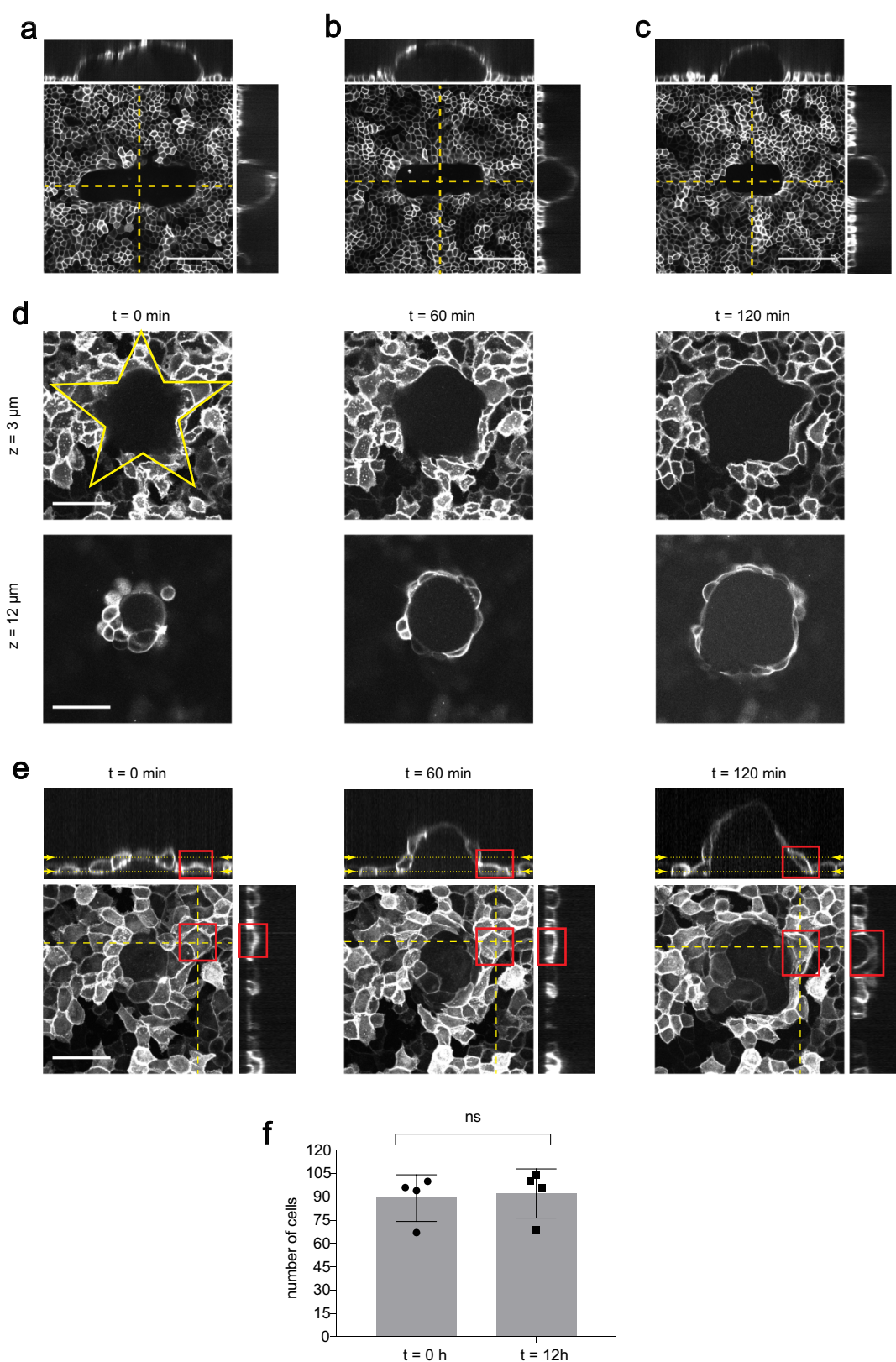
Code availability. MATLAB analysis procedures are available from the corresponding authors on reasonable request.

Reporting summary. Further information on research design is available in the Nature Research Reporting Summary linked to this paper.

Data availability

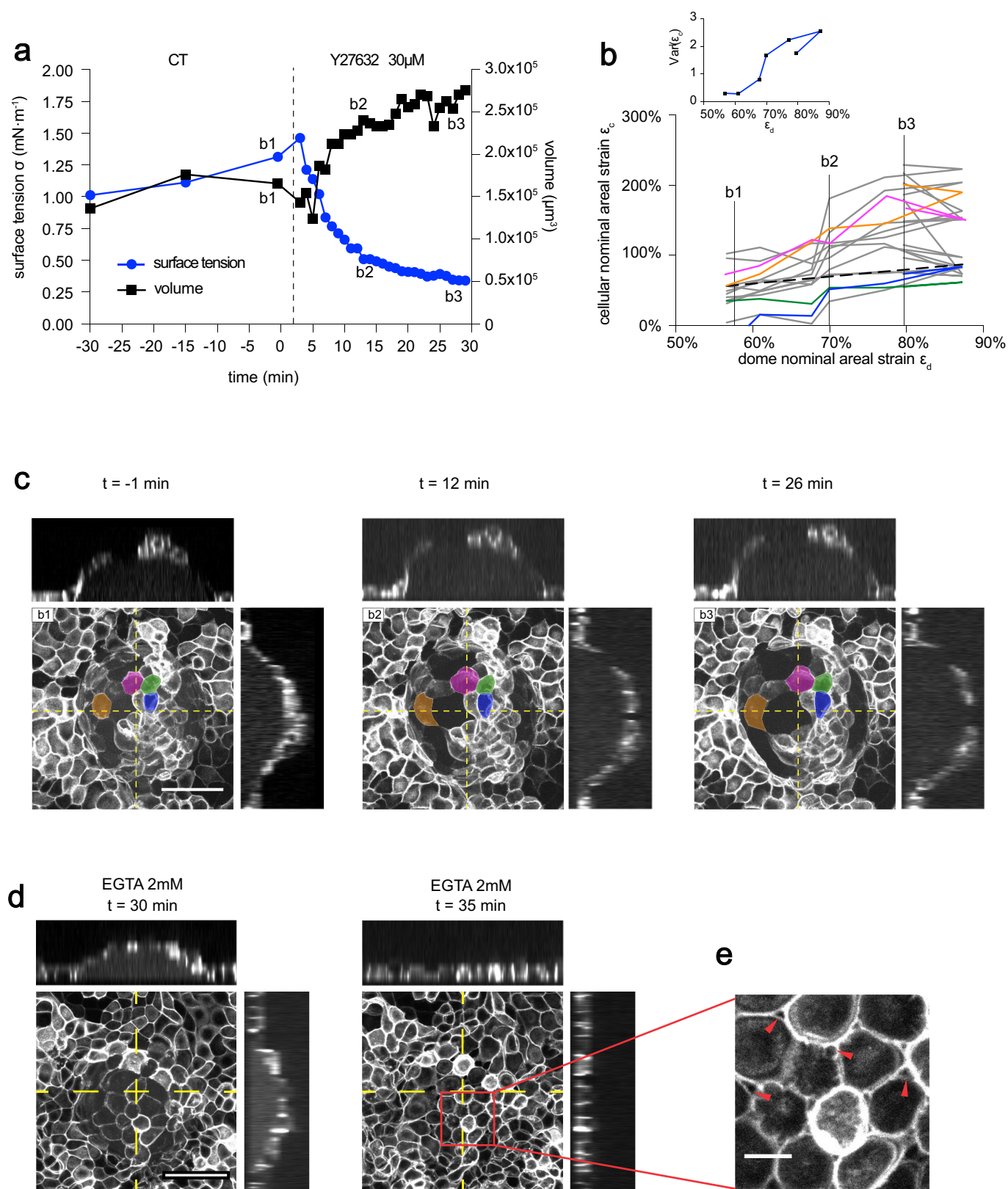
The data that support the findings of this study are available from the corresponding authors on reasonable request.

29. Style, R. W. et al. Traction force microscopy in physics and biology. *Soft Matter* **10**, 4047–4055 (2014).
30. Style, R. W., Hyland, C., Boltyanskiy, R., Wettlaufer, J. S. & Dufresne, E. R. Surface tension and contact with soft elastic solids. *Nat. Commun.* **4**, 2728 (2013).
31. Mertz, A. F. et al. Cadherin-based intercellular adhesions organize epithelial cell-matrix traction forces. *Proc. Natl Acad. Sci. USA* **110**, 842–847 (2013).
32. Vedula, S. R. et al. Epithelial bridges maintain tissue integrity during collective cell migration. *Nat. Mater.* **13**, 87–96 (2014).
33. Long, R., Hall, M. S., Wu, M. & Hui, C. Y. Effects of gel thickness on microscopic indentation measurements of gel modulus. *Biophys. J.* **101**, 643–650 (2011).
34. Mertz, A. F. et al. Scaling of traction forces with the size of cohesive cell colonies. *Phys. Rev. Lett.* **108**, 198101 (2012).
35. Bergert, M. et al. Confocal reference free traction force microscopy. *Nat. Commun.* **7**, 12814 (2016).
36. del Álamo, J. C. et al. Three-dimensional quantification of cellular traction forces and mechanosensing of thin substrata by Fourier traction force microscopy. *PLoS ONE* **8**, e69850 (2013).
37. Álvarez-González, B. et al. Three-dimensional balance of cortical tension and axial contractility enables fast amoeboid migration. *Biophys. J.* **108**, 821–832 (2015).
38. Bar-Kochba, E., Toyjanova, J., Andrews, E., Kim, K.-S. & Franck, C. A fast iterative digital volume correlation algorithm for large deformations. *Exp. Mech.* **55**, 261–274 (2015).
39. Yu, Y. S. & Zhao, Y. P. Elastic deformation of soft membrane with finite thickness induced by a sessile liquid droplet. *J. Colloid Interface Sci.* **339**, 489–494 (2009).
40. Das, S., Marchand, A., Andreotti, B. & Snoeijer, J. H. Elastic deformation due to tangential capillary forces. *Phys. Fluids* **23**, 072006 (2011).
41. Lubarda, V. A. Mechanics of a liquid drop deposited on a solid substrate. *Soft Matter* **8**, 10288–10297 (2012).
42. Yu, Y.-s. Substrate elastic deformation due to vertical component of liquid-vapor interfacial tension. *Appl. Math. Mech.* **33**, 1095–1114 (2012).
43. Edelstein, A. D. et al. Advanced methods of microscope control using µManager software. *J. Biol. Methods* **1**, e10 (2014).
44. Colombelli, J., Grill, S. W. & Stelzer, E. H. K. Ultraviolet diffraction limited nanosurgery of live biological tissues. *Rev. Sci. Instrum.* **75**, 472–478 (2004).
45. Schindelin, J. et al. Fiji: an open-source platform for biological-image analysis. *Nat. Methods* **9**, 676–682 (2012).



Extended Data Fig. 1 | The number of cells in the domes does not change significantly over time. **a–c**, Confocal x - y , y - z and x - z sections of domes of MDCK-CAAX cells, with rectangular basal shapes and varying size. Scale bar, 100 μm (representative of $n = 3$ micropatterned substrates). **d**, Time evolution (0, 60 and 120 min) of a representative dome with a star-shaped footprint. The patterned footprint (yellow) was obtained from images of the fibrinogen-labelled substrate. Each row shows a different z -plane (labelled by dotted yellow lines in the x - y profiles in **e** ($n = 3$

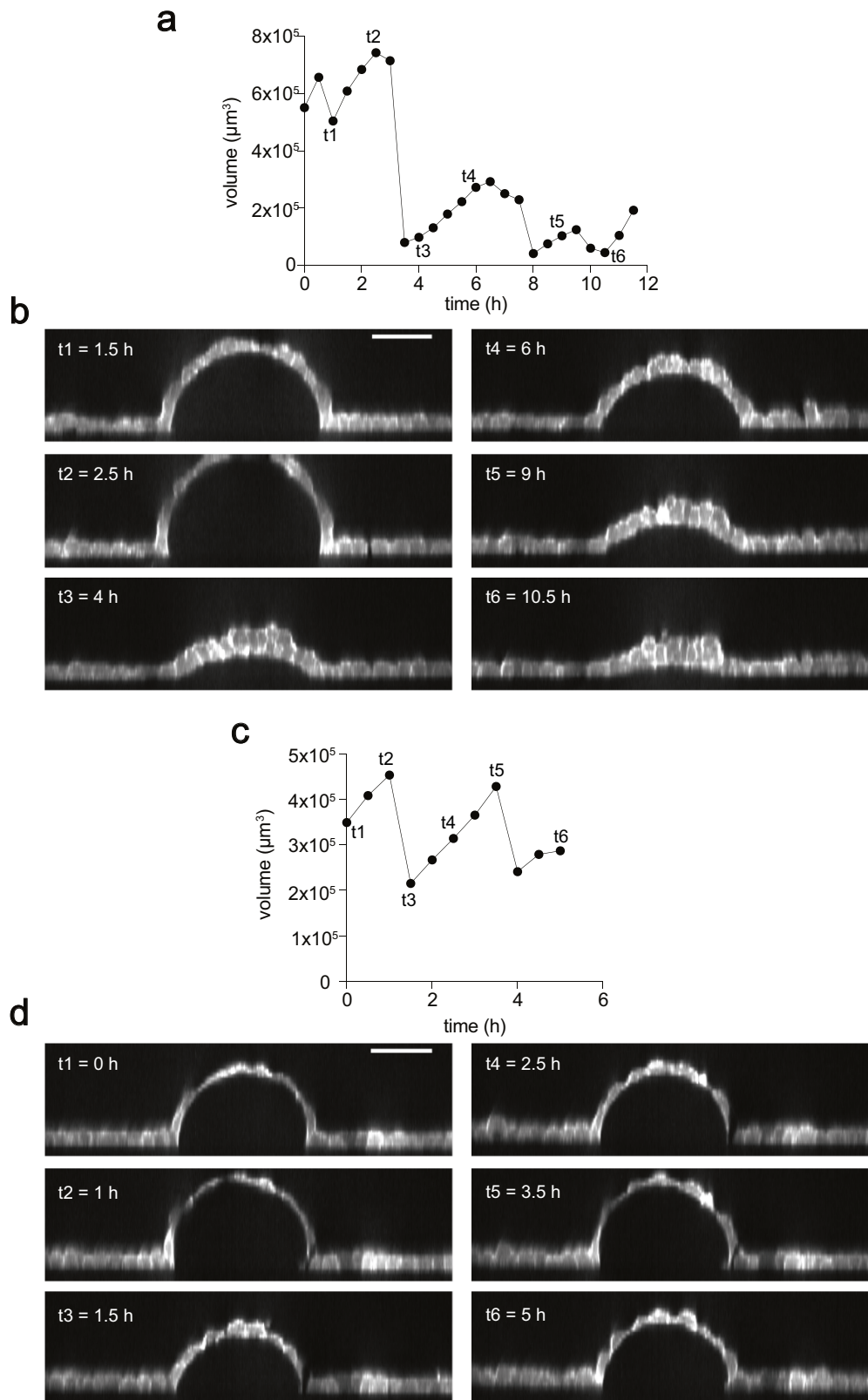
micropatterned substrates). Scale bar, 50 μm . **e**, Time evolution (0, 60 and 120 min) of the same star-shaped dome, showing the rare delamination of a single cell (red rectangle) at one tip of the star. Images are maximum intensity projections with confocal x - z and y - z sections along the yellow dashed lines ($n = 3$ micropatterned substrates). Scale bar, 50 μm . **f**, Quantification of the number of cells in circular domes at two time points 12 h apart ($n = 4$ domes). NS, not significant ($P = 0.4571$), two-tailed Mann-Whitney test. Data are shown as mean \pm s.d.



Extended Data Fig. 2 | See next page for caption.

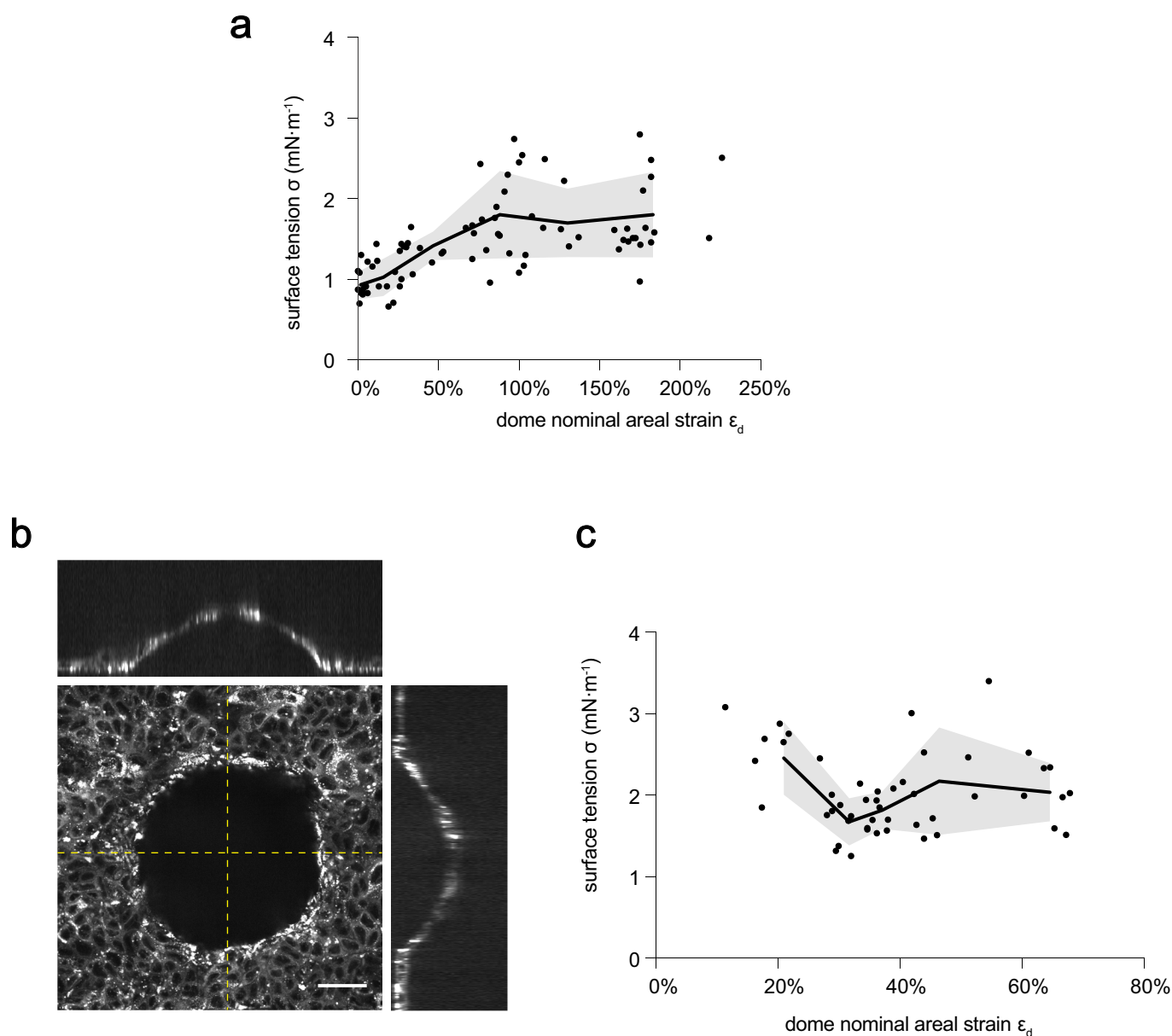
Extended Data Fig. 2 | Dome response to inhibition of tension and weakening of cell–cell adhesion. **a**, Time evolution of surface tension and volume of a representative dome in response to Y27632 (30 μ M, added at $t = 0$ min). **b**, Cellular areal strain ε_c as a function of dome nominal areal strain ε_d during dome swelling. Only a subset of cells is represented and most cells with $\varepsilon_c < \varepsilon_d$ have been omitted for clarity. Coloured lines represent the cells labelled in **c**. Dashed line represents the relation $\varepsilon_c = \varepsilon_d$. The inset represents the variance of ε_c within the dome as a function of ε_d . **c**, Maximum intensity projection and x – z and y – z confocal sections of an epithelial dome of MDCK–CAAX cells before (–1 min) and after (12 min

and 26 min) addition of Y27632 (30 μ M, added at $t = 0$ min). The time evolution of coloured cells is depicted in **b** using the same colour code. Scale bars, 50 μ m. Data are representative of $n = 3$ experiments. **d**, Maximum intensity projection and corresponding x – z and y – z profiles, showing the collapse of a dome of MDCK–CAAX cells after treatment with 2 mM EGTA (30 min and 35 min after the addition of EGTA). Data are representative of $n = 3$ experiments. Scale bar, 50 μ m. **e**, After dome collapse, gaps (red arrowheads) were apparent at tricellular junctions. Scale bar, 10 μ m.



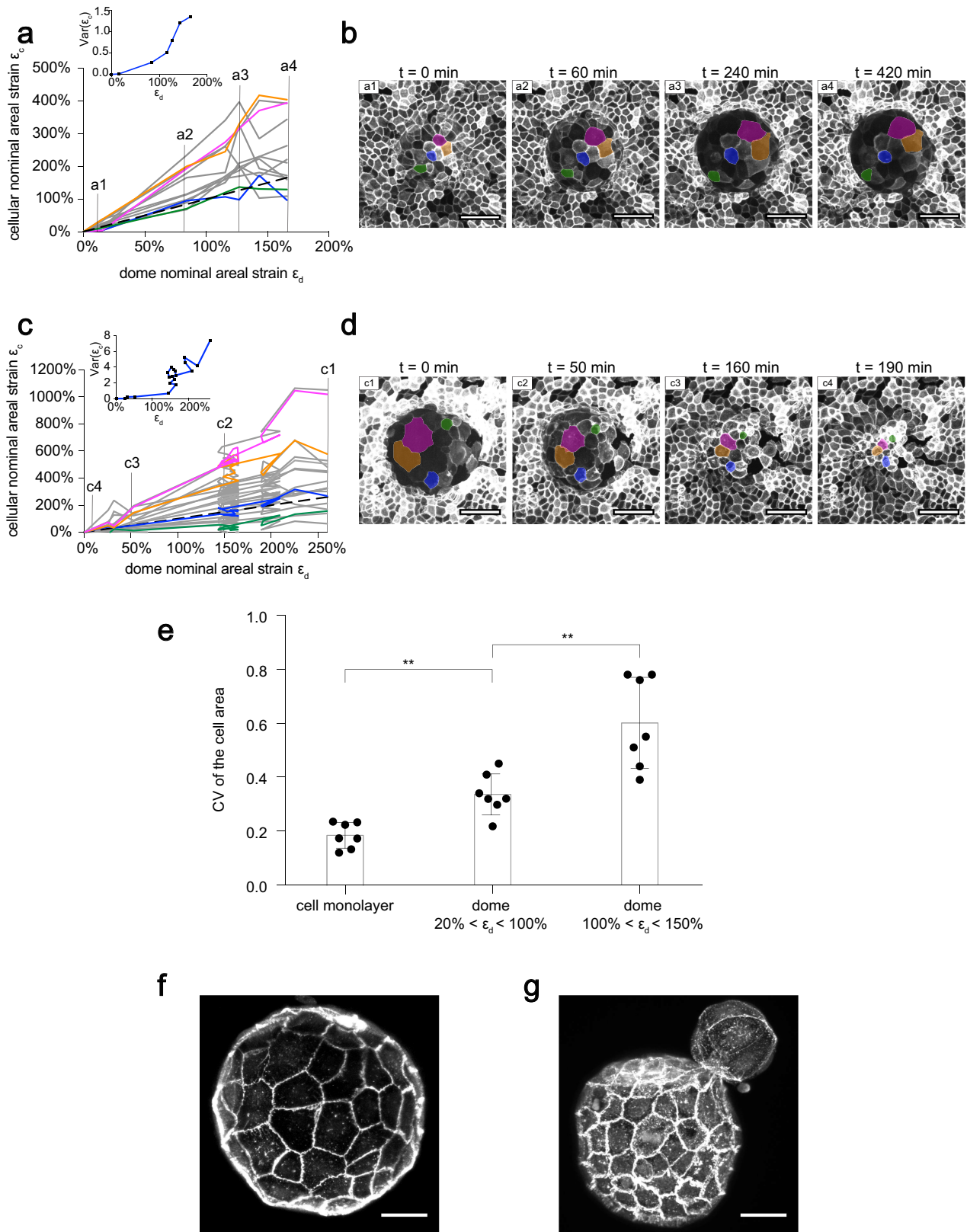
Extended Data Fig. 3 | Dome volume dynamics during spontaneous fluctuations. **a, c,** Time evolution of the dome volume in experiments that last 12 h (**a**) and 6 h (**c**). Cells are MDCK–LifeAct. **b, d,** Confocal x – z

sections of domes during these experiments. Data representative of $n = 10$ experiments. Scale bars, $50\ \mu\text{m}$.



Extended Data Fig. 4 | Tension–strain relations in MDCK–CAAX and Caco2 cells. **a**, Relation between surface tension and areal strain for MDCK–CAAX cells. Data include measurements at different time points from $n = 9$ domes. The tension–strain relation is qualitatively similar to the one obtained for MDCK–LifeAct cells (Fig. 3e), with small quantitative differences. The solid line and shaded area indicate the mean \pm s.d. obtained by binning the data ($n = 14$ points per bin). **b**, Image of a

representative Caco2-cell dome labelled with BODIPY FL C16 dye ($n = 3$ micropatterned substrates). Confocal x – y , x – z and y – z sections are shown. Scale bar, $50\,\mu\text{m}$. **c**, Relation between surface tension and areal strain for Caco2 cells. Data include measurements at different time points from $n = 6$ domes. Caco2 cells show a tensional plateau throughout the probed strain range. The solid line and shaded area indicate the mean \pm s.d. obtained by binning the data ($n = 10$ points per bin).



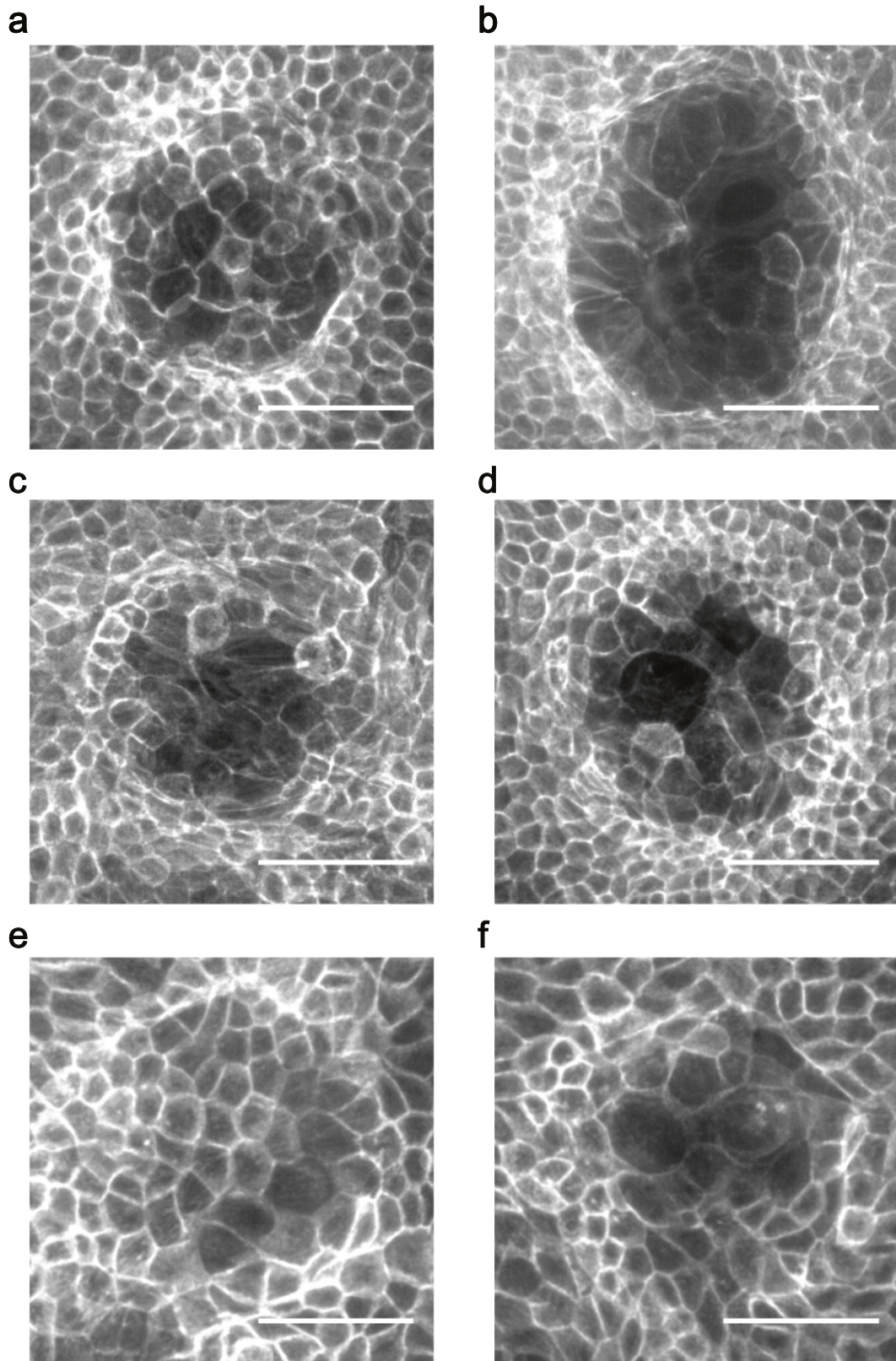
Extended Data Fig. 5 | See next page for caption.

Extended Data Fig. 5 | Dome cells exhibit large strain heterogeneity.

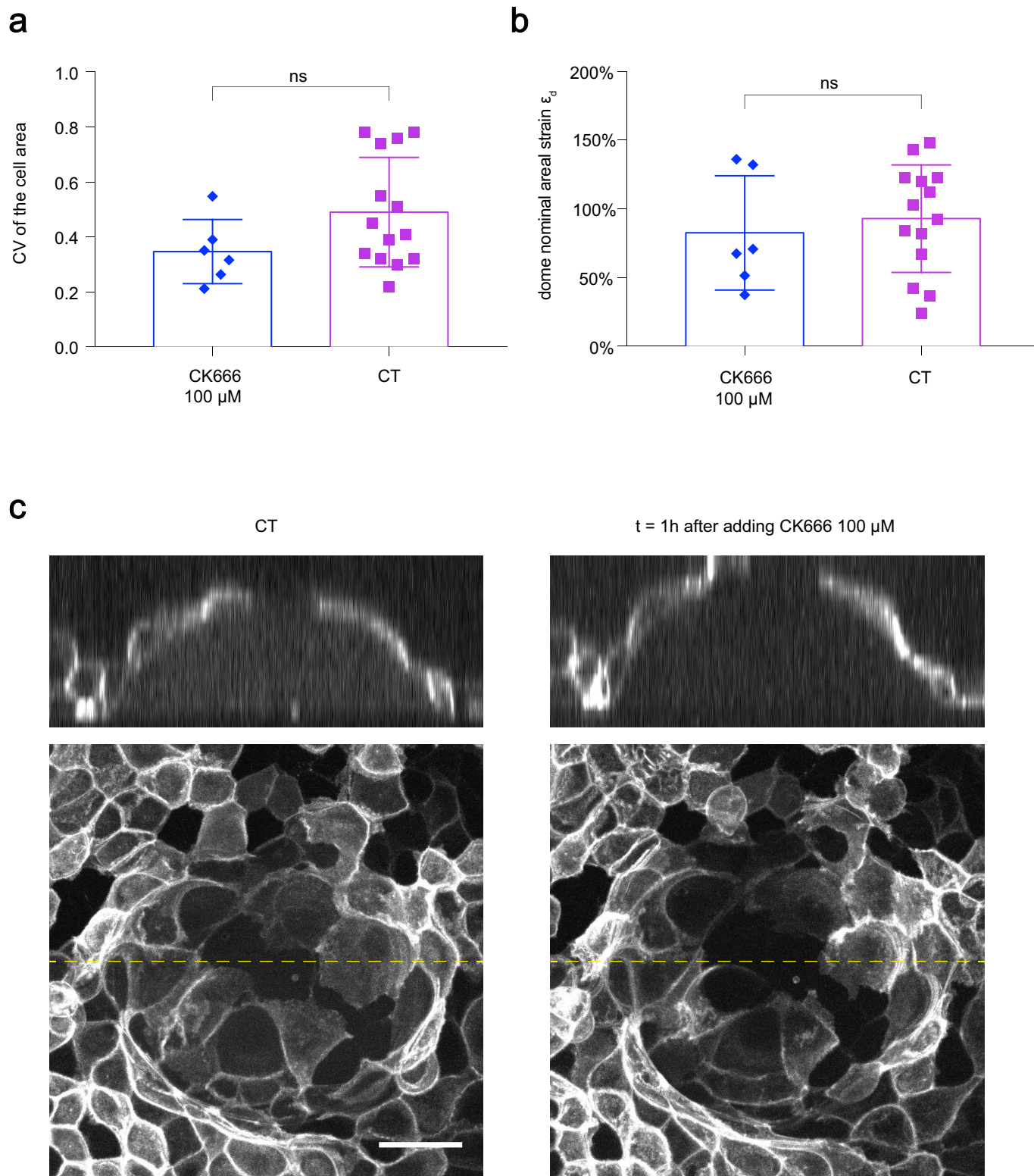
a, Cellular areal strain ε_c as a function of dome nominal areal strain ε_d during dome swelling. Only a subset of cells is represented and most cells with $\varepsilon_c < \varepsilon_d$ have been omitted for clarity. Coloured lines represent the cells labelled in **b**. Dashed line represents the relation $\varepsilon_c = \varepsilon_d$. The inset represents the variance of ε_c within the dome as a function of ε_d .

b, Maximum intensity projection of an epithelial dome of MDCK-CAAX cells at four different time points of the swelling event described in **a**. The time evolution of coloured cells is depicted in **a** using the same colour code. Scale bars, 50 μm . **c**, **d**, represent the same as **a**, **b**, for a different dome of MDCK-CAAX cells during slow deflation. **e**, Coefficient

of variation (CV) (defined as standard deviation divided by mean) of MDCK-CAAX cells in a 2D adherent cell monolayer, in weakly inflated domes (20–100% areal strain), and in highly inflated domes (100–150%). The coefficient of variation is a non-dimensional indicator of heterogeneity. The coefficient of variation was calculated by measuring area of 10 cells in $n=7$ cell monolayers, $n=7$ weakly inflated domes and $n=7$ highly inflated domes. $**P=0.0041$ (left), $**P=0.0041$ (right), two-tailed Mann-Whitney test. Data are shown as mean \pm s.d. **f**, **g**, Mouse blastocysts (labelled with E-cadherin) exhibiting heterogeneity in cell area in the trophectoderm, particularly during hatching (**g**) ($n=4$). Scale bars, 25 μm .

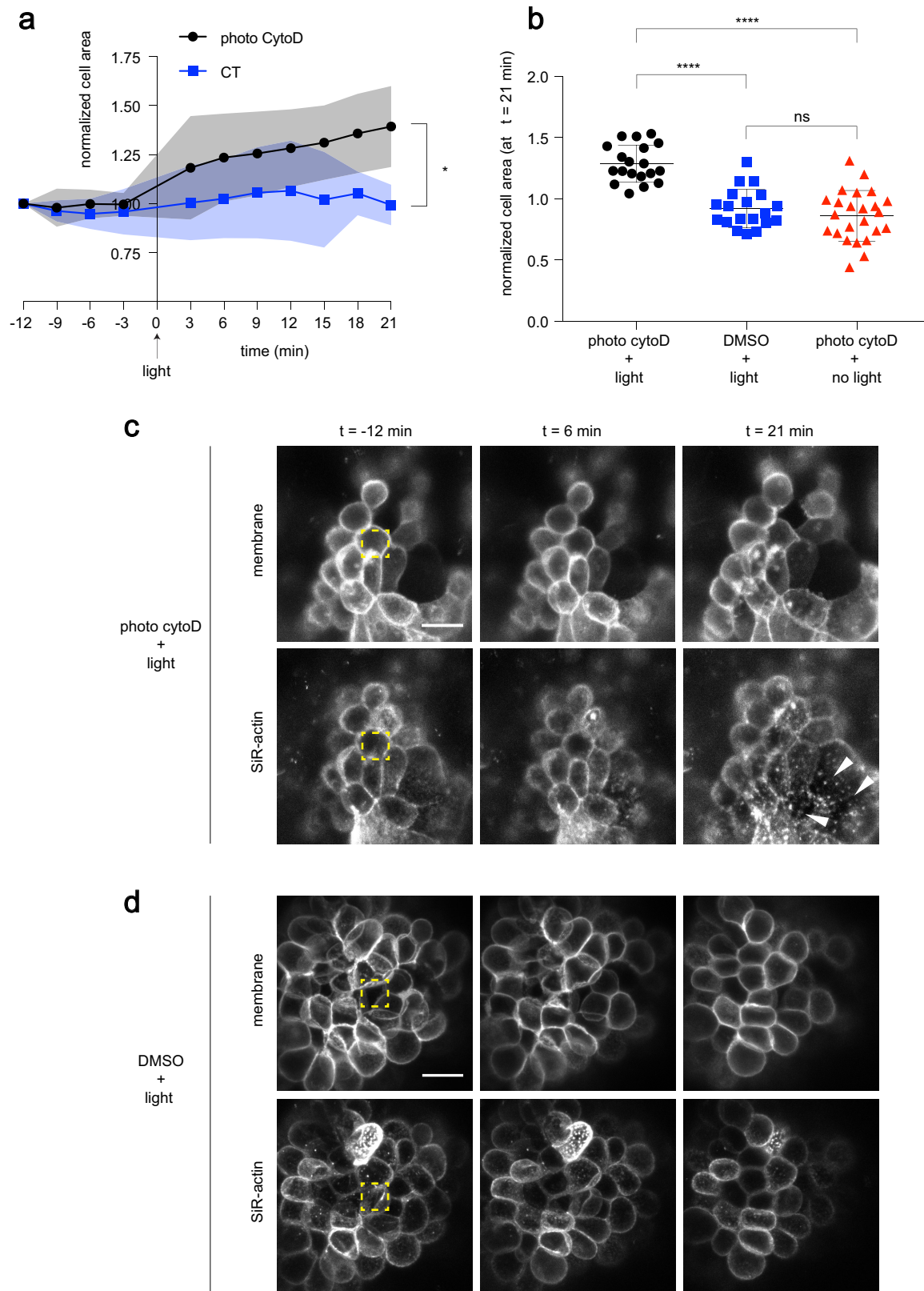


Extended Data Fig. 6 | Superstretched cells display a lower density of F-actin at the cortical surface. a–f, Sum of intensity projection of epithelial domes stained with phalloidin for F-actin. $n = 5$. Scale bars, 50 μm .



Extended Data Fig. 7 | Inhibition of ARP2/3 does not affect area heterogeneity in domes of MDCK cells. **a**, Coefficient of variation of the cell area in domes of MDCK-CAAX cells, treated with CK666 (100 μ M for 60 min), compared to control domes. The coefficient of variation is a non-dimensional indicator of heterogeneity. The coefficient of variation was calculated by measuring area of 10 cells in $n=6$ domes treated with CK666 and in $n=14$ control domes. NS, not significant ($P=0.1256$).

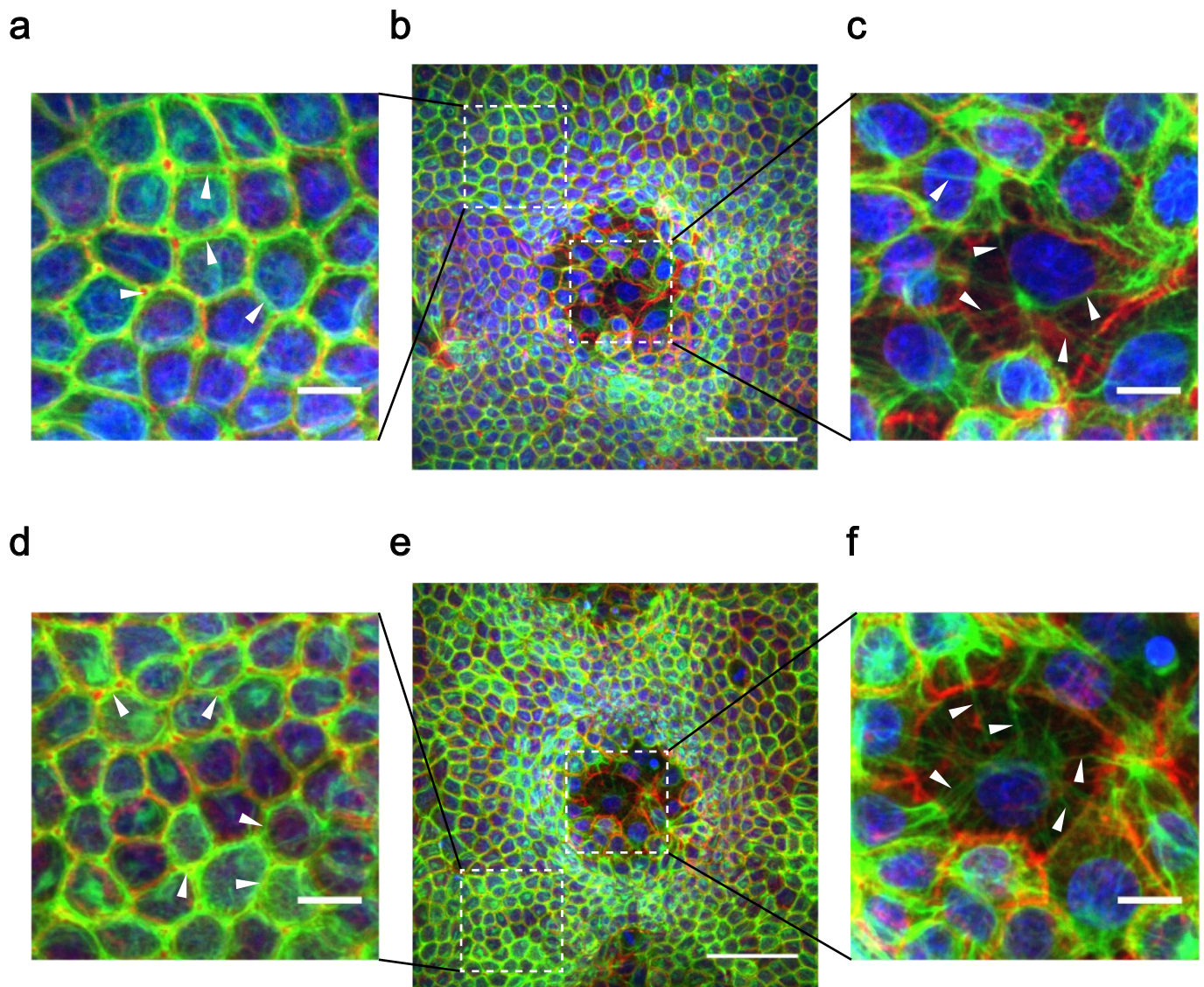
Two-tailed Mann-Whitney test. Data are shown as mean \pm s.d. **b**, Dome nominal areal strain in domes of MDCK-CAAX cells, treated with CK666 (100 μ M for 60 min, $n=6$), compared to control domes ($n=14$). NS, not significant ($P=0.7043$). Two-tailed Mann-Whitney test. Data are shown as mean \pm s.d. **c**, Maximum intensity projections and x-z sections of a representative control dome (left) and the same dome treated with CK666 100 μ M (60 min). Scale bar, 25 μ m.



Extended Data Fig. 8 | See next page for caption.

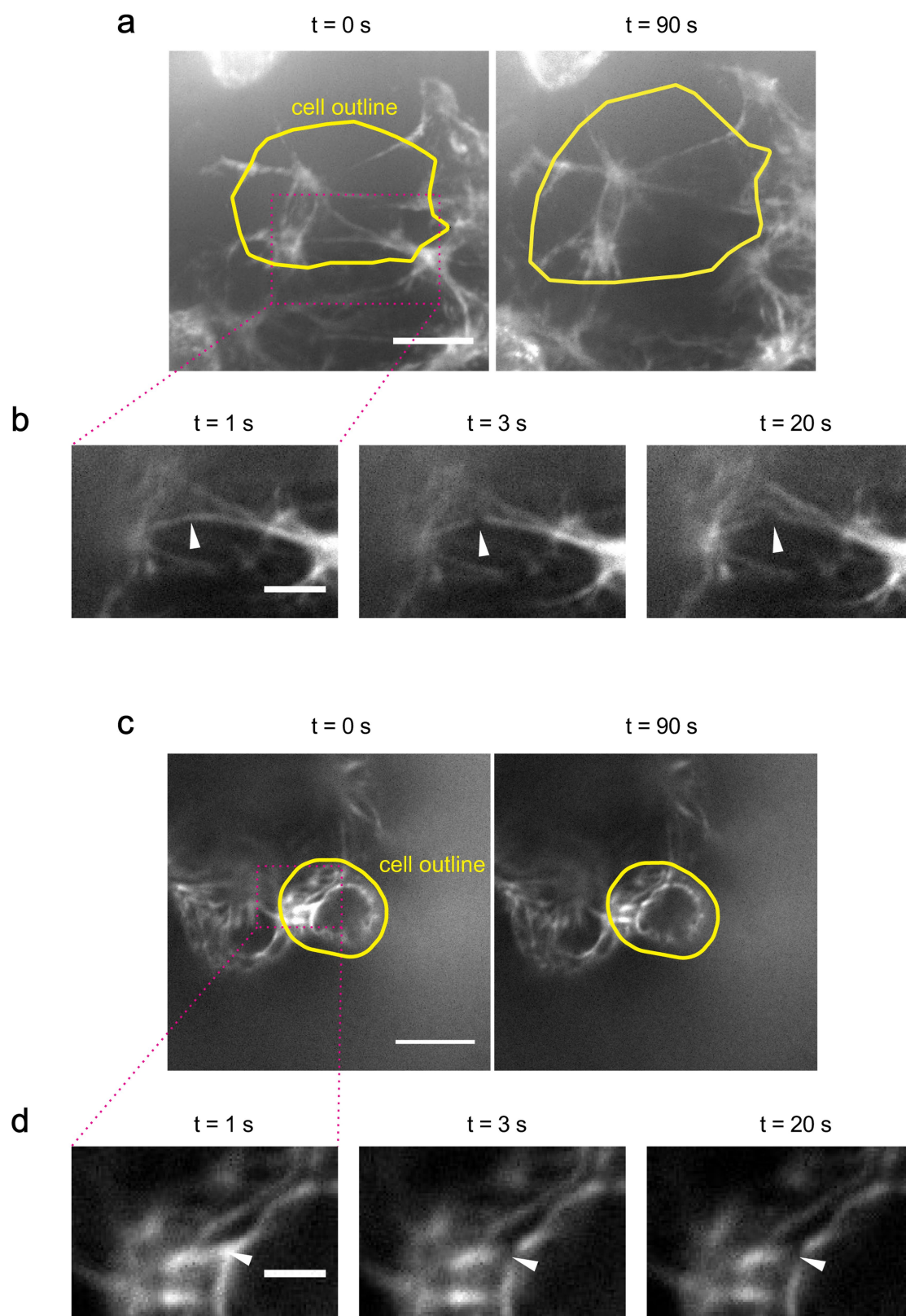
Extended Data Fig. 8 | Local perturbation of the actin cortex using photoactivatable cytochalasin D increases cell area. **a**, Time evolution of the normalized cell area in response to local photoactivation of cytochalasin D (black line, activation at $t = 0$ min, $n = 5$ domes; see Methods). The blue line shows the time evolution of control cells (same illumination protocol but no photoactivatable cytochalasin D in the medium, $n = 8$ domes). The area was normalized to the first time point. Solid lines and shaded areas indicate mean \pm s.d. At $t = 21$ min, normalized cell areas were significantly different ($*P = 0.0159$, two-tailed Mann–Whitney test). **b**, Normalized cell area 21 min after photoactivation in three experimental conditions: photoactivated cells (black circles, $n = 19$ cells from 5 domes), cells subjected to the same illumination protocol but without photoactivatable cytochalasin D in the medium (blue squares, $n = 19$ cells from 8 domes) and cells with photoactivatable cytochalasin D in the medium but without illumination (red triangles, $n = 24$ cells from

9 domes). Data include the immediate neighbours of the targeted cells because cytochalasin D quickly diffused after activation. $***P < 0.0001$, NS, not significant ($P = 0.4130$), two-tailed Mann–Whitney test. Data are shown as mean \pm s.d. **c**, Representative photoactivation experiments showing the apex of one dome before (-12 min) and after (6 min and 21 min) photoactivation of the cell marked with a yellow dashed rectangle ($n = 5$). Top panels show the fluorescently labelled membrane and bottom panels show the SiR-actin channel. Note the increase in cell area and granulation in the SiR-actin channel (white arrowheads), which indicates disruption of the actin cortex. Scale bar, $15\ \mu\text{m}$. **d**, Control experiment in which one cell at the apex of the dome (yellow dashed line) was subjected to the illumination protocol of **c** without photoactivatable cytochalasin D in the medium ($n = 8$). Top panels show the fluorescently labelled membrane and bottom panels show the SiR-actin channel. Scale bar, $15\ \mu\text{m}$. See also Supplementary Video 9.



Extended Data Fig. 9 | Intermediate filaments reorganize in superstretched cells. **a–f**, Immunofluorescence micrographs (see Methods)—represented using maximum intensity projection—of domes of MDCK keratin-18-GFP (in green) cells stained for F-actin (phalloidin, red), and nuclei (Hoechst, blue), $n = 3$. Scale bars, 50 μm . **a, d**, Zoomed-in area (marked with a dashed white square in **b, e**) showing

that the keratin-18 filament network links neighbouring cells and localizes at cell boundaries (white arrowheads). Scale bars, 10 μm . **c, f**, Zoomed-in area (marked with a dashed white square in **b, e**) showing that keratin-18 filaments are taut (white arrowheads) and have reorganized, with nodes at the cell centre connecting different cells. Scale bars, 10 μm .



Extended Data Fig. 10 | Intermediate filaments stabilize cell shape in superstretched cells. **a**, Representative MDCK keratin-18-GFP superstretched cell at the apex of a dome before (0 s) and after (90 s) laser cutting the keratin filament bundle marked in **b** with a white arrowhead. The yellow line marks the outline of the cell measured with bright-field imaging. Scale bar, 10 μm . **b**, Magnified view of the region labelled in **a** with a dotted magenta rectangle. Scale bar, 5 μm . **c**, Representative MDCK

keratin-18-GFP weakly stretched cell at the apex of a dome before (0 s) and after (90 s) laser cutting the keratin filament bundle shown in **d**. The yellow line marks the outline of the cell measured with bright-field imaging. Scale bar, 10 μm . **d**, Magnified view of the region labelled in **c** with a dotted magenta rectangle. The same laser cutting protocol and laser power were used to cut filaments in superstretched and weakly stretched cells. $n = 5$. Scale bar, 5 μm . See Fig. 4o, p for quantification and statistics.

Tc toxin activation requires unfolding and refolding of a β -propeller

Christos Gatsogiannis^{1,3}, Felipe Merino^{1,3}, Daniel Roderer^{1,3}, David Balchin², Evelyn Schubert¹, Anne Kuhlee¹, Manajit Hayer-Hartl² & Stefan Raunser^{1*}

Tc toxins secrete toxic enzymes into host cells using a unique syringe-like injection mechanism. They are composed of three subunits, TcA, TcB and TcC. TcA forms the translocation channel and the TcB–TcC heterodimer functions as a cocoon that shields the toxic enzyme. Binding of the cocoon to the channel triggers opening of the cocoon and translocation of the toxic enzyme into the channel. Here we show in atomic detail how the assembly of the three components activates the toxin. We find that part of the cocoon completely unfolds and refolds into an alternative conformation upon binding. The presence of the toxic enzyme inside the cocoon is essential for its subnanomolar binding affinity for the TcA subunit. The enzyme passes through a narrow negatively charged constriction site inside the cocoon, probably acting as an extruder that releases the unfolded protein with its C terminus first into the translocation channel.

Tc toxins are found in pathogenic bacteria that affect insects and humans¹. Tc toxins of insect pathogens are potential biopesticides and therefore the focus of crop protection research^{2,3}, and understanding the mechanism of action of Tc toxins of human pathogens is medically relevant^{4,5}. A *Photobacterium* toxin complex (Tc) is typically composed of three proteins, TcA, TcB and TcC (Fig. 1a). TcB and TcC form a heterodimeric cocoon of about 300 kDa. The C-terminal hypervariable region (HVR) of TcC¹ is autoproteolytically cleaved, generating a toxic enzyme of about 30 kDa^{6,7}. The HVR varies greatly in sequence among different TcC homologues; the enzymes therefore have diverse toxic activities. In the case of TccC3, a TcC protein from *Photobacterium luminescens*, the enzyme functions as an ADP-ribosyltransferase, which post-translationally modifies actin, leading to intracellular actin aggregation and cell death⁸. The enzyme is not resolved in the crystal structures of either TccC3 or its *Yersinia entomophaga* homologue YenC2^{6,7}, suggesting that it is at least partially unfolded inside the cocoon.

TcA is a 1.4-MDa protein, which forms a translocation channel that is shielded by a shell^{6,9}. A shift to higher or lower pH opens an electrostatic lock at the bottom of the shell, triggering its structural rearrangement^{6,9,10}. The translocation channel is released and the compaction of a stretched linker that connects channel and shell drives the membrane insertion of TcA^{6,10}. The anchoring of TcA on the membrane and the necessary counterforce for insertion are likely to be provided by binding to one or more receptors, which remain unidentified. Once inside the membrane, conformational changes result in the opening of the channel¹⁰.

Structural studies of the wild-type ABC holotoxin (ABC(WT)) from the *P. luminescens* strain W14, comprising TcA (TcdA1), TcB (TcdB2) and TcC (TccC3), have demonstrated that binding of TcB–TcC to TcA induces the opening of a gate formed by a distorted six-bladed β -propeller at the bottom of TcB–TcC⁶. However, the mechanism of gate control and opening remain unknown. We previously hypothesized that after gate opening the ADP-ribosyltransferase inside the TcB–TcC cocoon is translocated into the TcA channel, and ultimately released into the host cell⁶. However, clear densities corresponding to the β -propeller and ADP-ribosyltransferase were missing in the electron cryo-microscopy (cryo-EM) map of the holotoxin, limiting our understanding of the opening and initial translocation event.

Here we present two near-atomic cryo-EM structures of a complete Tc holotoxin complex, which reveal the precise mechanism of Tc toxin assembly, gate opening and release of the cytotoxic enzyme into the translocation channel.

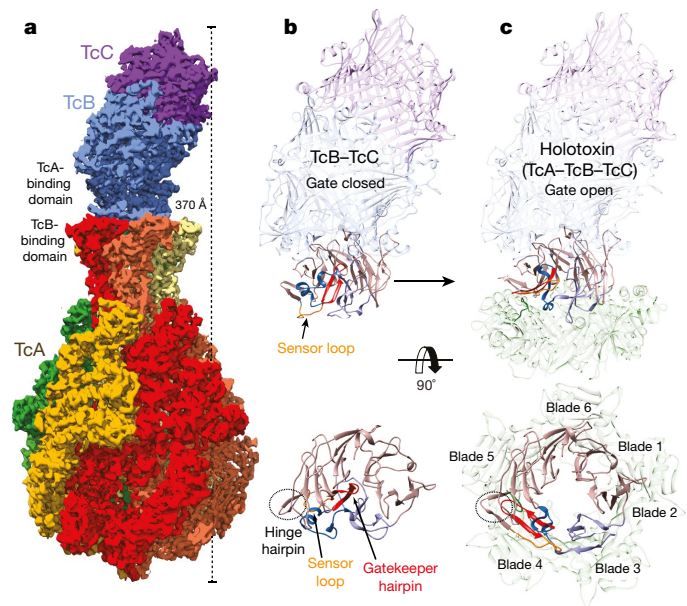


Fig. 1 | Cryo-EM structure of the ABC holotoxin. a, Side view of the 3D reconstruction of the ABC holotoxin complex (TcA (coloured by subunits), TcB (blue) and TcC (purple)). **b**, **c**, Side and top views of the closed (**b**, RCSB Protein Data Bank code (PDB) 4O9X⁶) and open (**c**) state of the β -propeller domain of TcB. Blades 1, 2, 5 and 6 (salmon), blades 3 and 4 (gatekeeper domain, blue and purple), gatekeeper hairpin residues (residues 514–524, red), the sensor loop (residues 527–536, orange) and the TcB-binding domain of TcA (green) are highlighted. The TcB–TcC cocoon is coloured according to **a**. The β -hairpin 537–546 (hinge hairpin), next to the TcB sensor loop, opens by 90°.

¹Department of Structural Biochemistry, Max Planck Institute of Molecular Physiology, Dortmund, Germany. ²Department of Cellular Biochemistry, Max Planck Institute of Biochemistry, Martinsried, Germany. ³These authors contributed equally: Christos Gatsogiannis, Felipe Merino, Daniel Roderer. *e-mail: stefan.raunser@mpi-dortmund.mpg.de

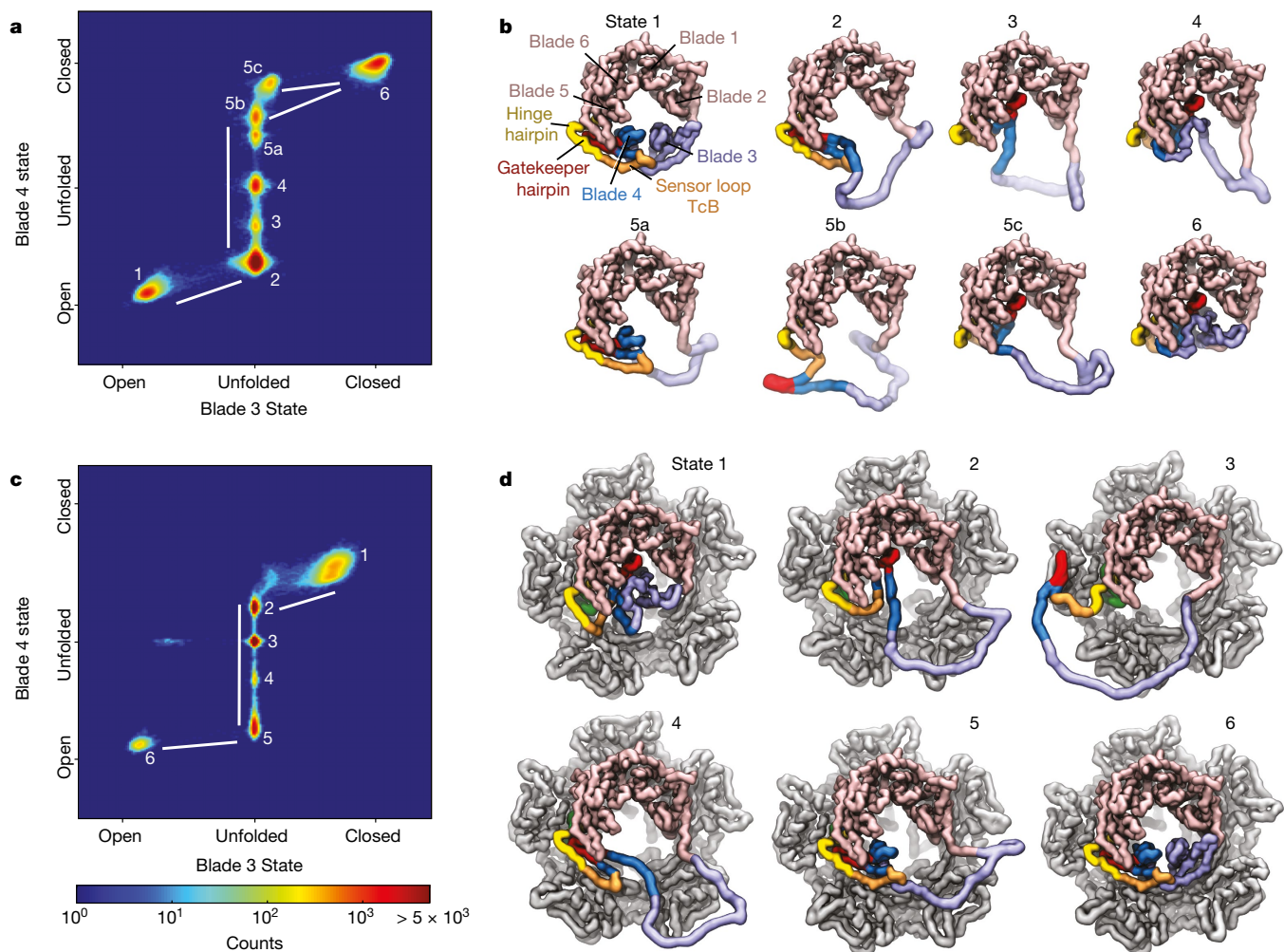


Fig. 2 | Transition between two states of the TcB β -propeller. **a, c**, 2D histogram of the states observed in the trajectories starting from open free TcB–TcC (**a**) or closed TcA-bound TcB–TcC (**c**). Lines indicate the typical sequence of conformational changes. **b, d**, Representative structures for

the states highlighted in **a** and **c**. Blades 1, 2, 5, 6 are coloured salmon, and blades 3 and 4 (gatekeeper domain) in shades of blue. The sensor loop, gatekeeper and hinge hairpin are shown in orange, red and yellow, respectively. In **d**, the TcB-binding domain of TcA is shown in grey.

Structure of the ABC holotoxin complex

To understand how TcA, TcB and TcC assemble, we solved the structure of ABC(WT) by cryo-EM and single-particle analysis using SPHIRE¹¹ (Fig. 1a, Extended Data Fig. 1a–f, Supplementary Table 1, Supplementary Video 1).

The TcA–TcB interface is formed by the β -propeller domain of TcB (TcA-binding domain) and the funnel-shaped TcB-binding domain of TcA (Fig. 1a, c). Whereas the conformation of TcA does not change upon binding (root mean square deviation (r.m.s.d.) 0.780 Å relative to free TcA), the β -propeller of TcB differs considerably from its unbound counterpart (Fig. 1b, c). The six blades of the β -propeller are ordered and adopt a pseudo-six-fold symmetry. The resulting inner diameter matches exactly the diameter of the channel of TcA, thereby forming a continuous passage (Fig. 1c). Binding of TcB to a five-fold symmetric TcA creates a symmetry mismatch, resulting in different interfaces at each β -propeller blade (Extended Data Fig. 2a). Similar symmetry mismatches have been identified in the proteases ClpAP and ClpXP^{12,13}, the 26S-proteasome¹⁴, the BpA-20S-proteasome complex¹⁵ and the tails of many bacteriophages¹⁶. Notably, similar to the proteasome case TcB–TcC adopts a tilted orientation, about 30° relative to the axis of symmetry of TcA. The tilted binding results in a large interface with high shape complementarity (Sc) ($Sc = 0.658$), comparable to that between protein antigens and antibodies ($Sc = 0.66$)¹⁷. The extensive interface explains the very high affinity between TcA and TcB–TcC (dissociation constant,

$K_D = 1.46 \pm 0.05 \times 10^{-10}$ M) (Extended Data Fig. 3a, b), which is about tenfold higher than previously estimated¹⁸.

In three TcA protomers, the conserved L2422 forms hydrophobic interactions with the β -propeller blades 3, 4 and 5 (Extended Data Fig. 2a). In each case, L2422 is positioned within a hydrophobic groove resembling a plug-and-socket interaction. The L2422E mutation reduced the affinity for the cocoon more than fiftyfold (Extended Data Fig. 3a, e, f, g), demonstrating the importance of this residue.

The positively charged residues R485 (blade 3), K534 (blade 4), R554 and R500 (blade 5) interact electrostatically with negatively charged patches on TcA (Extended Data Fig. 2a). However, most of these interactions are not conserved (Extended Data Fig. 2b, c). For the interfaces with blades 1 and 2, we could only identify putative hydrogen-bond interactions (Extended Data Fig. 2a).

Conformational changes in the open β -propeller

Structural alignment of free and bound TcB–TcC reveals that blades 1, 2, 5 and 6 of the β -propeller remain unchanged following binding (Fig. 1b, c). Conversely, blades 3 and 4 exhibit large conformational changes. In the unbound state, they are distorted, with a β -hairpin from blade 4 (residues 514–524) sealing the cocoon⁶ (Fig. 1b). Because the rearrangement of blades 3 and 4 results in the opening of the gate, we call them the gatekeeper domain, and call the β -hairpin of blade 4 the gatekeeper hairpin. A hairpin connecting blades 4 and 5 (residues

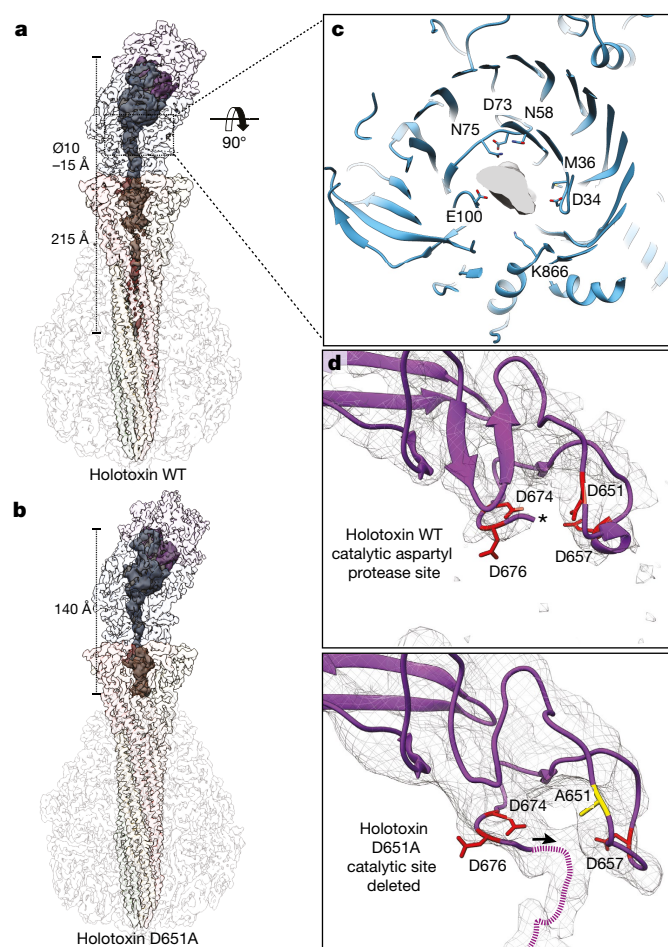


Fig. 3 | ADP-ribosyltransferase in ABC(WT) and ABC(D651A).

a, b, Three-dimensional reconstructions of ABC(WT) (**a**) and ABC(D651A) (**b**) with transparent surface. The density corresponding to the ADP-ribosyltransferase (light grey) is shown at lower threshold. **c**, Residues facing the interior of the channel at the constriction site. **d**, Cryo-EM map with the atomic model, highlighting the autoprotease site of ABC(WT) (top) and ABC(D651A) (bottom). In ABC(D651A) only, density is apparent beyond the cleavage site (indicated by an asterisk); the first residues of the toxic domain (dashed line) can be traced.

537–546) opens by 90° to allow the conformational changes in the gatekeeper domain (Fig. 1b, c); we therefore call this the hinge hairpin.

Gate opening is likely to be triggered by the clash of two loops, residues 2418–2430 in TcA and residues 527–536 in TcB (Extended Data Fig. 4a)—we call these sensor loops. The sensor loop of TcA does not change its conformation upon TcB binding. By contrast, the sensor loop of TcB undergoes a large conformational change; together, the hinge and gatekeeper hairpins and the TcB sensor loop form the β -sheet of blade 4 in the open β -propeller conformation (Fig. 1c). Because this loop connects blade 5 with the gatekeeper hairpin in blade 4 (Fig. 1b, c, Extended Data Fig. 4a) the initial clash can destabilize blade 4. To test this, we created several mutants, including sensor-loop deletions and the point mutations L2422E (TcA) and F532A or D530A/F532A (TcB). All but the TcA deletions (Extended Data Fig. 5a) could be expressed and purified. The affinity of all mutants is decreased by factors of between 3 and 50 compared to the wild type (Extended Data Fig. 3e, 5b–f). In spite of the lower affinity, holotoxins of TcA and all four TcB–TcC variants could be formed, with the point mutations being as toxic as TcB–TcC(WT) (Extended Data Fig. 5g–i). Deletion of the TcB sensor loop resulted in significantly decreased cytotoxicity even at a tenfold-higher toxin concentration (Extended Data Fig. 5g). This suggests that even though the holotoxin can be formed the gatekeeper domain does not switch to the

open conformation, owing to the absence of the TcB sensor loop. As a consequence, translocation of the toxic component from the cocoon to the TcA channel is blocked.

Further, combining the TcB–TcC mutants with the TcA mutant L2422E resulted in a near-complete loss of holotoxin formation (Extended Data Fig. 5h, i), which demonstrates the importance of the sensor loops for complex formation.

β -Propeller refolding

To further explore the gate-opening mechanism of TcB, we performed molecular dynamics simulations of free TcB–TcC in its closed (2.1 μ s) and open (4.2 μ s) β -propeller conformations. The simulations show that the TcB–TcC cocoon is stable in both conformations. However, the β -propeller—particularly around blade 3—is more dynamic in the open state (Extended Data Fig. 6a–f), suggesting that TcA stabilizes the open conformation of the β -propeller.

To further investigate the conformational change of the β -propeller, we performed molecular dynamics simulations using a structure-based model that included both states simultaneously (see Methods). Simulations that start from a closed β -propeller never fully transition to the open state (Extended Data Fig. 7a, b); on rare occasions blade 3 briefly unfolds before refolding back to the closed conformation (Extended Data Fig. 7b). This suggests that blade 3 is the most unstable region of the β -propeller. Notably, in many simulations that start from the open state, the gatekeeper domain quickly unfolds and later slowly adopts the closed conformation (Fig. 2a, b, Extended Data Fig. 7a, b, Supplementary Video 2). In all those trajectories, blade 3 unfolds first followed by blade 4, with refolding occurring in the reverse order (Fig. 2a, b).

In addition, we performed structure-based model simulations of the holotoxin to explore the effects of TcA on the β -propeller. Simulations that start from the open conformation maintain the same state (Extended Data Fig. 7c, d), demonstrating that TcA stabilizes the open β -propeller. However, simulations that start from the closed state never fully transition to the open conformation—the sensor-loop clash results in partial unfolding of the hinge hairpin (Extended Data Fig. 7c, d, g)—consistent with our interpretation that this is an early step in the conformational change.

We then performed simulations with a mildly destabilized β -propeller (see Methods). Again, simulations started from the open state preserve their conformation (Extended Data Fig. 7e, f). By contrast, blade 3 quickly unfolds in the simulations started from the closed state, with the sensor-loop clash resulting in the unfolding of blade 4 and subsequently the whole gatekeeper domain (Fig. 2c, d). Refolding occurs in a sequential manner, with blade 4 followed by blade 3 folding into the open state (Fig. 2c, d, Supplementary Video 3). Therefore, the transition occurs in the reverse order to that seen in the simulations of the free TcB–TcC (Fig. 2a, b). As we never observe a transition without unfolding, we propose that the β -propeller locally unfolds and refolds to switch between states. A similar refolding event switches the function of RfaH between transcription and translation factor¹⁹; however, the RfaH transition occurs through an intermediate that lies between both states²⁰.

In the simulations, blade 3 and 4 could either be unfolded or have the same state as the other blades. Therefore, whereas unfolding of blade 3 always initiates the transition, it is the relative stability of blade 4 that determines the final state. Therefore, in the holotoxin, the destabilization of blade 4 by the sensor loop pushes the protein towards the open conformation. A similar scenario has been proposed for haemagglutinin, in which destabilization of a small region has a key role in the conformational change required for membrane fusion²¹.

Initiation of translocation

We identified additional density corresponding to the ADP-ribosyltransferase inside the cocoon (Fig. 3a). The density appears at lower threshold than the rest of the map, with the lack of recognizable secondary structure indicating that the ADP-ribosyltransferase is

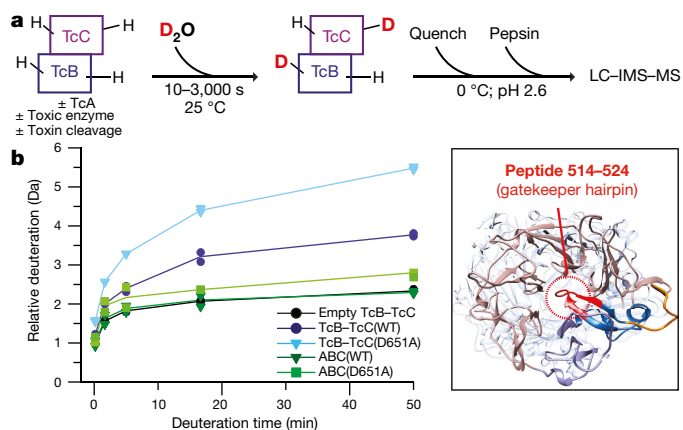


Fig. 4 | Analysis of the gatekeeper hairpin. **a**, Workflow for the measurements of TcB–TcC using HDX–MS. **b**, Equilibrium HDX behaviour of residues 514–524 (gatekeeper hairpin) in TcB–TcC(WT), empty TcB–TcC, TcB–TcC(D651A), ABC(WT) and ABC(D651A). Relative deuterium uptake of the residues as a function of incubation time in D₂O is shown. The data points represent two independent replicates, the solid lines represent the arithmetic mean values of both replicates.

flexible. The density fills almost the entire cocoon, continuing through the TcA translocation channel up to L2085 (Fig. 3a).

To test whether autoproteolysis of TcC is required for the ADP-ribosyltransferase to enter the translocation channel, we solved the structure of a holotoxin with a proteolytically inactive TcC (TcA–TcB–TcC(D651A); referred to collectively as ABC(D651A))⁶ (Extended Data Fig. 1g–l, Supplementary Table 1, Supplementary Video 4). In this case, the density also enters the TcA translocation channel, but only reaches down to P2020 (Fig. 3b). Consequently, a larger part of the ADP-ribosyltransferase is found in the cocoon (Supplementary Video 5). In contrast to ABC(WT), TcC(D651A) density continues after the cleavage site (Fig. 3d), indicating that the ADP-ribosyltransferase is indeed uncleaved. Because the ADP-ribosyltransferase is attached at its N terminus, the protein must have moved with its C terminus first. The similarity of the densities of the cleaved and uncleaved enzymes (Fig. 3, Supplementary Video 5) further suggests that the enzyme undergoes the same C-to-N-terminal translocation in ABC(WT). A similar mechanism has previously been proposed for diphtheria toxin²². By contrast, the anthrax lethal factor is translocated in an N-to-C-terminal direction²³. Similarly, protein translocation into the endoplasmic reticulum and other cell compartments is typically in an N-to-C-terminal direction. However, when the signal sequence of proteins targeted to mitochondria is placed at the C terminus instead of the N terminus, these proteins are also transported in C-to-N-terminal direction²⁴. Our study shows that toxins can probably also be translocated in this non-conventional ‘backwards’ fashion.

The TcB constriction site

After opening, the inner diameter of the β -propeller gate measures 11–15 Å. The narrowest passage in the entire ABC complex, the 10.5 Å constriction site, lies directly above the β -propeller (Extended Data Fig. 4b, c). This constriction site is composed of a ring of polar, mostly negatively charged residues (Fig. 3c), with a highly conserved aspartate (D34) positioned at the entrance (Extended Data Fig. 8a). The ring forms a band of negative electrostatic potential, similar to those in the lumen of the TcA channel¹⁰. Whereas there is little sequence conservation of the other residues at the constriction, the arrangement of charges is conserved among different Tc homologues (Extended Data Fig. 8).

The small diameter of the constriction site should prevent passage of any tertiary structures; this is supported by the shape of the ADP-ribosyltransferase density (Fig. 3a, b). We used molecular dynamics simulations to assess whether an α -helix can nevertheless traverse the constriction. The simulations show that a full helix can be accommodated with its secondary structure mostly preserved; hydrophobic

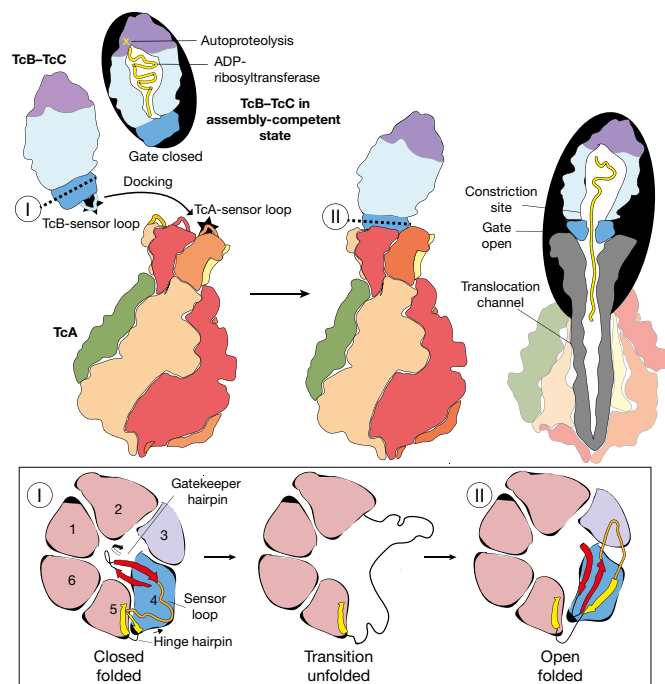


Fig. 5 | Model of Tc toxin activation. Cartoon representation of Tc toxin assembly and gate opening. The bottom panel shows sections indicated by Roman numerals in the top panel. TcB, blue; TcC, purple; ADP-ribosyltransferase, yellow; TcA-binding domain, dark blue.

residues of the helix nestle against hydrophobic patches in TcB, resulting in a peptide with partial hydration (Extended Data Fig. 9).

ADP-ribosyltransferase required for complex assembly

Binding experiments show that the values of K_D and association rate constant (k_{on}) for TcB–TcC(D651A) binding to TcA are comparable to those of the wild-type complex, indicating that the impaired cleavage of TcC does not influence holotoxin formation (Extended Data Fig. 3b, c). However, the affinity of a TcB–TcC complex without ADP-ribosyltransferase (empty TcB–TcC) to TcA is much lower; the K_D is three orders of magnitude higher, owing to a decrease of approximately 1,000-fold in k_{on} (Extended Data Fig. 3d). However, the values of dissociation rate constant (k_{off}) are similar for the empty and loaded TcB–TcC cocoons, demonstrating that the reduced affinity is not a result of missing interactions between the ADP-ribosyltransferase and TcA. This drop in affinity could be a mechanism to ensure that only fully functional TcB–TcC complexes are loaded onto TcA.

To better understand this effect, we determined the crystal structure of empty TcB–TcC at a resolution of 3.2 Å. Unexpectedly, the TcA-binding region was very similar to that of the wild-type complex (Extended Data Fig. 4b, d, e). However, this may be artificially stabilized, as the TcA-binding domain mediates some of the crystal contacts (Extended Data Fig. 4d, e).

To further probe the effect of the ADP-ribosyltransferase on TcB–TcC, we monitored the flexibility of empty TcB–TcC, TcB–TcC(WT), TcB–TcC(D651A), ABC(WT) and ABC(D651A) using hydrogen–deuterium exchange with mass spectrometry (HDX–MS) (see Methods and Fig. 4a). Whereas the sequence coverage for the holotoxins was only about 50% (Source Data for Fig. 4), a part of the gatekeeper hairpin (residues 514–524) (Fig. 4b) could be identified in all samples. We observed only low levels of deuterium incorporation for the empty TcB–TcC, ABC(WT) and ABC(D651A) (Fig. 4b, Extended Data Fig. 10a). By contrast, the TcB–TcC(D651A) complex showed substantial deuterium incorporation, indicative of structural destabilization, whereas TcB–TcC(WT) showed an intermediate level of deuterium incorporation (Fig. 4b, Extended Data Fig. 10a). A similar effect was observed for a

part of blade 4 (residues 463–471) of the β -propeller (Extended Data Fig. 10b, c). For both peptides, destabilization was more pronounced for TcB–TcC(D651A) (Fig. 4b, Extended Data Fig. 10c).

Our results show that TcA selectively stabilizes the gatekeeper hairpin and nearby TcB– β -propeller elements, consistent with the structure of the complex (Fig. 1b, c, Extended Data Fig. 4a). Moreover, in contrast to our crystallographic data, the HDX–MS data show that the ADP-ribosyltransferase destabilizes the gatekeeper domain of free TcB–TcC (Fig. 4b, Extended Data Fig. 10a). We therefore propose that the ADP-ribosyltransferase applies steric ‘pressure’ on the gatekeeper domain, facilitating TcA binding without opening the gate in the absence of TcA.

Conclusion

The results of the present study enable us to describe the mechanism of Tc toxin activation in detail. We have directly demonstrated the presence of a low-resolution density for the ADP-ribosyltransferase inside the cocoon. Therefore, as in our previous model⁶, we propose that the ADP-ribosyltransferase is partially unfolded (Fig. 5, left). We previously showed that the bottom of the cocoon is closed by a β -hairpin (gatekeeper hairpin) that blocks the central opening of the β -propeller (Fig. 5, left). Here we demonstrate that—without opening the cocoon—the ADP-ribosyltransferase influences the gatekeeper hairpin, probably by increasing the pressure within the cocoon, resulting in subnanomolar affinity of TcB–TcC for TcA.

The assembly-competent cocoon docks with its distorted β -propeller onto TcA (Fig. 5, middle), where the sensor loops of the two proteins clash. This destabilizes the gatekeeper domain and triggers a large conformational change in blades 3 and 4 of the β -propeller; they completely unfold and refold to form a pseudo-symmetrical six-bladed β -propeller. During this process the gatekeeper hairpin is rearranged and becomes part of the β -sheet of blade 4. The hinge hairpin, which is directly connected to the sensor loop, opens by 90°, allowing these large changes (Fig. 5, middle). Finally, this results in the opening of the gate, forming a continuous translocation channel with TcA. Despite the symmetry mismatch between TcA and TcB, the respective surfaces of the resulting interface are a close match. During translocation, the unfolded ADP-ribosyltransferase passes through a constriction site through which no tertiary structure can pass. Unusually, the protein begins translocating with its C terminus first. In the final state, the N terminus of the unfolded ADP-ribosyltransferase still resides within the TcB–TcC cocoon, whereas the C terminus extends to the centre of the TcA channel (Fig. 5, right). Threading into the translocation channel occurs spontaneously after gate opening. Further translocation is likely to require injection of the TcA channel into the membrane of the target cell and opening of the initially closed pore¹⁰.

Online content

Any methods, additional references, Nature Research reporting summaries, source data, statements of data availability and associated accession codes are available at <https://doi.org/10.1038/s41586-018-0556-6>.

Received: 10 January 2018; Accepted: 23 August 2018;
Published online 19 September 2018.

1. Waterfield, N. R., Bowen, D. J., Fetherston, J. D., Perry, R. D. & ffrench-Constant, R. H. The *tc* genes of *Photorhabdus*: a growing family. *Trends Microbiol.* **9**, 185–191 (2001).
2. ffrench-Constant, R. H. & Bowen, D. J. Novel insecticidal toxins from nematode-symbiotic bacteria. *Cell. Mol. Life Sci.* **57**, 828–833 (2000).
3. ffrench-Constant, R. H., Dowling, A. & Waterfield, N. R. Insecticidal toxins from *Photorhabdus* bacteria and their potential use in agriculture. *Toxicon* **49**, 436–451 (2007).
4. Pinheiro, V. B. & Ellar, D. J. Expression and insecticidal activity of *Yersinia pseudotuberculosis* and *Photorhabdus luminescens* toxin complex proteins. *Cell. Microbiol.* **9**, 2372–2380 (2007).

5. Zahaf, N.-I. et al. Targeted delivery of an ADP-ribosylating bacterial toxin into cancer cells. *Sci. Rep.* **7**, 41252 (2017).
6. Meusch, D. et al. Mechanism of Tc toxin action revealed in molecular detail. *Nature* **508**, 61–65 (2014).
7. Busby, J. N., Panjikar, S., Landsberg, M. J., Hurst, M. R. H. & Lott, J. S. The BC component of ABC toxins is an RHS-repeat-containing protein encapsulation device. *Nature* **501**, 547–550 (2013).
8. Lang, A. E. et al. *Photorhabdus luminescens* toxins ADP-ribosylate actin and RhoA to force actin clustering. *Science* **327**, 1139–1142 (2010).
9. Gatsogiannis, C. et al. A syringe-like injection mechanism in *Photorhabdus luminescens* toxins. *Nature* **495**, 520–523 (2013).
10. Gatsogiannis, C. et al. Membrane insertion of a Tc toxin in near-atomic detail. *Nat. Struct. Mol. Biol.* **23**, 884–890 (2016).
11. Moriya, T. et al. High-resolution single particle analysis from electron cryo-microscopy images using SPHIRE. *J. Vis. Exp.* **123**, (2017).
12. Bewley, M. C., Graziano, V., Griffin, K. & Flanagan, J. M. The asymmetry in the mature amino-terminus of ClpP facilitates a local symmetry match in ClpAP and ClpXP complexes. *J. Struct. Biol.* **153**, 113–128 (2006).
13. Baker, T. A. & Sauer, R. T. ClpXP, an ATP-powered unfolding and protein-degradation machine. *Biochim. Biophys. Acta* **1823**, 15–28 (2012).
14. Schweitzer, A. et al. Structure of the human 26S proteasome at a resolution of 3.9 Å. *Proc. Natl Acad. Sci. USA* **113**, 7816–7821 (2016).
15. Bolten, M. et al. Structural analysis of the bacterial proteasome activator Bpa in complex with the 20S proteasome. *Structure* **24**, 2138–2151 (2016).
16. Morais, M. C. et al. Cryoelectron-microscopy image reconstruction of symmetry mismatches in bacteriophage ϕ 29. *J. Struct. Biol.* **135**, 38–46 (2001).
17. Lawrence, M. C., Lawrence, M. C., Colman, P. M. & Colman, P. M. Shape complementarity at protein/protein interfaces. *J. Mol. Biol.* **234**, 946–950 (1993).
18. Lang, A. E., Konukiewicz, J., Aktories, K. & Benz, R. TcdA1 of *Photorhabdus luminescens*: electrophysiological analysis of pore formation and effector binding. *Biophys. J.* **105**, 376–384 (2013).
19. Burmann, B. M. et al. An α helix to β barrel domain switch transforms the transcription factor RfaH into a translation factor. *Cell* **150**, 291–303 (2012).
20. Ramírez-Sarmiento, C. A., Noel, J. K., Valenzuela, S. L. & Artsimovitch, I. Interdomain contacts control native state switching of RfaH on a dual-funneled landscape. *PLoS Comput. Biol.* **11**, e1004379 (2015).
21. Lin, X. et al. Order and disorder control the functional rearrangement of influenza hemagglutinin. *Proc. Natl Acad. Sci. USA* **111**, 12049–12054 (2014).
22. Murphy, J. R. Mechanism of diphtheria toxin catalytic domain delivery to the eukaryotic cell cytosol and the cellular factors that directly participate in the process. *Toxins (Basel)* **3**, 294–308 (2011).
23. Zhang, S., Finkelstein, A. & Collier, R. J. Evidence that translocation of anthrax toxin’s lethal factor is initiated by entry of its N terminus into the protective antigen channel. *Proc. Natl Acad. Sci. USA* **101**, 16756–16761 (2004).
24. Fölsch, H., Gaume, B., Brunner, M., Neupert, W. & Stuart, R. A. C- to N-terminal translocation of preproteins into mitochondria. *EMBO J.* **17**, 6508–6515 (1998).

Acknowledgements We thank O. Hofnagel for assistance in electron microscopy; A. Elsner and K. Vogel-Bachmayr for technical support; the SPHIRE developer team, in particular P. A. Penczek, for the software used in this study; and R. Matadeen and S. de Carlo (FEI) for acquisition of the ABC(D651A) dataset at the National Center for Electron Nanoscopy in Leiden. This work was supported by the Max Planck Society (to S.R.) and the European Research Council (FP7/2007–2013) (grant no. 615984) (to S.R.).

Reviewer information Nature thanks R. ffrench-Constant and the other anonymous reviewer(s) for their contribution to the peer review of this work.

Author contributions S.R. designed and managed the project. D.R. designed proteins and performed mutational and functional studies. C.G. and A.K. processed, and C.G. analysed, cryo-EM data. C.G. and F.M. built atomic models. F.M. calculated and analysed molecular dynamics simulations. E.S. determined the TcB–TcC structure. D.B. performed HDX–MS. D.B. and M.H.-H. analysed HDX–MS data. C.G., F.M., D.R. and E.S. prepared figures. All authors discussed the results and contributed to the writing of the manuscript.

Competing interests The authors declare no competing interests.

Additional information

Extended data is available for this paper at <https://doi.org/10.1038/s41586-018-0556-6>.

Supplementary information is available for this paper at <https://doi.org/10.1038/s41586-018-0556-6>.

Reprints and permissions information is available at <http://www.nature.com/reprints>.

Correspondence and requests for materials should be addressed to S.R.

Publisher’s note: Springer Nature remains neutral with regard to jurisdictional claims in published maps and institutional affiliations.

METHODS

Protein production. TcdA1 was expressed in BL21-CodonPlus(DE3)-RIPL in 10 l LB medium and purified as previously described¹⁰.

Fusion proteins TcdB2–TccC3 and cleavage-deficient TcdB2–TccC3(D651A)⁶ were expressed as previously described¹⁰ with the following modifications. Expression was performed in BL21-CodonPlus(DE3)-RIPL cells in 10 l LB medium starting from a single transformant with 30 μ M IPTG added immediately at the start of expression. Cells were grown for 4 h at 28 °C, followed by 20 h at 25 °C and 24 h at 20 °C. Cell lysis and protein purification were performed as previously described¹⁰.

The sequence of TcdB2–TccC3 without the HVR (empty TcB–TcC) was amplified from the TcdB2–TccC3 sequence using the primer pair GGATCCATGCAAAATTCACAAGATTTTAGTATTACGGAAGTGTAC and CTCGAGTTATAATCCATCAGGATCAAGGAGGGTAACTGG and cloned in pET28a via BamHI and XhoI, resulting in a TcdB2–TccC3 fusion construct terminated after L678 of TccC3. Empty TcdB2–TccC3 and all sensor-loop variants were expressed and purified as for the wild-type complex.

Cryo-EM data acquisition. ABC(WT) and ABC(D651A) were applied to glow-discharged holey carbon grids (C-Flats-2/1, Protochips) and blotted inside a Cryopluger3 (Cp3, Gatan) using 3-s blotting time at 94% humidity and plunge-frozen in liquid ethane. Grids were stored in liquid nitrogen.

A dataset of ABC(D651A) was collected at the National Center for Electron Nanoscopy in Leiden (NecEN) with a Cs-corrected FEI Titan-Krios equipped with a XFEG and operated at an acceleration voltage of 300 kV. Images were collected automatically using EPU (FEI). For every selected grid square, 4 positions within each hole were imaged. Images were collected at a magnification of 125,000 (nominal magnification 59,000 \times) using a back-thinned Falcon-II (FEI) direct electron detector, corresponding to a pixel size of 1.1 \AA /pixel on the specimen level.

Starting at 85 ms, seven frames (55 ms/frame) with a total dose of 15.4 $e^- \text{\AA}^{-2}$ and one integrated image (motion uncorrected) with a total dose of $\sim 35 e^- \text{\AA}^{-2}$ were acquired and used for further image processing. A total of 4,958 images were collected in a defocus range of 0.8 to 2.8 μ m.

A dataset of wild-type ABC was collected at the Max Planck Institute of Molecular Physiology, Dortmund using the same hardware setup (Cs-corrected Titan Krios equipped with a XFEG and a Falcon II). Images were recorded using the automated acquisition program EPU (FEI) at a magnification of 122,870, corresponding to a pixel size of 1.14 \AA /pixel on the specimen level. Movie-mode images (3,068) were acquired in a defocus range of 0.8 to 2.5 μ m. Each movie comprised of 24 frames acquired over 1 s with a total cumulative dose of $\sim 60 e^- \text{\AA}^{-2}$.

Image processing. After initial screening of all ABC(D651A) micrographs, 4,729 integrated images were selected for further processing. Single particles (137,733) were manually picked with e2boxer²⁵. The integrated images were also used to determine the contrast transfer function (CTF) parameters using CTER²⁶, implemented in the SPHIRE software package¹¹. Outlier images were removed using the graphical CTF assessment tool in SPHIRE¹¹. Reference-free 2D classification and cleaning of the dataset was performed with the iterative stable alignment and clustering approach ISAC²⁷ in SPHIRE. ISAC was performed with a pixel size of 6.875 \AA /pixel on the particle level. The ‘beautify’ tool of SPHIRE was then applied to obtain refined and sharpened 2D class averages at the original pixel size, showing high-resolution features (Extended Data Fig. 1h). Our previous 9.1 \AA 3D reconstruction of the ABC holotoxin (Electron Microscopy Data Bank code: EMD-2551) was used as initial reference for 3D refinement, after proper scaling and filtering to 25 \AA . Three-dimensional refinement without imposing symmetry was performed in SPHIRE using MERIDIEN, which is a maximum likelihood-based 3D-structure refinement program, driven by the gold-standard Fourier shell correlation (FSC). After each refinement cycle, we took advantage of the ‘user-function’ option of MERIDIEN and, with the help of a short Python script, automatically symmetrized the outer shell of the TcA component as previously described^{6,28}. In brief, after each refinement cycle, the density of TcA was masked out and symmetrized with C5 symmetry. The remaining density of TcB–TcC and the background were scaled to match the threshold of the density of TcA. Subsequently, the two densities were merged, automatically masked using an adaptive mask to remove background noise, and the resulting density was then forwarded and used as a reference for the subsequent refinement cycle. This procedure was performed to obtain global parameters. The user function was not applied and TcA was not symmetrized during the final local refinement rounds. Three-dimensional variability analysis, based on the final projection parameters using SPHIRE, revealed that the variance is mostly restricted within the TcB–TcC cocoon interior, thus further suggesting that the HVR is unfolded or flexible within the cocoon. Three-dimensional classification into five groups was performed using the SORT3D tool of SPHIRE with a 3D focused binary mask including only the cocoon interior. However, most probably owing to the intrinsic flexibility of the HVR, we were not able to improve the resolution for this structural region. Therefore, we continued with the complete dataset after ISAC, including 132,033 single particles, as the respective density map showed the highest resolution at the interface of TcA–TcB with TcC.

The seven movie frames were then aligned and averaged using MotionCorr²⁹. The 132,033 particles, obtained by processing of the integrated images, were then re-extracted from the low-dose and motion-corrected averages and were then subsequently subjected to few rounds of local refinement, using the ‘continue’ mode in MERIDIEN. The estimated accuracy of angles and shifts at the final iteration was measured to 0.72 degrees and 0.9 pixels, respectively. The resolution of the final density was estimated by using the FSC³⁰ (adjusted for the full-size of the dataset) and a soft Gaussian mask and reported an average resolution of 4.22 or 3.72 \AA , according to the FSC 0.5 or 0.143, respectively (Extended Data Fig. 1i), and a B-factor of -49.43\AA^2 . The two half volumes were then merged and the resulting volume was masked and sharpened accordingly. Local FSC calculation was performed using the ‘local resolution’ tool in SPHIRE. This analysis showed that the core of the TcA complex was resolved to 3.2 \AA resolution (at FSC 0.143), whereas the upper part of the cocoon (corresponding to TcC) showed the lowest resolution $\sim 4.5\text{--}5 \text{\AA}$ (at FSC 0.143). The rest of the density was resolved to the average resolution (Extended Data Fig. 1k). The reported values were consistent with the observed structural details. The density was filtered according to its local resolution using the 3D Local Filter tool in SPHIRE.

The frames of the movie-mode images of the ABC holotoxin dataset were motion-corrected, weighted and averaged using Unblur and Summovie³¹. In addition, we created averages of the first 8 motion-corrected frames, without dose weighting (total dose 20 $e^- \text{\AA}^{-2}$). CTF estimation was performed with CTER on full-dose unweighted motion-corrected sums. Outlier images were removed using the CTF assessment tool in SPHIRE and 100 selected micrographs of large defocus were then manually picked from the full-dose weighted sums and the extracted particles were subjected to 2D classification using ISAC. Selected class averages were then used as templates to pick the complete dataset using Gautamatch. 205,336 were picked, extracted and subjected to 2D classification using ISAC (Extended Data Fig. 1b). From the initial set of particles, the clean set used for 3D refinement contained 89,148 particles. For the refinement of this dataset we used the same multi-symmetry procedure as described above for the ABC(D651A) dataset. At the end of the refinement, we replaced the particles extracted from the full dose-weighted sums with particles extracted from the unweighted 20 $e^- \text{\AA}^{-2}$ motion-corrected sums and subsequently subjected this dataset to few rounds of local refinement, using the ‘continue’ mode in MERIDIEN. This improved the reconstruction significantly. The resolution of the final density was estimated after applying a soft Gaussian mask and reported an average resolution of 4.45 or 3.94 \AA according to FSC 0.5 or 0.143, respectively (Extended Data Fig. 1c). The B-factor was estimated to be -68.03\AA^2 . The estimated accuracy of angles and shifts at the final iteration was 0.69 degrees and 0.8 pixels, respectively. The local resolution of the density was calculated using the ‘local resolution’ tool in SPHIRE (Extended Data Fig. 1e), and finally the density was filtered accordingly using the ‘3D local filter’ tool. All steps of image processing above were performed using SPHIRE unless stated otherwise¹¹. Details related to data processing are summarized in Supplementary Table 1.

Bioinformatics tools. The geometry of the final refined model was evaluated with MolProbity³²; data statistics are summarized in Supplementary Table 1. Shape complementarity was calculated with Sc¹⁷, included in the ccp4-software package³³. Analysis of the channel size was performed with ChExVis³⁴. The interface of TcA–TcB with TcC was analysed using PDBePISA³⁵.

Homologues of TcdB2 were identified using protein BLAST³⁶ and sequences of 14 homologues were aligned in Clustal Omega³⁷. Sequence conservation in the TcA-binding region and in the acidic constriction site was analysed using the ConSurf server³⁸ and visualized in UCSF Chimera. Homology models of TcB sequences were created in UCSF Chimera³⁹ using the Modeller plugin⁴⁰. Analysis of electrostatic potentials of the models in the clamp region (15 \AA radius) and clustering of the models was performed in PISA⁴¹.

For visualization, analysis and preparation of figures and movies, we used Chimera³⁹, PyMOL (<http://www.pymol.org/>) and VMD⁴².

Hydrogen–deuterium exchange–mass spectrometry. All proteins were prepared at an initial concentration of 2 μ M in exchange buffer (40 mM HEPES pH 8.0, 200 mM NaCl, 1 mM TCEP and 10% glycerol). Hydrogen–deuterium exchange was initiated by adding 5 μ l protein to 45 μ l deuteration buffer (exchange buffer prepared in D₂O). Samples were incubated at 25 °C for different times (10–3000 s) before quenching by addition of 50 μ l ice cold quench buffer (100 mM sodium phosphate pH 2.2, 5 mM TCEP, 2 M GuHCl) to a final pH of 2.6.

Quenched samples were immediately injected into a Waters ACQUITY UPLC M-class with hydrogen–deuterium exchange via a 50- μ l sample loop. Digestion was performed using an Enzymate BEH-pepsin column (Waters) at a flow rate of 100 μ l min⁻¹ and temperature of 20 °C. Peptides were trapped and desalted for 3 min at 100 μ l min⁻¹ before transfer to a 1.0 \times 100 mm ACQUITY UPLC peptide CSH C18 column (Waters) held at 0 °C. Peptides were eluted over 7 min at 40 μ l min⁻¹ with an 8–40% acetonitrile gradient in 0.1 % formic acid pH 2.5. Mass analysis was performed on a Waters Synapt G2Si. T-wave ion mobility was used as

an orthogonal peptide separation step between the UPLC and mass spectrometer⁴³, and ion guide settings were adjusted to minimize gas-phase back exchange as previously described⁴⁴. Peptides were identified by analysing MS^E data (data-independent acquisition of product ion spectra) for 4–5 undeuterated control experiments using PLGS 3.01 (Waters). Mass spectra of deuterated peptides were processed in DynamX 3.0 (Waters) and peak selection was manually verified for all peptides. All experiments were performed under identical conditions. Deuterium levels were therefore not corrected for back exchange and are reported as relative⁴⁵. All experiments were performed in duplicate.

Crystallization of empty TcB–TcC, data collection and processing. The empty TcB–TcC complex first crystallized as thin sheets using the sitting-drop vapour diffusion method at 20 °C by mixing 1 µl TcB–TcC with 1 µl reservoir solution containing 0.1 M tri-sodium citrate pH 5.5, 10% PEG 8000 and 10% ethylene glycol. The thin sheets were used to prepare a seed solution. Final crystals were obtained within 5–7 days by mixing 1 µl TcB–TcC with 1.5 µl reservoir solution and 0.5 µl seed solution. Prior to flash-freezing in liquid nitrogen, the crystals were soaked in reservoir solution containing 20% glycerol as a cryoprotectant.

Diffraction data were collected at the PXII-X10SA beamline at the Swiss Light Source and were processed with the XDS package. Phases were determined by molecular replacement with PHASER⁴⁶ using the crystal structure of wild-type TcB–TcC(WT) (PDB 4O9X)⁶ as a search model. Empty TcB–TcC crystallized in primitive hexagonal space group *P*3₂21 with unit cell dimensions of 232 × 232 × 142 Å and one molecule per asymmetric unit. The structures were optimized by iteration of manual and automatic refinement using COOT⁴⁷ and phenix.refine implemented in the PHENIX package⁴⁸ to a final *R*_{free} of 25%. Details related to data processing are summarized in Supplementary Table 2.

Affinity determination using biolayer interferometry. Affinities of TcB–TcC(WT) and of all TcB–TcC variants to TcA were determined by biolayer interferometry (BLI) using an OctedRed 384 (forteBio, Pall Life Sciences) and streptavidin biosensors.

The different TcB–TcC complexes were biotinylated in 20 mM Hepes–NaOH pH 7.3, 200 mM NaCl, 0.05% Tween20 (labelling buffer) with Sulfo-NHS-LC-Biotin (Thermo Scientific) in a 1:3 molar ratio for 2 h at room temperature, followed by 16 h at 4 °C. Unreacted biotin label was washed out using AmiconUltra 100-kDa cut-off concentrators by diluting the sample two times with a tenfold volume of buffer and re-concentrating back to the original volume.

Biotinylated TcB–TcC was immobilized on streptavidin biosensors at a concentration of 10 µg/ml, followed by quenching with 5 µg/ml biotin. BLI sensorgrams were measured in three steps: baseline (300 s), association (20 s for TcB–TcC(WT) and TcB–TcC(D651A) and 600 s for empty TcB–TcC, respectively), and dissociation (200 s for TcB–TcC(WT) and TcB–TcC(D651A) and 600 s for empty TcB–TcC, respectively). The sensorgrams were corrected for background association of TcA on unloaded streptavidin biosensors. On- and off-rates of TcA binding were determined simultaneously by a global curve fit according to a 1:1 binding model. All BLI steps were performed in labelling buffer with 0.3 mg/ml BSA.

Intoxication assay. HEK293T cells (Thermo Fisher) were intoxicated with pre-formed holotoxin formed by TcA(WT) and TcB–TcC(WT) and sensor-loop variants. Cells (2 × 10⁴) were grown adherently in 400 µl DMEM/F12 medium (Pan Biotech) overnight and, subsequently, 0.5, 2 or 5 nM of holotoxin was added. Incubation was allowed to continue for 16 h at 37 °C before imaging. Experiments were performed in triplicate. Cells were not tested for *Mycoplasma* contamination.

Atomic modelling. We modelled the atomic structure of the ABC holotoxin complexes using an iterative combination of Rosetta de novo building⁴⁹, iterative refinement⁵⁰, relaxation, molecular dynamics flexible fitting (MDFF)⁵¹ and manual building in Coot⁴⁷. We performed all MDFF runs in VMD⁴² and NAMD⁵², using the CHARMM 36m forcefield⁵³ and an implicit solvation model. We started the modelling with the ABC(WT) complex. We fitted TcC into the density using MDFF, given the comparatively low local resolution at the top of the protein. For TcA, we started from the previously determined structure⁶ (PDB 1XVW1), and build an initial model using amino acids 21–2325 by iteratively relaxing the model into the density with Rosetta and MDFF. At this stage, we imposed C5 symmetry on the model, given that the symmetry is largely preserved in this region. For TcB, we split the molecule in several independent regions. In all cases, we started from the previously determined structure of the complex⁶ (PDB 4O9X). Amino acids 1258–1319 were built from a homology model based on the YenB structure⁷ (see below), and iteratively refined in Rosetta. Most of the β-propeller region of TcB (amino acids 370–700) was built de novo owing to the large conformational change. We started by relaxing the β-propeller into the density using Rosetta. Then, we removed all amino acids belonging to blades 3 and 4 (amino acids 442–553) and ran several consecutive rounds of Rosetta de novo building. We completed the β-propeller models using RosettaCM⁵⁴ and refined it using iterative rounds of Rosetta iterative local refinement and MDFF. Finally, we reassembled full TcB using iterative rounds of Rosetta relaxation and MDFF. We then combined TcB with amino acids 2326–2516 of TcA, relaxed the complex in Rosetta and further

added TcC into the model. We then relaxed this partial ABC holotoxin complex in Rosetta, and used it as input for all molecular dynamics simulations (see below). We finally combined to full ABC holotoxin complex and ran several iterative rounds of relaxation in Rosetta and MDFF. For MDFF at this step, we imposed symmetry locally in amino acids 21–2325 of the TcA. The final relaxation rounds were performed without imposing any symmetry. We used the ABC(WT) complex as input for modelling ABC(D651A), and refined the model using iterative rounds of Rosetta relaxation and MDFF.

Finally, amino acids without density support were removed from the final models. In all cases, the quality of the models was judged according to their Molprobit³², and EMRinger⁵⁵ scores, as well as the integrated FSC values reported by Rosetta⁵⁰.

Classical molecular dynamics simulations. To test the stability of the different conformations of TcB, we performed simulations of the TcB–TcC complex in its open and closed conformations. For the open state, we started the simulations directly from the partial ABC holotoxin models described above. Because the structure of the closed conformation is missing some amino acids, we used MODELLER⁵⁶ to complete the model of the protein based on the already known crystal structure⁶ (PDB 4O9X) and the structure of the homologue YenBC⁵⁷ (PDB 4IGL). We used Rosetta to relax this model back into the electron density, to correct any possible errors introduced during the modelling steps.

We assigned the protonation state of ionizable residues at neutral pH, according to the pK_a calculated using the Rosetta pH protocol⁵⁸. We solvated these models in a dodecahedral box of TIP3P water extending at least 1.5 nm away from every protein atom. We then neutralized the system with NaCl at an ionic strength of ~150 mM, resulting in typical system sizes of ~440,000 atoms. The systems were equilibrated using a step-wise protocol. After minimization, we restrained all the protein heavy atoms and slowly heated the system to 300 K (tau = 1 ps) during 0.1 ns at constant volume. We then maintained the temperature at 300 K and adjusted the pressure to 1 atm using a Berendsen barostat (tau = 2 ps) during 0.9 ns. We then switched to the Parrinello–Rahman barostat and simulated for another 1 ns. After this, we removed the positional restraints on the protein side chains and simulated for 5 ns. Finally, we removed all restraints on the protein and simulated for additional 5 ns. From here, we performed 1.05 µs of production run using the same settings. All simulations correspond to Langevin dynamics and were performed in GROMACS⁵⁹, using the CHARMM 36m force field⁵³. The real-space calculation of short-range-non-bonded interactions was truncated at 1.2 nm, with van der Waals forces switched slowly to 0 from 1 nm. Long-range electrostatics were calculated using the particle mesh Ewald algorithm. To use a time step of 2 fs we constrained all bonds involving hydrogen atoms using the SETTLE algorithm.

We performed two simulations for the closed β-propeller state and four for the open β-propeller state, each started from a system with randomized ion positions. Only the last 0.8 µs were considered in the final analysis of the trajectories. All analyses were performed with VMD and GROMACS.

To test whether a folded helix can be translocated through the constriction site of TcB, we performed another set of simulations. For this, we predicted the secondary structure of the ADP-ribosyltransferase using the NPS@ server⁶⁰. Two peptides, residues 815–825 (peptide 1) and 892–899 (peptide 2) of TcC, showed high helical propensity. We modelled them as ideal helices using MODELLER, placed their mass centre at the constriction site of TcB–TcC in the open state, and oriented them with their C terminus towards the exit of the channel. We capped the N and C termini of the peptide with an acetyl and *N*-methyl amide group, respectively, to prevent the charge of the termini from affecting the dynamics. We then prepared the systems for simulation using the same protocol described above, and equilibrated them with a small modification. Before the last step in which all restraints are released, we performed 5 ns simulation where the backbone atoms of TcB–TcC are still restrained but the ligand helices are free to move. To enforce the helical conformation, we used the α-r.m.s.d. coordinate in PLUMED⁶¹ and placed a soft lower wall (*k* = 500 kJ mol^{−1}; centres 5.5 and 2.5 for peptides 1 and 2, respectively) to prevent the helix from unwinding. To prevent the helices from scaping towards the cocoon, we also placed a soft upper wall controlling the distance between the centre of mass of the peptide's C_α atoms and the C_α atoms of residues 406, 461, 511, 567, 620 and 672 (*k* = 500 kJ mol^{−1} nm^{−2}, centre 2.2 nm). Finally, we kept the β-propeller of TcB from collapsing by placing a soft upper wall on the distance r.m.s.d. of the C_α atoms of residues 370–700 from TcB (*k* = 500 kJ mol^{−1} nm^{−2}, centre 1 nm). We used the staring open propeller as references and considered only inter-atomic distance between 0.3 and 0.8 nm. All wall restraints were included using PLUMED. For each system, we performed two 300-ns-long production runs. In one of these we released the helical restraint on the peptide ligand, whereas in the other we kept it for the full simulation time.

Structure-based molecular dynamics simulations. To simulate the transition between open and closed states of the TcB β-propeller region, we performed 120 structure-based molecular dynamics simulations of the TcB–TcC complex,

60 starting from the closed and 60 from the open state. To study the effect of the binding to TcA, we performed 80 simulations including amino acids 2326 to 2516 of TcA, 40 starting from the closed and 40 from the open state. We refer to these as holotoxin simulations. We used only the TcB-binding domain of TcA, primarily to save computational time. This is unlikely to affect the calculations as this region is connected by a single loop to the rest of TcA and has few tertiary contacts with the rest of the protein, essentially constituting an independent domain. In addition, the contact map calculated by SMOG (see below) extends only 0.6 nm away, guaranteeing that TcB will not interact with the rest of TcA. To further stimulate the conformational change, we performed 120 additional holotoxin simulations with a debilitated β -propeller (see below), 60 starting from the closed and 60 from the open state. All individual simulations were run at a $T=125$ using an integration step of 0.002 (Gromacs reduced units), and lasted 150,000,000 time steps.

In all cases, we used GROMACS and a Gaussian contact version of the SMOG force field⁶². To include both structures into the topology-based potential, we used a strategy similar to the one described²¹, with a modified potential of the form:

$$V = \sum_{\text{bonds}} \epsilon_r (r - r_0)^2 + \sum_{\text{angles}} \epsilon_\theta (\theta - \theta_0)^2 + \sum_{\text{impropers}} \epsilon_\chi (\chi - \chi_0)^2 \\ + \sum_{\text{backbone}} \epsilon_{\text{BB}} F_D(\phi) + \sum_{\text{side chains}} \epsilon_{\text{SC}} F_D(\phi) \\ + \sum_{\text{contacts}} \epsilon_C C_{ij}(r_{ij}) + \sum_{\text{bonds}} \epsilon_R \left(\frac{\mu_R}{r_{ij}} \right)^{12}$$

in which r_0 , θ_0 and χ_0 were taken from the native structures. The definition of all energy constants and their values have been described^{21,62,63}. For r_0 and θ_0 , we used the average between the two states, as they are mostly invariant. Improper restrain planar groups and the configuration of prolines. Therefore, we used also the average for χ_0 for any angle for which the difference between both structures was less than 10 degrees. In all other cases (some prolines), we transferred the term from the closed state, as this represents a model from a higher resolution map.

C_{ij} can be defined in two different ways. For all atomic contacts present in only one of the structures, we used a single Gaussian potential with an exclusion term. For contacts present in the open and closed conformations, we used a dual basin Gaussian potential, essentially as described²¹ (see Extended Data Fig. 6g, h). For the simulations with destabilized β -propeller region, we decreased the strength of all contacts involving β -propeller atoms to 90% of their original strength.

A dual dihedral energy term $F_D(\phi)$ was defined essentially as in ref. ²¹ (see Extended Data Fig. 6g, h). In brief, the term for a single dihedral is defined as

$$F_D(\phi) = 1 - \cos(\phi - \phi_0) + 0.5(1 - \cos(3(\phi - \phi_0)))$$

in which ϕ_0 represents the dihedral observed in the structure. To create a term that includes minima for two states (a and b) we defined a conditional function. We first identified $\text{av}1$, the average between the dihedral angles observed in each structure; we then identified $\text{av}2$, which corresponds to $\text{av}1 + 180^\circ$. Assuming that state a has the smallest dihedral angle, the new dual $F_D(\phi)$ function corresponds to $F_D(\phi)_a$ for $\text{av}2 < \phi < \text{av}1$, and to $F_D(\phi)_b$ for $\text{av}1 < \phi < \text{av}2$. To properly connect the halves of the function, we identified the appropriate extrema closest to $\text{av}1$ or $\text{av}2$, and connected them using the function $F_D(\phi) = k(\phi - q)^2(\phi - p)^2 + c$, in which k , q , p and c were chosen so that the first and second derivatives were the same as in the cosine function at the connecting points. For an overview of the final functions please see Extended Data Fig. 6g, h. All files for the simulations were prepared with a standalone version of SMOG2⁶⁴ and modified using in-house-built scripts. All analyses were performed in VMD. Two atoms were defined as forming their native contact if their distance was less than 1.2 times the distance observed in the native structure. Using the native contact maps, we defined a collective variable corresponding to the difference between the number of contacts in the closed and open states of each blade. We used this to follow the conformational change. To reduce the noise level, the collective variable trajectories were smoothed using running averages calculated with a window size of 150,000 time steps. Using these values, we considered that a blade had lost its state when it had less than 105 contacts formed. To characterize the conformational change mechanism, we combined all trajectories and used the new collective variable to build the histograms shown in Fig. 2 and Extended Data Fig. 7.

Reporting Summary. Further information on research design is available in the Nature Research Reporting Summary linked to this paper.

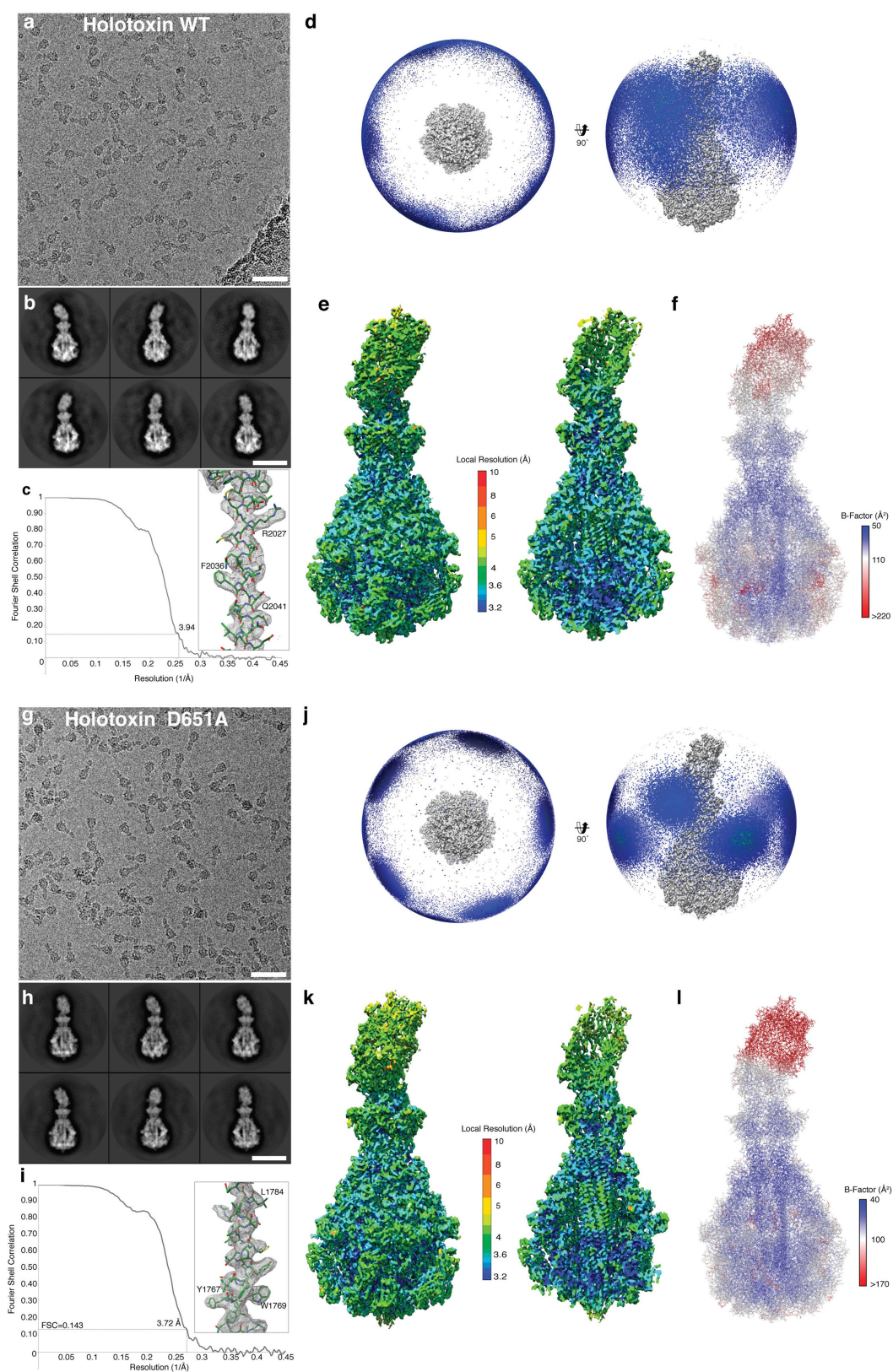
Data availability

The densities and atomic coordinates of ABC(WT) and ABC(D651A) have been deposited in the Electron Microscopy Data Bank under the accession numbers

EMD-0149 and EMD-0150, respectively, and in the Protein Data Bank under accession numbers 6H6E and 6H6F, respectively. The atomic coordinates of the crystal structure of TcdB2–TccC3 without HVR have been deposited in the Protein Data Bank under the accession number 6H6G. The HDX data are available in the Source Data for Fig. 4. The datasets generated and/or analysed during the current study are available from the corresponding author upon reasonable request.

- Tang, G. et al. EMAN2: an extensible image processing suite for electron microscopy. *J. Struct. Biol.* **157**, 38–46 (2007).
- Penczek, P. A. et al. CTER—rapid estimation of CTF parameters with error assessment. *Ultramicroscopy* **140**, 9–19 (2014).
- Yang, Z., Fang, J., Chittuluru, J., Asturias, F. J. & Penczek, P. A. Iterative stable alignment and clustering of 2D transmission electron microscope images. *Structure* **20**, 237–247 (2012).
- Gatsogiannis, C., Hofnagel, O., Markl, J. & Raunser, S. Structure of mega-hemocyanin reveals protein origami in snails. *Structure* **23**, 93–103 (2014).
- Li, X. et al. Electron counting and beam-induced motion correction enable near-atomic-resolution single-particle cryo-EM. *Nat. Methods* **10**, 584–590 (2013).
- Penczek, P. A. Resolution measures in molecular electron microscopy. *Methods Enzymol.* **482**, 73–100 (2010).
- Grant, T. & Grigorieff, N. Measuring the optimal exposure for single particle cryo-EM using a 2.6 Å reconstruction of rotavirus VP6. *eLife* **4**, e06980 (2015).
- Chen, V. B. et al. MolProbity: all-atom structure validation for macromolecular crystallography. *Acta Crystallogr. D* **66**, 12–21 (2010).
- Winn, M. D. et al. Overview of the CCP4 suite and current developments. *Acta Crystallogr. D* **67**, 235–242 (2011).
- Masood, T. B., Sandhya, S., Chandra, N. & Natarajan, V. CHEXVIS: a tool for molecular channel extraction and visualization. *BMC Bioinformatics* **16**, 179 (2015).
- Krissinel, E. & Henrick, K. Inference of macromolecular assemblies from crystalline state. *J. Mol. Biol.* **372**, 774–797 (2007).
- Altschul, S. F. et al. Basic local alignment search tool. *J. Mol. Biol.* **215**, 403–410 (1990).
- Sievers, F. et al. Fast, scalable generation of high-quality protein multiple sequence alignments using Clustal Omega. *Mol. Syst. Biol.* **7**, 539 (2011).
- Ashkenazy, H., Erez, E., Martz, E., Pupko, T. & Ben-Tal, N. ConSurf 2010: calculating evolutionary conservation in sequence and structure of proteins and nucleic acids. *Nucleic Acids Res.* **38**, W529–W533 (2010).
- Pettersen, E. F. et al. UCSF Chimera—a visualization system for exploratory research and analysis. *J. Comput. Chem.* **25**, 1605–1612 (2004).
- Webb, B. & Sali, A. in *Functional Genomics* (eds Kaufmann, M., Klinger, C. & Savelsbergh, A.) 39–54 (Springer, New York, 2017).
- Richter, S., Wenzel, A., Stein, M., Gabdoulline, R. R. & Wade, R. C. webPIPSA: a web server for the comparison of protein interaction properties. *Nucleic Acids Res.* **36**, W276–W280 (2008).
- Humphrey, W., Dalke, A. & Schulten, K. VMD: visual molecular dynamics. *J. Mol. Graph.* **14**, 33–38 (2008).
- Iacob, R. E., Murphy, J. P. III & Engen, J. R. Ion mobility adds an additional dimension to mass spectrometric analysis of solution-phase hydrogen/deuterium exchange. *Rapid Commun. Mass Spectrom.* **22**, 2898–2904 (2008).
- Guttman, M. et al. Tuning a high transmission ion guide to prevent gas-phase proton exchange during H/D exchange MS analysis. *J. Am. Soc. Mass Spectrom.* **27**, 662–668 (2016).
- Wales, T. E. & Engen, J. R. Hydrogen exchange mass spectrometry for the analysis of protein dynamics. *Mass Spectrom. Rev.* **25**, 158–170 (2005).
- McCoy, A. J. et al. Phaser crystallographic software. *J. Appl. Cryst.* **40**, 658–674 (2007).
- Emsley, P., Lohkamp, B., Scott, W. G. & Cowtan, K. Features and development of Coot. *Acta Crystallogr. D* **66**, 486–501 (2010).
- Adams, P. D. et al. PHENIX: a comprehensive Python-based system for macromolecular structure solution. *Acta Crystallogr. D* **66**, 213–221 (2010).
- Wang, R. Y.-R. et al. De novo protein structure determination from near-atomic-resolution cryo-EM maps. *Nat. Methods* **12**, 335–338 (2015).
- DiMaio, F. et al. Atomic-accuracy models from 4.5-Å cryo-electron microscopy data with density-guided iterative local refinement. *Nat. Methods* **12**, 361–365 (2015).
- Trabuco, L. G., Villa, E., Mitra, K., Frank, J. & Schulten, K. Flexible fitting of atomic structures into electron microscopy maps using molecular dynamics. *Structure* **16**, 673–683 (2008).
- Phillips, J. C. et al. Scalable molecular dynamics with NAMD. *J. Comput. Chem.* **26**, 1781–1802 (2005).
- Huang, J. et al. CHARMM36m: an improved force field for folded and intrinsically disordered proteins. *Nat. Methods* **14**, 71–73 (2017).
- Song, Y. et al. High-resolution comparative modeling with RosettaCM. *Structure* **21**, 1735–1742 (2013).
- Barad, B. A. et al. EMRinger: side chain-directed model and map validation for 3D cryo-electron microscopy. *Nat. Methods* **12**, 943–946 (2015).
- Sali, A. & Blundell, T. L. Comparative protein modelling by satisfaction of spatial restraints. *J. Mol. Biol.* **234**, 779–815 (1993).
- Busby, J. N. et al. Structural analysis of Chi1 chitinase from *Yen-Tc*: the multisubunit insecticidal ABC toxin complex of *Yersinia entomophaga*. *J. Mol. Biol.* **415**, 359–371 (2012).
- Kilambi, K. P. & Gray, J. J. Rapid calculation of protein pKa values using Rosetta. *Biophys. J.* **103**, 587–595 (2012).

59. Abraham, M. J. et al. GROMACS: high performance molecular simulations through multi-level parallelism from laptops to supercomputers. *SoftwareX* **1–2**, 19–25 (2015).
60. Combet, C., Blanchet, C., Geourjon, C. & Deléage, G. NPS@: network protein sequence analysis. *Trends Biochem. Sci.* **25**, 147–150 (2000).
61. Tribello, G. A., Bonomi, M., Branduardi, D., Camilloni, C. & Bussi, G. PLUMED 2: New feathers for an old bird. *Comput. Phys. Commun.* **185**, 604–613 (2014).
62. Lammert, H., Schug, A. & Onuchic, J. N. Robustness and generalization of structure-based models for protein folding and function. *Proteins* **77**, 881–891 (2009).
63. Whitford, P. C. et al. An all-atom structure-based potential for proteins: bridging minimal models with all-atom empirical forcefields. *Proteins* **75**, 430–441 (2009).
64. Noel, J. K. et al. SMOG 2: a versatile software package for generating structure-based models. *PLoS Comput. Biol.* **12**, e1004794 (2016).

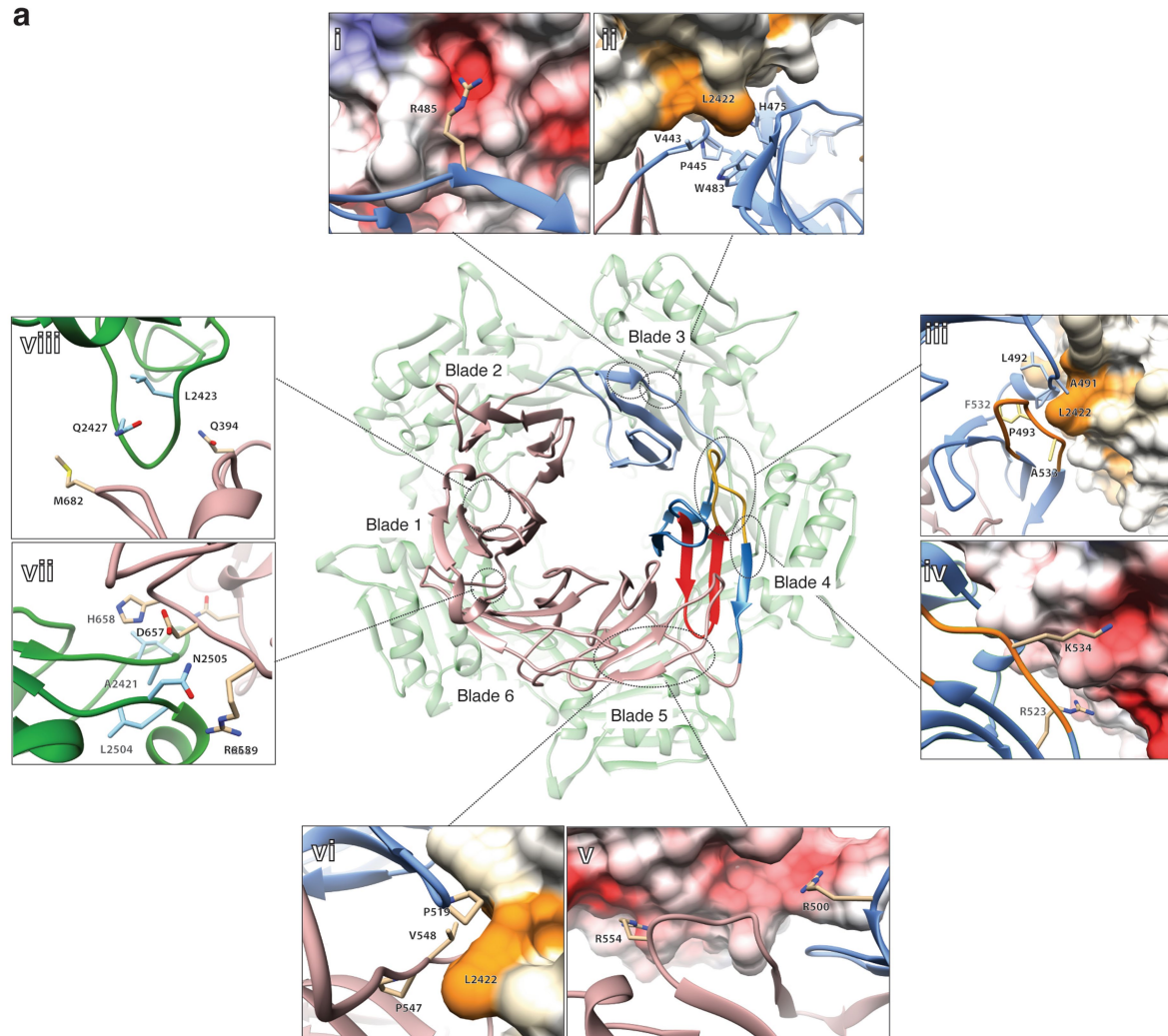
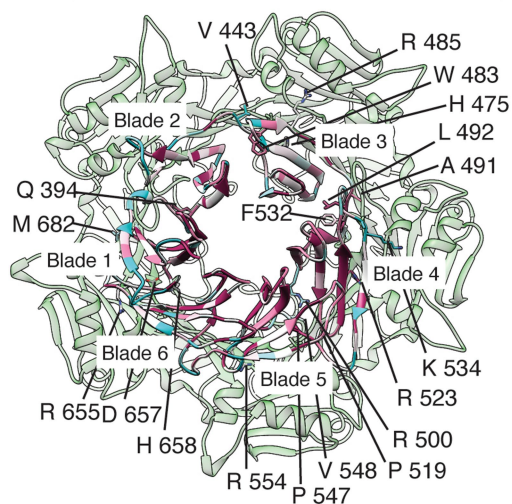


Extended Data Fig. 1 | See next page for caption.

Extended Data Fig. 1 | Cryo-EM of the wild-type ABC and

ABC(D651A) holotoxin complex. **a**, Typical digital micrograph area of vitrified wild-type holotoxin complexes at a defocus of 2 μm and a total dose of $60 \text{ e}^- \text{ \AA}^{-2}$ acquired with a Falcon II direct electron detector. Scale bar, 60 nm. **b**, Representative reference-free 2D class averages obtained by ISAC and subsequently resampled to the original pixel size, refined and sharpened, using the Beautifier tool implemented in the SPHIRE software package. Scale bar, 20 nm. **c**, Fourier shell correlation (FSC). The 0.143 FSC cut-off criterion indicates that the cryo-EM map has an average resolution of 3.94 \AA . The inset shows a representative area of the density map superimposed with the atomic model. **d**, Angular distribution for the final round of the refinement. Each stick represents a projection view. Size and colour of the stick is proportional to the number of particles. **e**, Surface and cross-section of the cryo-EM density map coloured according to the local resolution. **f**, Molecular model of the wild-type

holotoxin complex coloured by B-factor. **g**, Typical digital micrograph area of vitrified ABC(D651A) complexes at a defocus of 2 μm and a total dose of $35 \text{ e}^- \text{ \AA}^{-2}$. Scale bar, 60 nm. **h**, Characteristic reference-free 2D class averages of ABC(D651A) complexes. Scale bar, 20 nm. **i**, The 0.143 FSC cut-off criterion indicates that the cryo-EM map of ABC(D651A) has an average resolution of 3.72 \AA . The inset shows a representative area of the density map superimposed with the molecular model. **j**, Angular distribution for the final round of the refinement. **k**, Surface and cross section of the cryo-EM density map coloured according to the local resolution. **l**, Molecular model of the ABC(D651A) holotoxin complex coloured by B-factor. Note that the TcC density in both volumes shows comparatively low local resolution and the molecular models of these specific areas were obtained by flexible fitting of the available crystal structure using MDFF and subsequent local refinement with Rosetta.

a**b****c**

Consurf histogram

gii15787540BURPM_PA_TcB	481	491	501	511	521	531
gii15787540BURPM_PA_TcB	443 M	443 M	443 M	443 M	443 M	443 M
gii157810146BURPM_406e_TcB	443 M	443 M	443 M	443 M	443 M	443 M
gii103566602YEREN_YenB	458	458	458	458	458	458
gii530708567PHOTE_TE_TcB	458	458	458	458	458	458
gii339697549PHOTE_TE_TcB	458	458	458	458	458	458
gii3265037IPHOLU_TcB	458	458	458	458	458	458
gii78459183IPHOLU_LU_TcB	458	458	458	458	458	458
gii14085047YEREN_TcB	458	458	458	458	458	458
gii32699986YERFR_TcF2	458	458	458	458	458	458
gii733129602XENNE_WEB_TcB	469	469	469	469	469	469
gii733153959XENNE_AN_TcB	469	469	469	469	469	469
gii16416930IPHOLU_TcB1	458	458	458	458	458	458
gii27479675IPHOLU_TcB2	449	449	449	449	449	449
gii344311030PHOTE_TcB2	454	454	454	454	454	454

Consurf histogram

gii15787540BURPM_PA_TcB	541	551	561	571	581	591
gii15787540BURPM_PA_TcB	503 G	503 G	503 G	503 G	503 G	503 G
gii157810146BURPM_406e_TcB	503 G	503 G	503 G	503 G	503 G	503 G
gii103566602YEREN_YenB	517 G	517 G	517 G	517 G	517 G	517 G
gii530708567PHOTE_TE_TcB	517 G	517 G	517 G	517 G	517 G	517 G
gii339697549PHOTE_TE_TcB	517 G	517 G	517 G	517 G	517 G	517 G
gii3265037IPHOLU_TcB	517 G	517 G	517 G	517 G	517 G	517 G
gii78459183IPHOLU_LU_TcB	517 G	517 G	517 G	517 G	517 G	517 G
gii14085047YEREN_TcB	517 G	517 G	517 G	517 G	517 G	517 G
gii32699986YERFR_TcF2	515 G	515 G	515 G	515 G	515 G	515 G
gii733129602XENNE_WEB_TcB	529 G	529 G	529 G	529 G	529 G	529 G
gii733153959XENNE_AN_TcB	529 G	529 G	529 G	529 G	529 G	529 G
gii16416930IPHOLU_TcB1	514 G	514 G	514 G	514 G	514 G	514 G
gii27479675IPHOLU_TcB2	509 G	509 G	509 G	509 G	509 G	509 G
gii344311030PHOTE_TcB2	513 G	513 G	513 G	513 G	513 G	513 G

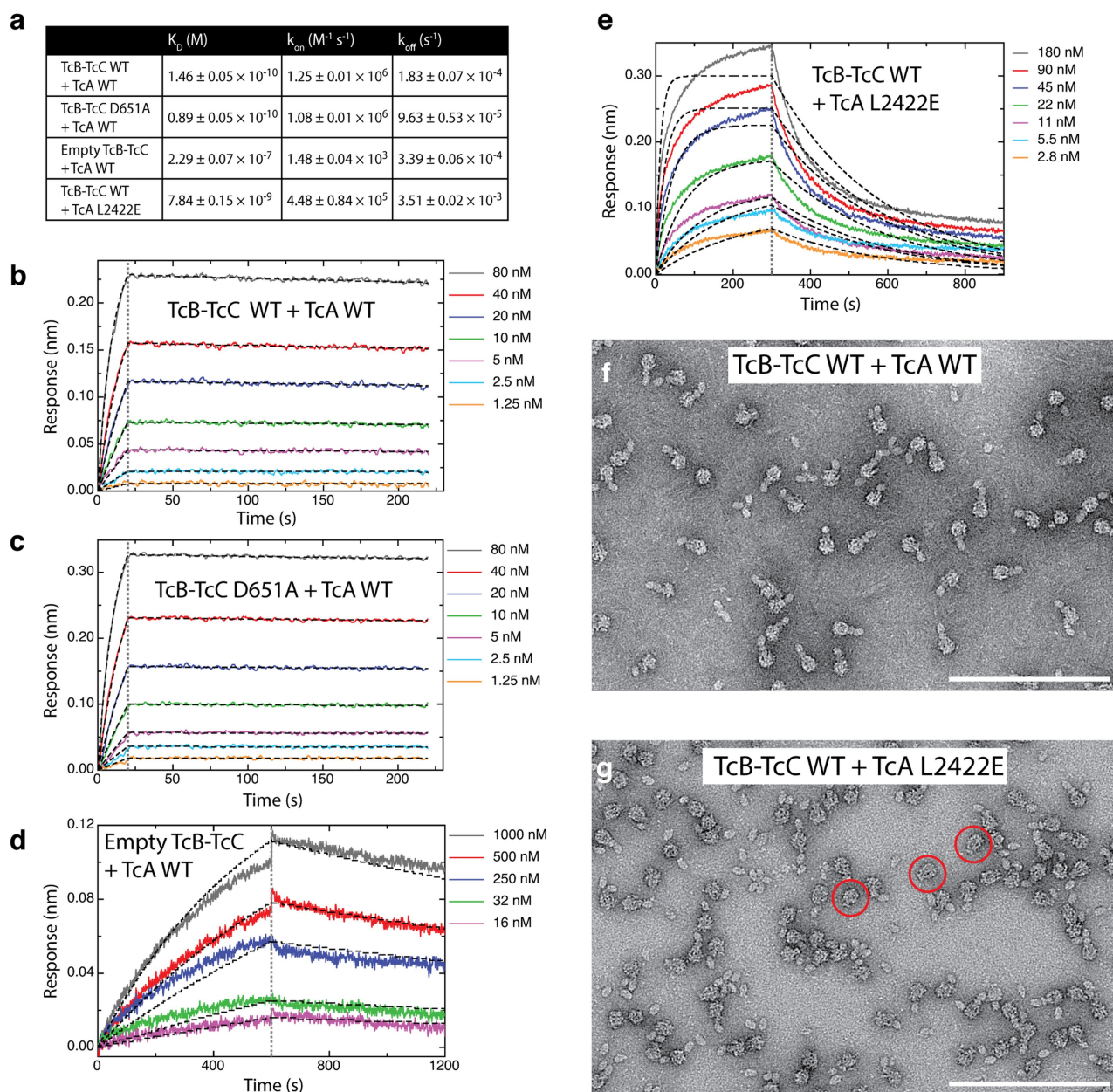
Consurf histogram

gii15787540BURPM_PA_TcB	661	671	681	691	701	711
gii15787540BURPM_PA_TcB	623 S	623 S	623 S	623 S	623 S	623 S
gii157810146BURPM_406e_TcB	623 S	623 S	623 S	623 S	623 S	623 S
gii103566602YEREN_YenB	637 S	637 S	637 S	637 S	637 S	637 S
gii530708567PHOTE_TE_TcB	637 S	637 S	637 S	637 S	637 S	637 S
gii339697549PHOTE_TE_TcB	637 S	637 S	637 S	637 S	637 S	637 S
gii3265037IPHOLU_TcB	637 S	637 S	637 S	637 S	637 S	637 S
gii78459183IPHOLU_LU_TcB	637 S	637 S	637 S	637 S	637 S	637 S
gii14085047YEREN_TcB	637 S	637 S	637 S	637 S	637 S	637 S
gii32699986YERFR_TcF2	635 S	635 S	635 S	635 S	635 S	635 S
gii733129602XENNE_WEB_TcB	648 A	648 A	648 A	648 A	648 A	648 A
gii733153959XENNE_AN_TcB	648 A	648 A	648 A	648 A	648 A	648 A
gii16416930IPHOLU_TcB1	634 A	634 A	634 A	634 A	634 A	634 A
gii27479675IPHOLU_TcB2	628 T	628 T	628 T	628 T	628 T	628 T
gii344311030PHOTE_TcB2	633 T	633 T	633 T	633 T	633 T	633 T

Extended Data Fig. 2 | See next page for caption.

Extended Data Fig. 2 | Details of the TcA–TcB interface. **a**, Interactions at the TcA–TcB interface. Binding of TcA to TcB–TcC is stabilized by interactions between the pseudo-six-fold symmetrical β -propeller of TcB and the five-fold symmetrical TcB-binding domain of TcA. The gatekeeper domain, shown in blue, undergoes the largest conformational changes during gate opening. In the open state, residues R485 (i) and K534 (iv) of blades 3 and 4, respectively, are positioned within negatively charged grooves of the TcB-binding domain of TcA. In addition, two copies of residue L2422 of two adjacent TcA subunits are positioned within a prominent hydrophobic groove of blade 3 (ii) and 4 (iii), respectively. Interacting residues of TcB are shown as sticks. Surfaces of TcA involved in the interfaces are coloured from high (orange) to low (white) hydrophobicity (ii, iii, vi) or according to the Coulomb potential (ranging from $-10 \text{ kcal mol}^{-1}$ (red) to 10 kcal mol^{-1} (blue) at pH 7.5 (i, iv, v)). Similar to the interfaces between blade 3 and 4 and TcA, blade 5 forms

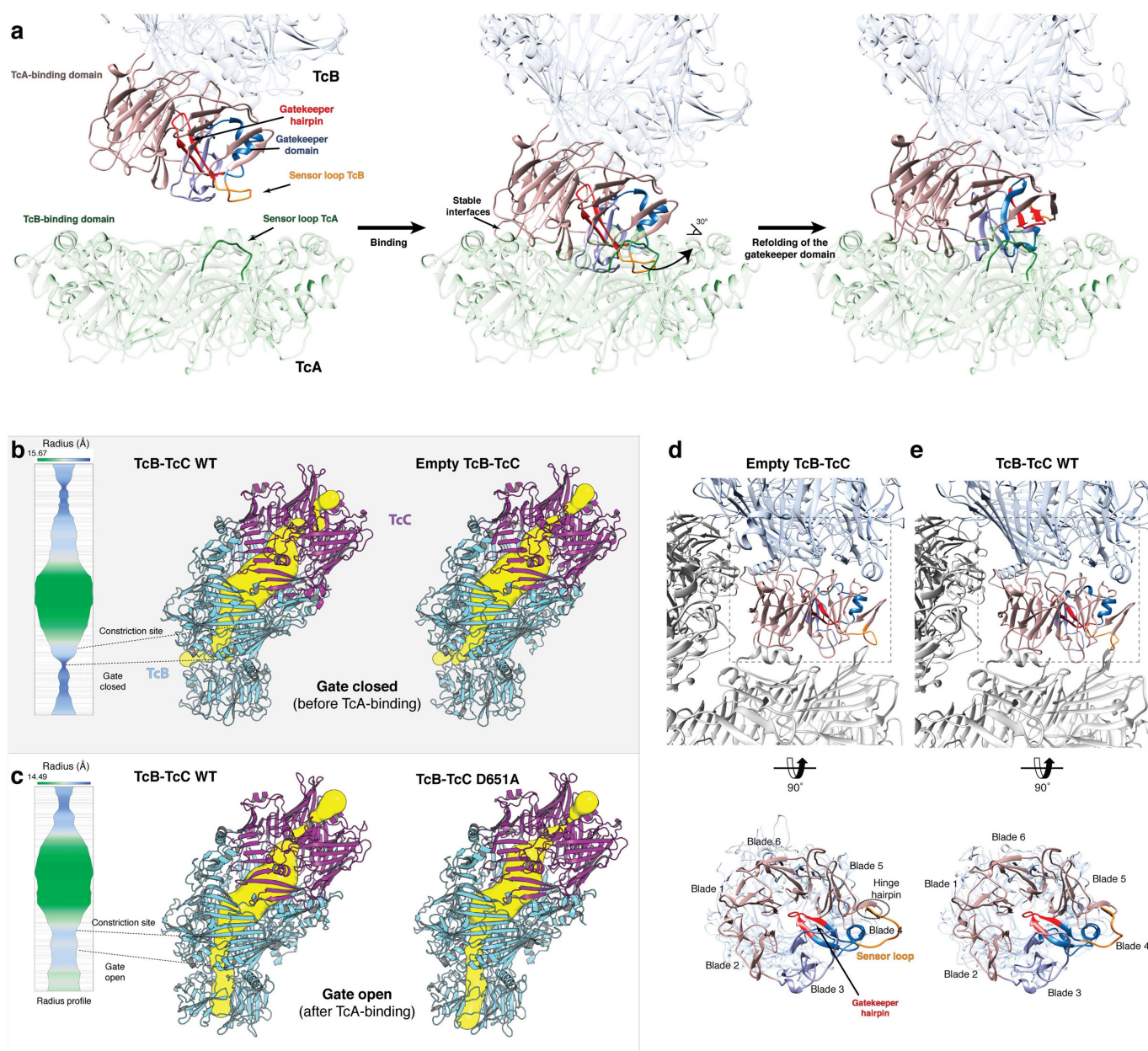
strong hydrophobic interactions with residue L2422 of TcA (vi) and electrostatic interactions with negatively charged patches of the opposing TcA domain (v). In contrast to the other blades, no prominent electrostatic or hydrophobic interactions can be observed with high certainty at this interface. Several candidates for amino acid residues were identified as putative hydrogen bond donors or acceptors (vii, viii). Colours correspond to those in Fig. 1. **b**, Conservation of residues at the TcA–TcB interface. Positions of residues of the β -propeller domain of TcB interacting with TcA are shown as in **a**. The model of the β -propeller domain is coloured according to sequence conservation, with cyan representing non-conserved residues and magenta representing highly conserved residues. The TcB-binding domain of TcA is shown in light green. **c**, Sequence alignment of TcB sequences. Asterisks indicate the positions of the residues highlighted in **b**. The sequence of *P. luminescens* TcdB2 is outlined. The alignment is coloured according to **b**.



Extended Data Fig. 3 | Binding affinities of TcB-TcC, TcB-TcC(D651A) and empty TcB-TcC for TcA and of TcB-TcC for TcA(L2422E).

a, Interaction of TcA with TcB-TcC(WT), empty TcB-TcC, or TcB-TcC_{D651A}, and interaction of TcA(L2422) with TcB-TcC were measured by BLI. K_D , k_{on} and k_{off} obtained from global fits are shown. Data are mean \pm error of fit; 5–7 individual curves were included in the global fits. **b–e**, BLI sensorgrams of TcA(WT) interacting with immobilized TcB-TcC(WT) (**b**), TcB-TcC(D651A) (**c**), empty TcB-TcC (**d**) and TcA(L2422E) interacting with immobilized TcB-TcC(WT) (**e**). TcA pentamer concentrations were 1.25 nM–80 nM in **b** and **c**, 16–1,000 nM in

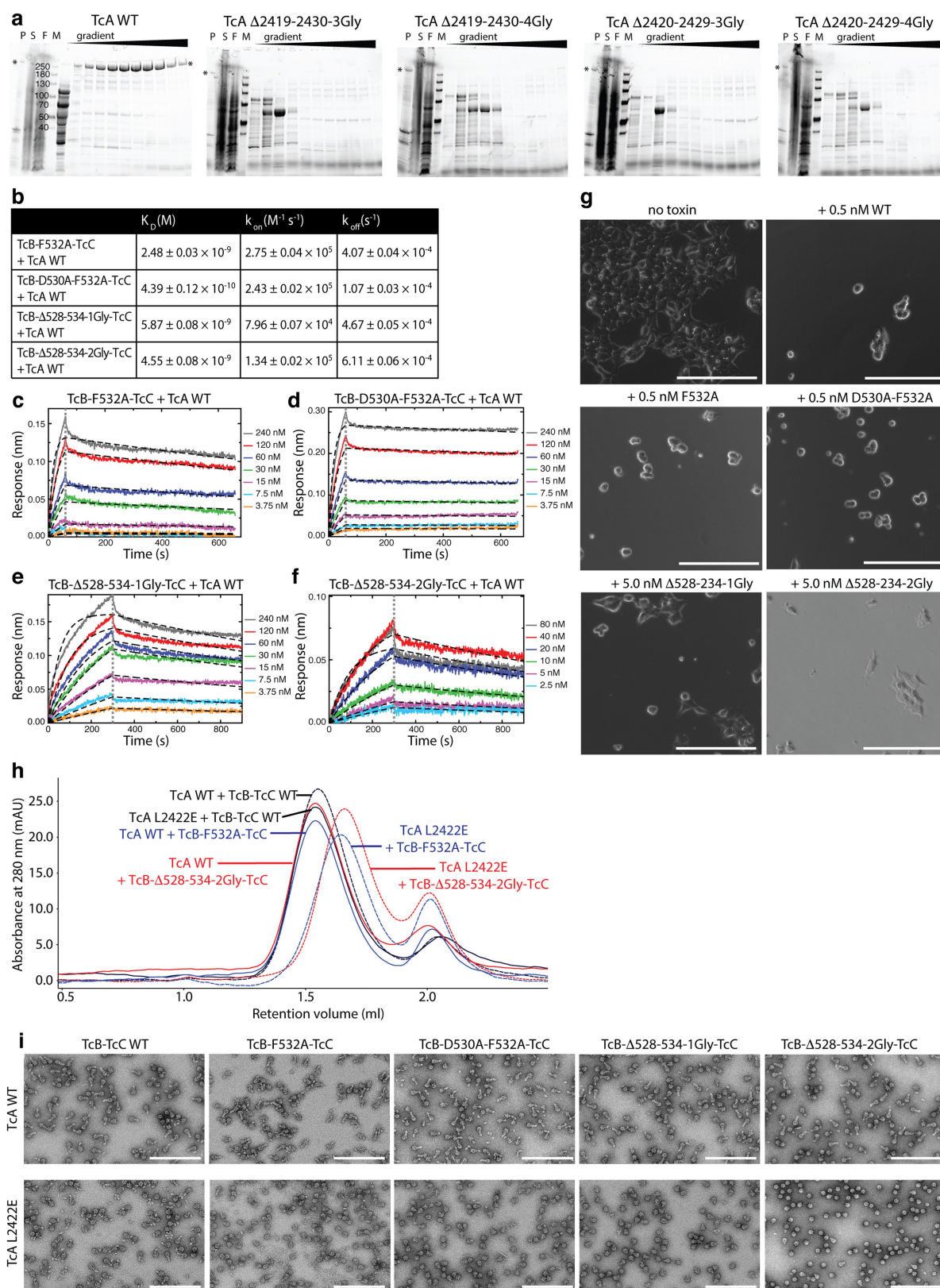
d and 2.8–180 nM in **e**. A global fit according to a 1:1 binding model was applied (black dashed curves). Resulting K_D , k_{on} and k_{off} values are shown. Association and dissociation phases are separated by a grey dotted line. **f**, **g**, Negative-stain electron micrographs of TcA(WT) (**f**) and TcA(L2422E) (**g**) incubated with wild-type TcB-TcC. TcA (200 nM) was incubated with TcB-TcC (300 nM), and the excess of free TcB-TcC was removed by size-exclusion chromatography before imaging. Red circles in **g** highlight side views of TcA without TcB-TcC. Experiments were performed three times with comparable results. Scale bar, 200 nm.



Extended Data Fig. 4 | Opening of the β -propeller gate of TcB.

a, Opening of the β -propeller gate is triggered by sensor loops. Side views of the closed, (left; before binding to TcA) (PDB 4O9X) and open (right; after binding to TcA) state of the TcA-binding six-bladed β -propeller domain of TcB-TcC. The structure of the closed state was structurally aligned with the structure of the open state and is shown together with the TcB-binding domain of TcA (middle). Note the clashing loops (sensor loops) between TcA (residues 2418–2430, green) and TcB (residues 527–536, orange). Colours correspond to those in Fig. 1. **b**, **c**, Effect of the ADP-ribosyltransferase on the structure of TcB-TcC. Crystal structures of unbound wild-type and empty TcB-TcC are shown in **b**. TcB-TcC structures obtained from the cryo-EM structures of ABC(WT) and ABC(D651A) are shown in **c**. For the structures of TcB-TcC(WT), the channel radius profile is shown as a function of distance along the

channel axis before and after TcA binding in **b** and **c**, respectively (left). The narrowest constriction of the channel lumen towards the TcA-binding domain (constriction site) has a diameter of 10.5 Å in the open state. For all structures, the mesh surface of the computed channel along the cocoon interior is shown in yellow. Note that the presence or absence of the ADP-ribosyltransferase does not affect the channel profile in the unbound state of the cocoon **b**. Note also, that cocoons with cleaved (TcB-TcC(WT)) or uncleaved (TcB-TcC(D651A)) ADP-ribosyltransferase show an almost identical channel profile following binding to TcA (**c**). **d**, **e**, Comparison of crystal contacts in the structures of empty TcB-TcC and TcB-TcC(WT). Top and side views of the crystal structures of empty TcB-TcC (**d**) and TcB-TcC(WT) (PDB 4O9X) (**e**) including crystal contacts. The TcA-binding domain of TcB is indicated by a dashed box and coloured as in Fig. 1b, c. The gatekeeper hairpin (residues 514–524) is highlighted in red.

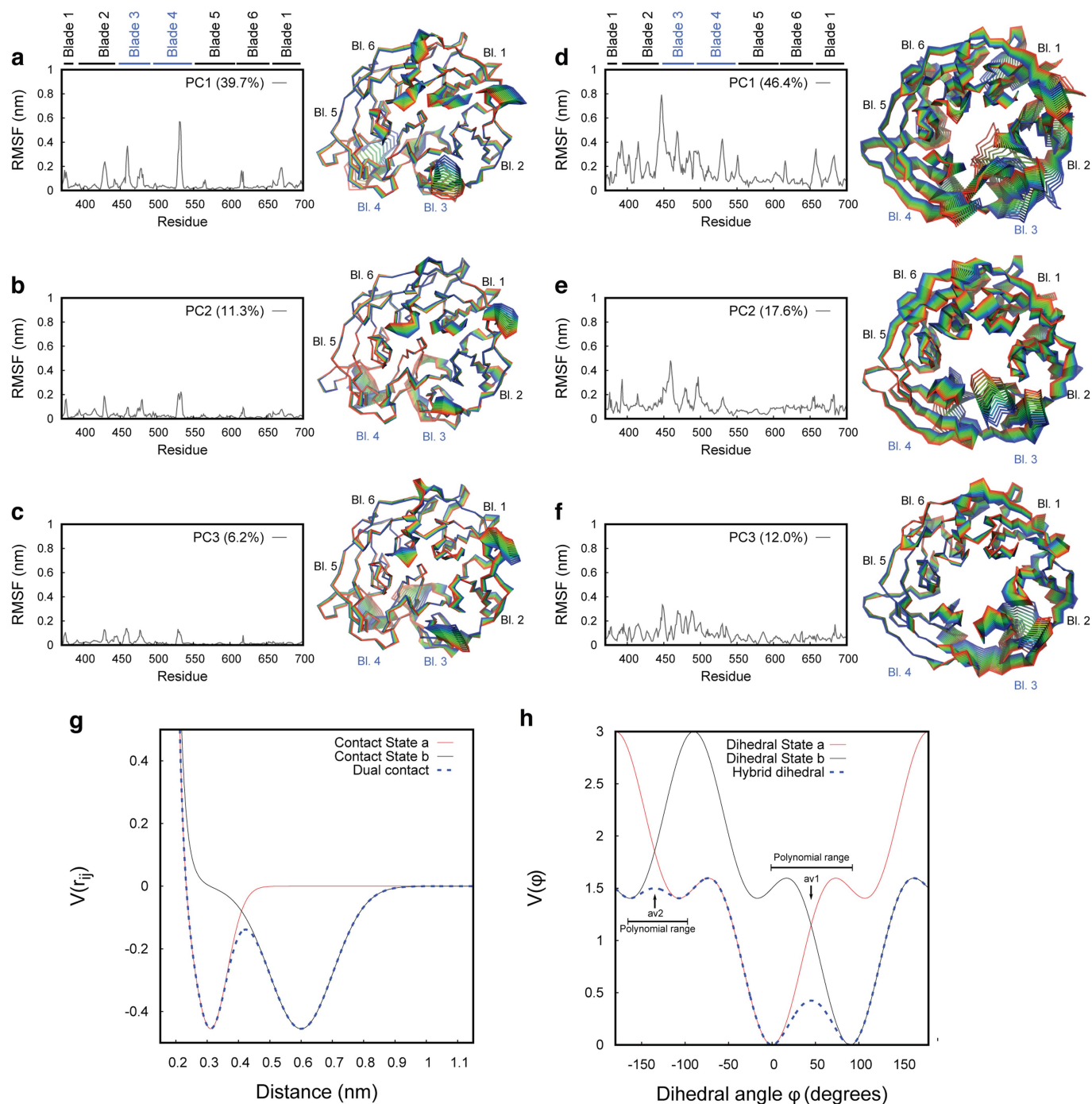


Extended Data Fig. 5 | See next page for caption.

Extended Data Fig. 5 | Analysis of TcA and TcB sensor-loop mutants.

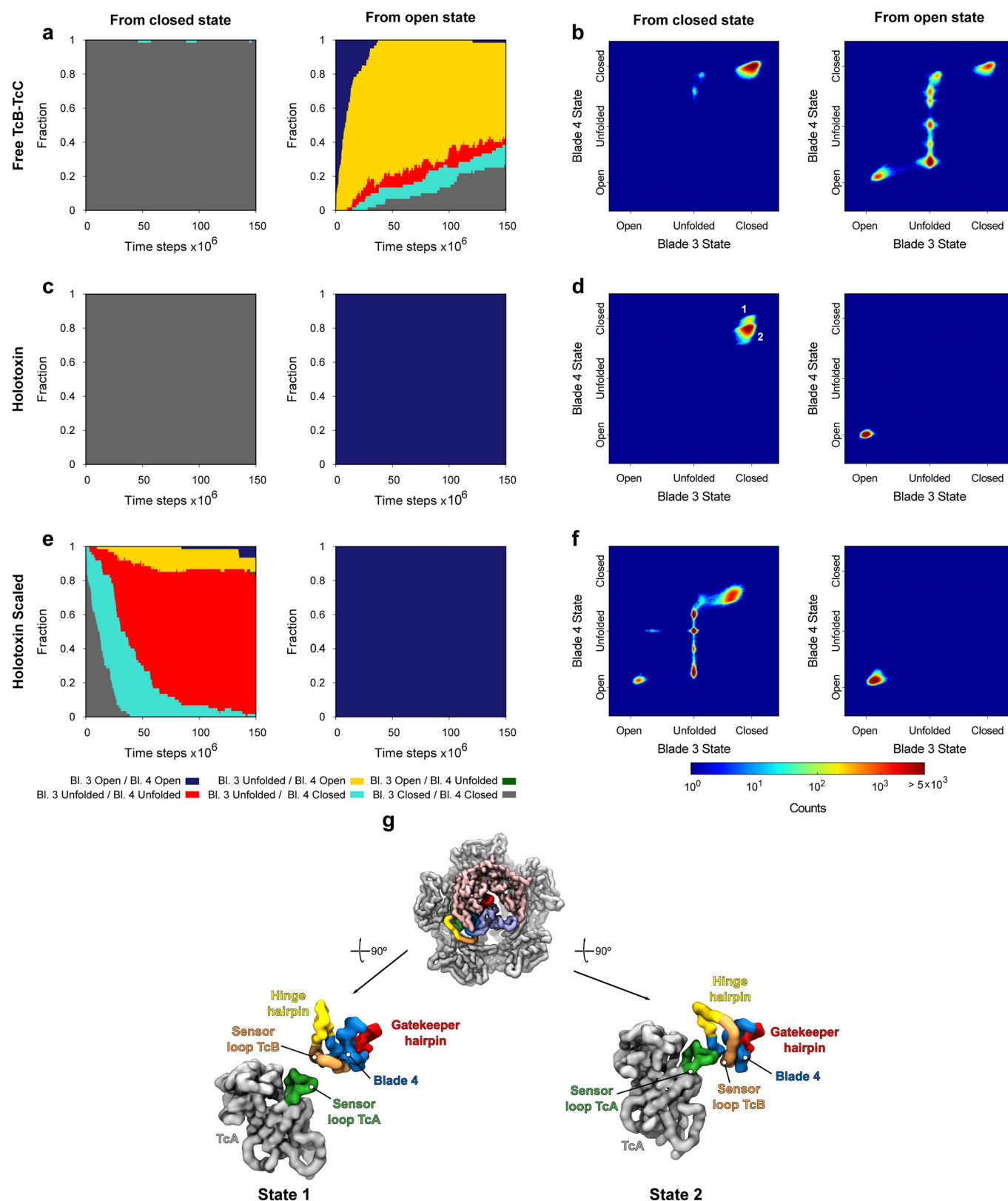
a, Analysis of the first purification step (Ni^{2+} -affinity chromatography) of TcA(WT) and sensor-loop deletion variants. P, insoluble fraction; S, soluble fraction; F, flow-through; M, protein marker. The gradient corresponds to 20–300 mM imidazole. Marker proteins: 250, 180, 130, 100, 70, 50 and 40 kDa. TcA is marked by an asterisk. Purification was performed once for each TcA variant. Purification of TcA(WT) resulted in comparable results for more than 5 experiments. **b**, K_D , k_{on} and k_{off} values of the global fits obtained from the BLI measurements (**c–f**), analogous to Extended Data Fig. 3a. Data are mean \pm error of fit; 6–7 individual curves were included in the global fits. **c–f**, BLI sensorgrams and binding affinities of TcB–TcC sensor-loop mutants with TcA. BLI sensorgrams of TcA(WT) interacting with immobilized TcB(F532A)–TcC (**c**), TcB(D530A/F532A)–TcC (**d**), TcB(Δ 528–534–1Gly)–TcC (**e**) and TcB(Δ 528–534–2Gly)–TcC (**f**) (-Gly indicates glycines replacing the TcB sensor loop). A global fit according to a 1:1 binding model was applied (black dashed lines). TcA pentamer concentrations were 3.75–240 nM in **c–e** and 2.5–80 nM in (**f**). Association and dissociation phases are separated by a grey dotted line. **g**, Intoxication of HEK293T cells with holotoxin formed

by TcA(WT) and the indicated TcB–TcC variants. Scale bars, 200 μm . Cells (2×10^4) in DMEM/F12 medium were incubated with 0.5 or 5 nM of holotoxin for 16 h at 37 °C before imaging. Experiments were performed in triplicate with qualitatively identical results. The wild-type holotoxin and the complexes with the two sensor-loop point mutations show strong cytotoxic effects. Both loop deletion variants, however, are not toxic to cells, even at 10 times higher concentration. **h**, **i**, Holotoxin complex formation between TcA(WT) and L2422E and TcB–TcC sensor-loop variants. **h**, Chromatograms of TcB–TcC(WT) and selected variants with TcA(WT) (solid lines) and TcA(L2422E) (dashed lines). TcA pentamer (200 nM) and TcB–TcC (400 nM) were incubated for 1 h at 22 °C before loading on a Superose 6 5/150 column (GE Life Science). Experiments were performed twice with identical results. **i**, Electron micrographs of different combinations of TcA and TcB–TcC. The main peaks of the chromatography runs (**h**) were negatively stained and imaged. Scale bar, 200 nm. Experiments were performed twice with qualitatively identical results. All sensor-loop mutants show almost exclusively holotoxins when mixed with TcA(WT), but practically no holotoxins with TcA(L2422E). TcB–TcC(WT), however, can form a holotoxin with TcA(L2422E).



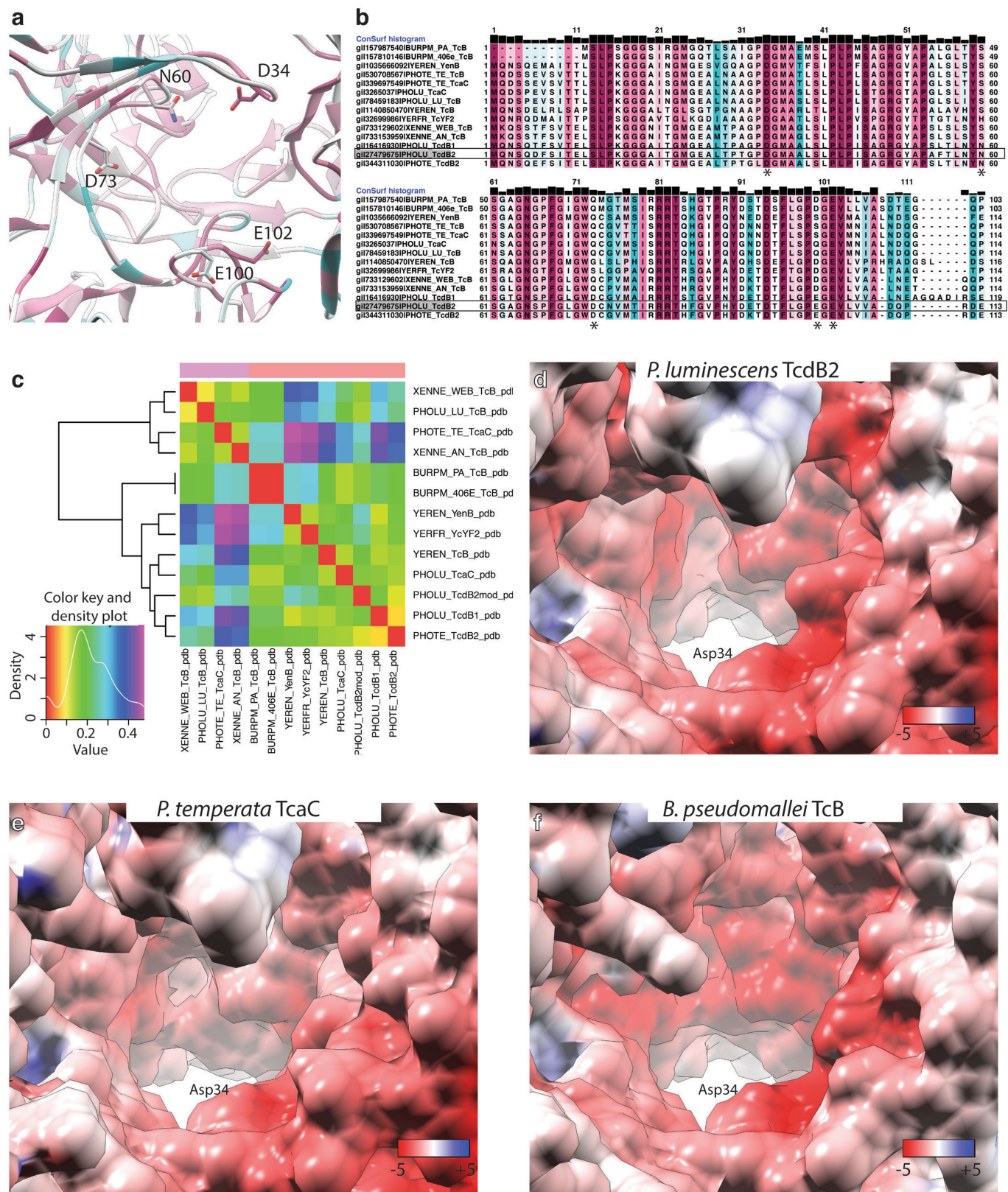
Extended Data Fig. 6 | Structural stability of the β -propeller of TcB during molecular dynamics simulations. Principal component analysis of the trajectories started from the closed (a–c) or open (d–f) states of the TcB–TcC complex. The plots show the root mean square fluctuation associated with the first (a, d), second (d, e) and third (c, f) principal components. The percentages in the legends indicate the fractional contribution that each component makes to the total variance. The structures show the range of conformations observed along their corresponding component. The colour scale in the structures represents the position along each principal component going between the extremes, from red to green to blue. For guidance, the blades of the β -propeller are labelled in structures and plots, with blades 3 and 4 highlighted in blue.

g, h, Graphical representation of the hybrid potentials used for the dual conformation structure-based SMOG force field. A Gaussian potential (**g**) can be used to create a contact term that includes exactly two minima (states a and b) with equal well depth, corresponding to the observed distance in two independent structures. In addition, by using a Gaussian potential the excluded volume of the contact can be independently controlled. A representation of the hybrid dihedral angle potential used in this study is shown in **h**. Starting from the dihedral functions for states a and b, the functions are combined as described in Methods. The regions between the averages (av1 and av2) and the closest extrema are connected using a polynomial function, to guarantee continuity and differentiability.



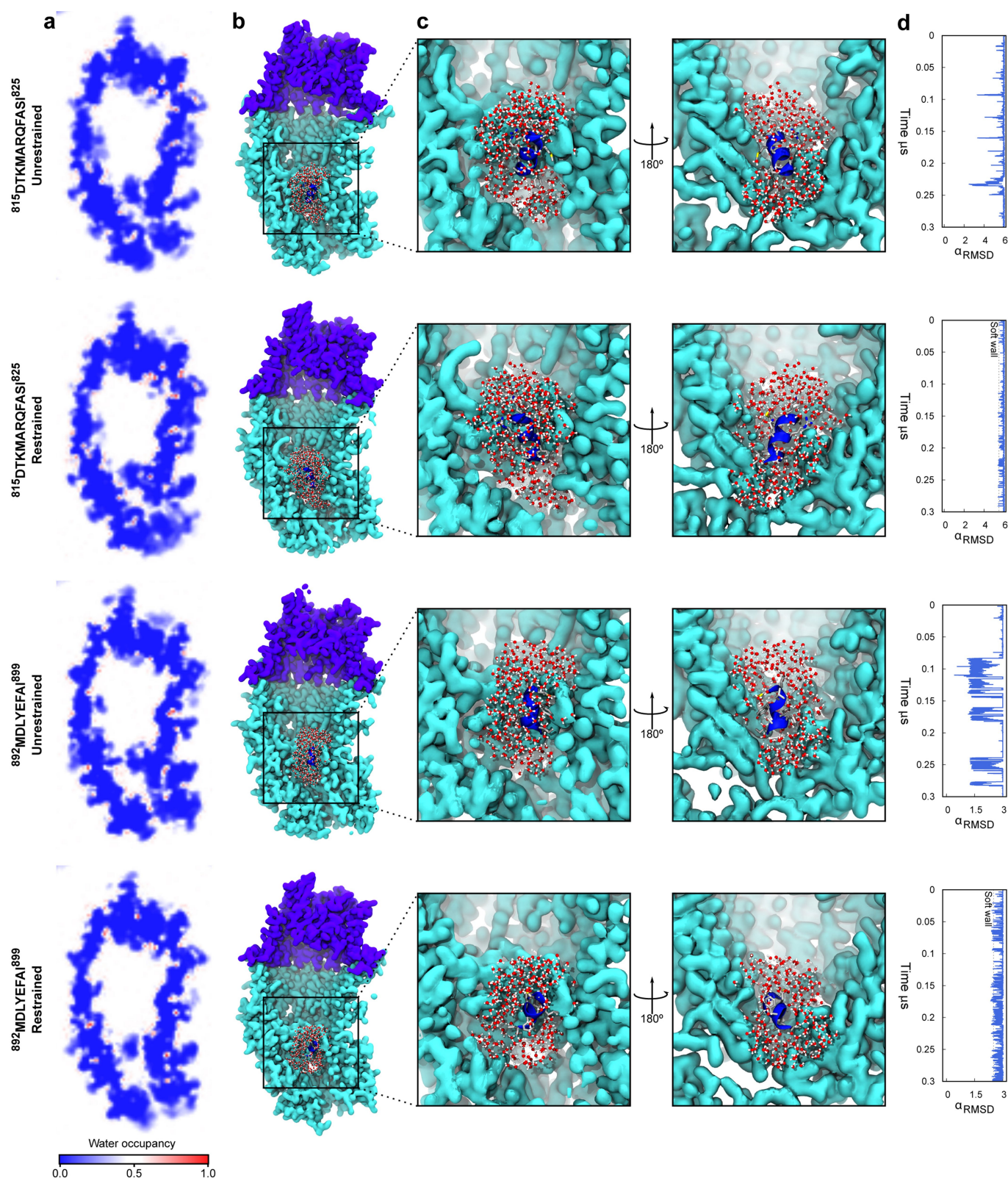
Extended Data Fig. 7 | Conformational distribution observed in the structure-based molecular dynamics simulations. **a**, Distribution of states of blades 3 and 4 during the simulations of free TcB-TcC. **b**, Histogram of the conformations sampled by the gatekeeper domain during the simulations of free TcB-TcC complex. **c**, Distribution of states of blades 3 and 4 during the simulations of the holotoxin. **d**, Histogram of the conformations sampled by the gatekeeper domain during the simulations of the holotoxin. In the simulations started from the closed state, the protein explores two minor conformations, which

are highlighted in the plot and shown in **g**. **e**, Distribution of states of blades 3 and 4 during the simulations of the holotoxin with destabilized β -propeller. **f**, Histogram of the conformations sampled by the gatekeeper domain during the simulations of the holotoxin with destabilized β -propeller. **g**, Representative structures for the two states highlighted in **d**. Colours correspond to those in Fig. 2. The histograms in **d** and **f** were calculated using running averages of the trajectories, using a window size of 150,000 time steps.



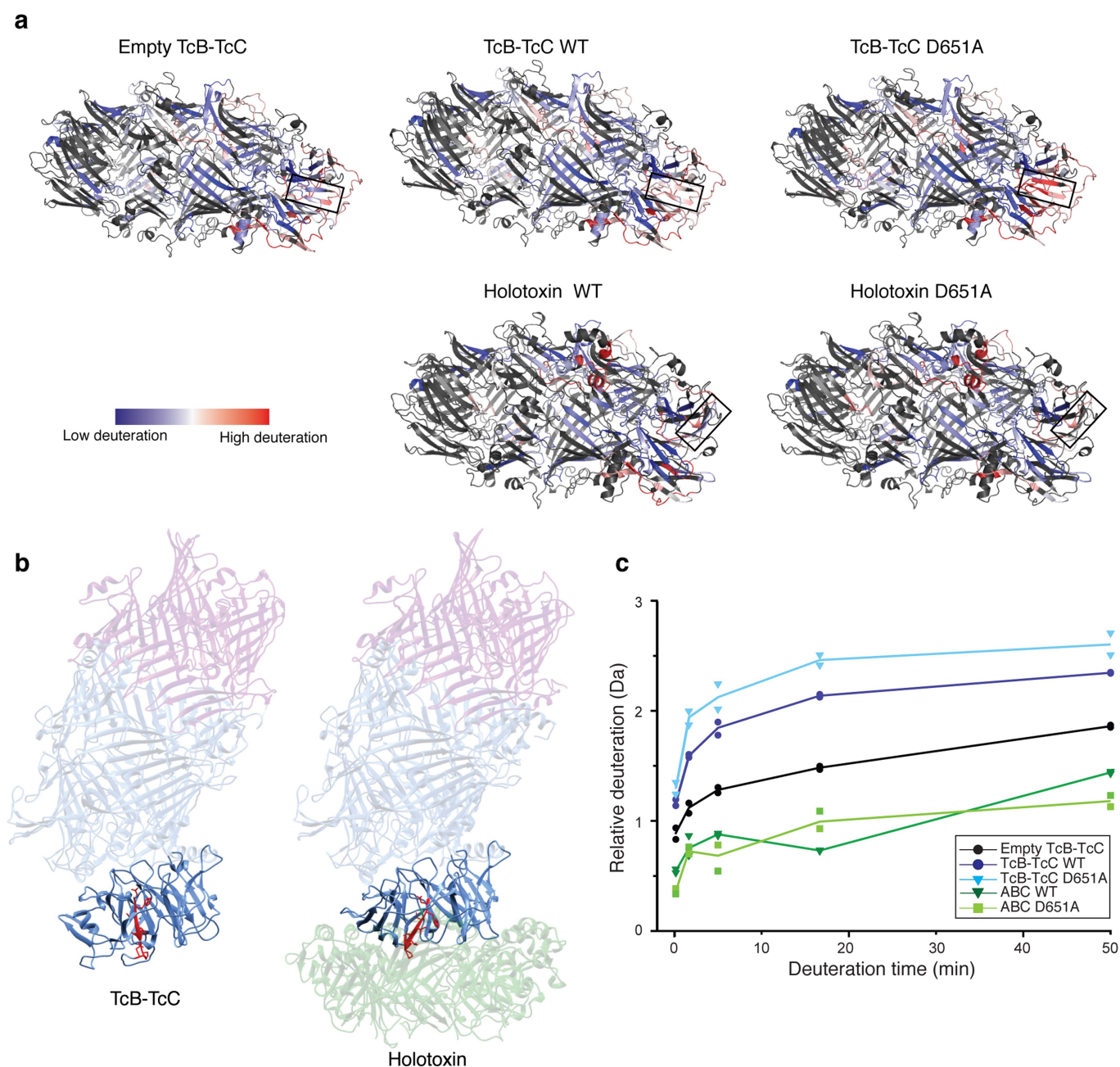
Extended Data Fig. 8 | Conservation of negatively charged residues that form a constriction between the barrel and the β -propeller domain of TcB. a, Positions of the residues D34, N60, D73, E100 and E120 in the constriction site of TcB. The model is coloured according to sequence conservation, with cyan representing non-conserved residues and magenta representing highly conserved residues. **b**, Sequence alignment of TcB sequences. Asterisks indicate the positions of the residues highlighted in **a**.

The sequence of *P. luminescens* TcdB2 is outlined. The alignment is coloured according to **a**. **c**, Dendrogram of TcdB2 homology models (from **b**), created by PIPSA. Models are clustered according to their surface electrostatic potential in the clamp region. **d–f**, Electrostatic surface potential representation of one representative model per cluster: *P. luminescens* TcdB2 (**d**), *Photobacterium temperata* TcaC (**e**) and *Burkholderia pseudomallei* TcB (**f**). The position of D34 is indicated.



Extended Data Fig. 9 | Modelling of a helical peptide at the constriction site of TcB–TcC. We placed two different peptides with predicted α -helical secondary structure from the HVR of TcC and performed simulations with the peptides free (unrestrained) or restrained to their helical conformation. **a**, Central section through TcB–TcC showing the average water occupancy during the 300-ns-long simulations. Bulk water is shown in white (~0.5 occupancy), whereas bound water molecules appear in red. Blue represents the regions that are never hydrated, which corresponds to the space occupied by the protein. The occupancy shows that there is still

a small channel of water next to the helical peptide. **b**, **c**, Representative snapshot of the trajectories. TcB (cyan) and TcC (violet) are shown as cut surfaces to illustrate the interior of the barrel. The bound helix is shown as a blue ribbon. Side chains of the bound helix and water molecules at most 8 Å away from it are shown in ball and stick representation. For each simulation, we included a close-up of the bound helix (**c**). **d**, Stability of the helical ligand bound to the constriction site. The variable $\alpha_{r.m.s.d.}$ represents the number of 6-residue-long segments with helical conformation within the peptide.



Extended Data Fig. 10 | HDX-MS of TcB-TcC and holotoxin complexes. **a**, Relative deuteration of TcB-TcC and holotoxin complexes at 50-min deuteration time. Relative deuteration values normalized to the maximum deuteration value of all peptides are shown in a gradient from 0.0 (blue) to 0.64 (red) relative deuteration level. Peptides without deuteration data are coloured grey. The position of the gatekeeper hairpin (residues 514–524, Fig. 4b) is indicated by a box. **b**, **c**, HDX-MS of residues 463–471 as part of the TcA interface in bound and unbound TcB-TcC. The position of residues 463–471 of the TcA-binding domain in unbound TcB-TcC

(**b**, left, red) and TcA-bound TcB-TcC (**b**, right, red) is indicated. The TcB-binding domain of TcA is shown in green (**b**, right). Equilibrium hydrogen-deuterium exchange at residues 463–471 in empty TcB-TcC (black circles), TcB-TcC(WT) (purple circles), TcB-TcC(D651A) (blue triangles), ABC(WT) (green triangles) and ABC(D651A) (light green squares) is displayed in **c**. Relative deuterium uptake of the residues as a function of incubation time in D₂O is shown. Data points show two independent replicates of each measurement. The solid lines represent the arithmetic mean of both replicates.

A population of luminous accreting black holes with hidden mergers

Michael J. Koss^{1,2*}, Laura Blecha³, Phillip Bernhard², Chao-Ling Hung⁴, Jessica R. Lu⁵, Benny Trakthenbrot^{6,7}, Ezequiel Treister⁸, Anna Weigel², Lia F. Sartori², Richard Mushotzky⁹, Kevin Schawinski², Claudio Ricci^{10,11,12}, Sylvain Veilleux⁸ & David B. Sanders¹³

Major galaxy mergers are thought to play an important part in fuelling the growth of supermassive black holes¹. However, observational support for this hypothesis is mixed, with some studies showing a correlation between merging galaxies and luminous quasars^{2,3} and others showing no such association^{4,5}. Recent observations have shown that a black hole is likely to become heavily obscured behind merger-driven gas and dust, even in the early stages of the merger, when the galaxies are well separated^{6–8} (5 to 40 kiloparsecs). Merger simulations further suggest that such obscuration and black-hole accretion peaks in the final merger stage, when the two galactic nuclei are closely separated⁹ (less than 3 kiloparsecs). Resolving this final stage requires a combination of high-spatial-resolution infrared imaging and high-sensitivity hard-X-ray observations to detect highly obscured sources. However, large numbers of obscured luminous accreting supermassive black holes have been recently detected nearby (distances below 250 megaparsecs) in X-ray observations¹⁰. Here we report high-resolution infrared observations of hard-X-ray-selected black holes and the discovery of obscured nuclear mergers, the parent populations of supermassive-black-hole mergers. We find that obscured luminous black holes (bolometric luminosity higher than 2×10^{44} ergs per second) show a significant ($P < 0.001$) excess of late-stage nuclear mergers (17.6 per cent) compared to a sample of inactive galaxies with matching stellar masses and star formation rates (1.1 per cent), in agreement with theoretical predictions. Using hydrodynamic simulations, we confirm that the excess of nuclear mergers is indeed strongest for gas-rich major-merger hosts of obscured luminous black holes in this final stage.

The Burst Alert Telescope (BAT) on the Neil Gehrels Swift Observatory has surveyed the entire sky at unprecedented depths in the ultra-hard X-ray band (14–195 keV) and primarily detects accretion onto supermassive black holes at the centres of nearby galaxies. Detection in the ultra-hard X-ray band is possible even when obscuring gas and dust in the host galaxy considerably attenuate the ultraviolet, optical or softer X-ray emission around the growing black holes. At the distance to the nearest luminous accreting black hole (about 220 Mpc or at a redshift of $z \approx 0.05$), ground-based optical imaging typically achieves a resolution of the order of $1''$, or 1 kpc, in the host galaxy. This spatial resolution is not sufficient to resolve the final merger stage in the host galaxies down to the hundreds of parsecs. However, these can be resolved with near-infrared adaptive optics, which provide an improvement by a factor of 10 in spatial resolution (about $0.1''$). These scales are still above the black-hole sphere of influence, which is of the order of 10–100 pc for black holes with masses of $10^7 M_\odot$ – $10^9 M_\odot$ (M_\odot , solar mass).

We observed 96 nearby ($z < 0.075$) black holes detected by Swift/BAT in the hard X-ray band. The black holes were selected at random over a wide range of luminosities using the adaptive optics system on the

Keck 2 telescope at the W. M. Keck Observatory with a near-infrared camera (NIRC2). These near-infrared observations ($2.1 \mu\text{m}$) include both obscured and unobscured accreting black holes and have an average spatial resolution of $0.13''$, about a factor of 10 better than previous ground-based surveys. We combined these adaptive-optics observations with available high-resolution archival Hubble Space Telescope (HST) near-infrared images of 64 Swift/BAT-detected active galactic nuclei (AGN) with an average spatial resolution of $0.17''$. These observations provide the first evidence of a sizeable population of double nuclei with very small separations (0.3–3 kpc) in late-stage mergers, which could not be detected in lower-resolution ground-based optical observations and were not detected in previous near-infrared samples of AGN observed with the HST (Fig. 1d–f).

We separated our sample into obscured and unobscured accreting black holes based on the presence of broad H β lines in optical spectroscopy images from past studies¹¹ and into low- and high-luminosity (below and above a bolometric luminosity of $L_{\text{bol}} = 2 \times 10^{44}$ erg s^{−1}, respectively) using their X-ray emission¹². We also compared our sample with 176 inactive galaxies matched in stellar masses and star formation rates that have high-resolution HST near-infrared images. Example high-resolution images of the inactive-galaxy sample are provided in Extended Data Fig. 3. A comparison of the stellar masses (Extended Data Fig. 4a), star formation rates (Extended Data Fig. 4b), physical resolutions (Extended Data Fig. 4c) and the consistency of the control sample with random inactive galaxies taken from the Sloan Digital Sky Survey (Extended Data Fig. 6) show that (Fig. 2a) the obscured luminous black holes show a significantly ($P < 0.001$) higher fraction (17.6%, 6/34) of nuclear mergers (< 3 kpc) than inactive galaxies (1.1%, 2/176), unobscured luminous black holes (1.8%, 1/55) and lower-luminosity black holes (2.7%, 2/73). When comparing the fractions of nuclear mergers for obscured and unobscured luminous black holes, the difference is also significant ($P \approx 0.01$). Finally, a higher proportion of nuclear mergers (separation $R < 3$ kpc) in obscured luminous AGN is also found when comparing them with lower-luminosity black holes ($P \approx 0.01$). At larger separations (3–10 kpc) the fraction of mergers in obscured luminous black holes is higher than in the other samples, but this difference is not statistically significant ($P > 0.29$). All the mergers identified at $R < 10$ kpc are listed in Extended Data Table 1. Finally, we note that even observations in the near-infrared band may sometimes miss nuclear mergers with very heavy extinction¹³, so these measurements should be seen as a lower limit.

While past work has found some nuclear mergers, our study is the first, to our knowledge, to demonstrate a significant excess ($P < 0.001$) of nuclear mergers in obscured luminous black holes in comparison to a matched sample of inactive galaxies. Past studies have typically focused on subsets of AGN galaxies at larger separations (for example, 10–30 kpc). For instance, some nuclear mergers have been identified

¹Eureka Scientific Inc, Oakland, CA, USA. ²Institute for Particle Physics and Astrophysics, ETH Zürich, Zürich, Switzerland. ³Department of Physics, University of Florida, Gainesville, FL, USA.

⁴Department of Physics, Manhattan College, New York, NY, USA. ⁵Department of Astronomy, University of California, Berkeley, CA, USA. ⁶Department of Physics, ETH Zürich, Zürich, Switzerland.

⁷School of Physics and Astronomy, Tel Aviv University, Tel Aviv, Israel. ⁸Instituto de Astrofísica, Facultad de Física, Pontificia Universidad Católica de Chile, Santiago, Chile. ⁹Department of

Astronomy and Joint Space-Science Institute, University of Maryland, College Park, MD, USA. ¹⁰Núcleo de Astronomía de la Facultad de Ingeniería, Universidad Diego Portales, Santiago, Chile.

¹¹Kavli Institute for Astronomy and Astrophysics, Peking University, Beijing, China. ¹²Chinese Academy of Sciences South America Center for Astronomy, Santiago, Chile. ¹³Institute for Astronomy, University of Hawaii at Manoa, Honolulu, HI, USA. *e-mail: mike.koss@eurekasci.com

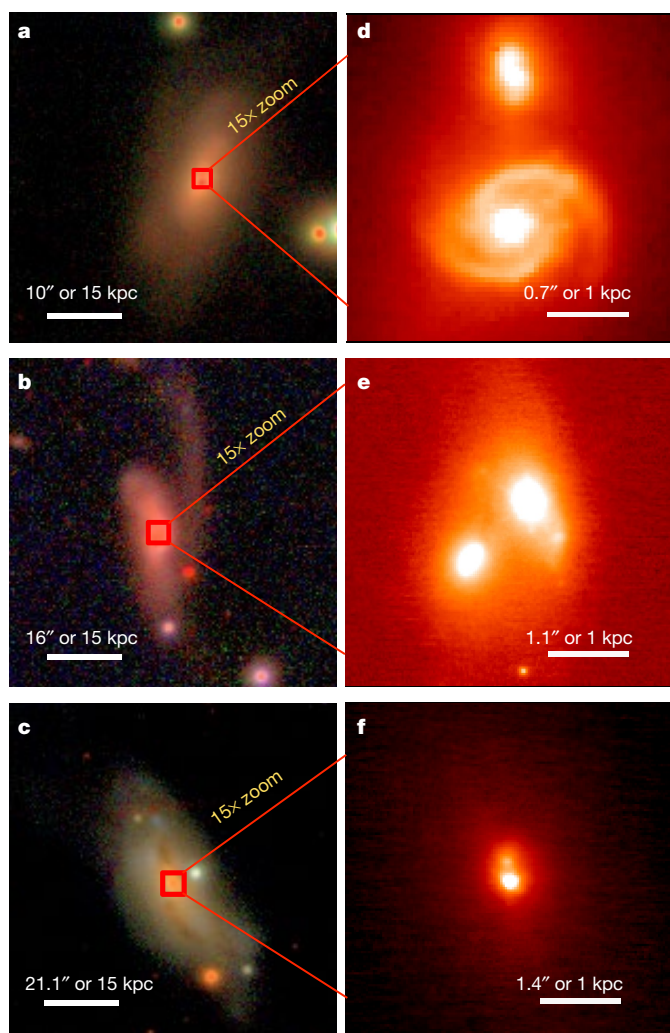


Fig. 1 | Example images of final-stage mergers. **a–c**, Tricolour optical images in the *gri* band from the Sloan Digital Sky Survey or the Kitt Peak survey with $1''$ angular resolution. The galaxies shown are 2MASX J01392400+2924067 (**a**), CGCG 341-006 (**b**) and MCG+02-21-013 (**c**). The images are $60 \text{ kpc} \times 60 \text{ kpc}$ in size. Red squares indicate the size of the zoomed-in adaptive optics image on the right. **d–f**, Corresponding near-infrared, K_p -band (effective wavelength, $2.12 \mu\text{m}$) adaptive optics images of nuclear mergers taken with the Keck/NIRC2 instrument. These images are $4 \text{ kpc} \times 4 \text{ kpc}$ in size.

in sources with double-peaked [O III] $\lambda 5,007$ emission lines, which result from the emission from both nuclei¹⁴. In a sample of 60 double-peaked sources observed with NIRC2¹⁵, only 4/60 (or 6.7%) were in major mergers with $<3 \text{ kpc}$ separations—a much smaller proportion than that seen in the obscured luminous black holes studied here. Some nuclear mergers have also been detected in the host galaxies¹⁶ of luminous infrared galaxies with accreting black holes, which have very high star formation rates, probably associated with the merger. However, only one of the ten nuclear mergers in our hard-X-ray sample is associated with a luminous infrared galaxy (NGC 6240), and none show double-peaked [O III] $\lambda 5,007$ emission lines. This indicates that both of these diagnostics are incomplete indicators of nuclear mergers.

When considering the fractions of galaxies found at various merger stages, it is critical to consider the corresponding observability timescale, because the time spent at small separations is thought to be much shorter than that spent at larger separations. For instance, in a recent merger simulation study¹⁷, the time spent at separations $R < 3 \text{ kpc}$ could be more than five times shorter than the time spent at separations of $3\text{--}10 \text{ kpc}$ (about 50 Myr versus 300 Myr). Thus, the excess fraction of nuclear

mergers in obscured luminous black holes that we find in our data is surprising, and it probably reflects a strong link between such mergers and intense black-hole accretion. To compare our observations with theoretical results more directly, we use a suite of state-of-the-art high-resolution hydrodynamical galaxy merger simulations with the galaxy stellar mass, black-hole mass and black-hole bolometric luminosity set up to reproduce the accreting black holes and their host galaxies observed in our study (GADGET-3 code¹⁸; see Methods). We also consider the simulated mergers at random orientations to the observer to account for the fact that some mergers would appear closer simply because of the projection effect (that is, their alignment with the observer's line of sight).

The simulations show that obscured luminous black-hole phases preferentially occur in the late stages of gas-rich ($M_{\text{gas}}/M_* < 0.1$) major ($M_1/M_2 < 5$) mergers, where M_{gas} is the gas mass, M_* is the stellar mass and M_1 (M_2) denotes the galaxy with the larger (smaller) stellar mass. Consistent with our observations, late-stage mergers are less prevalent in lower-luminosity black holes and inactive galaxies (Fig. 2b). Finally, our simulations show that obscured luminous black holes, which occur in the post-merger phase (after the two galactic nuclei and black holes have merged), contribute as much to the growth of the obscured black hole as the entire merger phase ($R < 30 \text{ kpc}$). We note that during the late stages of our simulated galaxy mergers, the black holes spend very little time in an unobscured luminous accreting-black-hole phase. These results are consistent with previous theoretical work¹⁹ that showed that merger-triggered accreting black holes are preferentially more luminous and obscured than those growing by stochastic feeding via slower secular processes. This explains the lack of nuclear mergers in low-luminosity AGN seen in a previous large-sample (>200) high-resolution study of AGN and normal galaxies using the HST²⁰. Moreover, simulations find that although global star formation is enhanced primarily in the early stages of the first merger passage, black-hole growth is minimal until the late merger stages²¹, when the galaxies pass within a few kiloparsecs of each other and cause tidal torques that increase nuclear gas inflows.

We simulated a set of mock HST images, targeting redshifted versions of our imaging datasets (see Methods) at the peak of black-hole growth at $z \approx 1\text{--}2$, and found that the HST would miss the majority of such systems (7/8) at merger separations below 3 kpc owing to insufficient spatial resolution and sensitivity, which is necessary to identify the nuclear mergers that we find in our low-redshift sample. The upcoming James Webb Space Telescope will provide substantial improvements in sensitivity. However, the resolution of such nuclear mergers requires the use of adaptive optics systems in the next generation of large-diameter ground-based telescopes (for example, the Thirty Meter Telescope, the European Extremely Large Telescope and the Giant Magellan Telescope). These will reach resolutions of 300 pc using adaptive optics at $z \approx 1\text{--}2$ —scales that are consistent with the smallest-separation mergers identified in this study.

With the discovery of gravitational waves emitted from the merger of stellar-mass black holes, interest in understanding gravitational waves produced from the merger of supermassive black holes has increased considerably. The study of nuclear mergers is therefore critical for comparison with cosmological merger-rate models, because it can help constrain the timescales for supermassive-black-hole inspiral and the rate of such events, which are likely to be found with gravitational wave detectors, such as pulsar timing arrays²² and the Laser Interferometer Space Antenna²³. Predictions of the detection rates for these instruments are based on parameterizations of the merger rates and the supermassive-black-hole-population²⁴, but these are highly uncertain and vary by orders of magnitude²⁵. Gravitational-wave observatories will also struggle with the localization of the sources, which is possible only with a resolution of the order of 10 square degrees²⁶, thus requiring a better characterization of their likely precursors. Thus, the study of nuclear merger fractions and their correlation with galaxy populations can provide crucial benchmarks for models of black-hole inspiral and the strength of gravitational-wave signals.

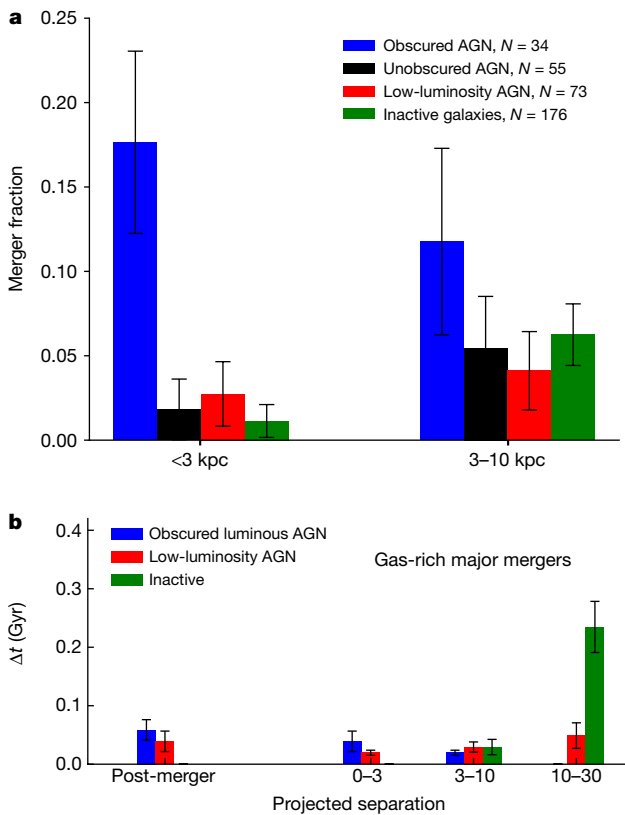


Fig. 2 | Fraction of close mergers. **a**, Fraction of mergers, determined using high-resolution images obtained with either Keck adaptive optics or the HST. The sample of high-luminosity obscured accreting black holes or AGN shows a strong excess of small-separation mergers (<3 kpc). Other types show no significant excess compared to inactive galaxies. Error bars correspond to 1σ confidence intervals. **b**, Results from a suite of gas-rich high-resolution hydrodynamical galaxy merger simulations for a range of viewing angles. Δt is the time spent at a separation range, and error bars represent the median absolute deviation. Our observed merger fractions are consistent with obscured and luminous accreting black holes occurring primarily in gas-rich major mergers.

Online content

Any methods, additional references, Nature Research reporting summaries, source data, statements of data availability and associated accession codes are available at <https://doi.org/10.1038/s41586-018-0652-7>.

Received: 17 October 2016; Accepted: 21 August 2018;

Published online 7 November 2018.

- Di Matteo, T., Springel, V. & Hernquist, L. Energy input from quasars regulates the growth and activity of black holes and their host galaxies. *Nature* **433**, 604–607 (2005).
- Goulding, A. D. et al. Galaxy interactions trigger rapid black hole growth: an unprecedented view from the Hyper Suprime-Cam survey. *Publ. Astron. Soc. Jpn* **70**, S37 (2018).
- Donley, J. L. et al. Evidence for merger-driven growth in luminous, high- z , obscured AGNs in the CANDELS/COSMOS field. *Astrophys. J.* **853**, 63 (2018).
- Villforth, C. et al. Host galaxies of luminous $z \sim 0.6$ quasars: major mergers are not prevalent at the highest AGN luminosities. *Mon. Not. R. Astron. Soc.* **466**, 812–830 (2017).
- Chang, Y.-Y. et al. Infrared selection of obscured active galactic nuclei in the COSMOS field. *Astrophys. J. Suppl. Ser.* **233**, 19 (2017).
- Glikman, E. et al. Major mergers host the most-luminous red quasars at $z \sim 2$: a Hubble Space Telescope WFC3/IR study. *Astrophys. J.* **806**, 218 (2015).
- Kocevski, D. et al. Are Compton-thick AGNs the missing link between mergers and black hole growth? *Astrophys. J.* **814**, 104 (2015).

- Koss, M. et al. A new population of Compton-thick AGNs identified using the spectral curvature above 10 keV. *Astrophys. J.* **825**, 85 (2016).
- Hopkins, P. F. et al. A physical model for the origin of quasar lifetimes. *Astrophys. J.* **625**, L71–L74 (2005).
- Baumgartner, W. H. et al. The 70 month Swift-BAT all-sky hard X-ray survey. *Astrophys. J. Suppl. Ser.* **207**, 19 (2013).
- Koss, M. et al. BAT AGN spectroscopic survey. I. Spectral measurements, derived quantities, and AGN demographics. *Astrophys. J.* **850**, 74 (2017).
- Ricci, C. et al. BAT AGN spectroscopic survey. V. X-ray properties of the Swift/BAT 70-month AGN catalog. *Astrophys. J. Suppl. Ser.* **233**, 17 (2017).
- Ohya, Y., Terashima, Y. & Sakamoto, K. Infrared and X-ray evidence of an AGN in the NGC 3256 southern nucleus. *Astrophys. J.* **805**, 162 (2015).
- Barrows, R. S., Comerford, J. M., Greene, J. E. & Pooley, D. Spatially offset active galactic nuclei. II. Triggering in galaxy mergers. *Astrophys. J.* **838**, 129 (2017).
- Fu, H., Myers, A. D., Djorgovski, S. G. & Yan, L. Mergers in double-peaked [O III] active galactic nuclei. *Astrophys. J.* **733**, 103 (2011).
- Haan, S. et al. The nuclear structure in nearby luminous infrared galaxies: Hubble Space Telescope NICMOS imaging of the GOALS sample. *Astron. J.* **141**, 100 (2011).
- Van Wassenhove, S. et al. Observability of dual active galactic nuclei in merging galaxies. *Astrophys. J.* **748**, L7 (2012).
- Springel, V. The cosmological simulation code GADGET-2. *Mon. Not. R. Astron. Soc.* **364**, 1105–1134 (2005).
- Hopkins, P. F., Richards, G. T. & Hernquist, L. An observational determination of the bolometric quasar luminosity function. *Astrophys. J.* **654**, 731–753 (2007).
- Hunt, L. K. & Malkan, M. A. Circumnuclear structure and black hole fueling: Hubble Space Telescope NICMOS imaging of 250 active and normal galaxies. *Astrophys. J.* **616**, 707–729 (2004).
- Capelo, P. R. et al. Growth and activity of black holes in galaxy mergers with varying mass ratios. *Mon. Not. R. Astron. Soc.* **447**, 2123–2143 (2015).
- Verbiest, J. P. W. et al. The International Pulsar Timing Array: first data release. *Mon. Not. R. Astron. Soc.* **458**, 1267–1288 (2016).
- Tang, Y., Haiman, Z. & MacFadyen, A. The late inspiral of supermassive black hole binaries with circumbinary gas discs in the LISA band. *Mon. Not. R. Astron. Soc.* **476**, 2249–2257 (2018).
- Sesana, A., Haiman, Z., Kocsis, B. & Kelley, L. Z. Testing the binary hypothesis: pulsar timing constraints on supermassive black hole binary candidates. *Astrophys. J.* **856**, 42 (2018).
- Mayer, L. Massive black hole binaries in gas-rich galaxy mergers; multiple regimes of orbital decay and interplay with gas inflows. *Class. Quantum Gravity* **30**, 244008 (2013).
- Lang, R. N. & Hughes, S. A. Advanced localization of massive black hole coalescences with LISA. *Class. Quantum Gravity* **26**, 094035 (2009).

Acknowledgements This work is dedicated to the memory of our friend and collaborator N. Gehrels. M.J.K. acknowledges support from the Swiss National Science Foundation (SNSF) through the Ambizione fellowship grant PZ00P2 154799/1 and from NASA through ADAP award NNN16CT03C. K.S., L.F.S. and A.W. acknowledge support from SNSF grants PP00P2 138979 and PP00P2 166159. L.B. acknowledges support from NSF award number 1715413. We acknowledge the work of the Swift/BAT team to make this study possible. This paper is part of the Swift/BAT AGN Spectroscopic Survey (BASS).

Reviewer information Nature thanks D. Kocevski and the other anonymous reviewer(s) for their contribution to the peer review of this work.

Author contributions M.J.K. drafted the manuscript, performed the observations and carried out much of the analysis. L.B. performed and interpreted the hydrodynamic simulations. P.B. carried out much of the initial data reduction. C.-L.H. ran the artificial redshifting code. J.R.L. provided the initial data reduction code and helped with the analysis. K.S. aided in the scientific interpretations and the reduction of the raw data. E.T. assisted in the initial observing runs. R.M., S.V. and D.B.S. aided in the initial proposal and scientific interpretations. B.T., L.F.S., A.W. and C.R. assisted in the scientific interpretations.

Competing interests The authors declare no competing interests.

Additional information

Extended data is available for this paper at <https://doi.org/10.1038/s41586-018-0652-7>.

Supplementary information is available for this paper at <https://doi.org/10.1038/s41586-018-0652-7>.

Reprints and permissions information is available at <http://www.nature.com/reprints>.

Correspondence and requests for materials should be addressed to M.J.K.

Publisher's note: Springer Nature remains neutral with regard to jurisdictional claims in published maps and institutional affiliations.

METHODS

Data analysis and sample overview. We selected our sources from the 70-month Swift/BAT catalogue, which contains 1,171 sources, 836 of which are accreting black holes or AGN. We cross-matched this sample with the Roma Blazar Catalog²⁷ to avoid beamed and radio-bright black holes, which have been extensively studied in past high-resolution studies. A full list of the observational aspects of all galaxies examined is provided in a machine-readable table in Supplementary Information.

We used the NIRC2 imager and an adaptive optics (AO) system to observe 96 low-redshift ($0.01 < z < 0.075$) Swift/BAT-detected black holes with suitable tip-tilt stars. The images were taken over nine nights spread between 2012 and 2014. For bright unobscured AGN, the nucleus was used as the point source for the tip-tilt correction. Images were taken in the K_p band (effective wavelength, $\lambda_{\text{eff}} \approx 2.12 \mu\text{m}$) and, when possible in good seeing conditions, in the J and H bands (1.25 and $1.63 \mu\text{m}$, respectively). We used a wide-field camera with a resolution of $40 \text{ mas pixel}^{-1}$ and a $40''$ field of view. We used a three-point dither pattern that avoids a known artefact in the lower left part of the field. For calibration purposes we took dark- and flat-field images for each night of observation.

The data were reduced using a custom JLU python code for NIRC2 reduction. The code was modified to ensure that extended galaxy emission features were not subtracted from the background using SExtractor²⁸. The images were combined by weighting by the Strehl ratio of each image.

To increase our sample size we also added 64 BAT-detected AGN that were observed with the HST NICMOS or WFC3 cameras. The images were taken with the F105W ($1.05 \mu\text{m}$) or F160W ($1.60 \mu\text{m}$) filters, with the majority (62/64, 97%) in the F160W band. Individual frames were co-added, corrected for cosmic rays and distortion, and registered using the default values in AstroDrizzle. For galaxies with $z < 0.01$, we used the mean value of redshift-independent distance measurements from the NASA Extragalactic Database, when available. We otherwise adopted a cosmology of $\Omega_m = 0.3$, $\Omega_\Lambda = 0.7$ and $H_0 = 70 \text{ km s}^{-1} \text{ Mpc}^{-1}$ (Ω_m , matter density; Ω_Λ , dark-energy density; H_0 , Hubble constant) for all distances computed.

Because most of the possible galaxy counterparts detected in the images do not have spectroscopic data available, we applied two methods to deal with possible stellar contamination from foreground stars. Nearby foreground stars and galaxies were identified using segmentation maps produced by SExtractor. We first applied the stellar classification technique provided by this tool, which uses a neural network as a classifier to assign the values 0 and 1 to non-stellar and stellar objects, respectively. To separate between galaxies and stars, every object with a stellarity index below 0.5 was considered as a secondary galaxy.

Because some of the AO observations relied on tip-tilt stars, the AO images typically had more foreground stars than the HST ones, which could lead to possible contamination. We therefore used a second technique to measure the number of stars in the entire field of view that are brighter than our second nearby source, divided by the total area searched in the image. This number was then compared to the search area used to find the nearest companion to provide an estimate for stellar contamination. We excluded counterparts with contamination likelihood greater than 10%, all of which also had a stellarity index below 0.5 and had already been excluded using the aforementioned SExtractor stellar classification technique.

All galaxies classified as extended, with low stellar contamination and within 2.5 mag ($\sim 1/10$) of the primary AGN or inactive galactic nucleus were classified as counterparts (see Extended Data Figs. 1, 2).

Inactive-galaxy control sample. We created a large control sample of inactive galaxies by aggregating over 20 years of past HST NICMOS and WFC3 surveys conducted using the F160W filter. For more massive galaxies, which were not well sampled in previous NICMOS surveys, we cross-matched all high-resolution HST near-infrared observations with the NASA-Sloan Atlas catalogue²⁹ which includes about 42,000 nearby ($z < 0.05$) massive ($M_* > 10^{10} M_\odot$, where M_\odot is the mass of the Sun) inactive galaxies within the footprint of the Sloan Digital Sky Survey. These were typically taken with the HST WFC3 near-infrared camera owing to the small field of view of NICMOS. We also cross-matched all nearby galaxies ($z < 0.05$) from the RC3 catalogue³⁰, which covers the entire sky, with the list of HST near-infrared observations. Finally, we cross-matched Version 2.1 of the Hubble Source Catalog, which includes all WFC3 near-infrared observations, with all nearby galaxies ($z < 0.05$) from the SIMBAD astronomical database. To ensure that our sample included only inactive galaxies, we excluded the 168,941 AGN in the 13th edition of the Véron-Cetty & Véron catalogue of quasars and active nuclei³¹. We also excluded any galaxies found in clusters, because of their very different environments and generally much higher stellar masses. Our final control sample included 385 inactive galaxies, obtained from 37 different HST programmes.

When possible, we used the Hubble Legacy Archive to download post-processed images. When these were not available, individual frames were co-added and corrected for cosmic rays and distortion, in the same way as the HST observations of the BAT AGN in our main sample. The NICMOS images were examined to ensure that the smaller field of view covered the nuclear regions without any size-

able artefacts after processing. As with our AGN sample, we used the average of redshift-independent distance measurements from NASA Extragalactic Database, when possible, and applied the same method to detect galaxy counterparts.

Control sample design. Although our matching procedure resulted in 385 inactive galaxies observed with the HST, many of the relevant HST programmes focused on nearby ($< 100 \text{ Mpc}$) inactive galaxies and with lower stellar masses than our AGN sample. This matching procedure for the control sample is crucial, as many studies have found that the merger activity and fraction depend on the stellar mass^{32,33}. We therefore measured H-band luminosities in both the inactive-galaxy and BAT AGN samples, as they are an excellent proxy for the stellar mass, with a small scatter of only³⁴ 0.2 dex. For photometry, we used the H-band elliptical aperture magnitudes from the 2MASS all-sky survey.

The merger fraction also depends on the star formation rate (SFR). We therefore used the IRAS $60\text{-}\mu\text{m}$ luminosity as a proxy for the SFR. When the IRAS $60 \mu\text{m}$ luminosity was measured as an upper limit, we used the $70\text{-}\mu\text{m}$ luminosity from the Herschel Photodetector Array Camera and Spectrometer or the Spitzer Multiband Imaging Photometer. We assumed a conversion factor of 1.15 between the $70\text{-}\mu\text{m}$ luminosity and the $60\text{-}\mu\text{m}$ luminosity based on the average number of sources in the sample with both measurements.

The inactive-galaxy sample was matched in stellar mass and SFR by excluding 117 low-stellar-mass galaxies ($(\log(L_H/L_\odot)) < 9.7$; L_H , H-band luminosity; L_\odot , luminosity of the Sun) and 95 low-SFR galaxies ($(\log(\nu L_\nu)_{60\mu\text{m}} < 43$; νL_ν is the luminosity expressed in units of erg s^{-1} and L_ν is the monochromatic specific luminosity per unit of frequency, ν). We note that although these 210 inactive galaxies were excluded from the analysis, we did not find any nuclear ($R < 3 \text{ kpc}$) mergers among them.

The sample of lower-luminosity black holes has a lower average H-band luminosity ($(\log(L_H/L_\odot)) = 9.9$) than the inactive control sample ($(\log(L_H/L_\odot)) = 10.1$) or the sample of obscured luminous black holes ($(\log(L_H/L_\odot)) = 10.1$). The sample of unobscured luminous black holes has slightly higher luminosity ($(\log(L_H/L_\odot)) = 10.2$) than the inactive control sample; however, for unobscured black holes, the light can contribute the majority of the emission even in the near-infrared bands³⁵, so the H-band luminosity may overestimate the stellar mass. As for the SFR, we find $(\log(\nu L_\nu)_{60\mu\text{m}}) = 44.1$ for the inactive galaxies, and the same value is obtained for the obscured luminous black holes and for all luminous black holes. This value is higher than that of the low-luminosity black holes ($(\log(\nu L_\nu)_{60\mu\text{m}}) = 43.6$).

A summary of the different programmes used in the HST control sample, based on their titles and descriptions, is provided in Extended Data Fig. 5 and in a machine-readable table in Supplementary Information. Most of the control sample was obtained from studies of star formation in luminous infrared galaxies or large samples of nearby galaxies (70%, 122/175). Nearly all of the inactive-galaxy images from the HST were taken with the F160W filter (172/175, 98%), with the remaining images taken with the F110W filter. The average image resolution typically corresponded to a full-width at half-maximum (FWHM) of $0.19''$ for the inactive-galaxy sample, slightly lower than that of the sample of accreting black holes (FWHM = $0.12''$). However, because the nearby inactive galaxies were typically at lower redshift ($\langle z \rangle = 0.021$) than the black-hole sample ($\langle z \rangle = 0.034$), the physical scales probed for inactive galaxies (FWHM = 79 pc) were actually smaller than those for the black-hole sample (FWHM = 97 pc), particularly for the obscured and unobscured luminous black holes (FWHM = 134 pc). The average Strehl ratio of the black-hole sample was 0.45, mainly owing to the low Strehl ratios in the AO sample, whereas the inactive galaxies selected solely from HST data had a higher Strehl ratio of 0.9. However, because our study focuses on identifying secondary nuclei that are within 2.5 mag of the bright black holes at the galaxy centres, the reduced sensitivity to very faint objects with AO does not affect our analysis or conclusions.

We also tested whether the parent sample of inactive galaxies from which the matched HST sample was drawn was itself representative, in a statistical sense, of the nearby-galaxy population. For the sample of nearby galaxies we used data from the Sloan Digital Sky Survey Data Release 7³⁶. We used spectroscopic redshifts from the New York Value-Added Galaxy Catalog³⁷ to limit the sample to the $0.01 < z < 0.05$ range to match the control sample. We extracted stellar masses and SFR measurements from the Max Planck Institute for Astrophysics–John Hopkins University (MPA JHU)^{38,39} catalogue, which contains data based on photometry and emission-line modelling. We only used sources that are flagged as galaxies in the MPA JHU catalogue (about 90,000). To convert the $60\text{-}\mu\text{m}$ emission of our HST sample to SFR we assumed standard galaxy templates⁴⁰. We found that the HST sample was representative of the nearby-galaxy population in terms of SFR, except for an excess of high-stellar-mass, high-SFR galaxies related to the large programmes that study luminous infrared galaxies (which are usually found among such high-stellar-mass, high-SFR galaxies in the nearby Universe)⁴¹. As galaxy mergers are thought to be correlated with increased star formation, the lack of nuclear mergers in these inactive galaxies is very surprising and strengthens

our findings of an excess of nuclear mergers among the obscured luminous AGN population compared to the control sample.

Finally, when comparing merger fractions between samples we used the binomial proportion confidence intervals, which are typically used to compare the fractions of different samples. The normal approximation interval is the simplest formula; however, for situations with a fraction very close to zero or small numbers, this formula is unreliable⁴² and may considerably underestimate the uncertainties. We therefore used the Jeffreys confidence interval to provide more reliable error estimates and Fisher's exact test to calculate the P value for the difference between the two sample fractions.

Simulations of galaxies at high redshift. We simulate the systematics of studying AGN at the peak of black-hole growth at higher redshift ($z \approx 1$) by artificially redshifting our imaging data to mimic the quality of the HST data at this redshift, following ref.⁴³. Because of the low redshift of our samples ($z = 0.04$), the physical resolution of our ground-based Pan-STARRS images is equal or superior to the HST data for a $z \approx 1$ sample. The images also have complete wavelength coverage in the g , r , i , z and y filters ($\lambda_{\text{eff}} = 4,776 \text{ \AA}$, $6,130 \text{ \AA}$, $7,485 \text{ \AA}$, $8,658 \text{ \AA}$ and $9,603 \text{ \AA}$, respectively), and thus we can properly consider the rest-frame wavelengths and spectral energy distributions of the artificially redshifted datasets. We assume that the redshifted galaxies are located at $z = 1$ and are observed in the WFC3 F160W band, achieving the same depth as the CANDELS and GOODS-S surveys⁴⁴. The FERENGI algorithm⁴⁵ is then used to determine the best-fit rest-frame spectral energy distribution templates using the *kcorrect* routine and to calculate the expected flux in the WFC3 F160W band. Finally, the output spatial flux distribution is convolved with the point-spread function of the WFC3 F160W band, and a noise frame is added using a blank region extracted from the CANDELS and GOODS-S surveys.

Our simulated observations (Extended Data Fig. 7) show that the HST can resolve only one of these late-stage mergers with tight double nuclei. This is not surprising, given the stark difference in physical scales between $z \approx 0.04$ and $z \approx 1$ ($D_A(z = 0.04)/D_A(z = 1) \approx 10$, where D_A is the angular-size distance at a given redshift) and the detection being based on the visibility of tight double nuclei. Although our asymmetric/disturbed structures at the outskirts of the galaxies may still be visible at $z \approx 1$ in a couple of cases with a considerably increased level of brightness owing to the increase in star formation activity at high redshift, the interpretation of these structures can be ambiguous, given that the morphology of high-redshift star-forming galaxies is often intrinsically less regular than nearby ($< 250 \text{ Mpc}$) galaxies.

Simulations of merging galaxies. We use high-resolution galaxy merger simulations performed with GADGET, a smoothed-particle hydrodynamics and N -body code that conserves energy and entropy and uses sub-resolution physical models for radiative heating and cooling, star formation, supernova feedback, metal enrichment and a multi-phase interstellar medium⁴⁶. Black holes are modelled as gravitational 'sink' particles that accrete gas via an Eddington-limited, Bondi-Hoyle-like prescription. Thermal AGN feedback is included by coupling 5% of the accretion luminosity ($L_{\text{bol}} = \epsilon_{\text{rad}} \dot{M} c^2$) to the surrounding gas as thermal energy, with a variable radiative efficiency ϵ_{rad} at low accretion rates⁴⁷ \dot{M} (where c is the speed of light in vacuum).

Our simulation suite includes seven major-merger simulations with galaxy mass ratios of 0.5 or 1. Each of the galaxies have a dark-matter halo, a disk of gas and stars (with initial gas fractions of 0.1–0.3), a stellar bulge-to-total ratio of 0 or 0.2, and a central black hole with initial mass scaled to the stellar bulge⁴⁸. The fiducial baryonic gravitational softening length and mass resolution are $\epsilon_{\text{grav}} = 48 \text{ pc}$ and $m_b = 2.8 \times 10^5 M_\odot$, respectively. We also run two simulations at ten-times-higher mass resolution to ensure that our results are not resolution-dependent. We stress that these details are not crucial for the purpose of the present work, where the simulations are used to assess the relative timescales in which merging galactic nuclei and black holes can be seen at various separations.

We also conduct radiative-transfer simulations in post-processing with the three-dimensional, polychromatic, dust radiative-transfer code SUNRISE^{49,50}. This publicly available code has been used extensively with GADGET-3 to model a wide range of isolated and merging galaxy populations^{51–53}. Stellar emission is calculated from age- and metallicity-dependent STARBURST99 spectral energy distributions for each stellar particle⁵⁴, and emission from H II regions (including dusty photo-dissociation regions) around young stars is calculated using the MAPPINGS III models⁵⁵. We implement an AGN spectral energy distribution based on the black-hole accretion rate, and our fiducial model is based on empirically derived, luminosity-dependent templates¹⁸.

After the dust distribution is calculated with SUNRISE from the gas-phase metal density distribution, we use SUNRISE to perform Monte Carlo radiative transfer through the dust grid, by computing the energy absorption (including dust self-absorption) and thermal re-emission to produce the emergent, spatially resolved ultraviolet-to-infrared spectral energy distributions. For each merger

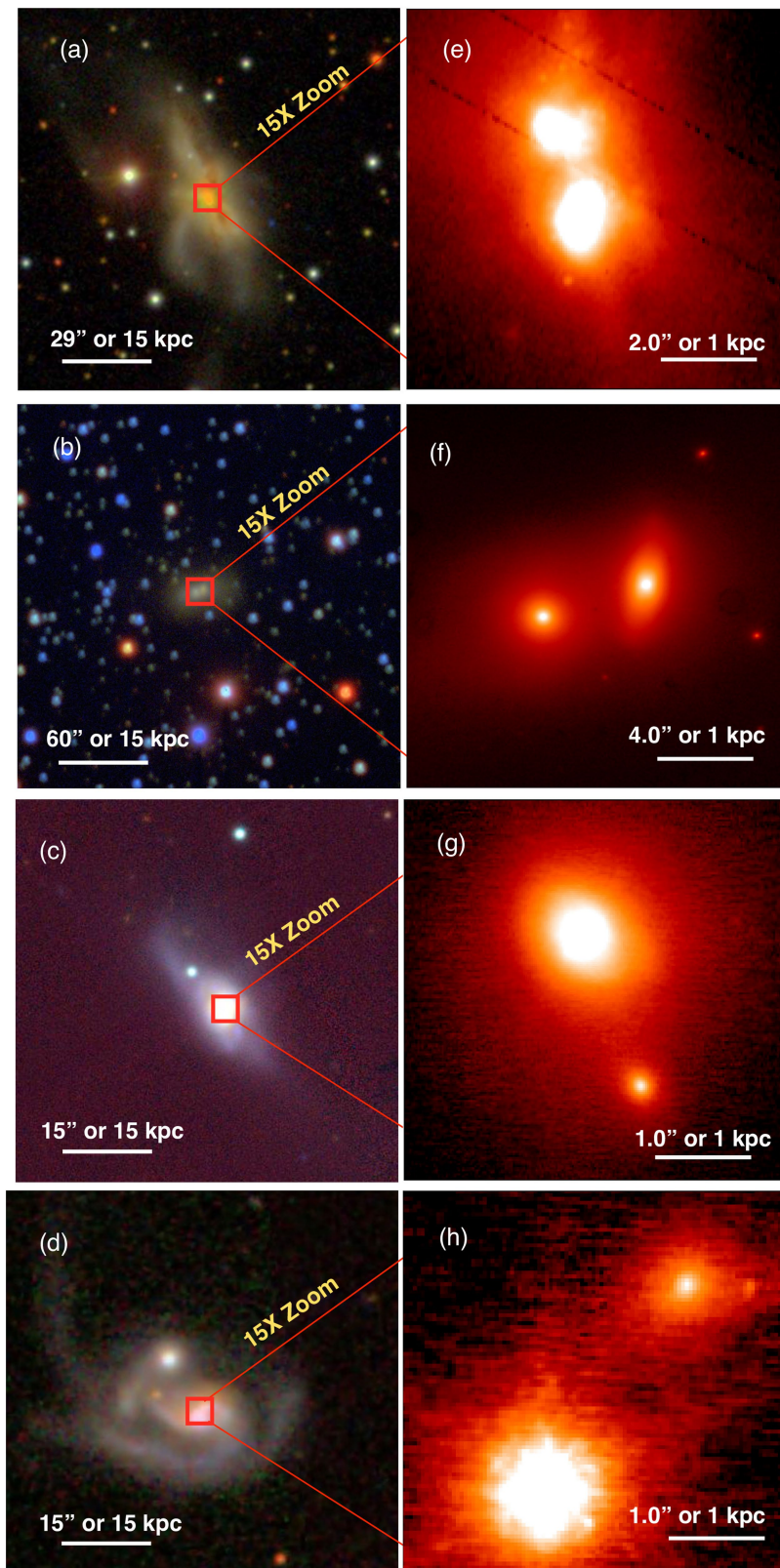
simulation, we run SUNRISE on snapshots at 10-Myr intervals during the merger phase ($R < 10\text{--}30 \text{ kpc}$) and post-merger phases, and at 100-Myr intervals during the early-merger phase, for seven isotropically distributed viewing angles, and the result is converted to the merger fraction that would be seen if observed from a single direction.

Code availability. The custom NIRC2 reduction software is available at <https://github.com/jluastro/JLU-python-code/tree/master/jlu>.

Data availability

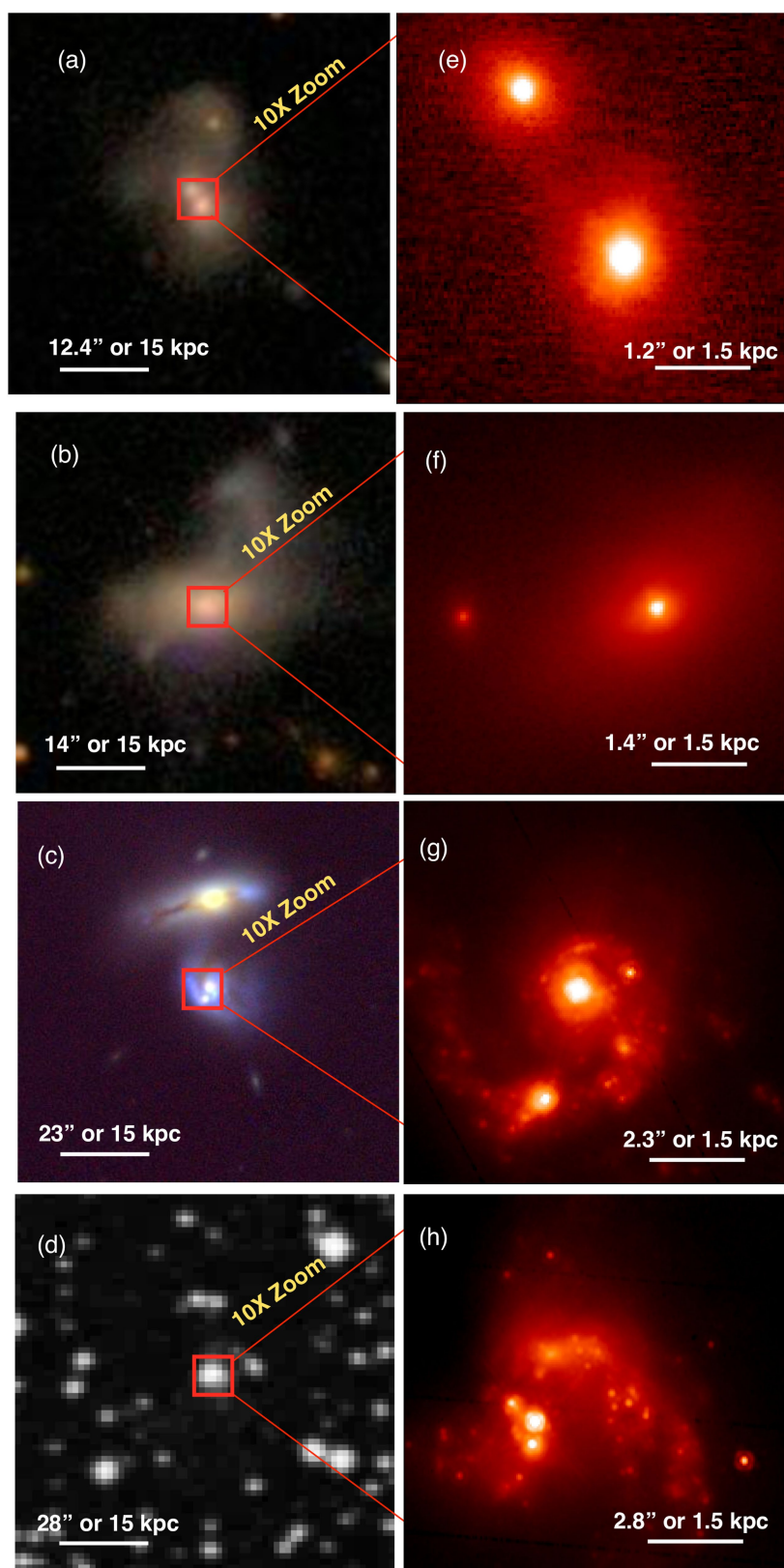
The reduced imaging datasets from the HST are available from the Hubble Legacy Archive. The raw imaging datasets from the near-infrared adaptive optics programmes are available from the Keck Observatory Archive. Other reduced datasets generated or analysed in this study are available from the corresponding author on reasonable request.

- Massaro, E. et al. Roma-BZCAT: a multifrequency catalogue of blazars. *Astron. Astrophys.* **495**, 691–696 (2009).
- Bertin, E. & Arnouts, S. SExtractor: software for source extraction. *Astron. Astrophys. Suppl. Ser.* **117**, 393–404 (1996).
- Blanton, M. R., Kazin, E., Muna, D., Weaver, B. A. & Price-Whelan, A. Improved background subtraction for the Sloan Digital Sky Survey images. *Astron. J.* **142**, 31 (2011).
- de Vaucouleurs, G. et al. *Third Reference Catalogue of Bright Galaxies* (Springer-Verlag, New York, 1991).
- Véron-Cetty, M. P. & Véron, P. A catalogue of quasars and active nuclei: 13th edition. *Astron. Astrophys.* **518**, A10 (2010).
- Patton, D. & Atfield, J. The luminosity dependence of the galaxy merger rate. *Astrophys. J.* **685**, 235 (2008).
- Weigel, A. K., Schawinski, K., Treister, E., Trakhtenbrot, B. & Sanders, D. B. The fraction of AGNs in major merger galaxies and its luminosity dependence. *Mon. Not. R. Astron. Soc.* **476**, 2308–2317 (2018).
- Davies, R. I. et al. Insights on the dusty torus and neutral torus from optical and X-ray obscuration in a complete volume limited hard X-ray AGN sample. *Astrophys. J.* **806**, 127 (2015).
- Koss, M. et al. Host galaxy properties of the Swift BAT ultra hard X-ray selected active galactic nucleus. *Astrophys. J.* **739**, 57 (2011).
- Abazajian, K. N. et al. The seventh data release of the Sloan Digital Sky Survey. *Astrophys. J. Suppl. Ser.* **182**, 543–558 (2009).
- Blanton, M. R., Eisenstein, D., Hogg, D. W., Schlegel, D. J. & Brinkmann, J. Relationship between environment and the broadband optical properties of galaxies in the Sloan Digital Sky Survey. *Astrophys. J.* **629**, 143 (2005).
- Kauffmann, G. et al. Stellar masses and star formation histories for 105 galaxies from the Sloan Digital Sky Survey. *Mon. Not. R. Astron. Soc.* **341**, 33–53 (2003).
- Brinchmann, J. et al. The physical properties of star-forming galaxies in the low-redshift Universe. *Mon. Not. R. Astron. Soc.* **351**, 1151–1179 (2004).
- Chary, R. & Elbaz, D. Interpreting the cosmic infrared background: constraints on the evolution of the dust-enshrouded star formation rate. *Astrophys. J.* **556**, 562–581 (2001).
- Vivian, U. et al. Spectral energy distributions of local luminous and ultraluminous infrared galaxies. *Astrophys. J. Suppl. Ser.* **203**, 9 (2012).
- DasGupta, A., Cai, T. T. & Brown, L. D. Interval estimation for a binomial proportion. *Stat. Sci.* **16**, 101–133 (2001).
- Hung, C.-L. et al. A comparison of the morphological properties between local and $z \sim 1$ infrared luminous galaxies: are local and high- z (U)LIRGs different? *Astrophys. J.* **791**, 63 (2014).
- Grogin, N. A. et al. CANDELS: the cosmic assembly near-infrared deep extragalactic legacy survey. *Astrophys. J. Suppl. Ser.* **197**, 35 (2011).
- Barden, M., Jahnke, K. & Häußler, B. FERENGI: redshifting Galaxies from SDSS to GEMS, STAGES, and COSMOS. *Astrophys. J. Suppl. Ser.* **175**, 105 (2008).
- Springel, V. & Hernquist, L. Cosmological smoothed particle hydrodynamics simulations: a hybrid multiphase model for star formation. *Mon. Not. R. Astron. Soc.* **339**, 289–311 (2003).
- Narayan, R. & McClintock, J. E. Advection-dominated accretion and the black hole event horizon. *New Astron. Rev.* **51**, 733–751 (2008).
- Kormendy, J. & Ho, L. C. Coevolution (or not) of supermassive black holes and host galaxies. *Annu. Rev. Astron. Astrophys.* **51**, 511–653 (2013).
- Jonsson, P. SUNRISE: polychromatic dust radiative transfer in arbitrary geometries. *Mon. Not. R. Astron. Soc.* **372**, 2–20 (2006).
- Jonsson, P., Groves, B. A. & Cox, T. J. High-resolution panchromatic spectral models of galaxies including photoionization and dust. *Mon. Not. R. Astron. Soc.* **403**, 17–44 (2010).
- Snyder, G. F. et al. Modeling mid-infrared diagnostics of obscured quasars and starbursts. *Astrophys. J.* **768**, 168 (2013).
- Blecha, L., Civano, F., Elvis, M. & Loeb, A. Constraints on the nature of CID-42: recoil kick or supermassive black hole pair? *Mon. Not. R. Astron. Soc.* **428**, 1341–1350 (2013).
- Leitherer, C. et al. Starburst99: synthesis models for galaxies with active star formation. *Astrophys. J. Suppl. Ser.* **123**, 3–40 (1999).
- Narayanan, D. et al. A physical model for $z \sim 2$ dust-obscured galaxies. *Mon. Not. R. Astron. Soc.* **407**, 1701–1720 (2010).
- Groves, B. et al. Modeling the pan-spectral energy distribution of starburst galaxies. IV. The controlling parameters of the starburst SED. *Astrophys. J. Suppl. Ser.* **176**, 438–456 (2008).



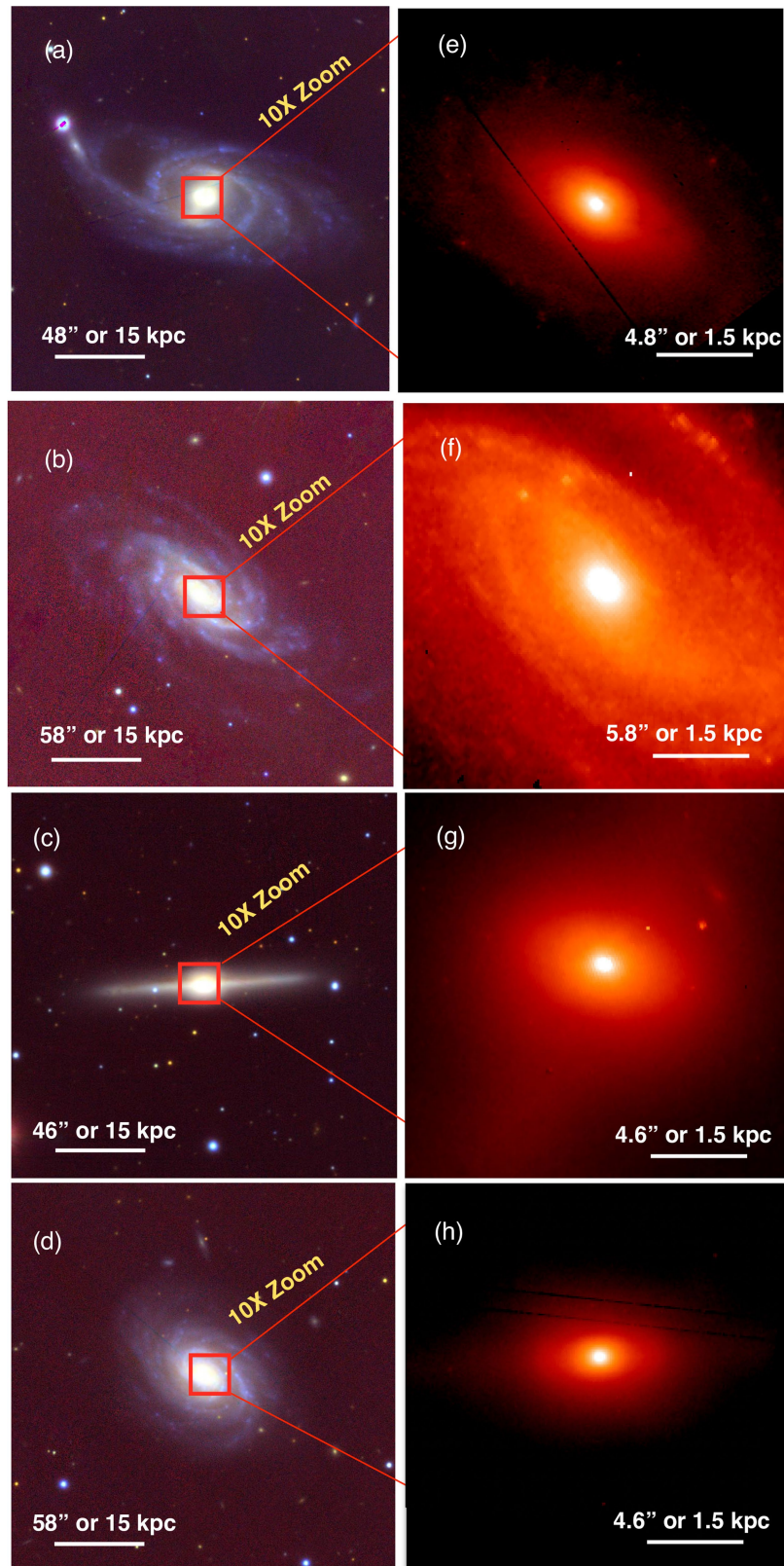
Extended Data Fig. 1 | Other close mergers. **a–d**, Tricolour optical images in the *gri* band from the Sloan Digital Sky Survey or the Kitt Peak survey with about $1''$ angular resolution. The galaxies shown are NGC 6240 (**a**), 2MASX J00253292+6821442 (**b**), ESO 509-G027 (**c**) and

Mrk 975 (**d**) from the AGN sample. The images are $60 \text{ kpc} \times 60 \text{ kpc}$ in size. Red squares indicate the size of the zoomed-in AO image on the right. **e–h**, High-spatial-resolution images of the nuclear mergers shown in **a–d**, $4 \text{ kpc} \times 4 \text{ kpc}$ in size.



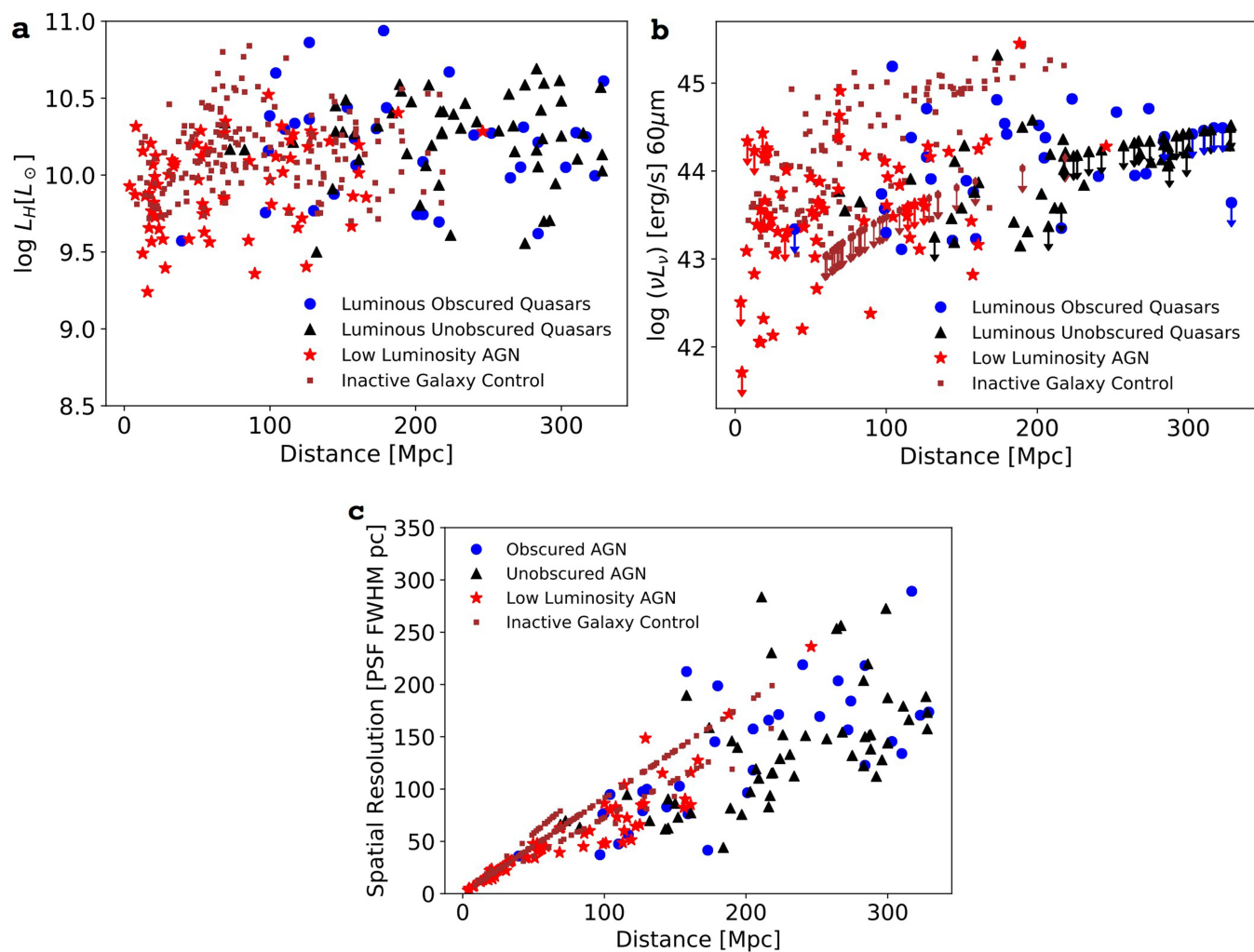
Extended Data Fig. 2 | Other close mergers. **a–c**, Tricolour optical images in the *gri* band from the Sloan Digital Sky Survey or the Kitt Peak survey with about $1''$ angular resolution. The galaxies shown are 2MASX J16311554+2352577 (**a**) and 2MASX J08434495+3549421 (**b**) from the AGN sample and 2MASX J08370182-4954302 (**c**) from the

inactive-galaxy sample. **d**, Lower-quality red Digitized Sky Survey image of UGC02369 NED01, for which no higher-quality imaging exists. The images in **a–d** are $60 \text{ kpc} \times 60 \text{ kpc}$ in size. Red squares indicate the size of the zoomed-in AO image on the right. **e–h**, High-spatial-resolution near-infrared images of the nuclear mergers shown in **a–d**, $4 \text{ kpc} \times 4 \text{ kpc}$ in size.



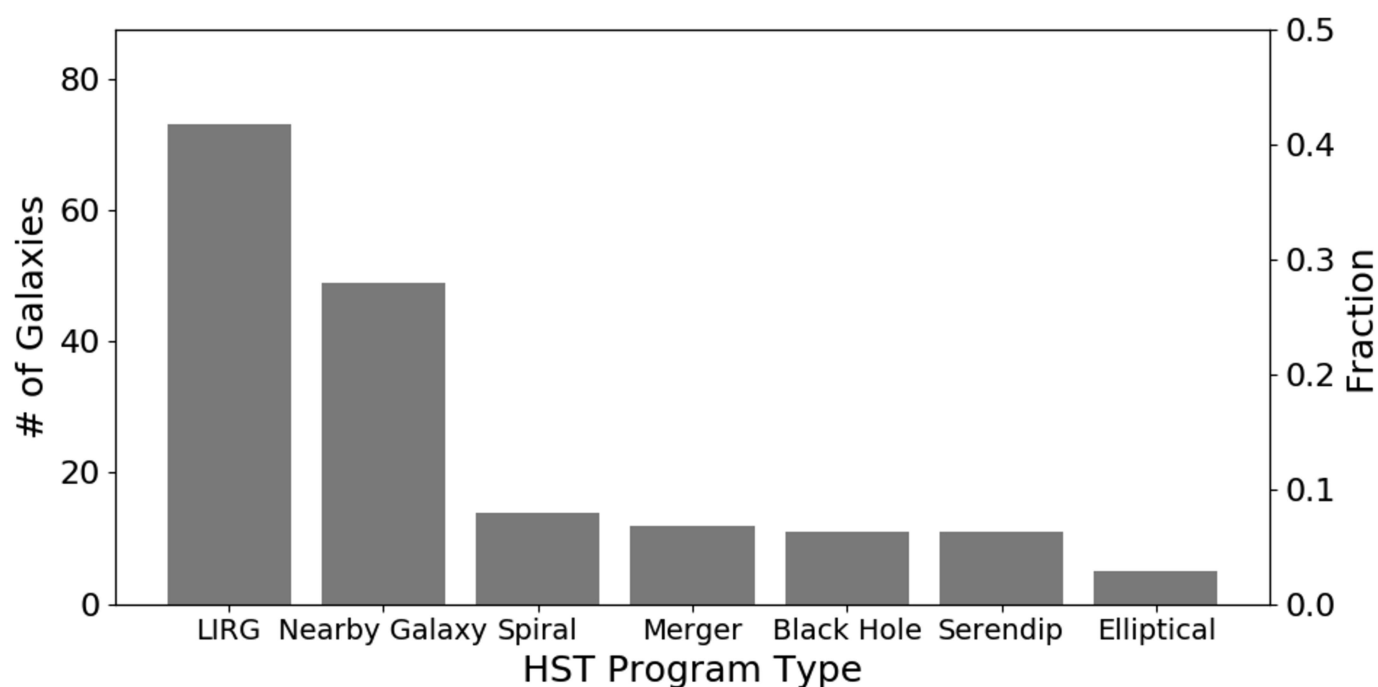
Extended Data Fig. 3 | Inactive-galaxy control sample. a–d, Tricolour optical images in the *gri* band from Pan-STARRS imaging with about $1''$ angular resolution. The images show inactive galaxies in the control sample that were matched in stellar mass and SFR to the AGN: NGC 214 (a), NGC 151 (b), NGC 2998 (c) and NGC 6504 (d). The images are

$60 \text{ kpc} \times 60 \text{ kpc}$ in size. Red squares indicate the size of the zoomed-in AO image on the right. **e–h,** High-spatial-resolution near-infrared images of the nuclear mergers shown in **a–d**, $4 \text{ kpc} \times 4 \text{ kpc}$ in size. Some white lines are present in NICMOS and Pan-STARRS imaging owing to bad pixels with very low or zero response or with very high or erratic dark current.



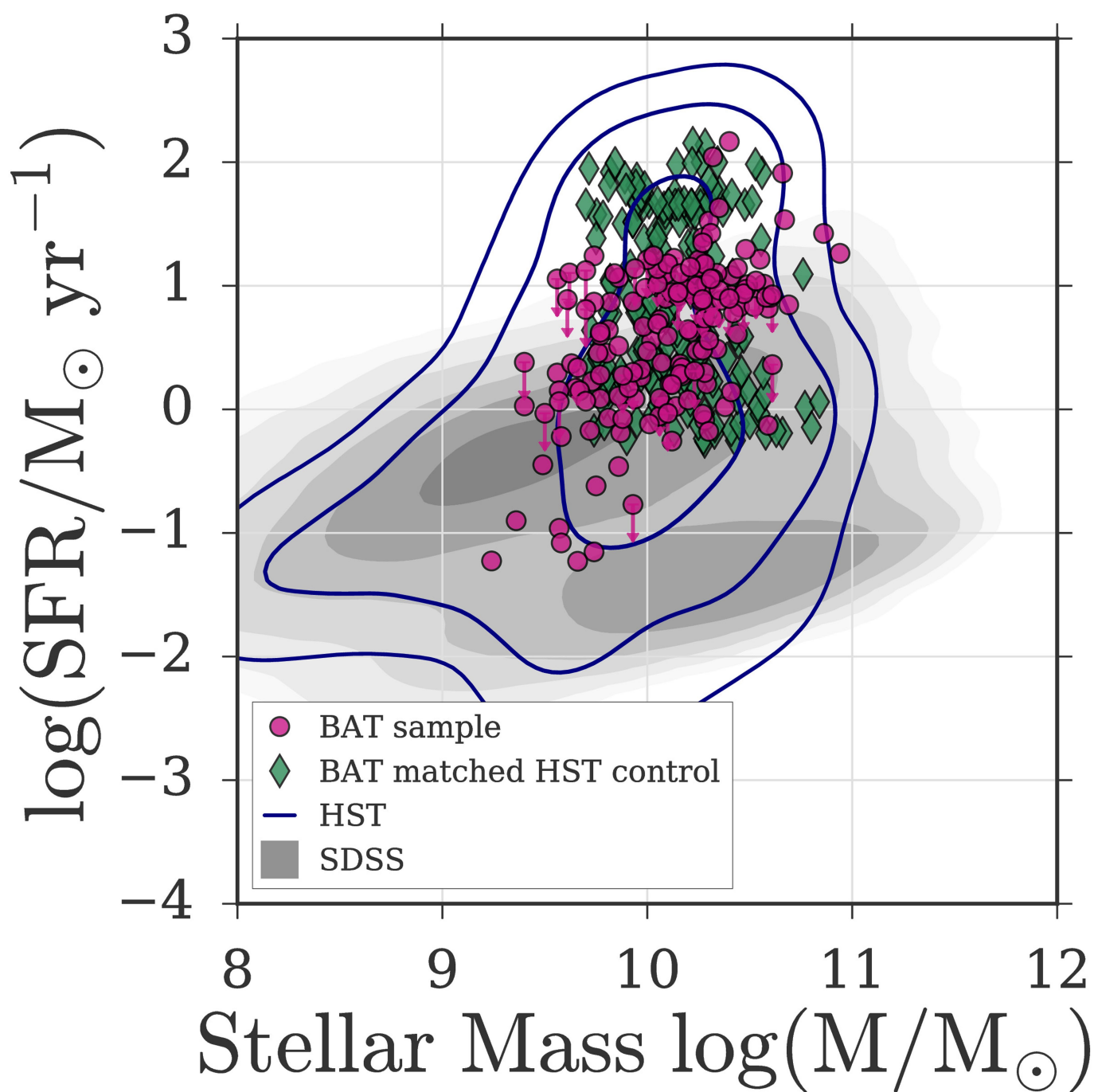
Extended Data Fig. 4 | Stellar mass, star formation rate and resolution of AGN and inactive galaxies. **a**, H-band luminosity of the different AGN and inactive galaxies. Inactive galaxies with considerably lower stellar masses than the AGN samples were excluded ($\langle \log(L_H/L_\odot) \rangle < 9.7$). **b**, 60- μm luminosity of the different AGN and inactive galaxies. Inactive galaxies with lower SFR were also excluded from the comparison ($\langle \log(\nu L_\nu)_{60\mu\text{m}} \rangle = 43.6$). For observations in which a galaxy was not

detected, we show a 3σ upper limit of the SFR, indicated by a downward arrow. **c**, Comparison of the maximum spatial resolution (in parsecs) of the different observations. The inactive-galaxy sample typically has higher physical spatial resolutions than the AGN samples. Many galaxies observed fall along a line because of the constant physical resolution of the HST.



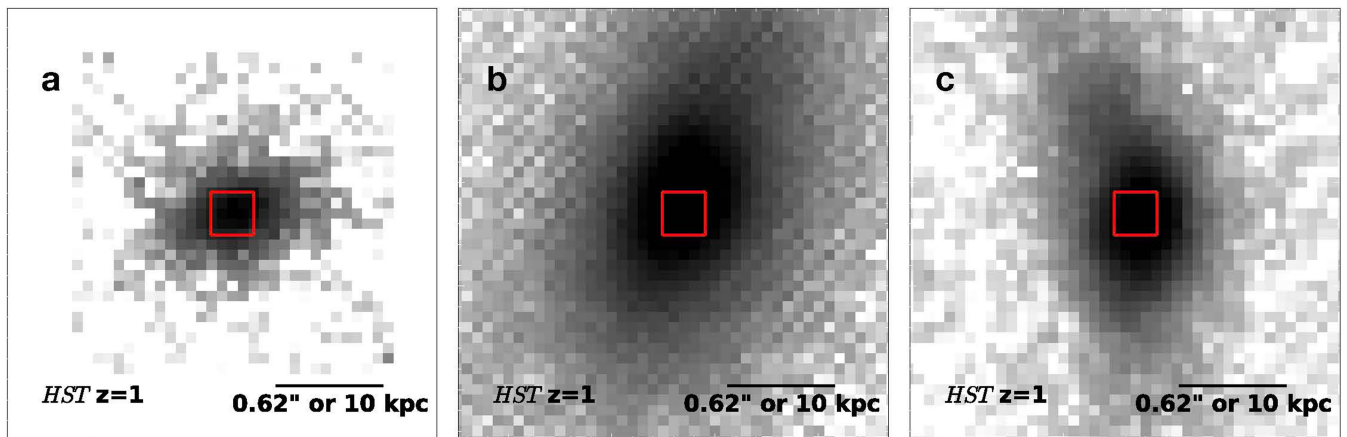
Extended Data Fig. 5 | Summary of programme types included in the HST control sample. The majority of archival control sample observations are of high-SFR luminous infrared galaxies ('LIRG') or from studies of volume-limited samples of nearby galaxies ('Nearby Galaxy'). The remaining samples originate from observations of spiral galaxies ('Spiral'),

galaxies in the merger sequence or late-stage mergers ('Merger'), galaxies with large or small black holes ('Black Hole') and elliptical galaxies ('Elliptical'). Finally, some nearby galaxies were observed serendipitously in observations of other sources or survey fields ('Serendip').



Extended Data Fig. 6 | SFR and stellar mass. Measurements of SFR and stellar mass for the BAT AGN sample (purple circles) and the HST-matched archival control sample of inactive galaxies (green diamonds). The full distribution of inactive galaxies from the Sloan Digital Sky Survey

(SDSS) is shown with grey shading and the full distribution of the HST archive with blue contours. The HST archival sample has an excess of high-stellar-mass, high-SFR inactive galaxies because of the large number of observations of luminous infrared galaxies.



Extended Data Fig. 7 | Simulated HST images of nuclear mergers at high redshift. Simulated images of three nuclear mergers (2MASXJ 01392400+2924067, CGCG 341-006, MCG+02-21-013) observed at $z=1$ with the HST F160W filter as part of the CANDELS survey ($60 \text{ mas pixel}^{-1}$) using optical imaging and FERENGI software. The

HST would be unable to detect these final stage mergers. All simulated images are displayed in the arcsinh scale in coupled-channel-device counts, as if observed in the HST F160W filter as part of the CANDELS survey.

Extended Data Table 1 | Galaxies with companions within 10 kpc

Galaxy	Class	d(")	d(kpc)	Stell.	Stellar Contam (%)	Diff mag
MCG+02-21-013	LumObs	0.4	0.3	0	--	1.4
NGC 6240	LumObs	1.8	0.9	0	--	0.8
2MASXJ08370182-4954302	Inactive	2.1	1.1	--	--	1
2MASX J00253292+6821442	LowLum	4.5	1.1	0	--	0.3
CGCG341-006	LumObs	1.3	1.3	0	--	0.6
UGC02369NED01	Inactive	3	1.9	--	--	0.5
2MASXJ01392400+2924067	LumObs	1.2	1.9	0	--	1.1
Mrk975	LumUnob	2.5	2.5	0	3.2	0.9
2MASXJ16311554+2352577	LumObs	2.3	2.8	0	--	0.8
2MASXJ08434495+3549421	LumObs	2.7	2.9	0	--	2.4
ESO099-G004	Inactive	5.2	3.1	--	--	1.6
MCG+12-02-001	Inactive	9.6	3.1	--	--	0.4
NGC985	LumUnob	3.7	3.3	0	--	2.1
IRAS23436+5257	Inactive	5.3	3.6	--	--	0.4
MCG-02-33-098	Inactive	11.4	3.6	--	--	0.1
Mrk739E	LowLum	6.1	3.8	0	--	0.3
NGC6090NED02	Inactive	6.6	3.9	--	--	1.3
NGC3588NED01	LowLum	7.6	4.1	0	--	1.1
Mrk463	LumObs	4.8	5	0	--	1.4
2MASXJ06094582-2140234	Inactive	8.1	6.1	--	--	1.2
Mrk423	LowLum	9.1	6.1	0	--	1.7
2MASXJ05442257+5907361	LumObs	4.8	6.6	0	--	2.2
IRAS21101+5810	Inactive	9.4	7.3	--	--	0.8
IIZw096NED02	Inactive	10.2	7.4	--	--	0.5
IRASF03359+1523	Inactive	10.8	7.7	--	--	0.2
NGC7212NED02	LowLum	14.3	7.9	0	--	0.9
Was49b	LumObs	6.7	8.7	0	--	0.7
NGC2672	Inactive	28.2	9.2	0.11	--	1.2
UGC04881	Inactive	11.3	9	--	--	0.3
2MASXJ17085915+2153082	LumUnob	6.7	9.8	0	--	1.3

The table lists the sources found to have counterparts within 10 kpc. Obscured and unobscured AGN are separated using the presence of broad H β lines in their optical spectra, and the separation between low- and high-luminosity AGN (below or above $L_{\text{bol}} = 2 \times 10^{44} \text{ erg s}^{-1}$, respectively) is based on their X-ray emission ('LowLum', low-luminosity AGN; 'LumUnob', luminous unobscured AGN; 'LumObs', luminous obscured AGN). The separation d between the two galaxy nuclei is given in arcseconds and kiloparsecs. The stellar contamination ('Stellar Contam') indicates the likelihood of a stellar source of this brightness occurring randomly in the same search area. Finally, the measured stellarity index from a neural net ('Stell.') and the difference (in mag) between the primary and secondary galaxies in the merger ('Diff mag') are also listed.

Observation of universal dynamics in a spinor Bose gas far from equilibrium

Maximilian Prüfer^{1*}, Philipp Kunkel¹, Helmut Strobel¹, Stefan Lannig¹, Daniel Linnemann¹, Christian-Marcel Schmied¹, Jürgen Berges², Thomas Gasenzer¹ & Markus K. Oberthaler¹

Predicting the dynamics of quantum systems far from equilibrium represents one of the most challenging problems in theoretical many-body physics^{1,2}. While the evolution of a many-body system is in general intractable in all its details, relevant observables can become insensitive to microscopic system parameters and initial conditions. This is the basis of the phenomenon of universality. Far from equilibrium, universality is identified through the scaling of the spatio-temporal evolution of the system, captured by universal exponents and functions. Theoretically, this has been studied in examples as different as the reheating process in inflationary Universe cosmology^{3,4}, the dynamics of nuclear collision experiments described by quantum chromodynamics^{5,6}, and the post-quench dynamics in dilute quantum gases in non-relativistic quantum field theory^{7–11}. However, an experimental demonstration of such scaling evolution in space and time in a quantum many-body system has been lacking. Here we observe the emergence of universal dynamics by evaluating spatially resolved spin correlations in a quasi-one-dimensional spinor Bose–Einstein condensate^{12–16}. For long evolution times we extract the scaling properties from the spatial correlations of the spin excitations. From this we find the dynamics to be governed by an emergent conserved quantity and the transport of spin excitations towards low momentum scales. Our results establish an important class of non-stationary systems whose dynamics is encoded in time-independent scaling exponents and functions, signalling the existence of non-thermal fixed points^{10,17,18}. We confirm that the non-thermal scaling phenomenon involves no fine-tuning of parameters, by preparing different initial conditions and observing the same scaling behaviour. Our analogue quantum simulation approach provides the basis with which to reveal the underlying mechanisms and characteristics of non-thermal universality classes. One may use this universality to learn, from experiments with ultracold gases, about fundamental aspects of dynamics studied in cosmology and quantum chromodynamics.

Isolated quantum many-body systems offer particularly clean settings for studying fundamental properties of the underlying unitary time evolution¹⁹. For systems initialized far from equilibrium, different scenarios have been identified, including the occurrence of many-body oscillations²⁰ and revivals²¹, the manifestation of many-body localization²², and quasi-stationary behaviour in a prethermalized stage of the evolution²³.

Here we observe a new scenario associated with the notion of non-thermal fixed points. This is illustrated schematically in Fig. 1a: starting from a class of far-from-equilibrium initial conditions, the system develops a universal scaling behaviour in time and space. This is a consequence of the effective loss of details about initial conditions and system parameters long before a quasi-stationary or equilibrium situation may be reached. The transient scaling behaviour is found to be governed by the transport of an emergent collective conserved quantity towards low momentum scales.

For our experimental study we employ an elongated Bose–Einstein condensate of about 70,000 ⁸⁷Rb atoms. We use the $F=1$ hyperfine manifold with its three magnetic sublevels $m_F=0, \pm 1$ as a spin-1 system with ferromagnetic interactions²⁴. Initially, all atoms are prepared in the $m_F=0$ sublevel, forming a spinor condensate with zero spin length. The dynamics is initiated by instantaneously changing the energy splitting of the $F=1$ magnetic sublevels by means of microwave dressing (see Methods). Consequently, spin excitations develop in the F_x – F_y plane¹² as sketched in Fig. 1b. Our experimental setup allows the extraction of the spin distribution in terms of the spin component $\hat{F}_x(y) = [\hat{\psi}_0^\dagger(y)(\hat{\psi}_{+1}(y) + \hat{\psi}_{-1}(y)) + \text{h.c.}]/\sqrt{2}$ where $\hat{\psi}_m^\dagger(y)$ is the creation operator of an atom in the magnetic sublevel m at position y and h.c. denotes the Hermitian conjugate. At a given time t this is achieved by a spin rotation from the F_x – F_y plane to the F_z -direction and subsequently detecting the atomic density difference $F_z(y) = n_{+1}(y) - n_{-1}(y)$ (see Methods for details). Representative absorption images are shown in Fig. 1c together with the extracted spin profiles (green lines). The histograms in Fig. 1c show the probability distribution of F_x for all positions y and experimental realizations for the corresponding evolution time (see Extended Data Fig. 1 for all evolution times). Results are presented for characteristic stages associated with the initial condition (1), the nonequilibrium instability regime (2), the universal scaling regime (3) and the departure from the non-thermal fixed point (4), as also indicated in Fig. 1a.

We find that during the time evolution the angular orientation θ of the transverse spin (see Fig. 1b) becomes the relevant dynamical degree of freedom. For short evolution times unstable longitudinal spin modes grow exponentially²⁵, well described by Bogoliubov theory, but non-linear evolution quickly takes over (after about 100 ms). This leads to a double-peaked structure of the histograms (see Fig. 1c) indicating that the spin has a mean length and a random orientation in the F_x – F_y plane. On the basis of this observation we extract the mean spin length $\langle |F_\perp(t)| \rangle$, where $F_\perp = F_x + iF_y$, and its fluctuations using a fit. Building on that knowledge, we extract the local angle from the profiles as $\theta(y, t) = \arcsin(F_x(y, t)/\langle |F_\perp(t)| \rangle)$ (see Methods for details).

The time evolution of the fluctuations of the spin orientation is described in terms of correlation functions of the scalar field $\theta(y, t)$. The fluctuations are analysed by evaluating the two-point correlation function $C(y, y'; t) = \langle \theta(y, t)\theta(y', t) \rangle$. To distinguish the role of different length scales we consider a momentum-resolved picture of the dynamics. Hence we evaluate the structure factor, which is the Fourier transform of $C(y, y'; t)$ with respect to the relative coordinate $\bar{y} = y' - y$, averaged over y :

$$f_\theta(k, t) = \int \int dy d\bar{y} C(y + \bar{y}, y; t) \exp(-i2\pi k\bar{y}) \quad (1)$$

In general, the structure factor f_θ is a function of momentum k which evolves in time t in a way determined by the system parameters and initial conditions. In Fig. 2a, we plot $f_\theta(k, t)$ as a function of k on a double-logarithmic scale for times between 4 s and 9 s. A characteristic shift of

¹Kirchhoff-Institut für Physik, Universität Heidelberg, Heidelberg, Germany. ²Institut für Theoretische Physik, Universität Heidelberg, Heidelberg, Germany. *e-mail: universaldynamics@matterwave.de

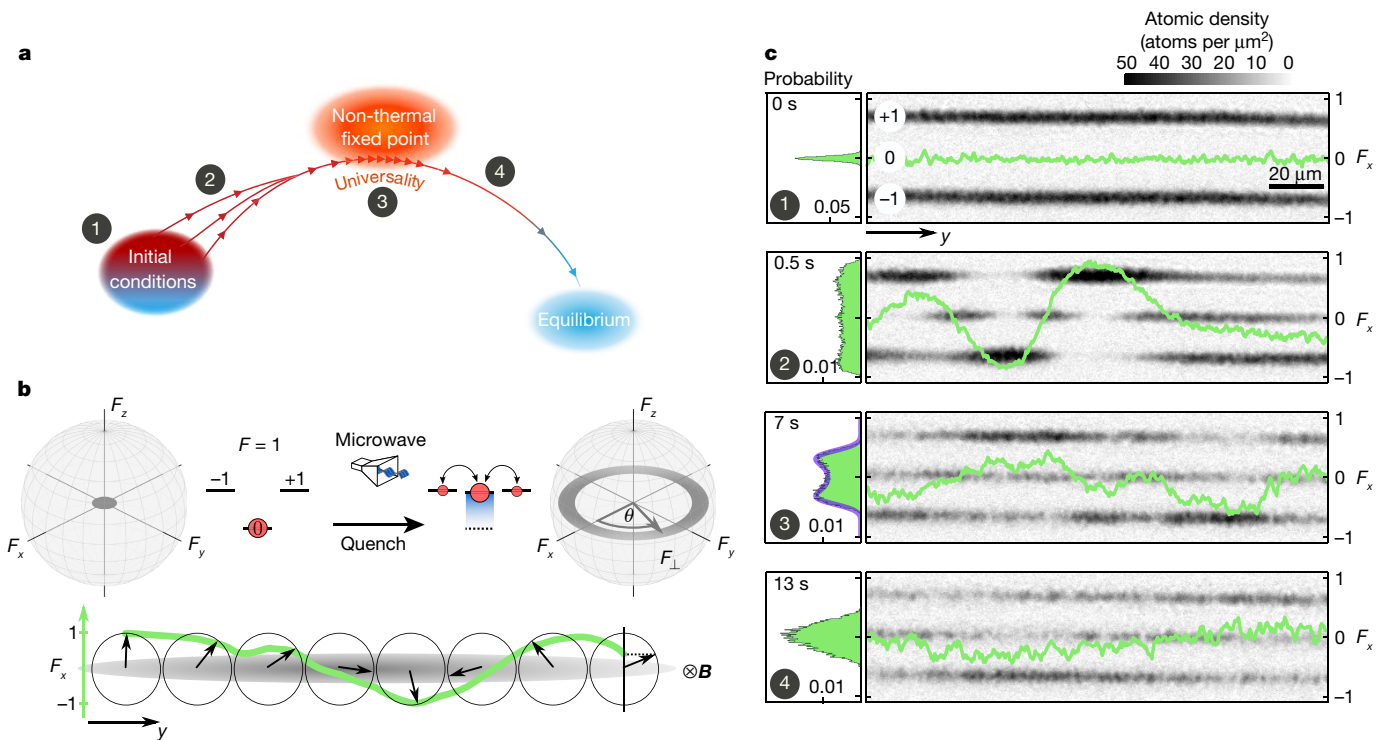


Fig. 1 | Universal dynamics and experimental procedure. **a**, Starting from a class of far-from-equilibrium initial conditions, universal dynamical evolution indicates the emergence of a non-thermal fixed point. Experimentally, we probe the system at different evolution times during the stages indicated by numbers 1 to 4. **b**, A condensate is prepared in the $m_F = 0$ state of the $F = 1$ hyperfine manifold, that is, with a vanishing mean spin length (left spin sphere). With microwave dressing (see Methods) we initiate spin-exchange dynamics, which leads to a growth of spin orthogonal to the magnetic field \mathbf{B} in the F_x – F_y plane (right spin sphere).

Subsequently, spatial structures of the spin orientation θ are found along the cloud. **c**, Exemplary absorption images of the three hyperfine levels taken after a $\pi/2$ spin rotation and Stern–Gerlach separation together with the inferred local spin $F_x(y)$ (green lines). Furthermore, histograms for around 160 experimental realizations are shown. In the universal regime (see step 3 in panel **a**) we extract the spin length and its fluctuation by a fit to the double-peaked structure of the histogram, as indicated in the corresponding plot (see Methods).

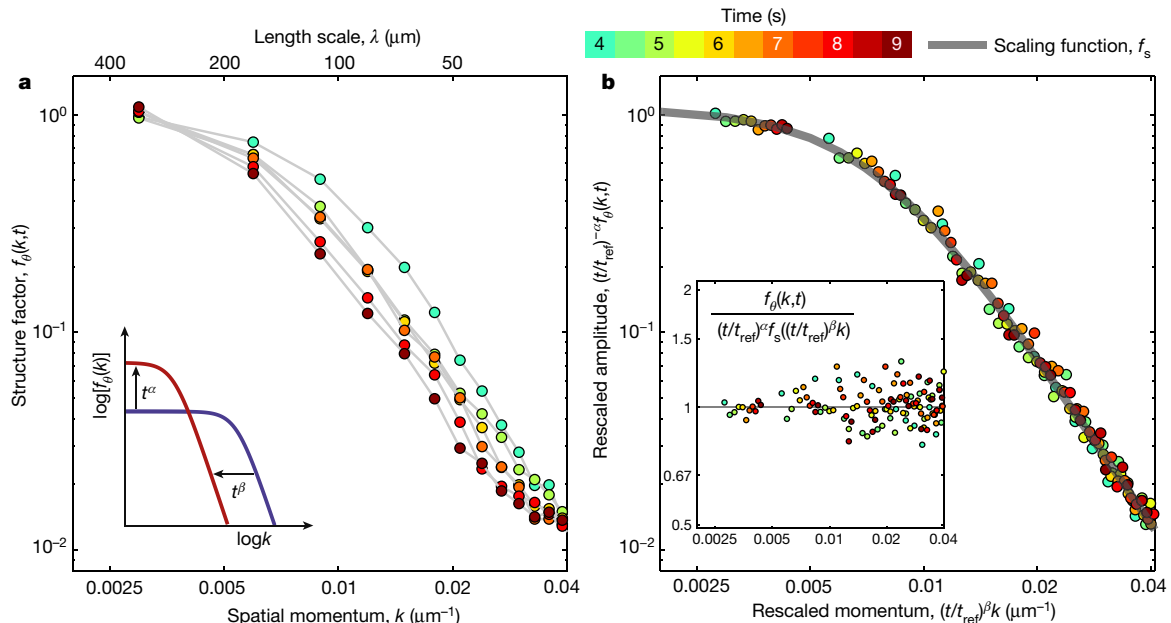


Fig. 2 | Scaling in space and time at a non-thermal fixed point. **a**, Structure factor $f_\theta(k, t)$ as a function of the spatial momentum $k = 1/\lambda$ in the scaling regime between 4 s and 9 s. The colour indicates the evolution time t . The statistical error is of the order of the size of the plot markers. In the infrared the structure factor shifts in time to smaller k (bigger wavelengths), which is connected to transport of excitations towards lower momenta. Characteristic for the non-thermal fixed point dynamics is the

rescaling of the amplitude with universal exponent α and rescaling of the length scale with β (see inset). **b**, By rescaling the data with $t_{\text{ref}} = 4.5$ s, $\alpha = 0.33$ and $\beta = 0.54$ the data collapses to a single curve. We parameterize the universal scaling function with $f_s \propto 1/[1 + (k/k_s)^\zeta]$. Using a fit (grey solid line) we find $\zeta \approx 2.6$ and $k_s \approx 1/133 \mu\text{m}^{-1}$. The quality of the rescaling is revealed by the small and symmetric scatter of the rescaled data divided by the fit (see inset).

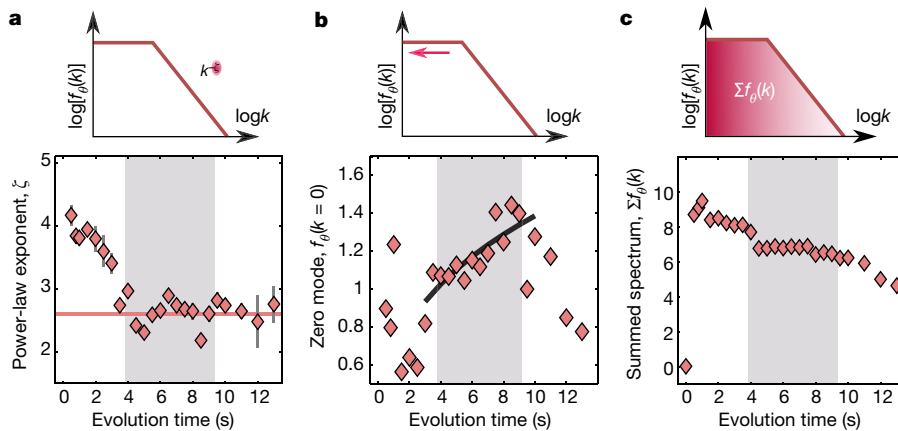


Fig. 3 | Characterization of the scaling regime. **a**, For each evolution time (see Fig. 2) we extract the power-law exponent ζ from a fit. After 4 s it settles to about 2.6 (red solid line), revealing the build-up of the universal scaling function. The grey-shaded region indicates the scaling regime. **b**, The transport to the infrared in the scaling regime is connected to a monotonic increase of the occupation of $k=0$. The solid line depicts

the expected scaling $f_0(k=0, t) \propto t^\alpha$ with $\alpha = 0.33$. After 9 s a rapid decay signals the departure from the scaling regime. **c**, The emergence of a conserved quantity is signalled by the sum over all k -modes of $f_0(k, t)$. After a fast initial growth this observable is approximately constant in the scaling regime and starts to decay after 9 s.

the structure factor towards smaller momenta as well as an increase of the low-momentum amplitude with time is observed.

In fact, instead of separately depending on k and t we find that in this regime the datasets collapse to a single curve if the rescaled distribution $t^{-\alpha} f_0$ is plotted as a function of the single variable $t^\beta k$. This implies that the data satisfy the scaling form

$$f_0(k, t) = t^\alpha f_s(t^\beta k) \quad (2)$$

with universal scaling exponents α , β and scaling function f_s . Figure 2b shows this collapse, where the same data points as in Fig. 2a are plotted with times normalized to the reference time $t_{\text{ref}} = 4.5$ s. The ability to reduce the full nonequilibrium time evolution of the correlation function in the scaling regime to a time-independent, so-called fixed-point distribution $f_s(k)$ and associated scaling exponents is a striking manifestation of universality.

We find the amplitude scaling exponent to be $\alpha = 0.33 \pm 0.08$ and the momentum scaling exponent to be $\beta = 0.54 \pm 0.06$. The errors correspond to one standard deviation obtained from a resampling technique (see Methods). However, the actual uncertainty for α is expected to be larger since the rescaling analysis is much less constraining on α than on β . We find that $f_0(k, t)$ develops a plateau at the lowest momenta and an approximate power-law fall-off above a characteristic length scale in the scaling regime. To parameterize the universal scaling function, we fitted the rescaled data with a function of the form²⁶: $f_s(k) \propto 1/[1 + (k/k_s)^\zeta]$ and find $\zeta \approx 2.6$, with $k_s \approx 1/133 \mu\text{m}^{-1}$ for our system. The value of ζ becomes constant after about 4 s (see Fig. 3a). Analysing $f_0(k=0, t)$ as shown in Fig. 3b reveals that the occupation of $k=0$, which cannot be seen on the logarithmic scale employed in Fig. 2, builds up in the scaling regime. This growth is consistent with the power law proportional to t^α with α obtained from the rescaling analysis, as indicated by the solid line. After 9 s the system departs from the scaling behaviour.

The nature of the observed scaling phenomenon is explained by the emergence of an approximately conserved quantity and its transport. In terms of our dynamical degree of freedom $\theta(y, t)$ we identify $\int dk \langle |\theta(k, t)|^2 \rangle \equiv \int dk f_0(k, t)$ as the conserved quantity. In fact, Fig. 3c shows that the sum over all modes k for different evolution times—after a fast initial rise due to the instability—settles around a constant within the scaling regime (see also Extended Data Fig. 2). According to the scaling (2), $\int dk f_0(k, t) = t^{\alpha-\beta} \int dk f_s(k) \approx \text{const.}$ corresponds to $\alpha \approx \beta$ so that in our case only one independent dynamical scaling exponent remains. A distinct feature is the transport of the conserved quantity directed towards the infrared, corresponding to a positive sign of β . Theoretically it is expected to find the scaling only for momenta smaller

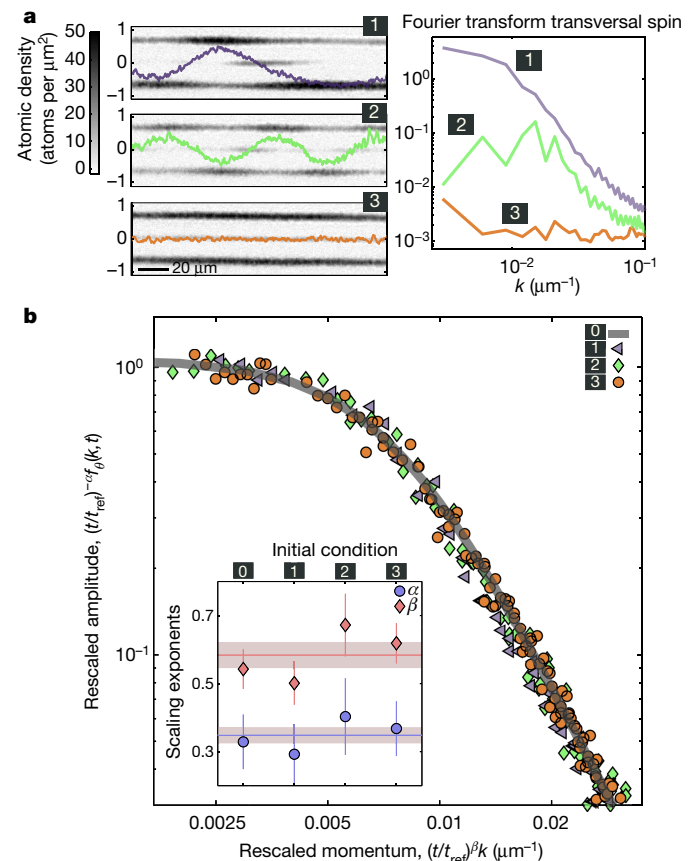


Fig. 4 | Robustness of universal dynamics at a non-thermal fixed point.

a, Absorption images of all three m_F components after spin rotation with the extracted transversal spin (solid lines) of three different initial conditions. The preparations show different initial amplitudes in the Fourier transform of the transversal spin. **b**, All initial conditions lead to scaling dynamics. The data shown were obtained in a time window between 4 s and 9 s after preparation of the initial state. In the inset the scaling exponents of all four initial conditions, including the preparation in $m_F = 0$ (see Fig. 1), are shown; the error bars are 1 s.d., obtained from a resampling method (see Methods). The mean values (red and blue solid lines) of α and β are used to rescale the data. We allow for overall scaling factors in k and amplitude for each initial condition.

than some scale¹⁰ (in our case about $0.04 \mu\text{m}^{-1}$; see Extended Data Fig. 3). The transport towards the infrared is in contrast to the turbulent transport into the ultraviolet observed in direct cascades²⁷.

These experimental findings of scaling behaviour, implying universality, allow comparison with predictions in a variety of models in the non-thermal universality class, which is defined by the scaling function f_s and $\alpha = d\beta$ for given spatial dimension d . N interacting Bose gases with equal intra- and interspecies Gross–Pitaevskii couplings are described by an $O(N)$ symmetric model. This is closely related to $O(N)$ symmetric scalar models²⁸, such as the relativistic Higgs sector of the Standard Model with $N = 4$ for $d = 3$. For these types of models, both Gross–Pitaevskii and relativistic, a universal value of $\beta \approx 0.5$ has been predicted and found to be insensitive to the spatial dimension¹⁰ for $d \geq 2$. This describes the self-similar transport of excitations of the relative phases between the components to lower wavenumbers. The scaling function f_s is known to depend on dimensionality²⁹ and has not yet been theoretically estimated for $d = 1$. Our setup is, to our knowledge, the first realization of an effective $N = 3$ model for the transport of conserved quantities associated with non-thermal fixed points in a quasi-one-dimensional situation. Finding scaling behaviour in one dimension was not expected and sheds new light on the concept of universality classes far from equilibrium.

We emphasize that the non-thermal scaling phenomenon studied here involves no fine-tuning of parameters. This is in contrast to equilibrium critical phenomena, which require a careful adjustment of system variables, such as the temperature, to a critical value³⁰. To illustrate this insensitivity we employ the high level of control of the atomic spin system and prepare three qualitatively different initial conditions (for details see Methods). The corresponding absorption images of single realizations are shown in Fig. 4a along with the Fourier transform of the spatial correlation function of $F_x(y)$.

We find universal dynamics for all initial conditions with comparable inferred scaling exponents (see inset of Fig. 4b). We rescale the data with the same exponents obtained from the mean of all four measurements and take into account overall scaling factors and reference momentum scales. This procedure leads to a collapse of all data, manifesting the robustness of non-thermal fixed point scaling.

The level of control demonstrated here and the accessible observables on our platform open the door to the discovery of further non-thermal universality classes. This represents a crucial step towards a comprehensive understanding of out-of-equilibrium dynamics with potential impact in various fields of science.

(We note that similar phenomena have recently been observed by the Schmiedmayer group³¹ in Vienna in a single-component Bose gas, where a scaling exponent $\beta \approx 0.1$ was extracted.)

Online content

Any methods, additional references, Nature Research reporting summaries, source data, statements of data availability and associated accession codes are available at <https://doi.org/10.1038/s41586-018-0659-0>.

Received: 29 March; Accepted: 28 September 2018;

Published online 7 November 2018.

- Polkovnikov, A., Sengupta, K., Silva, A. & Vengalattore, M. Nonequilibrium dynamics of closed interacting quantum systems. *Rev. Mod. Phys.* **83**, 863–883 (2011).
- Eisert, J., Friesdorf, M. & Gogolin, C. Quantum many-body systems out of equilibrium. *Nat. Phys.* **11**, 124–130 (2015).
- Kofman, L., Linde, A. & Starobinsky, A. A. Reheating after inflation. *Phys. Rev. Lett.* **73**, 3195–3198 (1994).
- Micha, R. & Tkachev, I. I. Relativistic turbulence: a long way from preheating to equilibrium. *Phys. Rev. Lett.* **90**, 121301 (2003).
- Baier, R., Mueller, A. H., Schiff, D. & Son, D. “Bottom-up” thermalization in heavy ion collisions. *Phys. Lett. B* **502**, 51–58 (2001).
- Berges, J., Boguslavski, K., Schlichting, S. & Venugopalan, R. Turbulent thermalization process in heavy-ion collisions at ultrarelativistic energies. *Phys. Rev. D* **89**, 074011 (2014).
- Lamacraft, A. Quantum quenches in a spinor condensate. *Phys. Rev. Lett.* **98**, 160404 (2007).

- Barnett, R., Polkovnikov, A. & Vengalattore, M. Prethermalization in quenched spinor condensates. *Phys. Rev. A* **84**, 023606 (2011).
- Hofmann, J., Natsu, S. S. & Das Sarma, S. Coarsening dynamics of binary Bose condensates. *Phys. Rev. Lett.* **113**, 095702 (2014).
- Piñeiro Orioli, A., Boguslavski, K. & Berges, J. Universal self-similar dynamics of relativistic and nonrelativistic field theories near nonthermal fixed points. *Phys. Rev. D* **92**, 025041 (2015).
- Williamson, L. A. & Blakie, P. B. Universal coarsening dynamics of a quenched ferromagnetic spin-1 condensate. *Phys. Rev. Lett.* **116**, 025301 (2016).
- Sadler, L. E., Higgie, J. M., Leslie, S. R., Vengalattore, M. & Stamper-Kurn, D. M. Spontaneous symmetry breaking in a quenched ferromagnetic spinor Bose–Einstein condensate. *Nature* **443**, 312–315 (2006).
- Kronjäger, J., Becker, C., Soltan-Panahi, P., Bongs, K. & Sengstock, K. Spontaneous pattern formation in an antiferromagnetic quantum gas. *Phys. Rev. Lett.* **105**, 090402 (2010).
- Bookjans, E. M., Vinit, A. & Raman, C. Quantum phase transition in an antiferromagnetic spinor Bose–Einstein condensate. *Phys. Rev. Lett.* **107**, 195306 (2011).
- De, S. et al. Quenched binary Bose–Einstein condensates: spin-domain formation and coarsening. *Phys. Rev. A* **89**, 033631 (2014).
- Nicklas, E. et al. Observation of scaling in the dynamics of a strongly quenched quantum gas. *Phys. Rev. Lett.* **115**, 245301 (2015).
- Berges, J., Rothkopf, A. & Schmidt, J. Nonthermal fixed points: effective weak coupling for strongly correlated systems far from equilibrium. *Phys. Rev. Lett.* **101**, 041603 (2008).
- Nowak, B., Sexty, D. & Gasenzer, T. Superfluid turbulence: nonthermal fixed point in an ultracold Bose gas. *Phys. Rev. B* **84**, 020506(R) (2011).
- Bloch, I., Dalibard, J. & Nascimbène, S. Quantum simulations with ultracold quantum gases. *Nat. Phys.* **8**, 267–276 (2012).
- Hung, C.-L., Gurarie, V. & Chin, C. From cosmology to cold atoms: observation of Sakharov oscillations in a quenched atomic superfluid. *Science* **341**, 1213–1215 (2013).
- Rauer, B. et al. Recurrences in an isolated quantum many-body system. *Science* **360**, 307–310 (2018).
- Schreiber, M. et al. Observation of many-body localization of interacting fermions in a quasirandom optical lattice. *Science* **349**, 842–845 (2015).
- Grimm, M. et al. Relaxation and prethermalization in an isolated quantum system. *Science* **337**, 1318–1322 (2012).
- Stamper-Kurn, D. M. & Ueda, M. Spinor Bose gases: symmetries, magnetism, and quantum dynamics. *Rev. Mod. Phys.* **85**, 1191–1244 (2013).
- Leslie, S. R. et al. Amplification of fluctuations in a spinor Bose–Einstein condensate. *Phys. Rev. A* **79**, 043631 (2009).
- Karl, M. & Gasenzer, T. Strongly anomalous non-thermal fixed point in a quenched two-dimensional Bose gas. *New J. Phys.* **19**, 093014 (2017).
- Navon, N., Gaunt, A. L., Smith, R. P. & Hadzibabic, Z. Emergence of a turbulent cascade in a quantum gas. *Nature* **539**, 72–75 (2016).
- Zinn-Justin, J. *Quantum Field Theory and Critical Phenomena* (Clarendon Press, Oxford, 2002).
- Chantesana, I., Piñeiro Orioli, A. & Gasenzer, T. Kinetic theory of non-thermal fixed points in a Bose gas. Preprint at <http://arXiv.org/abs/1801.09490> (2018).
- Hohenberg, P. C. & Halperin, B. I. Theory of dynamic critical phenomena. *Rev. Mod. Phys.* **49**, 435–479 (1977).
- Erne, S., Bücker, R., Gasenzer, T., Berges, J. & Schmiedmayer, J. Universal dynamics in an isolated one-dimensional Bose gas far from equilibrium. *Nature* <https://doi.org/10.1038/s41586-018-0667-0> (2018).

Acknowledgements We thank D. M. Stamper-Kurn, J. Schmiedmayer, A. Piñeiro Orioli, M. Karl, J. M. Pawłowski and A. N. Mikheev for discussions. This work was supported by the Heidelberg Center for Quantum Dynamics, the European Commission FET-Proactive grant AQuS (project number 640800), the ERC Advanced Grant Horizon 2020 EntangleGen (project ID 694561) and the DFG Collaborative Research Center SFB1225 (ISOQUANT).

Reviewer information Nature thanks M. Kolodrubetz and the other anonymous reviewer(s) for their contribution to the peer review of this work.

Author contributions The experimental concept was developed in discussion among all authors. M.P., P.K. and S.L. controlled the experimental apparatus. M.P., P.K., H.S., S.L. and M.K.O. discussed the measurement results and analysed the data. C.-M.S., J.B. and T.G. elaborated the theoretical framework. All authors contributed to the discussion of the results and the writing of the manuscript.

Competing interests The authors declare no competing interests.

Additional information

Extended data is available for this paper at <https://doi.org/10.1038/s41586-018-0659-0>.

Reprints and permissions information is available at <http://www.nature.com/reprints>.

Correspondence and requests for materials should be addressed to M.P.
Publisher's note: Springer Nature remains neutral with regard to jurisdictional claims in published maps and institutional affiliations.

METHODS

Microscopic parameters. The dynamics of the spinor Bose gas is described by the Hamiltonian

$$\hat{H} = \hat{H}_0 + \int dV \left[\frac{c_0}{2} \hat{n}^2 + \frac{c_1}{2} (\hat{F}_x^2 + \hat{F}_y^2 + \hat{F}_z^2) + q(\hat{n}_{+1} + \hat{n}_{-1}) + p\hat{F}_z \right] \quad (3)$$

where $\hat{n}_m = \hat{\psi}_m^\dagger \hat{\psi}_m$, with $\hat{\psi}_m^\dagger$ the bosonic field creation operator of the magnetic substate $m \in \{0, \pm 1\}$, and $:$ denotes normal ordering. \hat{H}_0 contains the spin-independent kinetic energy and trapping potential. The spin operators are given by $\hat{F}_x = [\hat{\psi}_0^\dagger(\hat{\psi}_{+1} + \hat{\psi}_{-1}) + \text{h.c.}]/\sqrt{2}$ and $\hat{F}_y = [i\hat{\psi}_0^\dagger(\hat{\psi}_{+1} - \hat{\psi}_{-1}) + \text{h.c.}]/\sqrt{2}$ and $\hat{F}_z = \hat{n}_{+1} - \hat{n}_{-1}$. The parameter p describes the linear Zeeman shift in a magnetic field. For the hyperfine spin $F=1$ of ^{87}Rb the spin interaction is ferromagnetic, that is, $c_1 < 0$.

For the experimental control parameter $q > 2n|c_1|$, with n being the total density, the mean-field ground state is the polar state, which corresponds to all atoms occupying the $m_F=0$ state. In the range $0 < q < 2n|c_1|$ a spin with non-vanishing length in the x - y plane is energetically favoured (easy-plane ferromagnet)³². This is the parameter regime employed in the experiment.

Experimental system. We prepare a Bose–Einstein condensate of about 70,000 atoms in the state $(F, m_F) = (1, 0)$ in an optical dipole trap of 1,030 nm light with trapping frequencies $\omega_{\parallel} \approx 2\pi \times 2.2$ Hz and $\omega_{\perp} \approx 2\pi \times 250$ Hz.

The control parameter q is given by $q = q_B - q_{\text{MW}}$, where $q_B \approx 2\pi \times 56$ Hz is the second-order Zeeman splitting in a magnetic field of $B \approx 0.884$ G and $q_{\text{MW}} = \Omega^2/4\delta$ is the energy shift due to the microwave dressing. For dressing³³ we use a power-stabilized microwave generator with resonant Rabi frequency $\Omega \approx 2\pi \times 5.3$ kHz and $\delta \approx 2\pi \times 137$ kHz blue detuned with respect to the $(1, 0) \leftrightarrow (2, 0)$ transition. For the spin dynamics we adjust Ω and δ so that $q \approx n|c_1|$ (with $n|c_1| \approx -2\pi \times 2$ Hz). To monitor the long-term stability of q we do a reference measurement every 4 h (corresponding to about 250 experimental realizations). For this we observe spin dynamics for a fixed evolution time of 4 s as a function of the control parameter q (changing the detuning δ). Analysing the integrated side mode population we infer that the drifts of q are well below 0.5 Hz.

Preparation of different initial conditions. We prepare three initial conditions (see Fig. 4) that differ from the polar state. For initial condition 1 the control parameter is first set to $q \approx n|c_1| + 1$ Hz. After 500 ms of spin dynamics at this value we quench to the final value $q \approx n|c_1|$. For the preparation of initial condition 2 we apply a resonant $\pi/5$ radio-frequency pulse to populate the $(1, \pm 1)$ states. After a hold time of 100 ms at a magnetic field gradient of around $0.2 \mu\text{G } \mu\text{m}^{-1}$ in the longitudinal trap direction we apply a second $\pi/5$ radio-frequency pulse. The combination of q and an inhomogeneous p during the hold time leads to a spatially modulated transversal spin on a length scale of $\lambda \approx 80 \mu\text{m}$. For initial condition 3

we populate homogeneously the $(1, \pm 1)$ states with a short radio-frequency pulse such that $(n_{+1} + n_{-1})/n \approx 0.1$.

Spin read-out. The spin dynamics is initiated by quenching the control parameter. After a fixed evolution time t we apply a short magnetic field gradient pulse (Stern–Gerlach) in the z -direction and switch off the waveguide potential. Following a short time of flight (about 1 ms) we perform high-intensity absorption imaging with a resonant light pulse of duration $15 \mu\text{s}$. The resolution of the imaging system is about $1.2 \mu\text{m}$, corresponding to three pixels on the charge-coupled-device camera³⁴; we accordingly bin the spin profiles by three pixels. As our Stern–Gerlach analysis is oriented in the z -direction, for the read-out of the spin in the x - y plane we apply, before the magnetic field gradient, a radio-frequency pulse resonant with the transitions $(1, 0) \leftrightarrow (1, \pm 1)$.

The radio-frequency pulse can be modelled as a spin rotation described by the Hamiltonian $\hat{H}_{\text{rf}} = \Omega_{\text{rf}} \hat{F}_y$ with resonant Rabi frequency $\Omega_{\text{rf}} \approx 2\pi \times 17.5$ kHz. Applying a $\pi/2$ -pulse of duration $14.3 \mu\text{s}$, the observable \hat{F}_x is mapped to the measurable density difference $n_{+1} - n_{-1}$.

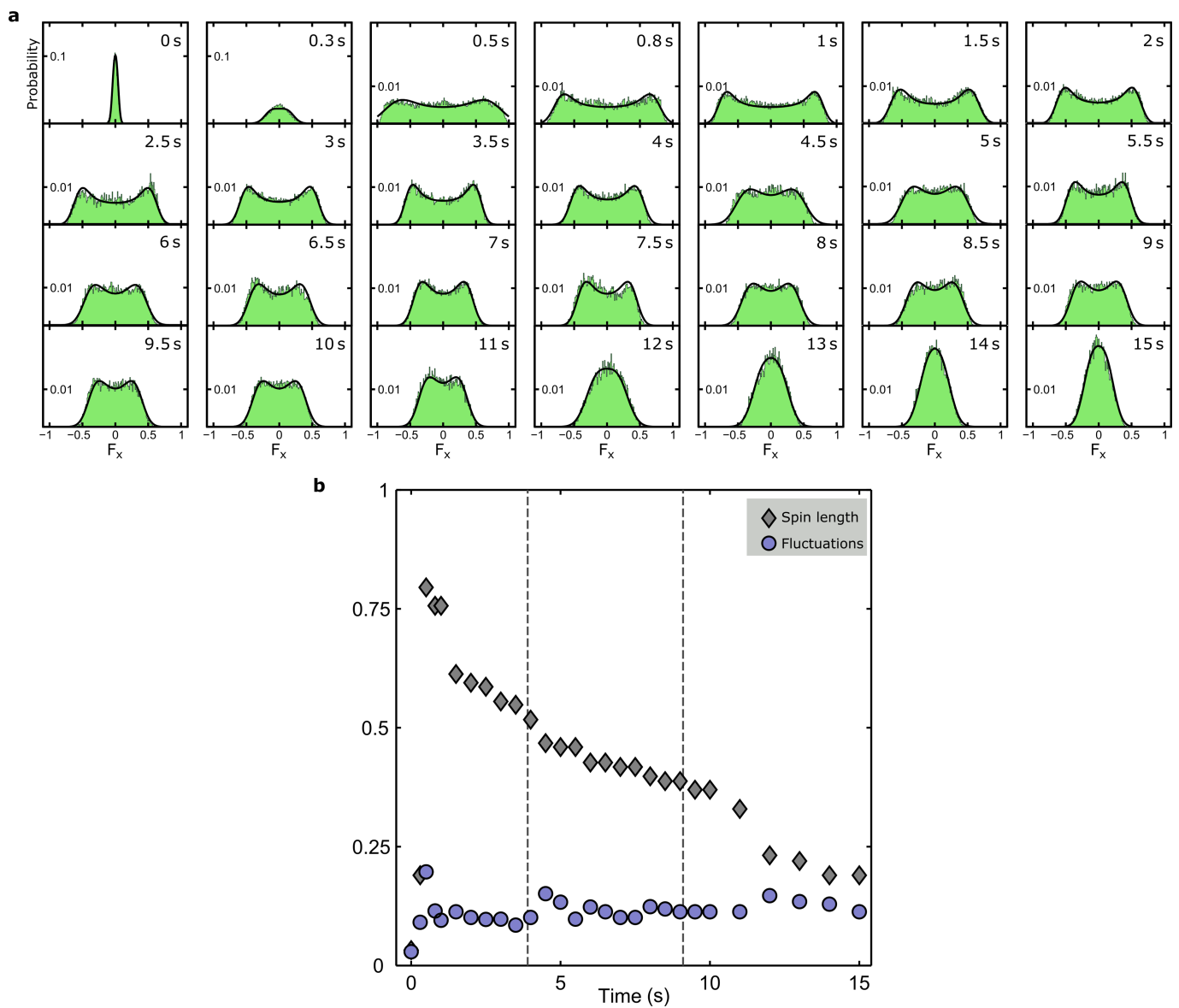
Inferring the spin orientation. The double-peaked spin distributions in the scaling regime (see Extended Data Fig. 1) resemble a distribution of a transversal spin with random orientation. To extract the corresponding ensemble average length $\langle |F_{\perp}| \rangle$ of the transversal spin and its fluctuation σ we fit a probability density of the form $p(F_x) \propto 1/\sqrt{1 - (F_x/\langle |F_{\perp}| \rangle)^2}$ convolved with a Gaussian distribution with root-mean-square σ . Under the assumption of a homogeneous spin length the spatial profile of the angular orientation is given by $\theta(y) = \arcsin(F_x(y)/\langle |F_{\perp}| \rangle)$. If the maximal amplitude is larger than $\langle |F_{\perp}| \rangle - \sigma$ we use the maximal amplitude of the single realization instead of $\langle |F_{\perp}| \rangle$.

Extraction of scaling exponents. After rescaling the results of the discrete Fourier transform according to equation (2) we interpolate with cubic splines to obtain a common k -grid for all evolution times. We vary the scaling exponents α and β to minimize the sum of the squared relative differences of all structure factors f_{θ} . To estimate the statistical error on the exponents we employ a jackknife resampling analysis³⁵.

Data availability

The data presented in this paper are available from the corresponding author upon reasonable request.

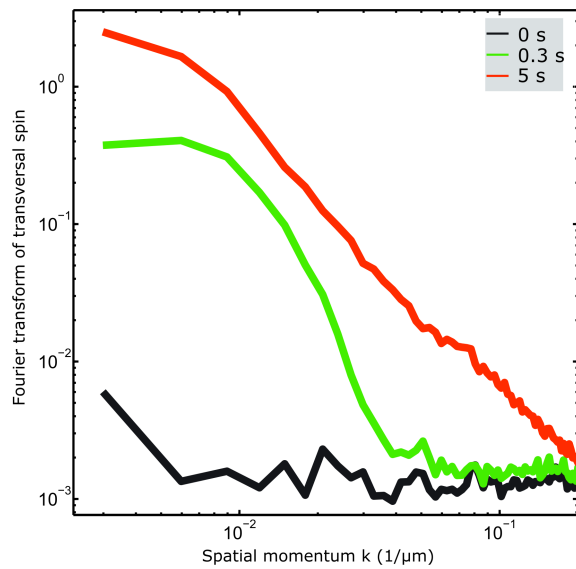
32. Kawaguchi, Y. & Ueda, M. Spinor Bose–Einstein condensates. *Phys. Rep.* **520**, 253–381 (2012).
33. Gerbier, F., Widera, A., Fölling, S., Mandel, O. & Bloch, I. Resonant control of spin dynamics in ultracold quantum gases by microwave dressing. *Phys. Rev. A* **73**, 041602(R) (2006).
34. Muesel, W. et al. Optimized absorption imaging of mesoscopic atomic clouds. *Appl. Phys. B* **113**, 69–73 (2013).
35. Miller, R. G. The jackknife—a review. *Biometrika* **61**, 1–15 (1974).



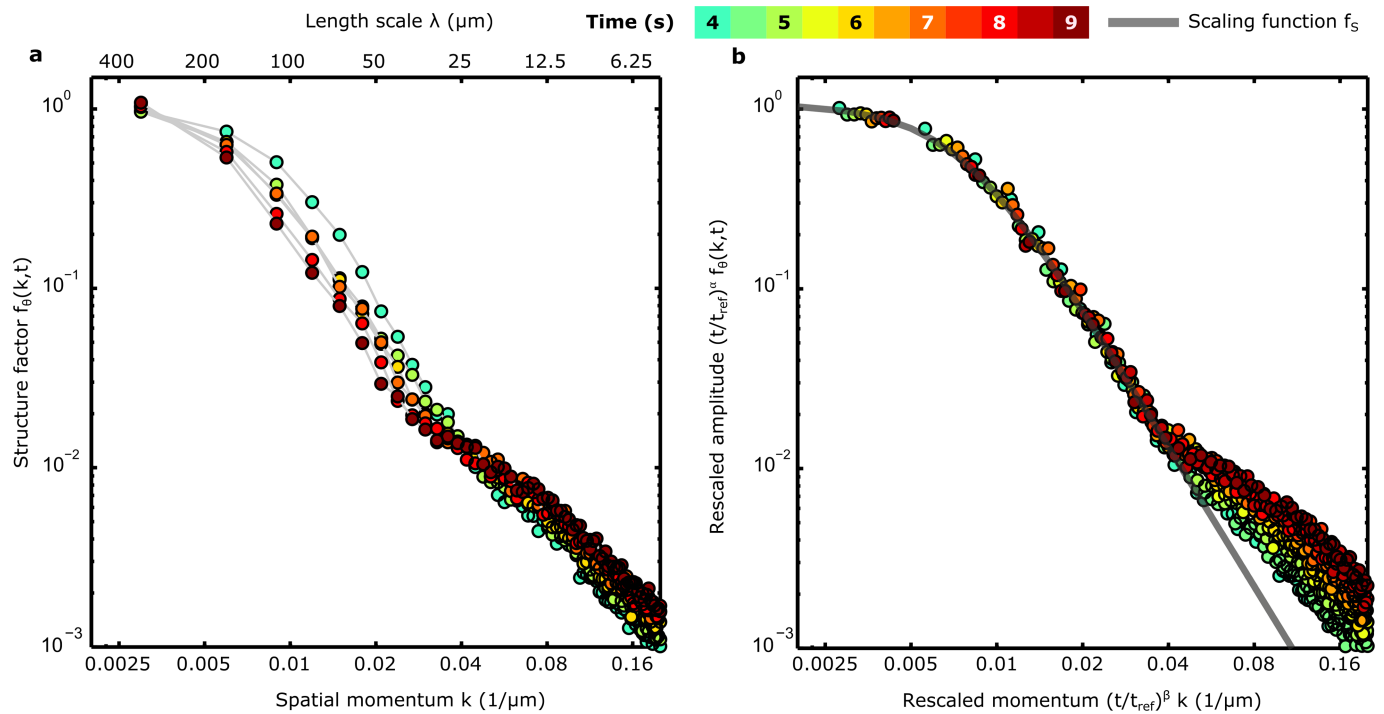
Extended Data Fig. 1 | Spin distributions for all evolution times.

a, The panels show the distributions of the transversal spin, F_x , measured at different evolution times as indicated. Initially, we find a narrow Gaussian distribution corresponding to the prepared coherent spin state. The excitations developing in the transversal spin lead to a double-peaked distribution within the interval of 2 s to 10 s. For long evolution times,

$t > 12$ s, the distribution resembles a Gaussian, which is much broader than the initial distribution. **b**, The spin length and its root-mean-square fluctuation as a function of evolution time are extracted by a fit (see Methods). We find a slow decay of the spin length and nearly constant root-mean-square fluctuations in the scaling regime.



Extended Data Fig. 2 | Build-up of transversal spin in momentum space. Since the angular orientation θ cannot be extracted reliably for short evolution times, we choose to show the Fourier transform of the transversal spin for regimes 1–3 (see Fig. 1). The initial condition, all atoms prepared in $m_F=0$, is characterized by a flat distribution. There is a fast build-up of long-wavelength spin excitations by more than two orders of magnitude within the first second. This process is followed by a redistribution of momenta leading to the scaling form for times longer than 4 s.



Extended Data Fig. 3 | Scaling of structure factor for all experimentally accessible length scales. Same data as shown in Fig. 2. **a**, Unscaled data. **b**, Data rescaled with the scaling exponents reported in the main text. The rescaling does not apply for large momenta, $k > 0.04 \mu\text{m}^{-1}$.

Universal prethermal dynamics of Bose gases quenched to unitarity

Christoph Eigen^{1*}, Jake A. P. Glidden¹, Raphael Lopes^{1,5}, Eric A. Cornell^{2,3}, Robert P. Smith^{1,4} & Zoran Hadzibabic^{1*}

Understanding strongly correlated phases of matter, such as the quark–gluon plasma and neutron stars, and in particular the dynamics of such systems, for example, following a Hamiltonian quench (a sudden change in some Hamiltonian parameter, such as the strength of interparticle interactions) is a fundamental challenge in modern physics. Ultracold atomic gases are excellent quantum simulators for these problems, owing to their tunable interparticle interactions and experimentally resolvable intrinsic timescales. In particular, they provide access to the unitary regime, in which the interactions are as strong as allowed by quantum mechanics. This regime has been extensively studied in Fermi gases^{1,2}. The less-explored unitary Bose gases^{3–11} offer possibilities¹² such as universal physics controlled solely by the gas density^{13,14} and new forms of superfluidity^{15–17}. Here, through momentum- and time-resolved studies, we explore degenerate and thermal homogeneous Bose gases quenched to unitarity. In degenerate samples, we observe universal post-quench dynamics in agreement with the emergence of a prethermal state^{18–24} with a universal non-zero condensed fraction^{22,24}. In thermal gases, the dynamic and thermodynamic properties generally depend on the gas density and the temperature, but we find that they can still be expressed in terms of universal dimensionless functions. Surprisingly, we find that the total quench-induced correlation energy is independent of the gas temperature. These measurements provide quantitative benchmarks and challenges for the theory of unitary Bose gases.

In ultracold atomic gases, two-body contact interactions are characterized by the *s*-wave scattering length *a*, and the unitary regime is realized in the limit $a \rightarrow \infty$, with *a* tuned using magnetic Feshbach resonances²⁵. In Bose gases, tuning *a* to infinity also enhances three-body recombination, which leads to particle loss and heating, making unitary Bose gases inherently dynamic, non-equilibrium systems. Experimentally, these systems are studied by rapidly quenching *a* to infinity (Fig. 1a), which initiates the non-equilibrium dynamics. If starting with a Bose–Einstein condensate (BEC) in the $k \approx 0$ momentum state, after the quench the momentum distribution broadens (the kinetic energy increases) owing to lossless correlation dynamics and to recombination heating (Fig. 1b). The interplay between these two processes raises many questions, such as whether the gas attains a strongly correlated quasi-equilibrium steady state before degeneracy is lost.

The timescales of the different processes are set by the natural length scales of the system. Within the universality hypothesis¹⁴, in a homogeneous degenerate unitary gas the only relevant length scale is the interparticle spacing $n^{-1/3}$, where *n* is the particle density, which (in analogy with Fermi gases) sets the Fermi momentum $\hbar k_n = \hbar(6\pi^2 n)^{1/3}$, energy $E_n = \hbar^2 k_n^2 / (2m)$ and time $t_n = \hbar / E_n$, where *m* is the particle mass and \hbar is the reduced Planck constant. Additional, potentially relevant length scales are the sizes of the Efimov trimer states that exist as a result of resonant two-body interactions^{17,26–31}. Three-body correlations⁸ and Efimov trimers⁹ have been observed experimentally, but all

degenerate-gas dynamics have been consistent with t_n being the only characteristic timescale^{6,9,10}. This universality has so far made it impossible to disentangle the lossless from the recombination-induced dynamics. Experimental evidence has suggested that the lossless processes are faster, sufficiently so that the gas attains a degenerate steady state^{6,10}; however, almost nothing could be established about the nature of this state. Here we isolate the effects of the lossless post-quench dynamics through momentum- and time-resolved studies of degenerate and thermal Bose gases.

We prepare a homogeneous ³⁹K Bose gas in an optical-box trap¹⁰ with a volume of around $3 \times 10^4 \mu\text{m}^3$ and use a Feshbach resonance centred at $402.70(3)$ G. Initially, we prepare either a quasi-pure BEC or a thermal gas. In both cases, we start with a weakly interacting system, with $na^3 < 10^{-4}$, then quench the gas to unitarity (within $2 \mu\text{s}$) and let it evolve for a time t_{hold} ; in our box trap, t_n is a global variable and after the quench all parts of the system evolve in the same way. After the time t_{hold} , we quench the gas back to low *a*, release it from

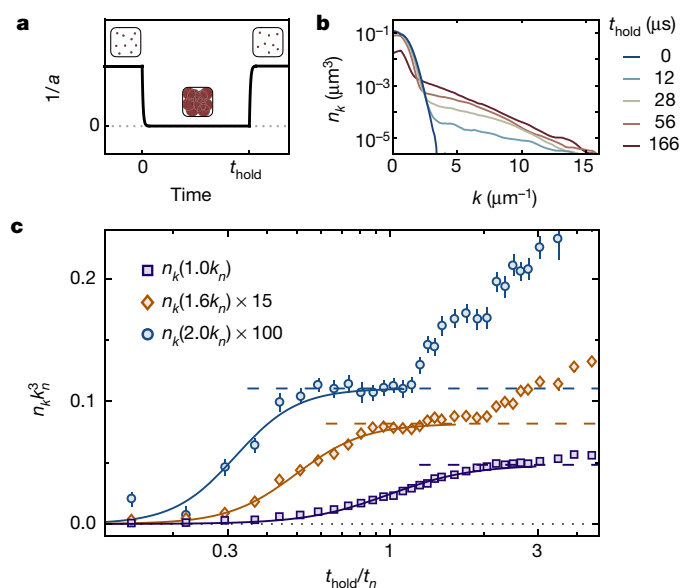


Fig. 1 | Dynamics of a degenerate Bose gas quenched to unitarity. **a**, Quench protocol. The red circles depict atoms, and their sizes the interaction strength, which is limited at unitarity by the interparticle spacing; *a* is the *s*-wave scattering length and t_{hold} is the hold time at unitarity. **b**, Momentum distribution $n_k(k)$ for different t_{hold} values; the initial gas density is $n = 5.1 \mu\text{m}^{-3}$, corresponding to a Fermi momentum of $k_n = 6.7 \mu\text{m}^{-1}$ and a Fermi time of $t_n = 27 \mu\text{s}$. **c**, Populations of individual *k* states show rapid initial growth, saturation at (quasi-)steady-state values of $\bar{n}_k(k)$ (dashed lines) and long-time heating. The error bars reflect 1 s.e.m. (not visible when smaller than the symbol size). The solid lines are sigmoid fits used to extract the initial-growth half-way times $\tau(k)$.

¹Cavendish Laboratory, University of Cambridge, Cambridge, UK. ²JILA, National Institute of Standards and Technology, University of Colorado, Boulder, CO, USA. ³Department of Physics, University of Colorado, Boulder, CO, USA. ⁴Clarendon Laboratory, University of Oxford, Oxford, UK. ⁵Present address: Laboratoire Kastler Brossel, Collège de France, CNRS, ENS-PSL University, UPMC-Sorbonne Université, Paris, France. *e-mail: ce330@cam.ac.uk; zh10001@cam.ac.uk

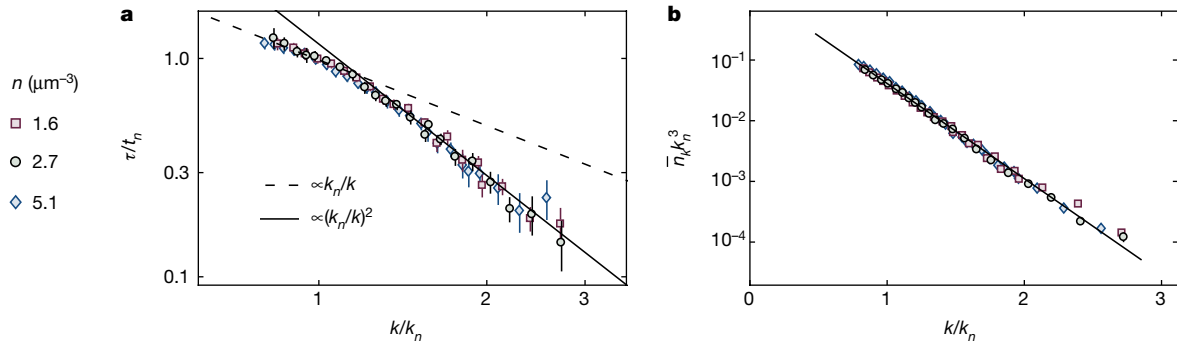


Fig. 2 | Universal post-quench dynamics and the steady-state momentum distribution in the degenerate Bose gas. a, b, The momentum-dependent half-way time $\tau(k)$ for reaching the steady state (a) and the steady-state momentum distribution $\bar{n}_k(k)$ (b), for three different BEC densities n . Expressing all quantities in dimensionless form, using the

the trap and measure its momentum distribution $n_k(k)$; we normalize n_k so that

$$\int 4\pi k^2 n_k dk = 1$$

See Methods for further experimental details.

We first present our study of degenerate gases. In Fig. 1b we show $n_k(k)$ for an initial BEC density of $n = 5.1 \mu\text{m}^{-3}$ and various t_{hold} . In Fig. 1c we illustrate our key experimental observation. By looking at n_k values for individual k states, we discern separate stages in the evolution of n_k : after a rapid initial growth, n_k reaches a (quasi-)steady-state plateau, before the long-time heating takes over. All timescales are of order t_n , but distinguishable. We discern such time separation for $k/k_n \gtrsim 0.8$. For each k in this range, we identify the plateau occupation \bar{n}_k (dashed lines in Fig. 1c) and use sigmoid fits (solid lines) to extract the characteristic time $\tau(k)$ for the initial rapid growth of n_k , defined such that $n_k(k, \tau(k)) = \bar{n}_k(k)/2$. We note that t_n and k_n correspond to the initial n ; for our longest τ we observe particle loss of approximately 20%.

In Fig. 1c we also see that the curves for different k values are not aligned in time; $n_k(2k_n)$ shows signs of heating before $n_k(k_n)$ reaches its steady-state value. This finding illustrates why lossless and recombination dynamics could not be separated quantitatively by considering all k at the same evolution time^{6,10}, such as by looking at the kinetic energy per particle $E(t_{\text{hold}})$ ¹⁰. Instead, we separately obtain \bar{n}_k for different k values and piece together the function $\bar{n}_k(k)$. Doing so does not give the momentum distribution at any specific time, but allows us to infer what the steady-state $n_k(k)$ would be if the gas did not suffer from losses and heating. We assume that at early times ($t_{\text{hold}} = \mathcal{O}(t_n)$), all non-zero- k states are primarily fed from the macroscopically occupied BEC (Fig. 1b).

In Fig. 2 we plot the dimensionless τ/t_n and $\bar{n}_k k_n^3$ versus the dimensionless k/k_n , for three BEC densities. By expressing all quantities in dimensionless form, all of our data fall onto universal curves (within experimental errors).

In the experimentally accessible range of momenta, our data are consistent with the scaling $\tau/t_n \propto k_n/k$ at low k and $\tau/t_n \propto (k_n/k)^2$ at high k . These scalings were predicted for the emergence of a prethermal steady state^{20–24}. According to this prediction, at short times after the quench, the excitations are similar to the Bogoliubov modes in a weakly interacting BEC—which are phonons at low k and particles at high k —but with the usual mean-field energy replaced by an energy of order E_n . The speed of sound is then of order $\hbar k_n/m$ and the crossover between the two regimes is at $k = \mathcal{O}(k_n)$. Finally, $\tau(k)$ is set by the dephasing time, which is given approximately by the inverse of the excitation energy.

The form of the universal $\bar{n}_k k_n^3$ curve was not anticipated and poses a new theoretical challenge. Empirically, over three orders of magnitude

Fermi time t_n and momentum k_n as the natural scales, collapses all of our data onto universal curves. The error bars show fitting errors (not visible when smaller than the symbol size). The solid line in b is an exponential fit, $\bar{n}_k k_n^3 = 1.53 \exp(-3.62 k/k_n)$.

of $\bar{n}_k k_n^3$, our data are well captured by a simple exponential, $A \exp(-Bk/k_n)$, with $A = 1.53(5)$ and $B = 3.62(2)$ (where the errors are 1σ fitting errors). This function implies a condensed fraction of

$$\eta = 1 - \int 4\pi k^2 \bar{n}_k dk = 19(4)\%$$

Up to $k \approx 3k_n$ we do not observe the asymptotic form $n_k \sim 1/k^4$ that is expected³² at very high k ; however, even if n_k changed to this more slowly decaying form immediately outside of our experimental range, η would change by less than 3%. Previous theoretical work^{22,24} has predicted values of η in the prethermal state that are close to our estimate, but the exponential form of $\bar{n}_k k_n^3$ has not previously been predicted. Explaining this experimental observation may require explicit consideration of the quench back to low a .

We now turn to thermal gases, which reveal some simplifications, but also more surprises. A simplification is that, while in a thermal gas the three-body recombination and the lossless dynamics are both slowed down compared to the degenerate-gas case, the three-body recombination is slowed down more^{4,5,33}. As shown in Fig. 3a, now $E(t_{\text{hold}})$ exhibits two separate stages in the post-quench dynamics: a rapid initial growth (here for $t_{\text{hold}} \lesssim 100 \mu\text{s}$) and long-time heating (for $t_{\text{hold}} \gg 100 \mu\text{s}$). The shape of the curve is similar to those for individual k states in Fig. 1c and the long-time energy growth matches the theory of recombination heating^{4,10}. These results reinforce our interpretation of the two-step dynamics, both for degenerate and for thermal gases. We now focus on the early-time dynamics. As we show in Fig. 3b, $n_k(k)$ is essentially identical at $60 \mu\text{s}$ and $126 \mu\text{s}$, meaning that on this timescale a steady state is established for all k .

In a thermal gas, even before the quench to unitarity, n_k is substantial for all $k \lesssim 1/\lambda$, where $\lambda = h/\sqrt{2\pi m k_B T}$ is the thermal wavelength, T is the initial temperature (before the quench to unitarity), k_B is the Boltzmann constant and $h = 2\pi\hbar$. We therefore look at the redistribution of particles in k space, in particular, the change $\delta n_k(k)$ with respect to $t_{\text{hold}} = 0$ and the corresponding change $\delta \varepsilon$ in the spectral energy density $\varepsilon = \hbar^2/(2m) \times 4\pi k^4 n_k$. An additional challenge in understanding the thermal-gas case is that we have two relevant length scales, $n^{-1/3}$ and λ , and it is not a priori clear whether the dynamic and thermodynamic properties can be expressed in terms of dimensionless universal functions.

In Fig. 3c we show time-resolved population changes in different spherical shells in k space, $4\pi k^2 \delta n_k$. For some special k_0 (dotted line), the population remains essentially constant. In Fig. 3d we show vertical cuts through Fig. 3c for $k < k_0$, $k = k_0$ and $k > k_0$. Away from k_0 , we use sigmoid fits (solid lines) to extract $\tau(k)$, both for diminishing and for growing populations. Near k_0 we see only a small wiggle in δn_k to which we cannot assign a single timescale.

In Fig. 3e, f we show $\tau(k)$ and the steady state $\bar{\delta \varepsilon}(k)$ for two different combinations of n and T . The $\bar{\delta \varepsilon}(k)$ curve conveys the

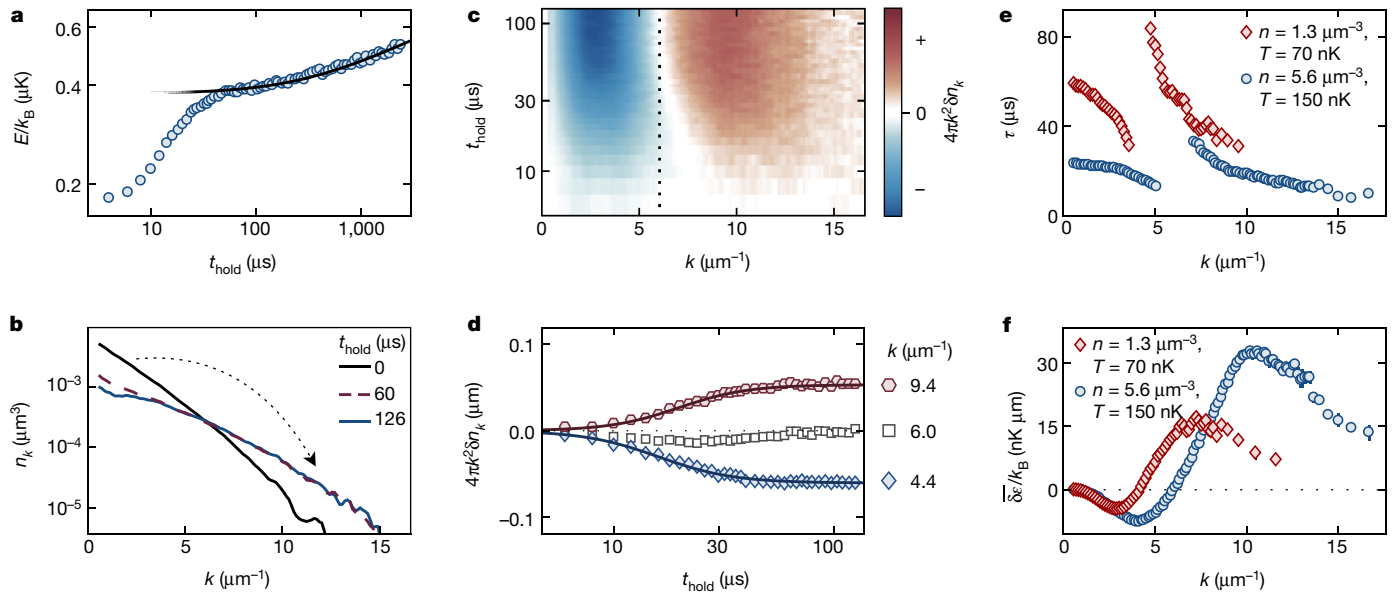


Fig. 3 | Thermal Bose gas quenched to unitarity. **a**, The kinetic energy per particle E shows rapid growth for $t_{\text{hold}} \lesssim 100 \mu\text{s}$ and substantial heating only for $t_{\text{hold}} \gg 100 \mu\text{s}$; the black line is the prediction for recombination heating. Here, and in **b–d**, the initial gas density and temperature are $n = 5.6 \mu\text{m}^{-3}$ and $T = 150 \text{ nK}$, respectively. **b**, Momentum distribution $n_k(k)$ for different hold times at unitarity. The initial redistribution of particles from low k to high k (indicated by the dotted arrow) is essentially complete within $60 \mu\text{s}$, and n_k is almost identical at $126 \mu\text{s}$ and $60 \mu\text{s}$. **c**, Population changes in different k -space shells, $4\pi k^2 \delta n_k(k)$; the

population in $k_0 = 6.0 \mu\text{m}^{-1}$ (dotted line) remains essentially unchanged. **d**, Vertical cuts through the plot in **c**. Solid lines are sigmoid fits used to extract the half-way time $\tau(k)$. **e**, **f**, $\tau(k)$ and the change in the spectral energy density (between the initial, pre-quench state and the post-quench steady state), $\delta \bar{\epsilon}(k) \propto k^4 \delta n_k(k)$. Here we show data for $n = 5.6 \mu\text{m}^{-3}$ and $T = 150 \text{ nK}$ (blue) and for $n = 1.3 \mu\text{m}^{-3}$ and $T = 70 \text{ nK}$ (red). For the data in **a** and **d**, 1 s.e.m. error bars are smaller than the symbol size. In **e** and **f**, the error bars (in most cases smaller than the symbol size) show fitting errors.

redistribution of particles from $k < k_0$ to $k > k_0$ and the resulting energy growth

$$\Delta E = \int \delta \bar{\epsilon} dk$$

The dispersive shape of $\tau(k)$ was not anticipated and invites further theoretical work. Here, we empirically investigate whether these curves can be scaled into universal dimensionless functions.

For the horizontal scaling we find that the natural scale for k is $1/\lambda$, independent of n . In Fig. 4a we plot $\tau(k)$ versus $k\lambda$, for 15 combinations of n and T (corresponding to phase-space densities $n\lambda^3$ between 0.2 and 2). Similarly, in Fig. 4d we plot $\delta \bar{\epsilon}(k)/\lambda$ versus $k\lambda$, so that the area under each curve is still $\Delta E(n, T)$. In both cases, we see horizontal alignment of all of the curves, with $k_0 = 4.4/\lambda$.

A more challenging question is whether these n - and T -dependent curves may be collapsed vertically, by scaling them by some time

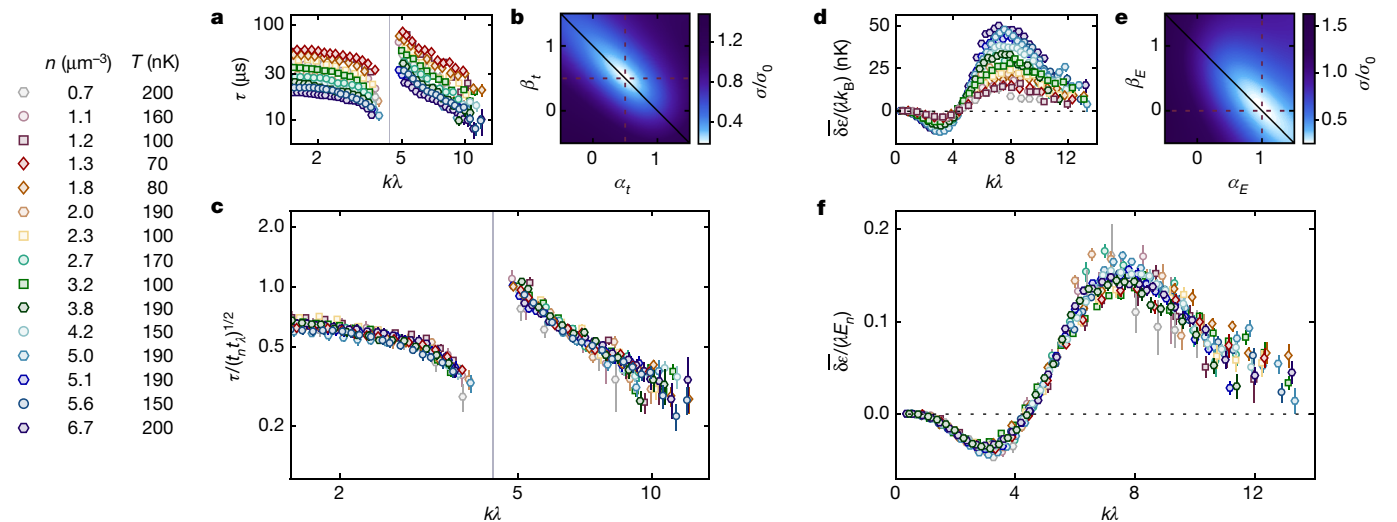


Fig. 4 | Universal dynamic and thermodynamic functions for the thermal Bose gas quenched to unitarity. **a**, **d**, Plotting the half-way time τ for reaching the post-quench steady state (**a**) and the change in the spectral energy density $\delta \bar{\epsilon}/\lambda$ (where λ is the thermal wavelength; **d**) versus $k\lambda$ horizontally aligns all of our curves for 15 different combinations of the initial gas density n and temperature T (see key). The vertical grey line corresponds to k_0 . **b**, Supposing that the characteristic timescale for the dynamics is $t_s \propto t_n^{\alpha_t} t_\lambda^{\beta_t}$, where $t_\lambda = \hbar/(k_B T)$, we obtain the best data collapse,

corresponding to the minimum of σ/σ_0 (see text for details), for $\alpha_t \approx \beta_t \approx 1/2$ (dashed cross indicates $\alpha_t = \beta_t = 1/2$). This suggests that $t_s = \sqrt{t_n t_\lambda}$. **e**, Similarly, for the energy scale $E_s \propto E_n^{\alpha_E} (k_B T)^{\beta_E}$, we find $\alpha_E \approx 1$ and $\beta_E \approx 0$, which suggests that $E_s = E_n$. **c**, **f**, The dimensionless $\tau/(t_n t_\lambda)^{1/2}$ (**c**) and $\delta \bar{\epsilon}/(\lambda E_n)$ (**f**) are, to within experimental errors, universal functions of the dimensionless $k\lambda$. All error bars (not visible when smaller than the symbol size) show fitting errors.

$t_s(n, T)$ and energy $E_s(n, T)$. We conjecture that $t_s \propto t_n^{\alpha_t} t_\lambda^{\beta_t}$, where $t_\lambda = \hbar/(k_B T)$, and similarly $E_s \propto E_n^{\alpha_E} (k_B T)^{\beta_E}$, and determine for which $\alpha_{t,E}$ and $\beta_{t,E}$ we get the best collapse. We treat $\alpha_{t,E}$ and $\beta_{t,E}$ as independent, but physically (if there are no other relevant scales) we expect $\alpha_t + \beta_t = \alpha_E + \beta_E = 1$.

We quantify the degree of the data collapse by a single number σ , which is obtained by calculating the standard deviation of the data for all n and T at a fixed $k\lambda$ and then summing over $k\lambda$. In Fig. 4b, e, we show plots of σ/σ_0 for τ and $\delta\varepsilon/\lambda$; here, σ_0 corresponds to no scaling.

For the temporal scaling, in Fig. 4b we find the lowest σ near $\alpha_t = \beta_t = 1/2$, which suggests that $t_s = \sqrt{t_n t_\lambda}$. In Fig. 4c we plot $\tau/\sqrt{t_n t_\lambda}$ and see that all of our data collapse onto a universal curve (within experimental scatter). For this scaling we have an intuitive interpretation. In a thermal gas, particles do not overlap, so to feel the unitary interactions after the quench they must first meet. The t_s that we find, $\sqrt{t_n t_\lambda} \propto n^{-1/3} \lambda m/\hbar$, matches the expected scaling for the characteristic time until meeting, which is given by the ratio of the interparticle spacing $n^{-1/3}$ and the characteristic thermal velocity $\hbar/(m\lambda)$.

In Fig. 4e we find that the optimal values of α_E and β_E are $\alpha_E \approx 1$ and $\beta_E \approx 0$, suggesting that $E_s = E_n$. This scaling implies that, surprisingly, whereas $\delta\varepsilon(k)$ naturally depends on n and T , its integral ΔE is independent of T ; in Fig. 4f we see that this scaling collapses all of our data onto a universal curve.

This lack of T dependence suggests that $\Delta E/E_n$ in a thermal gas should also be equal to \bar{E}/E_n in a degenerate gas (where $\Delta E = \bar{E}$). Bearing in mind the caveat that we do not observe very high- k tails experimentally, from the data in Fig. 4f we estimate that $\Delta E/E_n = 0.7(1)$ for a thermal gas; from the exponential $\bar{n}_k k_n^3$ in Fig. 2b, we obtain a consistent value of $\bar{E}/E_n = 0.74(4)$ for a degenerate gas.

Our experiments establish a comprehensive view of the prethermal dynamics and thermodynamics of homogeneous Bose gases quenched to unitarity, at low and high temperatures. They provide quantitative benchmarks and new questions for the theory of unitary Bose gases. Open problems include explaining the forms of our experimentally observed universal dynamic and thermodynamic functions, and elucidating the connections between these universal features and previously observed signatures^{8,9} of non-universal Efimov physics. Experimentally, an important future challenge is to probe the coherence and the potential superfluid properties of the prethermal state of a degenerate unitary Bose gas.

While this paper was under review, we learned of two other experiments that observe universality in the many-body dynamics of out-of-equilibrium quantum systems^{34,35}.

Online content

Any methods, additional references, Nature Research reporting summaries, source data, statements of data availability and associated accession codes are available at <https://doi.org/10.1038/s41586-018-0674-1>.

Received: 18 May; Accepted: 28 September 2018;

Published online 7 November 2018.

- Zwinger, W. (ed.) *The BCS-BEC Crossover and the Unitary Fermi Gas* (Springer, Berlin, 2011).
- Zwierlein, M. W. in *Novel Superfluids* Vol. 2 (eds Bennemann, K.-H. & Ketterson, J. B.) Ch. 18 (Oxford Univ. Press, Oxford, 2014).
- Navon, N. et al. Dynamics and thermodynamics of the low-temperature strongly interacting Bose gas. *Phys. Rev. Lett.* **107**, 135301 (2011).
- Rem, B. S. et al. Lifetime of the Bose gas with resonant interactions. *Phys. Rev. Lett.* **110**, 163202 (2013).
- Fletcher, R. J., Gaunt, A. L., Navon, N., Smith, R. P. & Hadzibabic, Z. Stability of a Unitary Bose Gas. *Phys. Rev. Lett.* **111**, 125303 (2013).
- Makotyn, P., Klauss, C. E., Goldberger, D. L., Cornell, E. A. & Jin, D. S. Universal dynamics of a degenerate unitary Bose gas. *Nat. Phys.* **10**, 116–119 (2014).
- Eismann, U. et al. Universal loss dynamics in a unitary Bose gas. *Phys. Rev. X* **6**, 021025 (2016).
- Fletcher, R. J. et al. Two- and three-body contacts in the unitary Bose gas. *Science* **355**, 377–380 (2017).

- Klauss, C. E. et al. Observation of Efimov molecules created from a resonantly interacting Bose gas. *Phys. Rev. Lett.* **119**, 143401 (2017).
- Eigen, C. et al. Universal scaling laws in the dynamics of a homogeneous unitary Bose gas. *Phys. Rev. Lett.* **119**, 250404 (2017).
- Fletcher, R. J. et al. Elliptic flow in a strongly interacting normal Bose gas. *Phys. Rev. A* **98**, 011601 (2018).
- Chevy, F. & Salomon, C. Strongly correlated Bose gases. *J. Phys. B* **49**, 192001 (2016).
- Cowell, S. et al. Cold Bose gases with large scattering lengths. *Phys. Rev. Lett.* **88**, 210403 (2002).
- Ho, T.-L. Universal thermodynamics of degenerate quantum gases in the unitarity limit. *Phys. Rev. Lett.* **92**, 090402 (2004).
- Radzihovsky, L., Park, J. & Weichman, P. B. Superfluid transitions in bosonic atom-molecule mixtures near a Feshbach resonance. *Phys. Rev. Lett.* **92**, 160402 (2004).
- Romans, M. W. J., Duine, R. A., Sachdev, S. & Stoof, H. T. C. Quantum phase transition in an atomic Bose gas with a Feshbach resonance. *Phys. Rev. Lett.* **93**, 020405 (2004).
- Piatecki, S. & Krauth, W. Efimov-driven phase transitions of the unitary Bose gas. *Nat. Commun.* **5**, 3503 (2014).
- Berges, J., Borsányi, Sz. & Wetterich, C. Prethermalization. *Phys. Rev. Lett.* **93**, 142002 (2004).
- Gring, M. et al. Relaxation and prethermalization in an isolated quantum system. *Science* **337**, 1318–1322 (2012).
- Yin, X. & Radzihovsky, L. Quench dynamics of a strongly interacting resonant Bose gas. *Phys. Rev. A* **88**, 063611 (2013).
- Sykes, A. G. et al. Quenching to unitarity: quantum dynamics in a three-dimensional Bose gas. *Phys. Rev. A* **89**, 021601 (2014).
- Kain, B. & Ling, H. Y. Nonequilibrium states of a quenched Bose gas. *Phys. Rev. A* **90**, 063626 (2014).
- Rançon, A. & Levin, K. Equilibrating dynamics in quenched Bose gases: characterizing multiple time regimes. *Phys. Rev. A* **90**, 021602 (2014).
- Yin, X. & Radzihovsky, L. Postquench dynamics and prethermalization in a resonant Bose gas. *Phys. Rev. A* **93**, 033653 (2016).
- Chin, C., Grimm, R., Julienne, P. & Tiesinga, E. Feshbach resonances in ultracold gases. *Rev. Mod. Phys.* **82**, 1225–1286 (2010).
- Efimov, V. Energy levels arising from resonant two-body forces in a three-body system. *Phys. Lett. B* **33**, 563–564 (1970).
- Kraemer, T. et al. Evidence for Efimov quantum states in an ultracold gas of caesium atoms. *Nature* **440**, 315–318 (2006).
- Smith, D. H., Braaten, E., Kang, D. & Platter, L. Two-body and three-body contacts for identical bosons near unitarity. *Phys. Rev. Lett.* **112**, 110402 (2014).
- Comparin, T. & Krauth, W. Momentum distribution in the unitary Bose gas from first principles. *Phys. Rev. Lett.* **117**, 225301 (2016).
- Colussi, V. E., Corson, J. P. & D’Incao, J. P. Dynamics of three-body correlations in quenched unitary Bose gases. *Phys. Rev. Lett.* **120**, 100401 (2018).
- D’Incao, J. P., Wang, J. & Colussi, V. E. Efimov physics in quenched unitary Bose gases. *Phys. Rev. Lett.* **121**, 023401 (2018).
- Tan, S. Energetics of a strongly correlated Fermi gas. *Ann. Phys.* **323**, 2952–2970 (2008).
- Li, W. & Ho, T.-L. Bose gases near unitarity. *Phys. Rev. Lett.* **108**, 195301 (2012).
- Prüfer, M. et al. Observation of universal dynamics in a spinor Bose gas far from equilibrium. *Nature* <https://doi.org/10.1038/s41586-018-0659-0> (2018).
- Erne, S., Bucker, R., Gasenzer, T., Berges, J. & Schmiedmayer, J. Universal dynamics in an isolated one-dimensional Bose gas far from equilibrium. *Nature* <https://doi.org/10.1038/s41586-018-0667-0> (2018).

Acknowledgements We thank R. Fletcher, N. Navon and T. Hilker for discussions and comments on the manuscript. This work was supported by the Royal Society, EPSRC (grant numbers EP/N011759/1 and EP/P009565/1), ERC (QBox), AFOSR and ARO. R.L. acknowledges support from the EU Marie Curie programme (grant number MSCA-IF-2015 704832) and Churchill College, Cambridge. E.A.C. acknowledges hospitality and support from Trinity College, Cambridge.

Reviewer information Nature thanks M. Kolodrubetz and the other anonymous reviewer(s) for their contribution to the peer review of this work.

Author contributions C.E., J.A.P.G. and R.L. collected the data. C.E. analysed the data and produced the figures. C.E., E.A.C., R.P.S. and Z.H. interpreted the data and wrote the manuscript.

Competing interests The authors declare no competing interests.

Additional information

Extended data is available for this paper at <https://doi.org/10.1038/s41586-018-0674-1>.

Reprints and permissions information is available at <http://www.nature.com/reprints>.

Correspondence and requests for materials should be addressed to C.E. or Z.H. **Publisher’s note:** Springer Nature remains neutral with regard to jurisdictional claims in published maps and institutional affiliations.

METHODS

Optical-box trap and sample preparation. As described previously^{36,37}, our box trap is formed by blue-detuned, 532-nm laser beams. It is cylindrical in shape, with a diameter of about 30 μm and a length of about 45 μm . We deduce n from the measured atom number, and take into account the fact that the trap walls are not infinitely steep³⁶, owing to the diffraction limit on the sharpness of the laser beams, so the effective trap volume depends slightly on the energy per particle in the initially prepared sample.

Our clouds are in the lowest hyperfine ground state and we initially prepare them at a field of approximately 399.1 G. At this field, the scattering length is $a_i \approx 400a_0$, where a_0 is the Bohr radius.

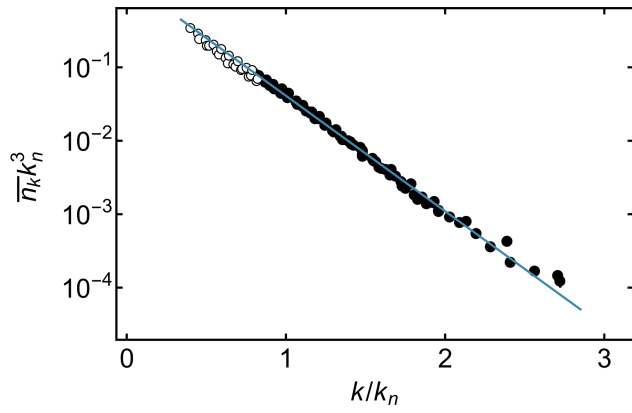
Quench protocol and measurement details. At the end of t_{hold} we quench a back to a_i using an exponential field ramp with a time constant of 1 μs . We use the fastest ramp that is technically possible to minimize the conversion of atoms into molecules^{9,10}. We then release the gas from the trap and simultaneously (within about 3 ms) completely turn off interactions ($a \rightarrow 0$). After letting the cloud expand for 6–12 ms of time of flight, we take an absorption image of it. We typically repeat each measurement about 20 times. To reconstruct $n_k(k)$ from the two-dimensional absorption images, which give the momentum distribution integrated along the line of sight, we average each image azimuthally, then average over the experimental repetitions, and finally perform the inverse Abel transform. Owing to the initial cloud size and non-infinite time of flight, our measurements of $n_k(k)$ are not quantitatively reliable for $k < 2 \mu\text{m}^{-1}$.

Extrapolation of $\bar{n}_k k_n^3$ in a degenerate gas. We also use our experimental data to estimate how the function $\bar{n}_k k_n^3$ extrapolates to lower k/k_n , without presuming its functional form. For $k/k_n < 0.8$, we do not see clear steady-state plateaux in $n_k(t_{\text{hold}})$, such as indicated by the dashed lines in Fig. 1c. However, we can extrapolate $\tau \propto t_n k_n/k$ according to the dashed line in Fig. 2a; then, assuming that heating effects are not yet substantial at $t_{\text{hold}} = \tau(k)$ and following our definition of τ , we estimate $\bar{n}_k = 2n_k(\tau)$, where $n_k(\tau)$ is the n_k measured at the extrapolated τ . These extrapolated values of $\bar{n}_k k_n^3$ are shown by open symbols in Extended Data Fig. 1. They fall on the same exponential curve that fits our directly measured values of $\bar{n}_k k_n^3$ (solid symbols), lending further support for this unexpected functional form.

Data availability

The data that support the findings of this study are available in the Apollo repository (<https://doi.org/10.17863/CAM.30242>). Any additional information is available from the corresponding authors on reasonable request.

36. Gaunt, A. L., Schmidutz, T. F., Gotlibovych, I., Smith, R. P. & Hadzibabic, Z. Bose–Einstein condensation of atoms in a uniform potential. *Phys. Rev. Lett.* **110**, 200406 (2013).
37. Eigen, C. et al. Observation of weak collapse in a Bose–Einstein condensate. *Phys. Rev. X* **6**, 041058 (2016).



Extended Data Fig. 1 | Extrapolation of $\bar{n}_k k_n^3$ in a degenerate gas to lower k/k_n . Solid symbols show directly measured values (also shown in Fig. 2b), here combining the data for all three BEC densities. Open symbols show experimentally extrapolated values, for all three densities, as described in Methods. The solid line is the same as in Fig. 2b.

Universal dynamics in an isolated one-dimensional Bose gas far from equilibrium

Sebastian Erne^{1,2,3}, Robert Bücke^{1,4}, Thomas Gasenzer^{2,5}, Jürgen Berges² & Jörg Schmiedmayer^{1*}

Understanding the behaviour of isolated quantum systems far from equilibrium and their equilibration is one of the most pressing problems in quantum many-body physics^{1,2}. There is strong theoretical evidence that sufficiently far from equilibrium a wide variety of systems—including the early Universe after inflation^{3–6}, quark–gluon matter generated in heavy-ion collisions^{7–9}, and cold quantum gases^{4,10–14}—exhibit universal scaling in time and space during their evolution, independent of their initial state or microscale properties. However, direct experimental evidence is lacking. Here we demonstrate universal scaling in the time-evolving momentum distribution of an isolated, far-from-equilibrium, one-dimensional Bose gas, which emerges from a three-dimensional ultracold Bose gas by means of a strong cooling quench. Within the scaling regime, the time evolution of the system at low momenta is described by a time-independent, universal function and a single scaling exponent. The non-equilibrium scaling describes the transport of an emergent conserved quantity towards low momenta, which eventually leads to the build-up of a quasi-condensate. Our results establish universal scaling dynamics in an isolated quantum many-body system, which is a crucial step towards characterizing time evolution far from equilibrium in terms of universality classes. Universality would open the possibility of using, for example, cold-atom set-ups at the lowest energies to simulate important aspects of the dynamics of currently inaccessible systems at the highest energies, such as those encountered in the inflationary early Universe.

Relaxation and thermalization generally result in loss of information about the details of the initial state of the system. However, the unitary quantum evolution of isolated systems preempts any such loss on a fundamental level. One way to resolve this contradiction reasons that the complexity of the many-body states involved and their dynamics lead to an insensitivity to the initial state for any realistic observable^{1,2}. Consequently, at late times, the system can be characterized by only a few conserved quantities.

Another path to loss of details about the underlying, microscale physics is through universality, such as critical scaling of correlations near phase transitions¹⁵. Aspects of universality in non-equilibrium systems have been discussed in many contexts, such as turbulence¹⁶, driven dissipative systems^{17,18}, defect formation when crossing a phase transitions^{19–21}, and the phenomenon of coarsening²² and ageing²³. Little is known about whether and how unitary time evolution from a general far-from-equilibrium state is connected to universality.

It has recently been proposed that isolated systems far from equilibrium can exhibit universal scaling in time and space associated with non-thermal fixed points^{3,4,7,10}. There is growing theoretical evidence for non-thermal universality classes, even away from any phase transition, that encompass relativistic and non-relativistic systems^{4,7}. In contrast to equilibrium critical phenomena, these non-equilibrium attractor solutions do not require any fine tuning of parameters. Moreover, the non-thermal scaling solutions do not

describe a time-translation-invariant state, whereas, for example, the scaling around a thermalized¹⁵ or pre-thermalized state does^{24–26}.

Here we study the dynamics of a repulsively interacting Bose gas after a strong cooling quench and identify a time window during which the system exhibits universal behaviour far from equilibrium. We start our experiment with a thermal gas of ultracold ⁸⁷Rb atoms in an extremely elongated, quasi-one-dimensional (in the *z* direction) harmonic trap (transverse confinement $\omega_{\perp} = 2 \times 10^4 \text{ s}^{-1}$, longitudinal confinement $\omega_{\parallel} = 30 \text{ s}^{-1}$) just above the critical temperature. In the final cooling step, the trap depth is lowered rapidly compared to the longitudinal thermalization timescale (Fig. 1a). This leads to fast removal of high-energy atoms, predominantly in the radially excited states, and hence constitutes an almost instantaneous cooling quench of the system. At the end of the cooling ramp, the trap depth lies below the first radially excited energy level and only longitudinal excitations remain. After a short holding period of 1 ms, which allows the atoms with large transverse energies to leave, we rapidly increase the trap depth. In this way, we prepare an isolated, far-from-equilibrium, one-dimensional system. The gas is then left to evolve in the deep potential for variable times *t* up to about 1 s, during which time the universal scaling dynamics takes place.

We probe the evolution of the system through two sets of measurements (see Methods for details). First, the in situ density $\rho(z, t)$ is measured using standard absorption imaging²⁷ after a short time of flight of $t_{\text{tof}} = 1.5 \text{ ms}$, during which the expansion is predominantly along the tightly confined radial direction. Second, the momentum distribution $n(k, t)$ of the trapped gas is measured after a long time of flight of $t_{\text{tof}} = 46 \text{ ms}$ using single-atom-resolved fluorescent imaging in a thin light sheet²⁸. For each hold time *t*, the distributions are averaged over many independent measurements (Methods).

A typical time evolution of each of these profiles is shown in Fig. 1b. The far-from-equilibrium state at early times exhibits strongly broadened density and momentum distributions. At early times, the momentum distribution $n(k)$ follows a characteristic exponential decay, $n(k) \propto \exp(-k\xi_s)$, for large *k*. At late times, the system relaxes to thermal equilibrium and is well described by a thermal quasi-condensate (Fig. 1c, Extended Data Fig. 1; see Methods for details). The momentum distribution is then described by only a Lorentzian function, with width given by the thermal coherence length $\lambda_T = 2\hbar^2\rho(z)/(mk_B T)$, where \hbar is the reduced Planck constant, *m* is the mass of the atoms, k_B is the Boltzmann constant and *T* is the temperature. During the evolution, a clear peak emerges at low momenta, signalling the quasi-condensation of the system in momentum space. In the following, we analyse the thermalization process, providing a link between the far-from-equilibrium state at early times and the final equilibrium state that is observed.

For the initial state of the far-from-equilibrium evolution, we find $n(k)$ in good agreement with a theoretical model of randomly distributed solitonic defects¹² (RDM; Fig. 1c). At low momenta, the RDM has a Lorentzian shape, $n(k) \propto [1 + (k/n_s)^2]^{-1}$, with width defined by the defect density n_s . At high momenta, $n(k)$ exhibits characteristic

¹Vienna Center for Quantum Science and Technology, Atominstitut, TU Wien, Vienna, Austria. ²Institut für Theoretische Physik, Ruprecht-Karls-Universität Heidelberg, Heidelberg, Germany.

³School of Mathematical Sciences, Centre for the Mathematics and Theoretical Physics of Quantum Non-Equilibrium Systems, University of Nottingham, Nottingham, UK. ⁴Max Planck Institute for the Structure and Dynamics of Matter, Hamburg, Germany. ⁵Kirchhoff-Institut für Physik, Ruprecht-Karls-Universität Heidelberg, Heidelberg, Germany. *e-mail: schmiedmayer@atomchip.org

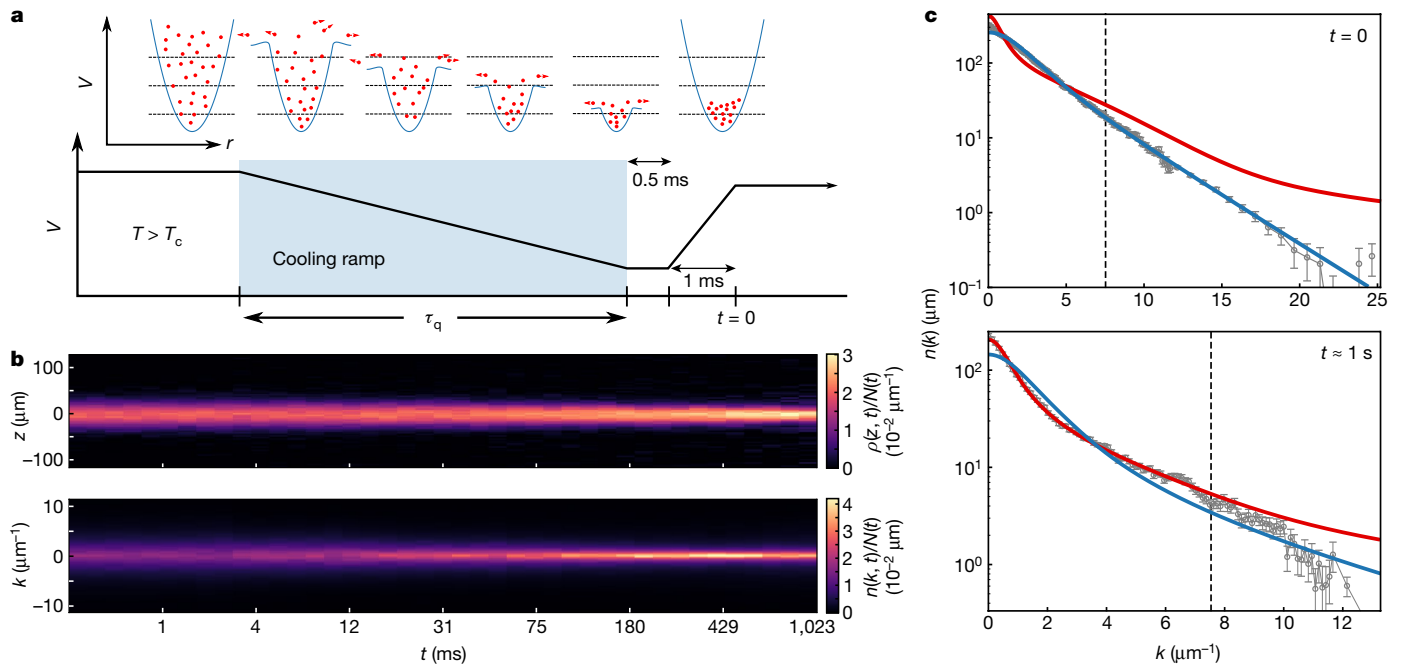


Fig. 1 | Cooling quench and late-time evolution. **a**, Schematic of the experimental cooling quench. During the quench (blue-shaded region), the trap depth V in the radial direction r (upper panel) is ramped linearly to its final value within a time $\tau_q \approx 7$ ms by applying radio-frequency radiation at a time-dependent frequency (radio-frequency knife; lower panel). The final value of V is below the first radially excited state (indicated by the dashed lines), which allows atoms (red dots) at higher energies to leave the trap (red arrows). The trap depth is held at its final position for approximately 0.5 ms to allow the hot atoms to leave and then raised within 1 ms to close the trap (see Methods). The resulting isolated, far-from-equilibrium, one-dimensional Bose gas is then measured after

a variable time t . **b**, Time evolution of the density $\rho(z, t)$ (upper panel; colour scale) and of the single-particle momentum distribution $n(k, t)$ (lower panel). Each distribution is normalized to the time-dependent atom number $N(t)$. **c**, Initial (upper panel) and final (lower panel) momentum distributions $n(k)$. The data for high momenta are binned over seven adjacent k values to lower the noise level. Error bars mark the standard error of the mean. The solid blue and red lines are theoretical fits using the random-soliton model and a thermal quasi-condensate, respectively (Extended Data Fig. 1). The vertical dashed lines correspond to the momenta of the first radially excited state.

exponential decay, $n(k) \propto \exp(-k\xi_s)$, determined by the width ξ_s of the localized density suppression associated with a solitonic defect.

Because we probe the system immediately after the almost instantaneous quench, these defects are not equilibrated (Extended Data Fig. 1); they have a reduced defect width of $\xi_s = 0.07 \mu\text{m} \approx \xi_h/3$ and a very high density of $n_s = 1.4 \mu\text{m}^{-1}$. The peak healing length $\xi_h = \hbar / \sqrt{2mg_{1D}n_0}$ determines the equilibrium width of a soliton, where $g_{1D} = 2\hbar a_s \omega_\perp$ is the one-dimensional interaction constant, a_s is the s -wave scattering length of ^{87}Rb and n_0 is the peak density. Although the nucleation of

solitons is predicted by the Kibble–Zurek mechanism¹⁹, the almost instantaneous quench creates an initial state with a strong overpopulation of high-energy modes. This very far-from-equilibrium state sets the initial conditions for the subsequent thermalization process and facilitates the observation of the emerging universal dynamics during the relaxation of the system.

The time evolution of the normalized momentum distribution $n(k, t)/N(t)$, where $N(t)$ is the total atom number at time t , is shown in Fig. 2a for the first 75 ms following the quench. The distribution

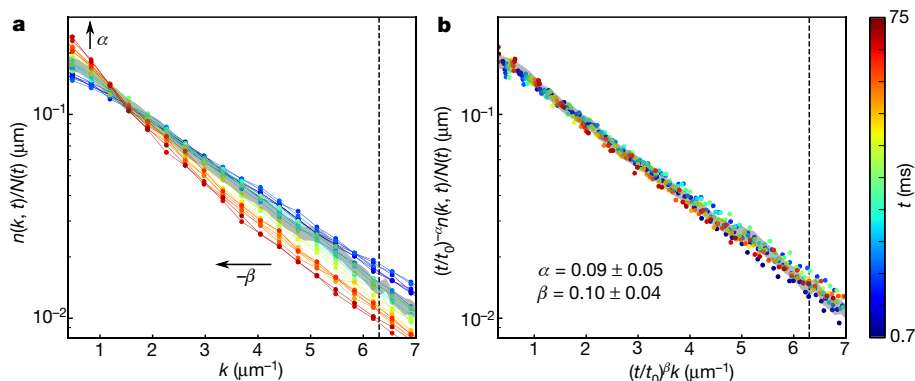


Fig. 2 | Universal scaling dynamics. **a**, Time evolution of the momentum distribution. For better visibility, the data are binned over three adjacent points in momentum space, with the time encoded by the colour scale. The grey line indicates the reference distribution at $t_0 = 4.7$ ms; its width depicts the 95% confidence interval at t_0 . The vertical dashed line marks the high-momentum cut-off for the scaling region. The arrows indicate the

scaling of the distribution in time according to equation (1). **b**, Momentum distribution rescaled according to equation (1). When depicted as a rescaled function $(t/t_0)^{-\alpha} n(\tilde{k}, t)$ of the rescaled variables $\tilde{k} = (t/t_0)^\beta k$, the data for all times collapse to a single curve, representing the distribution at the reference time t_0 . The exponents $\alpha = 0.09 \pm 0.05$ and $\beta = 0.10 \pm 0.04$ are determined from the maximum-likelihood function.

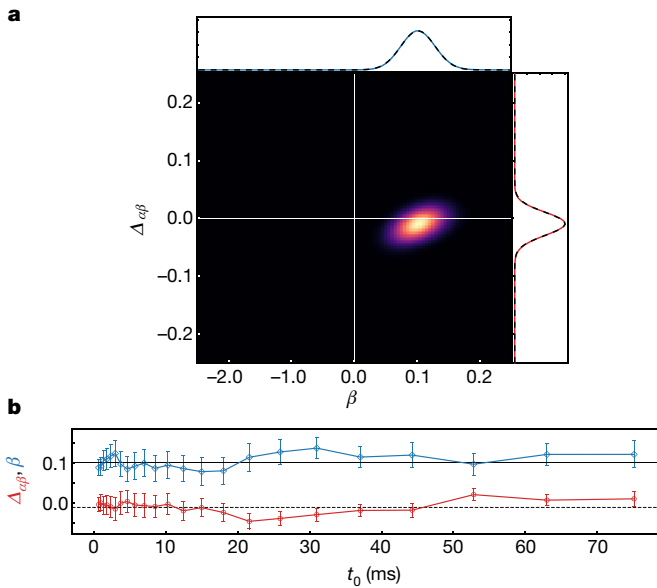


Fig. 3 | Scaling exponents. **a**, The combined two-dimensional likelihood function (colour scale), averaged over all times t and reference times t_0 within the scaling period and over three different initial conditions, reveals a clear peak that yields the non-vanishing scaling exponents $\alpha \approx \beta = 0.1 \pm 0.03$, with a deviation between the two exponents of $\Delta_{\alpha\beta} = \alpha - \beta = -0.01 \pm 0.02$. The error is estimated using a Gaussian fit (black dashed lines) to the marginal-likelihood function (top and right). **b**, Dependence of the scaling exponents on the reference time t_0 . The exponents are, to a good approximation, independent of t_0 and agree well with the mean predictions (black solid and dashed lines). The error bars denote the standard deviation obtained from a Gaussian fit to the marginal-likelihood functions at each reference time separately.

function shifts with time towards lower momentum scales while the occupancy grows in the infrared. In general, $n(k, t)$ depends on k and t separately.

However, it has been suggested⁴ that overpopulated fields far from equilibrium can give rise to universal behaviour, signalled by the infrared scaling property of the distribution function

$$n(k, t) = (t/t_0)^\alpha f_s((t/t_0)^\beta k) \quad (1)$$

where t_0 denotes an arbitrary reference time within the period when $n(k, t)$ exhibits the scaling behaviour.

Figure 2b demonstrates that scaling exponents α and β can indeed be found such that, in the infrared, the rescaled distributions $(t/t_0)^{-\alpha} n(\tilde{k}, t)$ as functions of the rescaled momenta $\tilde{k} = (t/t_0)^\beta k$ collapse to a single curve $f_s(\tilde{k}) = n(\tilde{k}, t_0)$. This indicates that below a characteristic momentum scale k_s , the distribution function $n(k, t)$ depends on space and time only through the scaling of a single universal function $f_s(\tilde{k})$. The scaling exponents are found to be $\alpha = 0.09 \pm 0.05$ and $\beta = 0.1 \pm 0.04$, which indicates that $\alpha \approx \beta$ (see Methods for details on the error estimation).

We demonstrate the predicted insensitivity of the universal properties to the initial state by comparing the evolution for different initial conditions before and after the cooling quench. We find excellent agreement for the scaling exponents, obtained independently by using a scaling analysis for each of the three measurements (Extended Data Figs. 2–5). This shows the generality and robustness of these non-equilibrium attractor solutions: in contrast to equilibrium critical phenomena, for which the temperature has to be adjusted to observe scaling, no fine-tuning of parameters is required.

The universal character allows us to relate the predictions for each measurement directly, resulting in the combined likelihood function presented in Fig. 3a. We consider, for the analysis, the approximately uncorrelated exponents β and $\Delta_{\alpha\beta} = \alpha - \beta$. In agreement with each individual measurement, we find a clearly non-vanishing exponent $\beta = 0.1 \pm 0.03$ and a vanishing (within errors) exponent $\Delta_{\alpha\beta} = -0.01 \pm 0.02$, and thus $\alpha = 0.09 \pm 0.03$. The expected independence of the scaling exponents α and β on the reference time t_0 is shown in Fig. 3b.

We further demonstrate that the shape of the scaling function $f_s(\tilde{k})$ in Fig. 4 is universal: the data for three different initial conditions follow a single universal function $f_s(\tilde{k})$ for all times during which the system shows scaling dynamics. This reflects an enormous reduction of the possible dependence of the dynamics on variations in time and momentum, because the scaling function depends on only the relevant parameters of the system. For instance, if an initial field amplitude represented a relevant parameter, then the scaling function would additionally depend on the product of time or momentum and this field amplitude, with a new scaling exponent. In this case, extracting the scaling function as in Fig. 2 or Fig. 4 as a function of only the product of time and momentum would fail to describe the data.

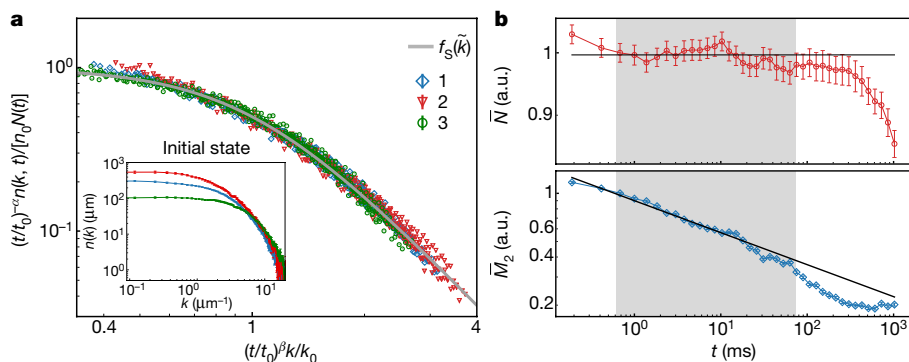


Fig. 4 | Universal scaling function and spatially averaged observables. **a**, Normalized universal scaling function for varying initial conditions: (1) blue, $N = 1,700$, $n_s = 1.4 \mu\text{m}^{-1}$; (2) red, $N = 2,800$, $n_s = 0.9 \mu\text{m}^{-1}$; (3) green, $N = 1,150$, $n_s = 2.3 \mu\text{m}^{-1}$. All initial conditions collapse to a single universal function f_s with exponent $\zeta = 2.39 \pm 0.18$ (grey solid line) for all times within the scaling region. The non-universal scales are the characteristic momentum scale, $k_0 = 2.61 \mu\text{m}^{-1}$ (blue), $2.28 \mu\text{m}^{-1}$ (red) and $3.97 \mu\text{m}^{-1}$ (green), and the global scaling factor of the momentum distribution, $n_0 = 0.14 \mu\text{m}$, $0.15 \mu\text{m}$ and $0.10 \mu\text{m}$, respectively. The rescaled experimental data are binned over three adjacent points in k for clarity. The small deviations at low momenta are due to the finite expansion time

of the gas (Methods). The initial single-particle momentum distribution $n(k)$ at the end of the quench is depicted in the inset. We note the double logarithmic scale, in contrast to Fig. 2. **b**, Scaling of averaged observables. The fraction of particles in the scaling region $\bar{N} \propto (t/t_0)^{\Delta_{\alpha\beta}}$ (upper panel) becomes approximately conserved (solid black line) within the scaling period (grey-shaded region) while being transported towards lower momenta. Deviations in the scaling of the mean kinetic energy per particle in the scaling region, $\bar{M}_2 \propto (t/t_0)^{-2\beta}$ (lower panel), from the predicted scaling (solid black line) indicates the extent of the scaling period in time. The error bars mark the 95% confidence interval. a.u., arbitrary units.

We consider the form $f_s \propto [1 + (\tilde{k}/k_0)^\zeta]^{-1}$ for the scaling function^{4,29}, where the exponent $\zeta = 2.39 \pm 0.18$ is obtained from a single maximum-likelihood fit to all experimental realizations simultaneously. For a fixed exponent, the non-universal scales—the global scaling factor of the momentum distribution and the momentum scale k_0 that rescales the dimensionless momentum \tilde{k}/k_0 —are determined from a least-squares fit for each experimental realization (Methods). The shape of the momentum distribution within the scaling period is markedly different from the thermal distribution (compare Fig. 1c and Extended Data Fig. 1), which clearly indicates a non-thermal scaling phenomenon.

The extent of the scaling region in time is visible from the scaling behaviour of the spatially averaged observables \bar{N} and \bar{M}_2 (Methods), which describe the fraction of particles and the mean energy per particle in the time-dependent scaling region of momentum space ($|k| \leq (t/t_0)^{\beta} k_s$), respectively. From the scaling ansatz in equation (1), we find $\bar{N} \propto (t/t_0)^{\Delta_{\alpha\beta}}$ and hence (because $\Delta_{\alpha\beta} \approx 0$) the emergence of a conserved quantity. This is confirmed in Fig. 4b, in which \bar{N} is approximately constant in the scaling period, whereas it shows a clear time dependence before and after.

The values for the scaling exponents α and β determine the direction and speed with which the particles are being transported. Because these values are positive, a given momentum k in this regime scales as $k/k_0 \propto t^{-\beta}$, so the transport is directed towards lower momenta (the infrared). This transport of particle number leads ultimately to the observed build-up of the quasi-condensate and the approach to thermal equilibrium at late times. The mean energy also exhibits power-law behaviour, $\bar{M}_2 \propto (t/t_0)^{-2\beta}$, and is in accordance with the determined scaling exponent β . Therefore, whereas the particle number in the scaling region is conserved, energy is transported outside this region to higher momenta. On the basis of the scaling properties of these global observables, we identify the scaling period to include the times $t \approx 0.7$ –75 ms.

The far-from-equilibrium universal scaling dynamics in isolated Bose gases following a strong cooling quench or for equivalent initial conditions has been studied theoretically using non-perturbative kinetic equations^{4,13}. In these studies, the universal scaling function is expected to depend on the dimensionality d . The predicted¹³ power-law fall-off $n(k) \propto k^{-\zeta}$, with $\zeta = d + 1$, is consistent with the approximate form of the scaling function given by the RDM and by the quasi-condensate at low momentum, but differs (slightly) from the experimental results. A scaling analysis of the kinetic quasiparticle transport⁴ yields the exponent $\beta = 1/2$ in equation (1) to be independent of d . However, this theory is not expected to apply fully. In particular, for $d = 1$, owing to the kinematic restrictions from energy and momentum conservation, the associated transport is expected to vanish.

The contributions of higher dimensions to the one-dimensional physics provide a plausible way of explaining the non-standard scaling function and scaling exponents observed. Initially, there is a small population of atoms with momenta large enough to excite thermalizing collisions³⁰, and a very small initial seed can lead to thermalization, as observed previously³¹. This is confirmed by a quasi-condensate fit to the final momentum distribution, which, assuming thermal equilibrium, yields an excited-state population of 11% ($T = 95$ nK $= 0.6\hbar\omega_{\perp}$). Our experimental results provide a quantum simulation near the dimensional crossover between one- and three-dimensional physics, establishing universal scaling dynamics far from equilibrium in a regime in which no theoretical predictions are currently available.

The direct experimental evidence that we have presented of scaling dynamics in an isolated far-from-equilibrium system is a crucial step towards a description of non-equilibrium evolution by non-thermal fixed points. Similar phenomena have recently been observed³² in a spin-1 system, but with a scaling exponent of $\beta \approx 1/2$. The concept of non-thermal fixed points has the potential to provide a unified description of non-equilibrium evolution, reminiscent of the characterization of equilibrium critical phenomena in terms of renormalization-group fixed points³³. Such a description may lead to a comprehensive

classification of systems on the basis of their universal properties far from equilibrium, which would be relevant for a large variety of systems at different scales.

Online content

Any methods, additional references, Nature Research reporting summaries, source data, statements of data availability and associated accession codes are available at <https://doi.org/10.1038/s41586-018-0667-0>.

Received: 30 May; Accepted: 28 September 2018;

Published online 7 November 2018.

- Polkovnikov, A., Sengupta, K., Silva, A. & Vengalattore, M. Colloquium: Nonequilibrium dynamics of closed interacting quantum systems. *Rev. Mod. Phys.* **83**, 863–883 (2011).
- Gogolin, C. & Eisert, J. Equilibration, thermalisation, and the emergence of statistical mechanics in closed quantum systems. *Rep. Prog. Phys.* **79**, 056001 (2016).
- Berges, J., Rothkopf, A. & Schmidt, J. Nonthermal fixed points: effective weak coupling for strongly correlated systems far from equilibrium. *Phys. Rev. Lett.* **101**, 041603 (2008).
- Piñeiro Orioli, A., Boguslavski, K. & Berges, J. Universal self-similar dynamics of relativistic and nonrelativistic field theories near nonthermal fixed points. *Phys. Rev. D* **92**, 025041 (2015).
- Micha, R. & Tkachev, I. I. Relativistic turbulence: a long way from preheating to equilibrium. *Phys. Rev. Lett.* **90**, 121301 (2003).
- Moore, G. D. Condensates in relativistic scalar theories. *Phys. Rev. D* **93**, 065043 (2016).
- Berges, J., Boguslavski, K., Schlichting, S. & Venugopalan, R. Universality far from equilibrium: from superfluid Bose gases to heavy-ion collisions. *Phys. Rev. Lett.* **114**, 061601 (2015).
- Baier, R., Mueller, A. H., Schiff, D. & Son, D. T. “Bottom-up” thermalization in heavy ion collisions. *Phys. Lett. B* **502**, 51–58 (2001).
- Berges, J., Boguslavski, K., Schlichting, S. & Venugopalan, R. Turbulent thermalization process in heavy-ion collisions at ultrarelativistic energies. *Phys. Rev. D* **89**, 074011 (2014).
- Scholle, J., Nowak, B. & Gasenzer, T. Critical dynamics of a two-dimensional superfluid near a nonthermal fixed point. *Phys. Rev. A* **86**, 013624 (2012).
- Swistunov, B. V. Highly nonequilibrium Bose condensation in a weakly interacting gas. *J. Moscow Phys. Soc.* **1**, 373–390 (1991).
- Schmidt, M., Erne, S., Nowak, B., Sexty, D. & Gasenzer, T. Non-thermal fixed points and solitons in a one-dimensional Bose gas. *New J. Phys.* **14**, 075005 (2012).
- Chantesana, I., Piñeiro Orioli, A. & Gasenzer, T. Kinetic theory of non-thermal fixed points in a Bose gas. Preprint at <https://arxiv.org/abs/1801.09490> (2018).
- Deng, J., Schlichting, S., Venugopalan, R. & Wang, Q. Off-equilibrium infrared structure of self-interacting scalar fields: universal scaling, vortex-antivortex superfluid dynamics, and Bose-Einstein condensation. *Phys. Rev. A* **97**, 053606 (2018).
- Hohenberg, P. C. & Halperin, B. I. Theory of dynamic critical phenomena. *Rev. Mod. Phys.* **49**, 435–479 (1977).
- Kolmogorov, A. N. The local structure of turbulence in incompressible viscous fluid for very large Reynolds numbers. *Dokl. Akad. Nauk SSSR* **30**, 299–303 (1941).
- Sieberer, L. M., Huber, S. D., Altman, E. & Diehl, S. Dynamical critical phenomena in driven-dissipative systems. *Phys. Rev. Lett.* **110**, 195301 (2013).
- Navon, N. et al. Synthetic dissipation and cascade fluxes in a turbulent quantum gas. Preprint at <https://arxiv.org/abs/1807.07564> (2018).
- del Campo, A. & Zurek, W. H. Universality of phase transition dynamics: Topological defects from symmetry breaking. *Int. J. Mod. Phys. A* **29**, 1430018 (2014).
- Navon, N., Gaunt, A. L., Smith, R. P. & Hadzibabic, Z. Critical dynamics of spontaneous symmetry breaking in a homogeneous Bose gas. *Science* **347**, 167–170 (2015).
- Clark, L. W., Feng, L. & Chin, C. Universal space-time scaling symmetry in the dynamics of bosons across a quantum phase transition. *Science* **354**, 606–610 (2016).
- Bray, A. J. Theory of phase-ordering kinetics. *Adv. Phys.* **43**, 357–459 (1994).
- Calabrese, P. & Gambassi, A. Ageing properties of critical systems. *J. Phys. A* **38**, R133–R139 (2005).
- Berges, J., Borsányi, S. & Wetterich, C. Prethermalization. *Phys. Rev. Lett.* **93**, 142002 (2004).
- Grim, M. et al. Relaxation and prethermalization in an isolated quantum system. *Science* **337**, 1318–1322 (2012).
- Chiocchetta, A., Gambassi, A., Diehl, S. & Marino, J. Dynamical crossovers in prethermal critical states. *Phys. Rev. Lett.* **118**, 135701 (2017).
- Smith, D. A. et al. Absorption imaging of ultracold atoms on atom chips. *Opt. Express* **19**, 8471–8485 (2011).
- Bücker, R. et al. Single-particle-sensitive imaging of freely propagating ultracold atoms. *New J. Phys.* **11**, 103039 (2009).
- Karl, M. & Gasenzer, T. Strongly anomalous non-thermal fixed point in a quenched two-dimensional Bose gas. *New J. Phys.* **19**, 093014 (2017).
- Mazets, I. E., Schumm, T. & Schmiedmayer, J. Breakdown of integrability in a quasi-1D ultracold Bosonic gas. *Phys. Rev. Lett.* **100**, 210403 (2008).

31. Li, C. et al. Dephasing and relaxation of bosons in 1D: Newton's cradle revisited. Preprint at <https://arxiv.org/abs/1804.01969> (2018).
32. Prüfer, M. et al. Observation of universal quantum dynamics far from equilibrium. *Nature* <https://doi.org/10.1038/s41586-018-0659-0> (2018).
33. Wilson, K. G. The renormalization group: critical phenomena and the Kondo problem. *Rev. Mod. Phys.* **47**, 773–840 (1975).

Acknowledgements We thank J. Brand, L. Carr, M. Karl, P. Kevrekidis, P. Kunkel, D. Linnemann, A. N. Mikheev, B. Nowak, M. K. Oberthaler, J. M. Pawłowski, A. Piñeiro Orioli, M. Prüfer, W. Rohringer, C. M. Schmied, M. Schmidt, J. Schole and H. Strobel for discussions. We thank T. Berrada, S. van Frank, J.-F. Schaff and T. Schumm for help with the experiment during data collection. This work was supported by the SFB 1225 'ISOQUANT' and grant number GA677/7,8 financed by the German Research Foundation (DFG) and Austrian Science Fund (FWF), the ERC advanced grant QuantumRelax, the Helmholtz Association (HA216/EMMI), the EU (FET-Proactive grant AQuS, project number 640800) and Heidelberg University (CQD). S.E. acknowledges partial support through the EPSRC project grant (EP/P00637X/1). J.S., J.B. and T.G. acknowledge the hospitality of the Erwin Schrödinger Institut in the framework of their thematic programme 'Quantum Paths'.

Reviewer information *Nature* thanks M. Kolodrubetz and the other anonymous reviewer(s) for their contribution to the peer review of this work.

Author contributions S.E. performed the analysis, adapted the theory and wrote the paper, J.S. designed the experiment; R.B. conducted the experiment and initial data analysis. All authors contributed to interpreting the data and writing the manuscript.

Competing interests The authors declare no competing interests.

Additional information

Extended data is available for this paper at <https://doi.org/10.1038/s41586-018-0667-0>.

Reprints and permissions information is available at <http://www.nature.com/reprints>.

Correspondence and requests for materials should be addressed to J.S.

Publisher's note: Springer Nature remains neutral with regard to jurisdictional claims in published maps and institutional affiliations.

METHODS

Preparation of the gas and cooling quench. The initial thermal Bose gas is prepared using a standard procedure to produce ultracold gases of ^{87}Rb on an atom chip³⁴. The description of the system at the microscale is given by the Bose Hamiltonian with contact interactions, determined by the s -wave scattering length $a_s = 5.2$ nm. We prepare a thermal cloud of typically $N = (2.7\text{--}3.2) \times 10^4$ atoms initially in an elongated, $\omega_{\parallel} = 2\pi \times 23$ Hz and $\omega_{\perp} = 2\pi \times 3.3$ kHz, deep trapping potential $V_i \approx h \times (130\text{--}160)$ kHz at a temperature $T \approx 530\text{--}600$ nK. The atoms are held in this configuration for 100 ms to ensure a well defined initial state. The thermal cloud is above both the dimensional crossover to an effective one-dimensional system and the critical temperature T_c for the phase transition to a three-dimensional Bose–Einstein condensate, and therefore has a large excess of particles in transversally excited, high-energy states. The trap depth is reduced to its final value V_f at a constant rate $R_q = (V_i - V_f)/\tau_q = h \times 25$ kHz ms^{-1} by applying radio-frequency radiation at a time-dependent frequency (RF-knife), leading to an energy-dependent transition of atoms from a trapped to an un-trapped spin state. This allows the high-energy particles to rapidly leave the trap, leading to the competing timescales τ_q of the cooling quench (see Fig. 1) and the typical collision times needed for re-equilibration of the system. The final trap depth is $V_f \approx h \times 2$ kHz, which is below the first radially excited state of the trapping potential, $hV_f < \hbar\omega_{\perp}$. At the end of the cooling ramp, the RF-knife is held at its final position for 0.5 ms before it is faded out within 1 ms, thereby raising the trap depth to $V \approx h \times 20$ kHz. In addition, because the RF-knife reduces the radial trapping frequency slightly, there is a small interaction quench (about 10%) of the one-dimensional system. The system is therefore rapidly quenched to the quasi-one-dimensional regime, finally occupying only the transverse ground state. Experimental realizations 1 to 3 reported in the main text have final atom numbers of $N \approx 1,700, 2,800$ and $1,150$, respectively, and agree well with the RDM with a defect density of $n_s = 1.4 \mu\text{m}^{-1}$, $0.9 \mu\text{m}^{-1}$ or $2.3 \mu\text{m}^{-1}$ and defect width of $\xi_s = 0.07 \mu\text{m}$, $0.06 \mu\text{m}$ or $0.05 \mu\text{m}$ (corresponding to $\xi_s/\xi_h = 0.3, 0.3$ or 0.17). The resultant far-from-equilibrium state is held for variables times of up to $t \approx 1$ s, during which the universal dynamics develops and takes place.

Measuring the density and momentum distributions. The density and momentum distribution of the gas are measured after finite time of flight for $t_{\text{tof}} = 1.5$ ms and $t_{\text{tof}} = 46$ ms of free expansion. This gives access to the in situ (IS) and time-of-flight (tof) density profiles, for which the atoms are detected using absorption and fluorescent imaging in a thin light sheet, respectively. We then calculate the radially centred and integrated density profiles in the longitudinal direction. We correct the profiles for possible random sloshing effects. The quench and measurement is repeated for each experimental shot and hold time t , 10–15 times for the in situ data and 25–50 times for the time-of-flight data. The fast expansion in the radial direction dilutes the gas and leads to ballistic expansion in the longitudinal direction. Because the momentum of the particles during the expansion is therefore approximately conserved, the density distribution after expansion converges to the in situ momentum distribution of the cloud. We checked the effects of a finite dilation time via numerical simulations of the Gross–Pitaevskii equation, using hydrodynamic models to determine the time dependence of the interaction constant g for early times of the expansion. For the parameters of the experiment, we did not find any substantial deviations from a completely ballistic expansion in the longitudinal direction.

The pulled-back momentum distribution converges rapidly for high k towards the true momentum distribution of the gas. For low k the finite in situ size of the cloud does not allow for a clear separation of different momentum modes and atoms of different momentum overlap in the measured density after time of flight. This means that for a cloud of size R , particles with momentum less than about $k_{\text{IS}} = Rm/(\hbar t_{\text{tof}})$ do not have time to propagate sufficiently far outside the in situ bulk density to be clearly separated. Therefore, the pulled-back momentum distribution for $k \lesssim k_{\text{IS}}$ resembles the in situ density profile rather than the actual momentum distribution of the gas.

Scaling analysis. We extract the universal scaling exponents α and β using a least-squares fit of the analytical prediction in equation (1), minimizing

$$\chi^2(\alpha, \beta) = \frac{1}{N_t} \sum_{t, t_0} \chi_{\alpha, \beta}^2(t, t_0) \quad (2)$$

where we average over all times t and reference times t_0 within the scaling period. The local $\chi_{\alpha, \beta}^2(t, t_0)$ is calculated via

$$\chi_{\alpha, \beta}^2(t, t_0) = \int_{k_1}^{k_h} \frac{[(t/t_0)^{\alpha} \bar{n}((t/t_0)^{\beta} k, t_0) - \bar{n}(k, t)]^2}{\bar{\sigma}((t/t_0)^{\beta} k, t_0)^2 + \bar{\sigma}(k, t)^2} dk$$

where σ denotes the standard error of the mean, and $\bar{n}(k, t) = n(k, t)/N(t)$ and $\bar{\sigma}(k, t) = \sigma(k, t)/N(t)$ are normalized by the total atom number to minimize the influence of atom loss during the evolution; however, the atom loss is negligible

during the time period when the system shows scaling behaviour. For later times the atom loss is roughly 10% per 100 ms, with a final atom number of approximately 40% at the end of the evolution. The rescaling of the momentum variable inevitably necessitates a comparison between the momentum distributions at momenta lying between the discrete values measured in the experiment. We therefore linearly interpolate the spectrum and its error at the reference time t_0 , which allows us to evaluate the experimental spectrum at all momenta $(t/t_0)^{\beta} k$. For the scaling analysis we symmetrize the spectrum by averaging the momentum distribution over $\pm k$ to lower the noise level.

Estimating the exponents and their error is done via the likelihood function. To decouple the two exponents we take $\alpha = \beta + \Delta_{\alpha\beta}$ and fit the deviation $\Delta_{\alpha\beta}$ of the exponent from the theoretical expectation $\alpha \equiv \beta$. We therefore define the likelihood function

$$L(\Delta_{\alpha\beta}, \beta) = \exp\left[-\frac{1}{2} \chi^2(\Delta_{\alpha\beta}, \beta)\right] \quad (3)$$

The most probable exponents are determined by the maximum of the likelihood function. The error of the estimate is determined by integrating the two-dimensional likelihood function along one dimension and extracting the variance of the remaining exponent using a Gaussian fit to the marginal-likelihood functions. We find excellent agreement between the marginal likelihood functions and the Gaussian fits. Therefore, the Gaussian estimate of the error is equivalent to the (asymmetric) estimate using a change in the log-likelihood function by 1/2. The reason for this good agreement is the aforementioned decoupling of the exponent, which results to a good degree in a two-dimensional, Gaussian likelihood function for $L(\Delta_{\alpha\beta}, \beta)$. The estimates of the scaling exponents for different reference times are calculated equivalently (neglecting the sum over t_0 in equation (2)). The estimate is insensitive to the upper cut-off k_h (within reasonable limits). The momentum k_s , which limits the scaling region in the ultraviolet, is determined as the characteristic scale for which the mean deviation of the rescaled momentum distributions for $|k| \leq k_s$ and averaged over all times t in the scaling period exceeds the 95% confidence interval at the reference time t_0 . The lower cut-off is taken as $k_l = 0$. Excluding momenta $|k| \leq k_s$ leads to a small shift in the exponents towards lower values, but agrees well within the estimated errors of the exponents (less than about 0.3σ deviation). The results of the scaling analysis for three independent experimental realizations are shown in Extended Data Figs. 2–4. We find similar results in all cases. The exponents and errors reported in the main text are estimated from the combined likelihood function $L = \prod_i L_i$, where i labels the independent experimental realizations.

The universal function f_s is determined equivalently, where for each fixed exponent ζ the non-universal scales are determined from a least-squares fit to each experimental realization separately. To minimize the influence of the finite expansion of the gas, we consider momenta $|k| > k_{\text{IS}}$ for the determination of f_s . The likelihood function is subsequently defined by the averaged residuals of the scaled data as compared to the universal scaling function $f_s = (1 + k^{\zeta})^{-1}$ for all realizations simultaneously. The error is again estimated using a Gaussian fit to the (one-dimensional) likelihood function. The non-universal scales for the most likely exponent $\zeta = 2.39 \pm 0.18$ for experimental realizations 1 to 3 are the characteristic momentum scale, $k_0 = 2.61 \mu\text{m}^{-1}$, $2.28 \mu\text{m}^{-1}$ and $3.97 \mu\text{m}^{-1}$, respectively, and the global scaling factor of the momentum distribution, $n_0 = 0.14 \mu\text{m}$, $0.15 \mu\text{m}$ and $0.10 \mu\text{m}$.

Global observables. We define the global observables

$$\bar{N} = \int_{|k| \leq (t/t_0)^{-\beta} k_s} \frac{n(k, t)}{N(t)} dk \propto (t/t_0)^{-\Delta_{\alpha\beta}} \quad (4)$$

$$\bar{M}_{n \geq 1} = \int_{|k| \leq (t/t_0)^{-\beta} k_s} \frac{|k|^n n(k, t)}{N(t)} dk \propto (t/t_0)^{-n\beta} \quad (5)$$

where $k_s = 6.5\text{--}8 \mu\text{m}^{-1}$ defines the high-momentum cut-off for the scaling region in k . In the main text, we consider the fraction of particles in the scaling region $\bar{N} \propto (t/t_0)^{-\Delta_{\alpha\beta}}$ and the mean kinetic energy per particle in the scaling region $\bar{M}_2 \sim (t/t_0)^{-2\beta}$. The global observables \bar{N} and \bar{M} show independent scaling in time with the exponents $\Delta_{\alpha\beta}$ and β , whereas the integral ranges depend non-trivially on β . The results for each experimental realization are shown in Extended Data Fig. 5. In the main text, we report the result obtained by averaging over all experimental realizations. **Model fits.** The density profile $\rho(z)$ is determined by a fit to the experimental in situ density, measured after $t_{\text{tof}} = 1.5$ ms of free expansion. In case of the RDM we consider for a fixed atom number $N(t)$ and a scaled density profile $\rho(z, t) = b^{-1}(t) \rho(zb^{-1}(t))$ in the Thomas–Fermi approximation, leaving the scaling factor $b(t)$ as the only free parameter (more precisely, a previous result³⁵ is used for the density profile, which takes the radial swelling of the condensate into account). We neglect possible finite-temperature fluctuations and any contributions

from radially excited states in the RDM, assuming the gas to be dominated by solitonic defects. For early times, the high-momentum modes do not have substantial thermal occupation, and we find good accordance with the RDM.

In case of the quasi-condensate, we determine the thermal density profile for a given temperature T and chemical potential μ using simulations of the stochastic Gross–Pitaevskii equation (see, for example, ref. ³⁶). The broadening of the density distribution is herein due to the finite temperature of the gas. The density profile is subsequently fitted via $\rho(z, t) = \rho_{\text{QC}}(z, T(t), \mu(t)) + \rho_{\perp}(z, T(t), \mu(t))$. Here we take into account the thermal occupation of radially excited states ρ_{\perp} within the semiclassical approximation, which are non-negligible for late times. The chemical potential μ is fixed by the total atom number, $\int \rho(z, t) dz = N(t)$.

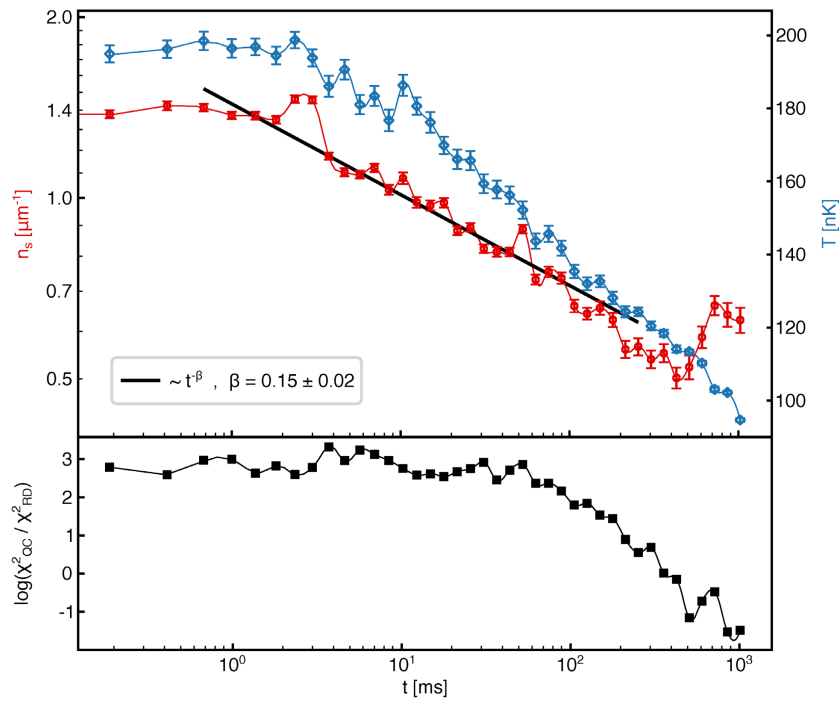
The fitted density profiles are used to determine the single-particle momentum distribution $n(k, t)$ of the inhomogeneous system from a least-squares fit of the experimental data to the theoretical predictions within the local density approximation. For both models we restrict the fitting region to $|k| > k_{\text{is}}$, owing to the simplified hydrodynamic model for the finite expansion of the gas. The RDM¹² is fitted over the full momentum range that is accessible in the experiment. For high defect densities, the RDM fit shows correlations between defect density and width because these two scales become of the same order for the far-from-equilibrium state. Because it is theoretically expected that the defect width is approximately conserved during evolution, we fix the defect width to its mean value within the first 25 ms of evolution, leaving the defect density as the only free parameter. We find reasonable agreement between the RDM results and the independent scaling analysis. In particular, the RDM is clearly preferred compared to a thermal distribution within the scaling period.

For the fits in thermal equilibrium we consider a quasi-condensate model³⁷, including thermal occupation of radially excited states³⁸. Considering the validity regime of the quasi-condensate model, we restrict the fitting procedure to momentum modes with energy less than $\hbar\omega_{\perp}$. We determine the chemical potential μ by fixing the atom number within this region of momentum space. This leads to a slight shift in the chemical potential compared to the in situ fits. For late times we find excellent agreement with the experimental data, demonstrating the relaxation of the system to thermal equilibrium.

Data availability

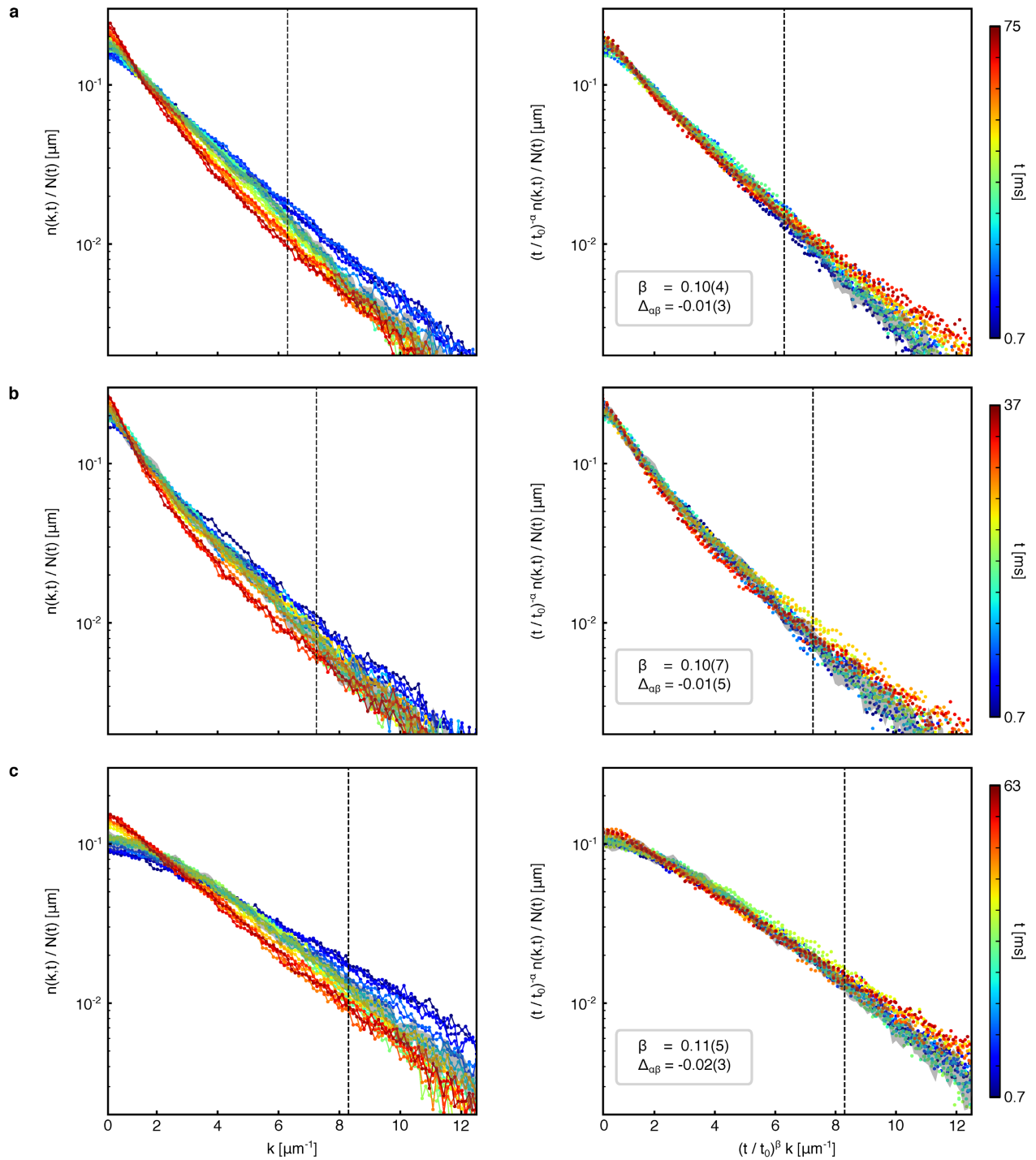
The data that support the findings of this study are available from the corresponding author on reasonable request.

34. Reichel, J. & Vuletic, V. *Atom chips* (John Wiley & Sons, Weinheim, 2011).
35. Gerbier, F. Quasi-1D Bose–Einstein condensates in the dimensional crossover regime. *Europhys. Lett.* **66**, 771–777 (2004).
36. Blakie, P. B., Bradley, A. S., Davis, M. J., Ballagh, R. J. & Gardiner, C. W. Dynamics and statistical mechanics of ultra-cold Bose gases using c-field techniques. *Adv. Phys.* **57**, 363–455 (2008).
37. Richard, S. et al. Momentum spectroscopy of 1D phase fluctuations in Bose–Einstein condensates. *Phys. Rev. Lett.* **91**, 010405 (2003).
38. Davis, M. J., Blakie, P. B., van Amerongen, A. H., van Druten, N. J. & Kheruntsyan, K. V. Yang–Yang thermometry and momentum distribution of a trapped one-dimensional Bose gas. *Phys. Rev. A* **85**, 031604 (2012).



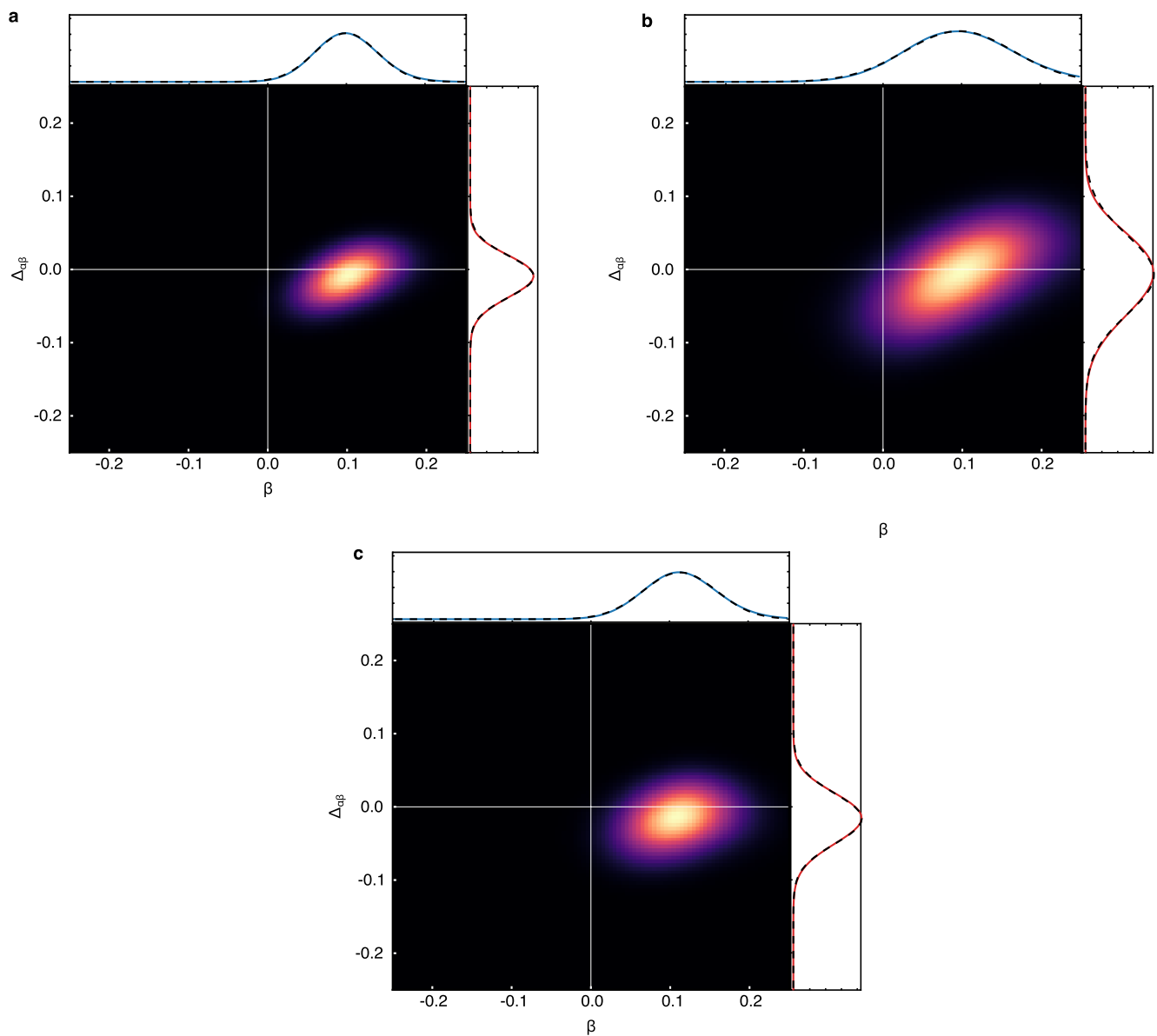
Extended Data Fig. 1 | Results of random-defect and quasi-condensate models. The time evolution of the characteristic scales for the experimental data presented in Fig. 4a (initial condition 1) are shown. The resulting temperature T (blue) and defect density n_s (red) are shown in the upper panel for the full time evolution. The defect width for the random-defect model is fixed to $\xi_s = 0.087 \mu\text{m}$, determined by the mean over the first 25 ms of the evolution. The defect density within the scaling region shows a power-law dependence consistent with the exponent β of the scaling evolution reported in the main text. For later times deviations

occur, signalling the end of the scaling region. The quality of the model fit is depicted in the lower panel (black squares), where positive and negative values favour the random-defect and quasi-condensate models, respectively. The random-defect model is strongly preferred for the first roughly 100 ms, after which the system converges to a thermal quasi-condensate within about 400 ms. The absolute values of the reduced χ^2 for the random-defect (RD) model are about 1 and 5 for early and late times, respectively; those for the quasi-condensate (QC) model are about 25 and 1.



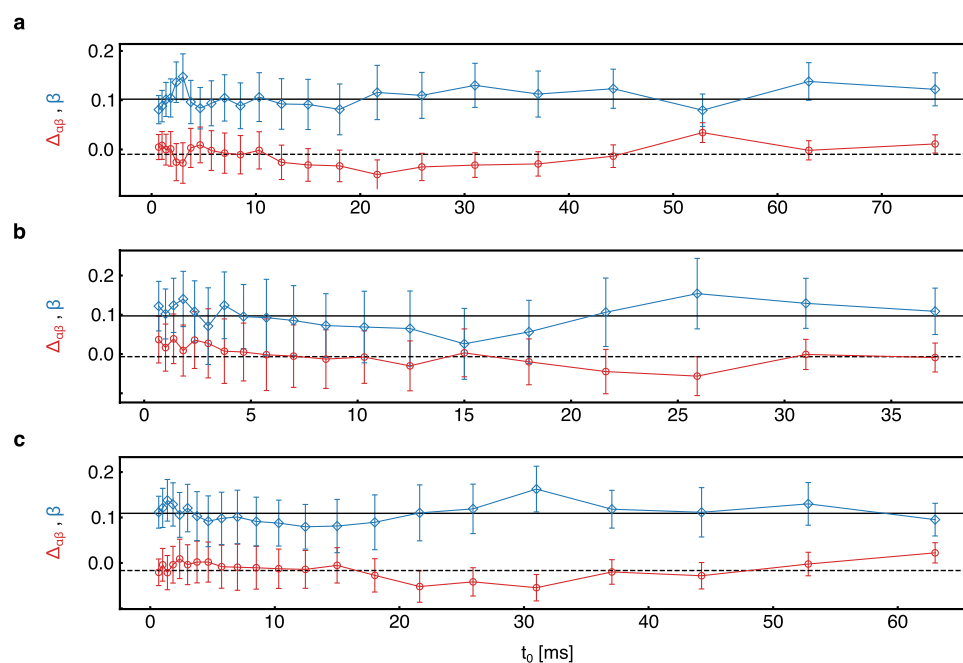
Extended Data Fig. 2 | Rescaling analysis for different initial conditions. a–c, Original (left) and rescaled (right) single-particle momentum distribution $n(k, t)$ for different initial conditions (a–c correspond to initial conditions 1–3 in Fig. 4a). Each distribution is normalized by the time-dependent atom number $N(t)$ and the time is encoded in the colour scale. The grey dashed vertical lines indicate

the scaling regime in k . The scaling exponents $\alpha \approx \beta$ and the deviation between them $\Delta_{\alpha\beta} = \alpha - \beta$ are in excellent agreement with the mean values reported in the main text. We note that here we compare the data for the full experimental resolution in k . The distribution at the reference time $t_0 = 4.7$ ms is given by the grey line; its width indicates the 95% confidence interval.



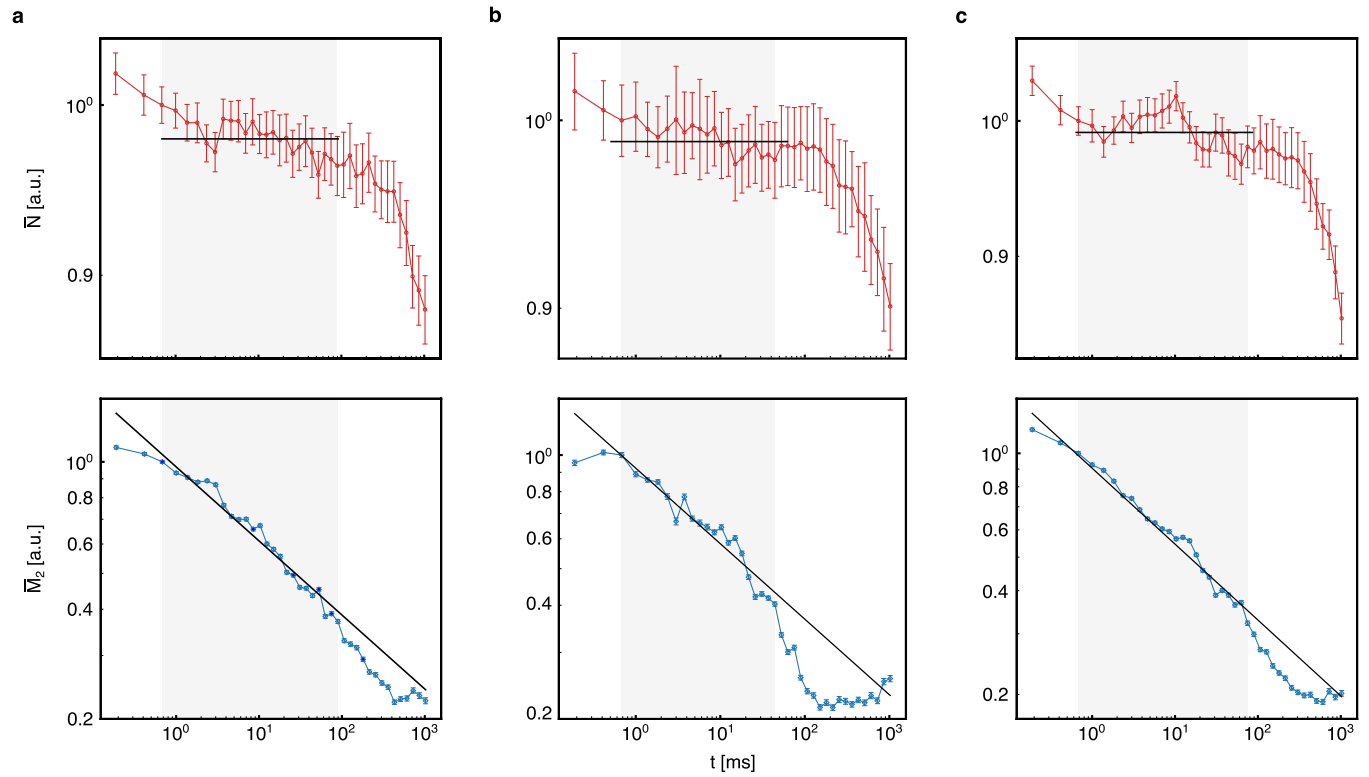
Extended Data Fig. 3 | Likelihood function for different initial conditions. **a–c,** Two-dimensional likelihood functions (colour scales) and marginal-likelihood functions (top and right) for different initial conditions (**a–c** correspond to initial conditions 1–3 in Fig. 4a). A clear peak at non-zero $\alpha \approx \beta$ is visible for each realization, whereas the deviation

between the two exponents is $\Delta_{\alpha\beta} = \alpha - \beta \approx 0$. For scan 2 (**b**), a small condensate may have been present before the quench, which led to the larger extent of the likelihood function. Gaussian fits are in excellent agreement with the marginal-likelihood functions and determine the error of the scaling exponents reported in Extended Data Fig. 2.



Extended Data Fig. 4 | Time evolution of scaling exponents for different initial conditions. **a–c**, Scaling exponents $\alpha \approx \beta$ (blue) and deviation between the two exponents $\Delta_{\alpha\beta} = \alpha - \beta$ (red) for different initial conditions (**a–c** correspond to initial conditions 1–3 in Fig. 4a),

determined from the likelihood function for each reference time t_0 , are in good agreement with the predicted mean (black solid and dashed lines). The error bars denote the standard deviation obtained from a Gaussian fit to the marginal-likelihood function at each reference time separately.



Extended Data Fig. 5 | Spatially averaged observables for different initial conditions. **a–c,** Time evolution of the fraction of particles in the scaling region $\bar{N} \propto (t/t_0)^{\Delta_{\alpha\beta}}$ (red) and the mean kinetic energy per particle in the scaling region $\bar{M}_2 \propto (t/t_0)^{-2\beta}$ (blue) for different initial conditions

(**a–c** correspond to initial conditions 1–3 in Fig. 4a). Within the scaling region (grey-shaded areas), \bar{N} is approximately conserved. The solid black lines are the approximately conserved value and scaling solutions (5). The error bars indicate the 95% confidence interval.

Vowel recognition with four coupled spin–torque nano–oscillators

Miguel Romera^{1,5}, Philippe Talatchian^{1,5}, Sumito Tsunegi², Flavio Abreu Araujo^{1,4}, Vincent Cros¹, Paolo Bortolotti¹, Juan Trastoy¹, Kay Yakushiji², Akio Fukushima², Hitoshi Kubota², Shinji Yuasa², Maxence Ernoult^{1,3}, Damir Vodenicarevic³, Tifenn Hirtzlin³, Nicolas Locatelli³, Damien Querlioz^{3*} & Julie Grollier^{1*}

In recent years, artificial neural networks have become the flagship algorithm of artificial intelligence¹. In these systems, neuron activation functions are static, and computing is achieved through standard arithmetic operations. By contrast, a prominent branch of neuroinspired computing embraces the dynamical nature of the brain and proposes to endow each component of a neural network with dynamical functionality, such as oscillations, and to rely on emergent physical phenomena, such as synchronization^{2–6}, for solving complex problems with small networks^{7–11}. This approach is especially interesting for hardware implementations, because emerging nanoelectronic devices can provide compact and energy-efficient nonlinear auto-oscillators that mimic the periodic spiking activity of biological neurons^{12–16}. The dynamical couplings between oscillators can then be used to mediate the synaptic communication between the artificial neurons. One challenge for using nanodevices in this way is to achieve learning, which requires fine control and tuning of their coupled oscillations¹⁷; the dynamical features of nanodevices can be difficult to control and prone to noise and variability¹⁸. Here we show that the outstanding tunability of spintronic nano-oscillators—that is, the possibility of accurately controlling their frequency across a wide range, through electrical current and magnetic field—can be used to address this challenge. We successfully train a hardware network of four spin-torque nano-oscillators to recognize spoken vowels by tuning their frequencies according to an automatic real-time learning rule. We show that the high experimental recognition rates stem from the ability of these oscillators to synchronize. Our results demonstrate that non-trivial pattern classification tasks can be achieved with small hardware neural networks by endowing them with nonlinear dynamical features such as oscillations and synchronization.

Spin-torque nano-oscillators are natural candidates for building hardware neural networks made of coupled nanoscale oscillators^{8–10,13,15,18,19}. These nanoscale magnetic tunnel junctions emit microwave voltages when they are driven by direct-current injection in a regime of sustained magnetization precession through the effect of spin torque. In addition, they have exceptional capacities to synchronize their rhythms to periodic electric and magnetic input signals and to other spin-torque nano-oscillators^{20–24}. This property originates from the high tunability of their frequency, in other words, the large frequency changes induced by applied d.c. currents and magnetic fields. Single spin-torque nano-oscillators can achieve impressive cognitive computations²⁵. However, it has not been shown experimentally that a coupled network of spin-torque nano-oscillators can learn to perform computational tasks through synchronization. Here, we use the ability of spin-torque nano-oscillators to modify their frequency in response to injected direct currents to train in real-time a network of coupled oscillators to categorize different input patterns into different synchronization configurations^{2,17,18}.

We transpose to hardware the neural network illustrated in Fig. 1a¹⁷ with the set-up illustrated in Fig. 1b. The four neurons in Fig. 1a are experimentally implemented with four spin-torque nano-oscillators (Fig. 1b), in our case circular magnetic tunnel junctions with 375 nm diameter and an FeB free layer with a vortex as ground state (see Methods)²⁶. The double arrow connections between neurons (blue in Fig. 1a) indicate that the output of neuron *i* influences the behaviour of neuron *j*, and vice versa. We implement these symmetric neural interconnections by connecting electrically the four oscillators using millimetre-long wires as schematized in Fig. 1b: in this configuration, the microwave current generated by each oscillator propagates in the electrical microwave loop and in turn influences the dynamics, and in particular the frequency, of the other oscillators through the microwave spin-torques it creates²⁴. The sum of all microwave emissions is detected by a spectrum analyser. Importantly, we can control the frequency of each oscillator by adjusting the direct current flowing through each (see Methods and Extended Data Fig. 1). Here, for computing, we choose direct currents leading to close but not identical frequencies. The light blue curve in Fig. 1c shows a four-peak spectrum typical of this regime of moderate coupling where the dynamics of the oscillators are correlated but do not lead to mutual synchronization.

The inputs to the neural network are encoded in the frequencies f_A and f_B of two fixed-amplitude microwave signals. Injected in a strip line fabricated above the active magnetic layers, they modify the dynamics of the oscillators through the radiofrequency magnetic fields they generate. Figure 1d shows that when the frequency of one of the microwave sources is swept, each oscillator synchronizes to the source in turn. Indeed, when the frequency of the source gets close to the frequency of one of the oscillators, the strong signal of the source pulls the adaptable frequency of the oscillator towards its own. In the locking range, the frequency of the oscillator becomes equal to the frequency of the source²⁷. The dark blue curve in Fig. 1c shows an example of spectrum measured when the two microwave inputs are injected simultaneously. Two peaks (in red) appear at frequencies f_A and f_B owing to capacitive coupling with the strip line. In comparison to the spectrum without inputs (light blue curve), the emission peaks of oscillators 1 and 2 are pulled towards f_A , whereas oscillator 4 is phase-locked to input B (its emission peak merges with the one of input B at f_B). We label this synchronization configuration as (4B).

The possible outputs of the neural network, represented in different colours in Fig. 1e, are the different synchronization configurations that appear for different frequencies of the two input signals, keeping the direct currents through the oscillators fixed. Depending on the frequencies of inputs, zero (grey regions), one, or two oscillators are phase-locked. For example, in the petrol-blue region labelled (2A), oscillator 2 is synchronized to input A. In the white region labelled (1A,3B), oscillators 1 and 3 are synchronized to inputs A and B, respectively.

¹Unité Mixte de Physique, CNRS, Thales, Université Paris-Sud, Université Paris-Saclay, Palaiseau, France. ²National Institute of Advanced Industrial Science and Technology (AIST), Spintronics Research Center, Tsukuba, Ibaraki, Japan. ³Centre de Nanosciences et de Nanotechnologies, CNRS, Université Paris-Sud, Université Paris-Saclay, Orsay, France. ⁴Present address: Institute of Condensed Matter and Nanosciences, UC Louvain, Louvain-la-Neuve, Belgium. ⁵These authors contributed equally: Miguel Romera, Philippe Talatchian. *e-mail: damien.querlioz@u-psud.fr; julie.grollier@cnrs-thales.fr

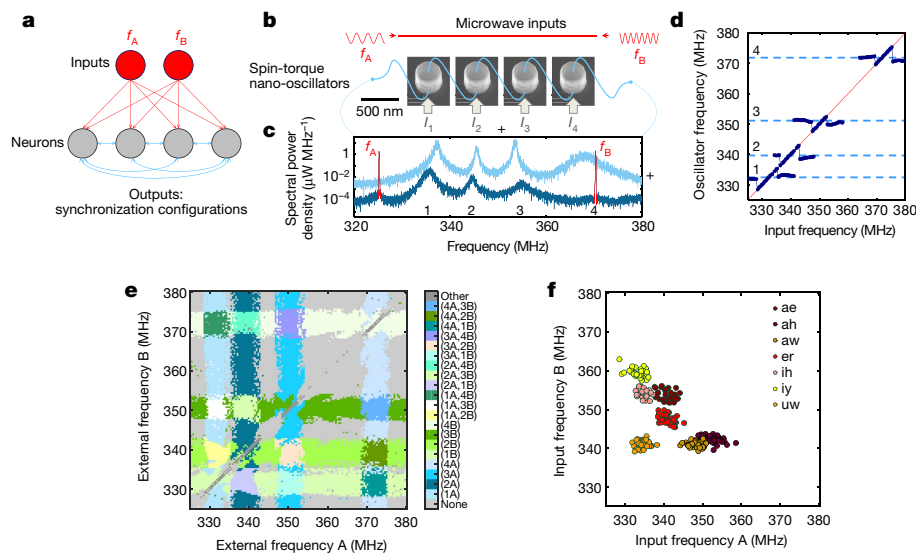


Fig. 1 | Approach for pattern classification with coupled spin-torque nano-oscillators. **a**, Schematic of the emulated neural network. **b**, Schematic of the experimental set-up with four spin-torque nano-oscillators electrically connected in series and coupled through their own emitted microwave currents. Two microwave signals encoding information in their frequencies f_A and f_B are applied as inputs to the system through a strip line, which translates into two microwave fields. The total microwave output of the oscillator network is recorded with a spectrum analyser. **c**, Microwave output emitted by the network of four oscillators without (light blue) and with (dark blue) the two microwave signals applied to the system. The two curves have been shifted vertically for clarity. The four peaks in the light blue curve correspond to the emissions of the four

oscillators. The two narrow red peaks in the dark blue curve correspond to the external microwave signals with frequencies f_A and f_B . **d**, Evolution of the four oscillator frequencies when the frequency of external source A is swept. One after the other, the oscillators phase-lock to the external input when the frequency of the source approaches their natural frequency. In the locking range, the oscillator frequency is equal to the input frequency. **e**, Experimental synchronization map as a function of the frequencies of the external signals f_A and f_B . Each colour corresponds to a different synchronization state. **f**, Inputs applied to the system, represented in the (f_A, f_B) plane. Each colour corresponds to a different spoken vowel, and each data point corresponds to a different speaker.

We now describe how this neural network can recognize patterns by classifying spoken vowels, which are naturally characterized by frequencies called formants²⁸. We use as input data a subset of the Hillenbrand database (available at <https://homepages.wmich.edu/~hillenbr/voweldata.html>; see Supplementary Information) comprising seven vowels pronounced by 37 different female speakers, where each vowel is characterized by 12 different frequencies. Formant frequencies are typically in the range between 500 Hz and 3,500 Hz, so a transformation is needed to obtain input frequencies (f_A, f_B) in the range of operation of our oscillators, between 325 MHz and 380 MHz. As detailed in Methods, we obtain f_A and f_B through two different linear combinations of the 12 formant frequencies that fit the grid-like geometry of the oscillator synchronization maps. In the resulting map shown in Fig. 1f, each point corresponds to one speaker. The spread in frequency for each vowel indicates that each speaker has a different pronunciation. Our goal is to recognize the vowel presented as input to the oscillator network independently of the speaker. For this purpose, the scattered points corresponding to each vowel pronounced by different speakers should all be contained inside a different region of the oscillator synchronization map in Fig. 1e.

As can be seen from Fig. 2a, in which the input vowel map and the oscillator synchronization map are superposed, initially they do not coincide: the initial oscillator frequencies have been set randomly and are not adequate to solve the problem. The oscillatory neural network must learn to perform the classification properly. During this training stage, the internal parameters of the network need to be finely tuned until each synchronization region encompasses the cloud of points corresponding to the vowel that it has been assigned. For this purpose, we take advantage of the highly tunable nature of spin-torque nano-oscillators to modify the synchronization map by tuning the direct current through each oscillator, adapting a training algorithm first proposed in ref.¹⁷. We have developed an automatic real-time learning procedure involving a feedback loop between the experimental setup and the computer that controls it (see Methods). At each training step, we consecutively apply seven inputs (f_A, f_B) to the oscillators, one

for each vowel, randomly picked between the different speakers. The oscillator emissions corresponding to each of the seven input microwave signals are recorded with a spectrum analyser. A computer identifies the corresponding synchronization states (see Methods). If all the seven vowels have been correctly classified in their assigned synchronization regions of the map (f_A, f_B) , the direct currents are not changed. If one or several vowels have not been correctly classified, direct currents in the oscillators are modified to bring the assigned synchronization regions closer to the corresponding input frequency pairs (f_A, f_B) and thus reduce the classification error (see Methods). In the next learning step, another set of seven vowels is applied, and so on.

Figure 2 shows synchronization maps obtained at different stages of the training process (Fig. 2a–d), together with the evolution of the direct currents applied to the oscillators (Fig. 2e), their frequencies (Fig. 2f) and the average recognition rates for the seven vowels (Fig. 2g) (for a short video (20 s), see Supplementary Information or <https://youtu.be/bbRqQxcx-po>; for a longer video (3 min 30 s), see <https://youtu.be/IHYnh0oJgOA>). After 48 training steps, an optimum is found, direct currents and frequencies stop evolving, and the recognition rates stop increasing, signifying that the training process can be stopped. During training, we do not use all the vowels in the database. We always retain 20% of the vowels to test the ability of the system to recognize unknown data. The final recognition rates on the training and testing datasets reach values up to 89% and 88%, respectively (Fig. 2g).

We now interpret these experimental recognition rates by comparing them to the performances that can be achieved with ideal oscillators trained on the same task with the same learning process. For this purpose, we model the oscillator dynamics with coupled van der Pol equations accounting for their collective magnetization coordinates (see Supplementary Information)²⁰. The simulated oscillators are noiseless and differ only by a 2% mismatch in their natural frequencies, analogous to the one observed experimentally. We first vary their ability to synchronize by modifying their frequency tunability (see Supplementary Information). Black circles in Fig. 3a show the recognition rate of the ideal simulated network as a function of the

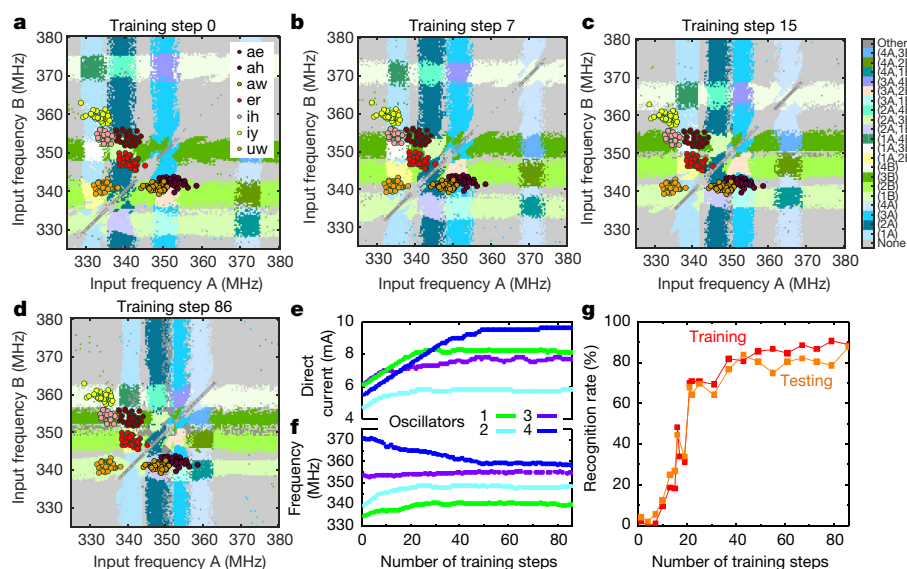


Fig. 2 | Learning to classify patterns by tuning the frequencies of oscillators. **a–d**, Experimental synchronization map as a function of the frequencies of the external signals, at different steps of the training procedure: **a**, step 0; **b**, step 7; **c**, step 15; and **d**, step 86. The coloured dots represent the inputs applied to the oscillatory network: vowels pronounced by different speakers. Different vowels are shown in different colours.

A video is provided as Supplementary Information. **e**, Direct current applied through each oscillator as a function of the number of training steps. **f**, Frequency of each oscillator as a function of the number of training steps. **g**, Recognition rates obtained with the sets of data points used for training and for testing, as a function of the number of training steps.

average locking range of the oscillators normalized by their frequency difference. The recognition rate increases linearly with the oscillator locking ranges (see dotted blue linear fit in Fig. 3a). Indeed, as shown in the simulated maps of Fig. 3b, when the oscillator locking ranges increase, the regions of synchronization grow, thus encompassing and classifying an increasing number of points in each of the different vowel clouds. As shown in Fig. 3c, d, the mutual coupling between oscillators also enhances their locking ranges²⁷, leading to increased recognition rates when the mutual interactions increase. The red star in Fig. 3a pinpoints where the experimental result features in this graph. The experimental vowel recognition rate of 89% is close to the maximum recognition rate of 94% that can be achieved with the same neural

network composed of ideal, noiseless oscillators. This high performance is due to the large experimental locking ranges resulting from the high tunability, coupling and low noise of the hardware spin-torque nano-oscillators.

We then compare the dynamical oscillator-based neural network studied in this paper to more conventional forms of neural networks. For this purpose, we first extract a reference value for the experimental recognition rate by repeating the training procedure experimentally several times with different combinations of training and testing sets (see Methods). This cross-validation technique yields an average value of 84.3% for the experimental recognition rate on the testing set that we can compare to other neural networks performances. First, we

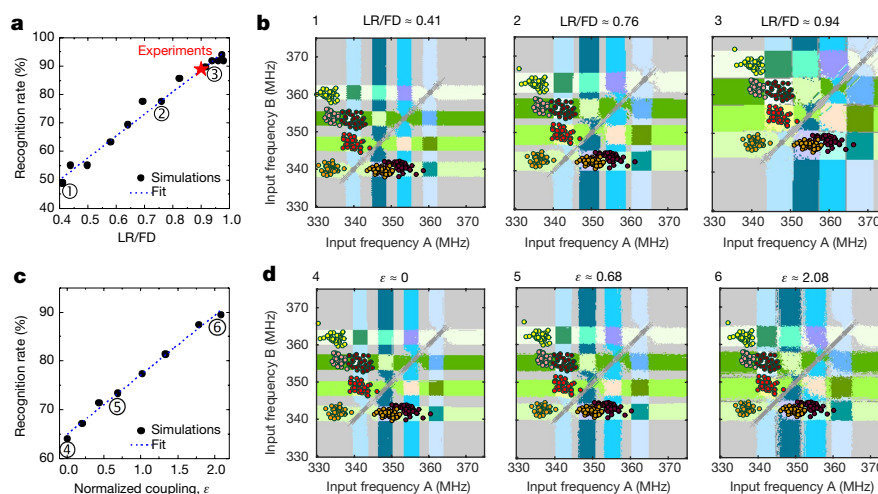


Fig. 3 | Comparing the recognition rates of experimental and ideal oscillators. Simulations of vowel recognition with a network of four identical oscillators trained with the same procedure as in the experiments are illustrated, in the absence of noise. The simulated oscillators differ only by a 2% mismatch in their natural frequencies. **a**, Recognition rate on the training set (black circles) as a function of the average oscillator locking range normalized by the frequency difference between oscillators (LR/FD). The locking range is varied by modifying the tunability of the oscillator frequency. The blue dotted line is a linear

fit to the simulation results. The red star indicates where experimental oscillators feature in this graph. **b**, Synchronization maps simulated with the network of oscillators used in **a**, for three different values of the normalized locking range. **c**, Recognition rate on the training set (black circles) as a function of the mutual coupling between oscillators normalized by their coupling to the microwave inputs. The blue dotted line is a linear fit to the simulation results. **d**, Synchronization maps simulated with the network of oscillators used in **c**, for three different values of the normalized coupling ϵ .

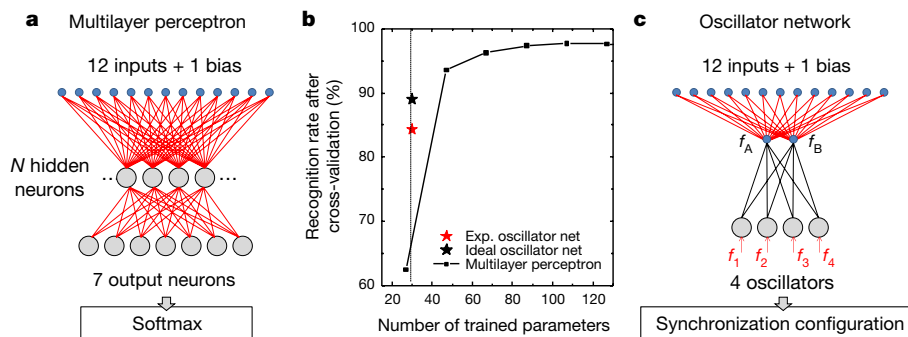


Fig. 4 | Benchmarking performances with classical neural networks. **a**, Flow chart of the simulated multilayer perceptron. The trained parameters are indicated in red. **b**, Recognition rate obtained through cross-validation versus the total number of trained parameters for the neural network in **a**, in which the number of hidden neurons is varied.

consider a conventional, static, multi-layer neural network. This kind of network can achieve better-than-human recognition rates at complex tasks, such as image classification. This performance, however, comes at the expense of the large number of parameters that need to be trained, a major hurdle for hardware implementation. Figure 4b shows the recognition rate of a multilayer perceptron, trained in software through backpropagation on the same database as the experimental neural network, with 30,000 vowel presentations (see Methods). As illustrated in Fig. 4a, this network, composed of static neurons, takes as inputs the 12 formant frequencies characterizing each pronounced vowel. The hidden layer neurons receive a weighted sum of these inputs (plus a bias term). The output layer, with softmax activation functions, has seven neurons, one for each vowel class (see Methods). As can be seen in Fig. 4b, the recognition rate is excellent, reaching 97% when the number of trained parameters is large (synaptic weights illustrated in red in Fig. 4a). However, the performance rapidly degrades for small numbers of trained parameters, diving below 65% for 27 trained parameters. This result is quite general: as can be seen from Extended Data Fig. 2, state-of-the-art networks with feedback such as standard recurrent neural networks or long short-term memory networks have limited performance when the number of trained parameters is small. In contrast, the recognition rate of our experimental oscillatory neural network is over 84% for only 30 trained parameters: as illustrated in red in Fig. 4c, the 26 weights converting formants to inputs, and the currents through the oscillators. For an ideal, noiseless, oscillatory network, the success rate reaches 89% after cross-validation. The network also learns rapidly (350 vowel presentations are used). This high performance with a small number of trained parameters comes from the combination of two phenomena: as shown in Fig. 3c, the oscillatory network can do better than the sum of its individual components, owing to its complex, coupled, dynamical features, and in addition, the oscillators collectively contribute to pattern recognition by synchronizing to the inputs. This result shows that the performance of hardware neural networks can be boosted by enhancing neuron functionalities beyond simple nonlinear activation functions, through oscillations and synchronization.

In the future, such dynamical neural networks will have to be scaled up to solve challenging classification problems on software-benchmarked databases. Spin-torque nano-oscillators offer numerous advantages towards this goal. Their energy consumption is comparable to or lower than complementary metal-oxide-semiconductor (CMOS) oscillators, and contrary to the latter, their lateral dimensions can be scaled down to a few nanometres in diameter (a detailed comparison is presented in Extended Data Table 2). Their quality factor can exceed several thousands²⁶, and their natural frequency can be controlled by the aspect ratio of the magnetic dot from hundreds of megahertz to several gigahertz in small pillars, opening the path to nano-oscillators assemblies with a wide range of natural frequencies¹⁹. In addition, their simple structure is similar to spin-torque magnetic random access memory cells, which means that they can be produced by billions

The red star corresponds to the experimental results with the network of spin-torque nano-oscillators. Exp., experimental. **c**, Flow chart of the experimental oscillatory neural network. The trained parameters are indicated in red.

on top of CMOS. Finally, their synchronization can be detected with CMOS circuits that count the number of oscillations²⁹ or measure the additional d.c. voltages produced by the oscillators when they phase-lock (see Methods and Extended Data Fig. 3)³⁰. Therefore, the wide variety of possible magnetic and electric couplings offered by spintronics^{21–24}, and the different ways of driving and controlling magnetization dynamics (spin torques, spin-orbit torques, electric fields), could be exploited in the future to implement large-scale hardware neural networks¹⁵.

Online content

Any methods, additional references, Nature Research reporting summaries, source data, statements of data availability and associated accession codes are available at <https://doi.org/10.1038/s41586-018-0632-y>.

Received: 24 November 2017; Accepted: 31 July 2018;

Published online 29 October 2018.

- Silver, D. et al. Mastering the game of Go without human knowledge. *Nature* **550**, 354–359 (2017).
- Borisov, R., Denham, M., Hoppensteadt, F., Kazanovich, Y. & Vinogradova, O. An oscillatory neural network model of sparse distributed memory and novelty detection. *Biosystems* **58**, 265–272 (2000).
- Jaeger, H. & Haas, H. Harnessing nonlinearity: predicting chaotic systems and saving energy in wireless communication. *Science* **304**, 78–80 (2004).
- Rabinovich, M., Huerta, R. & Laurent, G. Transient dynamics for neural processing. *Science* **321**, 48–50 (2008).
- Sussillo, D. Neural circuits as computational dynamical systems. *Curr. Opin. Neurobiol.* **25**, 156–163 (2014).
- Pikovsky, A. & Rosenblum, M. Dynamics of globally coupled oscillators: progress and perspectives. *Chaos* **25**, 097616 (2015).
- Kumar, S., Strachan, J. P. & Williams, R. S. Chaotic dynamics in nanoscale NbO₂ Mott memristors for analogue computing. *Nature* **548**, 318–321 (2017).
- Csaba, G. & Porod, W. Computational study of spin-torque oscillator interactions for non-Boolean computing applications. *IEEE Trans. Magn.* **49**, 4447–4451 (2013).
- Yogendra, K., Fan, D., Jung, B. & Roy, K. Magnetic pattern recognition using injection-locked spin-torque nano-oscillators. *IEEE Trans. Electron Dev.* **63**, 1674–1680 (2016).
- Macià, F., Kent, A. D. & Hoppensteadt, F. C. Spin-wave interference patterns created by spin-torque nano-oscillators for memory and computation. *Nanotechnology* **22**, 095301 (2011).
- Fang, Y., Yashin, V. V., Levitan, S. P. & Balazs, A. C. Pattern recognition with “materials that compute”. *Sci. Adv.* **2**, e1601114 (2016).
- Pickett, M. D., Medeiros-Ribeiro, G. & Williams, R. S. A scalable neuristor built with Mott memristors. *Nat. Mater.* **12**, 114–117 (2013).
- Pufall, M. R. et al. Physical implementation of coherently coupled oscillator networks. *IEEE J. Explor. Solid-State Comput. Devices Circuits* **1**, 76–84 (2015).
- Sharma, A. A., Bain, J. A. & Weldon, J. A. Phase coupling and control of oxide-based oscillators for neuromorphic computing. *IEEE J. Explor. Solid-State Comput. Devices Circuits* **1**, 58–66 (2015).
- Grollier, J., Querlioz, D. & Stiles, M. D. Spintronic nanodevices for bioinspired computing. *Proc. IEEE* **104**, 2024–2039 (2016).
- Parihar, A., Shukla, N., Jerry, M., Datta, S. & Raychowdhury, A. Computational paradigms using oscillatory networks based on state-transition devices. In *2017 International Joint Conference on Neural Networks (IJCNN)* 3415–3422 (IEEE, 2017).
- Vassiliev, E., Pinto, G., de Barros, J. A. & Suppes, P. Learning pattern recognition through quasi-synchronization of phase oscillators. *IEEE Trans. Neural Netw.* **22**, 84–95 (2011).

18. Vodenicarevic, D., Locatelli, N., Araujo, F. A., Grollier, J. & Querlioz, D. A nanotechnology-ready computing scheme based on a weakly coupled oscillator network. *Sci. Rep.* **7**, 44772 (2017).
19. Locatelli, N., Cros, V. & Grollier, J. Spin-torque building blocks. *Nat. Mater.* **13**, 11–20 (2014).
20. Slavin, A. & Tiberkevich, V. Nonlinear auto-oscillator theory of microwave generation by spin-polarized current. *IEEE Trans. Magn.* **45**, 1875–1918 (2009).
21. Kaka, S. et al. Mutual phase-locking of microwave spin torque nano-oscillators. *Nature* **437**, 389–392 (2005).
22. Mancoff, F. B., Rizzo, N. D., Engel, B. N. & Tehrani, S. Phase-locking in double-point-contact spin-transfer devices. *Nature* **437**, 393–395 (2005).
23. Houshang, A. et al. Spin-wave-beam driven synchronization of nanocontact spin-torque oscillators. *Nat. Nanotech.* **11**, 280–286 (2016).
24. Lebrun, R. et al. Mutual synchronization of spin torque nano-oscillators through a long-range and tunable electrical coupling scheme. *Nat. Commun.* **8**, 15825 (2017).
25. Torreon, J. et al. Neuromorphic computing with nanoscale spintronic oscillators. *Nature* **547**, 428–431 (2017).
26. Tsunegi, S. et al. High emission power and Q factor in spin torque vortex oscillator consisting of FeB free layer. *Appl. Phys. Express* **7**, 063009 (2014).
27. Romera, M. et al. Enhancing the injection locking range of spin torque oscillators through mutual coupling. *Appl. Phys. Lett.* **109**, 252404 (2016).
28. Hillenbrand, J., Getty, L. A., Wheeler, K. & Clark, M. J. Acoustic characteristics of American English vowels. *J. Acoust. Soc. Am.* **97**, 3099–3111 (1994).
29. Vodenicarevic, D., Locatelli, N., Grollier, J. & Querlioz, D. Synchronization detection in networks of coupled oscillators for pattern recognition. In *2016 International Joint Conference on Neural Networks (IJCNN)* 2015–2022 (IEEE, 2016).
30. Fang, B. et al. Giant spin-torque diode sensitivity in the absence of bias magnetic field. *Nat. Commun.* **7**, 11259 (2016).

Acknowledgements This work was supported by the European Research Council ERC under grant bioSPiNspired 682955, the French National Research Agency (ANR) under grant MEMOS ANR-14-CE26-0021, and a public grant overseen by the ANR as part of the ‘Investissements d’Avenir’ programme (Labex NanoSaclay, reference ANR-10-LABX-0035).

Reviewer information *Nature* thanks F. Hoppensteadt, A. Kent and the other anonymous reviewer(s) for their contribution to the peer review of this work.

Author contributions The study was designed by J.G. and D.Q. Samples were optimized and fabricated by S.T. and K.Y. The main experiments were performed by M.R. and P.T. Spin diode experiments were performed by P.T. and J.T. Numerical simulations were realized by P.T., M.E., M.R., T.H. and D.V. All authors contributed to analysing the results and writing the paper.

Competing interests The authors declare no competing interests.

Additional information

Extended data is available for this paper at <https://doi.org/10.1038/s41586-018-0632-y>.

Supplementary information is available for this paper at <https://doi.org/10.1038/s41586-018-0632-y>.

Reprints and permissions information is available at <http://www.nature.com/reprints>.

Correspondence and requests for materials should be addressed to D.Q. or J.G.

Publisher’s note: Springer Nature remains neutral with regard to jurisdictional claims in published maps and institutional affiliations.

METHODS

Samples. Magnetic tunnel junction (MTJ) films with a stacking structure of buffer/PtMn(15)/Co₇₁Fe₂₉(2.5)/Ru(0.9)/Co₆₀Fe₂₀B₂₀(1.6)/Co₇₀Fe₃₀(0.8)/MgO(1)/Fe₈₀B₂₀(6)/MgO(1)/Ta(8)/Ru(7) (thicknesses in nm) were prepared by ultrahigh-vacuum (UHV) magnetron sputtering. After annealing at 360 °C for 1 h, the resistance-area product was $RA \approx 3.6 \Omega \mu\text{m}^2$. Circular-shaped MTJs with a diameter of about 375 nm were patterned using Ar ion etching and e-beam lithography. The resistance of the samples is close to 40 Ω , and the magneto-resistance ratio is about 100% at room temperature. The FeB layer presents a structure with a single magnetic vortex as the ground state for the dimensions used here. In a small region called the vortex core (of about 12 nm diameter at remanence for our materials), the magnetization spirals out of plane. Under direct current injection and the action of the spin transfer torques, the core of the vortex steadily gyrates around the centre of the dot with a frequency in the range of 150 MHz to 450 MHz for the oscillators we used here.

Database and inputs. In this study, we classify seven spoken vowels with the oscillatory network. Spoken vowels are characterized by a set of frequencies called formants, which we obtain from a subset of the Hillenbrand database (<https://homepages.wmich.edu/~hillenbr/voweldata.html>) given in Supplementary Information. We use the first three formants (F_1 , F_2 and F_3) sampled at four different times of the duration of the spoken vowel: at the steady state and at 20%, 50% and 80% of the vowel duration (that is, 12 parameters in total). When one of these 12 parameters could not be measured, or when irresolvable formants mergers occurred, Hillenbrand et al.²⁸ put a zero in this parameter in the database. For our study, we have removed the vowel utterances whose corresponding set of formants is not complete. Moreover, we use the same number of speakers for each vowel. The resulting formant database comprising 37 female speakers that we used is provided as Supplementary Data.

We perform two linear combinations of these formants to obtain two characteristic frequencies (f_A and f_B) in the range of operation of the spin-torque nano-oscillators (between 325 MHz and 380 MHz for the applied field value that we are using):

$$\begin{aligned} f_A &= A_1 F_1^{\text{steady_state}} + B_1 F_2^{\text{steady_state}} + C_1 F_3^{\text{steady_state}} + D_1 F_1^{20\%} \\ &\quad + E_1 F_2^{20\%} + G_1 F_3^{20\%} + H_1 F_1^{50\%} + I_1 F_2^{50\%} + J_1 F_3^{50\%} + K_1 F_1^{80\%} \\ &\quad + L_1 F_2^{80\%} + M_1 F_3^{80\%} + N_1 \\ f_B &= A_2 F_1^{\text{steady_state}} + B_2 F_2^{\text{steady_state}} + C_2 F_3^{\text{steady_state}} + D_2 F_1^{20\%} \\ &\quad + E_2 F_2^{20\%} + G_2 F_3^{20\%} + H_2 F_1^{50\%} + I_2 F_2^{50\%} + J_2 F_3^{50\%} \\ &\quad + K_2 F_1^{80\%} + L_2 F_2^{80\%} + M_2 F_3^{80\%} + N_2 \end{aligned}$$

To choose the coefficients of the two linear combinations, we first record an experimental synchronization map that is used as a calibration of the network. The calibration map allows to assign a synchronization pattern to each vowel. Then, the linear transformation of the formants that best matches the data points of each vowel with its associated synchronization pattern is determined through fitting by least-square regression. The coefficients used in the two linear combinations and the two frequencies f_A and f_B corresponding to each vowel are provided as Supplementary Data.

Once this calibration is done and the coefficients and characteristic frequencies are calculated, the direct currents are reset to random values to begin the learning experiment. Two fixed-amplitude microwave signals with frequencies f_A and f_B are used as inputs to the experimental network of coupled nano-oscillators.

Experimental set-up. Extended Data Fig. 1 shows a schematic of the experimental set-up with the four coupled vortex nano-oscillators. A magnetic field of $\mu_0 H = 530$ mT is applied perpendicularly to the oscillator layers to get an efficient spin transfer torque acting on the oscillator vortex core. A direct current is injected into each oscillator to induce vortex dynamics, which leads to periodic oscillations of the magnetoresistance, giving rise to an oscillating voltage at the same frequency than the vortex core dynamics. The four oscillators are electrically connected in series by millimetre-long wires. They are therefore coupled through the microwave currents they emit, and too far away to be coupled through the magnetic dipolar fields that they radiate. Four direct currents (I_{DC1} , I_{DC2} , I_{DC3} , I_{DC4}) are supplied to the circuit by four different sources, allowing an independent control of the current flowing through each oscillator. The actual current flowing through each spin-torque oscillator is given by $I_{STO1} = I_{DC1}$, $I_{STO2} = I_{DC2} + I_{DC1}$, $I_{STO3} = I_{DC3} + I_{DC2} + I_{DC1}$ and $I_{STO4} = I_{DC4} + I_{DC3} + I_{DC2} + I_{DC1}$, respectively, where I_{STOi} corresponds to the current flowing through the i th oscillator. Two microwave sources are used to inject two external microwave signals with frequencies f_A and f_B and power $P = -9$ dBm through a strip line, creating two microwave fields as inputs to the oscillator network. The amplitude of the generated magnetic field, set by Ampere's law, depends only on the cross-section of the antenna (in addition to the distance between the strip line and the active magnetic layer of the oscillators). Therefore, the length of the antenna is only set by the number of oscillators it should cover. In our case, the strip line has a width of 2.5 μm and is fabricated 370 nm above the pillar (separated by an insulating layer). The resulting input microwave fields have an amplitude of

0.1 mT. They strongly affect the magnetization dynamics of the four oscillators, and thus the total microwave output emitted by the network. The microwave emissions are recorded with a spectrum analyser. As can be seen in Fig. 1d, the input signals from the antenna can be detected in addition to the oscillator emissions due to capacitive coupling between the strip line antenna and the metallic electrodes connecting the oscillator. The analysis of the output, which depends on the frequencies of the microwave inputs, can therefore easily be used to classify the spoken vowels.

Each spectrum recorded with the spectrum analyser is sent to the computer, where it is analysed by a program in real time. The information we use as input to this program is: (1) the value of the two frequencies of the external microwave signals (f_A , f_B) and (2) the oscillator frequencies at each direct current value in the absence of external microwave signals (f_1^0 , f_2^0 , f_3^0 , f_4^0). The output data that we extract from each spectrum analysis are the four values of the oscillator frequencies in the presence of microwave inputs. Then, another program takes these oscillator frequencies to calculate the synchronization states and check whether the applied vowel was properly recognized, as follows. If one of the detected frequencies coincides with the frequency of one of the external signals (± 0.5 MHz), we consider that the oscillator is synchronized to it. From this analysis, the synchronization pattern that corresponds to the input vowel is calculated. This is compared to the synchronization pattern initially assigned to that specific vowel to check whether it was successfully classified.

If we are in the training procedure and the vowel is not properly classified, the online learning algorithm calculates how the four direct currents should be modified to reduce the recognition error, as described in 'Real-time learning algorithm' below. This information is then sent back to the experimental set-up, where the currents are automatically modified.

Real-time learning algorithm. In this section, we present the supervised learning procedure that was applied to our spin-torque nano-oscillator network to learn to recognize different classes of input stimuli. Here these classes correspond to seven different spoken English vowels: ae, ah, aw, er, ih, iy and uw (see ref.²⁸ for details; the sounds can be heard at <https://homepages.wmich.edu/~hillenbr/voweldata.html>). Initially, we assign a synchronization pattern to each class of vowel (column 2 in Extended Data Table 1).

For a perfect recognition of one class of vowel, all data points in the frequency input map that corresponds to this vowel (Fig. 1f) must be contained in their assigned synchronization pattern in the experimental map (Fig. 1e). If this is not the case, for each association spoken vowel-synchronization pattern we define a frequency difference vector with four components (one for each oscillator; see third column in Extended Data Table 1) that will be used in the learning procedure.

Starting from a random map configuration (Fig. 1e), the automatic learning rule that we developed allows us to converge to a configuration where most data points for each vowel class are contained in their respective assigned synchronization pattern. The learning rule works in the following way.

(1) We present to the network a randomly chosen input data point i belonging to one vowel class, by sending two microwave inputs with frequencies f_A^i and f_B^i .

(2) From the resulting spectra, we extract the frequencies of the four spin-torque oscillators (f_1, f_2, f_3, f_4) in presence of the microwave inputs.

(3) We determine the resulting synchronization configurations by comparing the oscillator frequencies to the input frequencies f_A^i and f_B^i . Then, we compare the obtained synchronization configuration with the one assigned to this vowel.

(4) For each vowel presented to the network, we define an associated frequency difference vector, which describes the frequency distance between the applied input and the assigned synchronization region. For instance, if the presented data point belongs to the vowel class 'ae', we compute $\mathbf{d}_{ae} = [(f_A^i - f_1), 0, (f_B^i - f_3), 0]^T$.

If one of the two synchronization events assigned to 'ae' has occurred, we only compute the frequency difference that corresponds to the other event. For instance, if oscillator 1 is correctly synchronized to external source f_A^i , then we compute only $\mathbf{d}_{ae} = [0, 0, (f_B^i - f_3), 0]^T$.

(5) We repeat steps (1) to (4) for all seven vowel classes.

(6) We compute the sign of the vector sum of all seven associated frequency difference vectors $\mathbf{D}: \mathbf{D} = \text{sgn}(\mathbf{d}_{ae} + \mathbf{d}_{ah} + \mathbf{d}_{aw} + \mathbf{d}_{er} + \mathbf{d}_{ih} + \mathbf{d}_{iy} + \mathbf{d}_{uw}) = (D_1, D_2, D_3, D_4)^T$.

(7) We then compute the new direct current set (I_1', I_2', I_3', I_4'), which will be applied to the four oscillators:

$$\begin{pmatrix} I_1' \\ I_2' \\ I_3' \\ I_4' \end{pmatrix} = \begin{pmatrix} I_1 \\ I_2 \\ I_3 \\ I_4 \end{pmatrix} + \mu \begin{pmatrix} D_1 \text{sgn}\left(\frac{\partial \omega_1}{\partial I}\right)_{I=I_1} \\ D_2 \text{sgn}\left(\frac{\partial \omega_2}{\partial I}\right)_{I=I_2} \\ D_3 \text{sgn}\left(\frac{\partial \omega_3}{\partial I}\right)_{I=I_3} \\ D_4 \text{sgn}\left(\frac{\partial \omega_4}{\partial I}\right)_{I=I_4} \end{pmatrix}$$

In this equation, $\mu = 0.1$ mA is the learning rate of our algorithm. At each step, the applied direct current through each oscillator can be modified only by $\pm\mu$. Here $\text{sgn}[(\partial f_k / \partial I)_{I=I_k}]$ represents the sign of the frequency evolution versus injected direct current of the k th oscillator at the value of current I_k . For this, the frequency–current dependence of each independent oscillator has been previously characterized.

Upon modifying the direct currents following this learning procedure, the oscillator frequencies change. This translates into a displacement of the synchronization patterns in the experimental synchronization map (Fig. 2a–d).

(8) We repeat all previous steps (steps (1) to (7)) N times, where N is the total number of training steps. At each iteration, the synchronization map evolves towards an optimal configuration where the global frequency difference vector $\mathbf{d}_{\text{tot}} = \mathbf{d}_{\text{ae}} + \mathbf{d}_{\text{ah}} + \mathbf{d}_{\text{aw}} + \mathbf{d}_{\text{er}} + \mathbf{d}_{\text{ih}} + \mathbf{d}_{\text{iy}} + \mathbf{d}_{\text{uw}}$ is minimized. On increasing the number of training steps, we observe an increase of the recognition rate until it saturates after step 48, reaching a value of 89% (Fig. 2f). In our training experiment, we set the maximum number of training steps to $N = 87$, which corresponds to applying three times each of the 29 data points of the training database.

Cross-validation procedure. Training was realized using 80% of the total number of vowels in the database. The testing procedure was done using the remaining 20% data points. The cross-validation technique allows estimating accurately the recognition performances of the network by repeating the training/testing procedure five times over distinct data point samples. Each time, the selected data points used for testing are different: in the first (respectively second, third, fourth and fifth) cross-validation period, we use the first (respectively second, third, fourth and fifth) quintile (20%) of the data points for testing. The final recognition rate was obtained by averaging the testing recognition rates of the five cross-validation experiments. The same cross-validation procedure is used for all the neural networks (experimental and simulated).

Comparison of spin-torque nano-oscillators to CMOS oscillators. Extended Data Table 2 compares features of CMOS and spin-torque nano-oscillators. ‘Vortex spin-torque oscillators’ refer to the magnetic tunnel junctions used in this study; ‘10 nm spin-torque oscillators’ refer to state-of-the-art magnetic tunnel junctions currently used as memory cells.

Comparison with a multilayer perceptron. To benchmark the results of the experimental oscillatory network, we first ran a standard multi-layer perceptron, schematized in Fig. 4a, on the same vowel database.

The network takes as inputs the 12 formants of a given vowel in a database and has seven outputs, one for each vowel class. We have varied the number of hidden neurons between 1 and 20 to evaluate the recognition rate as a function of the number of trained parameters. More precisely, each formant has been rescaled between -1 and 1 before being fed into the first layer of neurons. The neuron activation functions are tanh functions at the hidden layer, and softmax at the output layer: the outputs z_i ($i = 1$ to 7) are defined as $z_i = e^{y_i} / \sum_{j=1}^7 e^{y_j}$, where y_j is the input to the output neuron j . The output with the largest z_i is taken as the vowel class corresponding to the input. We also tried ReLU activation functions, but they performed worse than tanh on this task.

For training the network we performed backpropagation, that is, gradient descent over the negative log-likelihood (or cross entropy).

As in the experimental conditions, the samples are picked and presented randomly to the network. One learning iteration corresponds to one forward pass of a given sample through the network, its subsequent gradient evaluation and weight update. The learning rate has been tuned to obtain the best result. Weights and biases before learning were randomly sampled from a Gaussian of mean 0 and variance 0.01.

For each trial, we ran training over 100,000 iterations to ensure convergence with a learning rate of 0.05. In practice, optimization techniques such as root-mean-square propagation or adaptive moment estimation could be used to accelerate training. All results are reported in Fig. 4b, where we show the recognition rate after cross validation as a function of the number of trained parameters.

Comparison with RNNs. In addition to the multilayer perceptron (Extended Data Fig. 2b), we also ran, on the same vowel database, a perceptron (Extended Data Fig. 2c), as well as a recurrent neural network (RNN; Extended Data Fig. 2d) and a long short-term memory network (LSTM) recurrent neural network (Extended Data Fig. 2e) with four hidden units. The procedure is similar to the multilayer perceptron. Formants are presented sequentially to the network which outputs a vowel once all of them have been swept through. Softmax activation functions were used at the output layer and tanh elsewhere. Outputs are encoded in a ‘one-hot’ fashion: for example, the ae vowel (out of the seven in total) is encoded by $(1, 0, 0, 0, 0, 0, 0)$. We take the maximum activation value as the classification result. As in the experimental conditions, the samples are picked and presented randomly to the network. One learning iteration corresponds to one forward pass of a given sample through the network, its subsequent gradient evaluation and weight update. For each architecture, the choice of the learning rate has been tuned to obtain the best result. Weights and biases before learning were randomly sampled from a

Gaussian of mean 0 and variance 0.01. No gradient inertia or learning rate adaptation technique was used. For the LSTM and the RNN, we ran training over 500,000 and over 1,000,000 iterations to ensure convergence with a learning rate of 0.01 and 0.0005, respectively. If needed, optimization techniques such as root-mean-square propagation or adaptive moment estimation could be used to accelerate training. Owing to the mini-batch size, gradient descent is highly stochastic, and we average the test and training rates over the last 5,000 iterations to obtain reliable training and error rate for a given trial. All results are reported in Extended Data Fig. 2a where we show the cross-validation success as a function of the number of parameters learnt.

Synchronization detection through oscillator rectified voltages. In the present work, synchronization of the oscillators is detected using a spectrum analyser, allowing a comprehensive understanding of the systems and of the physics of the oscillators. In a final integrated system, simpler techniques could be used to detect synchronization of oscillators. A possibility is given in ref. 29. Another method, involving less energy overhead, consists in exploiting the spin diode effect³¹, which causes synchronized oscillators to generate a supplementary direct voltage³². Extended Data Fig. 3a and b illustrates this effect in one of our oscillators. The appearance of a rectified voltage measured between the oscillator electrodes (Extended Data Fig. 3a) coincides with the locking range (Extended Data Fig. 3b). The generated rectified voltage is proportional to the fraction of the external microwave current I_{ext} flowing through the oscillator^{30,32}. In our experiments, I_{ext} is small: the input microwave signals are sent through a strip line isolated from the oscillators, in a geometry minimizing by design the capacitive coupling between oscillator and strip line ($I_{\text{ext}} = 7.5 \times 10^{-3} I_{\text{stripline}}$). As a result, the measured rectified voltages are small (approximately 0.5 mV). In the future, these values can be increased up to several tens of millivolts by optimizing the coupling between oscillator and strip line. Indeed, as demonstrated experimentally, rectification effects due to oscillator phase locking can be large, with sensitivities reaching 75.4 mV for the generated d.c. voltage per microwatt of injected microwave power³⁰.

We now present how synchronization detection through the resulting rectified voltages may be implemented in a final integrated circuit, using a differential method. We propose to use four reference resistors with the same resistance as the mean resistance of the nano-oscillators and polarized in the same manner. Comparing the voltage across a nano-oscillator and the corresponding reference resistance then allows detection of whether the oscillator is experiencing synchronization (Extended Data Fig. 3c). We designed a simple two-stage CMOS circuit to perform this comparison (Extended Data Fig. 3d,e). The first stage is composed of two differential amplifiers (voltage to current) in parallel. It is followed by a gain stage (current to voltage amplifier). The mismatch between the two amplifiers, a standard design technique, allows high gain. The output of the circuit is therefore a binary voltage, high if the oscillator is synchronized to the input signal, low otherwise. This voltage can be used directly by standard CMOS digital circuit to obtain the class of the input. In the circuit, bias voltages (V_{bias1} and V_{bias2}) can be adjusted to vary the speed and power consumption of the circuit.

We simulated this circuit in transient operation using the Cadence Spectre SPICE simulator, a standard tool in commercial integrated circuit design, with the design kit of a 28-nanometre commercial CMOS technology, and optimized the bias voltages for minimal energy consumption, while retaining a response time of the circuit below 600 ns. Extended Data Fig. 3f shows the energy consumed by the detection circuit as a function of the rectified direct voltage due to synchronization, taking into account the whole transient of the detection. This energy can be low: it is below 200 fJ for rectified direct voltages above 50 mV, which can be achieved in structures optimized for spin diode effect³⁰. For a full system, this detection must be performed twice (we send two input signals), for the four oscillators, leading to a detection energy of $2 \times 4 \times 200 \text{ fJ} = 1.6 \text{ pJ}$.

Using our current oscillators, this energy would be smaller than the energy dissipated by the oscillators and the reference resistors. By contrast, with scaled nano-oscillators (see Extended Data Table 2), this 1.6 pJ detection energy would become dominant.

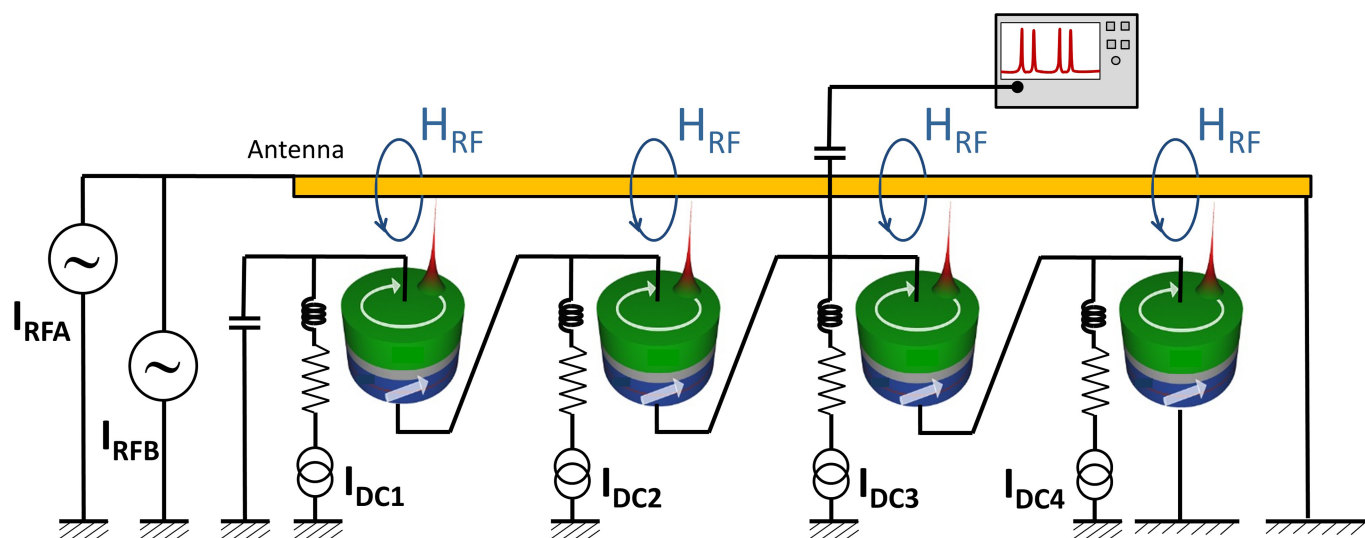
It is interesting to compare this quantity with the energy consumption of a purely CMOS neural network, implementing the multilayer perceptron of Fig. 4a. Optimized CMOS neural networks compute in reduced precision, usually 8-bit integers, which allows low energy consumption³³. Taking into account the arithmetic operations (sum and multiplications), in the same commercial 28-nanometre technology as the detection circuit that we implemented, we calculated that an 8-bit integer neural network implementing the second layer of the neural network of Fig. 4a consumes 2.2 pJ. We only took into account the second layer of the neural network, as it is the part implemented by the nano-oscillators. To obtain the energy estimation, we synthesized a Verilog description of a multiply and accumulate block and computed its energy consumption with the Cadence encounter tools using appropriate value change dump files generated by the Cadence ncsim simulator.

These energy considerations show that on our tiny control system, a nano-oscillator-based solution would provide an energy consumption slightly smaller than an optimized CMOS-based solution. We expect that the full benefit of the oscillator system will appear in deep networks composed of many layers of spin-torque nano-oscillators. Indeed, cascading the synchronization states from one layer to the next can be achieved directly through oscillatory interlayer coupling and does not require synchronization detection. Only at the last layer will detection circuits be required to communicate their state to other circuits. Therefore, we expect that in a deep network of oscillators, the energy consumption will be largely dominated by the oscillator energy consumption, which can be low for a scaled-down oscillator, as can be seen from Extended Data Table 2.

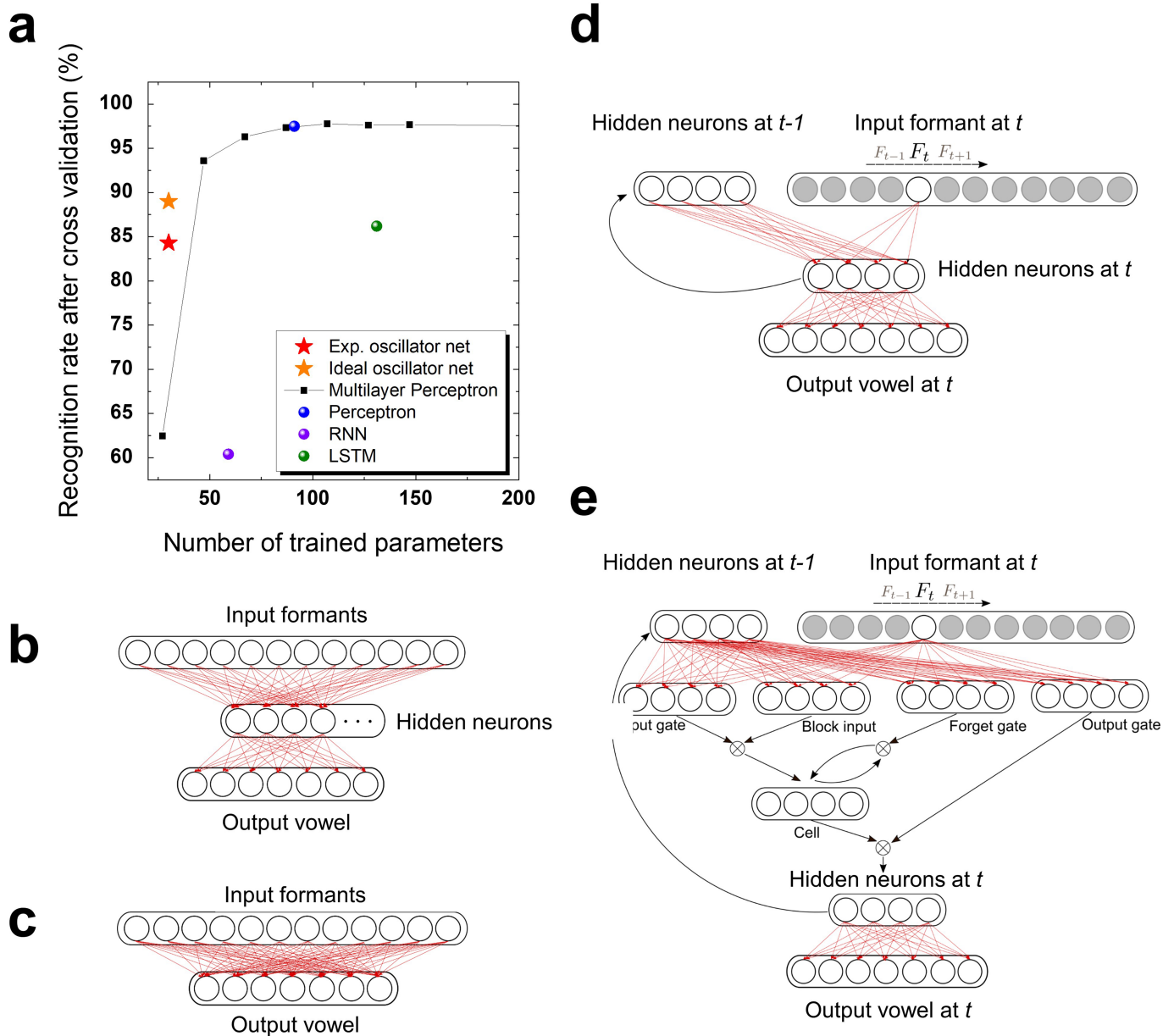
Data availability

The datasets generated and analysed during this study are available from the corresponding authors on reasonable request.

31. Tulapurkar, A. A. et al. Spin-torque diode effect in magnetic tunnel junctions. *Nature* **438**, 339–342 (2005).
32. Louis, S. et al. Low power microwave signal detection with a spin-torque nano-oscillator in the active self-oscillating regime. *IEEE Trans. Magn.* **53**, 1–4 (2017).
33. Jouppi, N. P. et al. Datacenter performance analysis of a tensor processing unit. In *Proc. 44th Annual International Symposium on Computer Architecture* 1–12 (ACM, 2017).
34. Livi, P. & Indiveri, G. A current-mode conductance-based silicon neuron for address-event neuromorphic systems. In *2009 IEEE International Symposium on Circuits and Systems* 2898–2901 (IEEE, 2009).
35. Qiao, N. & Indiveri, G. Scaling mixed-signal neuromorphic processors to 28 nm FD-SOI technologies. In *2016 IEEE Biomedical Circuits and Systems Conference (BioCAS)* 552–555 (IEEE, 2016).
36. Wijekoon, J. H. B. & Dudek, P. Compact silicon neuron circuit with spiking and bursting behaviour. *Neural Netw.* **21**, 524–534 (2008).
37. Tran, D. X. & Dang, T. T. An ultra-low power consumption and very compact 1.49 GHz CMOS voltage controlled ring oscillator. In *2014 International Conference on Advanced Technologies for Communications (ATC 2014)* 239–244 (IEEE, 2014).
38. Tomita, Y. et al. An 8-to-16 GHz 28 nm CMOS clock distribution circuit based on mutual-injection-locked ring oscillators. In *2013 Symposium on VLSI Circuits* C238–C239 (IEEE, 2013).
39. Gajek, M. et al. Spin torque switching of 20 nm magnetic tunnel junctions with perpendicular anisotropy. *Appl. Phys. Lett.* **100**, 132408 (2012).

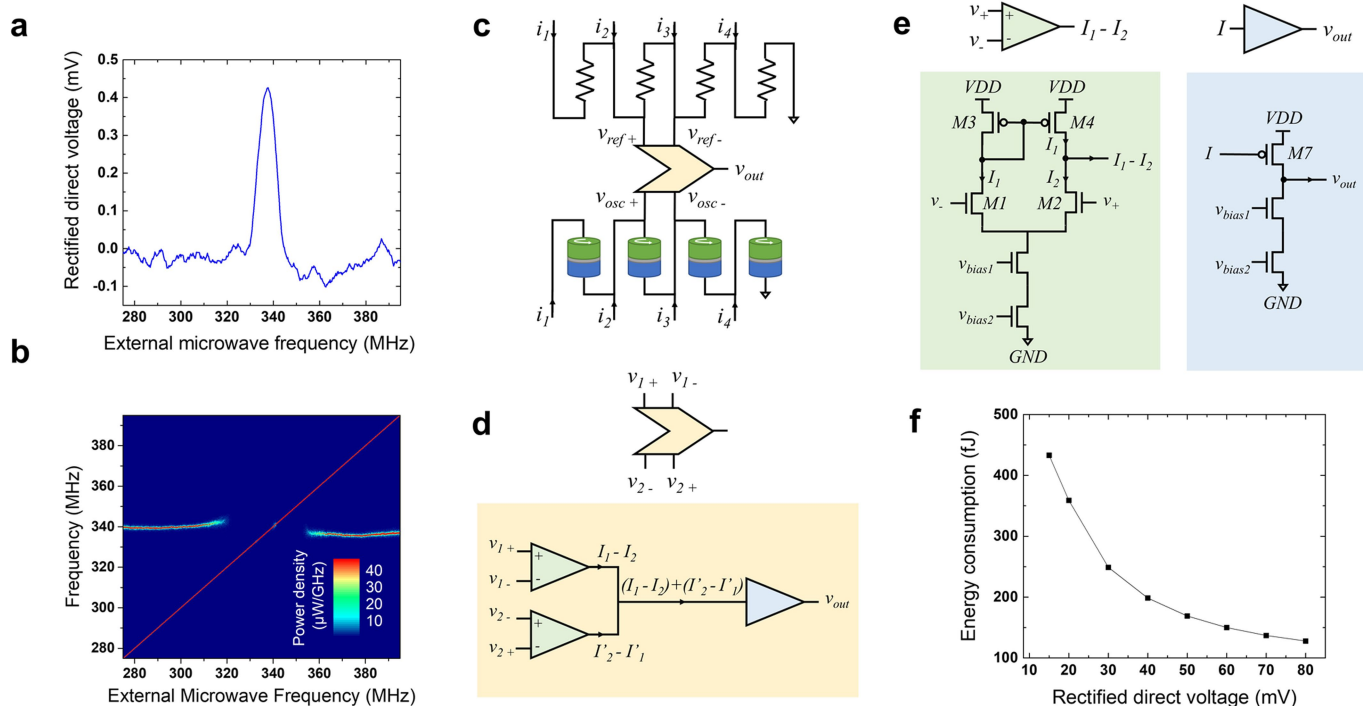


Extended Data Fig. 1 | Schematic of the experimental set-up. The four coupled vortex nano-oscillators are shown. I_{RFA} and I_{RFB} are the microwave currents injected in the strip line by the two microwave sources. H_{RF} is the resulting microwave field. I_{DC1-4} are the applied direct currents.



Extended Data Fig. 2 | Recognition rates obtained by different neural networks on the formant database. a, Recognition rates of different neural networks on the formant database as a function of the number of

trained parameters. **b–e**, Schematics of the simulated neural networks: **b**, multi-layer perceptron; **c**, perceptron; **d**, RNN; and **e**, LSTM.



Extended Data Fig. 3 | Synchronization detection by the spin diode effect. **a**, Rectified direct voltage measured between oscillator electrodes when the external microwave signal is injected in the strip line above the oscillator and its frequency is swept. Here, the direct current through the oscillator is 5 mA, the magnetic field is 585 mT and the injected microwave power is +1 dBm. **b**, Oscillator spectrum emission measured during the same frequency sweep as **a**. **c**, Proposed differential measurement

configuration for CMOS-based detection of synchronization-induced rectified voltages. **d**, Two-stage CMOS circuit. **e**, The first stage, composed of two differential amplifiers (green), is followed by a gain stage (blue). VDD, supply voltage; GND, ground. **f**, Energy consumption of the CMOS circuit for one synchronization detection event, as a function of the amplitude of the generated rectified direct voltages.

Extended Data Table 1 | Learning rule

7 different spoken vowel classes	Synchronization pattern	Associated frequency difference vector
ae	(1A, 3B)	$\mathbf{d}_{ae} = \begin{pmatrix} f_A^i - f_1 \\ 0 \\ f_B^i - f_3 \\ 0 \end{pmatrix}$
ah	(3A, 1B)	$\mathbf{d}_{ah} = \begin{pmatrix} f_B^i - f_1 \\ 0 \\ f_A^i - f_3 \\ 0 \end{pmatrix}$
aw	(2A, 1B)	$\mathbf{d}_{aw} = \begin{pmatrix} f_B^i - f_1 \\ f_A^i - f_2 \\ 0 \\ 0 \end{pmatrix}$
er	(1A, 2B)	$\mathbf{d}_{er} = \begin{pmatrix} f_A^i - f_1 \\ f_B^i - f_2 \\ 0 \\ 0 \end{pmatrix}$
ih	(3B)	$\mathbf{d}_{ih} = \begin{pmatrix} 0 \\ 0 \\ f_B^i - f_3 \\ 0 \end{pmatrix}$
iy	(4B)	$\mathbf{d}_{iy} = \begin{pmatrix} 0 \\ 0 \\ 0 \\ f_B^i - f_4 \end{pmatrix}$
uw	(1B)	$\mathbf{d}_{uw} = \begin{pmatrix} f_B^i - f_1 \\ 0 \\ 0 \\ 0 \end{pmatrix}$

Column 1, spoken vowel class; column 2, synchronization pattern assigned to each vowel; column 3, frequency difference vector between the spoken vowels and their associated patterns. The index i refers to the i th data point of a vowel class (i th speaker).

Extended Data Table 2 | Comparison of CMOS and spin-torque nano-oscillators for neuromorphic computing

	Lateral dimensions	Energy / oscillation	Frequency	Power consumption	Ability to synchronize	References
CMOS neuron	> 30 μm	265 pJ	10 Hz	2.65 nW	Yes	(34)
Scaled CMOS neuron	$\approx 7 \mu\text{m}$	50 pJ	30 Hz	1.5 nW	Yes	(35)
Accelerated CMOS neuron	$\approx 10 \mu\text{m}$	8.5 pJ	1 MHz	8.5 μW	Yes	(36)
CMOS ring oscillator	6 μm	6 fJ	200 KHz	1.2 nW	Unknown	(37)
CMOS ring oscillator	6 μm	33 fJ	1.5 GHz	50 μW	Unknown	(37)
CMOS ring oscillator	$\approx 300 \mu\text{m}$	1.4 pJ	16 GHz	23 mW	Yes	(38)
Vortex spin-torque oscillator	300 nm	3 pJ	300 MHz	1 mW	Yes	(24)
10 nm spin-torque oscillator (projection)	10 nm	100 aJ	10 GHz	1 μW	Yes	(39)

Data from refs ^{24,34–39}.

Palladium-mediated enzyme activation suggests multiphase initiation of glycogenesis

Matthew K. Bilyard¹, Henry J. Bailey², Lluís Raich³, Maria A. Gafitescu^{1,7}, Takuya Machida^{1,7}, Javier Iglésias-Fernández^{3,6}, Seung Seo Lee^{1,5}, Christopher D. Spicer¹, Carme Rovira^{3,4}, Wyatt W. Yue^{2*} & Benjamin G. Davis^{1*}

Biosynthesis of glycogen, the essential glucose (and hence energy) storage molecule in humans, animals and fungi¹, is initiated by the glycosyltransferase enzyme, glycogenin (GYG). Deficiencies in glycogen formation cause neurodegenerative and metabolic disease^{2–4}, and mouse knockout⁵ and inherited human mutations⁶ of GYG impair glycogen synthesis. GYG acts as a ‘seed core’ for the formation of the glycogen particle by catalysing its own stepwise autoglucosylation to form a covalently bound gluco-oligosaccharide chain at initiation site Tyr 195. Precise mechanistic studies have so far been prevented by an inability to access homogeneous glycoforms of this protein, which unusually acts as both catalyst and substrate. Here we show that unprecedented direct access to different, homogeneously glucosylated states of GYG can be accomplished through a palladium-mediated enzyme activation ‘shunt’ process using on-protein C–C bond formation. Careful mimicry of GYG intermediates recapitulates catalytic activity at distinct stages, which in turn allows discovery of triphasic kinetics and substrate plasticity in GYG’s use of sugar substrates. This reveals a tolerant but ‘proof-read’ mechanism that underlies the precision of this metabolic process. The present demonstration of direct, chemically controlled access to intermediate states of active enzymes suggests that such ligation-dependent activation could be a powerful tool in the study of mechanism.

The initial anchor point for the dendron-like structures that make up glycogen is the Tyr195 residue of GYG (using GYG1 numbering); glycogenesis is therefore a striking example of α -linked protein autoglucosylation⁷. Prior studies have suggested GYG to be a dimeric⁸, Mn²⁺-dependent enzyme belonging to the GT-8 family of retaining glycosyltransferases^{9,10}. GYG is—by virtue of its self-modifying nature—non-identical for each glucosylation step; that is, GYG, unlike nearly all biosynthetic enzymes, is strictly not a catalyst since it is itself changed at each step (Extended Data Fig. 1). This leads potentially to altered activity for each intermediate state and presumably to eventual inactivity once ‘buried’ in the polymer of glucose units that will emerge to make up the extended glycan portion of glycogen. This opens up the unusual possibility of distinct subphases and mechanisms occurring at different oligosaccharide chain lengths; crystal structures suggest possible intra-monomeric and inter-monomeric glucosylation modes within the GYG protein dimer¹⁰. Although bespoke biosynthetically deficient expression host strains can generate¹¹ a glycan-free, starting form of GYG, this allows access to only one catalyst state (Supplementary Text). As a result, any possible ‘(sub)phases’ subsequent to this starting state may be obscured if they follow faster kinetics. A lack of access to homogeneous GYG catalyst states therefore restricts our current understanding.

We reasoned that chemical construction of pure GYG in different glucosylation states might allow a strategy for direct, guided (‘shunted’) activation (and hence interrogation) of chosen intermediate states (Fig. 1, Extended Data Figs. 1, 2a). The unusual hybrid nature of these

catalyst states—part-catalyst, part-substrate—suggested a convergent (tag-and-modify¹²) construction process in which the desired (glycosyl acceptor) glycan moiety would be covalently attached in one step to key catalytic site 195 (Extended Data Fig. 1c). We have previously demonstrated that Pd(0)-mediated C–C-bond-forming ligation is feasible and benign in certain biological contexts^{13–17}. Pd-mediated approaches in biology have since been elegantly exploited by various groups^{18–20}. However, GYG is a testing target biomolecule on which to apply this method. Not only is site 195 in the heart of the active site, but GYG is also metal-dependent, raising the possibility of inhibitory ‘poisoning’ cross-competition^{21,22} by Pd at the metal co-factor site.

A suitable precursor GYG1 bearing a reactive ‘tag’ for Pd(0)-mediated C–C bond formation was generated via site-specific unnatural amino acid incorporation^{14,23,24}, giving a variant in which the *p*-hydroxy group of the natural, wild-type (WT) tyrosine residue at site 195 was exchanged for an iodide moiety (OH \rightarrow I, GYG-Tyr195 \rightarrow GYG-*p*I_{Phe}195, Fig. 1). Characterization confirmed no deleterious effects on overall enzyme structure. The structure of GYG-Y195X, determined in both apo (2.2 Å) and Mn²⁺ + UDP bound (2.4 Å) states (Supplementary Table 1; UDP, uridine diphosphate), revealed dimers that were highly superimposable on those in GYG-WT¹⁰ (Extended Data Fig. 2c). In the ligand-bound state, the *p*I_{Phe}195 group from one monomer is clearly visible (Extended Data Fig. 2d, inset), located within a partially unwound helix that adopts a catalytically poised position equidistant from either active site of the dimer (Extended Data Fig. 2d, red). Asymmetry at the dimer interface, consistent with previous unglucosylated GYG-WT structures¹⁰, suggested likely conformational flexibility needed as GYG transitions from unconjugated to differently glucosylated forms.

Studies on wild-type GYG (GYG-WT/GYG-Tyr195) revealed concentration-dependence of Pd inhibition and hence determination of essentially benign Pd concentrations that would successfully allow preservation of enzymatic activity (Extended Data Fig. 3, Supplementary Note); other cross-coupling components had minimal effect. These conditions allowed successful Pd-mediated C(sp²)–C(sp²) ligation of GYG-*p*I_{Phe}195 to a variety of designed, systematically altered ‘substrate templates’ (Fig. 1, Extended Data Figs. 2a, 4); all bore nucleophilic, hydroxyl groups as possible reaction sites for autoglucosylation (readily prepared as their corresponding C(sp²) boronic acid derivatives **1**, see Supplementary Methods). Small amounts of side-products were also identified (Extended Data Fig. 5): for example, unreacted GYG-*p*I_{Phe}195 or species attributable to dehalogenation¹⁷ using liquid chromatography-mass spectrometry (LC-MS) analysis and negative control studies (Supplementary Methods and Supplementary Text). Despite successful Pd-mediated ligation, ‘simple’ glycan-mimic templates (Extended Data Figs. 2a, 4) provided ineffective mimicry: irrespective of their systematically varied properties (orientation, length or pK_a), none led to activation of autoglucosylation. Activation of GYG requires therefore more than just an available hydroxyl nucleophile positioned

¹Department of Chemistry, University of Oxford, Oxford, UK. ²Structural Genomics Consortium, University of Oxford, Oxford, UK. ³Departament de Química Inorgànica i Orgànica (Secció de Química Orgànica) and Institut de Química Teòrica i Computacional (IQTC), Universitat de Barcelona, Barcelona, Spain. ⁴Institució Catalana de Recerca i Estudis Avançats (ICREA), Barcelona, Spain. ⁵School of Chemistry, University of Southampton, Southampton, UK. ⁶Present address: Institut de Química Computacional i Catalisi and Departament de Química, Universitat de Girona, Girona, Spain. ⁷These authors contributed equally: M. Gafitescu, T. Machida. *e-mail: wyatt.yue@sgc.ox.ac.uk; ben.davis@chem.ox.ac.uk

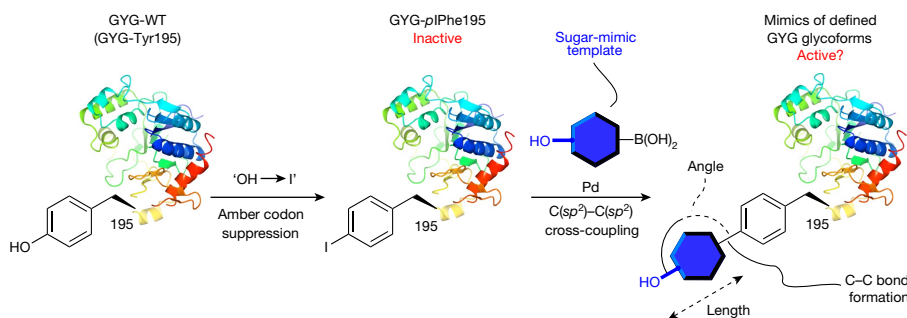


Fig. 1 | Palladium-mediated $C(sp^2)$ – $C(sp^2)$ ligation as a strategy for mechanistic investigation of glycogenin. First transformation, amber codon suppression enables ‘OH \rightarrow I’ replacement of the native Tyr195 acceptor of GYG-WT with an unnatural *L*-*p*-iodophenylalanine residue. This GYG-*p*I195 enzyme, which lacks a native glycosyl acceptor and thus cannot undergo glucosylation, represents a suitable substrate for Pd-

mediated Suzuki–Miyaura cross-coupling (second transformation) to a range of boronic acid sugar mimic templates, to generate potentially active enzyme species that mimic defined GYG glycoforms. In this way, inactive GYG-*p*I195 might be activated through C–C bond-forming ligation allowing pre-determined, ‘shunted’ access to intermediate catalyst states of GYG. See Extended Data Figs. 2, 4 for templates.

in the active site. However, for more complex substrate templates displaying glucosyl moieties inside GYG, not only did protein LC-MS analysis reveal successful C–C ligation but also concomitant activation (‘switch on’) and clear autoglucosylation activity in the resulting ‘shunted’ intermediate product GYG-Glc as well as the more advanced, chain-extended ‘shunted’ states GYG-Glc-Glc and GYG-Glc₆ (Fig. 2, Supplementary Information). Side-products from cross-coupling (Extended Data Fig. 5) were inactive to autoglucosylation and thus did not interfere in the assay.

This chemically generated access to ‘shunted’ functionally active intermediate states of GYG along the glycogen biosynthetic pathway allowed us to uniquely probe and compare activity using LC-MS monitoring of the sugars attached over time (Fig. 2c, d, Extended Data Figs. 6, 7, Supplementary Methods). Immediately contrasting behaviours from different states were observed. For more extended GYG-Glc-Glc, two distinct glucosylation phases were apparent: rapid glucosylation from 2 until about 4–5 Glc total, then substantially slower catalysis thereafter (Fig. 2c, d). Indeed, the initial step (GYG-Glc-Glc \rightarrow GYG-Glc-Glc-Glc) was extremely rapid; on-protein kinetic analyses conducted in replicate (see Supplementary Methods) revealed that about 90% of starting GYG-Glc-Glc was consumed within 20 s. In striking contrast, GYG-Glc exhibited a more gradual decline in glucosylation rate with increasing oligosaccharide length (Fig. 2c, d), consistent with a substantially slower initiation subphase for GYG-Glc (GYG-Glc \rightarrow GYG-Glc-Glc) that thus obscures the rapid phase immediately following (Extended Data Fig. 6d). Taken together, these data suggested a triphasic mechanism, in which a rapid intermediate phase is flanked by slower initiation (<2 glucoses) and elongation (>4/5 glucoses) phases (Extended Data Fig. 6d). Notably, only through the direct ‘shunt’ formation of intermediates (GYG-Glc, GYG-Glc-Glc, and so on) achieved through Pd-mediated ligation was unobscured analysis of each subphase made possible (Extended Data Fig. 7). Clear visualization of this kinetic profile was a consequence of our ability to both circumvent initial slow Tyr195 glucosylation and also probe discrete glucosylation states immediately after this. The presence of distinct (sub)phases is consistent with the proposed^{10,25,26} existence of different glucosylation mechanisms for GYG.

Use of ‘shunted’ intermediates GYG-Glc, GYG-Glc-Glc and GYG-Glc₆ allowed the determination of initial rates that gave apparent rate constants for each associated phase of $k_{app} = 0.016$, 0.126 and 0.003 s^{–1}, respectively (Extended Data Fig. 7b). These were also compared directly with kinetics determined from analysis of wild-type GYG in unglucosylated form (GYG-WT-Glc0, Extended Data Fig. 7). As expected, the inability to access intermediate states for GYG-WT failed to reveal the distinct phases shown by our chemically ‘shunted’ system. Nonetheless, global values for turnover proved consistent; we now show that one consequence of the triphasic regime is an accumulation of glucosylation at the end of the fast phase 2 mechanism regime (lengths 5–6 Glc) going into the slower phase 3. Taken together, this confirmed

quantitative mimicry at similar activity levels and highlighted the need for the chemical ‘shunted’ approach in revealing detailed mechanism.

Quantum mechanics/molecular mechanics (QM/MM) metadynamics^{27,28} simulations (see Supplementary Methods) allowed further insight through detailed reconstruction of the free-energy surface of reaction as a function of a few selected degrees of freedom (collective variables, CVs; Supplementary Methods). Michaelis complexes equivalent to GYG-Glc-Glc \rightarrow GYG-Glc-Glc-Glc (both in WT, GYG-WT-Glc3 \rightarrow GYG-WT-Glc4, and ‘shunted’, GYG-Glc-Glc \rightarrow GYG-Glc-Glc-Glc, form) were reconstructed from the structures determined here and of those in complex with UDP-Glc and cellotetraose¹⁰. Both wild-type and ‘shunted’ forms gave similar results (Extended Data Fig. 8), consistent with kinetic parameters. The free-energy surface revealed a short-lived intermediate (Extended Data Fig. 9) along the minimum free-energy pathway indicative of a front-face, ‘S_Ni-like’ reaction mechanism (see Supplementary Video)^{29,30}. The free-energy barrier of approximately 10 kcal mol^{–1} was very low compared with typical values obtained previously³⁰ for similar ‘S_Ni-like’ glucosyl transfer reactions (about 20 kcal mol^{–1}), suggesting potentially different rate-limiting processes. Thus, together our kinetic experimental and QM/MM data reveal unprecedentedly fast glucosyl-transfer for the second subphase of glycogen formation. The Michaelis complex (R’ in Extended Data Fig. 9b) exhibits a near-perfect approach between the O4’–H acceptor bond and the C1–O_p donor bond to assist the departure of UDP. The resulting very short C1...O4’ and H...O_p distances (3.3 and 2.0 Å, respectively, compared with 3.2 and 2.5 Å in prior, representative systems³⁰) for formed bonds provide excellent stabilization of charge developed at the phosphate, together with proper orientation for forthcoming front-face nucleophilic attack of O4’ onto C1 of Glc. The acceptor O–H in GYG thus creates a direct hydrogen bond H...O_p, unlike prior systems, resulting in a more stretched sugar–phosphate bond (C1–O_p) in GYG (1.58 Å compared to 1.51 Å; ref.³⁰) with a much lower associated bond energy (about 10 kcal mol^{–1} compared to approximately 18 kcal mol^{–1}).

To probe the selectivities of this multiphasic GYG mechanism, we next investigated the potential of GYG to use non-glucose sugar substrates³¹. The potential for GYG to use non-glucose acceptor sugar moieties has not been examined owing to the inability, until now, to directly access requisite intermediate enzyme states and to insert into those states non-glucose sugars. GYG-Glc and GYG-Glc-Glc generated by Pd-mediated ligation were capable of using the non-glucose donor sugar UDP-galactose with kinetic profiles essentially qualitatively similar to analogous autoglucosylation reactions (Fig. 3a), thereby forming GYG-Glc-(Gal)_n and GYG-Glc-Glc-(Gal)_n. Notably, however, the third kinetic (sub)phase observed for autoglucosylation was curtailed for autogalactosylation (Extended Data Fig. 6). Shunted access to GYG bearing common non-glucose but naturally occurring mammalian monosaccharides D-galactose (GYG-Gal) and D-mannose (GYG-Man) (Fig. 3b, Supplementary Information, using boronic acid reagents 1-Gal, 1-Man) revealed that both were capable of autoglucosylation to

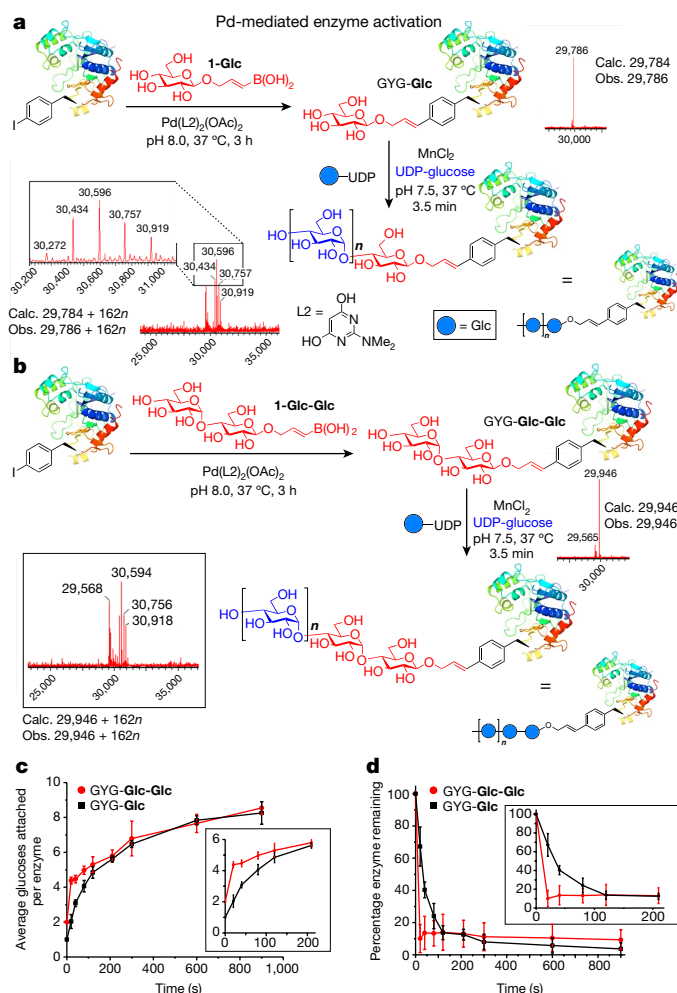


Fig. 2 | Generation of homogeneously glucosylated, catalytically active GYG glycoforms and kinetic studies of GYG-Glc and GYG-Glc-Glc.

a, Pd-mediated C–C bond-forming ligand of glucose-derived boronic acid **1-Glc** to GYG-Y195X generates in good yield the homogeneous glycoform GYG-Glc, which exhibits catalytic activity, as shown by LC-MS analysis. Similar results were obtained for at least four independent repeats. In all cases, non-glucosylated side-products present show no activity in the assay. **b**, Cross-coupling to **1-Glc-Glc** instead enables direct, ‘shunted’ access to a further catalytic intermediate of GYG-Glc, GYG-Glc-Glc, which also proved catalytically active, as also shown by LC-MS. Similar results were obtained for at least five independent repeats. In all cases, non-glucosylated side-products present show no activity in the assay. **c**, **d**, Kinetic profiles of overall glucosylation (**c**) and the initial glucosylation step as monitored through consumption of starting enzyme (**d** and inset) for GYG-Glc and GYG-Glc-Glc. The glucosylation levels and abundance of the starting enzyme were determined through LC-MS analysis (see also Extended Data Fig. 6 and Supplementary Methods). Whereas GYG-Glc-Glc exhibits a marked ‘fast → slow’ biphasic profile, these same phases, while necessarily present for GYG-Glc, are not visible, being instead obscured by a slower initiation step. For both **c** and **d**, data points represent mean averages of n independent replicate kinetic runs; $n = 4$ (GYG-Glc) and $n = 5$ (GYG-Glc-Glc). Error bars are ± 1 s.d.

form both GYG-Gal-(Glc) $_n$ and so on and GYG-Man-(Glc) $_n$ and so on (Fig. 3c). Kinetic analyses of this non-glucose acceptor activity of GYG revealed glucosylation rates for GYG-Gal and GYG-Man that are initially lower as a consequence of a substantially slower initiation step/(sub)phase. In contrast to their plasticity towards glucosylation, the non-glucose enzyme states GYG-Gal and GYG-Man did not catalyse autogalactosylation to any substantial extent (Supplementary Table 12). Molecular dynamics (MD) simulations (Extended Data Fig. 9) suggested that the altered configurations of non-glucose sugars—for example, Gal in GYG-WT-Glc-Gal or UDP-Gal—necessitated

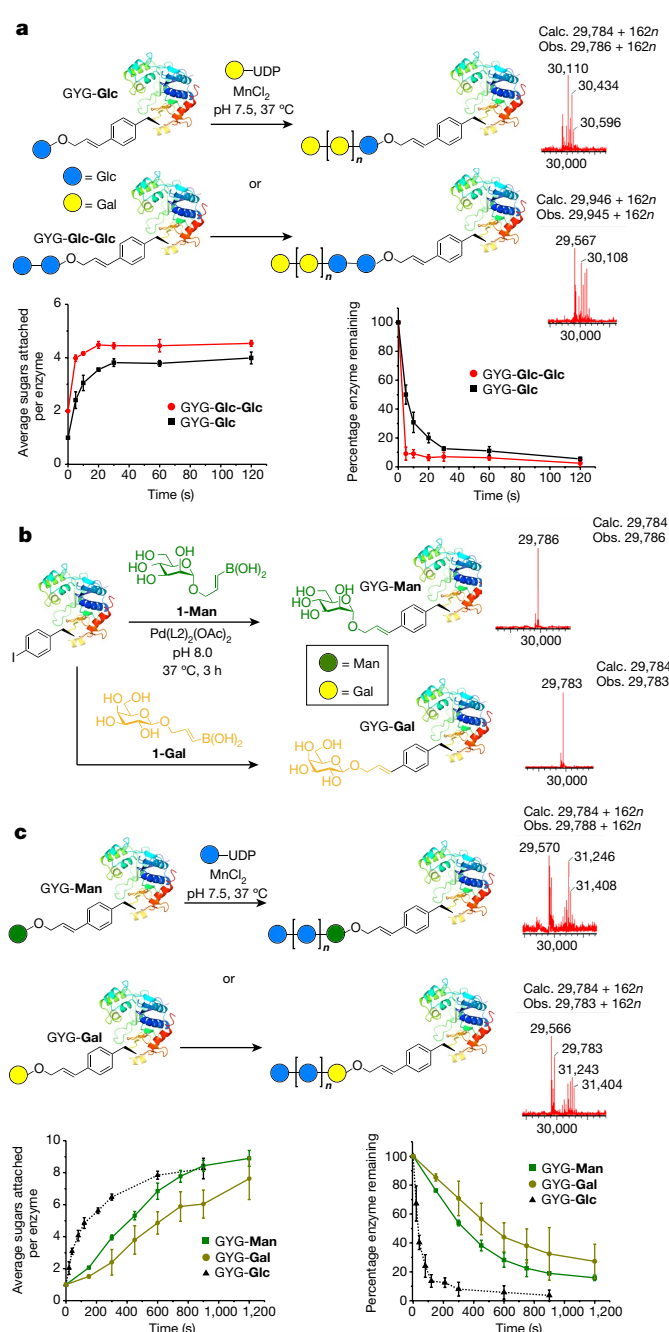


Fig. 3 | Donor and acceptor plasticity of GYG. **a**, GYG-Glc (top row) and GYG-Glc-Glc (middle row) are capable of using the unnatural donor UDP-galactose, as shown by LC-MS. Bottom row, kinetic profiles for overall galactosylation (left) and rate of initial galactosylation step (right). Data points represent mean averages of $n = 3$ independent replicate kinetic runs for both GYG-Glc and GYG-Glc-Glc galactosylation. Error bars are ± 1 s.d. **b**, Generation of non-natural GYG glycosyl acceptors GYG-Gal and GYG-Man (bottom and top respectively), as shown by LC-MS. Similar results were obtained for at least three independent repeats. **c**, Autoglucosylation activity of GYG-Man (top row) and GYG-Gal (middle row) compared to GYG-Glc, as shown by LC-MS. Bottom row, kinetic profiles analogous to those in **a**, overall glucosylation (left) and rate of initial glucosylation step (right) are shown. Data points represent mean averages of n independent replicate kinetic runs; $n = 4$ (GYG-Glc) and $n = 3$ (GYG-Gal, GYG-Man). Error bars are ± 1 s.d. In all cases, non-glucosylated side-products present show no activity in the assay.

slight reorientations but could be accommodated without substantially altering the interactions at the active site with key hydroxyl-binding residues. The result is that the distance of the putative nucleophile

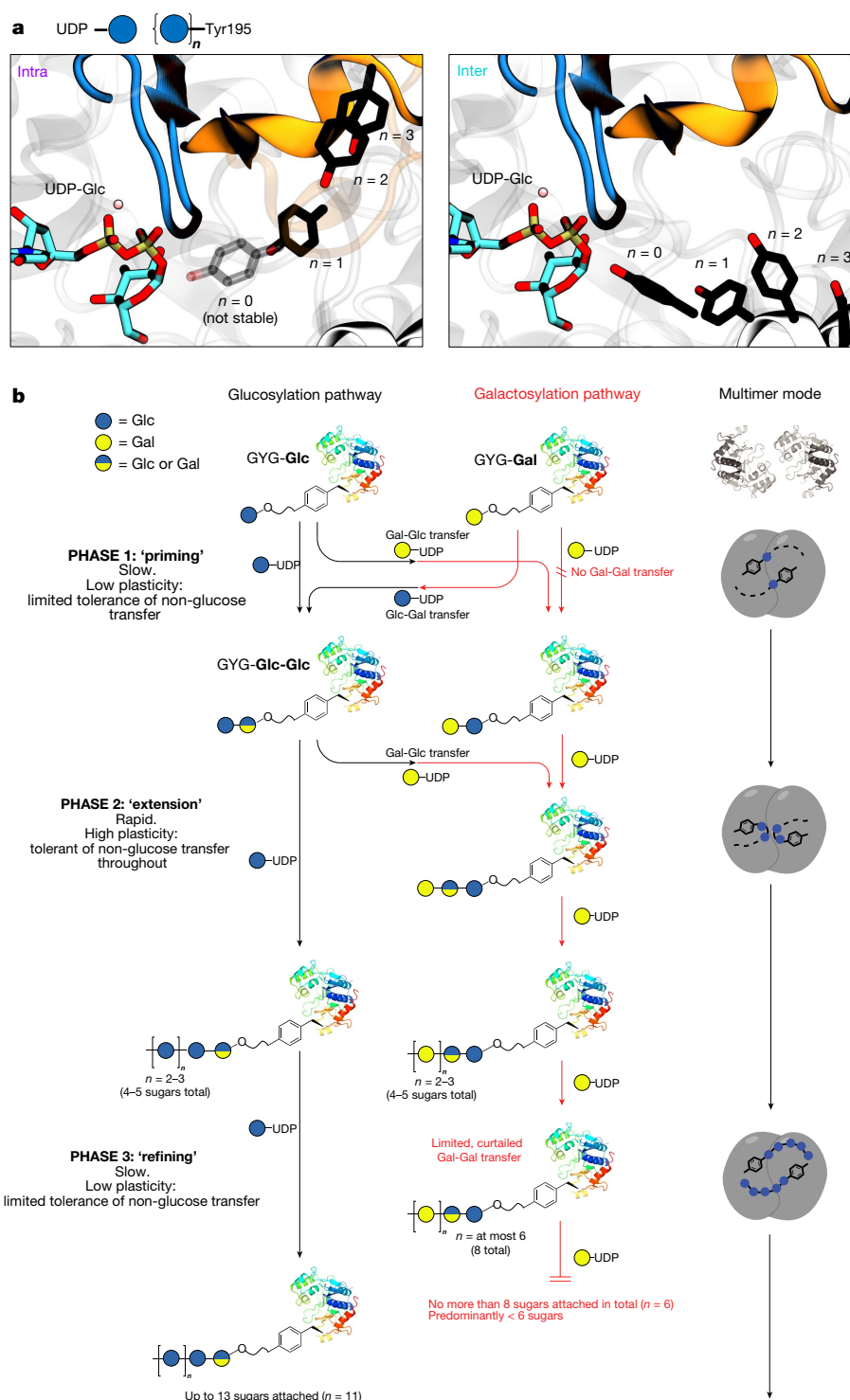


Fig. 4 | Natural and unnatural pathways of GYG catalysis further delineate a triphasic mechanism and reveal a possible proof-reading step. a, Motion of Tyr195 to accommodate acceptor substrates of various lengths and conformations (intra- and inter-monomeric). Results were obtained from MD simulations for each Michaelis complex. Acceptor sugar units have been omitted for clarity. The orange loop corresponds to the acceptor arm of the same subunit of the displayed active site (that is, intra), whereas the white loop is the acceptor arm of the opposite subunit (inter). The tyrosine residue represented as transparent indicates an unstable conformation due to steric hindrance with the 'blocking loop' coloured in blue. Notice that the tyrosine residue recoils one position for each sugar that is attached to it. Hydrogen atoms and acceptor

glucose units have been omitted for clarity. **b**, Comparison of the natural autoglucosylation pathway (and the unnatural autogalactosylation pathway for various GYG substrates) reveals that, while the slower first and third phases (which we speculate operate through inter-monomer multimer modes; see right hand column schematic) display limited Gal-Gal transfer, this reaction readily proceeds throughout the fast second phase (which we speculate is intra-monomer). The consequent absence of a third phase for autogalactosylation may function as a 'refining' step, preventing incorporation of poly-Gal oligosaccharides into glycogen and thus preventing accumulation of misformed, potentially toxic, glycogen particles. Phase characteristics are summarized on the left.

(OH-4) from the electrophilic anomeric carbon (in UDP-Gal or UDP-Glc, respectively) is not greatly perturbed ($O\cdots C1$ change $<0.5 \text{ \AA}$) and $O-C$ bond formation can thus evolve essentially ‘normally’ despite such changes, reflecting this experimentally observed plasticity.

Taken together, distinct mechanistic phases of GYG (Fig. 4) are therefore defined not only by different rates but also different donor/acceptor tolerance. Whereas the second, rapid phase (2 to 4/5 sugars) readily tolerates Gal-to-Gal transfer throughout (species with up to 5 sugars are quickly generated from GYG-Glc-Glc), the first and third phases show similarities in being linked by not only their slower glucosylation rates but also their apparent lower tolerance of non-glucose in both acceptor and donor at the same time. A plastic and rapid second phase is thus seemingly preceded by a slower step that can nonetheless be primed with unnatural sugars—immediately surprising given the presumed specific role of glycogen as a glucose-storage polymer—and is followed by a slower and much more selective third phase. Together these three phases appear to allow ‘priming’ with non-glucose sugars in the first phase (for example, Gal, Man) followed by more rapid and more plastic ‘extension’ in the second phase (with either UDP-Glc or UDP-Gal) before a third ‘refining’ phase that ensures use of only glucose in the more extended portions of the inner core of glycogen.

From data gathered here and earlier¹⁰, we speculate that these phases may reflect, in part, transitions between intra-monomeric and inter-monomeric modes of glucosylation within the active GYG protein dimer. From our structure of GYG-*pI*Phe195, we see that the anchor point for the oligosaccharide chain of glycogen is essentially equidistant from the two active sites in GYG dimer. MD simulations (Extended Data Fig. 8) with GYG bearing Glc-oligomer chains of different lengths (GYG-WT-Glc_n, $n = 0-5$) and conformations (intra-/inter-monomeric) suggest that the first glucosylation steps ($n = 0, 1$) are preferentially inter-monomeric. A ‘blocking loop’ in between the acceptor arm and the active site of the same subunit hampers intra-monomeric conformations. In contrast, sugar chains of subsequent steps ($n = 2, 3$) circumvent the blocking loop, allowing intramonomeric conformations. A key positioning residue GYG-Asp 125 binds the nucleophilic acceptor Glc terminus, allowing equilibration into a productive Michaelis complex and guides the OH-4 to the donor site from the α face of UDP-Glc, ready for the front-face attack (optimal for intermediate levels of GYG glucosylation). Key to this process is a striking flexibility of GYG-Tyr195, which steadily recoils step-by-step by the distance of one sugar ring to accommodate acceptor Glc_n chains of increasing lengths (Fig. 4).

Together these data suggest a first inter-monomer phase in which the nascent oligosaccharide chain is of insufficient length to easily provide the right orientation to be processed by the active site but can eventually equilibrate (‘hooked’ into place by Asp 125) to a productive Michaelis complex owing to flexibility of Tyr195. In the second phase, sufficient flexibility of the oligosaccharide chain allows correct orientation and a rapid intra-monomer extension, yet with low selectivity. Finally, in the third ‘refining’ phase, extension of the nascent oligosaccharide chain past the active site of its own protein monomer requires extension by the active site of another monomer in a much more closely linked dimer, which requires careful alignment of donor substrate (UDP-Glc only) recruitment with binding of the extending chain. Eventually, this chain too processes past the point of the second active site and GYG’s activity ceases at a longer chain length of more than 12 Glc units. This presents a Glc-terminated core-glycan particle ready for elaboration by glycogen synthase (GYS) and glycogen branching enzyme (GBE), respectively (Extended Data Fig. 1)^{1,32}.

The plasticity of GYG raises the question of whether non-glucose sugars can ever be incorporated into mature glycogen particles. Whereas natural incorporation of mannose from its most abundant nucleotide GDP-mannose is not feasible owing to the known specificity of GYG for pyrimidine nucleotide sugar donors³², UDP-Gal is readily available in vivo. In this light, the limited final kinetic phase for autogalactosylation is consistent with a ‘refining’ mechanism that prevents misformed glycogen particles due to, for example, poly-Gal incorporation

(Fig. 4). At the same time, GYG’s ability to utilize UDP-Gal in earlier phases may facilitate early glycogenesis during times in which UDP-Glc supplies are scarce. This suggests that the core of glycogen can carry priming glycans that may be non-glucose in nature. Our work here also highlights that while non-glucose sugars might serve this role, other simpler, hydroxyl-only templates fail. This, in turn, suggests that this core region does not serve as an energy storage polymer (since it would release incorrect sugars for metabolism) but instead acts to anchor glycogen to the glycogenin core protein. Together, these three phases—prime-extend-refine—therefore appear to represent a mechanistic solution to the delicate evolutionary balance between the difficult-to-achieve need to anchor glucose-polymer to a protein with the need to ensure precise glucose-only particle formation at its outer regions.

The chemical ligation approach used here has shown that, whereas natural C-O Tyr195-to-glucose linkages cannot be accessed via any current chemical modification approach (Extended Data Fig. 10), Pd-mediated formation of an irreversible C-C bond can yield sufficiently similar motifs to allow functional mimicry of GYG in glycogenesis. They reveal that GYG’s catalytic activity does indeed vary through these intermediate states and highlight how this ‘self-modulation’ seems to be exploited by nature in three phases with different function. We anticipate that this methodology may ultimately be expanded to access a wider range of precise glycogen structures, enabling study of other glucosylation and associated processing steps that will shine further light on the expanding number of glycogen-associated diseases^{1,2,4,33}.

More broadly, the demonstration of successful mimicry that we have achieved here by using chemistry to covalently and directly ‘bolt in’ a key residue alteration to create an intermediate catalytic state highlights that new protein chemistries are becoming accurate and subtle enough to allow precise (for example, ‘shunt’) mechanistic experiments that would be difficult through classical biochemical means. Although strategies for chemical rescue of enzymes via unmasking of caged natural residues have been elegantly explored^{19,34,35}, to our knowledge these experiments mark rare application of Pd-mediated C-C-bond-forming ligation as a mode of chemical enzyme activation. It suggests that such ligation-dependent activation (here using catalytic metal Pd(0) as a ‘switch’) could be a powerful tool not only in the study of mechanism but even potentially in the future ‘rescue’ of deficient enzymes.

Reporting summary

Further information on experimental design is available in the Nature Research Reporting Summary linked to this paper.

Data availability

Crystallographic data have been deposited and made available under PDB accession codes 6EQJ (apo) and 6EQL (with ligands). All raw MS data supporting Figures are given in the Supplementary Information and/or is available on request. All primary numerical data for graphical plots in Figures are available as spreadsheets. Key data have been deposited in the open-access depository ORA-data doi.org/10.5287/bodleian:2NAa0YogK.

Online content

Any methods, additional references, Nature Research reporting summaries, source data, statements of data availability and associated accession codes are available at <https://doi.org/10.1038/s41586-018-0644-7>.

Received: 30 September 2017; Accepted: 31 August 2018;

Published online 24 October 2018.

1. Roach, P. J., Depaoli-Roach, A. A., Hurley, T. D. & Tagliabracchi, V. S. Glycogen and its metabolism: some new developments and old themes. *Biochem. J.* **441**, 763–787 (2012).
2. Adeva-Andany, M. M., González-Lucán, M., Donapetry-García, C., Fernández-Fernández, C. & Arneiros-Rodríguez, E. Glycogen metabolism in humans. *BBA Clin.* **5**, 85–100 (2016).
3. Roach, P. J. Are there errors in glycogen biosynthesis and is laforin a repair enzyme? *FEBS Lett.* **585**, 3216–3218 (2011).
4. Zois, C. E., Favaro, E. & Harris, A. L. Glycogen metabolism in cancer. *Biochem. Pharmacol.* **92**, 3–11 (2014).

5. Testoni, G. et al. Lack of glycogenin causes glycogen accumulation and muscle function impairment. *Cell Metab.* **26**, 256–266 (2017).
6. Moslemi, A.-R. et al. Glycogenin-1 deficiency and inactivated priming of glycogen synthesis. *N. Engl. J. Med.* **362**, 1203–1210 (2010).
7. Alonso, M. D., Lomako, J., Lomako, W. M. & Whelan, W. J. Tyrosine-194 of glycogenin undergoes autocatalytic glucosylation but is not essential for catalytic function and activity. *FEBS Lett.* **342**, 38–42 (1994).
8. Hurley, T. D., Stout, S., Miner, E., Zhou, J. & Roach, P. J. Requirements for catalysis in mammalian glycogenin. *J. Biol. Chem.* **280**, 23892–23899 (2005).
9. Gibbons, B. J., Roach, P. J. & Hurley, T. D. Crystal structure of the autocatalytic initiator of glycogen biosynthesis, glycogenin. *J. Mol. Biol.* **319**, 463–477 (2002).
10. Chaikuad, A. et al. Conformational plasticity of glycogenin and its maltosaccharide substrate during glycogen biogenesis. *Proc. Natl Acad. Sci. USA* **108**, 21028–21033 (2011).
11. Hurley, T. D., Walls, C., Bennett, J. R., Roach, P. J. & Wang, M. Direct detection of glycogenin reaction products during glycogen initiation. *Biochem. Biophys. Res. Commun.* **348**, 374–378 (2006).
12. Chalker, J. M., Bernardes, G. J. L. & Davis, B. G. A “Tag-and-modify” approach to site-selective protein modification. *Acc. Chem. Res.* **44**, 730–741 (2011).
13. Chalker, J. M., Wood, C. S. C. & Davis, B. G. A convenient catalyst for aqueous and protein Suzuki-Miyaura cross-coupling. *J. Am. Chem. Soc.* **131**, 16346–16347 (2009).
14. Spicer, C. D. & Davis, B. G. Palladium-mediated site-selective Suzuki-Miyaura protein modification at genetically encoded aryl halides. *Chem. Commun.* **47**, 1698–1700 (2011).
15. Spicer, C. D., Triemer, T. & Davis, B. G. Palladium-mediated cell-surface labeling. *J. Am. Chem. Soc.* **134**, 800–803 (2012).
16. Spicer, C. D. & Davis, B. G. Rewriting the bacterial glycocalyx via Suzuki-Miyaura cross-coupling. *Chem. Commun.* **49**, 2747–2749 (2013).
17. Dumas, A. et al. Self-ligated Suzuki-Miyaura coupling for site-selective protein PEGylation. *Angew. Chem. Int. Edn Engl.* **52**, 3916–3921 (2013).
18. Li, J. & Chen, P. R. Moving Pd-mediated protein cross coupling to living systems. *ChemBioChem* **13**, 1728–1731 (2012).
19. Yang, M., Li, J. & Chen, P. R. Transition metal-mediated bioorthogonal protein chemistry in living cells. *Chem. Soc. Rev.* **43**, 6511–6526 (2014).
20. Jbara, M., Maity, S. K. & Brik, A. Palladium in the chemical synthesis and modification of proteins. *Angew. Chem. Int. Ed.* **56**, 10644–10655 (2017).
21. Boeggeman, E. & Qasba, P. K. Studies on the metal binding sites in the catalytic domain of β 1,4-galactosyltransferase. *Glycobiology* **12**, 395–407 (2002).
22. Nielsen, M. M. et al. Substrate and metal ion promiscuity in mannosylglycerate synthase. *J. Biol. Chem.* **286**, 15155–15164 (2011).
23. Young, T. S., Ahmad, I., Yin, J. A. & Schultz, P. G. An enhanced system for unnatural amino acid mutagenesis in *E. coli*. *J. Mol. Biol.* **395**, 361–374 (2010).
24. Davis, L. & Chin, J. W. Designer proteins: applications of genetic code expansion in cell biology. *Nat. Rev. Mol. Cell Biol.* **13**, 168–182 (2012).
25. Issoglio, F. M., Carrizo, M. E., Romero, J. M. & Curtino, J. A. Mechanisms of monomeric and dimeric glycogenin autoglucosylation. *J. Biol. Chem.* **287**, 1955–1961 (2012).
26. Bazán, S., Issoglio, F. M., Carrizo, M. E. & Curtino, J. A. The intramolecular autoglucosylation of monomeric glycogenin. *Biochem. Biophys. Res. Commun.* **371**, 328–332 (2008).
27. Laio, A. & Parrinello, M. Escaping free-energy minima. *Proc. Natl Acad. Sci. USA* **99**, 12562–12566 (2002).
28. Ardévol, A. & Rovira, C. Reaction mechanisms in carbohydrate-active enzymes: glycoside hydrolases and glycosyltransferases. insights from ab initio quantum mechanics/molecular mechanics dynamic simulations. *J. Am. Chem. Soc.* **137**, 7528–7547 (2015).
29. Lee, S. S. et al. Mechanistic evidence for a front-side, S_Ni -type reaction in a retaining glycosyltransferase. *Nat. Chem. Biol.* **7**, 631–638 (2011).
30. Ardévol, A. & Rovira, C. The molecular mechanism of enzymatic glycosyl transfer with retention of configuration: evidence for a short-lived oxocarbenium-like species. *Angew. Chem. Int. Edn Engl.* **50**, 10897–10901 (2011).
31. Carrizo, M. E., Miozzo, M. C., Goldraij, A. & Curtino, J. A. Purification of rabbit skeletal muscle proteoglycogen: studies on the glucosyltransferase activity of polysaccharide-free and -bound glycogenin. *Glycobiology* **7**, 571–578 (1997).
32. Alonso, M. D., Lomako, J., Lomako, W. M. & Whelan, W. J. A new look at the biogenesis of glycogen. *FASEB J.* **9**, 1126–1137 (1995).
33. Ashcroft, F. M., Rohm, M., Clark, A. & Brereton, M. F. Is type 2 diabetes a glycogen storage disease of pancreatic β cells? *Cell Metab.* **26**, 17–23 (2017).
34. Lee, H.-M., Larson, D. R. & Lawrence, D. S. Illuminating the chemistry of life: design, synthesis, and applications of “caged” and related photoresponsive compounds. *ACS Chem. Biol.* **4**, 409–427 (2009).
35. Li, J. et al. Palladium-triggered deprotection chemistry for protein activation in living cells. *Nat. Chem.* **6**, 352–361 (2014).

Acknowledgements This work was supported by grants from the EPSRC (DTA to C.D.S. and M.K.B.), MINECO (CTQ2017-85496-P to C.R.), AGAUR (2017SGR-1189 to C.R.), Spanish Structures of Excellence María de Maeztu (MDM-2017-0767 to C.R.), EU Horizon 2020 programme, Marie Skłodowska-Curie (67507) and the Royal Society (Wolfson Research Merit Award to B.G.D.). We thank G. Hemberg for useful discussions, P. G. Schultz for provision of initial pEVOL-pPhe plasmid, and BSC-CNS for computer resources and technical support at the MareNostrum supercomputer (RES-QCM-2018-2-0025). The Structural Genomics Consortium is a registered charity (number 1097737) that receives funds from AbbVie, Bayer Pharma AG, Boehringer Ingelheim, Canada Foundation for Innovation, Eshelman Institute for Innovation, Genome Canada, Innovative Medicines Initiative (EU/EFPIA) (ULTRA-DD grant number 115766), Janssen, Merck & Co., Novartis Pharma AG, Ontario Ministry of Economic Development and Innovation, Pfizer, São Paulo Research Foundation-FAPESP, Takeda, and Wellcome Trust (092809/Z/10/Z).

Author contributions M.K.B., S.S.L., C.D.S., W.W.Y. and B.G.D. designed the project. M.K.B., T.M. and M.A.G. carried out chemical synthesis, protein modification reactions, enzymatic assays and associated analysis. H.J.B., S.S.L., C.D.S., M.K.B., T.M. and M.A.G. carried out protein expression. H.J.B. performed protein expression optimization and crystallography experiments. L.R., J.I.-F. and C.R. performed computational experiments. M.K.B., C.R., W.W.Y. and B.G.D. wrote the manuscript. All authors read and commented on the manuscript.

Competing interests The authors declare no competing interests.

Additional information

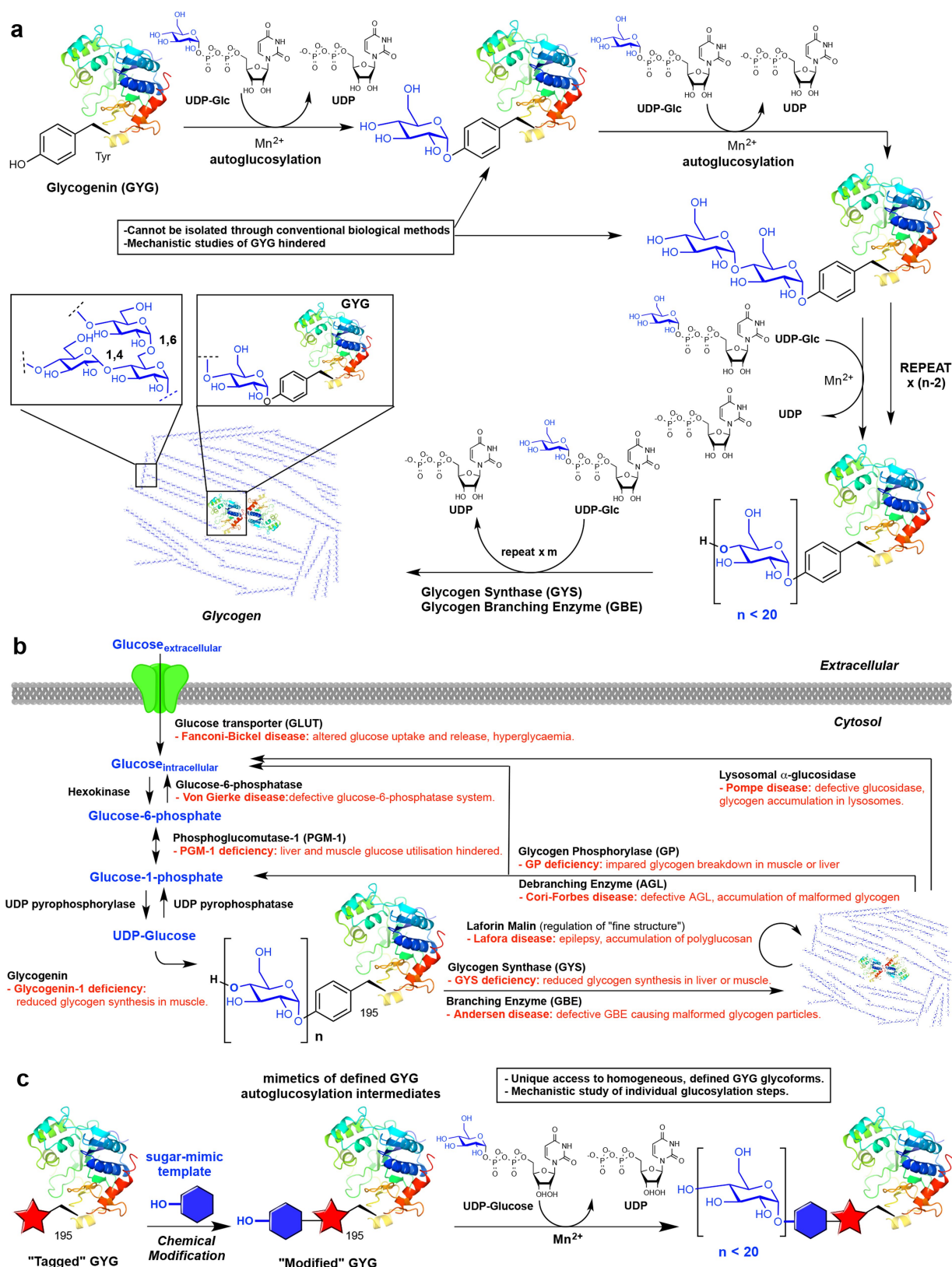
Extended data is available for this paper at <https://doi.org/10.1038/s41586-018-0644-7>.

Supplementary information is available for this paper at <https://doi.org/10.1038/s41586-018-0644-7>.

Reprints and permissions information is available at <http://www.nature.com/reprints>.

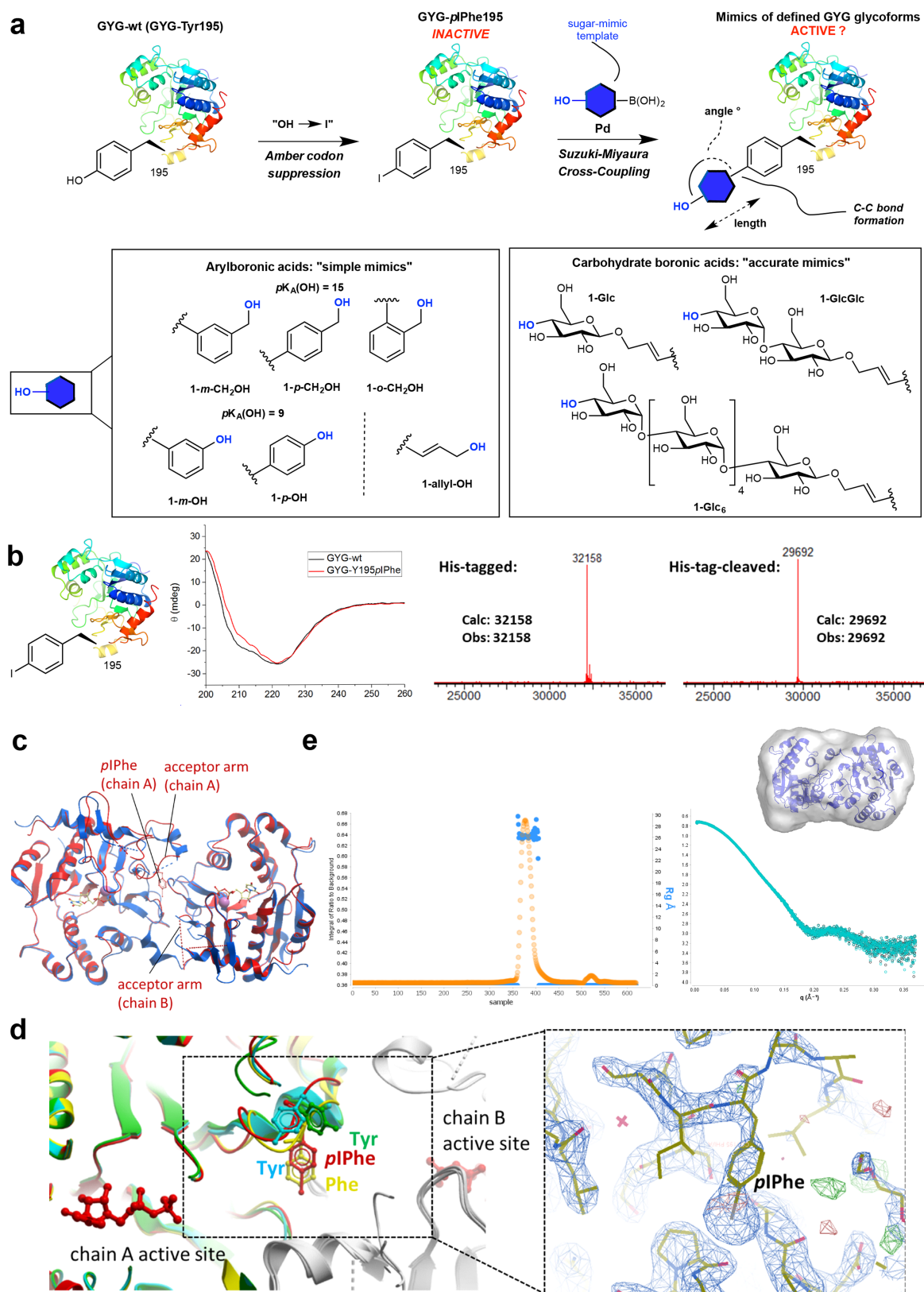
Correspondence and requests for materials should be addressed to W.W.Y. or B.G.D.

Publisher's note: Springer Nature remains neutral with regard to jurisdictional claims in published maps and institutional affiliations.



Extended Data Fig. 1 | Biological and chemical methods for glycogen assembly. **a**, Mechanism of glycogen biosynthesis in eukaryotes. The glycosyltransferase enzyme glycogenin (GYG; top left) catalyses its successive, stepwise autoglucosylation at Tyr195 to form a short enzyme-bound maltooligosaccharide, which undergoes further extension and branching catalysed by glycogen synthase (GYS) and glycogen branching enzyme (GBE) to form mature glycogen particles. Intermediate glucosylation states of glycogenin cannot be isolated in homogeneous form via conventional biological methods, hindering precise mechanistic studies. **b**, The formation of glycogen from GYG placed in the context

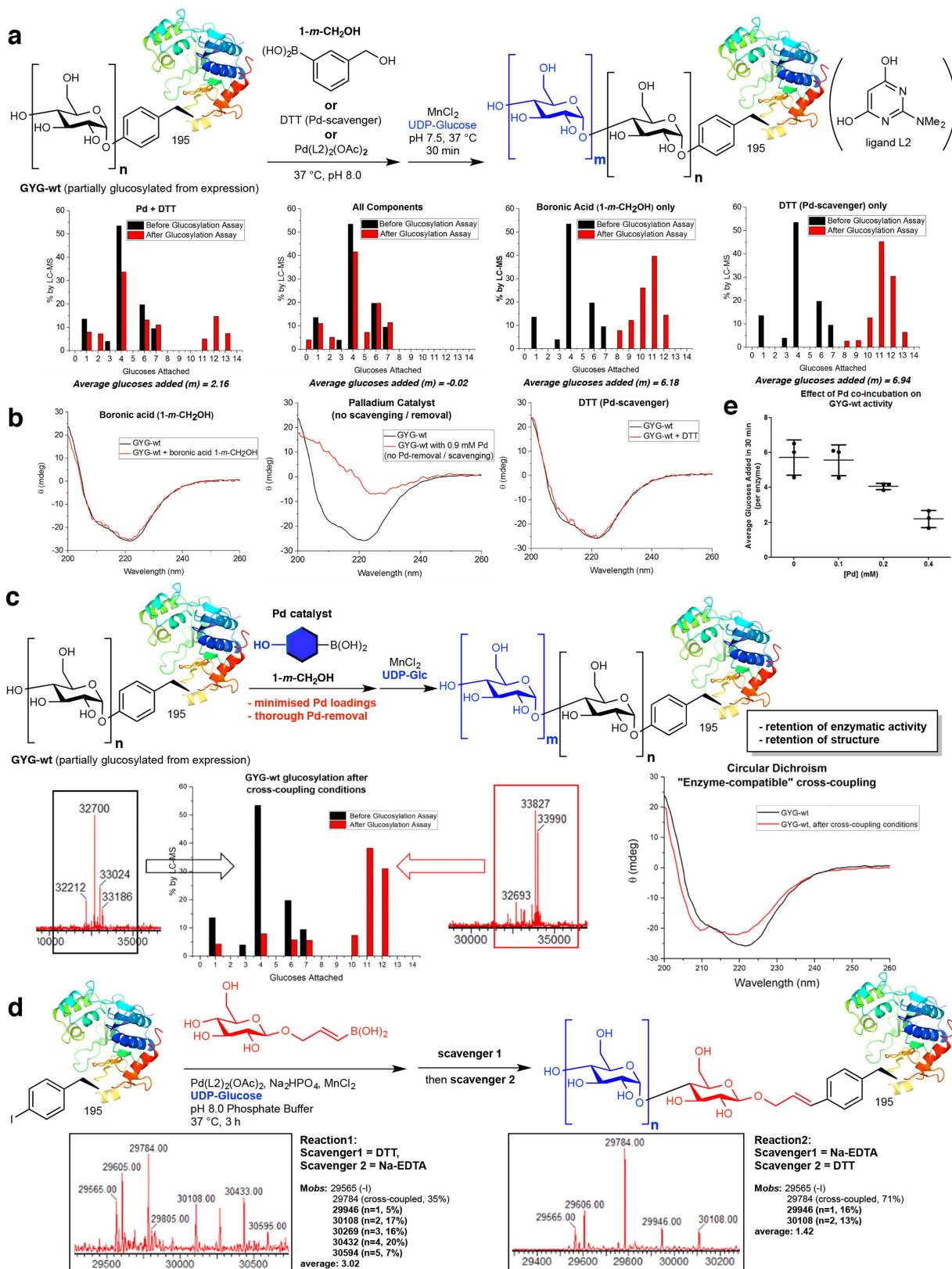
of the entire glycogenesis pathway (beginning from free glucose) and glycogenolysis pathway. A wide range of pathological conditions (text in red) are known to arise from malfunction of one of the many enzymes (text in black) involved. **c**, An alternative chemical method, involving site-selective ligation of sugar-mimic moieties to a GYG species bearing an amino acid 'tag' at the 195 site, may allow direct access to defined, homogeneous GYG glucosylation states corresponding to intermediates along the autoglucosylation pathway. This could, in turn, enable study of GYG mechanism with increased precision, through analysis of individual autoglucosylation steps.



Extended Data Fig. 2 | See next page for caption.

Extended Data Fig. 2 | Development of chemically addressable GYG scaffold as a strategy for mechanistic investigation. **a**, GYG-*p*IPhe195 enzyme (top, middle), which lacks a native glycosyl acceptor and thus cannot undergo glucosylation, represents a suitable substrate for Suzuki–Miyaura cross-coupling to a range of boronic acids (boxed), to generate potentially active enzyme species that mimic defined GYG glycoforms. In this way, inactive GYG-*p*IPhe195 might be activated through C–C bond-forming ligation allowing pre-determined, ‘shunted’ access to intermediate catalyst states of GYG. **b**, Expression of GYG-195*p*IPhe in *Escherichia coli* using a polyhistidine tag removable by TEV cleavage was confirmed by LC-MS (shown; *y* axis, *m/z* ratio) and showed structural similarity to wild-type enzyme. Similar LC-MS spectra were obtained for at least three analogous expressions. Circular dichroism plots (one shown, with ellipticity versus wavelength) are mean averages of three successive measurements of the same sample (*n* = 1). **c**, **d**, Overlay (**c**) and (**d**) enlarged view of the chain A acceptor arm for the structures of GYG-Y195X (Mn²⁺ + UDP; this study) (red), GYG-Phe (Mn²⁺ + UDPG)

(yellow), GYG-WT (Glc₄ + UDP) (blue), and GYG-WT (Glc₆ + UDP) (green). Inset to **d**, $2F_o - F_c$ electron density map for Y195*p*IPhe of the acceptor arm. The acceptor arm in chain B is disordered (marked by red-dashed line in **c**) and probably adopts multiple conformations to accommodate the equivalent *p*IPhe group. **e**, Evidence of dimer formation for GYG in solution. Left, SEC-SAXS signal plot. Each orange point represents the integrated area of the ratio of the sample SAXS curve to the estimated background. Each blue point shows radius of gyration (*R*_g) estimated from the Guinier region for each frame. Right, main panel, logarithmic intensity plot of subtracted and merged SAXS frames. Cyan circles represent averaged buffer frames subtracted from averaged sampled frames. Black circles represent the median of the buffer frames subtracted from the averaged sample frames. Above, aligned, averaged and refined DAMMIN ab initio model (grey) superimposed with the dimeric GYG1 crystal structure (PDB 6eqj) using *supcomb*. SAXS analysis was performed from 16 independent scattering measurements of one biological sample.

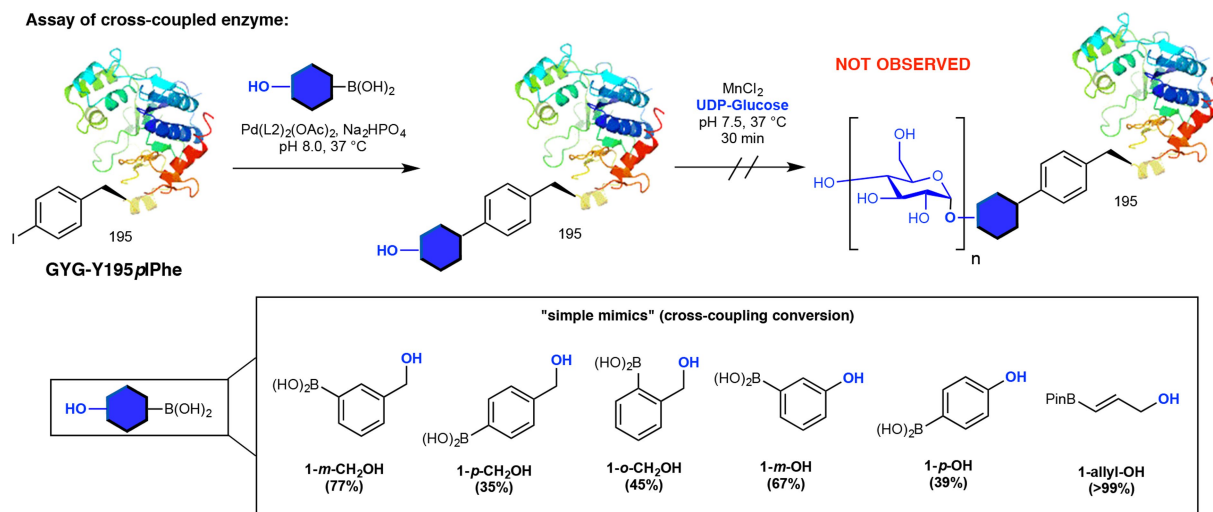


Extended Data Fig. 3 | See next page for caption.

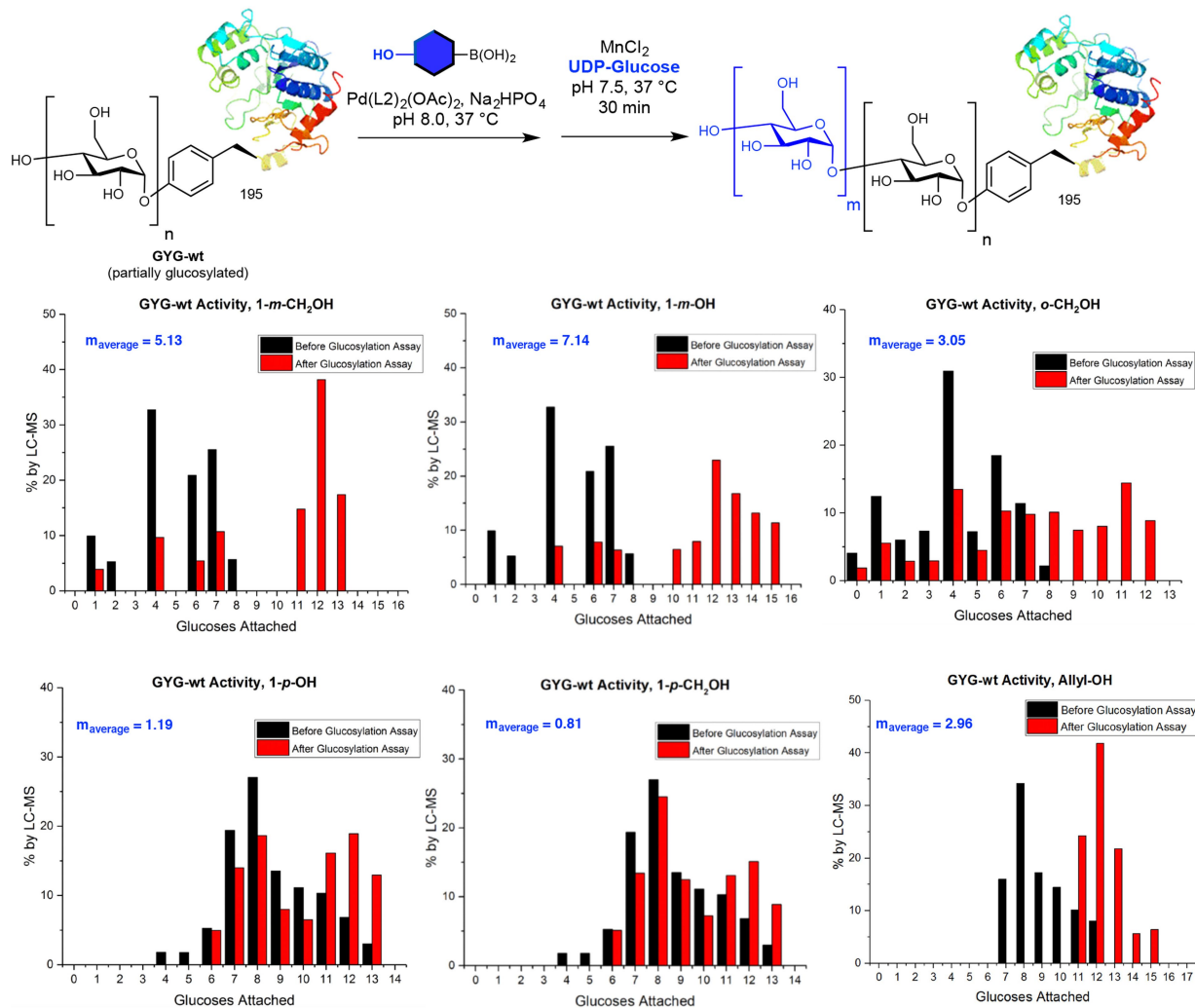
Extended Data Fig. 3 | Effect of Suzuki–Miyaura reagents and conditions on autoglucosylation activity and one-pot Suzuki–Miyaura autoglucosylation. **a**, Effect of different Suzuki–Miyaura reaction (scheme shown) components on GYG-WT activity. Bottom, plots illustrating proportions of glycoforms present before (black) and after (red) glucosylation assay, as calculated from the relative peak intensities of each glycoform in the corresponding LC-MS spectra, and represent single experiments ($n = 1$) carried out in parallel. Boronic acid and the Pd-scavenger DTT (dithiothreitol) did not appear to cause enzymatic inactivation in isolation. In the presence of palladium with limited Pd-removal/refolding steps, either far more limited activity (Pd + DTT) or no activity (all components) was seen. This highlighted that Pd was the key issue regarding GYG-WT activity. **b**, The effect of cross-coupling reaction components on GYG-WT structure, as shown by circular dichroism analysis. Neither DTT nor boronic acid (m -CH₂OH) caused any substantial alteration to secondary structure. Palladium catalyst, however, caused clear alteration of secondary structure. This effect could however be avoided through minimized Pd concentrations and thorough Pd-scavenging and removal (see **c**). Circular dichroism plots represent mean averages of three measurements of the same sample ($n = 1$). **c**, Demonstration of ‘enzyme-compatible’ Pd-mediated ligation.

Through minimizing the Pd concentrations employed, and post-reaction Pd removal, cross-coupling conditions compatible with retention of GYG-WT activity were developed (top row). The plot in the bottom row illustrates proportions of glycoforms present before (black) and after (red) glucosylation assay, as calculated from relative peak intensities of each glycoform in corresponding LC-MS spectra (boxed), and represents a single experiment ($n = 1$; note however that the ‘**1**- m -CH₂OH’ experiment in Extended Data Fig. 4 is near-identical, differing only in glucosylation time). Circular dichroism (rightmost plot, bottom row) additionally confirmed structural similarity of GYG-WT enzyme before and after subjection to optimized cross-coupling conditions. See also Extended Data Fig. 2 for more details of structural analyses by X-ray crystallography. Circular dichroism plots represent mean averages of three measurements of the same sample ($n = 1$). **d**, One-pot SMC of GYG-Y195X and autoglucosylation of GYG-Glc (top row). Autoglucosylation is greater when palladium scavenging is carried out before glucosylation assay quenching (reaction 1) than vice versa (reaction 2). LC-MS data represent single experiments run in parallel ($n = 1$). **e**, Average number of glucoses added per enzyme upon treatment of GYG-WT in the presence of varying final concentrations of Pd (0, 0.1, 0.2, 0.4 mM). Data are mean average of three independent replicates ($n = 3$); error bars are ± 1 s.d.

Assay of cross-coupled enzyme:



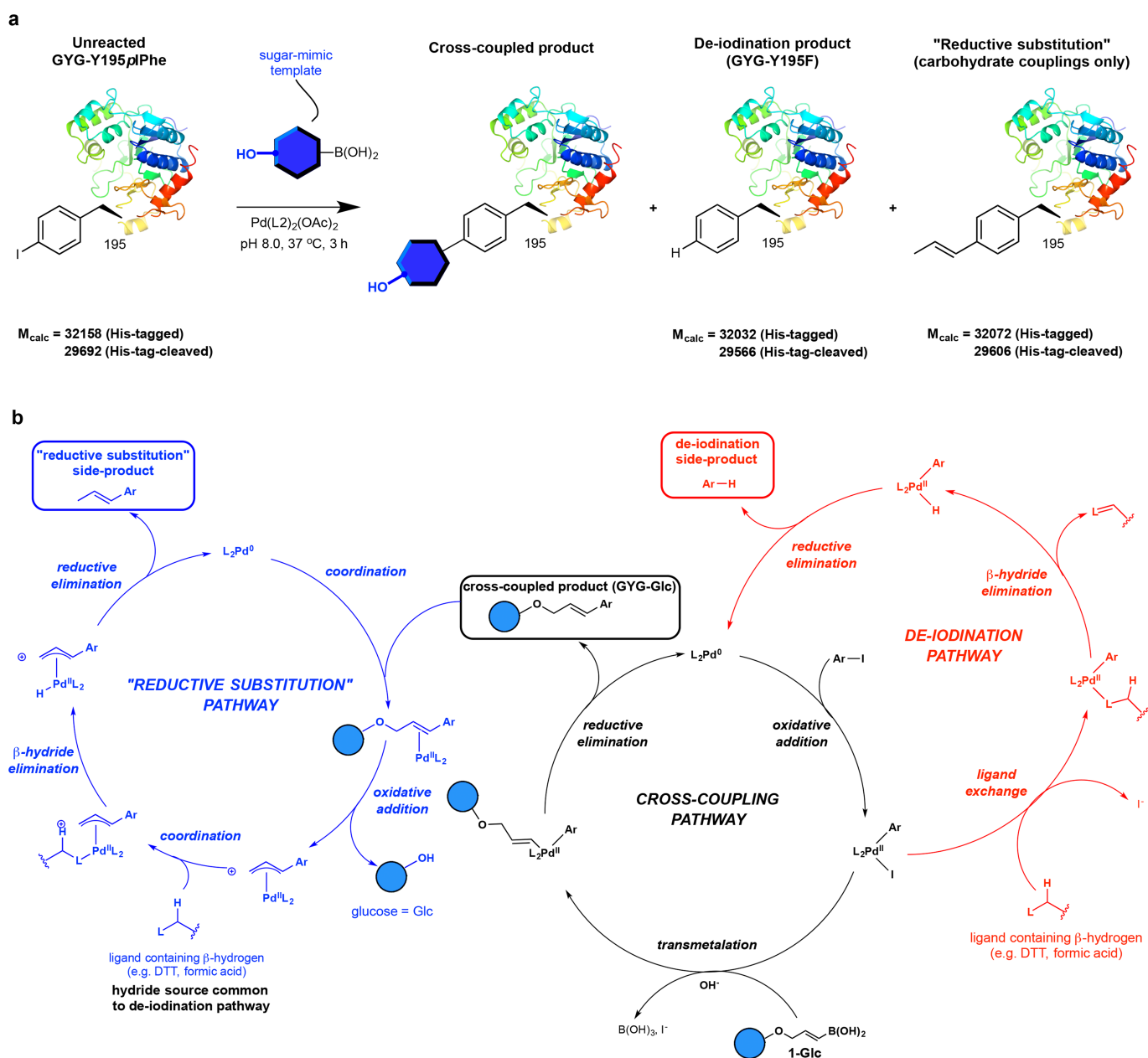
GYG-wt positive control, run in parallel:



Extended Data Fig. 4 | See next page for caption.

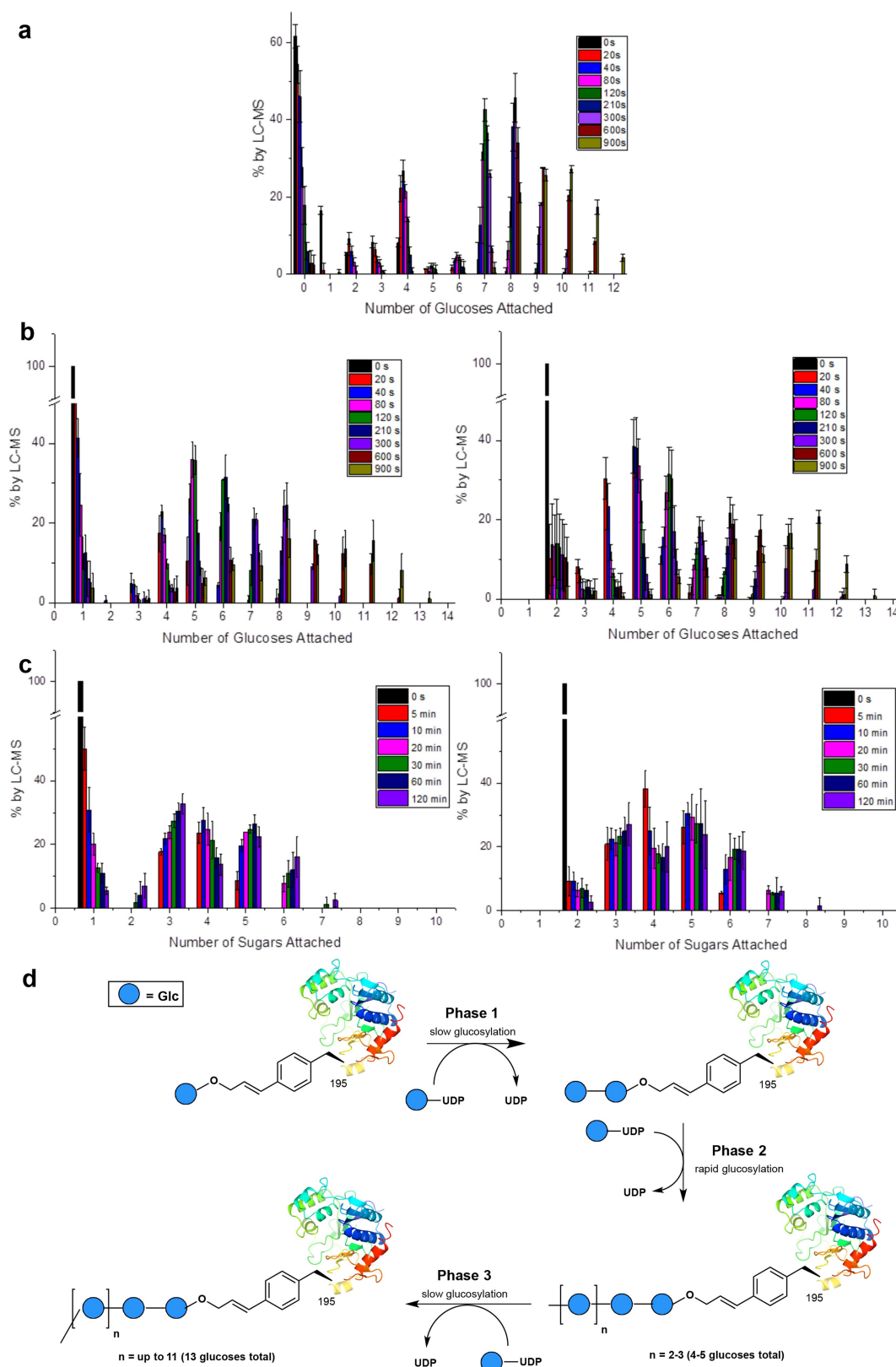
Extended Data Fig. 4 | Cross-coupling to ‘simple mimics’ and assessment of catalytic activity of products. Top row, ‘simple’ substrate templates were introduced using aryl boronic acids **1-*o*-CH₂OH**, **1-*m*-CH₂OH**, **1-*p*-CH₂OH** (exploring different angles of nucleophile display) and **1-*m*-OH**, **1-*p*-OH** (exploring reduced nucleophile length with similar angles) (shown in second row). These proceeded with useful to high conversions (Supplementary Methods, Section 6) to allow the direct creation of systematically altered GYG conjugates bearing substrate mimics: **GYG-*o*-CH₂OH**, **GYG-*m*-CH₂OH**, **GYG-*p*-CH₂OH**, **GYG-*m*-OH**, **GYG-*p*-OH**. LC-MS analysis showed that none of the cross-coupled products showed autoglucosylation activity (upper scheme, detail in Supplementary Methods, Section 6). Irrespective of the systematically varied nature of the glycan-mimic substrate templates (orientation,

length or pK_a), none led to efficient mimicry of substrate moiety and hence activation of autoglucosylation. Notably, also, the truncated, ‘linker-only’ variant **GYG-allyl-OH** was inactive, highlighting further the critical need of an effective mimic moiety for such ‘shunting’. Thus, despite successful Pd-mediated ligation, these ‘simple’ templates provided ineffective mimicry. Identically treated GYG-WT, run in parallel as a positive control in each case, showed detectable activity (central scheme). Bar charts (bottom two rows) are graphical representations of the LC-MS data for treated GYG-WT, showing abundances of each GYG glycoform before (black) and after (red) autoglucosylation assay. Bar charts are representations of single LC-MS experiments ($n = 1$, Supplementary Tables 13, 14).



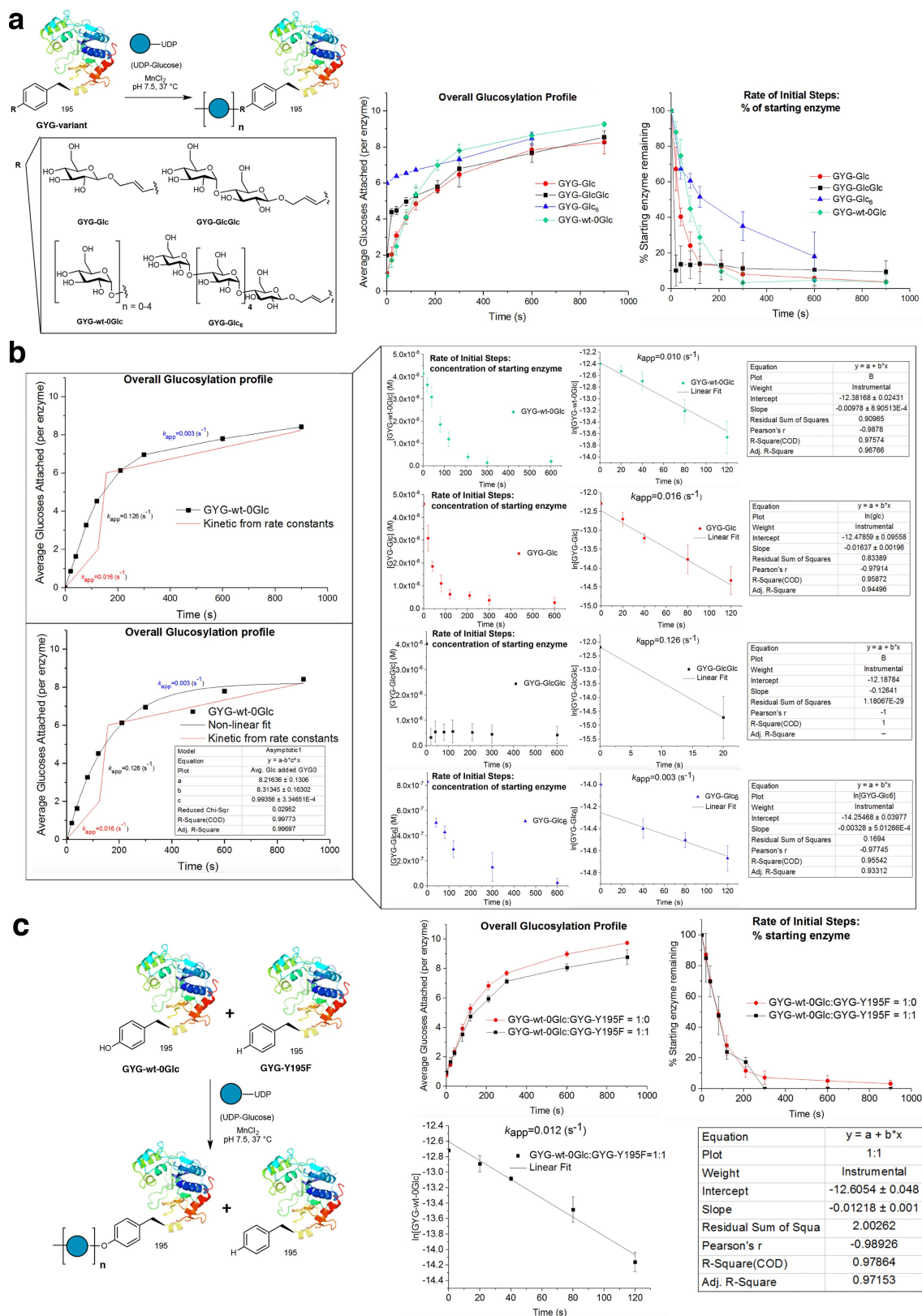
Extended Data Fig. 5 | Proposed species observed during cross-couplings to GYG-Y195X and possible mechanisms responsible for their formation. **a**, Left to right, unreacted GYG-Y195X (in certain cases), cross-coupled product, de-iodination product, and a species observed uniquely in carbohydrate couplings and proposed to result from 'reductive substitution' of the carbohydrate moiety (with 'hydride', probably from a hydrido-palladium species). **b**, Formation of cross-coupling side-products is illustrated using coupling to boronic acid **1-Glc** as an example. The relationship of these possible mechanisms to that of productive Suzuki–Miyaura cross-coupling is highlighted. The generally accepted mechanism for de-iodination (red) involves coordination of a β-hydride-containing ligand to Pd following the initial oxidative addition step of

cross-coupling; subsequent β-hydride elimination affords a hydrido-palladium species, reductive elimination from which affords de-iodinated side-product. 'Reductive substitution', seen here for carbohydrate systems only (blue), could be rationalized by the well documented ability of Pd to cleave C_{allyl}–O bonds, including those of allylic glycosides such as GYG-Glc, to form a π-allyl species. Quenching of the latter with the same hydrido-palladium complex as invoked in de-iodination—such use of a 'hydride scavenger' in Pd-catalysed de-allylation is a well documented process^{36–38}—would result in a 'reductive substitution' product, that is, replacement of the carbohydrate moiety (here, glucose) with hydride. Blue sphere, Glc, 'Ar–I', pI_Phe195 of GYG.



Extended Data Fig. 6 | Distributions of glycoforms in assays of GYG variants and the proposed triphasic mechanism. a, Species with up to 12 glucose sugar residues attached are observed during autoglucosylation of GYG-WT-0Glc after 900 s reaction time (the key shows reaction time). Glc-0 is slow to decline, while accumulation of later glycoforms (for example, Glc-7, Glc-8) is observed. This is consistent with the slow-fast-slow profile observed for the cross-coupled system, highlighting the relevance of the latter. **b,** Species with up to 13 sugars attached are observed during autoglucosylation of GYG-Glc (left) and

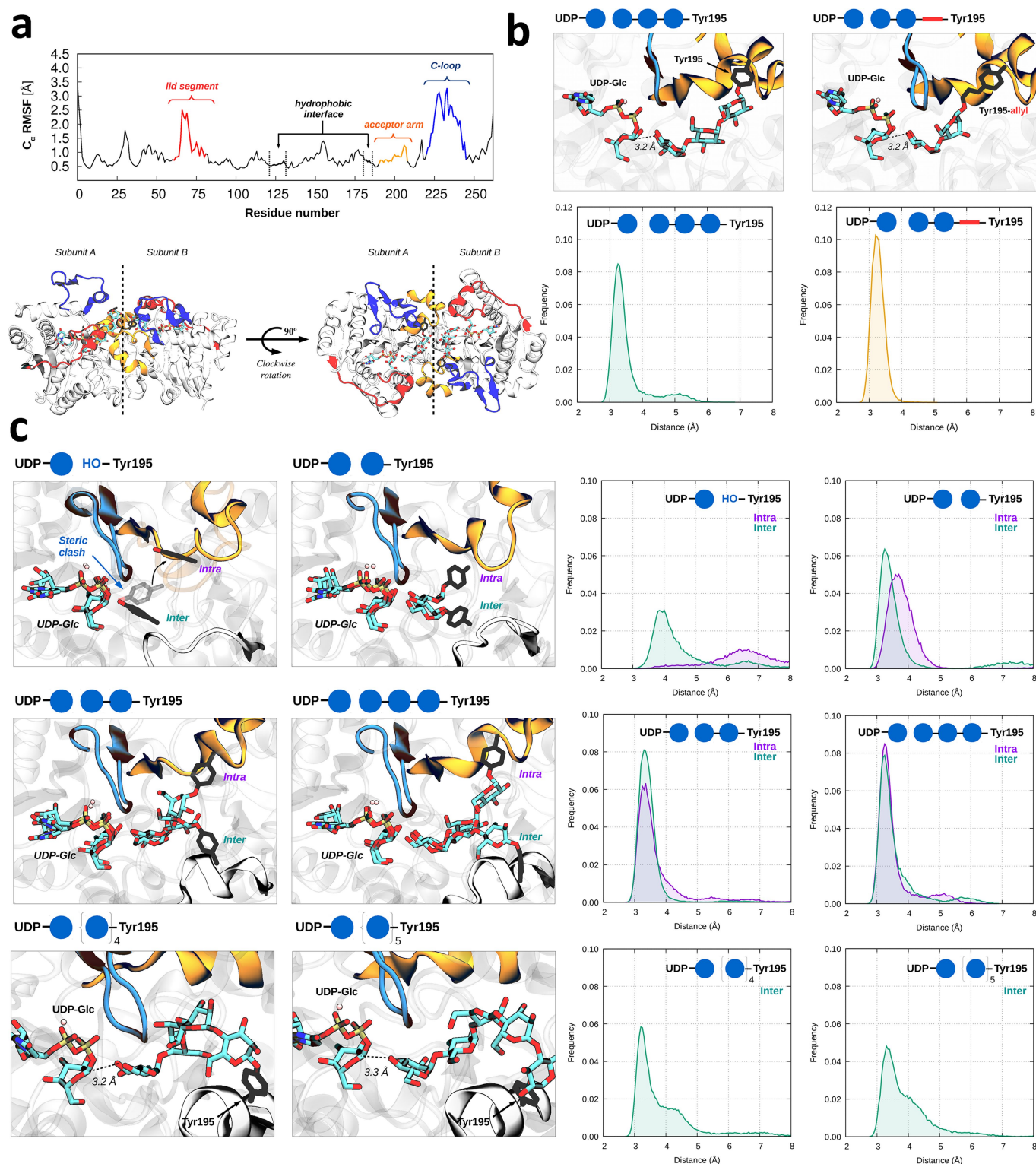
GYG-Glc-Glc (right). **c,** No species with more than 8 sugars is seen during autoglucosylation of the same enzymes even after 120 min reaction time. Data represent mean averages from n independent replicate kinetic assays ($n = 4$ for GYG-Glc glucosylation, $n = 5$ for GYG-Glc-Glc glucosylation, $n = 3$ for all others). Error bars are ± 1 s.d. **d,** Proposed triphasic mechanism inferred from kinetic experiments. GYG-Glc-Glc exhibits only two distinct phases (fast \rightarrow slow); the slower initiation step for GYG-Glc represents an additional first (slow) phase before reaching the disaccharide of GYG-Glc-Glc.



Extended Data Fig. 7 | See next page for caption.

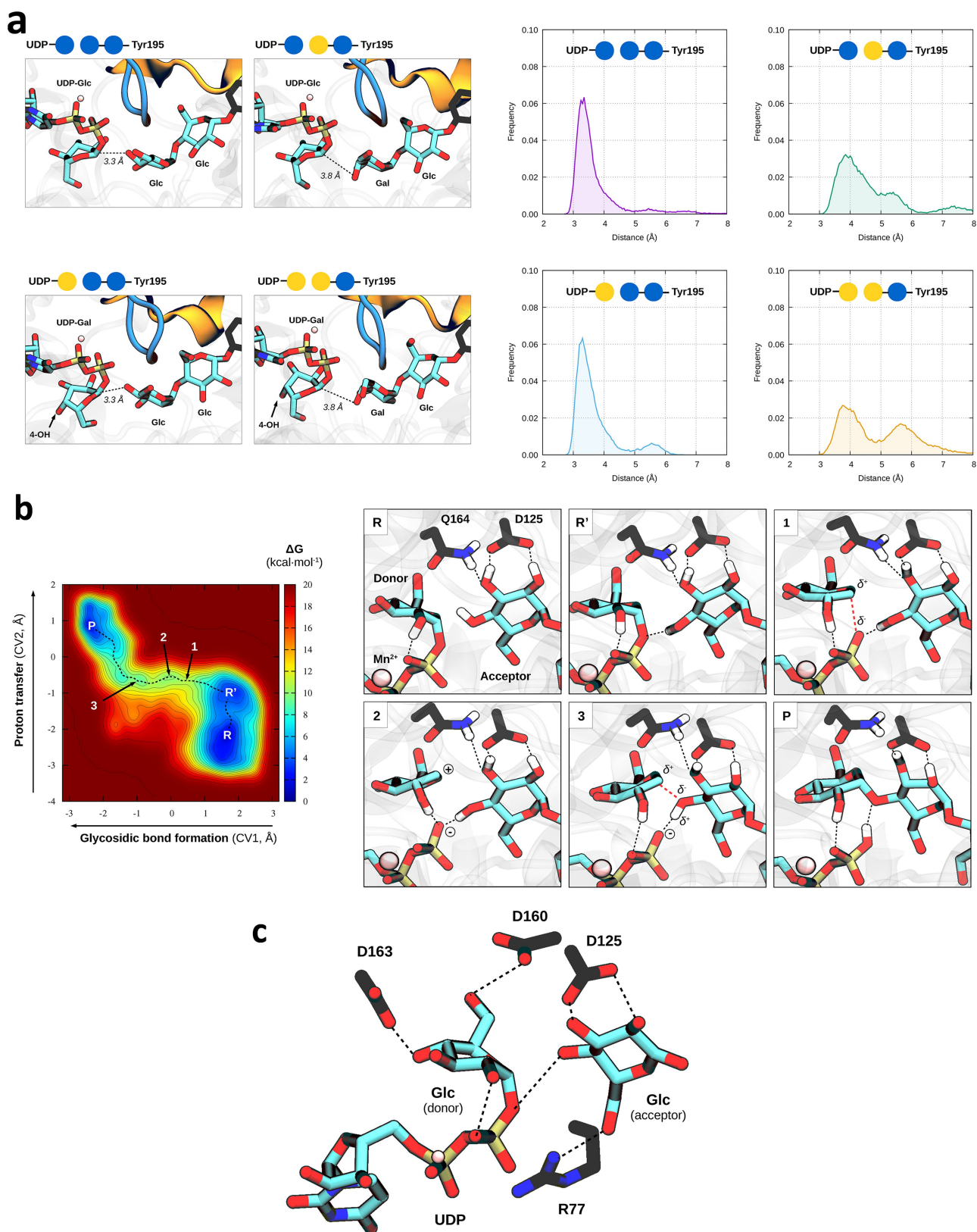
Extended Data Fig. 7 | Kinetic analyses and comparison of GYG-WT-0Glc with ‘shunted’ GYG-glycomimetics. **a**, Left, reaction scheme (top) with R variants under (boxed). Right, overlaid kinetic profiles (left plot) and initial rates (right plot) for GYG-WT-0Glc, GYG-Glc, GYG-Glc-Glc and GYG-Glc₆. Data are shown as mean \pm s.d. from n independent replicate kinetic assays ($n = 4$ for GYG-Glc, $n = 5$ for GYG-Glc-Glc, $n = 3$ for GYG-WT-0Glc, $n = 2$ for GYG-Glc₆). **b**, Apparent rate constants for autoglucosylation of GYG-WT-0Glc, GYG-Glc, GYG-Glc-Glc and GYG-Glc₆ allowed us to re-construct, using autoglucosylation kinetic parameters of each of the ‘shunted’ glycomimetics (right), an autoglucosylation profile in good agreement with the GYG-WT-0Glc kinetic data (left: top overlay, profile; bottom overlay, nonlinear fit). Data

are shown as mean \pm s.d. for n independent replicate kinetic assays ($n = 4$ for GYG-Glc, $n = 5$ for GYG-Glc-Glc, $n = 3$ for GYG-WT-0Glc, $n = 2$ for GYG-Glc₆). **c**, To ensure that there were no potential artefactual catalytic effects from a de-iodinated side-product giving rise to this previously unobserved rapid phase via intermolecular glucosylation, we also explored its effect when added in pure form to reactions (scheme shown left); rather than any enhancement it gave rise only to slight suppression, thereby discounting this possibility. Observed rates (k -values) are essentially independent of levels of GYG-Y195F, which lacks native acceptor capacity, highlighting that our conclusions are not influenced by such cross-coupling side products. Data are shown as mean \pm s.d. for n independent replicate kinetic assays ($n = 3$).



Extended Data Fig. 8 | Glycogenin dynamics, glycoform mimics and active site structure considering acceptors of different length. a, Root mean square fluctuation (RMSF) of the enzymatic C α atoms (top). Results are obtained from the MD simulations of the intra 'UDP-Glc + GYG-WT-Glc3' Michaelis complex. Coloured segments in plot correspond to the regions coloured in the structure below (see Supplementary Information for details). **b**, Top, modelled complex of the GYG glycoform mimic (right column), in comparison with the WT complex (left column). Blue balls represent Glc units, and the red and thin rectangle represents the allyl moiety. Bottom, normalized distributions of the donor-acceptor C1-O4 distances. Both inter and intra conformations gave similar results. **c**, Structural superposition of intra and inter conformations for 'UDP-Glc + GYG-WT-Glc n ' complexes, with $n = 0$ to $n = 5$ Glc units (six left-

hand panels). The orange loop corresponds to the acceptor arm of the same subunit of the active site that is displayed (that is, intra), and the white loop is the acceptor arm of the opposite subunit (inter). The protein loop coloured in blue hinders the approach of short acceptors in intra conformations. Specifically, the loop clashes with Tyr195 for the $n = 0$ (intra), causing it to move away from the donor, as indicated by the black arrow. The $n = 1$ (intra) is also affected by the loop, as reflected in the shift of the corresponding C1-O4 frequency peak. Frequency distributions are shown in the respective six right-hand panels. Each distribution was obtained from 0.4 μ s of simulation data. The maximum frequency peak for intra/inter conformations correspond to 6.4/3.8 Å ($n = 0$), at 3.6/3.2 Å ($n = 1$), 3.3/3.3 Å ($n = 2$) and 3.2/3.2 Å ($n = 3$). Hydrogen atoms have been omitted for clarity.



Extended Data Fig. 9 | Glycogenin plasticity and simulations of the glucosylation reaction mechanism. a, Modelled intra 'UDP-Glc + (Glc)₂-Tyr195' complexes (panels on left) and normalized distribution of the C1–O4 distances considering donor and acceptor Gal variants (panels on right). The change of Glc (blue) to Gal (yellow) in the acceptor displaces the reactive hydroxyl by 0.5 Å (from 3.3 Å to 3.8 Å). The Gal modification at the donor site displays alternative conformations (not shown) in which the OH-2 and OH-3 substituents interact with D163. Hydrogen atoms have been omitted for clarity. **b**, Computed free-energy landscape for the intra 'UDP-Glc + GYG-WT-Glc3' reaction catalysed by GYG (contour

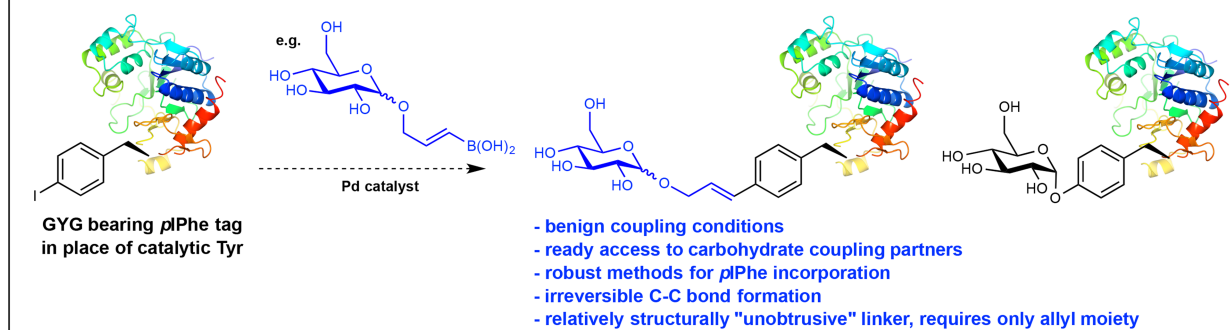
lines at 1 kcal mol^{−1}; left panel) and atomic rearrangement along the reaction pathway (six panels on the right). Hydrogen atoms have been omitted for clarity, except OH-2, OH-3 and OH-4 of the acceptor sugar, the OH-2 of the donor sugar and those of the side-chain amide NH₂ of Q164. Bonds being broken/formed are represented as dashed red lines (snapshots 1 and 3). **c**, Hydrogen-bond interactions (dashed lines; from PDBs 3T7O, 3U2V and 3U2U) that were restrained during the first steps of the initial classical MD simulations. Q164, interacting with the acceptor OH-3, is not shown for clarity.

Required "tagged" GYG

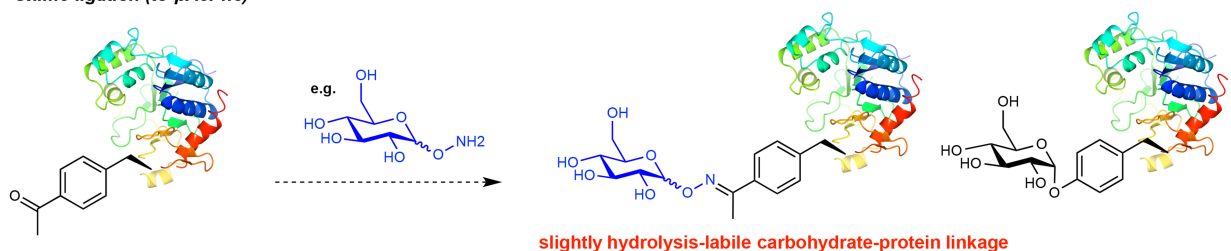
Resultant GYG Glycoform

Corresponding Natural Glycoform

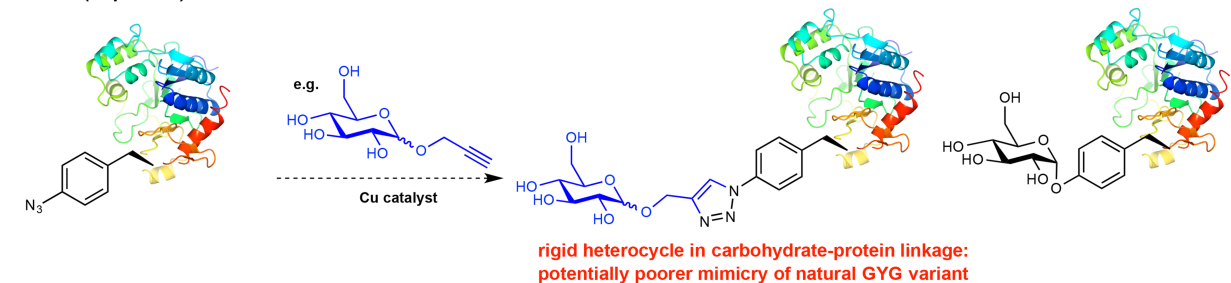
Suzuki-Miyaura cross-coupling (to pIPhe) - CHOSEN STRATEGY



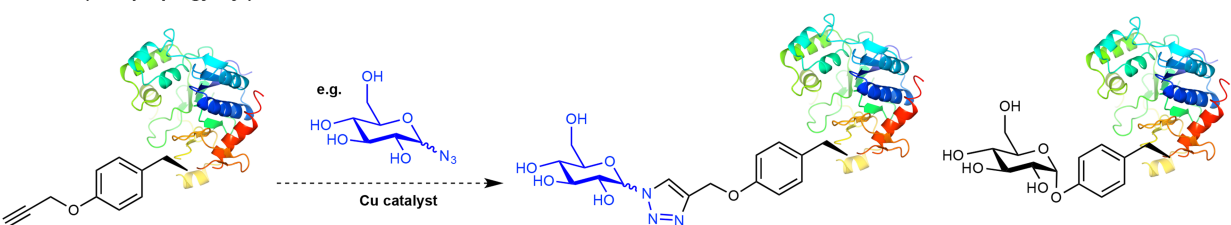
Oxime ligation (to pAcPhe)



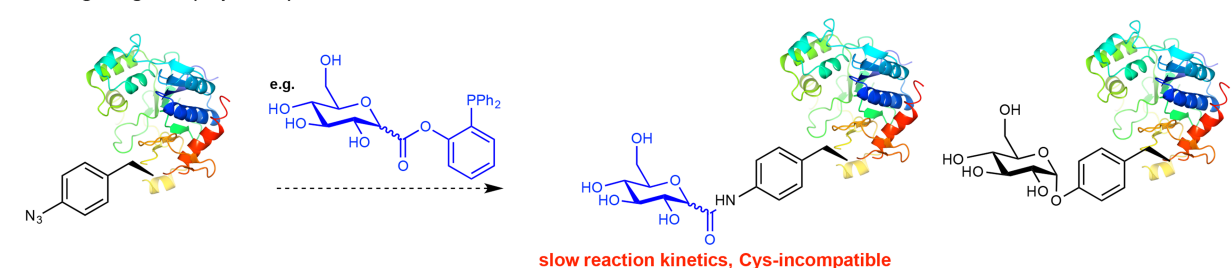
CuAAC (to pAzPhe)



CuAAC (to O-propargyl Tyr)



Staudinger Ligation (to pAzPhe)



36. Guibé, F. Allylic protecting groups and their use in a complex environment Part II: allylic protecting groups and their removal through catalytic palladium π -allyl methodology. *Tetrahedron* **54**, 2967–3042 (1998).
37. Tsuji, J. New general synthetic methods involving π -allylpalladium complexes as intermediates and neutral reaction conditions. *Tetrahedron* **42**, 4361–4401 (1986).
38. Tsuji, J. & Yamakawa, T. A convenient method for the preparation of 1-olefins by the palladium catalyzed hydrogenolysis of allylic acetates and allylic phenyl ethers with ammonium formate. *Tetrahedron Lett.* **20**, 613–616 (1979).

Reassessing evidence of life in 3,700-million-year-old rocks of Greenland

Abigail C. Allwood^{1*}, Minik T. Rosing², David T. Flannery¹, Joel A. Hurowitz^{3*} & Christopher M. Heirweh¹

The Palaeoarchean supracrustal belts in Greenland contain Earth's oldest rocks and are a prime target in the search for the earliest evidence of life on Earth. However, metamorphism has largely obliterated original rock textures and compositions, posing a challenge to the preservation of biological signatures. A recent study of 3,700-million-year-old rocks of the Isua supracrustal belt in Greenland described a rare zone in which low deformation and a closed metamorphic system allowed preservation of primary sedimentary features, including putative conical and domical stromatolites¹ (laminated accretionary structures formed by microbially mediated sedimentation). The morphology, layering, mineralogy, chemistry and geological context of the structures were attributed to the formation of microbial mats in a shallow marine environment by 3,700 million years ago, at the start of Earth's rock record. Here we report new research that shows a non-biological, post-depositional origin for the structures. Three-dimensional analysis of the morphology and orientation of the structures within the context of host rock fabrics, combined with texture-specific analyses of major and trace element chemistry, show that the 'stromatolites' are more plausibly interpreted as part of an assemblage of deformation structures formed in carbonate-altered metasediments long after burial. The investigation of the structures of the Isua supracrustal belt serves as a cautionary tale in the search for signs of past life on Mars, highlighting the importance of three-dimensional, integrated analysis of morphology, rock fabrics and geochemistry at appropriate scales.

Earth's earliest fossil assemblages are important for understanding the origins of life on Earth and, by analogy, how and where to search for signs of primitive life in the rock record of other planets². The oldest widely accepted evidence of life on Earth is in marine metasedimentary rocks of the Pilbara Craton, Australia, in the form of a microbial stromatolite reef^{3,4} and fossil biofilms⁵ of the 3,450-million-year-old (Myr) Strelley Pool Formation. Putative microfossils⁶ (Strelley Pool Formation) and stromatolites (3,490-Myr-old Dresser Formation)⁷ also occur in the Pilbara Craton, but their biogenicity is equivocal⁸. In Greenland, geochemical features compatible with microbial activity exist^{9,10}, but their interpretation has been questioned^{11–13}. The presence of 3,700-Myr-old stromatolites in Greenland's Isua supracrustal belt (ISB), if true, would represent an entirely new and compelling type of biosignature in Earth's oldest rocks and establish the start of the fossil record 200 Myr earlier than previously thought¹.

The putative stromatolites, discovered approximately 150 km northeast of Nuuk (Extended Data Fig. 1), were described¹ as elongate cones and domes 1–4 cm high, with apices pointing upward relative to overturned sedimentary bedding. Combining those attributes with: (1) internal stromatolitic lamination that is continuous across the crests of the structures; (2) diverse morphologies similar to younger stromatolites; (3) associated shallow-water sedimentary features, including sedimentary onlap; (4) differences in chemical composition inside the structures compared to surrounding sedimentary rock; (5) the presence of low temperature dolomite; and (6) seawater-like rare earth element

and yttrium (REE + Y) composition of the dolomite, it was proposed in the previous study¹ that the structures are stromatolites produced by microbial communities in a shallow marine, carbonate-platform environment similar to the stromatolites in the Strelley Pool Formation^{3,4}. Preservation of these features was attributed to an approximately 30-m × 70-m low-deformation lacuna in the hinge of an anticline¹.

We located the discovery outcrops using data from the previous study¹. Site A consists of brownish-grey layered dolomitic rock, with light-grey triangular features mostly oriented apex-up relative to the overturned layering. However, some are apex-down (Fig. 1a and Extended Data Fig. 2c), which is inconsistent with upward growth of the structures from a palaeo-seafloor. Dolomitic breccia nearby (site C) was previously interpreted as a tempestite (storm deposit), which in turn was taken as evidence of a shallow-water, ice-free sedimentary environment¹. However, a wider view of the outcrop shows ductile and brittle deformation of the clasts, including extreme elongation when viewed from the side (Extended Data Fig. 3), indicating that the breccia has a tectonic origin and has no bearing on water depth, ice or other sedimentary conditions.

A sample was acquired approximately 0.5 m from the original 'stromatolite' sample site of site A¹⁴, including one of the triangular structures (Extended Data Fig. 2). Cut parallel to the weathered face (face 1, Fig. 1c–e), the sample shows irregularly layered light- and medium-grey quartz–dolomite layers with dark micaceous layers and foliation. An array of millimetre- to centimetre-scale convex-up features, of which the triangle structure is the largest, all have subparallel axial planes (Fig. 1c, d). Notably, the base of the triangular structure is also convex-up and conformable with small convex-up features in the underlying quartzose layers. The fabric is extensively disrupted by planar discontinuities, or spaced cleavage, subparallel to the axial planes of the convex-up features (Fig. 1c). By contrast, when viewed orthogonally (face 2, Fig. 1b), the rock shows flat, even layering without any stromatolites, bumps or irregularities (Fig. 1b, e and Extended Data Fig. 4).

Such orientation-dependent, contrasting fabrics are inconsistent with sedimentary processes. Rather, they are typical deformation fabrics found in a multi-layered rock that has been shortened in one direction (parallel to layering), producing minor folds, cleavage and other compressional features similar to those observed on face 1; and substantially lengthened in an orthogonal direction, producing extensional rod-like features such as those observed on face 2. The type of deformation indicated is consistent with the structural setting of the rock, within the hinge of an anticline¹.

Accordingly, cuts parallel to face 1 show that the 'stromatolites' are not cones or elongate cones, but ridges extending at least 10 cm (our sampling depth) into the rock, aligned with the lengthening direction. The ridges probably extend further, given the extreme elongation of the rock fabric observed in the outcrop. Photographs published in the previous study¹ suggest that the structure that they sampled is also ridge-shaped. Although ridge morphology alone does not preclude biological origins, it is easier to produce ridges abiotically than cones^{3,4}. More importantly, a deformational origin is more plausible given the

¹Jet Propulsion Laboratory, California Institute of Technology, Pasadena, CA, USA. ²Natural History Museum of Denmark, University of Copenhagen, Copenhagen, Denmark. ³Department of Geosciences, Stony Brook University, Stony Brook, NY, USA. *e-mail: abigail.c.allwood@jpl.nasa.gov; joel.hurowitz@stonybrook.edu

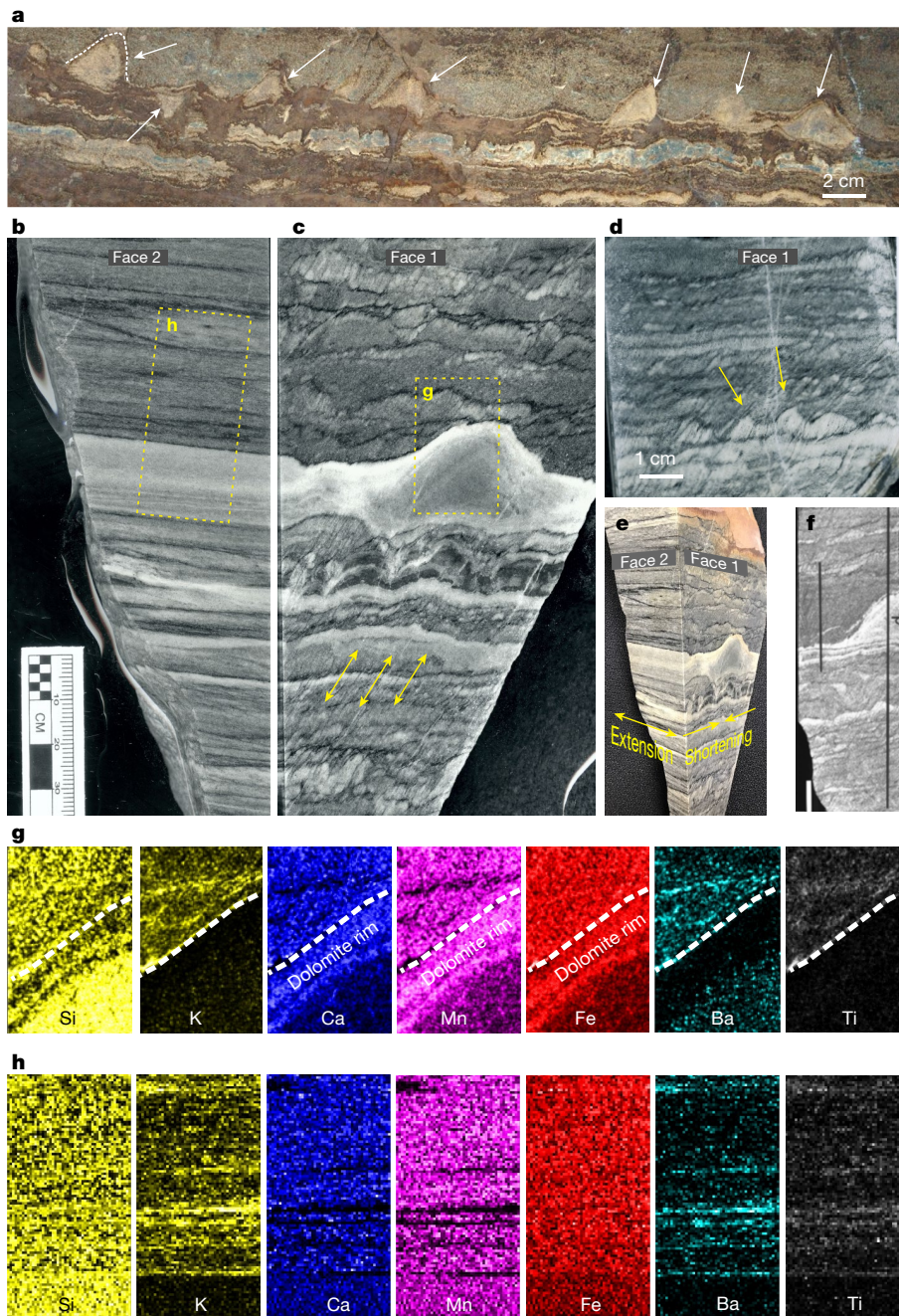


Fig. 1 | Putative stromatolites of Greenland. **a**, Seven structures in outcrop (arrows, white dashed line). **b–d**, Sample from site A. **b**, Face 2 shows even, parallel layering. **c**, **d**, Face 1 shows irregularly layered fabric with planar discontinuities (arrows in **c**) and convex-up features (two yellow arrows in **d**). Yellow dashed boxes indicate panels expanded in **g**, **h** as indicated. **e**, Oblique view of the sample. **f**, Sample from the previous study¹, equivalent to face 1. Lines indicate the path of X-ray fluorescence

scans in the previous study¹. The ‘d’ denotes their scan through the stromatolite. **g**, PIXL element maps of stromatolite and matrix (yellow box in **c**). Dashed line marks the edge of the structure, below which the composition shows a gradient from a Ca–Mn–Fe-rich rim to a Si-rich interior. **h**, PIXL maps of the light-grey layer (yellow box in **b**) show elemental composition, including Ti and K depletion, identical to the ‘stromatolite’.

alignment of the ridges with the lengthening direction indicated by the rock fabrics.

The previous study¹ included outcrop photographs of thin, recessive laminae that tangentially truncate against a structure, which the authors use as evidence of seafloor growth of a stromatolite. However, similar truncation occurs in our sample where micaceous foliation terminates against the triangular structure—an observation that is consistent with the presence of a rigid object (the quartzose ridge) in a ductilely deforming rock, leading to deflection and pressure solution of the mica and carbonate foliation on the shortening side. Tangentially truncated laminae observed in the thin section¹ occurred at site B. However, the

putative stromatolitic structures from site B illustrated in the previous study¹ are very different from those at site A: the published image only shows an undulose lithologic contact (Fig. 2b of the previous study¹).

PIXL (planetary instrument for X-ray lithochemistry) micro-X-ray fluorescence maps of elemental composition cast new light on putative evidence for biological activity¹. First, maps of the distribution of the elements calcium, iron and manganese show that ‘stromatolitic’ lamination internal to the structures is actually a dolomitic alteration rim on a quartzose interior (Fig. 1g) and that there is no other compositional relict of internal lamination in the structures. Second, titanium and potassium are depleted not only in the ‘stromatolites’ but also throughout the

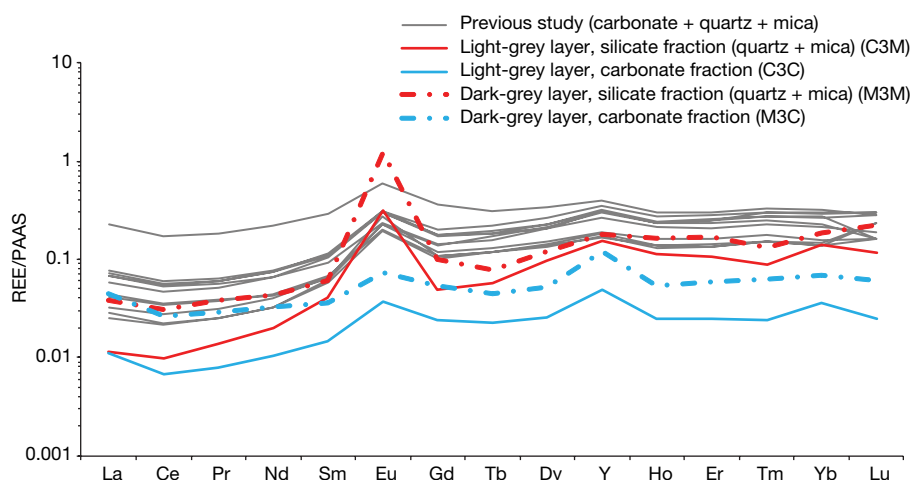


Fig. 2 | Relative abundance of REE + Y for different components of the Isua rock samples. Blue and red lines, our sample, which was separated into silicate and carbonate fractions. Grey lines, sample analysed in the previous study¹, combining carbonate and silicate. All have light rare earth elements (LREE) element depletion (Pr/Yb of $\ll 1$), Y/Ho ratio of ≥ 30 ,

quartzose layers (Fig. 1h), owing to the fact that they have considerably less potassium- and titanium-bearing mica compared to the dark layers. Finally, the iron and silicon maps show iron-rich/silicon-poor dark layers and silicon-rich/iron-poor light layers, suggesting that the rock may have originally consisted of intercalated cherty and iron-rich strata, which is consistent with previous studies and our observations of carbonate-altered banded iron formation and cherty metasediments in nearby outcrops¹⁵.

In the previous study, low-temperature dolomite formation was inferred from C and O isotopes, and this was interpreted as evidence of biogenic dolomite formation in the sedimentary environment¹. However, the role of microbes in low-temperature dolomite formation is equivocal¹⁶. Furthermore, low temperature does not preclude secondary origins—an hypothesis supported by the presence of dolomite alteration rims observed in PIXL maps (Fig. 1g).

The REE + Y geochemistry of dolomite was mentioned as evidence of primary marine carbonate sedimentation in the previous study¹. However, synchrotron X-ray fluorescence element maps show that the 800- μm -wide laser-ablation inductively coupled plasma-mass spectroscopy scans collected by Nutman et al.¹ would have sampled a mixture of dolomite, quartz and micas. Therefore, their REE + Y patterns cannot be attributed to dolomite alone. Micas, in particular, are important trace element carriers in these rocks (Extended Data Fig. 6 and Supplementary Information).

To resolve this uncertainty, we separated carbonate and silicate (quartz and mica) fractions (Extended Data Fig. 5) by acid digestion and measured the REE + Y by mass spectroscopy (Fig. 2 and Extended Data Table 1). Both have REE + Y patterns broadly consistent with the properties of Archean to Paleoproterozoic seawater^{17–19}. However, the overall abundance is higher in the silicates than carbonates, and higher in the mica-rich silicate sample than in the mica-poor silicate sample. These observations can be attributed to a high REE + Y concentration in micas. The silicate REE + Y pattern also has a larger positive Eu anomaly than the carbonate, indicating a different origin of the silicates compared to carbonate. Given the observed carbonate alteration of quartz (Fig. 1g), the most plausible interpretation is that the carbonate REE + Y composition was inherited from diagenetic and/or metasomatic fluids. In summary, the texture-specific distribution of major and minor elements, and the REE + Y composition of the rocks are consistent with original deposition in a marine environment, followed by secondary carbonate alteration any time between early diagenesis²⁰ and late carbonate metasomatism—the latter process having been well-documented in nearby ISB meta-sedimentary rocks¹⁵.

positive La and Eu anomalies, broadly consistent with Archean seawater origins. However, carbonate and silicate fractions are different in abundance (due to mica) and pattern, including a more pronounced positive Eu anomaly in the silicate fractions. PAAS, post-Archean Australian Shale composite.

Therefore, we propose that none of the previously published results support the interpretation of the ISB structures as stromatolites: they lack internal lamination and we found no evidence of synsedimentary growth. Their triangular ridge shape is not an indicator of biogenicity and they do not exhibit unique chemical compositions that indicate a localized microbial influence on the sedimentary processes¹. We agree that the host rock protolith formed in a marine environment; however, there is no evidence for shallow water depth, and there is no unambiguous evidence that carbonate was part of the primary sedimentary assemblage. The inherent attributes of the structures, their geological setting in a fold hinge, the deformation fabrics observed in the host rock, and the shape and alignment of the structures within the overall rock fabrics—all indicate non-biological origins. In our view, it is very reasonable to interpret the ISB structures as products of structural deformation and carbonate alteration of layered rocks. On the other hand, we believe that the current evidence does not support the interpretation of these structures as 3,700-Myr-old stromatolites.

Online content

Any methods, additional references, Nature Research reporting summaries, source data, statements of data availability and associated accession codes are available at <https://doi.org/10.1038/s41586-018-0610-4>.

Received: 21 December 2017; Accepted: 31 August 2018;

Published online 17 October 2018.

- Nutman, A. P., Bennett, V. C., Friend, C. R. L., Van Kranendonk, M. J. & Chivas, A. R. Rapid emergence of life shown by discovery of 3,700-million-year-old microbial structures. *Nature* **537**, 535–538 (2016).
- Allwood, A. et al. Conference summary: life detection in extraterrestrial samples. *Astrobiology* **13**, 203–216 (2013).
- Allwood, A. C., Walter, M. R., Kamber, B. S., Marshall, C. P. & Burch, I. W. Stromatolite reef from the Early Archean era of Australia. *Nature* **441**, 714–718 (2006).
- Allwood, A. C., Walter, M. R., Burch, I. W. & Kamber, B. S. 3.43 billion-year-old stromatolite reef from the Pilbara Craton of Western Australia: ecosystem-scale insights to early life on Earth. *Precamb. Res.* **158**, 198–227 (2007).
- Allwood, A. C. et al. Controls on development and diversity of Early Archean stromatolites. *Proc. Natl Acad. Sci. USA* **106**, 9548–9555 (2009).
- Sugitani, K. et al. Biogenicity of morphologically diverse carbonaceous microstructures from the ca. 3400 Ma Strelley pool formation, in the Pilbara Craton, Western Australia. *Astrobiology* **10**, 899–920 (2010).
- Walter, M. R., Buick, R. & Dunlop, S. R. Stromatolites 3,400–3,500 Myr old from the North Pole area, Western Australia. *Nature* **284**, 443–445 (1980).
- Mojzsis, S. J. et al. Evidence for life on Earth before 3,800 million years ago. *Nature* **384**, 55–59 (1996).
- Rosing, M. T. ^{13}C -depleted carbon microparticles in >3700-Ma sea-floor sedimentary rocks from West Greenland. *Science* **283**, 674–676 (1999).

10. Schidlowski, M., Appel, P. W., Eichmann, R. & Junge, C. E. Carbon isotope geochemistry of the 3.7×10^9 -yr-old Isua sediments, West Greenland: implications for the Archaean carbon and oxygen cycles. *Geochim. Cosmochim. Acta* **43**, 189–199 (1979).
11. van Zuilen, M. A., Lepland, A. & Arrhenius, G. Reassessing the evidence for the earliest traces of life. *Nature* **418**, 627–630 (2002).
12. Lindsay, J. F. et al. The problem of deep carbon—an Archean paradox. *Precamb. Res.* **143**, 1–22 (2005).
13. Shields, G. & Veizer, J. Precambrian marine carbonate isotope database: version 1.1. *Geochem. Geophys. Geosyst.* **3**, 1–12 (2002).
14. Nutman, A., Van Kranendonk, M. *Sampling of the World's Oldest Stromatolites from Isua (Greenland): Damage to a Globally-Unique Locality*. Technical Report (2017).
15. Fedo, C. M., Myers, J. S. & Appel, P. W. U. Depositional setting and paleogeographic implications of Earth's oldest supracrustal rocks, the >3.7 Ga Isua Greenstone belt, West Greenland. *Sediment. Geol.* **141–142**, 61–77 (2001).
16. Machel, H. G. Concepts and models of dolomitization: a critical reappraisal. *Geol. Soc. Spec. Publ.* **235**, 7–63 (2004).
17. Bau, M. & Dulski, P. Distribution of yttrium and rare-earth elements in the Penge and Kuruman iron-formations, Transvaal Supergroup, South Africa. *Precamb. Res.* **79**, 37–55 (1996).
18. Nutman, A. P., Friend, C. R. L., Bennett, V. C., Wright, D. & Norman, M. D. >3700 Ma pre-metamorphic dolomite formed by microbial mediation in the Isua supracrustal belt (W. Greenland): simple evidence for early life? *Precamb. Res.* **183**, 725–737 (2010).
19. Planavsky, N. et al. Rare earth element and yttrium compositions of Archean and Paleoproterozoic Fe formations revisited: new perspectives on the significance and mechanisms of deposition. *Geochim. Cosmochim. Acta* **74**, 6387–6405 (2010).
20. Qing, H. & Mountjoy, E. W. Rare earth element geochemistry of dolomites in the Middle Devonian Presqu'île barrier, Western Canada Sedimentary Basin: implications for fluid–rock ratios during dolomitization. *Sedimentology* **41**, 787–804 (1994).

Acknowledgements Part of this research was carried out at the Jet Propulsion Laboratory, California Institute of Technology, under a contract with the National Aeronautics and Space Administration (NASA). Funding for the work was provided by the NASA Mars 2020 PIXL flight project. We thank the Government of Greenland, Ministry of Mineral Resources for provision of

access to the field sites, sampling permits and specifically geologist A. Juul-Nielsen for accompanying us on the field expedition, participating in discussions to determine an acceptable sampling strategy, and approving the final sample collection; T. Elam for providing the PIQUANT quantification code and descriptions of its architecture for the PIXL prototype; J. Thieme and E. Fogelqvist for assistance with data collection and reduction at the SRX beamline; T. Rasbury and K. Wooton for assistance with sample digestion and REE + Y analysis; I. Burch for field assistance including sample acquisition; K. Bourke for cutting and polishing the rock samples; and I. Fast for assistance in the field. J.A.H. acknowledges partial support from the Stony Brook University-Brookhaven National Laboratory Seed Grant program.

Reviewer information *Nature* thanks M. M. Tice, M. van Zuilen and the other anonymous reviewer(s) for their contribution to the peer review of this work.

Author contributions A.C.A. led the research and field expedition, determined analytical strategy for samples, interpreted data, analysed the structures and wrote the manuscript. M.T.R. coordinated field logistics, including sampling permits and inclusion of Greenland government staff in the fieldwork and sampling operations, made field observations, interpreted metamorphic history, provided regional geologic context and contributed to manuscript writing. J.A.H. performed synchrotron X-ray fluorescence analyses, REE + Y analyses and interpreted geochemical data, contributed to manuscript writing and helped to write the Methods. D.T.F. acquired and analysed PIXL maps, performed thin section petrography and contributed to manuscript revisions. C.M.H. processed the PIXL data used in elemental maps and helped to write the Methods.

Competing interests The authors declare no competing interests.

Additional information

Extended data is available for this paper at <https://doi.org/10.1038/s41586-018-0610-4>.

Supplementary information is available for this paper at <https://doi.org/10.1038/s41586-018-0610-4>.

Reprints and permissions information is available at <http://www.nature.com/reprints>.

Correspondence and requests for materials should be addressed to A.C.A. or J.A.H.

Publisher's note: Springer Nature remains neutral with regard to jurisdictional claims in published maps and institutional affiliations.

METHODS

Data reporting. No statistical methods were used to predetermine sample size. The experiments were not randomized and the investigators were not blinded to allocation during experiments and outcome assessment.

PIXL analysis at the Jet Propulsion Laboratory. PIXL (planetary instrument for X-ray lithochemistry) is a microfocus X-ray fluorescence instrument developed at the Jet Propulsion Laboratory to fly aboard NASA's Mars 2020 rover mission. The PIXL engineering prototype used in this study employs a Moxtek 12-Watt 60-kV MAGPRO Rh X-ray tube, in 180° emission geometry, mated with an XOS (6319) glass polycapillary focusing optic. The optic delivers a sub-millimetre (around 100 µm diameter at 7 keV) focused X-ray beam spot at a nominal 2-cm stand-off distance from the target. Two Ketek Vitus H50 AXAS-D detectors (model: D5C2T0-H50-ML9BEV), oriented at 20° relative to the beam axis, provide a near-backscatter geometry for optimized X-ray detection. Analogue-to-digital conversion of X-ray signals and multi-channel binning of pulses is performed by the Ketek-built electronics. Data were acquired using an in-house-designed acquisition software built using a National Instruments LabVIEW platform.

Measurements of the Greenland rock were performed in air using 28 kV/100 µA X-ray tube-operating conditions. The rock sample was cut, polished and cleaned. The data of Fig. 1g were acquired by rastering the X-ray beam across the sample surface in *x* and *y* directions in 100-µm steps, with 15-s integration at each step, to produce a 10 × 15-mm² image containing 15,000 data points. For Fig. 1h, a 200-µm step size was selected and a 10 × 20-mm² area, containing 5,000 data points, was imaged.

To accurately identify the elements present, all of the spectra in each map were summed together to produce a whole-map summed spectrum. Principal elemental peaks of the major elements of interest were identified and peak areas under the characteristic X-ray peaks were derived using the in-house software package PIQUANT²¹, designed to process and fit spectral data generated by PIXL. PIQUANT uses a rigorously applied linear least-squares spectrum peak-fitting approach to ensure robust identification of elements, the fitting routine of PIQUANT applies Gaussian functions to each of the X-ray lines that describe a peak. The analytic integral of the combined Gaussians produces the net peak intensity. Peak intensity is one of the fitted variables. Also variable are two parameters associated with the peak widths and two more to describe the channel bin-to-peak energy conversion. The 'noise' corresponding primarily to the bremsstrahlung background that underlies the X-ray peaks is fitted separately using a SNIP¹⁷-fitting algorithm. The background contribution is subtracted as part of deriving the net peak intensities. This approach enables accurate distinction of element peaks even when the peaks overlap. In the Greenland rock maps, the Ba L α X-ray peak (4.47 keV) and Ti K α X-ray peak (4.51 keV) are an example of this. Both appear almost as part of one peak, broadened by the contribution and with 40-eV separation of the two elemental lines. With PIQUANT, the individual lines are distinguished, given that the line energies are constrained to a fixed energy and the peak widths and channel energy calibration parameters are constrained by values derived from the dominant lines of neighbouring elements (for example, Ca and Fe). Harnessing these constraints enables separation of Ti from Ba.

One challenge that persists through these spectra is that coherent scatter diffraction peaks appear in the energy range of spectra in which Ti and Ba peaks reside. Their presence has the potential to be registered falsely as a characteristic X-ray response. The PIQUANT software does not yet possess a treatment process that would allow for correction of this contribution. Therefore, a very small amount of data from this region may represent diffraction scatter instead of a X-ray response.

PIQUANT utilizes the databases from a previous study²², although a number of those databases have been, or are currently being, modified.

REE + Y analyses at Stony Brook University. Four samples were prepared and analysed by inductively coupled plasma mass spectrometry (ICP-MS) for their rare earth element (REE) and Y concentrations (REE + Y). A slab of the sample shown in Fig. 1b, c was sectioned with a tile saw (Extended Data Fig. 5) to separate a portion of the carbonate-rich rim on the light-grey part of the rock (subsample 'C') and a portion of the overlying dark-grey part of the rock (subsample 'M'). These two subsamples were hand crushed in a ceramic mortar and then powdered in an agate shatterbox. Half a gram of each powder was weighted out and sonicated with 2% nitric acid for 30 min to leach carbonate from the samples. The supernatant was then removed, diluted and analysed by ICP-MS; these are samples C3C and M3C. About 40 mg (dry weight) of the remaining leached sediment was then dried and dissolved in a mixture of hydrofluoric and nitric acid for 12 h in sealed Teflon vials on a hotplate at around 120°C. They were then dried and dissolved in aqua regia for 12 h in sealed Teflon vials on a hotplate at around 120°C.

Once completely dissolved, the aqua regia was dried off and the samples were reconstituted in nitric acid, which was then diluted and analysed by ICP-MS; these are samples C3M and M3M.

Elemental concentration analyses were performed in the FIRST (Facility for Isotope Research and Student Training) Laboratory in the Department of Geosciences at Stony Brook University on an Agilent 7500cx quadrupole ICP-MS. Samples were diluted to match to the signal of mixed calibration standards and unknown concentrations were calculated based on standard calibration curves, with standards run frequently between unknowns to monitor for drift in signal intensity. The U.S.G.S. Cody shale standard, SCO-1, was used to calculate the elemental concentrations for these samples. The REEs and Y concentrations in parts per million (p.p.m.) are shown in Extended Data Table 1. Concentrations were calculated for the carbonate leach of each sample assuming only carbonate was dissolved in 2% nitric acid using Ca and Mg concentrations to calculate the carbonate mass dissolved.

High-resolution X-ray fluorescence mapping at NSLS-II. High-resolution synchrotron X-ray fluorescence (XRF) spectra were collected on the Sub-micron Resolution X-ray spectroscopy (SRX) beamline at the National Synchrotron Light Source 2 (NSLS-II) at the Brookhaven National Laboratory. The capabilities of the SRX beamline have previously been described^{23,24}. In brief, SRX is a hard X-ray microprobe that performs scanning micro-fluorescence microscopy (μ -XRF) and X-ray absorption near-edge structure (μ -XANES) analysis using the high-brightness NSLS-II as a source of incident radiation. The SRX optics allow investigation of elemental distribution and chemical speciation at the sub-micrometre scale. For our analyses, we used an incident beam energy of 12 keV. The beam was focused to a spot size of 1 µm and XRF spectra were collected for 0.6 s at each spot. Motorized stages were used to move the sample under the beam with a 2-µm step size, thus generating a two-dimensional map of the elemental composition of this sample. Fluorescent X-rays were detected using an energy dispersive X-ray detector (Hitachi Vortex silicon drift detector). We analysed two areas, called 'map 1' and 'map 2' (Extended Data Fig. 6, Supplementary Information), on a cut and polished slab sample from locality A. This slab contains one of the putative stromatolite-like features, bounded above and below by alternating light and dark layers. XRF spectra for map 1 were collected on a 1–2 mm thick dark-black layer bounded above and below by thicker grey coloured layers. XRF spectra for map 2 were collected from within the core of the stromatolite-like feature. The dimensions of the maps are 200 × 200 µm² and 125 × 125 µm², respectively. To generate element maps, the individual X-ray spectra from each map were first summed into single bulk spectra (that is, one for map 1 and another for map 2) and fitted using the PyXRF analysis package developed at NSLS-II²⁵. PyXRF uses a nonlinear least-squares method to determine global parameters such as peak width, energy calibration values, parameters related to the Compton and elastic scattering peaks, and element identities. Once elements were identified in the summed spectra, individual spectra were searched for those elements, their peak areas were fitted, and maps of elemental distribution and fluorescence intensity were generated.

Reporting summary. Further information on research design is available in the Nature Research Reporting Summary linked to this paper.

Code availability. PIQUANT software used in the study is available from the corresponding authors upon reasonable request.

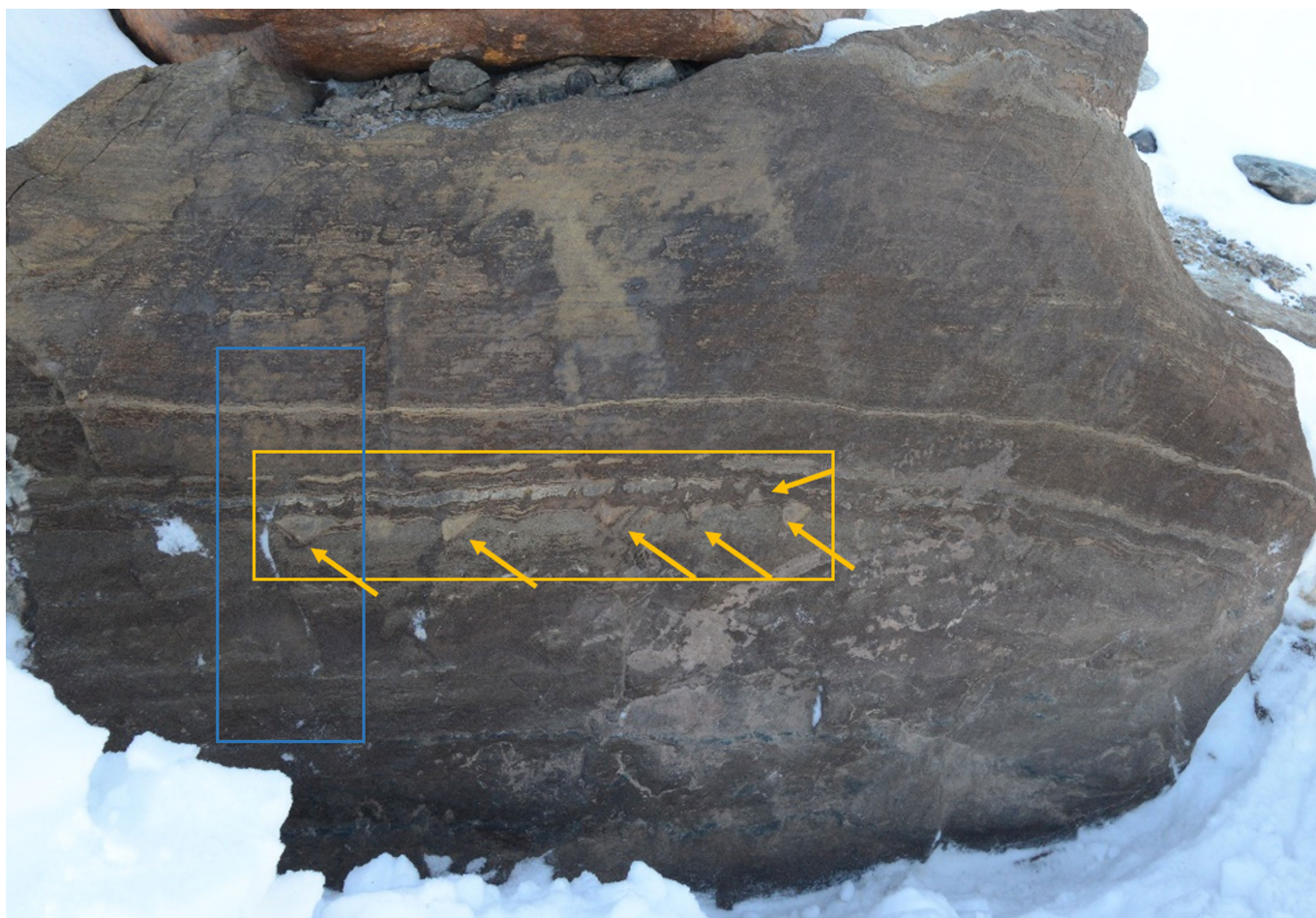
Data availability

The datasets generated during and/or analysed during the current study are available from the corresponding authors upon reasonable request.

- Heirwegh, C. M., Elam, W. T., Flannery, D. T. & Allwood, A. C. An empirical derivation of the X-ray optic transmission profile used in calibrating the Planetary Instrument for X-ray Lithochemistry (PIXL) for Mars 2020. *Powder Diff.* 162–165 (2018).
- Elam, W. T. et al. A new atomic database for the X-ray spectroscopic calculations. *Radiat. Phys. Chem.* **63**, 121–128 (2002).
- De Andrade, V. et al. The sub-micron resolution X-ray spectroscopy beamline at NSLS-II. *Nucl. Instrum. Methods Phys. Res. A* **649**, 46–48 (2011).
- Chen-Wiegart, Y. C. K. et al. Early science commissioning results of the sub-micron resolution X-ray spectroscopy beamline (SRX) in the field of materials science and engineering. In *Proc. 23rd International Conference on X-Ray Optics and Microanalysis* (eds Thieme, J. & Siddons, D. P.) (ICXOM23, American Institute of Physics, 2016).
- Li, L., Yan, H., Xu, W., Yu, D. & Heroux, A. PyXRF: Python-based X-ray fluorescence analysis package. *Proc. 10389 X-Ray Nanoimaging, Instruments and Methods III* 103890U (SPIE Optical Engineering & Applications, 2017).

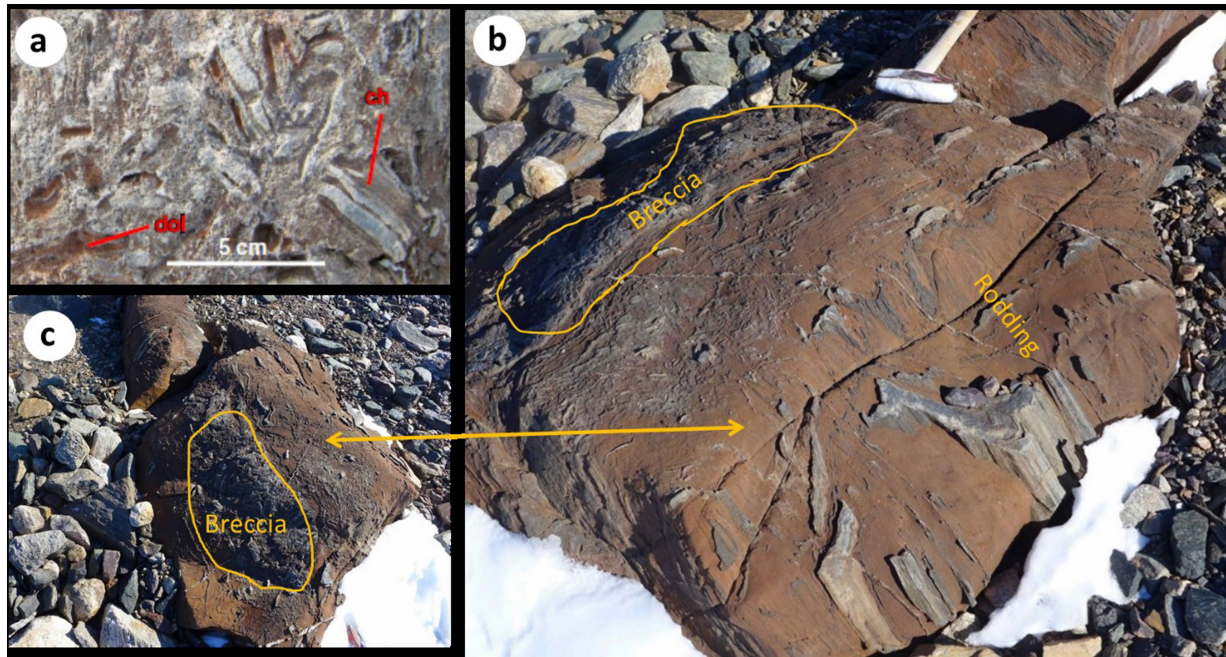


Extended Data Fig. 1 | Satellite image showing the approximate outline and location of the Isua Structural Belt and the study area. The satellite image of the study area. The image was obtained from Google Maps.



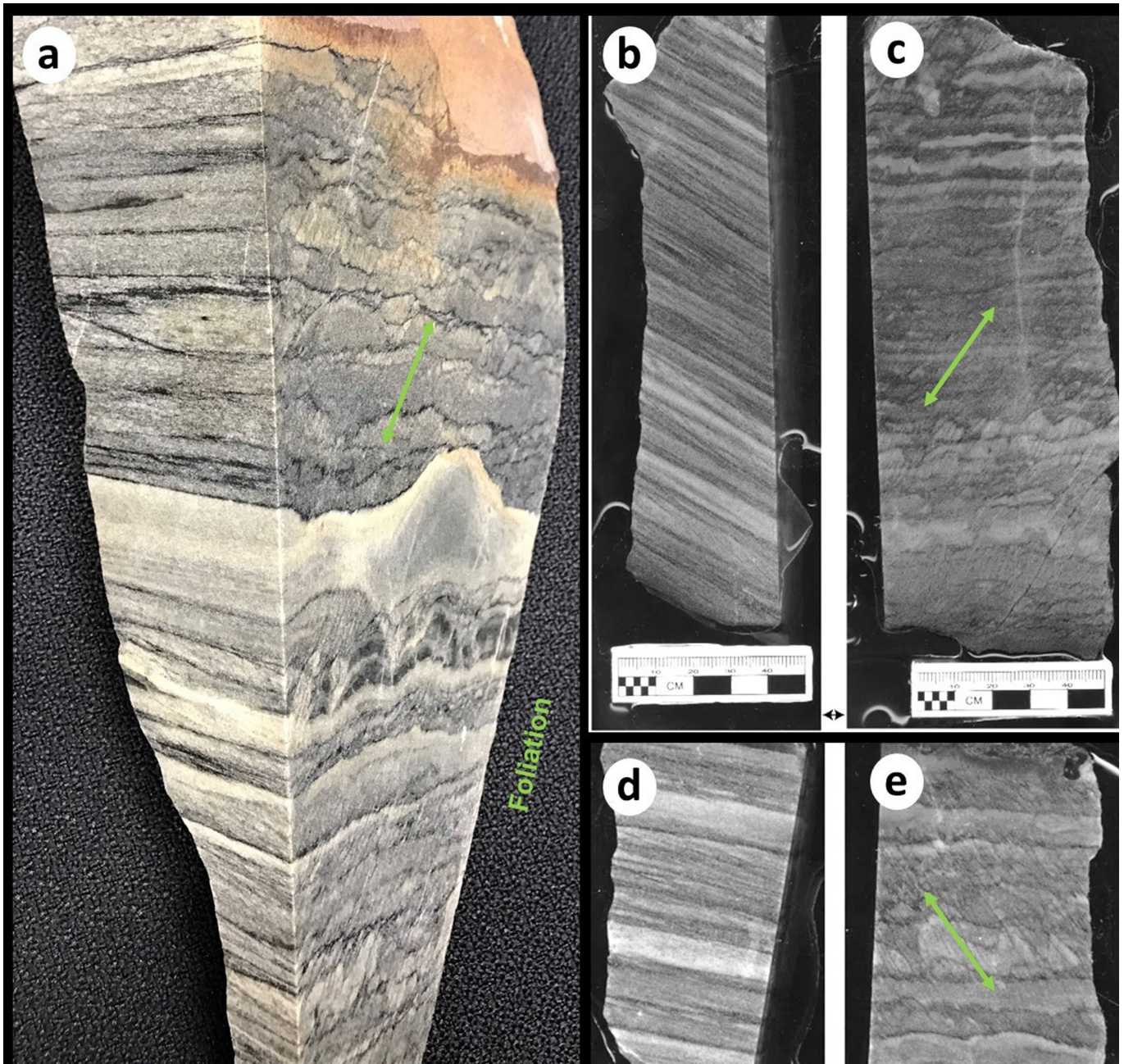
Extended Data Fig. 2 | Putative stromatolites of the ISB at site A. Yellow arrows point to triangular shapes with apices mostly pointing down relative to layering. Note, the stratigraphy was inverted, as the layers have

been overturned¹. Each of the triangles is approximately 4 cm across. The blue box shows the approximate outline of the sample acquired for the present study. The yellow box shows the area shown in Fig. 1.



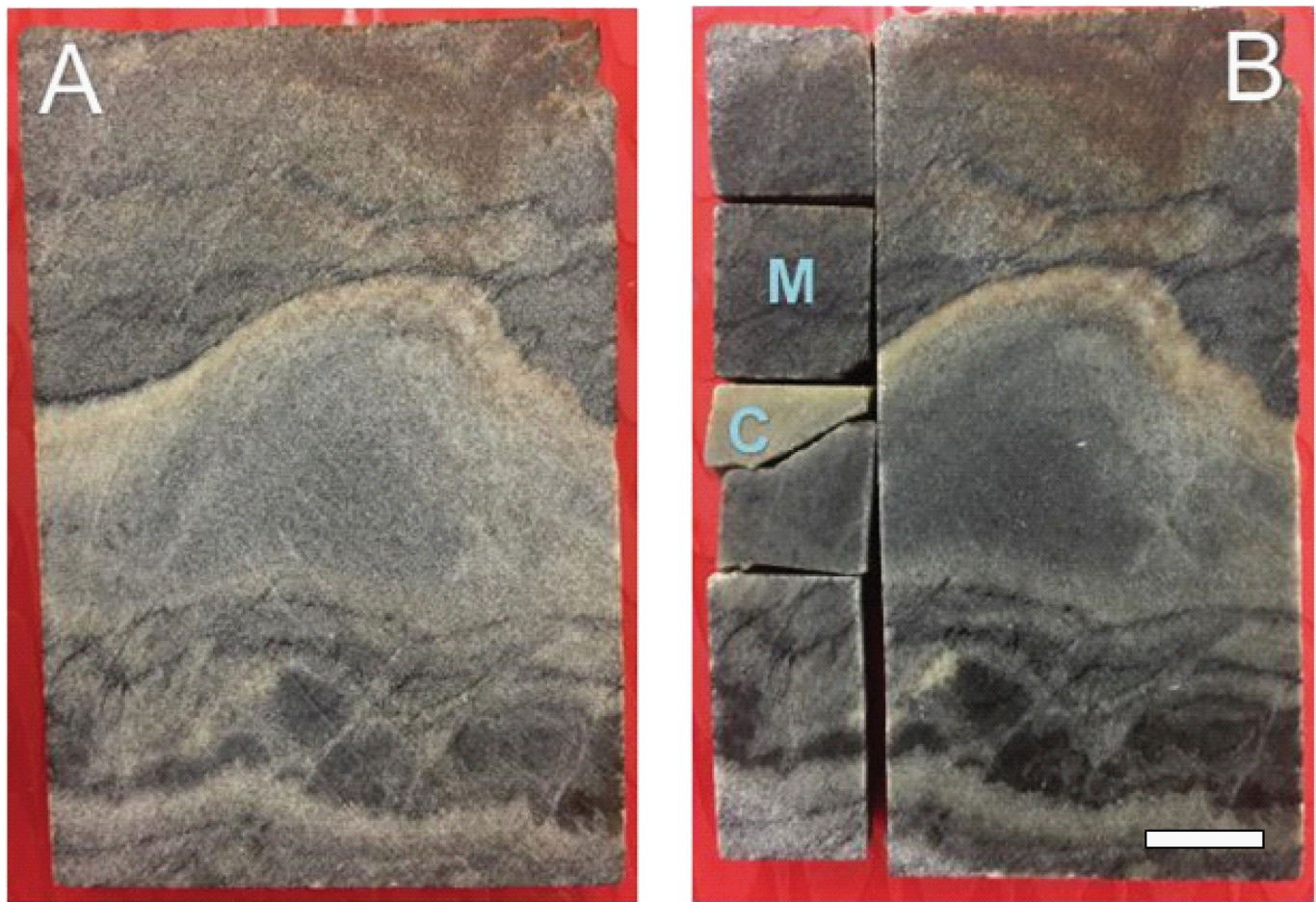
Extended Data Fig. 3 | Breccia at site C. **a**, Close-up view of breccia, from the previous study¹. Ch, chert; dol, dolomite. **b**, Larger field of view showing the same breccia block as in **a**, showing the location of the

elongated rod-like fabric (rodding) on the upper right side of the rock. **c**, Top view of the breccia-containing block from **a**—note the contrasting appearance of the rock fabric.



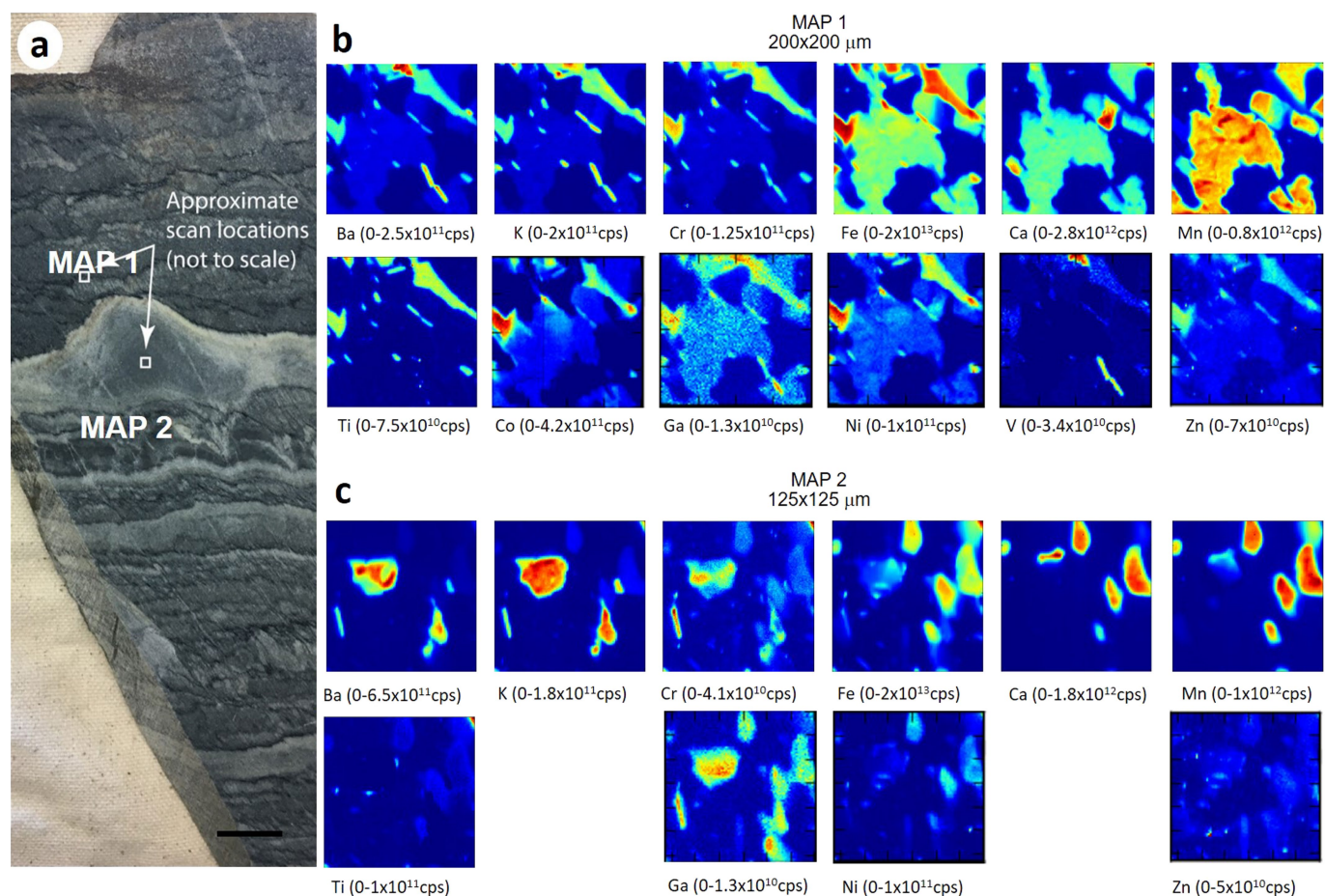
Extended Data Fig. 4 | Photographs of details from the deformation fabrics of site A. The photographs show details of the observed deformation fabrics on the cut and polished faces of all three pieces of the columnar sample that we collected from site A. Each piece was cut to show rock fabrics on orthogonal faces. **a**, Largest piece, which includes one of

the 'stromatolites' on the right face. Note contrasting fabrics on adjacent faces. **b–e**, Additional pieces of the rock sample, showing further examples of the contrasting rock fabrics. Green arrows on all images indicate the orientation of the spaced cleavage.



Extended Data Fig. 5 | Petrographic context of samples that were digested for REE + Y analyses. a, Slab sample before cutting. **b,** Slab sample after cutting. 'M' denotes the subsample from which analyses

'M3M' and 'M3C' were derived. 'C' denotes the subsample from which analyses 'C3M' and 'C3C' were derived. Scale bar, 10 mm.



Extended Data Fig. 6 | Synchrotron XRF element maps of the ISB sample. The distribution of trace elements relative to minerals is shown. **a**, Photograph of the sample. White squares show map locations. Scale bar, 10 mm. **b**, Distribution and X-ray intensity of detected elements for map 1. **c**, Distribution and X-ray intensity of detected elements for map 2.

b, c, X-ray intensity variations were used to colour the element maps. Blue, zero X-ray intensity; red, maximum X-ray intensity. X-ray intensity ranges (counts per second (cps)) are shown beneath each map. All maps are for K-shell X-rays except for Ba, which was detected using L-shell X-rays.

Extended Data Table 1 | REE + Y concentrations (p.p.m.) from acid digestion and ICP-MS analysis

I.D.	La	Ce	Pr	Nd	Sm	Eu	Gd	Tb	Dy	Y	Ho	Er		Tm	Yb	Lu
Carbonate fraction from “Stromatolite”																
C3C	0.414	0.530	0.070	0.332	0.082	0.040	0.113	0.017	0.113	1.335	0.025	0.072		0.010	0.100	0.011
Carbonate fraction from “Sediment”																
M3C	1.670	2.080	0.260	1.047	0.203	0.080	0.252	0.034	0.230	3.209	0.053	0.170		0.025	0.190	0.026
Silicate fraction from “Stromatolite”																
C3M	0.430	0.781	0.124	0.636	0.226	0.343	0.226	0.044	0.421	4.182	0.112	0.310		0.035	0.393	0.050
Silicate fraction from “Sediment”																
M3M	1.438	2.456	0.341	1.398	0.344	1.358	0.468	0.060	0.528	4.812	0.161	0.485		0.052	0.519	0.096

Credibility-enhancing displays promote the provision of non-normative public goods

Gordon T. Kraft-Todd^{1*}, Bryan Bollinger², Kenneth Gillingham³, Stefan Lamp⁴ & David G. Rand^{5*}

Promoting the adoption of public goods that are not yet widely accepted is particularly challenging. This is because most tools for increasing cooperation—such as reputation concerns¹ and information about social norms²—are typically effective only for behaviours that are commonly practiced, or at least generally agreed upon as being desirable. Here we examine how advocates can successfully promote non-normative (that is, rare or unpopular) public goods. We do so by applying the cultural evolutionary theory of credibility-enhancing displays³, which argues that beliefs are spread more effectively by actions than by words alone—because actions provide information about the actor's true beliefs. Based on this logic, people who themselves engage in a given behaviour will be more effective advocates for that behaviour than people who merely extol its virtues—specifically because engaging in a behaviour credibly signals a belief in its value. As predicted, a field study of a programme that promotes residential solar panel installation in 58 towns in the United States—comprising 1.4 million residents in total—found that community organizers who themselves installed through the programme recruited 62.8% more residents to install solar panels than community organizers who did not. This effect was replicated in three pre-registered randomized survey experiments (total $n = 1,805$). These experiments also support the theoretical prediction that this effect is specifically driven by subjects' beliefs about what the community organizer believes about solar panels (that is, second-order beliefs), and demonstrate generalizability to four other highly non-normative behaviours. Our findings shed light on how to spread non-normative prosocial behaviours, offer an empirical demonstration of credibility-enhancing displays and have substantial implications for practitioners and policy-makers.

Public goods are crucial to human welfare but pose a challenge when contributing is costly to the individual. Field experiments—which verify the conclusions of countless models and laboratory experiments—have demonstrated the power of reputation concerns and social norms for promoting contributions to public goods⁴. However, such interventions are typically only effective when most people already contribute to the public good in question (a descriptive social norm exists) or at least believe that people should contribute to it (an injunctive social norm exists)².

Here we investigate how to promote public goods that are not already normative—that is, how new prosocial norms can be spread. We focus on 'bottom-up' approaches in which individuals influence those around them, rather than 'top-down' approaches based on institutional sanctions or policies⁵, and ask why some individuals are more successful than others in promoting the adoption of new prosocial norms. To shed light on this question, we leverage a theory from the study of cultural evolution that has primarily been used to explain religious commitment^{6–8}: credibility-enhancing displays (CREDs)³.

The essence of this theory is that your actions help to shape my second-order beliefs (that is, what I believe about what you believe), which in turn influences my adoption of your beliefs. In particular, the

theory of CREDs focuses on actions that are expected to be beneficial to people who hold the belief but expected to be costly to people who do not hold the belief. If I see you engage in such an action, it provides a credible signal that you actually hold the belief and thus think the action is beneficial—a much stronger signal than if you simply say that you believe it. The canonical example involves assessing the edibility of a mushroom. If the mushroom is inedible, eating it can be extremely costly. Thus, seeing someone eat the mushroom after they say it is edible gives you much greater confidence that they truly believe it is safe to eat, relative to someone who merely says that the mushroom is edible—and this, in turn, makes you more likely to believe the mushroom is edible.

The logic of CREDs generates a clear prediction regarding bottom-up attempts to promote public goods: advocates who themselves engage in a given behaviour should be more effective at convincing others to also adopt that behaviour—specifically because they are perceived as believing that the behaviour is more beneficial. To test these predictions, we focus on one particular public-goods problem: the installation of residential solar panels. The use of residential solar panels helps to reduce carbon dioxide emissions and resultant climate change, and thereby benefits society at large. But the immediate financial cost of installation, combined with the search cost of learning about solar panels and suitable installers, may outweigh any personal benefit to the homeowner who chooses to install. The installation of solar panels remains descriptively non-normative (only 0.4% of American households had solar panels in 2014, during data collection; see Supplementary Information section 4.4 for details)⁹ and—as shown by a norming study (see Methods and Extended Data Figs. 1, 2 for details)—there is also not currently a strong injunctive norm that stipulates that people should be installing solar panels.

We examine the role of CREDs in the ability of community organizers to promote the installation of solar panels by using data from a series of 'Solarize Connecticut' campaigns^{10–12}, run in 58 towns (with a total population size of 1.4 million) in the state of Connecticut by the non-profit organization SmartPower from 2012 to 2015. These campaigns promoted the Solarize programme, which included a volunteer 'solar ambassador' in each town who encouraged other residents to install solar panels through the programme (see Supplementary Information section 4 and Extended Data Fig. 3 for further details).

Ambassadors were recruited on the basis of their centrality in the community social network rather than their own solar installation choices. As a result, only a minority of the ambassadors (32.7%) themselves installed solar panels through the Solarize programme. Examining the number of Solarize installations achieved in each town confirms the key prediction of CREDs: more people installed solar panels through the Solarize programme in towns in which the ambassador also installed through Solarize, compared to towns in which the ambassador did not install through Solarize (Fig. 1; linear regression including controls for the type and timing of the Solarize campaign, $b = 17.89$, 95% confidence interval (CI) = 3.36–32.41, $P = 0.017$). This result is robust to controlling for important characteristics of the towns and the ambassadors: the number of residential solar panel installations

¹Department of Psychology, Yale University, New Haven, CT, USA. ²Fuqua School of Business, Duke University, Durham, NC, USA. ³School of Forestry & Environmental Studies, Yale University, New Haven, CT, USA. ⁴Toulouse School of Economics, University of Toulouse Capitole, Toulouse, France. ⁵Sloan School and Department of Brain and Cognitive Sciences, Massachusetts Institute of Technology, Cambridge, MA, USA. *e-mail: gordon.kraft-todd@yale.edu; drand@mit.edu

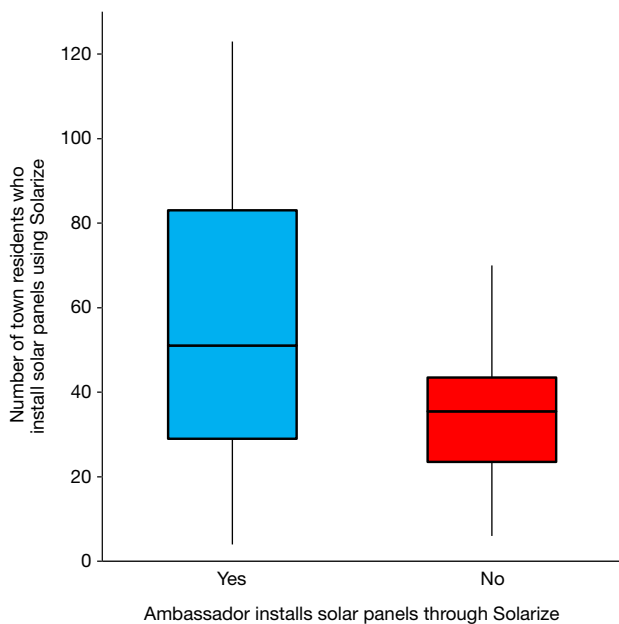


Fig. 1 | Ambassadors who install solar panels through the Solarize programme are more successful at convincing others to participate than ambassadors who do not. The number of people per town who installed solar panels using the Solarize programme is shown as a function of whether the solar ambassador of that town installed through the Solarize programme (blue, $n = 18$) or did not (red, $n = 40$). Box-and-whiskers plot indicates the minimum, 25th percentile, 50th percentile (median), 75th percentile and maximum values.

in the town before the Solarize campaign, the number of homes suitable for solar panel installation in the town, the gender of the ambassador, whether the ambassador served in an official town government role and whether the ambassador had already installed solar panels before the Solarize campaign (see Supplementary Information section 2 for further details).

To help to support a causal interpretation of this correlational finding, we perform an instrumental variable regression, which is a standard econometric technique for inferring causality from observational data (for details, see Supplementary Information section 3). We instrument for whether the ambassadors installed through the Solarize programme with a variable for whether the ambassador's home was suitable for solar installation. Given that ambassadors could only install through the Solarize programme if their house was suitable, suitability is a useful instrument: a test of suitability demonstrates that it is not a weak instrument (F ratio of 25.23) and it significantly predicts whether the ambassador installed using the Solarize programme ($b = 0.58$, 95% CI = 0.34–0.82, $P < 0.001$). We believe that suitability is a valid instrument because it is highly unlikely that suitability is correlated with potential unobserved confounding variables—such as ambassador motivation or installer quality—because suitability is based on predetermined features of the roof structure and shading of ambassadors' houses (for further discussion of validity, see Supplementary Information section 3). In our instrumented regression, we continue to find a significant positive effect of ambassador installation on the number of townspeople installations ($b = 23.82$, 95% CI = 1.77–45.88, $P = 0.034$), supporting our causal interpretation.

Thus, this field study supports our hypothesis based on CREDs: ambassadors who installed solar panels through the Solarize programme were more effective at convincing others to perform similar installations, when compared to those ambassadors who advocated installation without any accompanying action.

We complement this field study with three pre-registered experiments that were run using the online labour market Amazon Mechanical Turk, which is substantially more demographically diverse than undergraduate subject pools¹³. Of particular relevance, 52% of our subjects indicated that they were past or current homeowners,

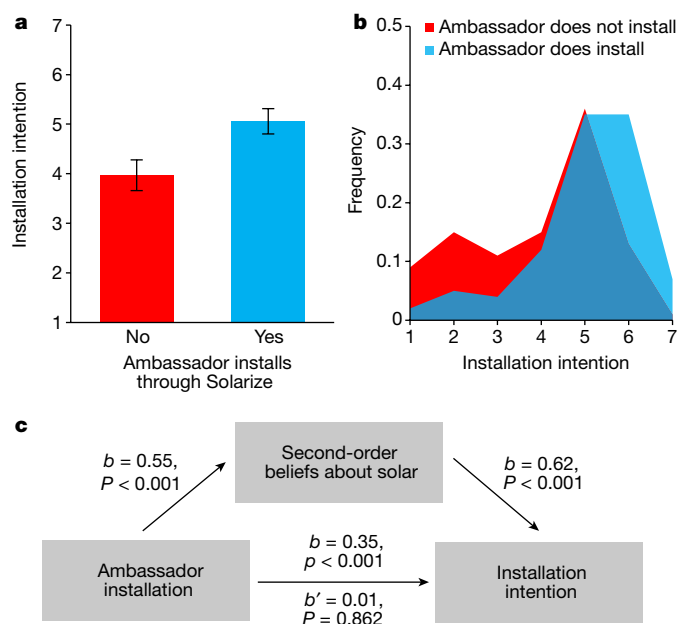


Fig. 2 | Ambassador installation influences subjects' intentions to install through the Solarize programme. a, Means (with 95% CIs) (a) and distributions (b) of intentions to install (1–7 Likert scale), as a function of whether the ambassador installed solar panels through the Solarize programme (blue, $n = 100$) or did not (red, $n = 100$). c, Subjects' second-order beliefs fully mediate the effect of ambassador installation on subjects' installation intentions. All variables are standardized for this analysis. The correlations between ambassador installation and second-order beliefs, second-order beliefs and subjects' intentions to install, and ambassador installation and subjects' intentions to install (without (b) and with (b') second-order beliefs as a covariate) are shown.

and all of our results replicate when restricting to these subjects (see Supplementary Information section 5.2).

Experiments 1 and 2 recreated the main contrast of the field study: subjects were presented with a description of the Solarize campaign, a description of a solar ambassador who did or did not choose to install solar panels through Solarize and an appeal from the solar ambassador that detailed the benefits of the programme. Subjects then indicated how likely they would be to install solar panels through the Solarize programme.

As in the field study, experiment 1 ($n = 200$ individuals) finds a significant effect of ambassador installation: subjects reported a higher likelihood of installing through the Solarize programme if the ambassador installed through Solarize ($m = 5.06$, 95% CI = 4.80–5.32) than if the ambassador did not ($m = 3.97$, 95% CI = 3.66–4.28, $t_{198} = 5.31$, $d = 0.75$, $P < 0.001$; Fig. 2a, b). Experiment 1 also provides an initial test of our prediction that this effect is driven by subjects' second-order beliefs (that is, their beliefs about what the ambassador believes about solar panels). To do so, we developed a 12-item second-order-belief scale ($\alpha = 0.96$), in which subjects indicated their beliefs about the ambassador's beliefs about the benefits of the Solarize campaign. As predicted, responses to the second-order-belief scale significantly and fully mediate the effect of ambassador installation on the subjects' intentions to install (97% of the effect; Fig. 2c) (see Methods and Supplementary Information section 5.1 for details).

Experiment 2 ($n = 399$ individuals) used an experimental mediation design¹⁴ to provide further support for the key role of second-order beliefs in driving the effect of ambassador installation, and to rule out two competing explanations. We implemented a 2×2 between-subjects design that crossed the manipulation of whether the ambassador installed through the Solarize programme (from experiment 1) with a direct manipulation of second-order beliefs regarding the benefits of residential solar panels: subjects were informed about accidentally

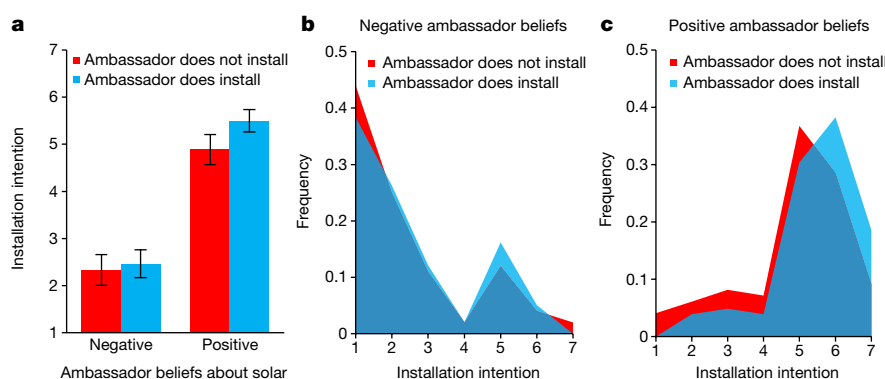


Fig. 3 | Second-order beliefs explain the effect of ambassador installation on the installation intentions of subjects. **a**, Mean (with 95% CI) installation intentions (1–7 Likert scale) as a function of whether the ambassador did not install solar panels through the Solarize programme and did not believe in the benefits of solar panels (red, left; $n = 100$), did install but did not believe in the benefits (blue, left; $n = 98$), did not install but believed in the benefits (red, right; $n = 99$), or did install and believed

in the benefits (blue, right; $n = 102$). **b**, **c**, The distributions of installation intentions in each condition are shown. We see that when information about the ambassador's beliefs is provided directly in experiment 2, there is little effect of whether the ambassador installed on installation intentions of the subjects. This result is in contrast to experiment 1, providing evidence for the mediating role of second-order beliefs.

overhearing the ambassador express, in confidence, either a positive or negative view of residential solar panels. Thus, in experiment 2 subjects did not need to rely on the installation behaviour of the ambassador to gain insight into what the ambassador truly believed about solar panels—and thus, the CREDS account predicts that ambassador installation should have much less effect in experiment 2 compared to experiment 1. A two-way ANOVA finds a significant main effect of second-order beliefs such that subjects reported a higher likelihood of installing when the ambassador expressed a belief that residential solar panels are beneficial ($m = 5.20$, 95% CI = 5.01–5.39), compared to when the ambassador expressed a belief that residential solar panels are not beneficial ($m = 2.40$, 95% CI = 2.17–2.63, $F_{1,395} = 340.79$, $d = 1.83$, $P < 0.001$). There was also a significant, but small, main effect of ambassador installation such that subjects reported a slightly higher likelihood of installing if the ambassador also installed ($m = 4.00$, 95% CI = 3.71–4.30) than if the ambassador did not ($m = 3.60$, 95% CI = 3.31–3.88, $F_{1,395} = 6.08$, $d = 0.17$, $P = 0.014$) (Fig. 3). There was no significant interaction between ambassador installation and second-order beliefs ($F_{1,395} = 2.48$, $P = 0.116$). Critically, the coefficient on ambassador installation is 62% smaller in experiment 2 than in experiment 1, which provides causal evidence that second-order beliefs mediate the effect of ambassador installation (subjects were randomly assigned simultaneously across experiments 1 and 2 to enable this comparison; see Methods and Supplementary Information section 5.1 for details).

Experiment 2 also provides evidence for CREDS over two alternative explanations of the effect of ambassador installation that are based directly on actions rather than second-order beliefs. First, subjects might dislike or distrust the non-installing ambassador because their behaviour is hypocritical¹⁵ and therefore ignore their recommendation to install through the Solarize programme¹⁶. Second, the ambassador's installation decision might directly influence subjects' count of the number of people who install and therefore influence their intention to install via perceived descriptive normativity². Contrary to these accounts, however, subjects reported a higher likelihood of installing in the condition with an ambassador who did not install—and therefore was hypocritical and projected a norm of non-installation—but was overheard expressing a belief in the benefits of solar panels ($m = 4.89$, 95% CI = 4.59–5.19) than in the condition with an ambassador who installed—and was therefore not a hypocrite and projected a norm of installation—but was overheard to not truly believe in the benefits of solar panels ($m = 2.46$, 95% CI = 2.14–2.79, $t_{195} = 10.83$, $d = 1.54$, $P < 0.001$). Thus, when put in conflict, information about the beliefs of ambassadors overrides their actions.

Finally, experiment 3 ($n = 1,206$ individuals) replicated the design of experiment 1; however, solar panel installation was replaced by one of

four other behaviours that are strongly non-normative from both a descriptive and injunctive perspective (see Methods and Extended Data Figs. 2, 3 for details). For each behaviour, we compare subjects' intention to engage in the behaviour across conditions in which the ambassador does versus does not engage in the behaviour. A random-effects meta-analysis on the four effect sizes reveals a significant positive effect of the ambassador engaging in the behaviour ($d = 0.33$, 95% CI = 0.21–0.44, $Z = 5.63$, $P < 0.001$), and no evidence of heterogeneity in effect size across behaviours ($\chi^2_3 = 2.37$, $P = 0.499$) (Fig. 4). Finally, aggregating over the four behaviours we find that the second-order-belief scale ($\alpha = 0.91$) significantly and fully mediates the effect of ambassador engagement (89% of the effect) (see Methods, Supplementary Information section 5 and Extended Data Fig. 4 for details). Thus, experiment 3 shows that the CREDS-based effect documented in the field study and experiments 1 and 2 can promote a range of highly non-normative public goods other than solar panels.

These results are of substantial importance for theories of cultural evolution, in which CREDS have a major role: despite the influence

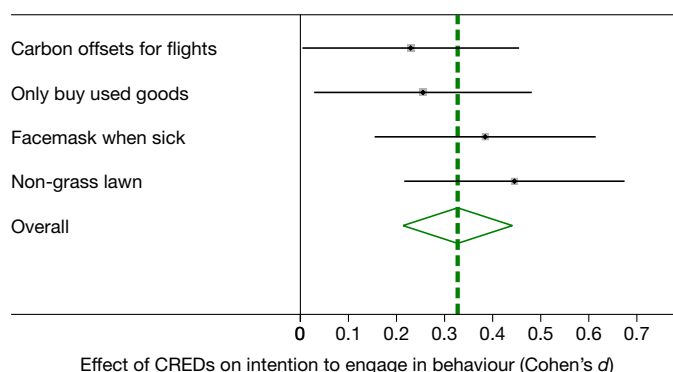


Fig. 4 | Ambassador engagement promotes contribution to highly non-normative public goods. Random-effects meta-analysis of the effect of the ambassador engaging in the behaviour they are advocating on subjects' intentions to engage in that behaviour (1–7 Likert scale). This was performed across four highly non-normative public goods: purchasing carbon offsets for flights ($n = 305$), only buying used goods ($n = 303$), wearing a facemask in public when sick ($n = 297$) and replacing grass lawns with more sustainable ground cover ($n = 301$). Effect sizes are shown as Cohen's d ; error bars indicate 95% CI. The relative sizes of the grey boxes indicate the weighting assigned to the studies by the meta-analysis. ANOVA produces equivalent results (see Supplementary Information section 5.3).

that this theory has had, there has previously been little empirical evidence that directly supports CREDs—notable exceptions include two previous studies^{7,17}—or that specifically demonstrates the mechanism of second-order beliefs. Our experiments provide such support. Furthermore, although it has previously been theorized that CREDs may help to explain prosocial behaviour more broadly¹⁸, we apply the logic of CREDs to the spread of non-normative public goods in particular, which demonstrates an important role for this theory in solving one of the major outstanding challenges in cooperation research. Finally, we present an experimental methodology that can be used to empirically investigate the effects of CREDs in a wide range of contexts beyond that of public goods.

Our results also contribute to the literature on influence, persuasion and attitudes^{19,20}, as well as community organizing and the diffusion of solar panels in particular¹⁰, by empirically demonstrating the importance of ‘practicing what you preach’. Although this result might seem obvious in retrospect, the data suggest that it was not in fact self-evident in prospect: only 32.7% of solar ambassadors recruited as Solarize Connecticut community organizers were people who themselves installed residential solar panels through the programme.

Problems of cooperation and the provision of public goods are becoming increasingly important and urgent. The results presented here suggest that whether we are advocating for residential solar panels, public transportation, supporting local businesses or civil liberties, our campaigns will be more effective if they are built on a foundation not only of words but also of action.

Online content

Any methods, additional references, Nature Research reporting summaries, source data, statements of data availability and associated accession codes are available at <https://doi.org/10.1038/s41586-018-0647-4>.

Received: 28 August 2017; Accepted: 15 August 2018;
Published online 24 October 2018.

- Nowak, M. A. & Sigmund, K. Evolution of indirect reciprocity. *Nature* **437**, 1291–1298 (2005).
- Cialdini, R. B. & Trost, M. R. in *The Handbook of Social Psychology* (eds Fiske, S. T. et al.) 151–192 (McGraw-Hill, New York, 1998).
- Henrich, J. The evolution of costly displays, cooperation and religion: credibility enhancing displays and their implications for cultural evolution. *Evol. Hum. Behav.* **30**, 244–260 (2009).
- Kraft-Todd, G. T., Yoeli, E., Bhanot, S. & Rand, D. G. Promoting cooperation in the field. *Curr. Opin. Behav. Sci.* **3**, 96–101 (2015).
- Tankard, M. E. & Paluck, E. L. Norm perception as a vehicle for social change. *Soc. Issues Policy Rev.* **10**, 181–211 (2016).
- Norenzayan, A. & Shariff, A. F. The origin and evolution of religious prosociality. *Science* **322**, 58–62 (2008).
- Lanman, J. A. & Buhrmester, M. D. Religious actions speak louder than words: exposure to credibility-enhancing displays predicts theism. *Religion Brain Behav.* **7**, 3–16 (2017).
- Willard, A. K. & Cingl, L. Testing theories of secularization and religious belief in the Czech Republic and Slovakia. *Evol. Hum. Behav.* **38**, 604–615 (2017).
- Rogers, J. & Wisland, L. *Solar Power on the Rise* https://www.ucsusa.org/clean_energy/our-energy-choices/renewable-energy/solar-power-technologies-and-policies.html (Union of Concerned Scientists, 2014).
- Bollinger, B. & Gillingham, K. Peer effects in the diffusion of solar photovoltaic panels. *Mark. Sci.* **31**, 900–912 (2012).
- Graziano, M. & Gillingham, K. Spatial patterns of solar photovoltaic system adoption: the influence of neighbors and the built environment. *J. Econ. Geogr.* **15**, 815–839 (2015).
- Irvine, L., Sawyer, A. & Grove, J. *Solarize Guidebook: A Community Guide to Collective Purchasing of Residential PV Systems* (National Renewable Energy Laboratory, Golden, 2011).
- Arechar, A. A., Kraft-Todd, G. & Rand, D. G. Turning overtime: how participant characteristics and behavior vary over time and day on Amazon Mechanical Turk. *J. Econ. Sci. Assoc.* **3**, 1–11 (2017).
- Imai, K., Tingley, D. & Yamamoto, T. Experimental designs for identifying causal mechanisms. *J. R. Stat. Soc. A* **176**, 5–51 (2013).
- Jordan, J. J., Sommers, R., Bloom, P. & Rand, D. G. Why do we hate hypocrites? Evidence for a theory of false signaling. *Psychol. Sci.* **28**, 356–368 (2017).
- Attari, S. Z., Krantz, D. H. & Weber, E. U. Statements about climate researchers’ carbon footprints affect their credibility and the impact of their advice. *Clim. Change* **138**, 325–338 (2016).
- Bryan, J. H. & Walbek, N. H. The impact of words and deeds concerning altruism upon children. *Child Dev.* **41**, 747–757 (1970).
- Chudek, M. & Henrich, J. Culture-gene coevolution, norm-psychology and the emergence of human prosociality. *Trends Cogn. Sci.* **15**, 218–226 (2011).
- Cialdini, R. B. *Influence: The Psychology of Persuasion* (Collins, New York, 2009).
- Petty, R. E. & Cacioppo, J. T. *Attitudes and Persuasion: Classic and Contemporary Approaches* (Routledge, New York, 2018).

Acknowledgements This research was made possible by US Department of Energy (award DE-EE0006128), the Templeton World Charity Foundation (grant no. TWCF0209) and the Defense Advanced Research Projects Agency NGS2 programme (grant no. D17AC00005). The authors thank S. Carattini, C. Moya and M. Hoffman for their helpful feedback on drafts of this manuscript, and D. Banko and C. Borden for research assistance.

Reviewer information Nature thanks A. Grønhoj, L. Stanca and the other anonymous reviewer(s) for their contribution to the peer review of this work.

Author contributions K.G. and B.B. designed and conducted the field study. G.T.K.-T. and S.L. analysed the results of the field study. G.T.K.-T. and D.G.R. designed the online experiments. G.T.K.-T. conducted the online experiments and analysed the results. G.T.K.-T., B.B., K.G., S.L. and D.G.R. wrote the paper.

Competing interests The authors declare no competing interests.

Additional information

Extended data is available for this paper at <https://doi.org/10.1038/s41586-018-0647-4>.

Supplementary information is available for this paper at <https://doi.org/10.1038/s41586-018-0647-4>.

Reprints and permissions information is available at <http://www.nature.com/reprints>.

Correspondence and requests for materials should be addressed to G.T.K. or D.G.R.

Publisher’s note: Springer Nature remains neutral with regard to jurisdictional claims in published maps and institutional affiliations.

METHODS

No statistical methods were used to predetermine sample size. The field study was not randomized, and the experiments were randomized. Investigators were not blinded to allocation during experiments and outcome assessment.

Field study. The Solarize Connecticut campaign was run in five rounds over 2012–2015 in 58 towns in Connecticut (see Supplementary Information section 4 for more detail on the rounds and round types). Solarize Connecticut was an initiative of the Connecticut Green Bank administered by the non-profit organization SmartPower (similar campaigns have also been conducted in New York, Massachusetts and Washington¹², and are underway in several additional states including North Carolina, South Carolina, Pennsylvania, Montana and California). There were four main marketing principles of the campaign: town-supported outreach and education, pre-selected solar installers, discount pricing through a tiered pricing structure and a clear termination date to the campaign. Solarize programmes were designed to limit the time and number of approved installers of residential photovoltaic systems or solar panels within a town.

The campaigns were organized by local volunteers—‘solar ambassadors’—who were primarily recruited from town selectpeople, town managers and members of the town clean-energy task forces, because they were expected to be key nodes in the community social network, and therefore more influential. Before the campaigns, solar installation rates were extremely low among the towns studied ($m < 1\%$), so it is not surprising that most ambassadors did not have solar panels themselves before the campaign. Although many towns had multiple ambassadors, there was always a point person for SmartPower, who was the ‘primary’ ambassador. In this study, we focus on the one primary ambassador (identified by SmartPower, who were blind to the hypotheses tested here). In the field study, ambassadors in $n = 18$ towns installed solar through the Solarize programme and ambassadors in $n = 40$ towns did not. Because the ambassadors were recruited based on their centrality in the community social network rather than their own solar installation choices, it is not surprising that a majority of the ambassadors (67.3%) did not themselves participate in the Solarize programme.

Data from this field experiment originate from three sources: (1) Connecticut Green Bank recorded installations and their timing; and after the conclusion of the Solarize campaign, solar ambassadors were (2) sent an online survey and (3) interviewed in person. Connecticut Green Bank data were used to ascertain installations as the dependent variable in the analysis of the field study, and ambassador interviews and surveys were used to derive the individual difference measures of ambassadors that were the predictors in the field study. We obtained county-level data on the suitability of rooftops for solar photovoltaics from the company GeoStellar. Yale University’s Institutional Review Boards reviewed the use of this data and approved it under protocol 1303011727.

Experiments. Our experiments were conducted using Qualtrics survey software and subjects were recruited using the crowdsourcing tool Amazon Mechanical Turk. Informed consent was obtained from all subjects and was approved by Yale University’s Institutional Review Boards protocol 1307012383.

Experiments 1 and 2 were designed to capture the key features of the field study in a vignette context (see Supplementary Information section 6 for full experimental materials for each experiment). The vignettes began on screen 1 with an initial description that provided basic information about the Solarize Connecticut campaign. Then, screen 2 provided information about a hypothetical solar ambassador (for maximal similarity to the field study, subjects were only provided with information about the ambassador that would have been evident to a community member in conversation with an ambassador). At the end of screen 2, subjects in experiment 1 and experiment 2 were randomized to receive information that indicated that the ambassador did or did not install solar panels through the Solarize programme. Then, on screen 3 the ambassador gave subjects the ‘pitch’ for Solarize, which was copied from the Solarize Connecticut website (<http://solarizect.com/about-solarize/>). In experiment 2, subjects next saw an additional screen in which

they learned about the ambassador’s private beliefs as a result of being behind the ambassador in the checkout line at the grocery store and overhearing him speaking on the phone to his wife (this screen was not included in experiment 1). Subjects in experiment 2 were randomized to either learn that the ambassador’s beliefs regarding solar panels were positive or negative. On the next screen, subjects in both experiments indicated their likelihood of participating in the Solarize programme using a seven-point Likert scale. This question is our dependent variable. Subjects in experiment 1 were then shown an additional screen with the second-order-belief scale that we developed for this study ($\alpha = 0.96$). The scale consisted of twelve items, each of which assessed different aspects of subjects’ second-order beliefs regarding Solarize (see Supplementary Information section 6.1.2 for the full scale). Finally, subjects in both experiments completed comprehension and demographic questions—including whether they were a homeowner—and were thanked for their participation.

In summary, experiment 1 had two conditions (ambassador installed versus ambassador did not install) and experiment 2 had four conditions, in a 2×2 (ambassador installed versus ambassador did not install) \times 2 (ambassador had positive beliefs about solar panels versus ambassador had negative beliefs about solar panels) design. To enable comparison of behaviour across experiment 1 and experiment 2, subjects for both experiments were recruited at the same time and were randomly assigned to one of the six total conditions. Our pre-registered target sample size was 100 subjects per condition, and we recruited $n = 200$ (64.5% female, average age = 34.6 years) for experiment 1 and $n = 399$ (61.1% female, average age = 34.6 years) for experiment 2. Subjects completed the survey in 7 min on average and were compensated 0.50 US dollars (US\$).

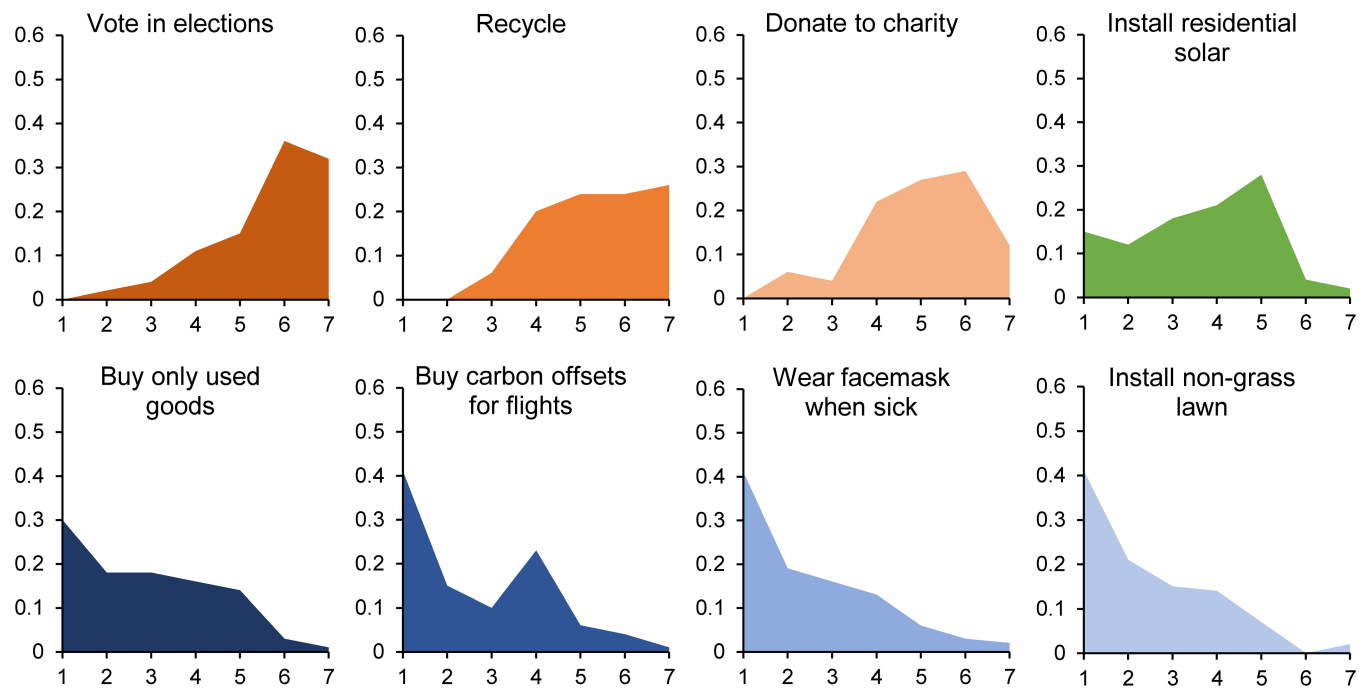
Experiment 3 aimed to test whether the results of the two-condition study of experiment 1 generalized to four highly non-normative behaviours. Thus, subjects were randomly assigned to one of eight between-subjects conditions in a 2×4 (ambassador engaged versus ambassador did not engage in the behaviour they were advocating) \times 4 (behaviour being advocated: purchasing carbon offsets for flights, only buying used goods, wearing a facemask in public when sick and replacing grass lawns with more sustainable ground cover) design. The format of experiment 3 was identical to experiment 1, except that all text related to installing solar panels though Solarize was replaced with relevant text about one of the four behaviours. Full experimental materials are shown in Supplementary Information section 6.4. Our pre-registered sample size was $n = 150$ subjects per condition, and we recruited $n = 1,206$ subjects (63.3% female, average age = 34.8 years), who completed the survey in 5 min on average and were compensated US\$0.50.

Subjects in the norming study were asked for their normativity judgments on various behaviours associated with contributions to public goods (presented in randomized order): wearing a face mask in public when sick with the flu or a cough; replacing grass lawns with more sustainable ground cover; buying carbon offsets for flights; buying only used consumer goods; installing residential solar panels; donating to charity; recycling; and voting in elections. For each behaviour (presented in randomized order), subjects were asked for their judgments of injunctive normativity, with the question: ‘in your opinion, how much do people in your community think this behaviour is what you are supposed to do?’. Responses were given on a seven-point scale from 1 (very little) to 7 (very much). The same was performed for descriptive normativity, with the question: ‘in your opinion, how many people in your community do this behaviour?’ (responses from 1 (very few) to 7 (very many)). Our pre-registered sample size was $n = 100$, and we recruited $n = 100$ subjects (45% female, average age = 36.2 years), who completed the study in 4 min on average and were compensated US\$0.50.

Reporting summary. Further information on research design is available in the Nature Research Reporting Summary linked to this paper.

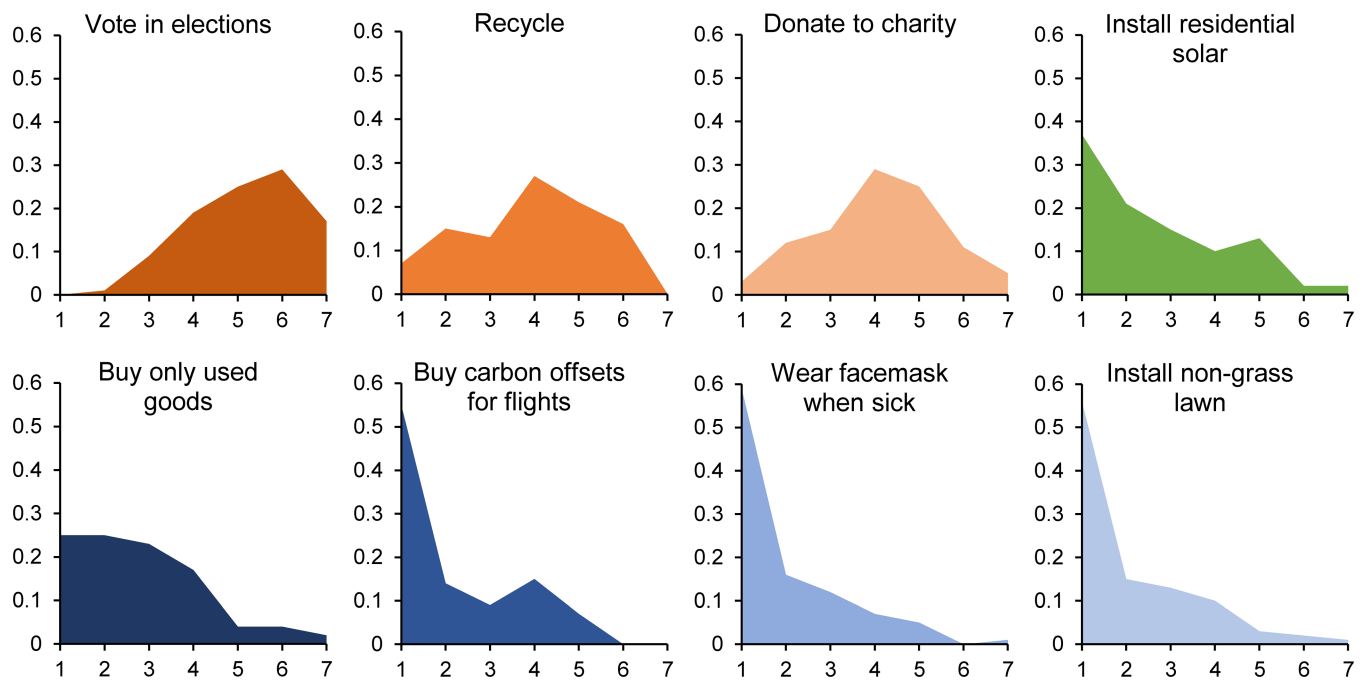
Data availability

All data are publicly available at: <http://osf.io/wbmjc>.



Extended Data Fig. 1 | Results of the norming study regarding injunctive norms. Distributions are shown of subjects' ($n = 100$) responses to the question: 'in your opinion, how much do people in your

community think doing this behaviour is what you are supposed to do?'. Responses were given on a Likert scale between 1 ('very little') and 7 ('very much').

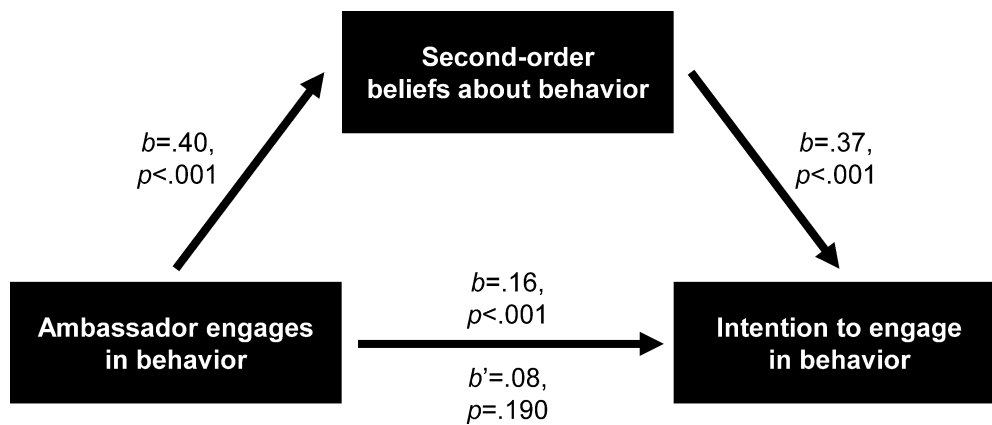


Extended Data Fig. 2 | Results of the norming study regarding descriptive norms. Distributions are shown of subjects' ($n=100$) responses to the question: 'in your opinion, how many people in your

community do this behaviour?'. Responses were given on a Likert scale between 1 ('very few') and 7 ('very many').



Extended Data Fig. 3 | Example photographs from Solarize campaigns. a–c, A live installation event (a), a campaign kick-off event (b) and flyers and signs for an informational event (c) are shown. Photographs courtesy of SmartPower.



Extended Data Fig. 4 | Mediation analysis for experiment 3. Because there is no evidence of heterogeneity in the effect of CREDs across non-normative public-good scenarios, we collapse across scenario (total $n = 1,206$) and see that subjects' second-order beliefs fully mediate the effect of ambassador engagement on subject intentions to engage in the behaviour in question. All variables are standardized for this analysis.

The correlations between ambassador engagement and second-order beliefs, second-order beliefs and subjects' intentions to engage in the behaviour, and ambassador engagement and subjects' intentions to engage in the behaviour (without (b) and with (b') second-order beliefs as a covariate) are shown.

m⁶A facilitates hippocampus-dependent learning and memory through YTHDF1

Hailing Shi^{1,2,3,4,17}, Xuliang Zhang^{5,6,17}, Yi-Lan Weng^{7,8,17}, Zongyang Lu⁵, Yajing Liu⁵, Zhike Lu^{1,2,3,4}, Jianan Li⁵, Piliang Hao⁵, Yu Zhang⁵, Feng Zhang^{7,8}, You Wu⁹, Jary Y. Delgado¹⁰, Yijing Su^{7,8}, Meera J. Patel¹⁰, Xiaohua Cao¹¹, Bin Shen¹², Xingxu Huang⁵, Guo-li Ming^{7,8,13,14,15}, Xiaoxi Zhuang¹⁰, Hongjun Song^{7,8,14,15,16,18*}, Chuan He^{1,2,3,4,18*} & Tao Zhou^{5,18*}

N⁶-methyladenosine (m⁶A), the most prevalent internal RNA modification on mammalian messenger RNAs, regulates the fates and functions of modified transcripts through m⁶A-specific binding proteins^{1–5}. In the nervous system, m⁶A is abundant and modulates various neural functions^{6–11}. Whereas m⁶A marks groups of mRNAs for coordinated degradation in various physiological processes^{12–15}, the relevance of m⁶A for mRNA translation in vivo remains largely unknown. Here we show that, through its binding protein YTHDF1, m⁶A promotes protein translation of target transcripts in response to neuronal stimuli in the adult mouse hippocampus, thereby facilitating learning and memory. Mice with genetic deletion of *Ythdf1* show learning and memory defects as well as impaired hippocampal synaptic transmission and long-term potentiation. Re-expression of YTHDF1 in the hippocampus of adult *Ythdf1*-knockout mice rescues the behavioural and synaptic defects, whereas hippocampus-specific acute knockdown of *Ythdf1* or *Mettl3*, which encodes the catalytic component of the m⁶A methyltransferase complex, recapitulates the hippocampal deficiency. Transcriptome-wide mapping of YTHDF1-binding sites and m⁶A sites on hippocampal mRNAs identified key neuronal genes. Nascent protein labelling and tether reporter assays in hippocampal neurons showed that YTHDF1 enhances protein synthesis in a neuronal-stimulus-dependent manner. In summary, YTHDF1 facilitates translation of m⁶A-methylated neuronal mRNAs in response to neuronal stimulation, and this process contributes to learning and memory.

The discovery of reversible RNA methylation and the development of transcriptome-wide mapping methods of m⁶A have sparked extensive research into the functions of m⁶A methylation in diverse biological processes^{16–19}, with several studies showing that m⁶A governs mRNA stability during cell fate transition and animal development^{1,12–15}. In addition, m⁶A affects mRNA translation. In HeLa cells, the m⁶A binding protein YTHDF1 facilitates the initiation of translation of m⁶A-modified mRNAs³. In MCF7 cells, m⁶A and YTHDF1 appear to have more complex effects on translation²⁰. Therefore, it remains to be discovered how m⁶A modulates mRNA translation and to what extent this function affects physiological events in intact biological systems.

Previous studies have suggested that m⁶A modulates neuronal functions, including dopaminergic signalling in the mouse midbrain⁶, flight and locomotor behaviours in flies⁷, neurogenesis in adult mice⁸, and axon regeneration in mice⁹. Upregulation of m⁶A has been observed to occur with brain maturation¹⁹, behavioural experience¹⁰, and memory

formation¹¹, suggesting a link between m⁶A accumulation and brain activity. Learning and memory are fundamental functions of brains, and long-term memory formation is believed to require activity-induced protein synthesis²¹. We therefore investigated whether learning and memory processes could be affected by the translational effects of m⁶A and YTHDF1.

In the mouse brain, *Ythdf1* mRNA is preferentially expressed in the hippocampus²², a key region in spatial learning and memory. We constructed *Ythdf1* CRISPR–Cas9 knockout (*Ythdf1*-KO) mice²³ (Extended Data Fig. 1a–d), in which complete elimination of YTHDF1 protein was verified in the hippocampus and other brain regions (Fig. 1a; Extended Data Fig. 1e, f). Compared to wild-type control littermates, *Ythdf1*-KO mice developed normally up to four months of age (the end of the experiment) and appeared to have normal gross hippocampal histology (Fig. 1b), adult hippocampal neurogenesis (Extended Data Fig. 2a, b), and cortical morphology (Extended Data Fig. 2c, d). Moreover, loss of YTHDF1 did not alter the motor abilities or general emotional states of the mice (Extended Data Fig. 2e–m).

We first examined hippocampus-dependent spatial learning and memory in these mice using Morris water maze (MWM) tests²⁴ (Extended Data Fig. 3a; see Methods). In visible platform training, *Ythdf1*-KO mice performed as proficiently as wild-type mice (Fig. 1c), indicating that they could see and acquire procedural learning normally. However, in hidden platform training, *Ythdf1*-KO mice spent a longer time navigating to the platform than control mice (Fig. 1d), suggesting that their spatial learning was impaired. In the probe test, *Ythdf1*-KO mice failed to remember the previous platform location, spending a similar time in each quadrant despite showing normal swimming activity (Fig. 1e; Extended Data Fig. 3b, c), suggesting defects in spatial memory.

To further confirm the importance of YTHDF1 in hippocampus-dependent learning and memory, we performed classical fear conditioning tests (Extended Data Fig. 3d; see Methods). Contextual fear memory is sensitive to hippocampal defects, whereas auditory fear memory depends on the amygdala²⁵. We titrated the electric shock intensity to establish fear conditioning protocols that did not saturate fear responses (Extended Data Fig. 3e). Under a moderate training protocol (0.5 mA, 2 s, 1 pair), *Ythdf1*-KO mice showed a smaller freezing response during inter-trial intervals (ITIs) but not when the tone sounded (Fig. 1f; Extended Data Fig. 3f), suggesting that contextual but not auditory learning was impaired. Twenty-four hours after conditioning, *Ythdf1*-KO mice showed deficits in contextual but not auditory fear

¹Department of Chemistry, The University of Chicago, Chicago, IL, USA. ²Department of Biochemistry and Molecular Biology, The University of Chicago, Chicago, IL, USA. ³Institute for Biophysical Dynamics, The University of Chicago, Chicago, IL, USA. ⁴Howard Hughes Medical Institute, The University of Chicago, Chicago, IL, USA. ⁵School of Life Science and Technology, ShanghaiTech University, Shanghai, China. ⁶Laboratory Animal Center, Zhejiang University, Hangzhou, China. ⁷Department of Neuroscience Perelman School of Medicine, University of Pennsylvania, Philadelphia, PA, USA. ⁸Mahoney Institute for Neurosciences, Perelman School of Medicine, University of Pennsylvania, Philadelphia, PA, USA. ⁹School of Life Sciences and Technology, Tongji University, Shanghai, China. ¹⁰Department of Neurobiology, The University of Chicago, Chicago, IL, USA. ¹¹Key Laboratory of Brain Functional Genomics, Ministry of Education, Shanghai Key Laboratory of Brain Functional Genomics, School of Life Sciences, East China Normal University, Shanghai, China. ¹²State Key Laboratory of Reproductive Medicine, Department of Histology and Embryology, Nanjing Medical University, Nanjing, China. ¹³Department of Psychiatry, Perelman School of Medicine, University of Pennsylvania, Philadelphia, PA, USA. ¹⁴Department of Cell and Developmental Biology, Perelman School of Medicine, University of Pennsylvania, Philadelphia, PA, USA. ¹⁵Institute for Regenerative Medicine, Perelman School of Medicine, University of Pennsylvania, Philadelphia, PA, USA. ¹⁶The Epigenetics Institute, Perelman School of Medicine, University of Pennsylvania, Philadelphia, PA, USA. ¹⁷These authors contributed equally: Hailing Shi, Xuliang Zhang, Yi-Lan Weng. ¹⁸These authors jointly supervised this work: Hongjun Song, Chuan He, Tao Zhou. *e-mail: shongjun@pennmedicine.upenn.edu; chuanhe@uchicago.edu; zhoutao@shanghaitech.edu.cn

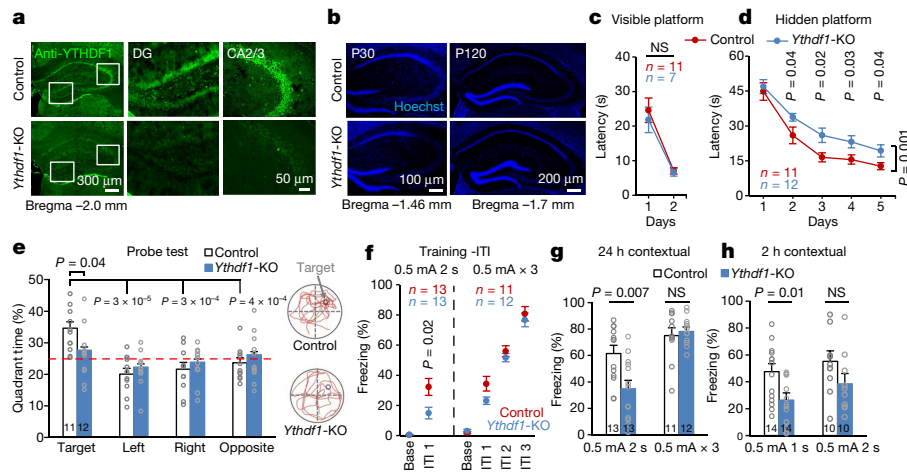


Fig. 1 | Impaired spatial learning and memory in *Ythdf1*-KO mice.

a, b, Representative images of YTHDF1 immunostaining (**a**) and Hoechst staining (**b**) in control and *Ythdf1*-KO hippocampus. DG, dentate gyrus; P30 and P120, postnatal days 30 and 120. **c, d**, Learning curves of control (red) and *Ythdf1*-KO (blue) mice in MWM tests with visible (**c**) and hidden (**d**) platform. **e**, Quadrant time (per cent; left) and representative swimming paths (right) of control and *Ythdf1*-KO mice in the MWM probe test. The red dashed line represents the chance level (25%).

memory (Fig. 1g; Extended Data Fig. 3g). Under a weaker training protocol (0.5 mA, 1 s, 1 pair), contextual but not auditory fear memory of the mice was impaired two hours after training (Fig. 1h; Extended Data Fig. 3h). Together, these data support the idea that genetic deletion of *Ythdf1* disrupts learning and memory formation in the mouse hippocampus.

We next used electrophysiological characterization to study how YTHDF1 depletion affects hippocampal synaptic functions. We used whole-cell patch-clamp to examine the basal synaptic properties of hippocampal CA1 neurons (see Methods). In *Ythdf1*-KO CA1 neurons, spontaneous miniature excitatory postsynaptic currents (mEPSCs) were substantially decreased in amplitude and frequency, compared to control neurons (Fig. 2a, b). Analysis of paired-pulse ratios (PPRs) also indicated reduced presynaptic release probability in *Ythdf1*-KO CA1 neurons (Extended Data Fig. 4a, b), confirming the defects in basal synaptic transmission. Morphologically, *Ythdf1*-KO CA1 neurons had reduced dendritic spine density but unaltered spine size (Extended Data Fig. 4c, d).

Long-term potentiation (LTP) is an important cellular model for explaining learning and memory. To test whether YTHDF1 modulates long-term synaptic plasticity, we recorded LTP induced by high-frequency stimulation (HFS) in the CA1 region of hippocampal slices. Compared to wild-type controls, *Ythdf1*-KO slices did not generate normal levels of field excitatory postsynaptic potential (fEPSP) after two rounds of HFS induction (Fig. 2c, d). Initial potentiation following HFS was similar between control and *Ythdf1*-KO slices (Fig. 2c); therefore, it is less likely that the decreased LTP was due only to impairments in basal synaptic transmission. *Ythdf1*-KO slices were also defective in late-phase LTP (induced by four rounds of HFS; Fig. 2e, f), which requires activity-induced synaptic protein synthesis. Indeed, depletion of YTHDF1 noticeably reduced the abundance of key proteins involved in LTP in the postsynaptic density (PSD) fraction of hippocampal neurons (Fig. 2g, h; Extended Data Fig. 4e), although such decreases were not observed for those proteins in whole hippocampal tissue (Extended Data Fig. 4f). Together, these results suggest that depletion of YTHDF1 in mice impairs basal synaptic transmission and LTP in hippocampal neurons, contributing to the observed defects in learning and memory.

To confirm that the observed defects resulted from the loss of YTHDF1 specifically in the hippocampus, we investigated whether re-expressing YTHDF1 in the hippocampus of adult *Ythdf1*-KO mice would be sufficient to rescue the phenotypes. We delivered an

f, Learning curves of control (red) and *Ythdf1*-KO mice (blue) for contextual fear conditioning in moderate (left) or strong (right) training sessions. Base, baseline; ITI, inter-trial interval. **g, h**, Contextual fear memory assessed 24 h (**g**) or 2 h (**h**) after the indicated fear conditioning. *P* values, two-way ANOVA with two-tailed *t*-test (relative to “Target” or between genotypes) (**e**), two-way repeated measures ANOVA with post hoc test (**c, d, f**), and two-tailed *t*-test (**g, h**). Numbers in bars, numbers of mice. Data shown as mean \pm s.e.m.

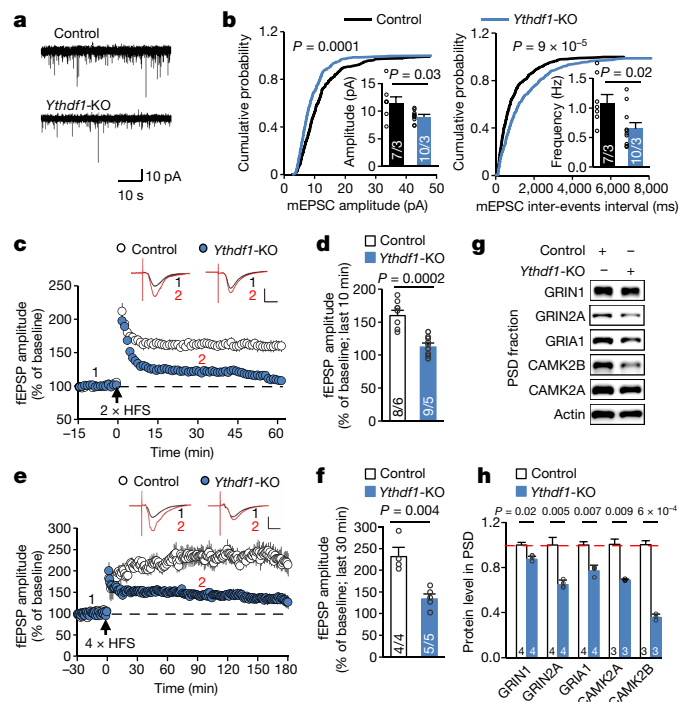


Fig. 2 | Deficient basal transmission and plasticity in *Ythdf1*-KO hippocampal synapses.

a, b, Representative traces (**a**) and quantification of amplitude (**b**, left) and frequency (**b**, right) of spontaneous mEPSCs in control and *Ythdf1*-KO hippocampal CA1 neurons. **c, d**, Summary plots (**c**) and average amplitude (**d**) of LTP induced by 2 \times HFS in the CA1 region of control and *Ythdf1*-KO acute slices. **e, f**, Summary plots (**e**) and average amplitude (**f**) of late-phase LTP induced by 4 \times HFS. Top, sample traces taken at time points 1 and 2 indicated above the summary plots; scale bars, 10 ms (horizontal) and 0.2 mV (vertical) (**c, e**). **g, h**, Representative western blots (**g**) and quantification (**h**) of LTP-related proteins in control and *Ythdf1*-KO hippocampal postsynaptic density (PSD) fractions. *P* values, Kolmogorov–Smirnov test for cumulative distributions followed by comparisons with Mann–Whitney *U* test (**b**) and two-tailed *t*-test (**d, f, h**). Numbers in bars, numbers of neurons/mice (**b**), slices/mice (**d, f**), and mice (**h**). Data shown as mean \pm s.e.m.

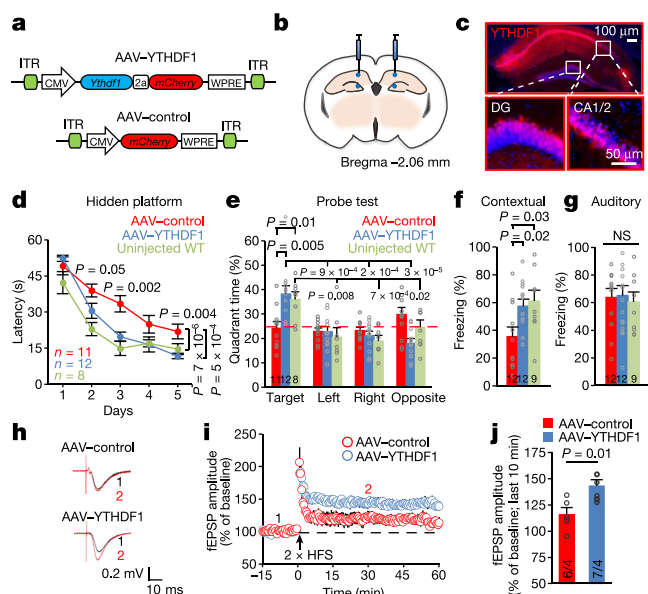


Fig. 3 | Selective YTHDF1 re-expression in the hippocampus rescues defects in memory and synaptic plasticity. **a**, Schematics of AAV constructs overexpressing YTHDF1 (AAV-YTHDF1) or control (AAV-control). ITR, inverted terminal repeats; CMV, cytomegalovirus promoter; WPRE, woodchuck hepatitis virus posttranscriptional regulatory element. **b**, Illustration of bilateral viral injections into the mouse hippocampus. Mouse brain reproduced with permission from the atlas of Paxinos and Franklin²⁹. **c**, Representative fluorescence images of the mouse hippocampus after AAV infection. Hoechst, blue; YTHDF1 co-expressed with mCherry, red. **d–g**, Learning curves in MWM hidden-platform training (**d**), quadrant time (per cent) in MWM probe tests (**e**), and contextual (**f**) and auditory (**g**) fear memories assessed 24 h after fear conditioning, of *Ythdf1*-KO mice injected with AAV-control (red) or AAV-YTHDF1 (blue), compared to uninjected wild-type (WT, green). **h–j**, Representative traces (**h**), summary plots (**i**), and average amplitude (**j**) of LTP induced by $2 \times$ HFS in acute slices from *Ythdf1*-KO mice injected with AAV-YTHDF1 or AAV-control. Sample traces (**h**) were taken at time points 1 and 2 indicated in the summary plots (**i**). *P* values, two-way repeated measures ANOVA with post hoc two-tailed *t*-test (horizontal *P* values, AAV-YTHDF1 relative to AAV-control; vertical *P* values, comparisons between curves) (**d**), two-way ANOVA with post hoc two-tailed *t*-test (comparison within group or with ‘Target’) (**e**), one-way ANOVA with post hoc Fisher test (**f**, **g**), and two-tailed *t*-test (**j**). Numbers in bars, numbers of mice (**e–g**) and slices/mice (**j**). Data shown as mean \pm s.e.m.

adeno-associated virus (AAV) expressing either YTHDF1 (AAV-YTHDF1) or a control fluorescent protein mCherry (AAV-control) specifically to the hippocampus by bilateral stereotactic injection (Fig. 3a, b), resulting in selective re-expression in injected regions (Fig. 3c; Extended Data Fig. 5a–c). Hippocampal re-expression of YTHDF1 in *Ythdf1*-KO mice substantially enhanced their learning and memory performances in MWM tests (Fig. 3d, e; Extended Data Fig. 5d) and restored contextual fear memory to normal levels (Fig. 3f), with no obvious effect on auditory fear memory, anxiety-like behaviour, or motor activity (Fig. 3g; Extended Data Fig. 5e–h); it also reversed the hippocampal LTP deficiency in *Ythdf1*-KO mice (Fig. 3h–j).

To test whether acute loss of YTHDF1 in the hippocampus was sufficient to induce the phenotypes of *Ythdf1*-KO mice, we injected an AAV expressing a short hairpin RNA specifically targeting *Ythdf1* transcripts (AAV-RNAi) to the hippocampus of adult wild-type mice (Extended Data Fig. 6a, b). In mice injected with AAV-RNAi, learning and memory in MWM tests were markedly impaired (Extended Data Fig. 6c–f), as was contextual fear memory but not emotional state or auditory fear memory (Extended Data Fig. 6g–i). Moreover, hippocampus-specific knockdown of *Mettl3* (Extended Data Fig. 7a) also phenocopied the effects of YTHDF1 depletion, leading to defects in spatial memory and

contextual fear memory without affecting auditory fear memory or locomotor activity (Extended Data Fig. 7b–f). These knockdown results further support the idea that the observed phenotypes in *Ythdf1*-KO mice come from direct depletion of YTHDF1 instead of potential developmental defects caused by lack of YTHDF1 and are m⁶A-dependent.

We next proceeded to investigate the underlying molecular mechanisms of these effects. We mapped YTHDF1 binding sites and m⁶A sites on hippocampal mRNAs using crosslinking and immunoprecipitation-based sequencing methods (CLIP-seq; Supplementary Table 1). Biological triplicates of YTHDF1 CLIP-seq identified 3,552 common peaks as high-confidence peaks (Extended Data Fig. 8a) on 1,042 transcripts (defined as ‘YTHDF1-CLIP targets’; Supplementary Table 2), with validated pull-down efficiency of YTHDF1 (Extended Data Fig. 8b). About two-thirds of the high-confidence YTHDF1-CLIP peaks were mapped to mature mRNAs (Fig. 4a) and enriched near the stop codon and 3’UTR (Fig. 4b). Functional annotation of YTHDF1-CLIP targets revealed substantial enrichment for synaptic transmission and LTP (Fig. 4c; Supplementary Table 2), consistent with the neuronal phenotypes observed in *Ythdf1*-KO mice.

Biological triplicates of m⁶A-CLIP-seq, using purified hippocampal poly(A)⁺ RNA, yielded about 11,000 common peaks with the GGACU consensus sequence and enrichment at the coding sequence and 3’UTR (Extended Data Fig. 8c–e) on 3,460 transcripts (defined as ‘m⁶A-modified transcripts’; Supplementary Tables 1, 3). Similarly, genes that mediate neuronal biological processes were overrepresented in m⁶A-modified transcripts (Extended Data Fig. 8f; Supplementary Table 3). At the transcript level, YTHDF1-CLIP targets on average have higher numbers of m⁶A-CLIP peaks and crosslinking-induced mutations detected in the m⁶A-CLIP-seq data, either compared to transcripts without YTHDF1-CLIP peaks (defined as ‘non-YTHDF1-CLIP transcripts’), or compared to m⁶A-modified transcripts (Fig. 4d); at the peak level, 30% of YTHDF1-CLIP peaks overlap (>1 nucleotide) with m⁶A-CLIP peaks (Extended Data Fig. 8g; in comparison, 0.65–0.72% of background peaks overlap with m⁶A-CLIP peaks; see Supplementary Table 3, Methods). These results indicate that YTHDF1 preferentially recognizes m⁶A sites in the adult mouse hippocampus. Key synaptic plasticity transcripts, including *Gria1*, *Grin1*, and *Camk2a*, contain one or more overlapped YTHDF1-CLIP peaks and m⁶A-CLIP peaks (Extended Data Fig. 8h). We then profiled mRNA and protein abundance in the hippocampus of *Ythdf1*-KO and control mice. Note that YTHDF1-CLIP targets and m⁶A-modified transcripts exhibit a slight decrease in mRNA abundance (Extended Data Fig. 8i; Supplementary Tables 1, 4) and no observable changes in global protein level (Extended Data Fig. 8j; Supplementary Table 5) in the hippocampus of *Ythdf1*-KO mice compared to control mice.

These mild changes prompted us to investigate whether YTHDF1 functions in a neuronal-stimulus-dependent manner. To test this, we monitored nascent protein synthesis²⁶ in cultured wild-type and *Ythdf1*-KO hippocampal neurons before and after potassium chloride depolarization (KCl, 50 mM). KCl stimulation induced noticeable protein synthesis in control neurons but much less in *Ythdf1*-KO neurons (Fig. 4e, f; Extended Data Fig. 9a–c). We found the same difference between AAV-mediated control and YTHDF1-knockdown neurons (Extended Data Fig. 9d, e). We also constructed a reporter system in which the N terminus of YTHDF1 (YTHDF1-N) was tethered to the 3’ UTR of the firefly luciferase (F-Luc) coding sequence, mimicking direct binding of YTHDF1 onto m⁶A-modified transcripts; *Renilla* luciferase was co-transfected for normalization³ (Fig. 4g). YTHDF1-N tethering did not affect F-Luc protein level before KCl stimulation (Fig. 4h, left), consistent with proteomics results (Extended Data Fig. 8j). However, increased F-Luc production was observed 2 and 4 h after KCl stimulus for YTHDF1-N tethering compared to the control (Fig. 4h), supporting the idea that YTHDF1 promotes protein synthesis upon neuronal stimulation. Indeed, *Bsn*, one of the top YTHDF1-CLIP targets, showed attenuated protein expression after fear conditioning in the *Ythdf1*-KO hippocampus, as did *Camk2a* in the *Ythdf1*-KO PSD fraction (Extended Data Fig. 10a). After fear conditioning, YTHDF1 protein increased by

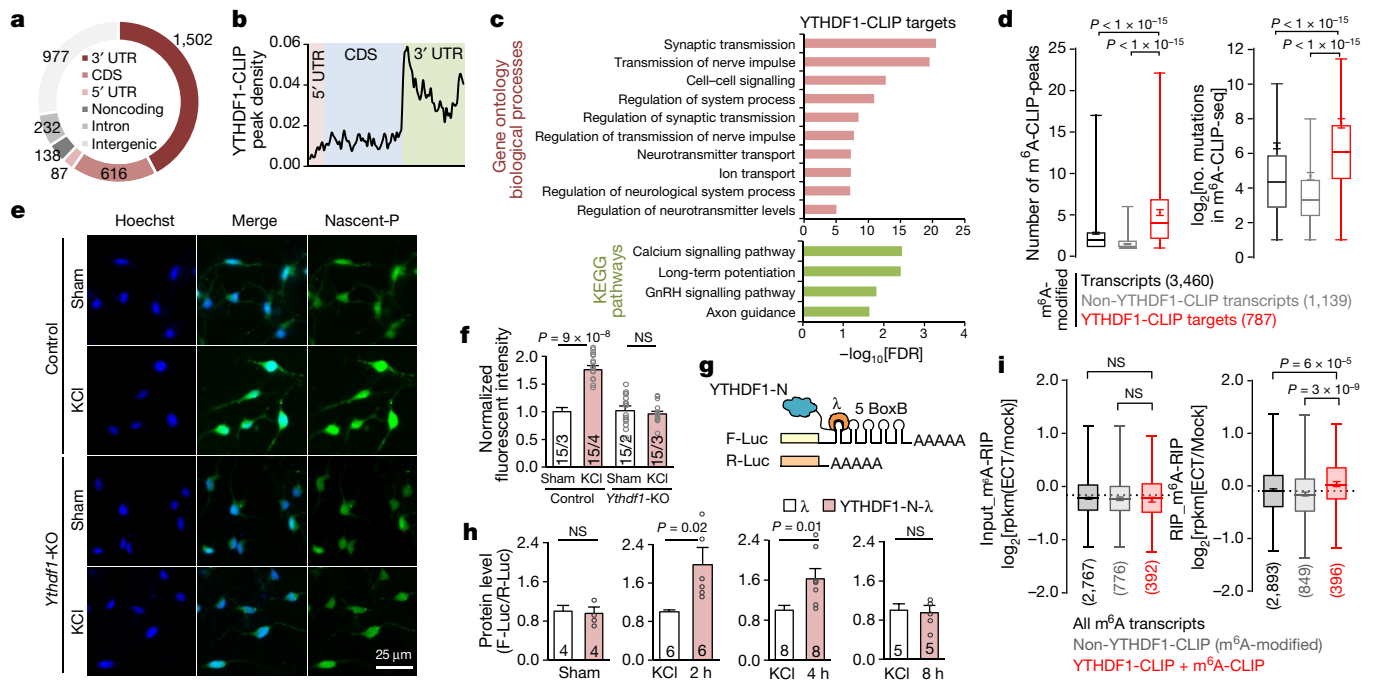


Fig. 4 | YTHDF1 facilitates translation of m⁶A-modified targets in response to neuronal stimulation. **a, b**, Distributions of high-confidence YTHDF1-CLIP peaks in different regions of genome (**a**) and transcripts (**b**). **c**, Functional annotation of YTHDF1-CLIP targets ($n = 1,032$) in the adult mouse hippocampus. **d**, Box-plots of the number of m⁶A-CLIP peaks (left) and the log₂ number of m⁶A-CLIP-seq mutations (right) on m⁶A-modified transcripts, non-YTHDF1-CLIP transcripts, and YTHDF1-CLIP targets. **e, f**, Representative images (**e**) and quantification (**f**) of nascent protein (Nascent-P) synthesis in cultured control and *Ythdf1*-KO hippocampal neurons before (sham) and 2 h after KCl depolarization. Nascent-P signals were normalized to that of control neurons under sham condition. **g**, Schematic of a tether reporter system that mimics binding between YTHDF1 and 3' UTR m⁶A sites of target transcripts. YTHDF1-N, truncated N-terminal mouse YTHDF1 (amino acids 1–389); F-Luc/R-Luc, firefly/*Renilla* luciferase. **h**, Normalized F-Luc reporter expression

in cultured hippocampal neurons tethered with YTHDF1-N or control (λ), before (sham) and after KCl depolarization. **i**, Box-plots of transcript abundance log₂ fold change between electroconvulsive treated (ECT) and untreated (Mock) dentate gyrus, for m⁶A-modified transcripts, m⁶A-modified non-YTHDF1-CLIP transcripts, and transcripts with overlapped YTHDF1-CLIP and m⁶A-CLIP peaks, in 'Input' (left) and m⁶A-enriched 'RIP' (right) RNA-seq libraries. Dashed lines, median log₂ fold change of all reliably detected transcripts (reads per kilobase of transcript per million mapped reads (rpkm) > 1). Box-plot elements: centre line, median; box limits, upper and lower quartiles; whiskers, 1–99%; error bars, 95% confidence interval of mean; number in parentheses, number of genes (**d, i**). P values, two-sided unpaired Kolmogorov–Smirnov test (**d, i**) and two-tailed t -test (**f, h**). Numbers in bars, numbers of images/mice (**f**) and biologically independent samples (**h**). Bar plots show mean \pm s.e.m. (**f, h**).

30% in the PSD fraction, although no change occurred at the tissue level (Extended Data Fig. 10b, c). This suggests that YTHDF1 may undergo translocation to the PSD in response to stimulation, which could contribute to localized translation in synapses and thus synaptic plasticity.

We also examined potential changes in the m⁶A landscape in the dentate gyrus in an electroconvulsive treatment (ECT) model, in which dentate granule cells are synchronously activated^{27,28}. The m⁶A RNA immunoprecipitation (RIP)-seq of dentate gyrus mRNAs (Extended Data Fig. 10d; see Methods) showed that although the level of YTHDF1-CLIP targets was not differentially regulated compared to other transcripts in response to ECT, the m⁶A-methylated copies of YTHDF1-CLIP targets were upregulated in abundance after ECT (Fig. 4i; Supplementary Tables 1, 6), suggesting that an increase in binding of YTHDF1 to its m⁶A-methylated targets may occur upon stimulation to both facilitate translation and help to stabilize these targets (Supplementary Discussion).

In summary, we show that m⁶A methylation of mRNAs facilitates learning and memory formation in the mouse hippocampus, mainly by promoting translation of target transcripts upon neuronal stimulation, and that this effect is mediated through the m⁶A-binding protein YTHDF1. Depletion of YTHDF1 impairs basal transmission and LTP at hippocampal synapses. The presence of YTHDF1 could expedite new protein synthesis that is required for long-lasting changes in synaptic plasticity and thus memory formation; in the hippocampus of *Ythdf1*-KO mice, stimulus-dependent protein synthesis is attenuated, resulting in less efficient synaptic strengthening and a lower probability of reaching thresholds for memory formation (Extended Data Fig. 10e).

Promotion of translation by m⁶A could be stimulation-induced, as shown here for YTHDF1, and this might represent an important aspect of RNA methylation-dependent translational regulation¹.

Online content

Any methods, additional references, Nature Research reporting summaries, source data, statements of data availability and associated accession codes are available at <https://doi.org/10.1038/s41586-018-0666-1>.

Received: 9 November 2017; Accepted: 21 August 2018;

Published online 31 October 2018.

- Roundtree, I. A., Evans, M. E., Pan, T. & He, C. Dynamic RNA modifications in gene expression regulation. *Cell* **169**, 1187–1200 (2017).
- Wang, X. et al. N⁶-methyladenosine-dependent regulation of messenger RNA stability. *Nature* **505**, 117–120 (2014).
- Wang, X. et al. N⁶-methyladenosine modulates messenger RNA translation efficiency. *Cell* **161**, 1388–1399 (2015).
- Xiao, W. et al. Nuclear m⁶A reader YTHDC1 regulates mRNA splicing. *Mol. Cell* **61**, 507–519 (2016).
- Roundtree, I. A. et al. YTHDC1 mediates nuclear export of N⁶-methyladenosine methylated mRNAs. *eLife* **6**, e31311 (2017).
- Hess, M. E. et al. The fat mass and obesity associated gene (Fto) regulates activity of the dopaminergic midbrain circuitry. *Nat. Neurosci.* **16**, 1042–1048 (2013).
- Lence, T. et al. m⁶A modulates neuronal functions and sex determination in *Drosophila*. *Nature* **540**, 242–247 (2016).
- Li, L. et al. Fat mass and obesity-associated (FTO) protein regulates adult neurogenesis. *Hum. Mol. Genet.* **26**, 2398–2411 (2017).
- Weng, Y.-L. et al. Epitranscriptomic m⁶A regulation of axon regeneration in the adult mammalian nervous system. *Neuron* **97**, 313–325.e6 (2018).

10. Widagdo, J. et al. Experience-dependent accumulation of N^6 -methyladenosine in the prefrontal cortex is associated with memory processes in mice. *J. Neurosci.* **36**, 6771–6777 (2016).
11. Walters, B. J. et al. The role of the RNA demethylase FTO (Fat Mass and Obesity-Associated) and mRNA methylation in hippocampal memory formation. *Neuropsychopharmacology* **42**, 1502–1510 (2017).
12. Zhao, B. S. et al. m^6A -dependent maternal mRNA clearance facilitates zebrafish maternal-to-zygotic transition. *Nature* **542**, 475–478 (2017).
13. Ivanova, I. et al. The RNA m^6A reader YTHDF2 is essential for the post-transcriptional regulation of the maternal transcriptome and oocyte competence. *Mol. Cell* **67**, 1059–1067.e4 (2017).
14. Li, H.-B. et al. m^6A mRNA methylation controls T cell homeostasis by targeting the IL-7/STAT5/SOCS pathways. *Nature* **548**, 338–342 (2017).
15. Yoon, K. J. et al. Temporal control of mammalian cortical neurogenesis by m^6A methylation. *Cell* **171**, 877–889.e17 (2017).
16. Jia, G. et al. N^6 -methyladenosine in nuclear RNA is a major substrate of the obesity-associated FTO. *Nat. Chem. Biol.* **7**, 885–887 (2011).
17. Zheng, G. et al. ALKBH5 is a mammalian RNA demethylase that impacts RNA metabolism and mouse fertility. *Mol. Cell* **49**, 18–29 (2013).
18. Dominissini, D. et al. Topology of the human and mouse m^6A RNA methylomes revealed by m^6A -seq. *Nature* **485**, 201–206 (2012).
19. Meyer, K. D. et al. Comprehensive analysis of mRNA methylation reveals enrichment in 3' UTRs and near stop codons. *Cell* **149**, 1635–1646 (2012).
20. Slobodin, B. et al. Transcription impacts the efficiency of mRNA translation via co-transcriptional N^6 -adenosine methylation. *Cell* **169**, 326–337.e12 (2017).
21. Sutton, M. A. & Schuman, E. M. Dendritic protein synthesis, synaptic plasticity, and memory. *Cell* **127**, 49–58 (2006).
22. Lein, E. S. et al. Genome-wide atlas of gene expression in the adult mouse brain. *Nature* **445**, 168–176 (2007).
23. Shen, B. et al. Efficient genome modification by CRISPR-Cas9 nickase with minimal off-target effects. *Nat. Methods* **11**, 399–402 (2014).
24. Morris, R. G. M., Garrud, P., Rawlins, J. N. P. & O'Keefe, J. Place navigation impaired in rats with hippocampal lesions. *Nature* **297**, 681–683 (1982).
25. LeDoux, J. E. Emotion circuits in the brain. *Annu. Rev. Neurosci.* **23**, 155–184 (2000).
26. Liu, J., Xu, Y., Stoleru, D. & Salic, A. Imaging protein synthesis in cells and tissues with an alkyne analog of puromycin. *Proc. Natl Acad. Sci. USA* **109**, 413–418 (2012).
27. Ma, D. K. et al. Neuronal activity-induced Gadd45b promotes epigenetic DNA demethylation and adult neurogenesis. *Science* **323**, 1074–1077 (2009).
28. Guo, J. U., Su, Y., Zhong, C., Ming, G. L. & Song, H. Hydroxylation of 5-methylcytosine by TET1 promotes active DNA demethylation in the adult brain. *Cell* **145**, 423–434 (2011).
29. Franklin, K. & Paxinos, G. *The Mouse Brain in Stereotaxic Coordinates 2nd edn* (Academic, San Diego, 2004).

Acknowledgements This study was supported by the National Key R&D Program of China (2016YFA0500903 to X.H.), the National Institute of Health (HG008935 and GM113194 to C.H.; DA043361 to X. Zhuang), the National Natural Science Foundation of China (31500866 to T.Z. and 31471077 to X.C.), the Simons Foundation Autism Research Initiative (SFARI) to H. Song, and the Dr. Miriam and Sheldon G. Adelson Medical Research Foundation (AMRF) to G.-I.M. C.H. is an investigator of the Howard Hughes Medical Institute. T.Z. is sponsored by the Shanghai Rising-Star Program. X.H. is sponsored by the Startup Foundation of ShanghaiTech University. X. Zhang is sponsored by Zhejiang Public Welfare Technology Application Research Project (2018C37118). We thank P. Cao, and X. Wang for discussions; Z. Qiu and T. Cheng for help with primary neuron culture; M. Wu for suggestions on proteomics data analyses; and J. Tauler, P. J. Hsu, and A. C. Zhu for editing help.

Author contributions C.H. and T.Z. conceived the study. H. Shi, X. Zhang, Y.-L.W., C.H., H. Song, and T.Z. designed experiments. X. Zhang and T.Z. performed animal and cell biology experiments. H. Shi, X. Zhang, and T.Z. performed biochemistry experiments. H. Shi, Zhike Lu, and Y.-L.W. analysed sequencing data. Zongyang Lu helped with primary neuron culture and virus packaging. J.L. helped with plasmid construction. P.H. performed mass spectrometry experiments and data analysis. X.C. helped with behavioural tests and electrophysiological recordings. Y.-L.W., F.Z., Y.S., G.-I.M., and H. Song performed in vivo ECT stimulation. X.H. and B.S. helped with generation of knockout mice. Y.L. and Y.Z. helped with cell culture and RNAi testing. Y.W. helped with CLIP-seq experiments. J.Y.D., M.J.P., and X. Zhuang helped with mouse tissue dissection. H. Shi, X. Zhang, C.H., and T.Z. wrote the manuscript with input from all authors.

Competing interests C.H. is a scientific founder of Accent Therapeutics, Inc. and a shareholder of Epican Genetech.

Additional information

Extended data is available for this paper at <https://doi.org/10.1038/s41586-018-0666-1>.

Supplementary information is available for this paper at <https://doi.org/10.1038/s41586-018-0666-1>.

Reprints and permissions information is available at <http://www.nature.com/reprints>.

Correspondence and requests for materials should be addressed to H.S. or C.H. or T.Z.

Publisher's note: Springer Nature remains neutral with regard to jurisdictional claims in published maps and institutional affiliations.

METHODS

Data reporting. No statistical methods were used to predetermine sample size. The sample sizes in this manuscript were similar to previous papers^{3,30}. Experimenters were blind to the genotype and treatment for all behavioural tests.

Animals. All mice were maintained under a 12–12-h light–dark cycle with lights on at 07:00, and temperature and humidity were kept at $22 \pm 1^\circ\text{C}$, $55\% \pm 5\%$, with ad libitum access to food and water. Male adult (8–16 weeks of age) mice were used for behavioural tests. Animal experiments, except for electroconvulsive treatment (ECT), were carried out in accordance with protocols approved by the Institutional Animal Care and Use Committee of the School of Life Science and Technology of Shanghai University and with the Guidance Suggestions for the Care and Use of Laboratory Animals, formulated by Ministry of Science & Technology of the People's Republic of China. Animal procedures used in ECT were performed in accordance with protocols approved by the Institutional Animal Care and Use Committee of Johns Hopkins University School of Medicine and University of Pennsylvania School of Medicine.

Cell lines. The N2A cell line used in *in vitro* transfection experiments was purchased from Cell Bank of Chinese Academy of Sciences and authenticated by the supplier. It is not in the list of commonly misidentified cell lines maintained by the International Cell Line Authentication Committee (ICLAC). Cells were tested negative for mycoplasma contamination before use.

Generation of *Ythdf1*-KO mice. The YTH domain family protein-1 knockout mice (*Ythdf1*-KO) were generated using CRISPR–Cas9. sgRNA expression plasmids were generated by annealing and cloning oligos that were designed to target exon 4 of *Ythdf1* into the BsaI sites of pUC57-sgRNA (Addgene 51132). mYTHDF1-E4-1 T7 gRNA up: TAGGATAGTAACCTGGACAGGTA; mYTHDF1-E4-1 gRNA down: AAACCTACCTGTCCAGTTACTAT; mYTHDF1-E4-2 T7 gRNA up: TAGGCACCATGGTCCACTGCAG; mYTHDF1-E4-2 gRNA down: AAACCTGCAGTGGACCATGGTG.

In vitro transcription and microinjection of CRISPR–Cas9 were performed as previously described²³. In brief, the Cas9 expression construct pST1374-Cas9-N-NLS-Flag-linker-D10A (Addgene 51130) was linearized with AgeI and transcribed using the mMACHINE T7 Ultra Kit (Ambion, AM1345). Cas9 mRNA was purified using RNeasy Mini Kit (Qiagen, 74104). pUC57-sgRNA expression vectors were linearized by DraI and transcribed using the MEGAshortscript Kit (Ambion, AM1354). sgRNAs were purified by MEGAclear Kit (Ambion, AM1908). A mixture of Cas9 mRNA (20 ng/ μl) and two sgRNAs (5 ng/ μl each) was injected into cytoplasm and male pronucleus of zygotes obtained by mating of CBF1. Injected zygotes were transferred into pseudo-pregnant CD1 female mice. Founder mice used for experiments were backcrossed to C57BL/6 for at least five generations. *Ythdf1*-KO mice used for the experiments were killed at 8–16 weeks of age and did not show obvious development defects before this point. mYTHDF1-E4 C9 For: CACCTGAGTTCAGATCATTAC; mYTHDF1-E4 C9 Rev: GCTCCAGACTGTTTCATCC. Amplicon length: 650 bp. Applicable to genotyping founders and targeted ESC.

Genotyping. Mice were weaned at the third postnatal week and genotyped by PCR. *Ythdf1*-KO and wild-type alleles were detected by PCR assays in which primer F1 (5'-GTGTATGAGGTGGTCAGCAT-3') and primer R1 (5'-CTTGTGAGGGAGTCACTGT-3') amplified a 465-bp fragment (wild-type) and a 286-bp fragment (*Ythdf1*-KO) (Extended Data Fig. 1d).

Open-field test. Mice were exposed to a square open arena (40 cm \times 40 cm) with opaque base and walls (40 cm high). Each mouse was allowed 30 min to explore the area and its activity was recorded and analysed using the Tru Scan Activity System (Coulbourn Instruments). The surface was cleaned with 70% ethanol after each mouse was tested.

Elevated-plus maze. The elevated-plus maze apparatus consists of two open arms (50 cm \times 9 cm), two enclosed arms (50 cm \times 9 cm \times 39 cm) and a central area (9 cm \times 9 cm). The maze is elevated 70 cm above ground in a room with normal light. Mice were placed in the central area individually and allowed 5 min to explore the maze. The time each mouse spent in the open arms during the 5-min exploration was counted by Anymaze software.

Light–dark box transition test. The light and the dark compartments of the light–dark transition box (35 cm \times 35 cm \times 40 cm) were separated by an opaque plexiglass board with a hole. The light compartment was illuminated by strong light (400 lx). During the test, mice were individually placed at the centre of the light compartment facing away from the hole and allowed 30 min to explore freely in the box. The activity of each mice was monitored. The time mice spent in the light compartment as well as the number of transitions between the two compartments were automatically calculated by Tru Scan Activity System (Coulbourn Instruments).

Tail-suspension test. The tail-suspension test was used to assess behavioural despair of mice. Each mouse was suspended by its tail with adhesive tape for 6 min and was video recorded. Total immobility time during the test was scored by independent observers. Mice were considered immobile only when they hung passively and motionlessly for at least 2 s.

Morris water maze task. The MWM test was specifically designed to evaluate spatial reference memory abilities²⁴ (Extended Data Fig. 3a). The Morris water-tank consists of a circular pool (diameter 120 cm, height 50 cm) filled with water maintained at room temperature ($23 \pm 1^\circ\text{C}$) and made opaque with nontoxic white paint. The pool is located in an experimental room with many extra-maze visual cues and virtually divided into four equal quadrants. A circular platform, 10 cm in diameter, is placed in the middle of one fixed quadrant ('target') of the pool, just above water surface (visible platform) or 1 cm underneath the water surface (hidden platform). For visible platform training, mice were trained for four trials with 30 min inter-trial intervals each day for two consecutive days, and they were released from each starting point in a random order. For hidden platform training, mice were trained for four trials each day for five consecutive days. Twenty-four hours after the last trial of training (day 6), the platform was removed and all mice were given one probe trial for 60 s searching (probe test). The escape latency to visible or hidden platform and the exploring time in each quadrant of the pool were automatically recorded by water maze system (Coulbourn, Inc.). Mice were trained at the same time of a day during their light phase.

Contextual and auditory fear conditioning. The fear conditioning test was performed as previously described³¹ (Extended Data Fig. 3d). Mice were first handled for 5 min each day for three consecutive days and habituated to the conditioning chamber for 5 min the day before training. On the day of training, after 3 min exploration in the conditioning chamber, each mouse received one pairing of a tone (2,800 Hz, 75 dB, 30 s) with a short co-terminating foot shock (0.5 mA, 1 s) for the weak training protocol, a long foot shock (0.5 mA, 2 s) for the moderate protocol, or three pairings of a tone (2,800 Hz, 75 dB, 30 s) with a long co-terminating foot shock (0.5 mA, 2 s) for the strong protocol, after which they remained in the chamber for additional 30 s and were then returned to home cages. Two hours and 24 h after the conditioning, mice were tested for freezing (behavioural immobility) in response to the training context (training chamber) and to the tone (in the training chamber with a new environment and odour). The percentage of freezing time was calculated as an index of fear learning and memory. For contextual fear memory tests, mice were returned to the conditioning chamber for 3 min and freezing behaviour was counted using StartFear Combined system (Panlab). For auditory fear memory tests, mice were placed in a changed chamber and freezing responses were recorded during the last 3 min when the tone was delivered. Tests of contextual and auditory fear memory were done in a counterbalanced manner.

Electrophysiological recording of hippocampal slices. Extracellular field recordings and whole-cell miniature excitatory postsynaptic current (mEPSC) recordings in the hippocampal CA1 region were conducted in 380- μm -thick acute brain slices from 6–9-week-old wild-type control and *Ythdf1*-KO mice of either sex. Coronal sections that contained hippocampal formations were prepared according as previously described³². In brief, mice were anaesthetized with sodium pentobarbital and were killed by decapitation. Transverse slices of the hippocampus (380 μm) were cut using the vibratome at 4°C in a modified artificial cerebrospinal fluid (mACSF) consisting of 110 mM choline chloride, 2.5 mM KCl, 0.5 mM CaCl_2 , 7 mM MgSO_4 , 25 mM NaHCO_3 , 1.25 mM NaH_2PO_4 , 25 mM D-glucose, and 3.1 mM sodium pyruvate, which was saturated with 95% O_2 and 5% CO_2 . Slices were transferred to an incubating chamber with oxygenated (95% O_2 and 5% CO_2) normal ACSF containing 120 mM NaCl, 2.5 mM KCl, 2.5 mM CaCl_2 , 1.3 mM MgSO_4 , 26 mM NaHCO_3 , 1 mM NaH_2PO_4 , 10 mM D-glucose (pH 7.3–7.4) and incubated at 30°C for at least 2 h before recording. Data were collected with a MultiClamp 700B (Molecular Devices), digitized using Digidata 1440A and pClamp 10.1 data acquisition system (Molecular Devices). Frequency, duration, and magnitude of extracellular stimulus were controlled with a Master 8 pulse stimulator (A-M Systems). Evoked synaptic responses were triggered with a bipolar electrode.

LTP and PPF. To record the extracellular field excitatory postsynaptic potentials (fEPSPs), a glass micro-electrode (4–8 M Ω , filled with 0.5 M sodium acetate) was placed in the stratum radiatum of the CA1 region, and a bipolar tungsten stimulating electrode was placed along the Schaffer collateral fibres 100–150 μm away from the recording pipette. The intensity of the stimulation was adjusted to produce an fEPSP with an amplitude of 30–40% of the maximum response. Test stimulation was delivered once per 30 s (0.033 Hz) or per minute (0.017 Hz). After recording a stable baseline for at least 30 min, early-phase LTP or later-phase LTP was induced by two (100 Hz for 1 s, 30 s interval) or four trains (100 Hz for 1 s, 5 min interval) of HFS, respectively. Magnitudes of LTP and later-phase LTP were calculated based on the averaged fEPSP values during the last 10 min and 30 min of summary plots, respectively.

For paired-pulse facilitation (PPF) recording, a second stimulus was delivered following the first one with different time intervals. The two stimuli were separated by 20, 40, 60, 80, 100, 200, 400, 600, 800, or 1,000 ms. The amplitude of the population response to the second stimulus was compared with that to the first one to obtain the PPF ratio.

Miniature EPSCs. Voltage clamp recordings were obtained from neurons in hippocampus slices equilibrated for at least 1 h in the recording chamber.

Micropipettes (tip diameter: 1.5–2.0 μm ; resistance: 4–6 $\text{M}\Omega$) were pulled from borosilicate capillaries (P-97; Sutter Instruments) and filled with an internal solution (adjusted to pH 7.2) composed of 145 mM potassium gluconate, 5 mM NaCl, 1 mM MgCl_2 , 0.2 mM EGTA, 10 mM HEPES, 2 mM magnesium ATP, 0.1 mM sodium-guanosine-5'-triphosphate, and 10 mM phosphocreatine disodium. For mEPSC recordings, 0.5 μM tetrodotoxin was added to the perfusion solution. Picrotoxin (100 μM) was present in all of experiments to block γ -aminobutyric acid (GABA) type A receptor-mediated inhibitory synaptic currents. Neuronal signals, which were amplified using an Axoclamp-700B amplifier (bandwidth filter set at 1 kHz for voltage clamp recordings), were digitized (Digidata 1440A, pClamp 10.1; Molecular Devices). The series resistance was 12–20 $\text{M}\Omega$ and was monitored throughout the experiment. Data were discarded when access resistance changed by more than 15% during the experiment.

Plasmid constructs and viruses. For reporter assay, pPB-CAG-Flag-YTHDF1-N- λ and pPB-CAG-Flag- λ were constructed by inserting the Flag-YTHDF1-N- λ (YTHDF1-N: N terminus of mouse YTHDF1, 1–389 aa) and Flag- λ fragments into pPB-CAG backbone vector between BglII and XhoI restriction sites, respectively. For AAV vectors, pAAV-CMV-mouse-YTHDF1-2a-mCherry-WPRE, pAAV-CMV-mCherry-WPRE, pAAV-CMV-RFP-U6-YTHDF1-shRNA, pAAV-CAG-eGFP-H1-YTHDF1-shRNA, and pAAV-CAG-eGFP-H1-METTL3-shRNA were all designed and constructed by standard methods. The following oligonucleotide sequences were used for knockdown: mouse YTHDF1-shRNA: 5'-GATCCTTACCTGTCCAGTTAC-3'; mouse METTL3-shRNA: 5'-GCACACTGATGAATCTTTAGG-3'; Scramble control: 5'-AACAGTCGCGTTTGCAGCTGG-3'. AAV viruses were prepared by Taitool Biotech (Shanghai).

In vivo stereotactic injections. For viral injection, male mice (8–10 weeks of age) were anaesthetized with 5% chloral hydrate (100 μl /10 g body weight) by intraperitoneal (i.p.) injection and placed on a stereotaxic apparatus. Small bilateral holes were drilled into the skull at -1.7 mm posterior and -1.5 mm lateral to bregma for injections into the hippocampal CA1 and dentate gyrus (DG) regions. A glass cannula filled with a virus solution was lowered to CA1 (-1.5 mm) and DG (-2.0 mm), and the virus solution (0.6 μl) was injected using a Nanoject II (Drummond) system at a rate of 0.1 μl per min sequentially into each side of the hippocampus. The injection cannula was slowly withdrawn 5 min after the virus infusion. The scalp was then sealed and injected mice were monitored as they recovered from anaesthesia. Behavioural experiments or electrophysiological recordings were performed at least 10 days after virus injection. Virus infection was examined at the end of all the behavioural tests.

Immunohistochemistry. *Ythdf1*-KO and wild-type male mice (from P28 to 16 weeks old) were perfused with phosphate-buffered saline (PBS) followed by 4% paraformaldehyde in PBS. After post-fixation in 4% PFA for 12 h at 4°C and dehydration in 30% sucrose-PBS solution for another 24 h, the brains were frozen-sectioned into coronal slices (35 μm) for next step use. For anti-YTHDF1 and anti-DCX staining, slices were incubated in diluted antibody solution at 4°C overnight then detected by Alexa Fluor-conjugated second antibodies. All slices were counterstained with Hoechst in the final step incubation. Fluorescent image acquisition was performed using an Axioimager Z2 microscope or LSM 510 confocal microscope (Zeiss). Images were analysed with Image-Pro Plus and ImageJ software. Brain slices from mice injected with AAV-CMV-mouse-YTHDF1-2a-mCherry-WPRE (AAV-YTHDF1) and AAV-CMV-mCherry-WPRE (AAV-control) were used for the YTHDF1 overexpression quantification assay (Extended Data Fig. 5a, b). For Extended Data Fig. 2d, female mice (P60) were anaesthetized and perfused with ice-cold 4% paraformaldehyde (PFA). Brains were removed from perfused animals, post-fixed overnight in 4% PFA in PBS, and cryoprotected in 30% sucrose (w/v) for 2–3 days. Samples were sectioned on a microtome at 40 μm thickness. Primary antibody was applied at 4°C overnight. Secondary antibody was applied for 2 h at room temperature.

Western blot. Samples were homogenized in RIPA buffer (Beyotime) containing 1 mM PMSF, 1 \times protease inhibitor cocktail and 1 \times phosphatase inhibitor cocktail (Sigma). Lysates were boiled at 100°C with 6 \times loading buffer (Beyotime) for 8 min and then stored at -80°C for next step use. A total of 30 μg protein per sample was resolved on SDS-PAGE (10%) at 80 V for 20 min and then 110 V for 110 min. Proteins on the gel were transferred onto PVDF membranes (Millipore) and blocked in 5% milk blocking solution for 1 h at room temperature, incubated in a diluted primary antibody solution at 4°C overnight, and incubated in a dilution of secondary antibody conjugated to HRP for 2 h at room temperature (dilution folds indicated in the section of antibodies). Protein bands were detected using ECL western blotting detection reagents (Millipore) and Amersham Imager 600 system (GE).

Dissociated neuron culture and reporter assay. Hippocampal neurons from E18 C57BL/6 mouse embryos of either sex were cultured at a density of 200,000 cells per well on poly-D-lysine pre-coated 6-well plates. Neuron cultures were maintained in complete medium (neurobasal medium supplemented with 0.5 mM GlutaMAX-I

and 2% B-27). Plasmid transfection was conducted using 4D-Nucleofector System (Lonza) immediately after neuron dissociation.

The reporter plasmid (pmirGlo-5BoxB) and the effector plasmid (Flag- λ , or Flag-YTHDF1-N- λ in pPB-CAG vector) were used to transfect neuron cultures at a ratio of 1:9 as previously reported^{2,3}. After transfection, neurons were plated in plating medium (neurobasal medium supplied with 0.5 mM GlutaMAX-I, 2% B-27 and 5% FBS) for 6 h, then changed to complete medium for further culturing. Three days after transfection, neurons were treated with KCl at the final concentration of 50 mM for 2, 4, or 8 h. Then neurons were collected and assayed using Dual-Glo Luciferase Assay Systems (Promega) to test protein production.

Quantitative mass spectrometry. Hippocampal samples from wild-type control and *Ythdf1*-KO mice (8–12 weeks, male) were freshly isolated and snap frozen in liquid nitrogen. For each mouse, 100 mg tissue was used for further preparation. Tissues were ground into fine powder in liquid nitrogen then lysed with 500 μl freshly prepared lysis buffer (20 mM triethylammonium bicarbonate (TEAB, pH 8.5), 8 M urea, protease inhibitor cocktail (Roche), and 1 mM DTT). The yielded lysate was treated with ultrasonication at 4°C for 30 s to shear DNA, followed by centrifugation at 16,000g for 10 min at 4°C. The resultant supernatant was carefully separated and transferred into a new tube. Protein concentrations were measured using BCA Protein Assay Kit (Thermo Scientific). For each condition, a total of 100 μg protein was reduced with 5 mM tris(2-carboxyethyl)phosphine (TCEP) for 3 h at 30°C, then alkylated with 10 mM methyl methanethiosulfonate (MMTS) for 45 min at room temperature (protected from light). Samples were then diluted with 20 mM TEAB to obtain a final concentration of 1 M urea before digestion with 2.5 μg trypsin overnight at 37°C. Resultant tryptic peptides were finally labelled with TMT10plex Mass Tag Labelling Kit (Thermo Scientific) according to manufacturer's protocol and followed with liquid chromatography with tandem mass spectrometry (LC-MS/MS) analysis.

PSD preparation. Hippocampal tissues from wild-type and *Ythdf1*-KO mice (8–12 weeks, male) were isolated, snap frozen in liquid nitrogen, and stored at -80°C before use. PSD fraction preparation was prepared as previously described³²; hippocampal tissues were homogenized in homogenization buffer (320 mM sucrose, 5 mM sodium pyrophosphate, 1 mM EDTA, 10 mM HEPES (pH 7.4), 1 \times protease inhibitor cocktail, and 1 \times phosphatase inhibitor cocktail (Sigma)). The resultant homogenate was centrifuged at 800g for 10 min at 4°C to yield post-nuclear pelleted fraction 1 (P1) and supernatant fraction 1 (S1). S1 was further centrifuged at 15,000g for 20 min at 4°C. Then pellet P2 (which contains the synaptosome) was resuspended in 4 mM HEPES (pH 7.4) and incubated with agitation at 4°C for 30 min. Suspended P2 was centrifuged at 25,000g for 20 min at 4°C. The resulting pellet was resuspended in 50 mM HEPES (pH 7.4), mixed with an equal volume of 1% Triton X-100, and incubated with agitation at 4°C for 15 min. The PSD fraction was generated by centrifugation at 32,000g for 20 min at 4°C. The final PSD pellet was resuspended in 50 mM HEPES followed by protein quantification and then boiled with 6 \times loading buffer for western blot.

Lucifer yellow labelling by intracellular injection. Wild-type control and *Ythdf1*-KO mice (8–12 weeks, male) were perfused with 4% PFA in PBS and their brains were removed to perform intracellular injection of the fluorescent dye Lucifer yellow (LY). The brains were post-fixed for 24 h in 4% PFA in PBS, and coronal sections were obtained (200 μm). Intracellular injections were performed as previously described³³. In brief, sections were placed under a differential interference contrast (DIC) microscope to find healthy CA1 neurons and a continuous current (5–10 nA) was used to inject cells with LY. At least five CA1 pyramidal cells per mouse were injected individually with LY, with the current applied until the distal tips of each dendrite fluoresced brightly (5–10 min). Images (z-stacks) for spine density counting were acquired using an LSM 510 confocal microscope with a 63 \times oil objective. Spine counting and spine morphology analyses were performed using Neurostudio software.

Protein synthesis assay. Wild-type control and *Ythdf1*-KO mouse hippocampal neurons were cultured on pre-coated glass cover slides. Twelve days later, a protein synthesis assay was conducted using Click-iT Plus OPP Alexa Fluor 488 Protein Synthesis Assay Kit (Invitrogen, C10456) following the manufacturer's protocol. In brief, the neurons were treated with 50 mM KCl for 10 min before the complete culture medium was changed back. Click-iT OPP (Component A) was diluted 1:1,000 in pre-warmed culture medium as a 20 μM working solution. Two or four hours after the KCl treatment, the culture medium was replaced with the working solution for another 30-min incubation under culturing conditions. The medium was then removed, and the neurons were washed once with PBS before being fixed with 4% PFA for 15 min and permeabilized with 0.5% Triton X-100 (in PBS) for another 15 min at room temperature. After two more rounds of wash with PBS, the neurons were incubated with a freshly prepared Click reaction cocktail for 30 min at room temperature in the dark and rinsed once with the reaction rinse buffer. Finally, neurons were counterstained with NuclearMask Blue Staining working solution and washed twice with PBS before imaging and analysis. For assays using AAV-mediated knockdown (Extended Data Fig. 9d, e), wild-type

mouse hippocampal neurons were cultured on pre-coated glass cover slides, and in three days transfected with AAV-YTHDF1-RNAi-GFP (pAAV-CAG-eGFP-H1-YTHDF1-shRNA) or AAV-control-GFP. Four to five days after virus transfection, a protein synthesis assay was conducted as described above using Click-iT Plus OPP Alexa Fluor 594 Protein Synthesis Assay Kit (Invitrogen, C10457). All the pictures were acquired using identical settings and analysed using Image-Pro Plus. The Integrated Optical density (IOD) of fluorescent signals was divided by area value of Hoechst signals for each picture to derive the signal intensity of each neuron. For comparison, fluorescence intensities from experimental groups were normalized to that from control neurons under sham conditions.

YTHDF1-CLIP-seq. Fifteen micrograms of rabbit anti-YTHDF1 antibody (Proteintech, 17479-1-AP), 50 μ l Protein A beads (ThermoFisher), 50 μ l Protein G beads (ThermoFisher), and four pairs of hippocampi from C57BL/6 mice (9 weeks, male) were used for each biological replicate. Three biological replicates were performed.

For each replicate, Protein A and G beads were washed three times with PBST (PBS with 0.05% Tween-20) and resuspended with anti-YTHDF1 antibody in 250 μ l PBST before overnight rotation at 4°C. On the following day, mouse hippocampal tissues were dissected, homogenized in 500 μ l HBSS buffer, and crosslinked in 6-well plates on ice four times with 254 nm UV light, 0.15 J/cm² per time (UV stratalinker 2400, Stratagene). Lysis buffer (1.5 ml; 150 mM NaCl, 0.5% NP-40, 50 mM Tris-HCl (pH 7.5), 2 mM EDTA, 1% protease inhibitor cocktail (Roche), 0.5 mM DTT) was added to the crosslinked tissue pellet for a 40-min rotation at 4°C. After being cleared by maximum-speed centrifuge, the lysate underwent a first round of RNA digestion with 0.2 U/ μ l RNase T1 (ThermoFisher, EN0541) for 15 min at room temperature followed by a five-min quenching on ice. A 100- μ l aliquot of the resultant lysate was saved as 'Input', and the remaining lysate was incubated with the Protein A and G beads conjugated with anti-YTHDF1 antibody. After three hours of rotation at 4°C, the beads were washed three times with 1 ml immunoprecipitation (IP) wash buffer (50 mM Tris-HCl (pH 7.5), 300 mM KCl, 0.05% NP-40, 0.5 mM DTT, 1% protease inhibitor cocktail), and resuspended in 200 μ l IP wash buffer supplemented with 10 U/ μ l RNase T1 for a second round of RNA digestion for 8 min at room temperature. The previously saved 'Input' was digested in parallel, and immediately supplemented with 4 \times Laemmli sample buffer (Bio-Rad). After a 5-min quenching on ice, the beads were washed three times with high-salt wash buffer (50 mM Tris-HCl (pH 7.5), 500 mM NaCl, 0.05% NP-40, 0.5 mM DTT, 1% protease inhibitor cocktail, 1% SUPERase In) and another three washes with PNK buffer (50 mM Tris-HCl (pH 7.5), 50 mM NaCl, 10 mM MgCl₂). The RNA fragments co-immunoprecipitated with Protein A and G beads ('CLIP') were subject to end-repair by: (1) 1 U/ μ l T4 PNK (ThermoFisher, EK0031) in 100 μ l 1 \times PNK buffer A (ThermoFisher) at 37°C for 20 min with vigorous shaking; and then (2) 1 mM ATP (final concentration) with another 0.5 U/ μ l T4 PNK at 37°C for another 20 min. The beads were washed with PNK buffer another five times and then resuspended in 100 μ l 2 \times Laemmli sample buffer. The YTHDF1-RNA complex was size-selected by SDS-PAGE (size indicated in Extended Data Fig. 8b), and the gel slice at the same molecular weight was cut for 'Input' samples in parallel. To extract RNA, the gel slices were mashed and digested with 2 mg/ml protease K (ThermoFisher, RNA-grade, 25530049) at 55°C for 1 h. Then gel particles were filtered out, and the RNA was purified by acid-phenol:chloroform extraction and overnight ethanol precipitation. The 'Input' RNA fragments were end-repaired using T4 PNK and further cleaned up using RNA Clean & Concentrator-5 (Zymo Research). RNA libraries were generated using NEBNext multiplex small RNA library preparation kit (NEB, E7300S) for both Input and CLIP samples.

m⁶A-CLIP-seq. Total RNA was extracted from hippocampal tissue dissected from C57BL/6 mice (8–16 weeks, male) using Trizol (Invitrogen) and isopropanol precipitation. Poly(A)⁺ RNA was purified using Dynabeads mRNA DIRECT Purification Kit (Invitrogen) following the manufacturer's instructions.

For the m⁶A-CLIP-seq, we followed the protocol reported¹² with a smaller amount of starting material: 300 ng purified poly(A)⁺ RNA, with 2.5 μ g anti-m⁶A antibody (Synaptic System, 202 003) and 25 μ l Protein A/G beads. Three biological replicates were performed, and the pair of hippocampi from one mouse were pooled for each replicate.

RNA-seq. Total RNA from wild-type littermate control and *Ythdf1*-KO mouse (8–16 weeks, male) hippocampus was extracted using Trizol (Invitrogen) and isopropanol precipitation. mRNA extraction was performed by poly(A)⁺ RNA selection once using Dynabeads mRNA DIRECT Purification Kit (Invitrogen). The RNA libraries were prepared using Truseq stranded mRNA sample preparation kit (Illumina) according to the manufacturer's protocol. Three biological replicates were performed for each genotype, and two hippocampi from one mouse were pooled for each replicate.

ECT and m⁶A-RIP-seq of dentate gyrus. Adult male, 6–8-week old C57BL/6 mice were used (Charles River) and housed in a standard facility. ECT was achieved with pulses consisting of 1.0 s, 100 Hz, 16–18 mA stimulus of 0.3 ms delivered using the

Ugo Basile ECT unit (Model 57800) as previously described³⁴. Mock-treated mice were handled in parallel without the electrical current delivery.

m⁶A-RIP-seq. Total RNA from adult mouse dentate gyrus was isolated using TRIzol reagent according to the manufacturer's instructions (Invitrogen). mRNA purification was performed with poly(A)⁺ RNA selection twice using Dynabeads Oligo (dT)25 (Thermo Fisher; 61006). A total of 150 ng of mRNA was subjected to m⁶A-SMART-seq using anti-m⁶A rabbit polyclonal antibody (Synaptic Systems, 202003) as previously described⁹. In brief, 5 μ g of anti-m⁶A polyclonal antibody was conjugated to Dynabeads Protein A (Thermo Fisher; 10001D) and used for each affinity pull-down. The m⁶A RNA was eluted twice with 6.7 mM N⁶-methyladenosine (Sigma-Aldrich; M2780) in 1 \times IP buffer (10 mM Tris-HCl (pH 7.5), 150 mM NaCl, and 0.1% (vol/vol) Igepal CA-630) and recovered by RNA Clean and Concentrator-5 (Zymo Research). Libraries were generated using the SMART-seq protocol as described³⁵. Three biological replicates for each condition were sequenced using Illumina NextSeq 550 from a single end for 75 bases.

Data analysis of high-throughput sequencing data. *General processing.* (for all sequencing samples unless specified). Sequencing was carried out on NextSeq500 with single end 80-bp read length or NextSeq550 with single end 75-bp according to the manufacturer's instructions. Sequencing data were mapped to mouse genome version mm10 downloaded from UCSC using Tophat v2.0.14³⁶. For RNA-seq analysis, rpkm were calculated by Cuffnorm³⁷. For CLIP-seq experiments, after removing the adaptor using Cutadapt³⁸, the reads were aligned to the mouse genome (mm10) by Bowtie 2³⁹. More information could be found in Supplementary Table 1.

Peak calling in YTHDF1-CLIP-seq. All mapped reads were treated as background and mutations were treated as signals for peak calling. PARalyzer⁴⁰ was used for peak calling in CLIP-seq samples with a few modifications: (1) mutations in both CLIP and Input were removed from CLIP; (2) sites with 100% mutations rate were also removed. The remaining mutations were used for peak calling. At least two mutation sites are needed in each peak (MINIMUM_CONVERSION_LOCATIONS_FOR_CLUSTER = 2).

Peak calling in m⁶A-CLIP-seq. We followed the same peak calling method as reported¹². The consensus motif was determined using HOMER⁴¹ for the m⁶A-CLIP peaks identified in each replicate.

m⁶A-RIP-seq analysis. Low-quality bases and adaptor sequences from original reads were removed using Trimmomatic⁴². The remaining reads were then mapped to the mouse genome (mm10) using STAR aligner⁴³. Mapped reads between samples were normalized using DESeq2⁴⁴. The Input and RIP libraries were normalized.

Integrative analysis. (1) Definitions for groups of transcripts: (i) The common peaks (peaks from replicate 1 with >1 nt overlap in peak location with those from both replicate 2 and 3) of CLIP-seq are defined as high-confidence CLIP peaks. (ii) Transcripts with high-confidence YTHDF1-CLIP peaks are defined as YTHDF1-CLIP targets (Fig. 4c, d, i; Extended Data Fig. 8i, j). (iii) Transcripts without YTHDF1-CLIP peaks in any of the three YTHDF1-CLIP-seq replicates are defined as non-YTHDF1-CLIP targets, and they were used as a control group for analysing gene expression change in the absence of YTHDF1 (Fig. 4d, i; Extended Data Fig. 8i, j). (iv) Transcripts with high-confidence m⁶A-CLIP peaks are defined as m⁶A-modified transcripts (Fig. 4d, i; Extended Data Fig. 8f, h, i, j). (v) Transcripts with overlapped high-confidence YTHDF1-CLIP peaks and high-confidence m⁶A-CLIP peaks (>1 nt in peak location) are defined as YTHDF1-CLIP + m⁶A-CLIP transcripts (Fig. 4i; Extended Data Fig. 8i, j). (2) Functional annotation of a list of genes was generated by DAVID^{45,46}, for YTHDF1-CLIP targets (Fig. 4c) and m⁶A-modified transcripts with no fewer than five mutations in m⁶A-CLIP-seq (Extended Data Fig. 8f). (3) Only genes with sufficient expression (rpkm >1 in RNA-seq of wild-type triplicates; rpkm >1 in m⁶A-RIP-seq input or RIP libraries) were kept and subject to further analyses. The median rpkm value of the sequencing triplicates was used for differential analyses.

Antibodies. The antibodies used in this study are listed below in the format of name (application; catalogue; supplier; dilution fold): rabbit anti-YTHDF1 (western blot, 17479-1-AP, Proteintech, 500-1,000; IF, 200); rabbit anti-YTHDF2 (western blot, 24744-1-AP, Proteintech, 500); rabbit anti-YTHDF3 (western blot, 25537-1-AP, Proteintech, 500); rabbit anti-YTHDC1 (western blot, 14392-1-AP, Proteintech, 500); rabbit anti-YTHDC2 (western blot, ab176846, Abcam, 1,000); rabbit anti-METTL3 (western blot, ab195352, Abcam, 1,000); mouse anti-GAPDH (western blot, G8795, Sigma, 3,000); rabbit anti-DCX (IF, ab18723, Abcam, 1,000); mouse anti-ACTIN (western blot, A4700, Sigma, 1,000); rabbit anti-GRIA1 (western blot, AB1504, Merck, 1,000); rabbit anti-CAMK2 (western blot, 4436S, Cell Signaling, 1,000); rabbit anti-GRIN1 (western blot, 5704S, Cell Signaling, 1,000); rabbit anti-GRIN2A (western blot, 4205S, Cell Signaling, 1,000); mouse anti-BSN (western blot, ab82958, Abcam, 500); goat anti-mouse IgG HRP-conjugated (western blot, AP308P, Merck, 5,000); goat anti-rabbit IgG HRP-conjugated (western blot, AP307P, Merck, 5,000); rat anti-CTIP2 (IF, ab18465, Abcam, 300); mouse anti-SATB2 (IF, ab51502, Abcam, 300); Alexa Fluor 488 goat anti-mouse IgG (IF, A11029, ThermoFisher, 1,000); Cy3 AffiniPure donkey anti-rat

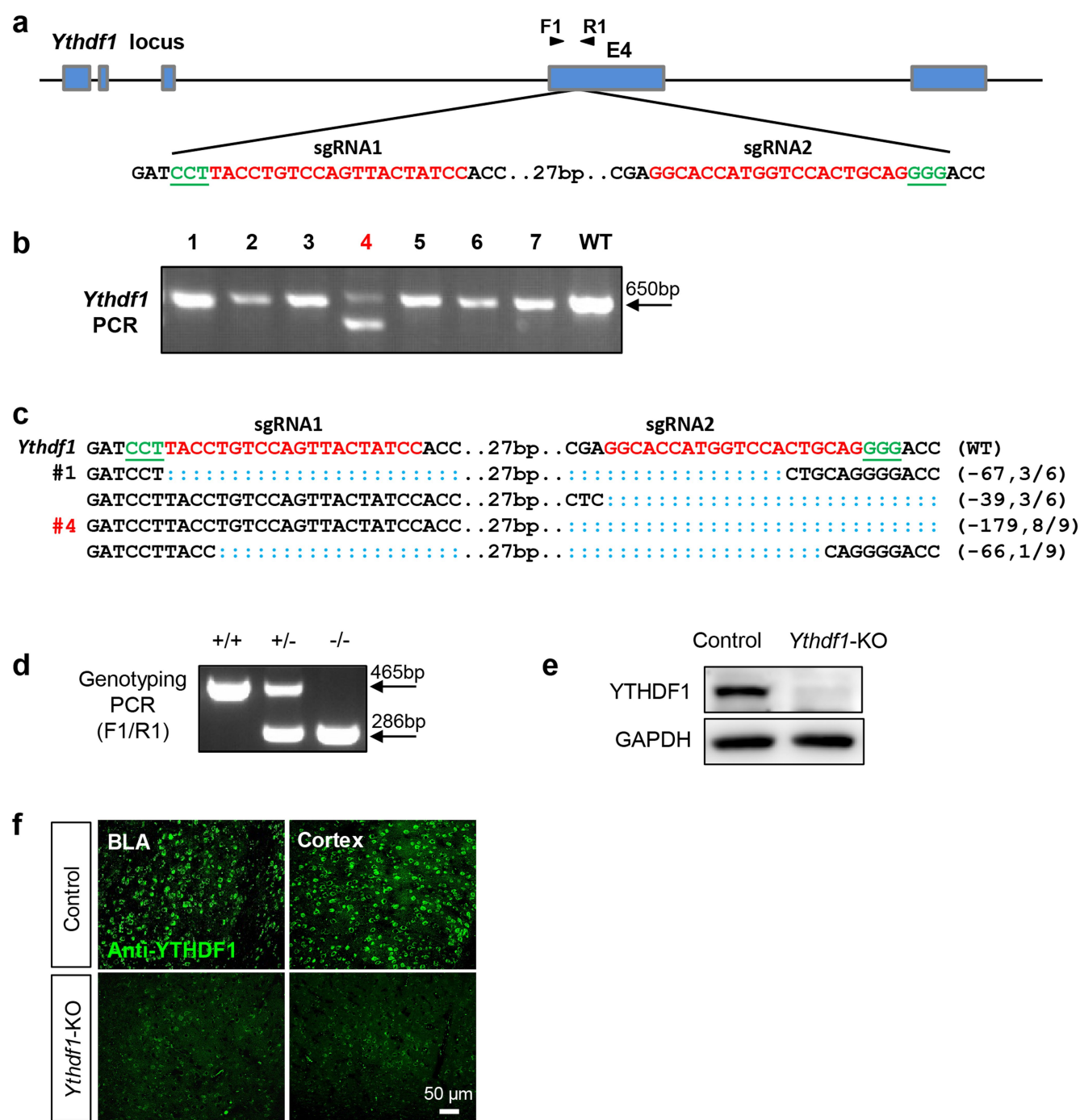
IgG (H+L) (IF, 712-165-153, Jackson ImmunoResearch, 500); Cy5 AffiniPure donkey anti-mouse IgG (H+L) (IF, 715-175-150, Jackson ImmunoResearch, 500); biotin-SP-conjugated goat anti-rabbit IgG (IF, 111-065-003, Jackson ImmunoResearch, 500); Cy2-conjugated streptavidin (IF, 016-220-084, Jackson ImmunoResearch, 1,000).

Reporting summary. Further information on experimental design is available in the Nature Research Reporting Summary linked to this paper.

Data availability

High-throughput sequencing data can be accessed in the Gene Expression Omnibus under accession number GSE106607. Source data for bar graphs and box-plots in Figures and Extended Data Figures are provided in separate excel files.

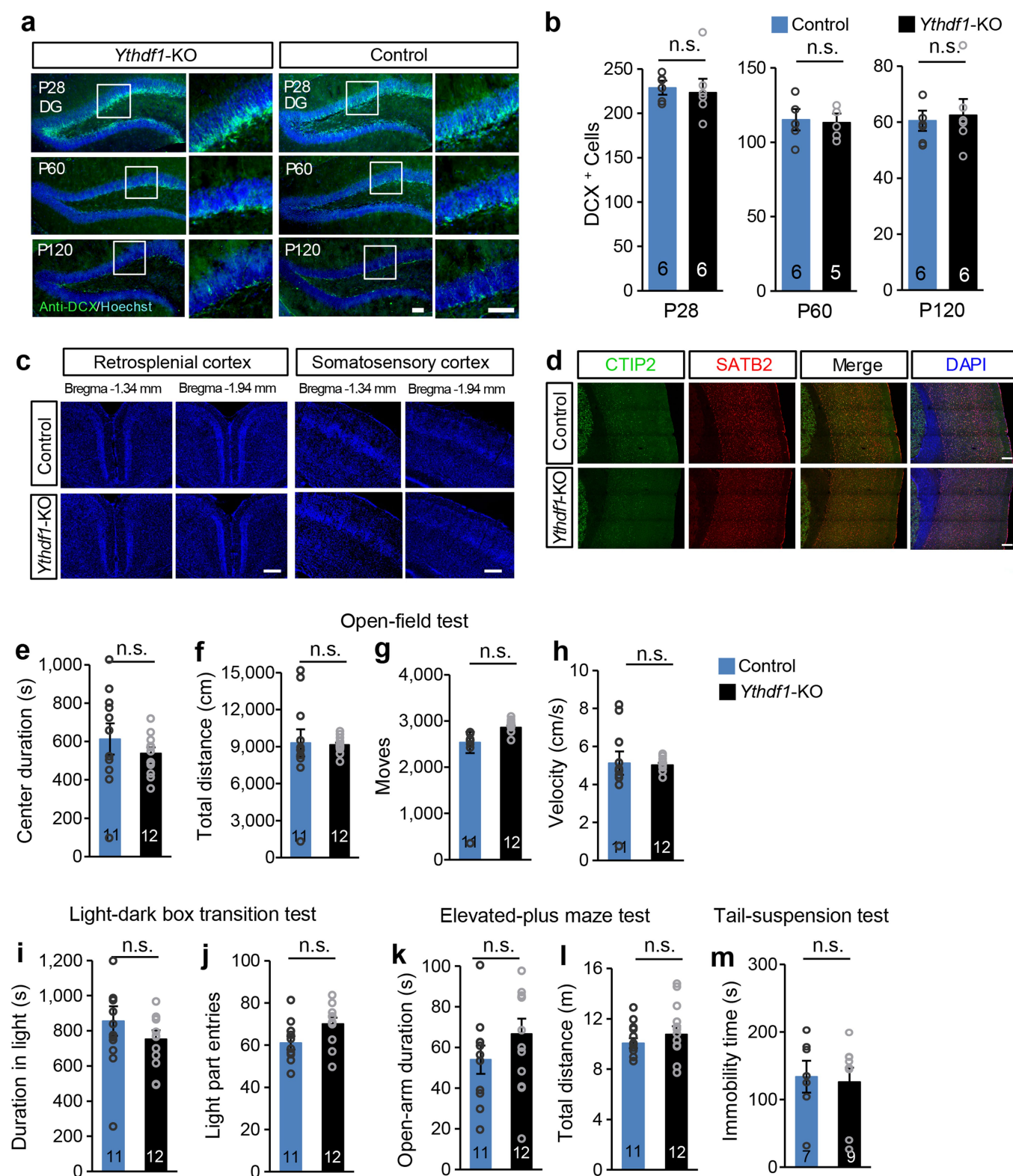
30. Li, K. et al. β CaMKII in lateral habenula mediates core symptoms of depression. *Science* **341**, 1016–1020 (2013).
31. Huang, W. et al. mTORC2 controls actin polymerization required for consolidation of long-term memory. *Nat. Neurosci.* **16**, 441–448 (2013).
32. Chiu, S. L. et al. GRASP1 regulates synaptic plasticity and learning through endosomal recycling of AMPA receptors. *Neuron* **93**, 1405–1419.e8 (2017).
33. Shioda, N. et al. Aberrant calcium/calmodulin-dependent protein kinase II (CaMKII) activity is associated with abnormal dendritic spine morphology in the ATRX mutant mouse brain. *J. Neurosci.* **31**, 346–358 (2011).
34. Su, Y. et al. Neuronal activity modifies the chromatin accessibility landscape in the adult brain. *Nat. Neurosci.* **20**, 476–483 (2017).
35. Picelli, S. et al. Full-length RNA-seq from single cells using Smart-seq2. *Nat. Protocols* **9**, 171–181 (2014).
36. Kim, D. et al. TopHat2: accurate alignment of transcriptomes in the presence of insertions, deletions and gene fusions. *Genome Biol.* **14**, R36 (2013).
37. Trapnell, C. et al. Transcript assembly and quantification by RNA-seq reveals unannotated transcripts and isoform switching during cell differentiation. *Nat. Biotechnol.* **28**, 511–515 (2010).
38. Martin, M. Cutadapt removes adapter sequences from high-throughput sequencing reads. *EMBnet journal* **17**, 10–12 (2011).
39. Langmead, B. & Salzberg, S. L. Fast gapped-read alignment with Bowtie 2. *Nat. Methods* **9**, 357–359 (2012).
40. Corcoran, D. L. et al. PARalyzer: definition of RNA binding sites from PAR-CLIP short-read sequence data. *Genome Biol.* **12**, R79 (2011).
41. Heinz, S. et al. Simple combinations of lineage-determining transcription factors prime cis-regulatory elements required for macrophage and B cell identities. *Mol. Cell* **38**, 576–589 (2010).
42. Bolger, A. M., Lohse, M. & Usadel, B. Trimmomatic: a flexible trimmer for Illumina sequence data. *Bioinformatics* **30**, 2114–2120 (2014).
43. Dobin, A. et al. STAR: ultrafast universal RNA-seq aligner. *Bioinformatics* **29**, 15–21 (2013).
44. Love, M. I., Huber, W. & Anders, S. Moderated estimation of fold change and dispersion for RNA-seq data with DESeq2. *Genome Biol.* **15**, 550 (2014).
45. Huang, W., Sherman, B. T. & Lempicki, R. A. Systematic and integrative analysis of large gene lists using DAVID bioinformatics resources. *Nat. Protocols* **4**, 44–57 (2009).
46. Huang, W., Sherman, B. T. & Lempicki, R. A. Bioinformatics enrichment tools: paths toward the comprehensive functional analysis of large gene lists. *Nucleic Acids Res.* **37**, 1–13 (2009).



Extended Data Fig. 1 | Generation and evaluation of *Ythdf1*-KO mice.

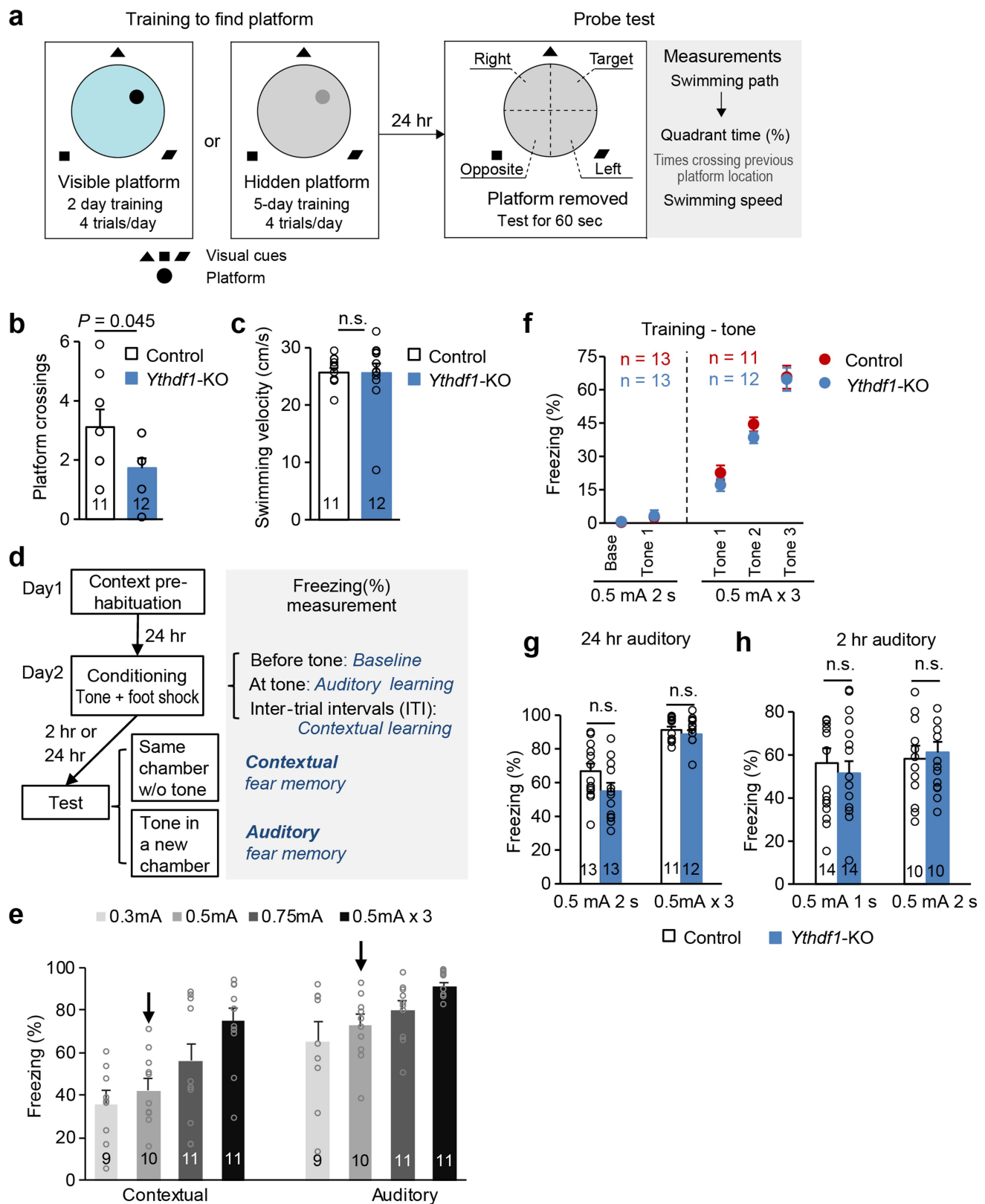
a, Schematic diagram of the targeting strategy for generating *Ythdf1*-KO mice using CRISPR-Cas9. Two sgRNAs (red) were designed to target the fourth exon (E4) of *Ythdf1*. PAM sequence, underlined, green; F1 and R1, genotyping primers. **b**, Genotyping PCR products of the seven founders co-injected with 20 ng Cas9 mRNA and the two sgRNAs (5 ng each). **c**, Genotypes of sequenced mice. PCR products were cloned and

sequenced. Founder #4 with a 179-bp deletion was crossed with C57BL/6 wild-type mice for further analysis. **d**, Representative genotyping PCR products of offspring mice with different genotypes. **e**, Validation of *Ythdf1* knockout by western blot using mouse hippocampal tissues. For gel source data, see Supplementary Fig. 1. **f**, Representative images of YTHDF1 immunostaining in the mouse basal lateral amygdala (BLA) and the cortex.



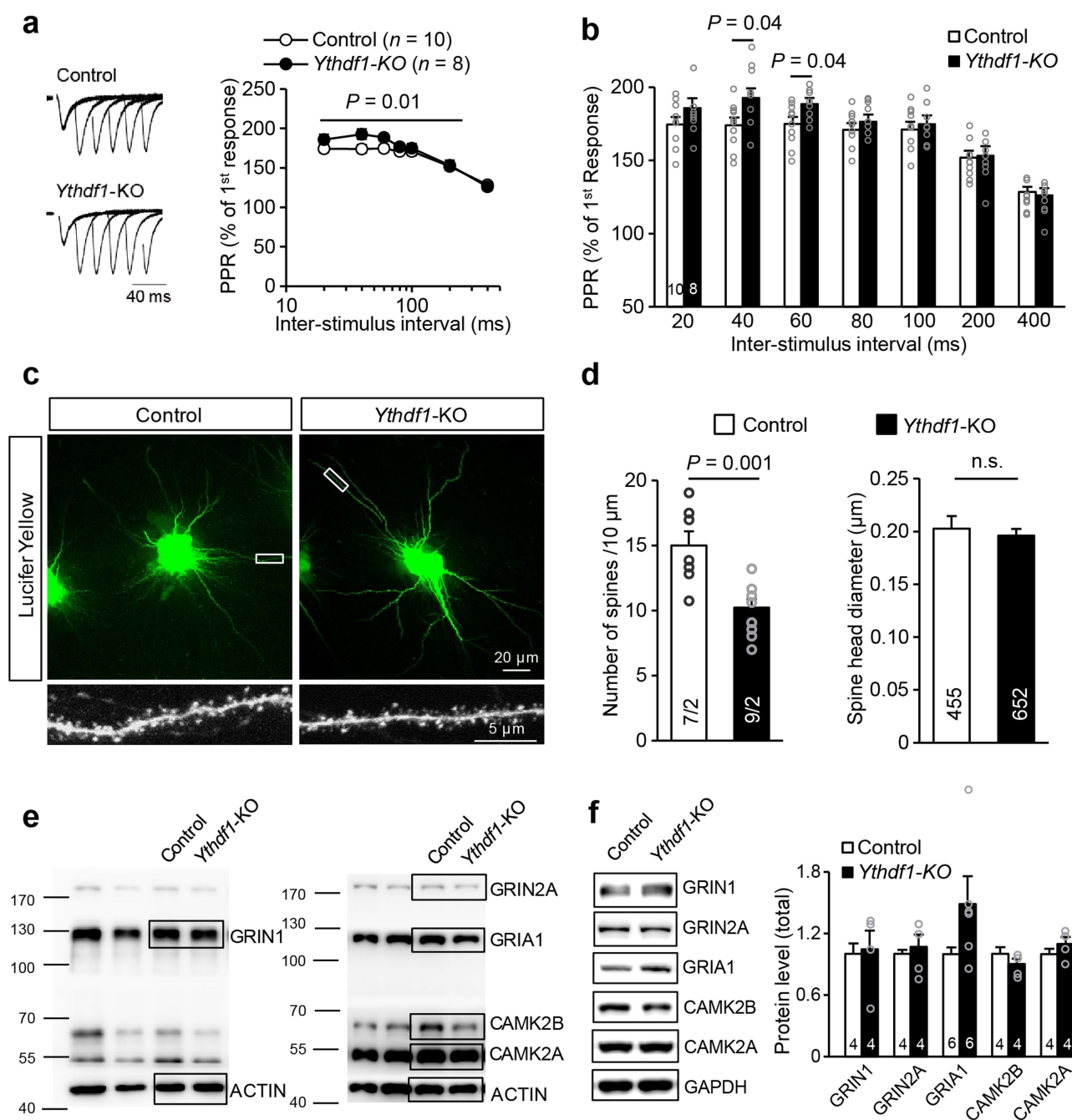
Extended Data Fig. 2 | *Ythdf1*-KO mice are normal in hippocampal neurogenesis, cortical morphology, motor activities, anxiety-like behaviour, and depressive-like behaviour. **a, b**, Representative images of Doublecortin (DCX, a marker of neurogenesis) immunostaining (**a**) and quantification of the number of DCX⁺ cells (**b**) in the dentate gyrus (DG) region of *Ythdf1*-KO and wild-type control mice at different postnatal development stages. Scale bar, 100 μ m. **c**, Representative images of cortical morphology staining using Hoechst in adult control and *Ythdf1*-KO mice. Scale bar, 200 μ m. **d**, Representative confocal immunostaining of CTIP2

(a marker for deep layer cortical neurons) and SATB2 (a marker for upper layer cortical neurons) in the cortex of adult control and *Ythdf1*-KO mice. Scale bar, 200 μ m. **e-h**, Motor activities measured by various parameters as listed in the open-field test. **i-l**, Anxiety-like behaviour measured by the light-dark box transition test (**i, j**) and the elevated-plus maze test (**k, l**). **m**, Depressive-like behaviour measured by tail suspension test. *P* values, two tailed *t*-test. Numbers in bars, numbers of mice. Data shown as mean \pm s.e.m.



Extended Data Fig. 3 | MWM tests and fear conditioning tests in *Ythdf1*-KO mice. **a**, Schematics of procedure of MWM training and MWM probe tests. **b**, **c**, Number of crossings over previous platform location (**b**) and swimming velocity (**c**) of control and *Ythdf1*-KO mice in MWM probe tests. **d**, Schematics of the fear conditioning procedures (left) and freezing responses measured at different stages (right). **e**, Titration curves of the freezing level of wild-type mice 24 h after training with different foot shock intensities. The conditioning protocols used in later

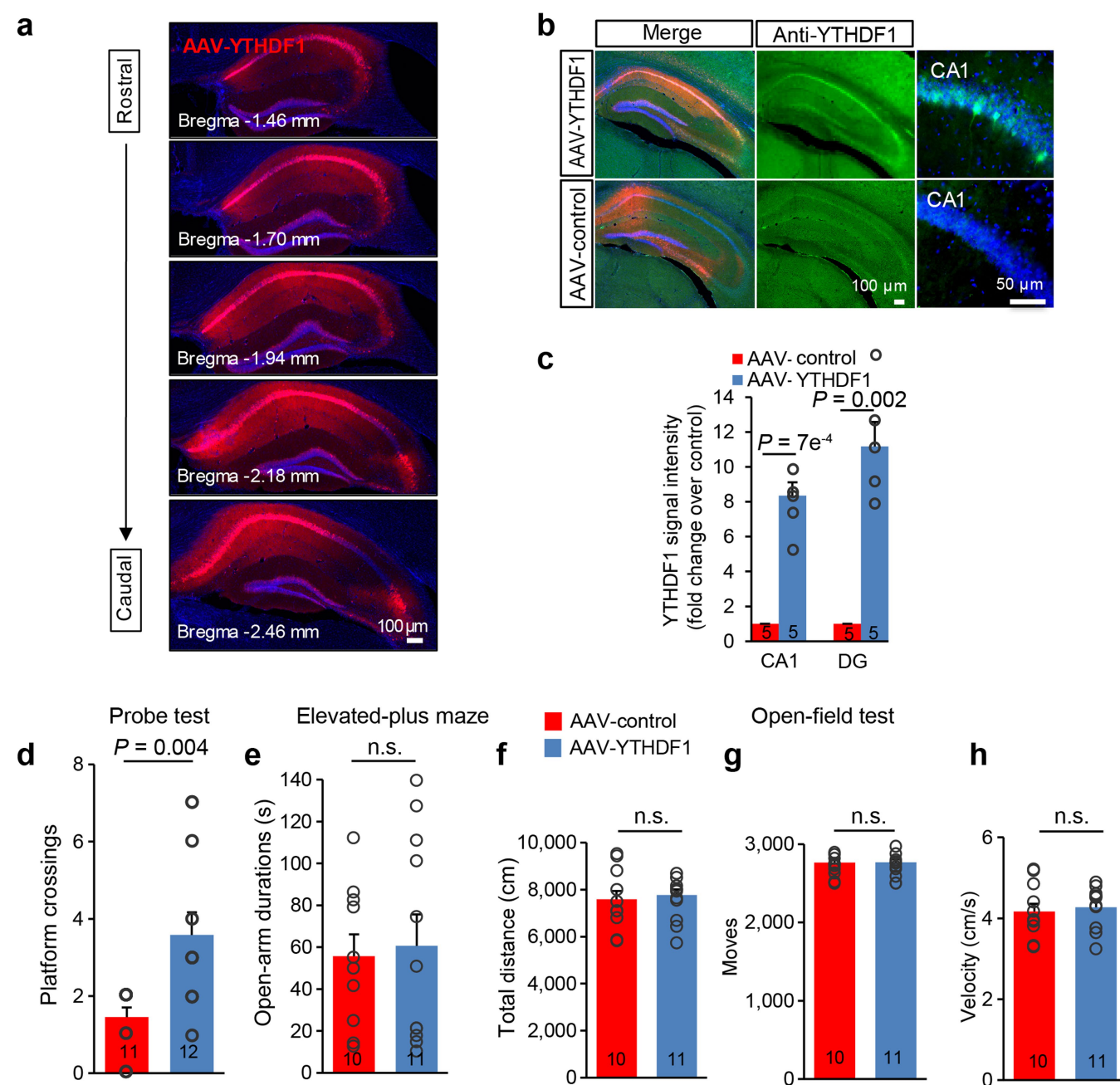
experiments (moderate protocols) are indicated by arrows. **f**, Learning curves for auditory fear conditioning under moderate (left) or strong (right) training protocols. The training sessions were separated into two parts: baseline (base) and tone periods (tone). **g**, **h**, Auditory fear memory of control and *Ythdf1*-KO mice assessed 24 h (**g**) and 2 h (**h**) after the indicated training sessions. *P* values, two-way repeated measures ANOVA (**d**) and two tailed *t*-test (**b**, **c**, **f**–**h**). Numbers in bars, numbers of mice. Data shown as mean \pm s.e.m.



For Fig. 2g

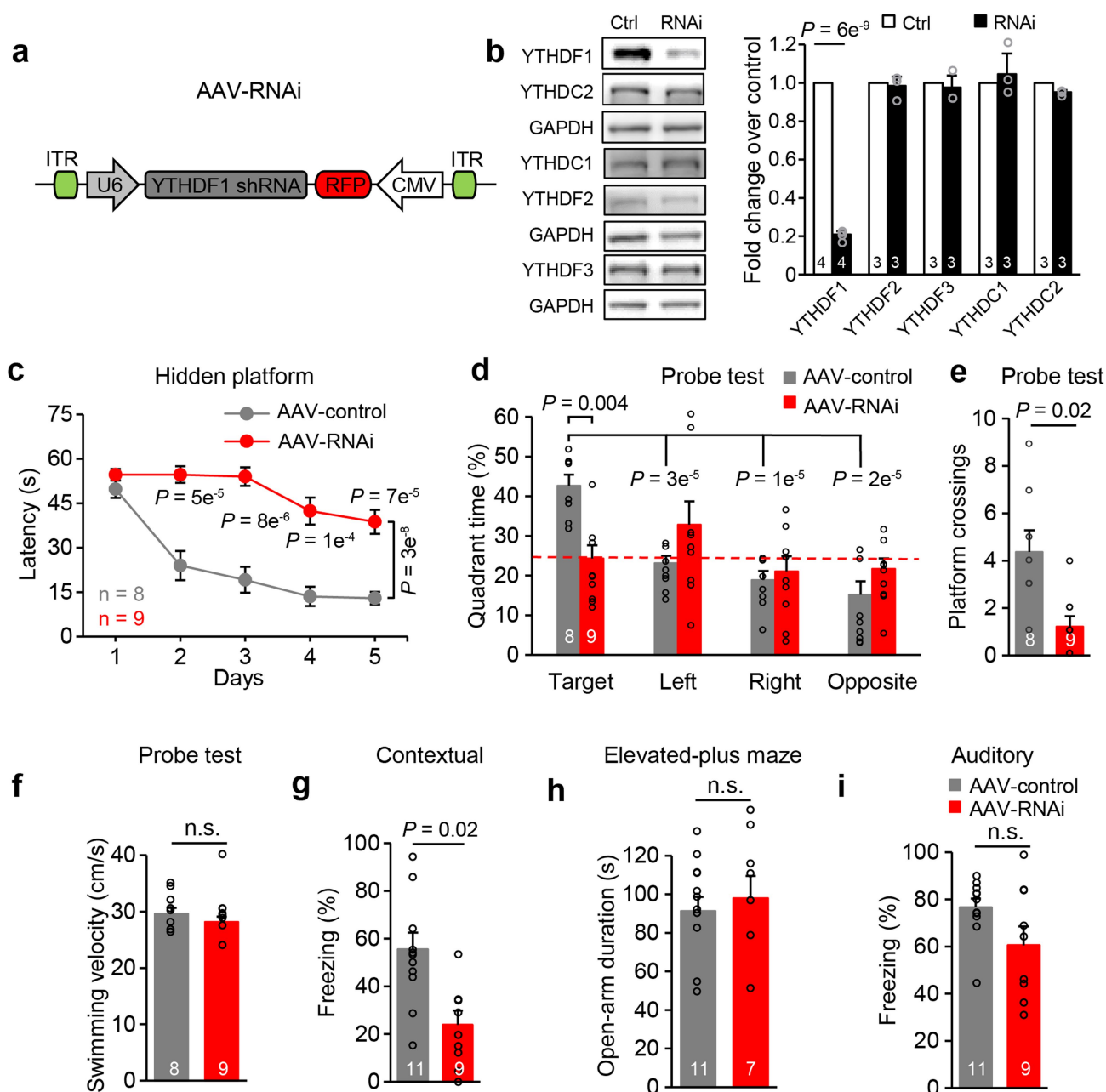
Extended Data Fig. 4 | PPRs, spine morphology, and total protein levels of various LTP-related genes in *Ythdf1*-KO mouse hippocampus. Related to Fig. 2. **a, b**, PPR with different inter-stimulus intervals in CA1 neurons from wild-type control and *Ythdf1*-KO mice. **c, d**, Representative images of Lucifer yellow staining (**c**) and statistical analyses of spine density (**d**, left) and spine size (**d**, right) in CA1 neurons from adult control and *Ythdf1*-KO brains. **e**, Uncropped western blot images for Fig. 2g.

f, Total protein levels of a set of LTP-related genes in control and *Ythdf1*-KO mouse hippocampus. For gel source data, see Supplementary Fig. 1. *P* values, two-way repeated measures ANOVA with post hoc two-tailed *t*-test (**a**) and two-tailed *t*-test (**b, d, f**). Numbers in bars, numbers of slices (**b**), neurons/mice (**d**, left), spines (**d**, right), or mice (**f**). Data shown as mean \pm s.e.m.



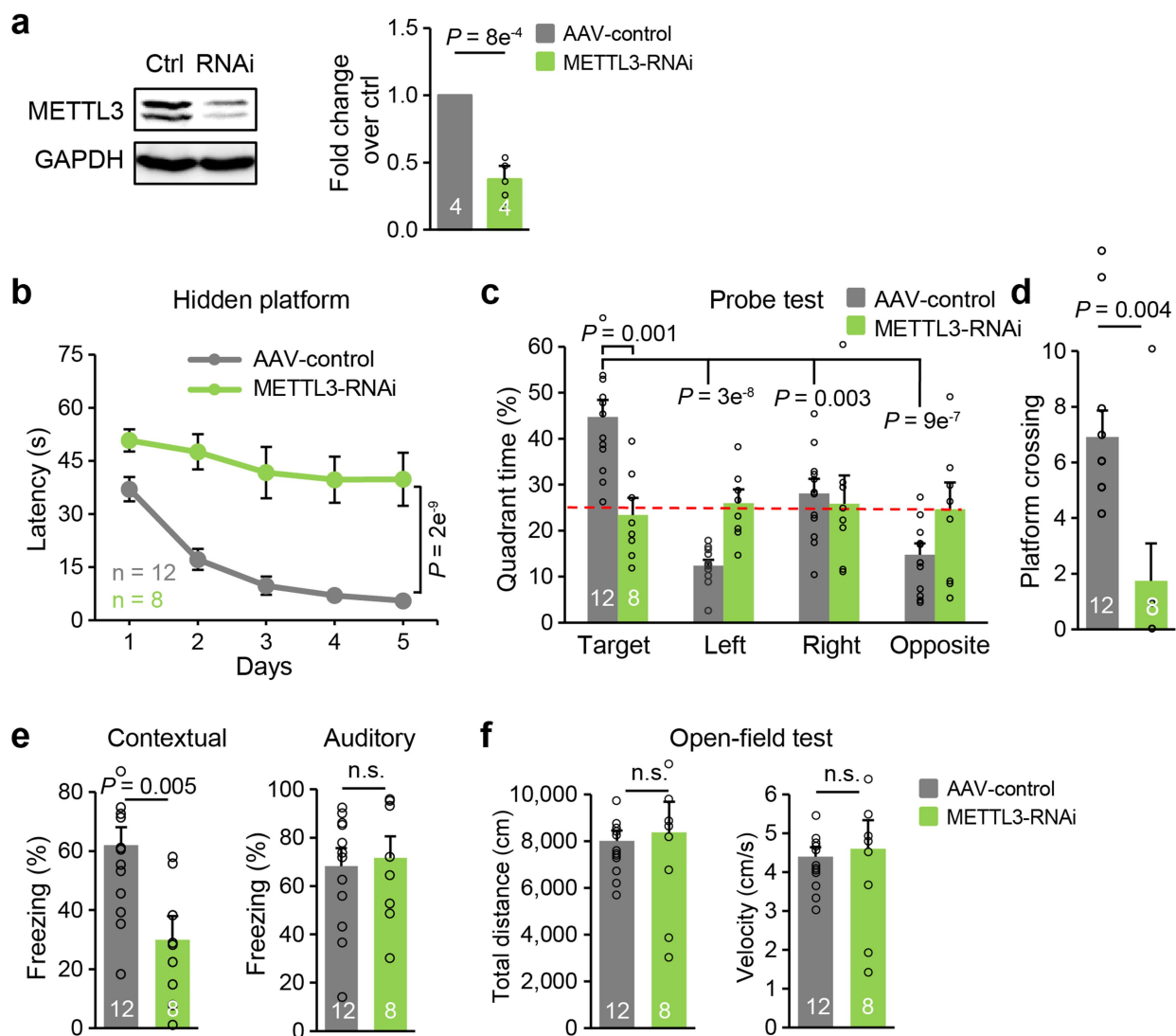
Extended Data Fig. 5 | Viral targeting in *Ythdf1*-KO mouse hippocampus and behavioural analyses of *Ythdf1*-KO mice injected with AAV virus. Related to Fig. 3. a, Representative fluorescence images of brain slices from rostral to caudal positions dissected from a mouse injected with AAV-YTHDF1 virus. Hoechst, blue; YTHDF1 co-expressed with mCherry, red. **b**, Representative images of virus expression (mCherry, red) and YTHDF1 immunostaining (green) in the mouse hippocampus after AAV-control or AAV-YTHDF1 infection. Hoechst, blue. **c**, YTHDF1 protein overexpression level indicated by immunofluorescent signal

intensity in the CA1 and DG regions. **d**, Number of crossings over the previous platform location for *Ythdf1*-KO mice injected with AAV-YTHDF1 or AAV-control in MWM probe tests. **e**, Anxiety-like behaviour of the injected mice measured as open-arm durations in elevated-plus maze. **f–h**, Motor activities of the injected mice measured as total distance (**f**), number of moves (**g**), and average velocity (**h**) in the open-field test. *P* values, two tailed *t*-test (**c–h**). Numbers in bars, numbers of mice. Data shown as mean \pm s.e.m.



Extended Data Fig. 6 | Impaired spatial learning and memory after selective knockdown of YTHDF1 in the hippocampus of wild-type mice. **a**, Schematics of the AAV construct expressing YTHDF1 shRNA. **b**, Western blot and quantification of protein expression level of YTH proteins in N2A cells after YTHDF1-shRNA (RNAi) or control vector (Ctrl) transfection. For gel source data, see Supplementary Fig. 1. **c**, Spatial learning curves in the hidden-platform MWM training sessions for RNAi (red) and control (grey) mice. **d–f**, Spatial memory performances measured by quadrant time (%) (**d**) and number of platform crossings (**e**),

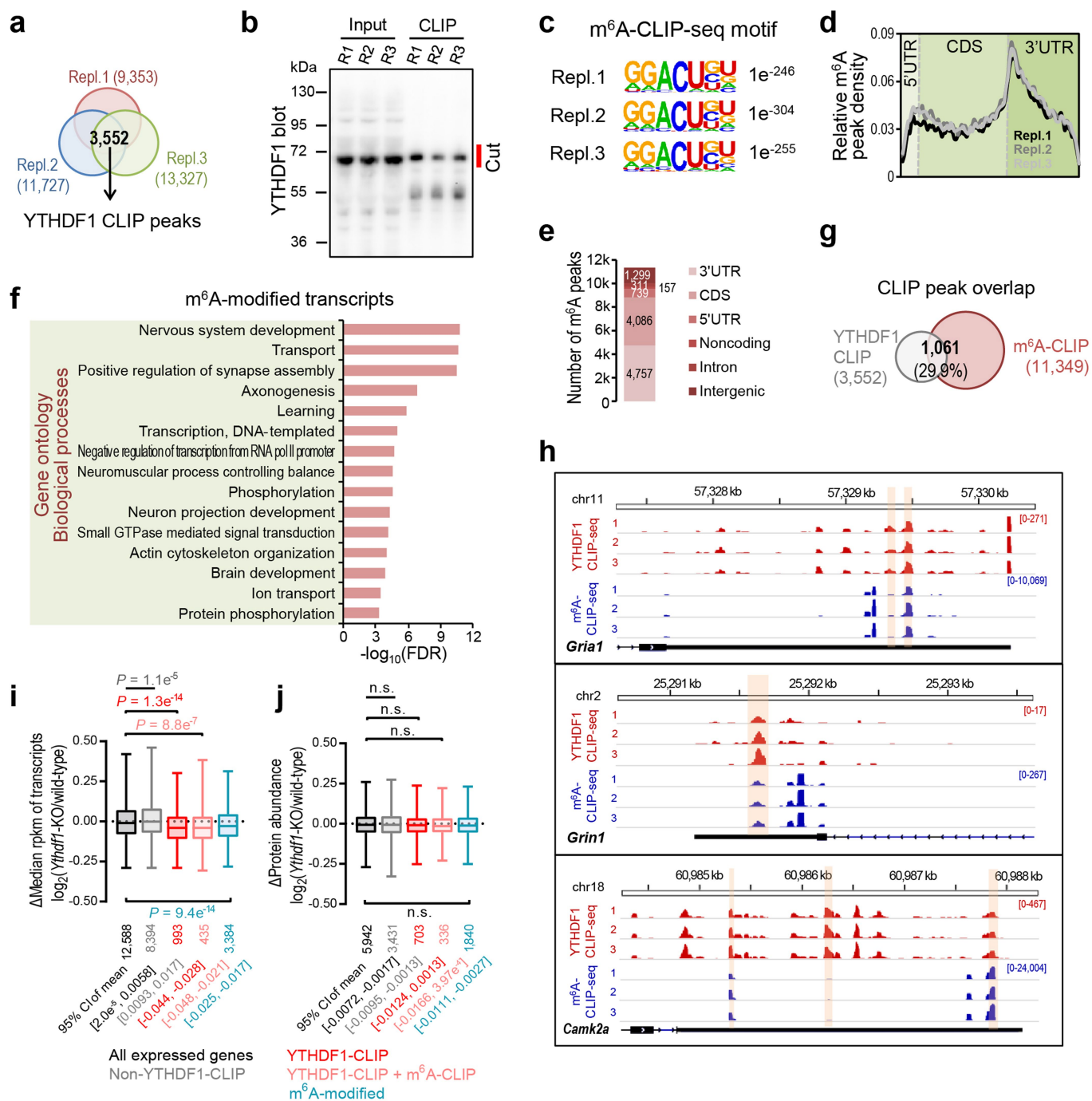
and motor activities (**f**) of RNAi (red) and control (grey) mice in MWM probe tests. **g**, **i**, Contextual (**g**) and auditory (**i**) fear memories assessed 24 h after fear conditioning in RNAi and control mice. **h**, Anxiety level of mice assessed by open-arm durations in elevated-plus maze. *P* values, two-way repeated measures ANOVA with post hoc two-tailed *t*-test (**c**), two-way ANOVA with two-tailed *t*-test (comparison between group or to 'Target') (**d**), and two-tailed *t*-test (**b**, **e–i**). Numbers in bars, numbers of biologically independent samples (**b**) and mice (**d–i**). Data shown as mean \pm s.e.m.



Extended Data Fig. 7 | Impaired spatial learning and memory after acute knockdown of METTL3 in the hippocampus of wild-type mice.

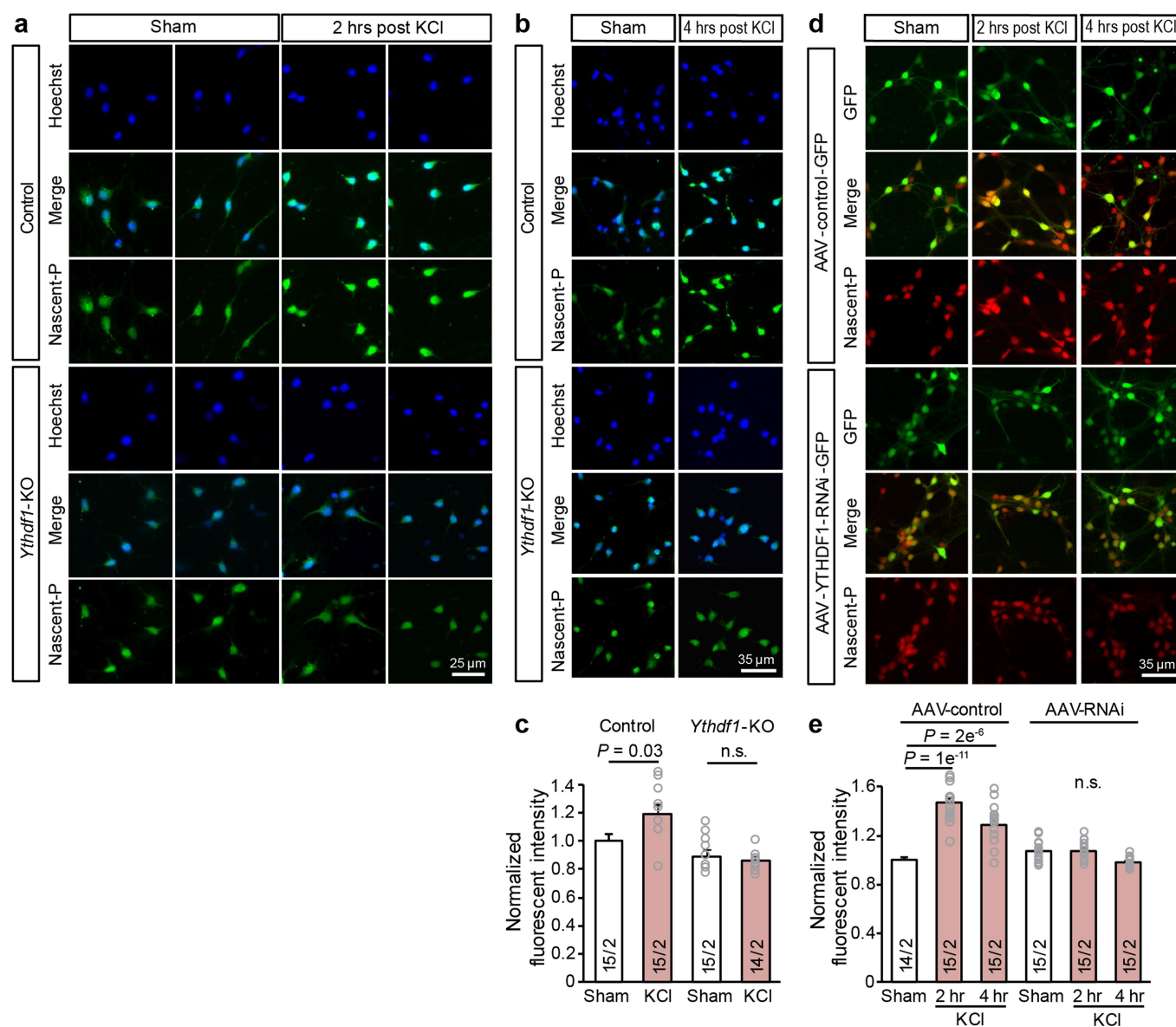
a, Representative western blot (left) and quantification (right) of METTL3 protein level in N2A cells transfected with METTL3-shRNA (RNAi) or control vector (Ctrl). For gel source data, see Supplementary Fig. 1. **b–d**, Spatial learning curves in the hidden-platform MWM training sessions (**b**), and spatial memory performance measured by quadrant time (per cent) (**c**) and the number of platform crossings (**d**) in MWM

probe tests, for METTL3-RNAi and control mice. **e**, Contextual (left) and auditory (right) fear memories measured by freezing levels 24 h after fear conditioning in METTL3-RNAi and control mice. **f**, Motor activities of mice accessed in the open-field test. *P* values, two-way repeated measures ANOVA with post hoc two-tailed *t*-test (**b**), two-way ANOVA with two-tailed *t*-test (comparison between groups or to 'Target') (**c**), and two-tailed *t*-test (**a**, **d–f**). Numbers in bars, numbers of biologically independent samples (**a**) and mice (**c–f**). Data shown as mean \pm s.e.m.



Extended Data Fig. 8 | YTHDF1 binding sites and m⁶A sites in the hippocampus of adult mice, and YTHDF1-mediated effects of m⁶A on hippocampal transcriptome and proteome. **a**, Peak overlap among three biological replicates of YTHDF1-CLIP-seq. **b**, Validation of immunoprecipitation efficiency for YTHDF1-CLIP-seq. The position of the gel slice cut during the step of protein–RNA complex size selection is indicated in red (see Methods). **c**, Consensus motif and its *P* value generated by HOMER⁴⁰ of the three sets of hippocampal m⁶A sites from biological replicates of m⁶A-CLIP-seq. **d**, **e**, Distribution of m⁶A-CLIP peaks along the different regions of transcripts (**d**) and genome (**e**). **f**, Functional annotation of m⁶A-modified transcripts in the adult mouse hippocampus (number of mutations in m⁶A-CLIP-seq ≥ 5 , $n = 2,922$). **g**, Peak overlap between high-confidence YTHDF1-CLIP peaks and high-confidence m⁶A-CLIP peaks. The percentage of YTHDF1-CLIP

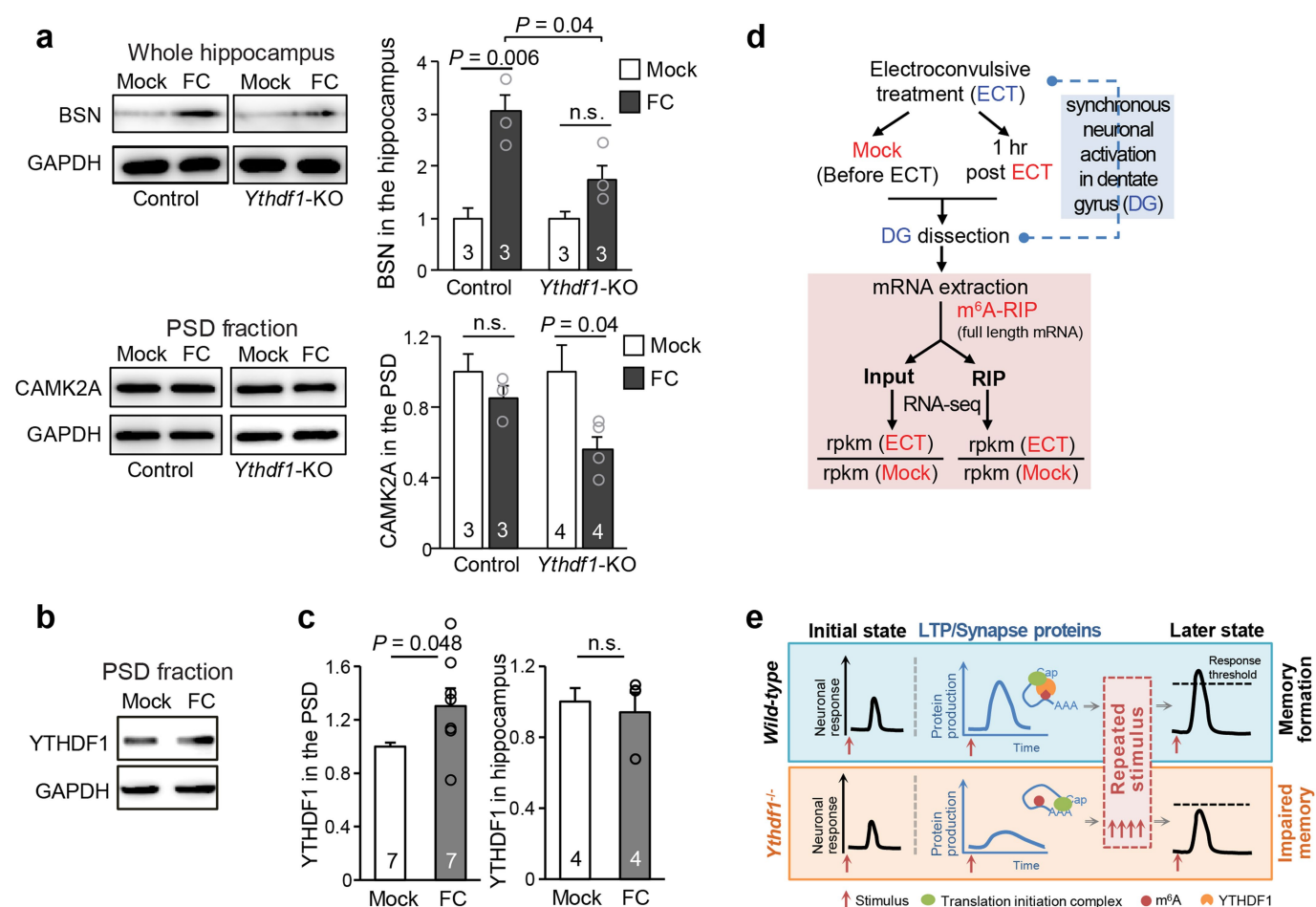
peaks overlapped is indicated. **h**, Integrative Genomics Viewer (IGV) screenshots of the piled mutated reads for the each of the biological triplicates of YTHDF1-CLIP-seq (red) and m⁶A-CLIP-seq (blue). Three examples of synaptic plasticity transcripts were presented; the overlapped peak regions are highlighted in orange. **i, j**, Box-plots of mRNA abundance (**i**) and protein abundance (**j**) log₂ fold changes (Δ) between *Ythdf1*-KO hippocampus and wild-type control for all expressed genes (black), non-YTHDF1-CLIP transcripts (grey), YTHDF1-CLIP targets (red), transcripts with overlapped YTHDF1-CLIP peaks and m⁶A-CLIP peaks (pink), and m⁶A-modified transcripts (blue). Box-plot elements: centre line, median; box limits, upper and lower quartiles, whiskers, 1–99%; *P* values, two-sided unpaired Kolmogorov–Smirnov test; number of genes and 95% confidence interval of mean are indicated for each box (**i, j**).



Extended Data Fig. 9 | Effects of YTHDF1 on nascent protein synthesis in cultured hippocampal neurons in response to KCl stimulus.

a, Additional representative images of nascent protein (Nascent-P) synthesis in cultured wild-type control and *Ythdf1*-KO hippocampal neurons before (sham) and 2 h after KCl depolarization, related to Fig. 4e, f. **b**, **c**, Representative images (**b**) and quantification (**c**) of Nascent-P in wild-type control and *Ythdf1*-KO hippocampal neurons before (sham)

and 4 h after KCl depolarization. **d**, **e**, Representative images (**d**) and quantification (**e**) of Nascent-P in AAV-control and AAV-YTHDF1-RNAi treated hippocampal neurons before (sham), 2 h, and 4 h after KCl depolarization. Intensities of Nascent-P were normalized to that of wild-type control (**c**) or AAV-control (**e**) neurons under the sham condition. *P* values, two-tailed *t*-test (**c**, **e**). Numbers in bars, numbers of images/biologically independent samples. Data shown as mean \pm s.e.m.



Extended Data Fig. 10 | Neuronal-stimulus-dependent functions of YTHDF1 in the mouse hippocampus and potential underlying mechanisms. a, Representative western blot (left) and quantification (right) of the protein levels of BSN (top) and CAMK2A (bottom), in the whole hippocampus and the PSD fraction, respectively, before (Mock) and 2 h after fear conditioning (FC). The protein quantification was normalized to the Mock condition for each genotype separately. For gel source data, see Supplementary Fig. 1. **b, c**, Representative western blot (b) and quantification of YTHDF1 protein level in the hippocampal postsynaptic density (PSD) fraction (c, left) and the whole hippocampus (c, right) before (Mock) and 2 h after fear conditioning. For gel source

data, see Supplementary Fig. 1. **d**, Schemes of the experimental design to quantify the change in the extent of m^6A methylation for each transcript in the dentate gyrus region before (Mock) and 1 h after ECT. **e**, A proposed mechanism for how YTHDF1 contributes to memory formation: YTHDF1 promotes translation of m^6A -modified target transcripts, including transcripts related to synaptic transmission and LTP, in response to learning stimulus, thus facilitating synapse strength adequately for a memory to occur. P values, two-tailed t -test (a, c). Numbers in bars, numbers of biologically independent samples. Data shown as mean \pm s.e.m.

Resting zone of the growth plate houses a unique class of skeletal stem cells

Koji Mizuhashi¹, Wanida Ono¹, Yuki Matsushita¹, Naoko Sakagami¹, Akira Takahashi¹, Thomas L. Saunders², Takashi Nagasawa³, Henry M. Kronenberg⁴ & Noriaki Ono^{1*}

Skeletal stem cells regulate bone growth and homeostasis by generating diverse cell types, including chondrocytes, osteoblasts and marrow stromal cells. The emerging concept postulates that there exists a distinct type of skeletal stem cell that is closely associated with the growth plate^{1–4}, which is a type of cartilaginous tissue that has critical roles in bone elongation⁵. The resting zone maintains the growth plate by expressing parathyroid hormone-related protein (PTHrP), which interacts with Indian hedgehog (Ihh) that is released from the hypertrophic zone^{6–10}, and provides a source of other chondrocytes¹¹. However, the identity of skeletal stem cells and how they are maintained in the growth plate are unknown. Here we show, in a mouse model, that skeletal stem cells are formed among PTHrP-positive chondrocytes within the resting zone of the postnatal growth plate. PTHrP-positive chondrocytes expressed a panel of markers for skeletal stem and progenitor cells, and uniquely possessed the properties of skeletal stem cells in cultured conditions. Cell-lineage analysis revealed that PTHrP-positive chondrocytes in the resting zone continued to form columnar chondrocytes in the long term; these chondrocytes underwent hypertrophy, and became osteoblasts and marrow stromal cells beneath the growth plate. Transit-amplifying chondrocytes in the proliferating zone—which was concertedly maintained by a forward signal from undifferentiated cells (PTHrP) and a reverse signal from hypertrophic cells (Ihh)—provided instructive cues to maintain the cell fates of PTHrP-positive chondrocytes in the resting zone. Our findings unravel a type of somatic stem cell that is initially unipotent and acquires multipotency at the post-mitotic stage, underscoring the malleable nature of the skeletal cell lineage. This system provides a model in which functionally dedicated stem cells and their niches are specified postnatally, and maintained throughout tissue growth by a tight feedback regulation system.

We first defined the formation of PTHrP⁺ chondrocytes in the growth plate using a *Pthrp-mCherry* (*Pthrp* is also known as *Pthlh*) knock-in reporter allele (Extended Data Fig. 1a, see also Supplementary Information). During the fetal stage, PTHrP-mCherry⁺ cells were mitotically active and localized within the Sox9⁺ perichondrial region (Extended Data Fig. 1b). Although this pattern continued at birth (Fig. 1a), a distinct group of PTHrP-mCherry⁺ chondrocytes appeared in the central area of the growth plate that is devoid of proliferation at postnatal day (P)3 (Extended Data Fig. 1c). These PTHrP-mCherry⁺ chondrocytes increased markedly in number between P6 and P9, and occupied a well-defined zone in the growth plate (Fig. 1b–d, Extended Data Fig. 1c); these chondrocytes were less proliferative than their counterparts in the proliferating zone (EdU⁺; $6.1 \pm 2.3\%$ of mCherry⁺ cells versus $30.5 \pm 3.2\%$ of proliferating chondrocytes at P9, $n = 3$ mice). Therefore, PTHrP-mCherry⁺ chondrocytes in the resting zone ('resting chondrocytes') develop in the postnatal growth plate, which is closely associated with the formation of secondary ossification centres. Flow cytometry analysis revealed that PTHrP-mCherry⁺ cells were exclusively found in the CD45^{neg} cell population in the

growth plate (Fig. 1e), and were completely absent in the CD45^{neg} population in bone and bone marrow cells (Extended Data Fig. 2a). PTHrP-mCherry⁺ cells in the growth plate did not express Col1a1(2.3kb)-GFP (Extended Data Fig. 2b), which indicates that PTHrP-mCherry is specifically expressed by growth-plate chondrocytes but not by osteoblasts or bone marrow stromal cells. We next asked whether PTHrP-mCherry⁺ resting chondrocytes express a panel of cell-surface markers for transplantable skeletal stem and progenitor cells³—particularly three subsets of skeletal stem and progenitor populations (integrin alpha V (CD51)⁺Thy-1 (CD90)[−]; mouse skeletal stem cells (mSSCs) (CD105[−]CD200⁺), pre-bone, cartilage and stromal progenitors (pre-BCSPs) (CD105[−]CD200[−]), and bone, cartilage and stromal progenitors (BCSPs) (CD105⁺). A large majority of CD45[−]Ter119[−]CD31[−] growth-plate cells—including both mCherry[−] and mCherry⁺ fractions—were in a CD51⁺CD90[−] skeletal stem and progenitor population (Fig. 1f, left panels). Among CD45[−]Ter119[−]CD31[−]CD51⁺CD90[−] mCherry⁺ cells, $49.2 \pm 8.4\%$, $23.4 \pm 8.4\%$ and $27.4 \pm 16.5\%$ were CD105[−]CD200⁺ (mSSCs), CD105[−]CD200[−] (pre-BCSPs) and CD105⁺ (BCSPs), respectively (Fig. 1f, right panels; see also Extended Data Fig. 2c, d). Conversely, $41.6 \pm 4.4\%$, $31.7 \pm 6.2\%$ and $53.4 \pm 16.9\%$ of mSSCs, pre-BCSPs and BCSPs, respectively, were positive for PTHrP-mCherry (Extended Data Fig. 2e). Therefore, PTHrP-mCherry⁺ resting chondrocytes represent a substantial subset of immunophenotypically defined skeletal stem and progenitor cells in the growth plate.

We next determined whether PTHrP⁺ resting chondrocytes behave as stem cells in vivo, by using a *Pthrp-creER* bacterial artificial chromosome transgenic line (L909, Extended Data Fig. 3a; see also Supplementary Information, Supplementary Methods and Extended Data Fig. 10 for establishment of this system and validation of tamoxifen-negative controls). Analysis of *Pthrp*^{mCherry/+}; *Pthrp-creER*; *R26R^{ZsGreen}* mice revealed that ZsGreen⁺ cells largely overlapped with mCherry⁺ cells shortly after a tamoxifen pulse at P6 (Extended Data Fig. 3b–d). The percentage of CD105⁺ cells within the ZsGreen⁺ cell population was significantly lower than that within the mCherry⁺ cell population (Extended Data Fig. 3e), which indicates that *Pthrp-creER* preferentially marks an immature subset of PTHrP-mCherry⁺ cells. An EdU label-exclusion assay of *Pthrp-creER*; *R26R^{tdTomato}* mice pulsed with tamoxifen at P6 revealed that a large majority of tdTomato⁺ cells were resistant to EdU incorporation (Extended Data Fig. 3f, EdU⁺; $7.7 \pm 2.0\%$ of tdTomato⁺ cells versus $61.1 \pm 11.5\%$ of proliferating-zone chondrocytes, $n = 3$ mice), which demonstrates that *Pthrp-creER* specifically marks resting chondrocytes (Extended Data Fig. 3g). These PTHrP⁺ resting chondrocytes did not express Grem1⁴ (Extended Data Fig. 3h). Subsequently, we traced the fate of PTHrP⁺ resting chondrocytes labelled on P6 (hereafter, PTHrP^{CE}-P6 cells) in vivo. After remaining within the resting zone at P12 (Fig. 2a; see also Extended Data Fig. 3g), PTHrP^{CE}-P6 cells first formed short columns (composed of <10 cells) (Fig. 2b, arrowhead) and subsequently formed longer columns (composed of >10 cells) that originated from the

¹University of Michigan School of Dentistry, Ann Arbor, MI, USA. ²Transgenic Animal Model Core, University of Michigan Medical School, Ann Arbor, MI, USA. ³Laboratory of Stem Cell Biology and Developmental Immunology, Graduate School of Frontier Biosciences, Osaka University School of Medicine, Suita, Japan. ⁴Endocrine Unit, Massachusetts General Hospital and Harvard Medical School, Boston, MA, USA. *e-mail: norionao@umich.edu

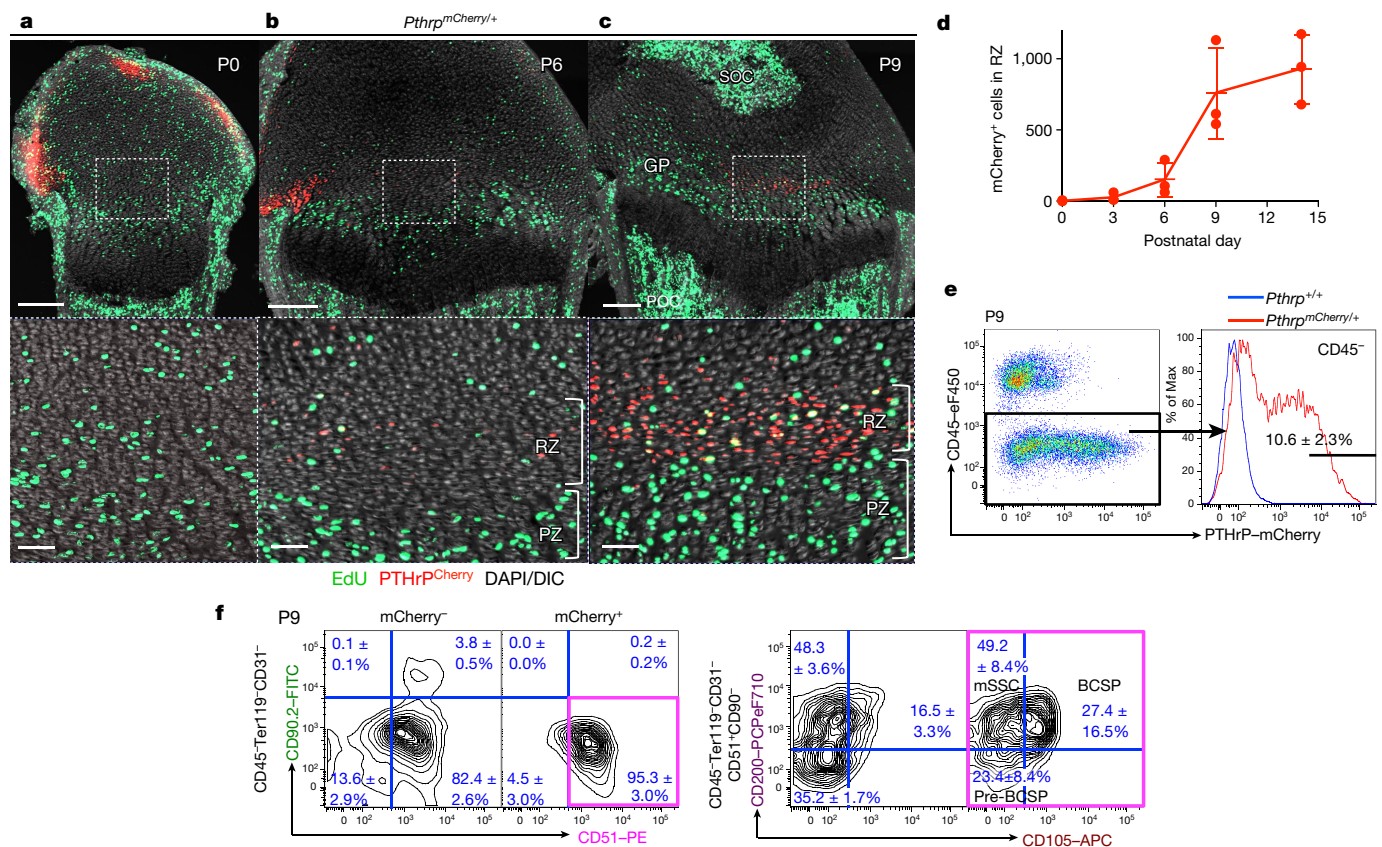


Fig. 1 | Formation of PTHrP-mCherry⁺ chondrocytes in the resting zone of the growth plate. **a–c**, *Pthrp*^{mCherry/+} distal-femur growth plates with EdU administration shortly before analysis. Bottom panels show magnified views of central growth plates. RZ, resting zone; PZ, proliferating zone; GP, growth plate; POC, primary ossification centre; SOC, secondary ossification centre. Grey, DAPI and DIC. Scale bars, 200 μ m (top panels), 50 μ m (bottom panels). **d**, Quantification of mCherry⁺ cells. $n = 3$ mice per group, data are presented as

mean \pm s.d. **e**, Flow cytometry analysis of *Pthrp*^{mCherry/+} growth-plate cells. $n = 8$ mice, data are presented as mean \pm s.d. **f**, Skeletal stem and progenitor cell-surface-marker analysis of *Pthrp*^{mCherry/+} growth-plate cells. mCherry[−], mCherry⁺ fraction of *Pthrp*^{mCherry/+} cells; mCherry[−], mCherry⁺ fraction of *Pthrp*^{mCherry/+} cells. Magenta box, CD45[−] Ter119[−] CD31[−] CD90[−] mCherry⁺ fraction. $n = 3$ mice per group, data are presented as mean \pm s.d.

resting zone, at around P18 (Fig. 2c, arrows). After a month of chase, PTHrP^{CE}-P6 cells constituted the entire column from the resting zone to the hypertrophic zone (Fig. 2d). The number of tdTomato⁺ resting chondrocytes transiently increased during the first week of chase and decreased thereafter, owing to the formation of columnar chondrocytes (Fig. 2e). The number of short tdTomato⁺ columns peaked at P18 and decreased thereafter, whereas long tdTomato⁺ columns appeared at P18 and continued to increase until P36 (Fig. 2f). Thus, *Pthrp*-creER⁺ resting chondrocytes stay within the resting zone for the first week, and establish columnar chondrocytes starting from the second week of chase. Analysis of *Pthrp*-creER;R26R^{Confetti} mice revealed that each column was marked by its unique colour (CFP, YFP or tdTomato, Fig. 2g), which demonstrates that single *Pthrp*-creER⁺ resting chondrocytes can give rise to multiple types of chondrocytes. Additional analysis of *Col2a1*-creER;R26R^{Confetti} mice further supported the existence of clonal cell populations (Extended Data Fig. 4a). Together, these findings support the notion that individual PTHrP⁺ resting chondrocytes are multipotent and can clonally establish columnar chondrocytes in the growth plate.

To investigate whether *Pthrp*-creER⁺ resting chondrocytes undergo self-renewing asymmetric divisions, we performed an EdU label-retention assay. Analysis of PTHrP^{CE}-P6 cells with serial pulses of EdU revealed that, after three weeks of chase, these cells gradually diluted the EdU signal as they differentiated towards the hypertrophic zone (Fig. 2h). Further, PTHrP^{CE}-P6 cells in the resting zone expressed PTHrP-mCherry, whereas those in the proliferating zone lost this expression (Fig. 2i). Therefore, *Pthrp*-creER⁺ chondrocytes maintain themselves in the resting zone as PTHrP⁺ cells and become the

source of columnar chondrocytes in the growth plate, by providing the transit-amplifying progeny. Analysis of *Pthrp*-creER;R26R^{tdTomato} mice after being pulsed at various preceding pre-natal and early post-natal time points revealed that *Pthrp*-creER⁺ chondrocytes started to be formed within the resting zone at embryonic day (E)17.5 (Extended Data Fig. 4b–e); a tamoxifen pulse on a later day laterally expanded the domain of tdTomato⁺ cells. However, once they were marked, tdTomato⁺ cells did not expand laterally upon further chase (Extended Data Fig. 4f,g), which indicates that PTHrP⁺ resting chondrocytes are dedicated—at least to some degree—to making columnar chondrocytes longitudinally. Additional analysis of *Dlx5*-creER;R26R^{tdTomato} mice revealed that chondrocytes in the proliferating and hypertrophic zone could only form short columns (<10 cells) that eventually disappeared from the growth plate (Extended Data Fig. 5a–d), indicating that *Dlx5*-creER⁺ proliferating chondrocytes are not the source of columnar chondrocytes in the growth plate.

During an extended chase period, PTHrP^{CE}-P6 cells continued to form columnar chondrocytes within the growth plate for at least a year after the pulse (Fig. 3a–c for *Col1a1*(2.3kb)-GFP; Extended Data Fig. 6a–d for *Cxcl12*-GFP¹²): the number of tdTomato⁺ columns in the growth plate gradually decreased until six months after the pulse, and reached a plateau thereafter (Fig. 3d). A majority of tdTomato⁺ columns extended beyond the hypertrophic layer and continued into the primary spongiosa and the metaphyseal bone marrow, an area beneath the growth plate¹³. These chondrocytes became Cxcl12-GFP⁺ stromal cells beneath tdTomato⁺ columns (Extended Data Fig. 6e), and reticular cells near trabecular bones (Fig. 3a, bottom). These chondrocytes also became *Col1a1*(2.3kb)-GFP⁺ osteoblasts on the trabecular surface

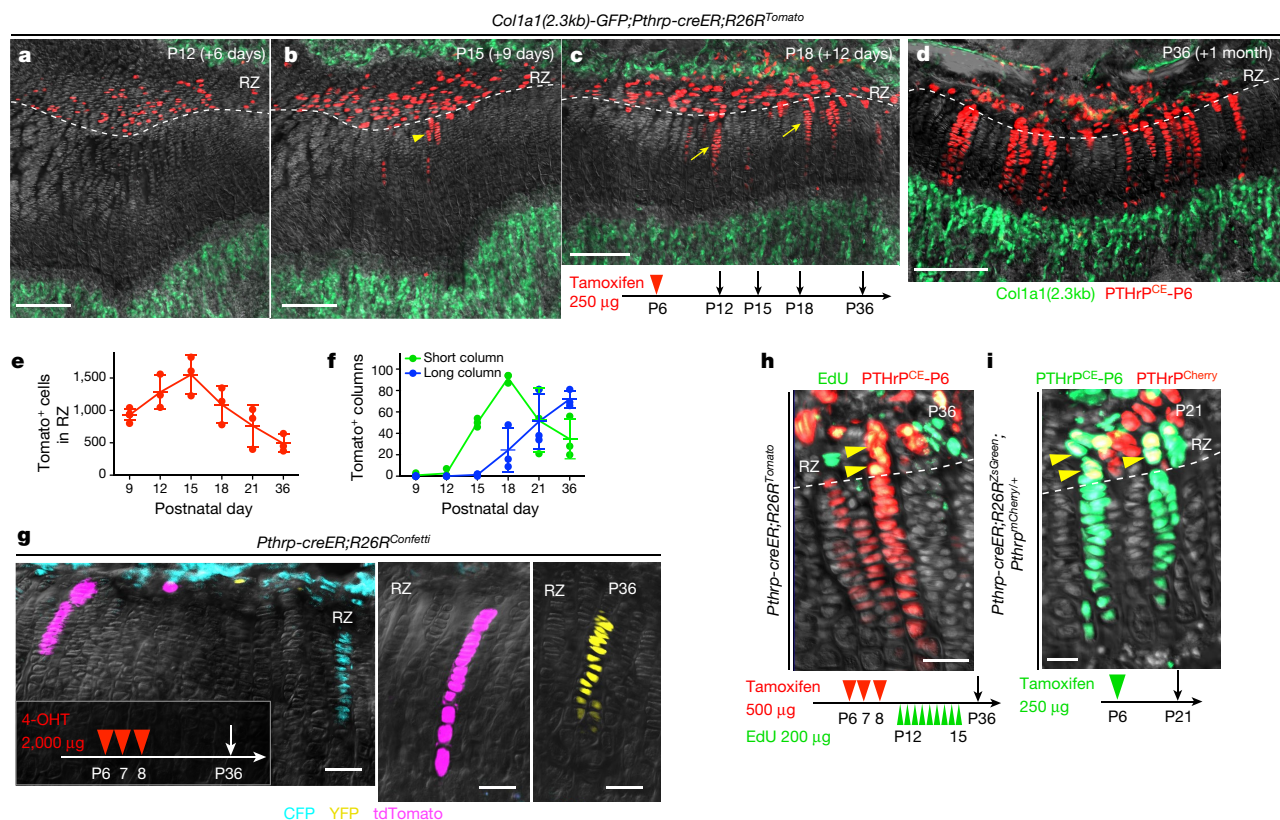


Fig. 2 | *Pthrp-creER*⁺ resting chondrocytes are the source of columnar chondrocytes. **a–d**, Cell-fate analysis of *Pthrp-creER*⁺ resting chondrocytes. *Col1a1(2.3kb)-GFP;Pthrp-creER;R26R^{tdTomato}* (pulsed on P6) distal-femur growth plates. Arrowhead, short column (<10 cells); arrows, long columns (>10 cells). Scale bars, 200 µm. **e, f**, Quantification of tdTomato⁺ cells in resting zone (red line) (**e**) and columns in growth plate, short columns (<10 cells, green line) and long columns (>10 cells, blue line) (**f**). *n* = 5 (P9), *n* = 3 (P12–P36) mice per group, data are presented as mean ± s.d. **g**, In vivo clonal analysis of *Pthrp-creER*⁺

(Fig. 3a, bottom) and in the primary spongiosa (Fig. 3b, bottom). The number of *Cxcl12-GFP*⁺tdTomato⁺ stromal cells and *Col1a1(2.3kb)-GFP*⁺tdTomato⁺ osteoblasts increased for the first three months of chase; subsequently, the number of *Col1a1(2.3kb)-GFP*⁺tdTomato⁺ osteoblasts decreased, whereas the number of *Cxcl12-GFP*⁺tdTomato⁺ stromal cells reached a plateau (Fig. 3e). These cells did not become bone marrow adipocytes in the presence of a high-fat diet that contained a PPAR-γ agonist rosiglitazone (LipidTOX⁺, 0 out of 443 cells examined; Extended Data Fig. 6f). Therefore, a subset of *Pthrp-creER*⁺ resting chondrocytes can continue to reproduce themselves within the resting zone in the long term; their descendants first differentiate into hypertrophic chondrocytes within the growth plate, and then become multiple types of cells beyond the growth plate, such as osteoblasts and bone marrow stromal cells—but not adipocytes—in vivo.

We next performed a colony-forming assay to test whether *Pthrp-creER*⁺ resting chondrocytes behave as skeletal stem cells in cultured conditions^{14,15}. PTHrP^{CE}-P6 cells formed distinct and large tdTomato⁺ colonies (>50 cells) composed of small Sox9⁺ spherical cells (about 20 µm in diameter) (Extended Data Fig. 7a, b). By contrast, *Dlx5*⁺ proliferating chondrocytes labelled on P7 failed to form tdTomato⁺ colonies (Extended Data Fig. 7b, right), which indicates that *Pthrp-creER*⁺ resting chondrocytes uniquely possess the capacity to form colonies when cultured ex vivo (Extended Data Fig. 7c). We next isolated individual primary PTHrP^{CE}-tdTomato⁺ colonies and sub-cultured them further to determine whether individual colony-forming cells can self-renew in vitro (Extended Data Fig. 7d, see also Supplementary Information). Although a small fraction of P9 PTHrP^{CE}-tdTomato⁺ primary colonies had the ability to establish secondary colonies

resting chondrocytes. *Pthrp-creER;R26R^{Confetti}* distal-femur growth plates (pulsed on P6, P7 and P8). 4-OHT, 4-hydroxytamoxifen. Scale bars, 50 µm. *n* = 3 mice. **h**, EdU label-retention assay of *Pthrp-creER;R26R^{tdTomato}* distal-femur growth plates (pulsed on P6, P7 and P8). Arrowheads, EdU-retaining tdTomato⁺ cells. Scale bars, 50 µm. *n* = 3 mice. **i**, PTHrP-mCherry expression in *Pthrp-creER;R26R^{ZsGreen};Pthrp^{mCherry}/+* distal-femur growth plates (pulsed on P6). Arrowheads, PTHrP-mCherry⁺ZsGreen⁺ cells. Scale bars, 20 µm. Grey, DAPI and DIC. *n* = 3 mice.

(17 out of 518 clones, 3.3%), none of them could survive a further passage (Extended Data Fig. 7e). By contrast, an increased fraction of P12 PTHrP^{CE}-tdTomato⁺ colonies established secondary colonies (16 out of 98 clones, 16.3%), and a fraction of these clones (2 out of 16 clones, 12.5%) could be further passaged for at least nine generations (Fig. 4a). Thus, *Pthrp-creER*⁺ colony-forming cells appear to acquire robust in vitro self-renewability when the secondary ossification centre actively develops. Further, individual PTHrP^{CE}-tdTomato⁺ cells (passage 4–7) could generate Alcian blue⁺ spheres, Alizarin red⁺ mineralized matrix and LipidTOX⁺ oil droplets under chondrogenic, osteogenic and adipogenic differentiation conditions, respectively (Figs. 4b, 4 out of 4 clones, 100%). Upon subcutaneous transplantation into immunodeficient mice, these cells robustly differentiated into *Col1a1(2.3kb)-GFP*⁺ osteoblastic cells (Fig. 4c) and effectively gave rise to Alcian blue⁺ and Alizarin red⁺ matrix, but produced Oil red O⁺ lipid droplets only ineffectively (Extended Data Fig. 7f). These findings indicate that PTHrP⁺ skeletal stem cells are predisposed to become chondrocytes and osteoblasts in vivo, and possess a baseline potential to become adipocytes in an inductive condition in vitro.

Lastly, we set out to investigate the functional importance of PTHrP⁺ resting chondrocytes. Inducible cell ablation experiments using *Pthrp-creER;R26^{Isl-tdTomato}/+* (control) and *Pthrp-creER;R26^{Isl-tdTomato}/iDTA* (hereafter, DTA) littermates revealed that *Pthrp-creER*⁺ cells were only incompletely ablated; tdTomato⁺ resting chondrocytes and columns were still observed in the induced tissue of DTA mice (Fig. 5a, b). Nonetheless, the height of each layer of the growth plate was altered in the induced tissue of DTA mice, in which the proliferating zone was significantly reduced in association with the

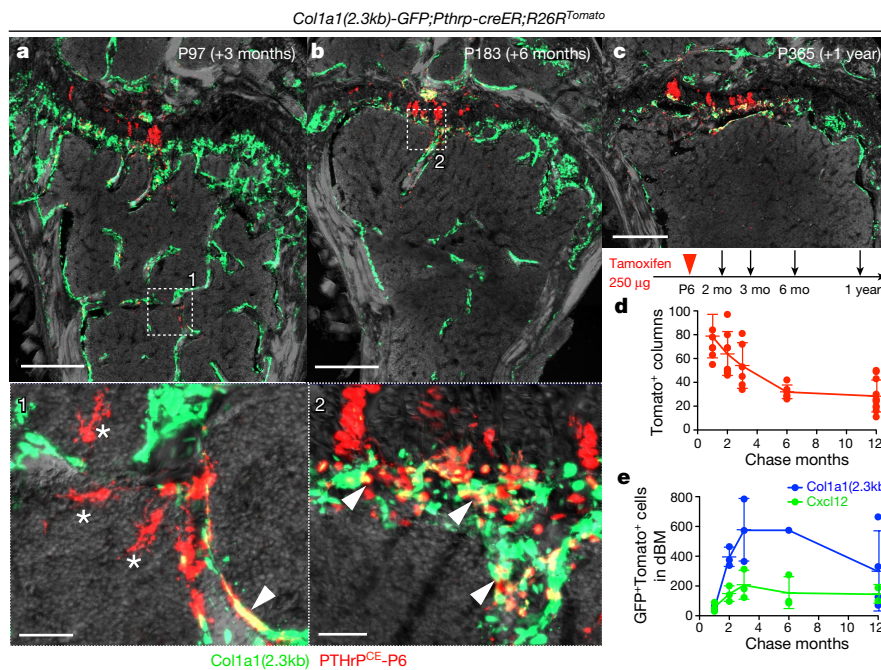


Fig. 3 | *Pthrp-creER*⁺ resting chondrocytes behave as skeletal stem cells in vivo. **a–c**, Long-chase analysis of *Pthrp-creER*⁺ resting chondrocytes. *Col1a1(2.3kb)-GFP;Pthrp-creER;R26R^{tdTomato}* distal femurs (pulsed on P6). In **a**, **b**, the bottom panel shows a magnified view of marrow space (white box in top panel). Arrowheads, *Col1a1(2.3kb)-GFP*⁺tdTomato⁺ osteoblasts; asterisks, tdTomato⁺ reticular stromal cells. Grey, DAPI and DIC. Scale bars, 500 μ m (top panels), 50 μ m (bottom panels). $n = 3$ mice per group, except in **b**, $n = 1$ mouse. **d**, Quantification of tdTomato⁺ columns in growth plate (red line) during the chase. $n = 8$ (1 month,

2 months), $n = 6$ (3 months, 6 months), $n = 11$ (12 months) mice per group, data are presented as mean \pm s.d. **e**, Quantification of *Col1a1(2.3kb)-GFP*⁺tdTomato⁺ osteoblasts (blue line) and *Cxcl12-GFP*⁺tdTomato⁺ stromal cells (green line) in distal bone and bone marrow (dBm, up to 5 mm from the growth plate) during the chase. $n = 3$ (1 month, 2 months, 3 months for *Col1a1(2.3kb)-GFP* and *Cxcl12-GFP*, 6 months for *Cxcl12-GFP*, $n = 4$ (12 months for *Col1a1(2.3kb)-GFP*, $n = 2$ (12 months for *Cxcl12-GFP*) mice per group, data are presented as mean \pm s.d., $n = 1$ (6 months for *Col1a1(2.3kb)-GFP*) mouse.

significant expansion of the hypertrophic and resting zones (Fig. 5c). Therefore, partial loss of PTHrP⁺ cells in the resting zone is sufficient to alter the integrity of the growth plate by inducing premature hypertrophic differentiation of chondrocytes in the proliferating zone.

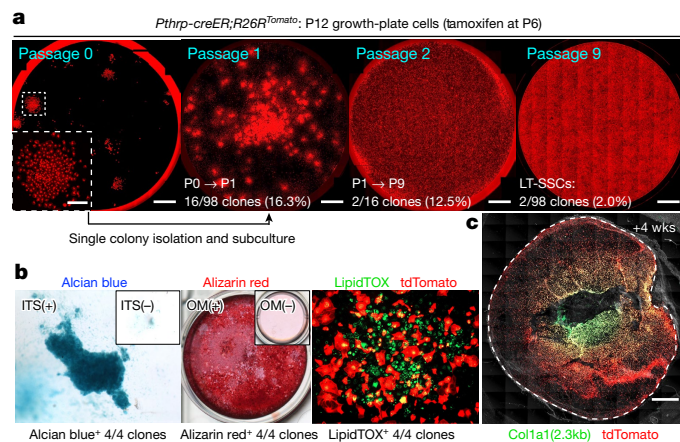


Fig. 4 | Skeletal stem cell activities of *Pthrp-creER*⁺ resting chondrocytes ex vivo. **a**, Colony-forming assay and subsequent passaging of individual PTHrP^{CE}-tdTomato⁺ colonies. Inset, magnified view of single colony. Red, tdTomato. Scale bars, 5 mm, 1 mm (inset). LT-SSCs, long-term skeletal stem cells. $n = 98$ independent experiments. **b**, Trilineage differentiation of PTHrP^{CE}-tdTomato⁺ clones (passage 4 to 7). Chondrogenic (left), osteogenic (centre) and adipogenic (right) differentiation conditions. Insets, differentiation-medium negative controls. ITS, insulin–transferrin–selenium, OM, osteogenic differentiation medium. Four independent clones were tested. **c**, Subcutaneous transplantation of PTHrP^{CE}-tdTomato⁺ clones into immunodeficient mice. Dotted line, contour of the plug. Grey, DIC. Scale bars, 1 mm. $n = 8$ mice.

Moreover, global manipulation of Hedgehog (Hh) signalling using Smo agonist (SAG) and antagonist (LDE225) in *Pthrp-creER;R26R^{tdTomato}* mice pulsed on P6 revealed that these regimens predominantly affected chondrocytes in the proliferating zone, without directly affecting PTHrP^{CE}-P6 cells in the resting zone (Extended Data Fig. 8a–c). Both regimens resulted in a significantly reduced number of tdTomato⁺ columns (Fig. 5d; see also Extended Data Fig. 8d–k), indicating that uninterrupted Hh signalling is essential to maintaining the proper cell fates of PTHrP⁺ resting chondrocytes. *Pthrp-creER*⁺ cells directly differentiated into *Col1a1(2.3kb)-GFP*⁺ osteoblasts in response to micro-perforation injury (Extended Data Fig. 8l, m), which indicates that PTHrP⁺ skeletal stem cells lose their physiological fate in the absence of an intact proliferating zone.

Here we identified that the resting zone of the growth plate houses a unique class of skeletal stem cells, the transit-amplifying progeny of which are lineage-restricted as chondrocytes that exhibit multipotency only at the post-mitotic stage (see Extended Data Fig. 9a, b). PTHrP⁺ cells are one of the stem-cell subgroups organized within the resting zone and—together with other as-yet unidentified cells—these cells can concertedly contribute to long-term tissue renewal. PTHrP⁺ skeletal stem cells are dedicated to making columnar chondrocytes longitudinally, and appear to derive from PTHrP[−] cells. PTHrP⁺ stem cells are highly hierarchical; approximately 2–3% of these cells acquire long-term self-renewability (Extended Data Fig. 9b). In addition, these stem cells are endowed with the ability to maintain the integrity of the growth plate, by sending a forward signal (that is, PTHrP) for transit-amplifying chondrocytes to maintain their proliferation and delay their hypertrophy in a non-cell autonomous manner. Therefore, PTHrP⁺ stem cells can also provide the niche for transit-amplifying cells, which is compatible with a model previously proposed for the epithelium¹⁶. Conversely, transit-amplifying cells—which are maintained in a Hedgehog-responsive manner—appear to provide instructive cues to determine the cell fates of PTHrP⁺ stem cells within the growth

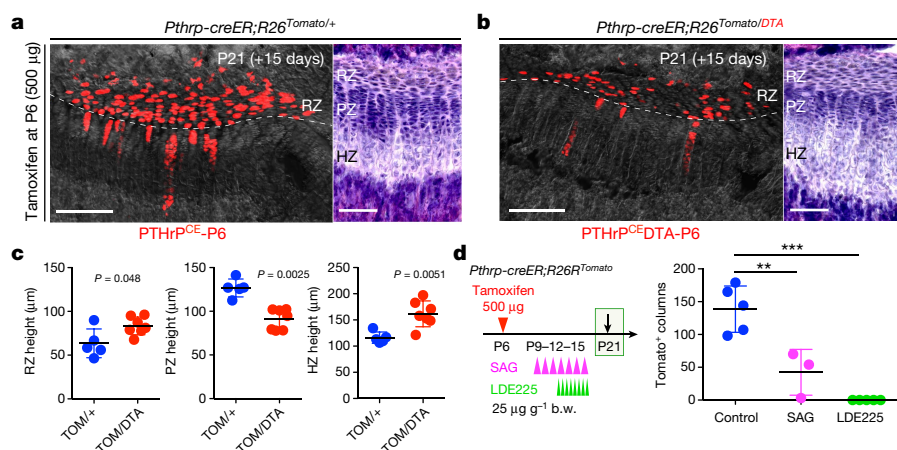


Fig. 5 | Reciprocal interactions between *PTHrP-creER*⁺ resting chondrocytes and their niche. **a–c**, DTA-mediated ablation of *Pthrp-creER*⁺ resting chondrocytes. **a**, *Pthrp-creER;R26^{Isl-tdTomato}/+* (control). **b**, *Pthrp-creER;R26^{Isl-tdTomato}/DTA* (DTA) distal-femur growth plates (pulsed on P6). HZ, hypertrophic zone. Grey, DAPI and DIC. Right panels, haematoxylin and eosin staining. Scale bars, 200 µm (left panels) and 100 µm (right panels). **c**, Quantification of resting (left), proliferating (centre) and hypertrophic (right) zone height. TOM, tdTomato. $n = 5$ mice for control, $n = 7$ mice for DTA, data are presented as mean \pm s.d., P values from Mann–Whitney's U -test, two-tailed. **d**, Pharmacological

manipulation of Hedgehog signalling. Quantification of tdTomato⁺ columns in *Pthrp-creER;R26^{Isl-tdTomato}* distal-femur growth plates (pulsed on P6). $n = 5$ (control), $n = 3$ (SAG) and $n = 5$ (LDE225) mice per group, data are presented as mean \pm s.d., $^{**}P < 0.01$, $^{***}P < 0.001$. Control versus SAG, mean difference = 96.2, 95% confidence interval (41.6, 150.9); control versus LDE225, mean difference = 138.6, 95% confidence interval (91.3, 185.9); SAG versus LDE225, mean difference = 42.3, 95% confidence interval (–12.3, 97.0). One-way ANOVA followed by Tukey's multiple comparison test. b.w., body weight.

plate, which implies a reciprocal interaction between the stem cells and their progeny. We assume that PTHrP[–] short-term precursors are the principal driver for extensive bone growth that occurs during postnatal development, reminiscent of a model proposed for haematopoietic stem cells^{17,18}. It is possible that PTHrP⁺ skeletal stem cells are mainly involved in the long-term maintenance of skeletal integrity, although further details need to be clarified.

Data availability

Source Data are provided in the online version of the paper. The datasets generated during and/or analysed during the current study are available in Dryad Digital Repository (<https://doi.org/10.5061/dryad.3qq5bm7>).

Online content

Any methods, additional references, Nature Research reporting summaries, source data, statements of data availability and associated accession codes are available at <https://doi.org/10.1038/s41586-018-0662-5>.

Received: 23 September 2017; Accepted: 10 September 2018;

Published online 31 October 2018.

- Ono, N. & Kronenberg, H. M. Bone repair and stem cells. *Curr. Opin. Genet. Dev.* **40**, 103–107 (2016).
- Ono, N., Ono, W., Nagasawa, T. & Kronenberg, H. M. A subset of chondrogenic cells provides early mesenchymal progenitors in growing bones. *Nat. Cell Biol.* **16**, 1157–1167 (2014).
- Chan, C. K. et al. Identification and specification of the mouse skeletal stem cell. *Cell* **160**, 285–298 (2015).
- Worthley, D. L. et al. Gremlin 1 identifies a skeletal stem cell with bone, cartilage, and reticular stromal potential. *Cell* **160**, 269–284 (2015).
- Kronenberg, H. M. Developmental regulation of the growth plate. *Nature* **423**, 332–336 (2003).
- St-Jacques, B., Hammerschmidt, M. & McMahon, A. P. Indian hedgehog signaling regulates proliferation and differentiation of chondrocytes and is essential for bone formation. *Genes Dev.* **13**, 2072–2086 (1999).
- Kobayashi, T. et al. PTHrP and Indian hedgehog control differentiation of growth plate chondrocytes at multiple steps. *Development* **129**, 2977–2986 (2002).
- Kobayashi, T. et al. Indian hedgehog stimulates periarticular chondrocyte differentiation to regulate growth plate length independently of PTHrP. *J. Clin. Invest.* **115**, 1734–1742 (2005).
- Chen, X. et al. Initial characterization of PTH-related protein gene-driven lacZ expression in the mouse. *J. Bone Miner. Res.* **21**, 113–123 (2006).
- Mak, K. K., Kronenberg, H. M., Chuang, P. T., Mackem, S. & Yang, Y. Indian hedgehog signals independently of PTHrP to promote chondrocyte hypertrophy. *Development* **135**, 1947–1956 (2008).
- Abad, V. et al. The role of the resting zone in growth plate chondrogenesis. *Endocrinology* **143**, 1851–1857 (2002).

- Ara, T. et al. A role of CXC chemokine ligand 12/stromal cell-derived factor-1/pre-B cell growth stimulating factor and its receptor CXCR4 in fetal and adult T cell development *in vivo*. *J. Immunol.* **170**, 4649–4655 (2003).
- Yang, L., Tsang, K. Y., Tang, H. C., Chan, D. & Cheah, K. S. Hypertrophic chondrocytes can become osteoblasts and osteocytes in endochondral bone formation. *Proc. Natl Acad. Sci. USA* **111**, 12097–12102 (2014).
- Bianco, P. et al. The meaning, the sense and the significance: translating the science of mesenchymal stem cells into medicine. *Nat. Med.* **19**, 35–42 (2013).
- Bianco, P. 'Mesenchymal' stem cells. *Annu. Rev. Cell Dev. Biol.* **30**, 677–704 (2014).
- Pardo-Saganta, A. et al. Parent stem cells can serve as niches for their daughter cells. *Nature* **523**, 597–601 (2015).
- Sun, J. et al. Clonal dynamics of native haematopoiesis. *Nature* **514**, 322–327 (2014).
- Busch, K. et al. Fundamental properties of unperturbed haematopoiesis from stem cells *in vivo*. *Nature* **518**, 542–546 (2015).

Acknowledgements We thank D. Holcomb and M. Curtis of Carl Zeiss Microscopy for assistance in imaging, G. Gavriliina and W. Fillipak of the University of Michigan Transgenic Animal Model Core for assistance with transgenesis. This research was supported by NIH R01DE026666 and R00DE022564 (to N.O.), R03DE027421 (to W.O.), P01DK011794 (to H.M.K.), 2017 Fred F. Schudy Memorial Research Award from the American Association of Orthodontists Foundation (to N.O.) and University of Michigan MCubed 2.0 Grant (to N.O. and W.O.).

Reviewer information Nature thanks O. Klein, M. T. Longaker and the other anonymous reviewer(s) for their contribution to the peer review of this work.

Author contributions K.M. and N.O. conceived the project and designed the experiments; K.M. and N.O. performed the mouse genetic experiments with assistance from W.O., N.S. and A.T., who performed genotyping; K.M. performed histological experiments and imaging analysis; K.M. performed cell culture experiments; K.M. and N.O. performed flow cytometry experiments and analysis; Y.M. performed the surgery and cell transplantation; K.M. and N.O. analysed the data; N.O. supervised the project; T.L.S. generated the mice; T.N. provided the mice; K.M. and N.O. wrote the manuscript; T.N., W.O. and H.M.K. critiqued the manuscript.

Competing interests The authors declare no competing interests.

Additional information

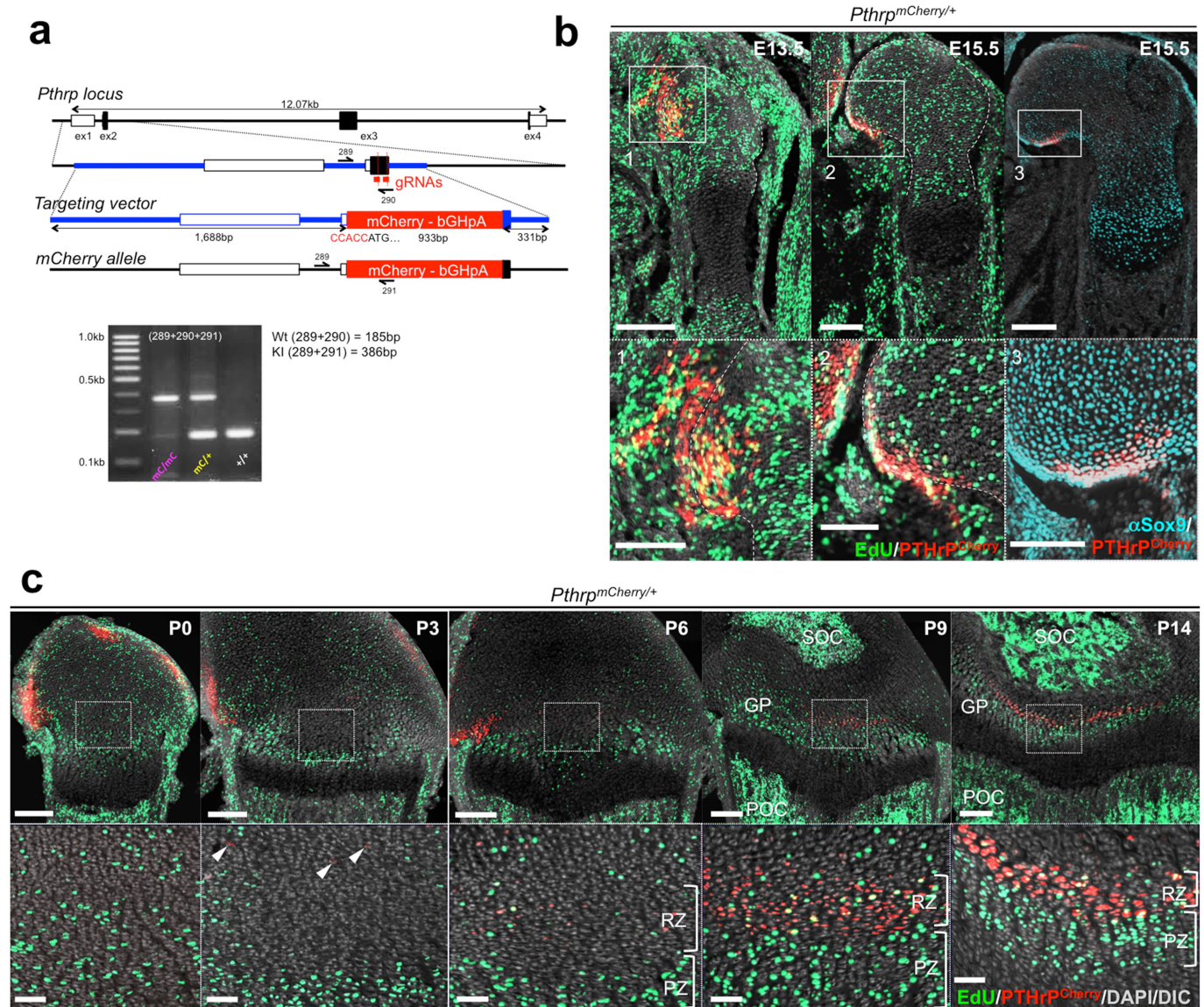
Extended data is available for this paper at <https://doi.org/10.1038/s41586-018-0662-5>.

Supplementary information is available for this paper at <https://doi.org/10.1038/s41586-018-0662-5>.

Reprints and permissions information is available at <http://www.nature.com/reprints>.

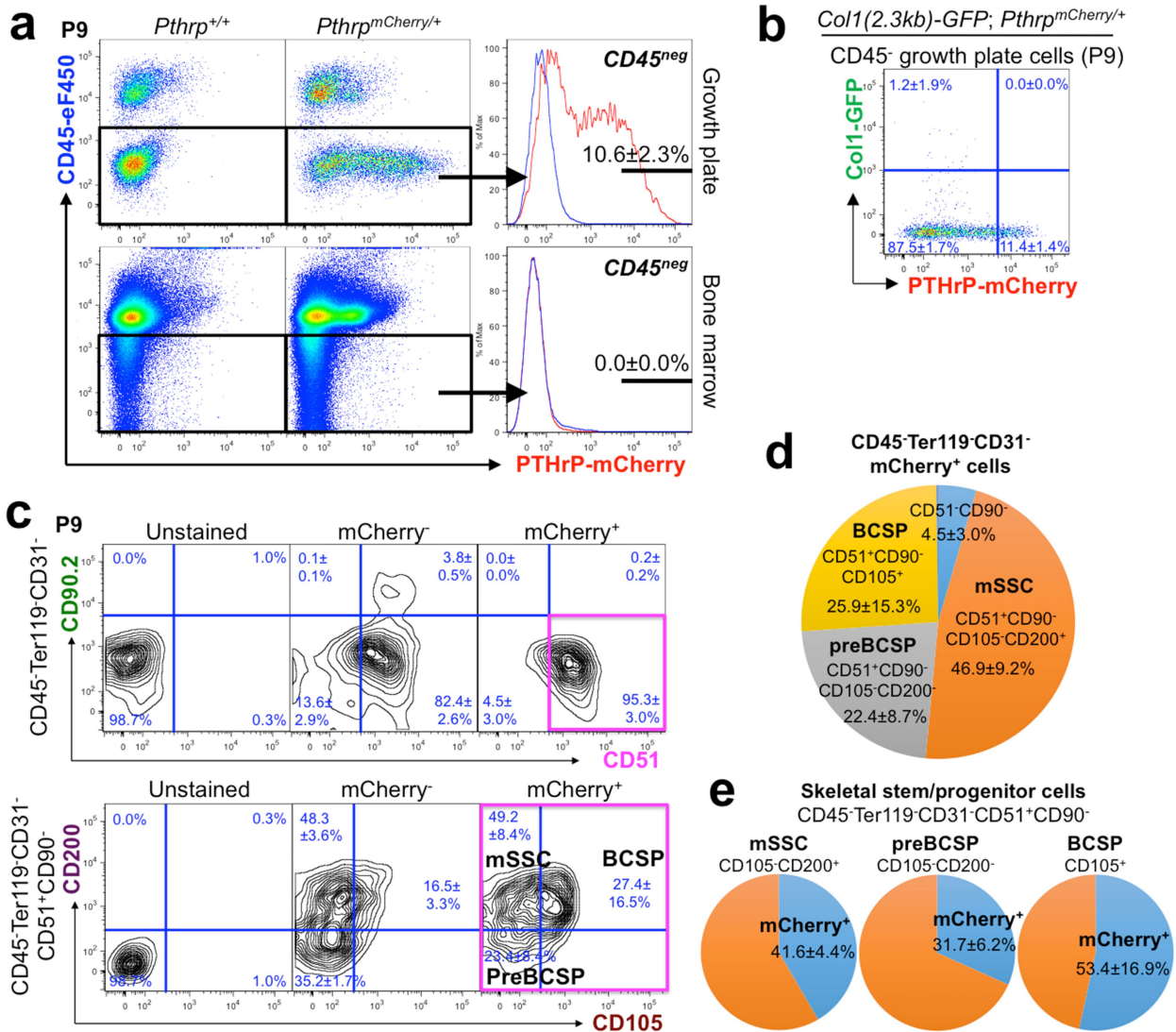
Correspondence and requests for materials should be addressed to N.O.

Publisher's note: Springer Nature remains neutral with regard to jurisdictional claims in published maps and institutional affiliations.



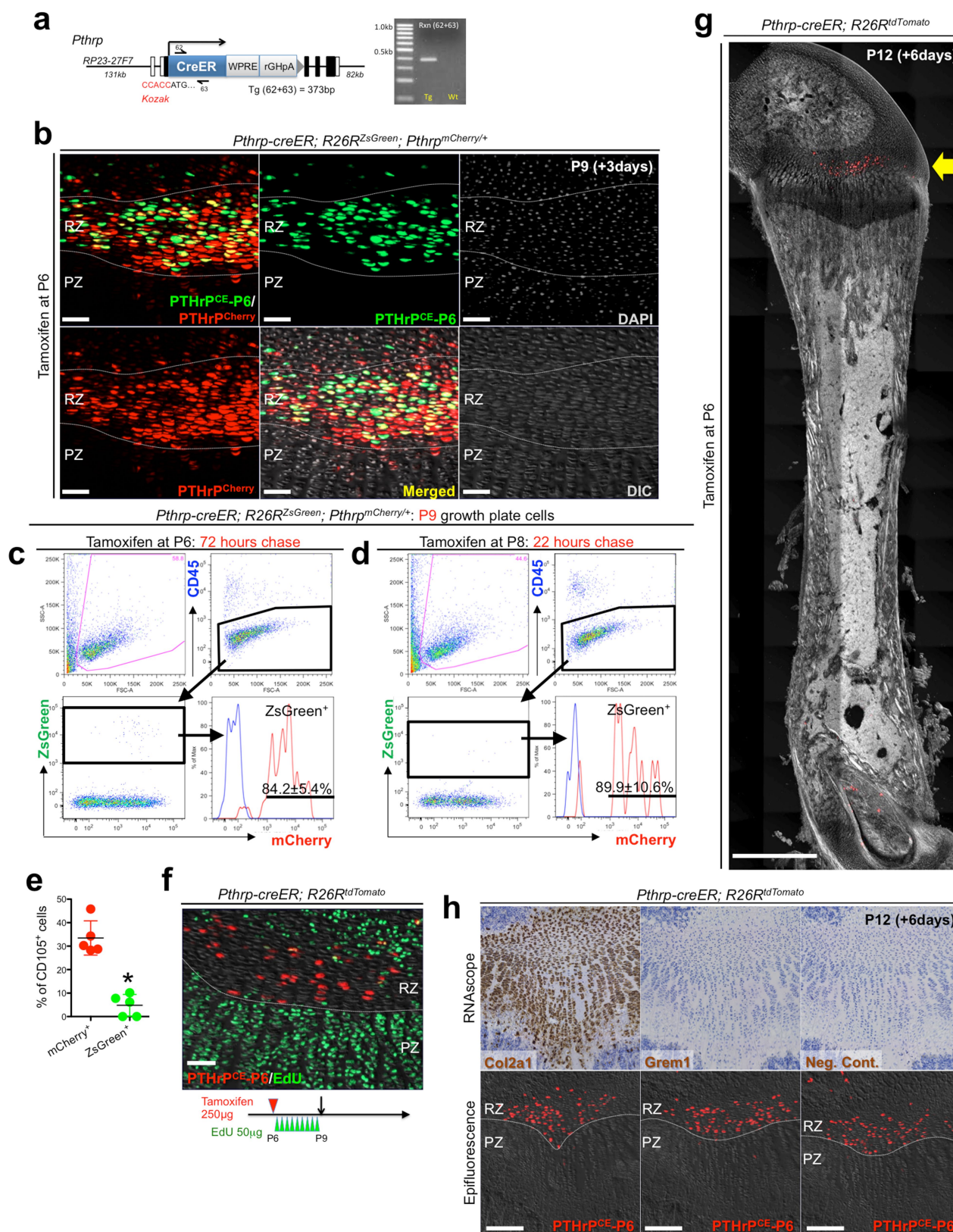
Extended Data Fig. 1 | Generation and characterization of *Pthrp-mCherry* knock-in allele. **a**, CRISPR-Cas9 generation of *Pthrp-mCherry* knock-in allele. Structure of the genomic *Pthrp* locus, targeting vector and knock-in allele after homologous recombination. White boxes, untranslated region; black boxes, coding region; ex, exon. Blue bars, homology arms; red bars, guide RNAs (gRNAs) as part of CRISPR-Cas9 reagents; red boxes, *Kozak-mCherry-bGHpA* cassette replacing the native start codon. Half arrows, primers; wild-type forward (289), wild-type reverse (290) and mutant reverse (291). Bottom, PCR genotyping using 289, 290 and 291 primer mix; wild-type (WT) allele, 185 bp; knock-in

(KI) allele, 385 bp. At least $n = 100$ independent experiments with similar results. **b**, *Pthrp*^{mCherry/+} fetal distal femurs with EdU administration shortly before analysis (3 h). Bottom panels show magnified views of perichondrium. Dotted lines, borders of bone anlage. Grey, DAPI and DIC. Scale bars, 200 μm (top panels), 100 μm (bottom panels). $n = 2$ (E13.5, E15.5) mice, $n = 1$ (α -Sox9) mouse. **c**, *Pthrp*^{mCherry/+} distal-femur growth plates with EdU administration shortly before analysis (3 h). Bottom panels show magnified views of central growth plates. Arrowheads, mCherry⁺ cells. Grey, DAPI and DIC. Scale bars, 200 μm (top panels), 50 μm (bottom panels).



Extended Data Fig. 2 | Skeletal stem and progenitor cell-marker expression in PTHrP-mCherry⁺ resting chondrocytes. **a**, Flow cytometry analysis of *Pthrp*^{mCherry/+} growth-plate cells (top panels) and bone-marrow cells (bottom panels). *n* = 8 mice for *Pthrp*^{mCherry/+} and *n* = 3 mice for *Pthrp*^{+/+}, data are presented as mean ± s.d. **b**, Flow cytometry analysis of *Col1a1(2.3kb)-GFP;Pthrp*^{mCherry/+} growth-plate cells. *n* = 5 mice per group, data are presented as mean ± s.d. **c**, Skeletal stem and progenitor cell-surface-marker analysis of *Pthrp*^{mCherry/+} growth-plate cells. Unstained, *Pthrp*^{+/+} cells mice only stained for CD45, Ter119 and CD31; mCherry⁻, mCherry⁻ fraction of *Pthrp*^{mCherry/+} cells;

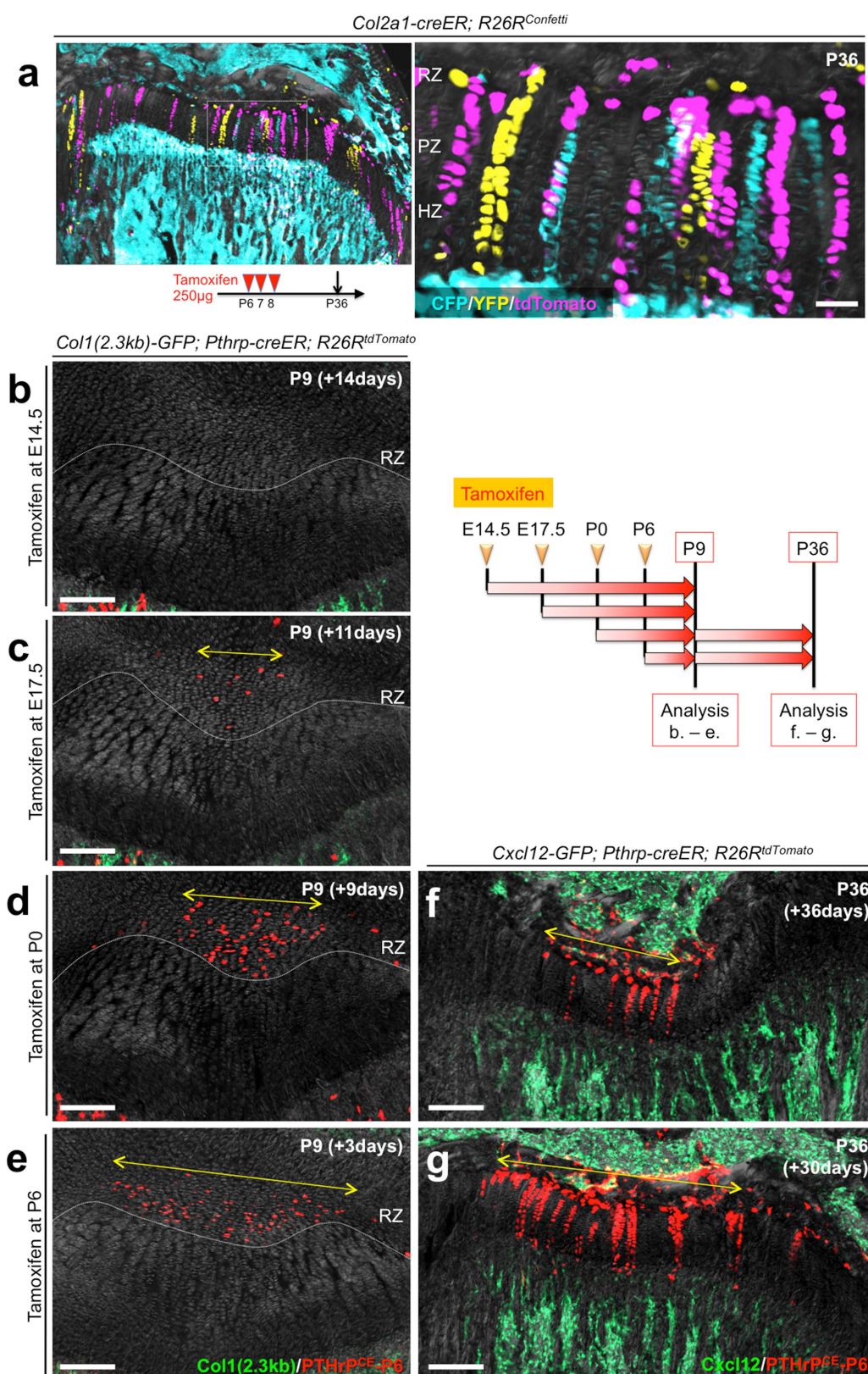
mCherry⁺, mCherry⁺ fraction of *Pthrp*^{mCherry/+} cells. Magenta box, CD45⁻Ter119⁻CD31⁻CD51⁺CD90⁻mCherry⁺ fraction. *n* = 3 mice for *Pthrp*^{mCherry/+}, data are presented as mean ± s.d., *n* = 1 mouse for *Pthrp*^{+/+}. **d**, Composition of CD45⁻Ter119⁻CD31⁻mCherry⁺ growth-plate cells. *n* = 3 mice per group, data are presented as mean ± s.d. **e**, Percentage of mCherry⁺ cells among mSSCs (left, CD105⁻CD200⁺), pre-BCSPs (center, CD105⁻CD200⁻) and BCSPs (right, CD105⁺), gated under CD45⁻Ter119⁻CD31⁻CD51⁺CD90⁻ fraction. *n* = 3 mice per group, data are presented as mean ± s.d.



Extended Data Fig. 3 | See next page for caption.

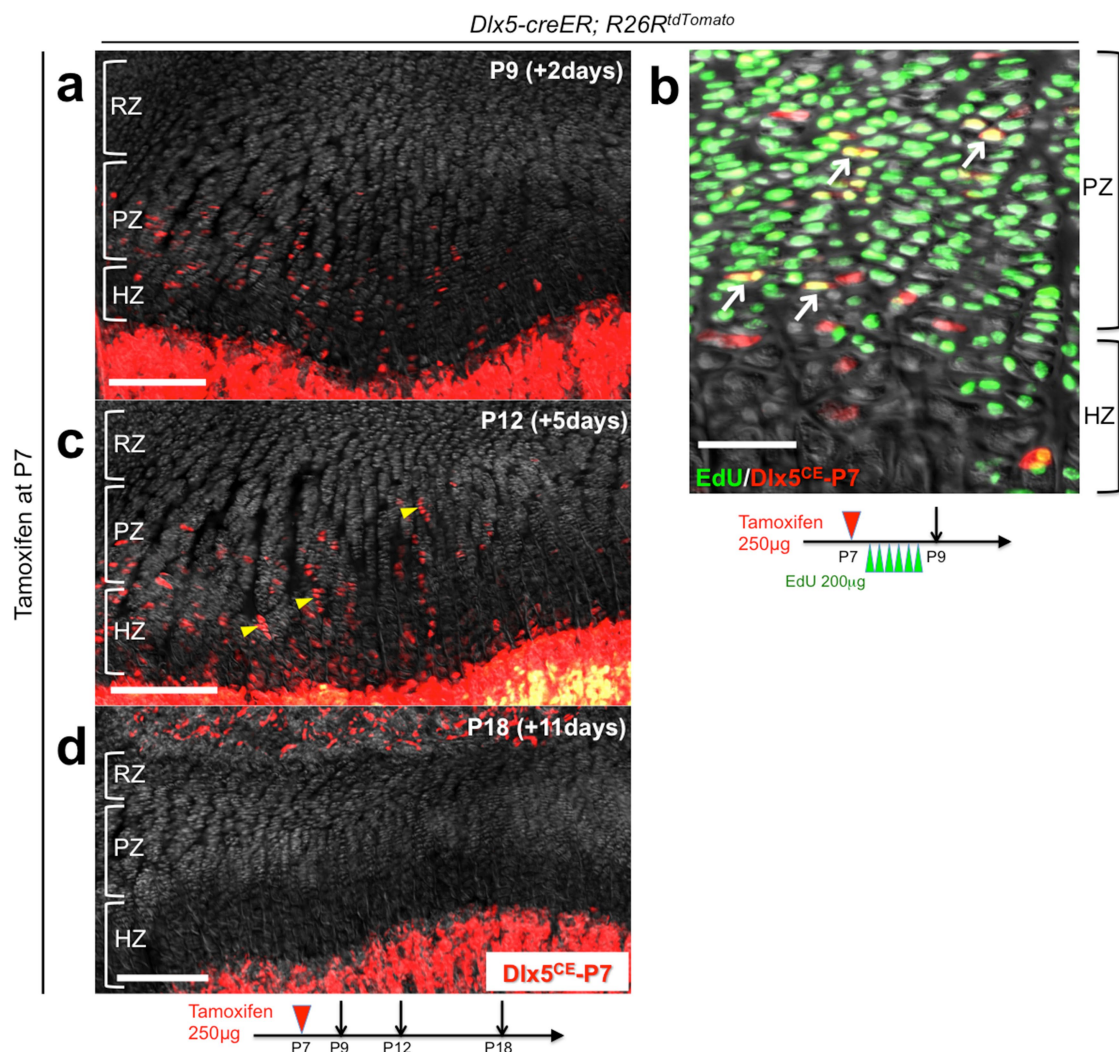
Extended Data Fig. 3 | Generation and characterization of *Pthrp-creER* bacterial artificial chromosome transgenic line. **a**, Generation of *Pthrp-creER* bacterial artificial chromosome (BAC) transgenic mice. Structure of the *Pthrp-creER-WPRE-rGHpA* BAC construct. *Kozak-Pthrp-creER-WPRE-rGHpA-frt-Neo^R-frt* cassette containing 62-bp homology arms was recombined into a BAC clone RP23-27F7 containing 131-kb upstream and 82-kb downstream genomic sequences of the *Pthrp* gene. *Neo^R* and backbone *lox* sites were removed before pronuclear injection. Half arrows, forward (62) and reverse (63) primers. Right, PCR genotyping using 62 and 63 primer mix; transgenic (Tg), 373 bp. White boxes, exons; black boxes, introns. At least $n = 100$ independent experiments with similar results. **b**, Short-chase analysis of *Pthrp-creER;R26R^{ZsGreen};Pthrp^{mCherry/+}* distal-femur growth plates (pulsed on P6). Scale bars, 50 μm . $n = 3$ mice. **c–e**, Short-chase flow cytometry analysis of *Pthrp-creER;R26R^{ZsGreen};Pthrp^{mCherry/+}* growth-plate cells, with tamoxifen injection at 72 h (**c**, **e**) or 22 h (**d**) in advance. Red lines, ZsGreen⁺ cells;

blue lines, control cells without PTHrP-mCherry. $n = 5$ mice (72 h) or $n = 3$ mice (22 h) per group. **e**, Percentage of CD105⁺ cells within mCherry⁺ (red) and ZsGreen⁺ (green) cells. $n = 5$ mice per group, data are presented as mean \pm s.d., * $P = 0.012$, Mann–Whitney's *U*-test, two-tailed. **f**, *Pthrp-creER;R26R^{tdTomato}* distal-femur growth plates (pulsed on P6) at P9. EdU (50 μg) was serially injected 9 times at 8-h intervals between P6 and P9. Grey, DIC. Scale bars: 50 μm . $n = 3$ mice. **g**, Scanning of *Pthrp-creER;R26R^{tdTomato}* whole femur (pulsed on P6) at P12. Arrow, tdTomato⁺ cells localized within the resting zone of distal femur. Grey, DAPI and DIC. Scale bars, 1 mm. $n = 3$ mice. **h**, High sensitivity in situ hybridization (RNAscope) analysis of *Pthrp-creER;R26R^{tdTomato}* distal-femur growth plates (pulsed on P6) at P12. Top and bottom panels represent the identical section, before (bottom panels) and after (top panels) hybridization. Left panels, *Col2a1* (positive control); centre panels, *Grem1*; right panels, negative control. Grey, DAPI and DIC. Scale bars, 200 μm . $n = 3$ independent experiments.



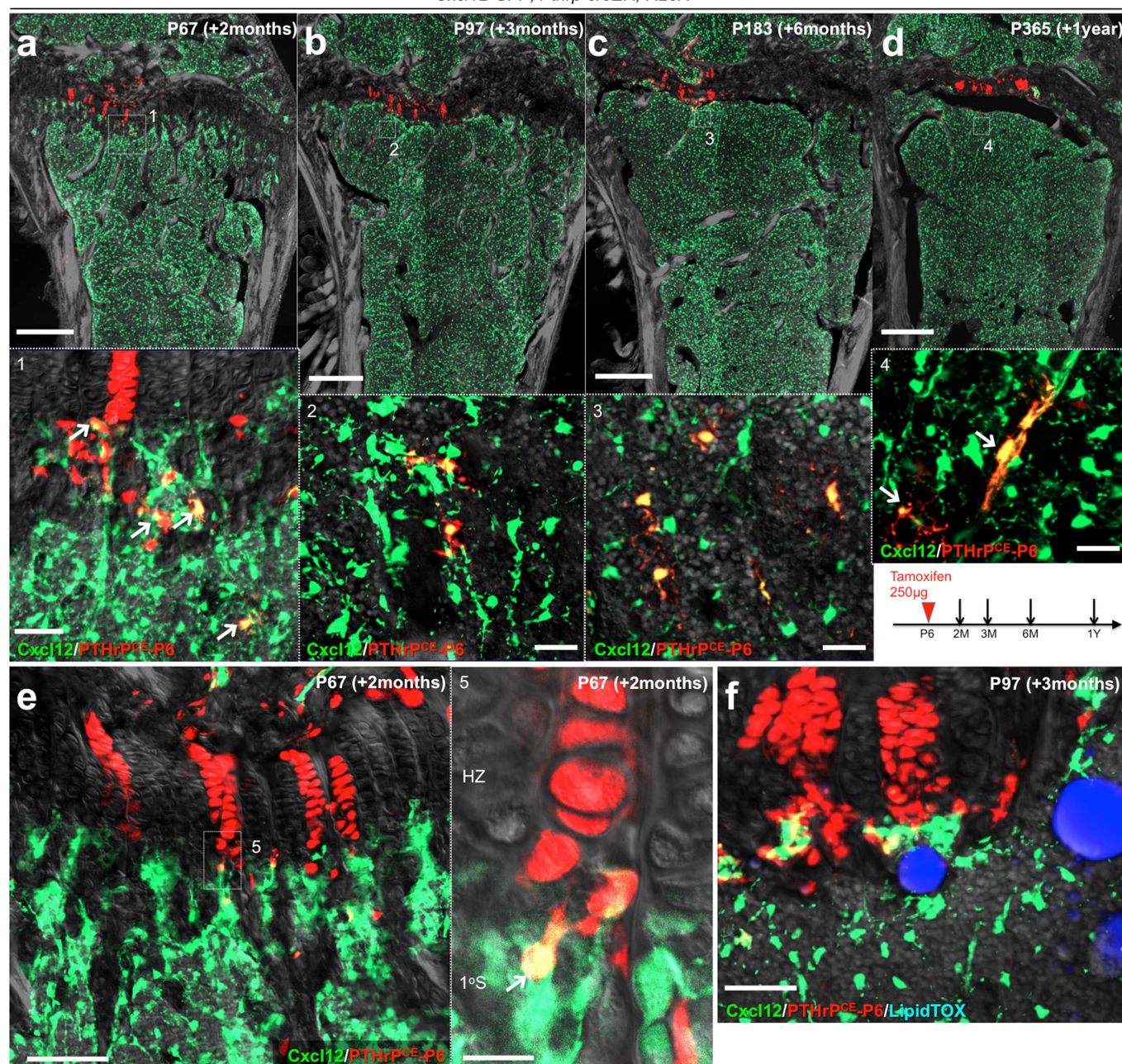
Extended Data Fig. 4 | PTHrP⁺ resting chondrocytes are functionally dedicated to columnar chondrocyte formation. **a**, In vivo clonal analysis of *Col2a1-creER*⁺ growth-plate chondrocytes. *Col2a1-creER; R26R^{Confetti}* distal-femur growth plates (pulsed on P6, P7 and P8). Scale bars, 50 μ m. $n = 2$ mice. **b–e**, *Col1a1(2.3kb)-GFP; Pthrp-creER; R26R^{tdTomato}* distal-femur growth plates, shown at P9 after being pulsed at various preceding

time points. Yellow double-headed arrows, tdTomato⁺ domain within the resting zone. Grey, DAPI and DIC. Scale bars, 200 μ m. $n = 3$ mice per group. **f, g**, *Cxcl12-GFP; Pthrp-creER; R26R^{tdTomato}* distal-femur growth plates, shown at P36 after being pulsed on P0 (**f**) and P6 (**g**). Yellow double-headed arrows in **f, g** indicate the same width as those shown in **d, e**. Grey, DAPI and DIC. Scale bars, 200 μ m. $n = 3$ mice per group.



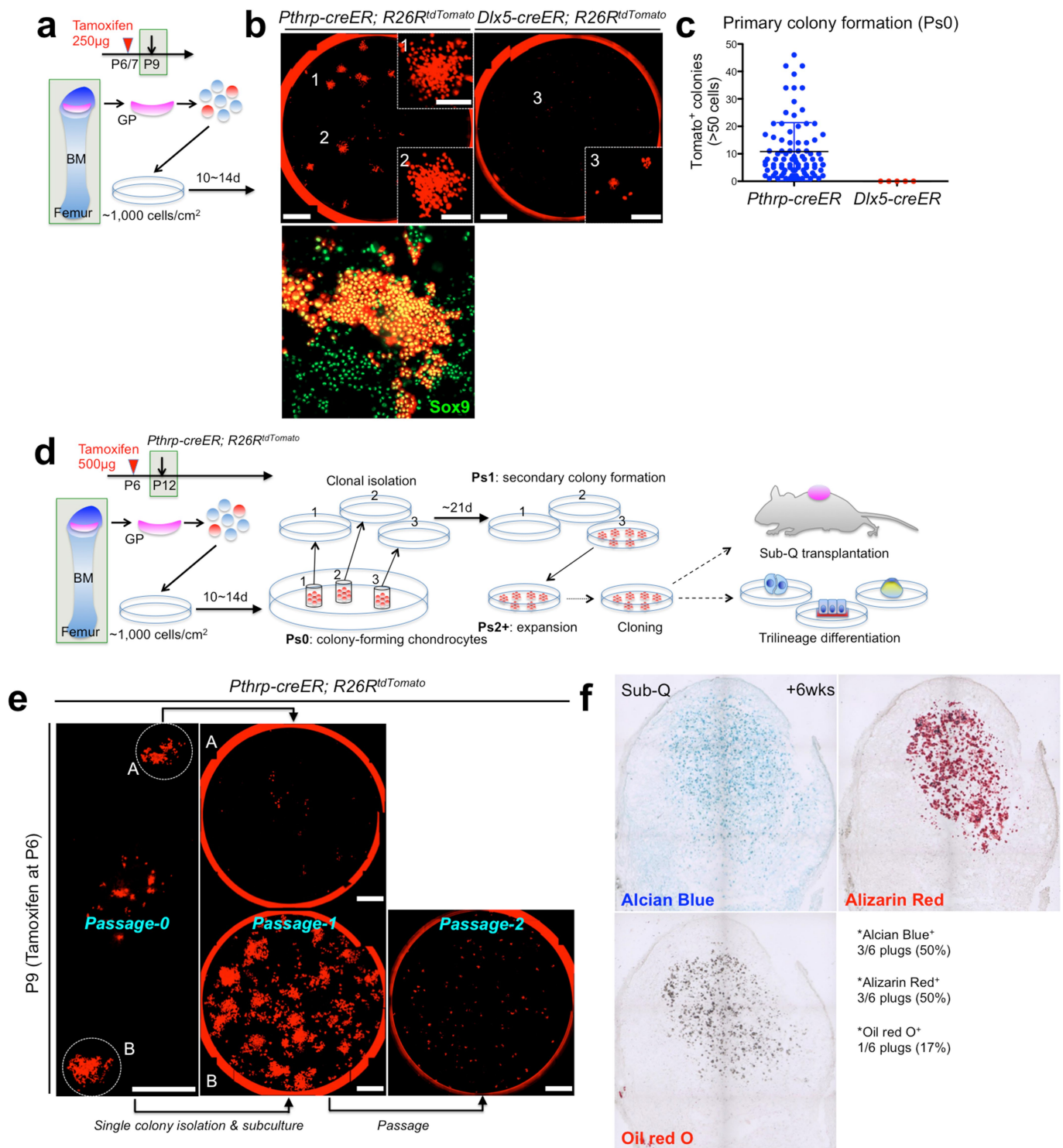
Extended Data Fig. 5 | *Dlx5-creER*⁺ proliferating chondrocytes are not the source of columnar chondrocytes. **a–d**, Cell-fate analysis of *Dlx5-creER*⁺ proliferating chondrocytes. *Dlx5-creER;R26R^{tdTomato}* distal-femur growth plates (pulsed on P7). **b**, EdU (200 µg) was serially injected

6 times at 8-h intervals, between P7 and P9. Arrows, EdU⁺tdTomato⁺ cells; arrowheads, short columns (<10 cells). Grey, DAPI and DIC. Scale bars, 200 µm (left panels), 50 µm (right panel). *n* = 3 mice at each time point.

Cxcl12-GFP; Pthrp-creER; R26R^{tdTomato}

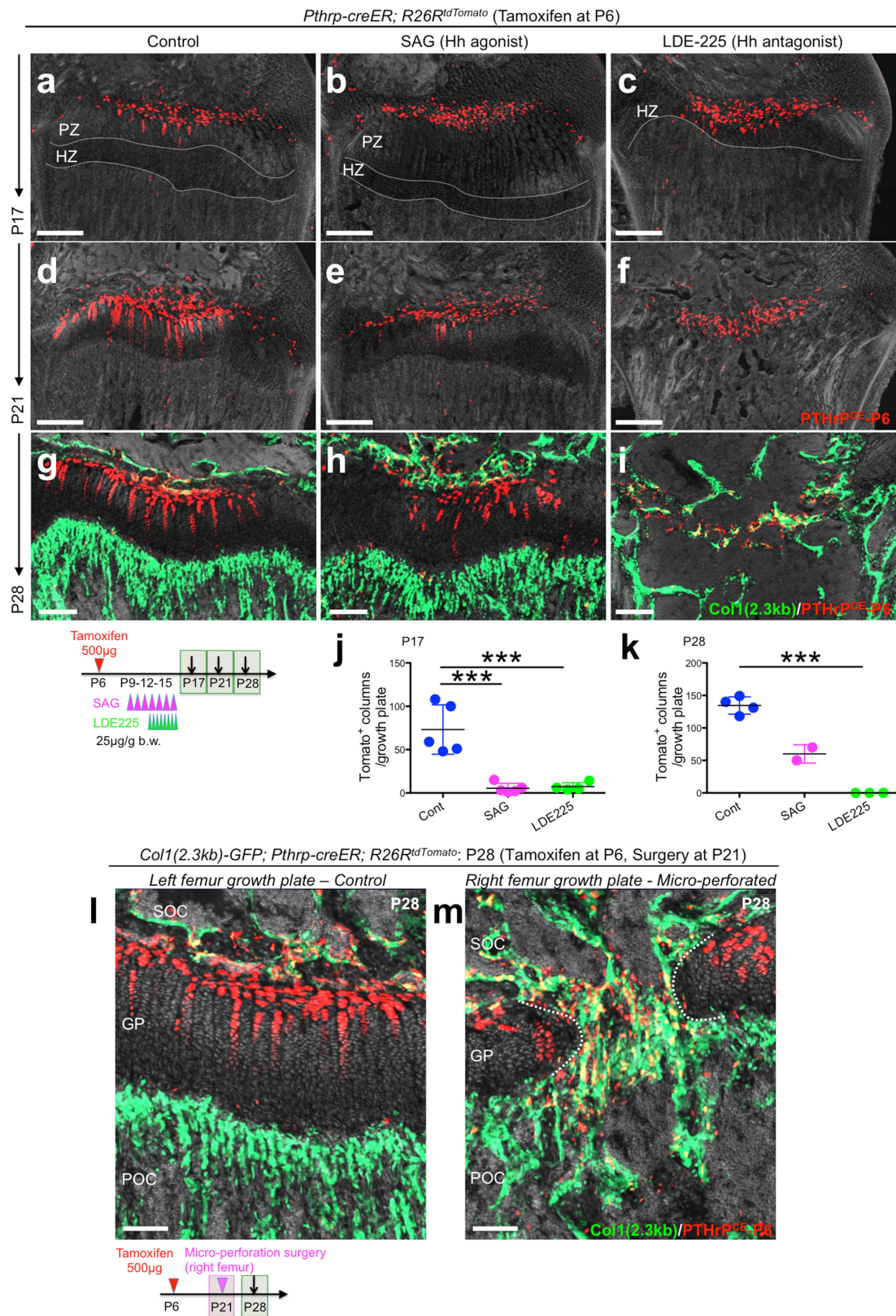
Extended Data Fig. 6 | *Pthrp-creER*⁺ resting chondrocytes are precursors for bone marrow reticular stromal cells. *Cxcl12-GFP;Pthrp-creER;R26R^{tdTomato}* distal femurs (pulsed on P6). **a–d**, Bottom panels show magnified views of the dotted areas beneath growth plates. Arrows, *Cxcl12-GFP*⁺*tdTomato*⁺ reticular stromal cells. **e**, Magnified view of the junction between hypertrophic layer and primary spongiosa. Arrow, *Cxcl12-GFP*⁺*tdTomato*⁺ reticular stromal cells immediately below the

hypertrophic zone. 1°S: primary spongiosa. **f**, Magnified view of the metaphyseal bone marrow. Mice were fed with high-fat diet containing rosiglitazone between P56 and P97. Grey, DAPI and DIC. Scale bars, 500 µm (**a–d**, **f**), 100 µm (**e**), 50 µm (bottom panels of **a–c**), 20 µm (bottom panel of **d**, right panel of **e**). *n* = 3 mice for each group, except *n* = 2 mice for P365.



Extended Data Fig. 7 | *Pthrp-creER*⁺ resting chondrocytes uniquely possess colony-forming capabilities ex vivo. **a**, Diagram of colony-forming assay. Growth-plate cells were isolated from *Pthrp-creER;R26R^{tdTomato}* (pulsed on P6) or *Dlx5-creER;R26R^{tdTomato}* (pulsed on P7) mice at P9, and cultured at a clonal density (~1,000 cells per cm²) for 10–14 days to initiate colony formation. BM, bone marrow. **b**, Colony-forming assay. Left top, *Pthrp-creER;R26R^{tdTomato}*; right, *Dlx5-creER;R26R^{tdTomato}*. Insets 1, 2 and 3 show magnified views of the corresponding areas (labelled with 1, 2, 3). Bottom left, Sox9 staining of primary *Pthrp-creER* tdTomato⁺ colonies. Red, tdTomato. Scale bars, 5 mm (top panels), 1 mm (top panel insets), 200 µm (bottom panel). *n* = 88 mice for *Pthrp-creER;R26R^{tdTomato}*, *n* = 5 for *Dlx5-creER;R26R^{tdTomato}*.

c, Quantification of tdTomato⁺ colonies (>50 cells) established from *Pthrp-creER;R26R^{tdTomato}* (*n* = 88) and *Dlx5-creER;R26R^{tdTomato}* (*n* = 5) mice. Data are presented as mean ± s.d. **d**, Diagram of colony-forming assay and subsequent analyses on self-renewal, trilineage differentiation and transplantation of individual colony-forming cells. **e**, Isolation of single PTHrP^{CE}-tdTomato⁺ colonies and subsequent subculture of isolated clones. A, exhausting clone; B, self-renewing clone establishing secondary colonies. Right, clone B did not proliferate at passage 2 upon bulk culture. Red, tdTomato. Scale bars, 5 mm. *n* = 518 independent experiments. **f**, Subcutaneous transplantation of PTHrP^{CE}-tdTomato⁺ clones into immunodeficient mice. *n* = 8 mice.



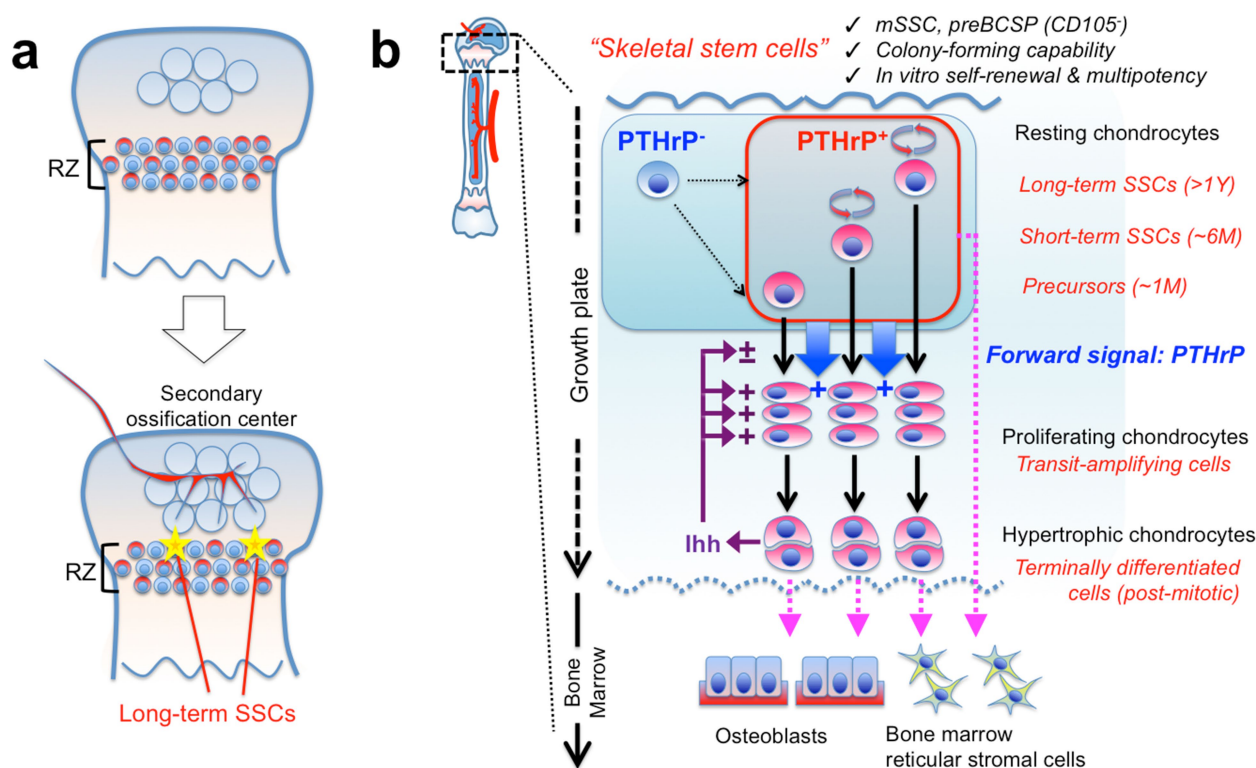
Extended Data Fig. 8 | See next page for caption.

Extended Data Fig. 8 | *Pthrp-creER*⁺ resting chondrocytes form columnar chondrocytes in a Hedgehog-responsive, niche-dependent manner. **a–i**, Pharmacological manipulation of Hedgehog signalling.

Pthrp-creER;R26R^{tdTomato} distal-femur growth plates (pulsed on P6). Left panels, vehicle control; centre panels, SAG (Hh agonist)-treated samples; right panels, LDE225 (Hh antagonist)-treated samples. Grey, DAPI and DIC. Scale bars, 200 μm . **j**, **k**, Quantification of tdTomato⁺ columns in *Pthrp-creER;R26R^{tdTomato}* distal-femur growth plates (pulsed on P6).

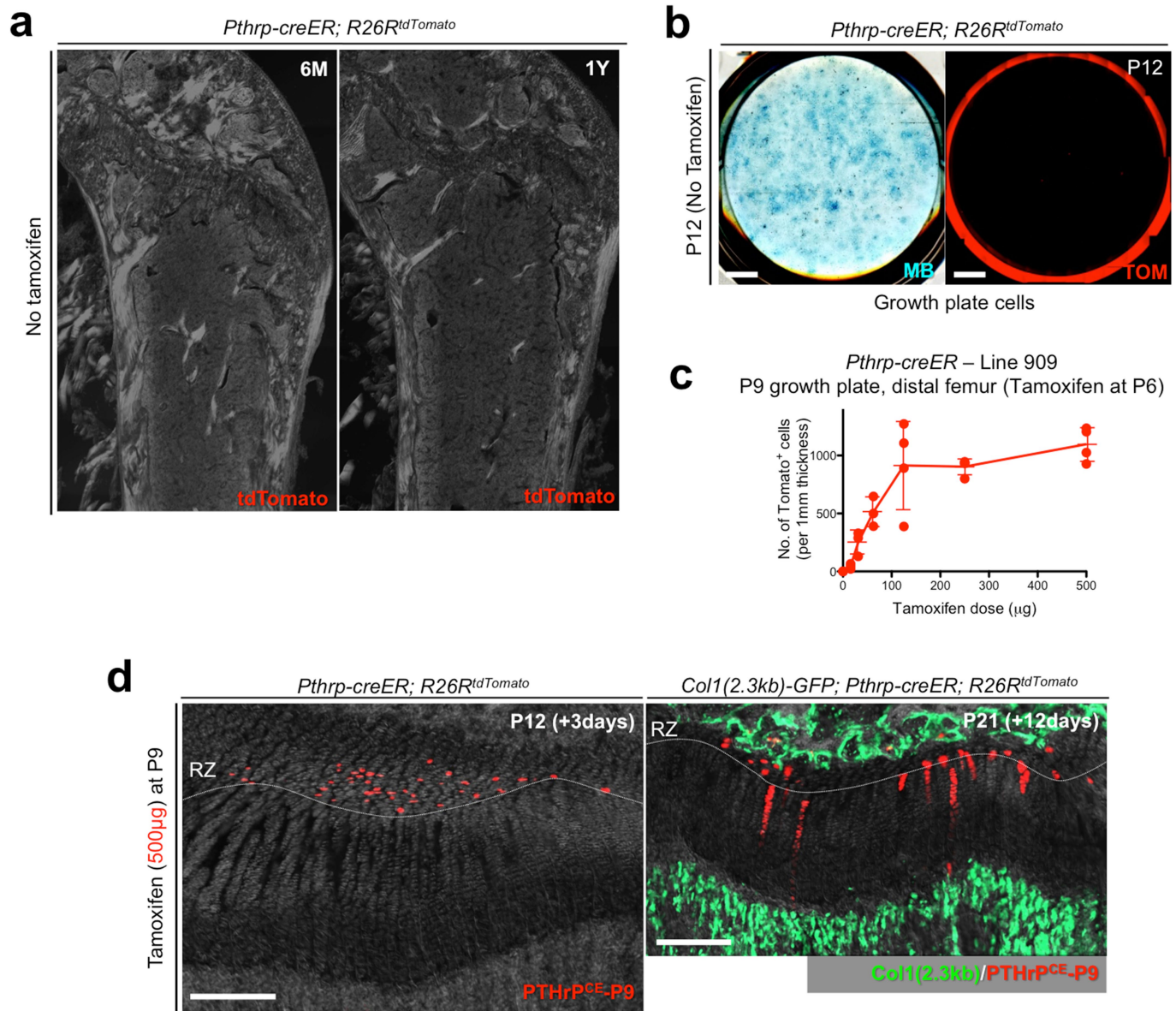
P17, $n = 5$ (control), $n = 5$ (SAG), $n = 4$ (LDE225) mice per group. P28, $n = 4$ (control), $n = 3$ (LDE225) mice per group. Data are presented as mean \pm s.d. P28, $n = 2$ (SAG). *** $P < 0.001$; P17 control versus SAG,

mean difference = 67.8, 95% confidence interval (37.5, 98.1); P17 control versus LDE225, mean difference = 66.0, 95% confidence interval (33.9, 98.0); P17 SAG versus LDE225, mean difference = -1.85, 95% confidence interval (-33.9, 30.2); P28 control versus LDE225, mean difference = 134.5, 95% confidence interval (108.7, 160.3). One-way ANOVA followed by Tukey's multiple comparison test. **l**, **m**, Micro-perforation injury of growth plates. *Col1a1(2.3kb)-GFP;Pthrp-creER;R26R^{tdTomato}* distal femurs (pulsed on P6) at P28. Micro-perforation surgery was performed at P21. **l**, Left femur growth plate (control). **m**, Right femur growth plate (micro-perforated). Dotted line, micro-perforated area. Grey, DAPI and DIC. Scale bars, 100 μm . $n = 3$ mice.



Extended Data Fig. 9 | Resting zone of the growth plate contains a unique class of skeletal stem cells. a, Formation of PTHrP⁺ skeletal stem cells within the growth plate. A small subset of PTHrP⁺ chondrocytes in the resting zone acquire properties as long-term skeletal stem cells in conjunction with the formation of the highly vascularized secondary ossification centre. **b,** PTHrP⁺ skeletal stem cells are heterogeneously composed of long-term, short-term and transient populations, and undergo asymmetric divisions and maintain themselves within the

resting zone. These cells may be supplemented by PTHrP⁻ cells. PTHrP⁺ cells perform two different functions: (1) these cells differentiate into proliferating chondrocytes, hypertrophic chondrocytes and eventually become osteoblasts and bone marrow stromal cells at the post-mitotic stage. (2) These cells send a forward signal (PTHrP) to control chondrocyte proliferation and differentiation. Indian hedgehog (Ihh) secreted by hypertrophic chondrocytes maintains the proliferation of chondrocytes and formation of columnar chondrocytes.



Extended Data Fig. 10 | Absence of tamoxifen-independent recombination in *Pthrp-creER* line. **a**, No tamoxifen controls of *Pthrp-creER; R26R^{tdTomato}* mice at 6 months (left) and 1 year (right) of age. Red, tdTomato; blue, DAPI; grey, DIC. Scale bars, 500 μm. $n = 3$ mice per group. **b**, No tamoxifen controls of primary colonies (passage 0) isolated from *Pthrp-creER; R26R^{tdTomato}* mice at P12 without tamoxifen injection. Left, methylene blue (MB) staining; right, red tdTomato (TOM). Scale bar, 5 mm. $n = 3$ mice. **c**, Dose-response curve of recombination based on *Pthrp-creER*. Quantification of tdTomato⁺ cells in resting zone at P9 in

Pthrp-creER; R26R^{tdTomato} mice upon a single dose of tamoxifen at P6. x axis, dose of tamoxifen (μg); y axis, the number of tdTomato⁺ cells per 1-mm thickness. $n = 3$ (0, 31.3 and 62.5 μg), $n = 4$ (15.6, 125, 250 and 500 μg) mice per group, data are presented as mean \pm s.d. **d**, Tamoxifen-induced recombination in growth plates pulsed on P9. *Pthrp-creER; R26R^{tdTomato}* distal-femur growth plates at P12 (left) and *Col1a1(2.3kb)-GFP; Pthrp-creER; R26R^{tdTomato}* mice at P21 (right). Tamoxifen (500 μg) was injected at P9. Green, Col1a1(2.3kb)-GFP; red, tdTomato; grey, DAPI and DIC. Scale bars, 200 μm. $n = 3$ mice.

Transcriptional regulation of nitrogen-associated metabolism and growth

Allison Gaudinier¹, Joel Rodriguez-Medina¹, Lifang Zhang², Andrew Olson², Christophe Liseron-Monfils², Anne-Maarit Bågman¹, Jessica Foret¹, Shane Abbitt³, Michelle Tang^{1,4}, Baohua Li⁴, Daniel E. Runcie⁴, Daniel J. Kliebenstein^{4,5}, Bo Shen³, Mary J. Frank³, Doreen Ware^{2,6} & Siobhan M. Brady^{1*}

Nitrogen is an essential macronutrient for plant growth and basic metabolic processes. The application of nitrogen-containing fertilizer increases yield, which has been a substantial factor in the green revolution¹. Ecologically, however, excessive application of fertilizer has disastrous effects such as eutrophication². A better understanding of how plants regulate nitrogen metabolism is critical to increase plant yield and reduce fertilizer overuse. Here we present a transcriptional regulatory network and twenty-one transcription factors that regulate the architecture of root and shoot systems in response to changes in nitrogen availability. Genetic perturbation of a subset of these transcription factors revealed coordinate transcriptional regulation of enzymes involved in nitrogen metabolism. Transcriptional regulators in the network are transcriptionally modified by feedback via genetic perturbation of nitrogen metabolism. The network, genes and gene-regulatory modules identified here will prove critical to increasing agricultural productivity.

The root system takes up and metabolizes bio-available nitrogen and transduces nitrogen signals. In response to reduced nitrogen availability, plant development is adjusted—this includes increased lateral root elongation to forage for nitrogen³. Above ground, rosette size is decreased and plants flower earlier⁴. Diverse molecular events underlie these morphological changes. Nitrogen transporters, assimilation enzymes and signalling factors are transcriptionally regulated in response to changes in available nitrogen⁵. Post-transcriptional, calcium- and phosphorylation-dependent signalling cascades are also critical regulators of this transcriptional response⁶. Concomitantly, carbon metabolism and hormone pathways are also altered to adjust metabolic pathways and plant growth⁷. Sixteen transcription factors in *Arabidopsis thaliana* have previously been identified to have a role in nitrogen metabolism^{8–19} (Supplementary Table 1), through a range of approaches that includes systems-level studies^{16,20}. Despite the importance of the root system in regulating responses to nitrogen, only seven of these transcription factors have previously been shown to regulate root development in a nitrogen-dependent manner^{8,9,11,14–17}.

Using enhanced yeast one-hybrid assays, we screened for transcription factors that regulate nitrogen metabolism^{21,22}. Because nitrogen metabolism is interconnected with a range of different processes, we included target promoters from genes associated with nitrogen transport (12 promoters), assimilation (11 promoters), signalling (2 promoters), connections to nitrogen metabolism through amino acid metabolism (5 promoters), carbon metabolism (10 promoters), carbon transport (4 promoters), organ growth (5 promoters) and hormone responses (7 promoters) as well as associated transcription factors (12 promoters) (Supplementary Table 2). We screened these promoters against transcription factors expressed in roots. The resulting network comprises 1,660 interactions between 431 genes, 345 transcription factors and 98 promoters (Fig. 1a, Extended Data Fig. 1, Supplementary Table 3a). We call this network the ‘yeast one-hybrid network for

nitrogen-associated metabolism’ (YNM). Our assays captured previously characterized interactions: NLP7 physically binds to and regulates expression of *NIR1* and *CIPK8*, and NLP6 binds to and regulates expression of *NIR1*^{13,23}. Within the YNM we found what is, to our knowledge, a previously undescribed putative hierarchical regulation of transcription factors—including both known nitrogen-regulatory transcription factors and transcription factors identified in this study—that bind to promoters of genes in many processes, such as the nitrate assimilation pathway (Fig. 1b, Supplementary Table 3b). A signalling cascade that links the nitrate-mediated regulation of Ca²⁺-sensor protein kinases to transcriptional regulation via NLP7 is also significantly overrepresented in the YNM⁶ ($P = 2.14 \times 10^{-9}$) (Extended Data Fig. 2a, Supplementary Table 4a). Moreover, the YNM is enriched for hormone-regulated genes, which supports previous findings that hormone signalling is integrated into the regulation of nitrogen metabolism^{9,24} (see Methods, Extended Data Figs. 2b–h, Supplementary Table 4b–h). The highly combinatorial nature of interactions is consistent with previous studies that suggest that transcription factors that are central within the YNM may regulate multiple processes that are related to nitrogen metabolism²³. NLP7 bound to promoters of seven nitrogen-associated categories (Supplementary Table 3c). One hundred and seventy-five transcription factors from the YNM were found to bind to gene promoters that are involved in more than one nitrogen-associated process (Supplementary Table 2d).

We used a variety of datasets and approaches to rank transcription factors in the YNM for functional validation. First, under the premise that transcription factors and their targets are co-expressed upon changes in nitrogen availability, we prioritized highly correlated transcription factors and targets for a nitrogen treatment and a cell-type-specific dataset (Supplementary Tables 5, 6). This approach does not exclude the possibility of detecting self-regulating repressors or activators. Second, we used the network analysis algorithm NeCorr (see Methods, Supplementary Table 7). Third, transcription factors were evaluated for their outgoing connectivity (Supplementary Table 3e). Additionally, transcription factors were considered given the total number and percentage of targets that are classical nitrogen-metabolism genes (Supplementary Table 8). As a positive control, we included mutants of the transcription factors NLP7 and GNC, and the transceptor NPF6.3 (also known as NRT1.1 or CHL1)^{11,25,26}. Perturbation of nitrogen metabolism in *npf6.3* (also known as *nrt1.1* or *chl1*) and *nrt2.1* plants alters lateral root initiation and/or lateral root elongation^{27,28}. With the hypothesis that these transcription factors regulate nitrogen metabolism and nitrogen status, we examined their mutant root system architecture (RSA) (see Methods) under limiting (1 mM KNO₃) and sufficient nitrogen (10 mM KNO₃) (Extended Data Fig. 3, Supplementary Table 2c).

Mutant alleles of seventeen genes that we identify here showed significant changes in at least one RSA trait relative to wild type (Supplementary Tables 9, 10, Supplementary Data 1, 2). *chl1-5*—a

¹Department of Plant Biology and Genome Center, University of California, Davis, Davis, CA, USA. ²Cold Spring Harbor Laboratory, Cold Spring Harbor, Cold Spring Harbor, NY, USA. ³DuPont Pioneer, Johnston, IA, USA. ⁴Department of Plant Sciences, University of California, Davis, Davis, CA, USA. ⁵DynaMo Center of Excellence, University of Copenhagen, Frederiksberg C, Denmark. ⁶US Department of Agriculture, Agricultural Research Service, Ithaca, NY, USA. *e-mail: sbrady@ucdavis.edu

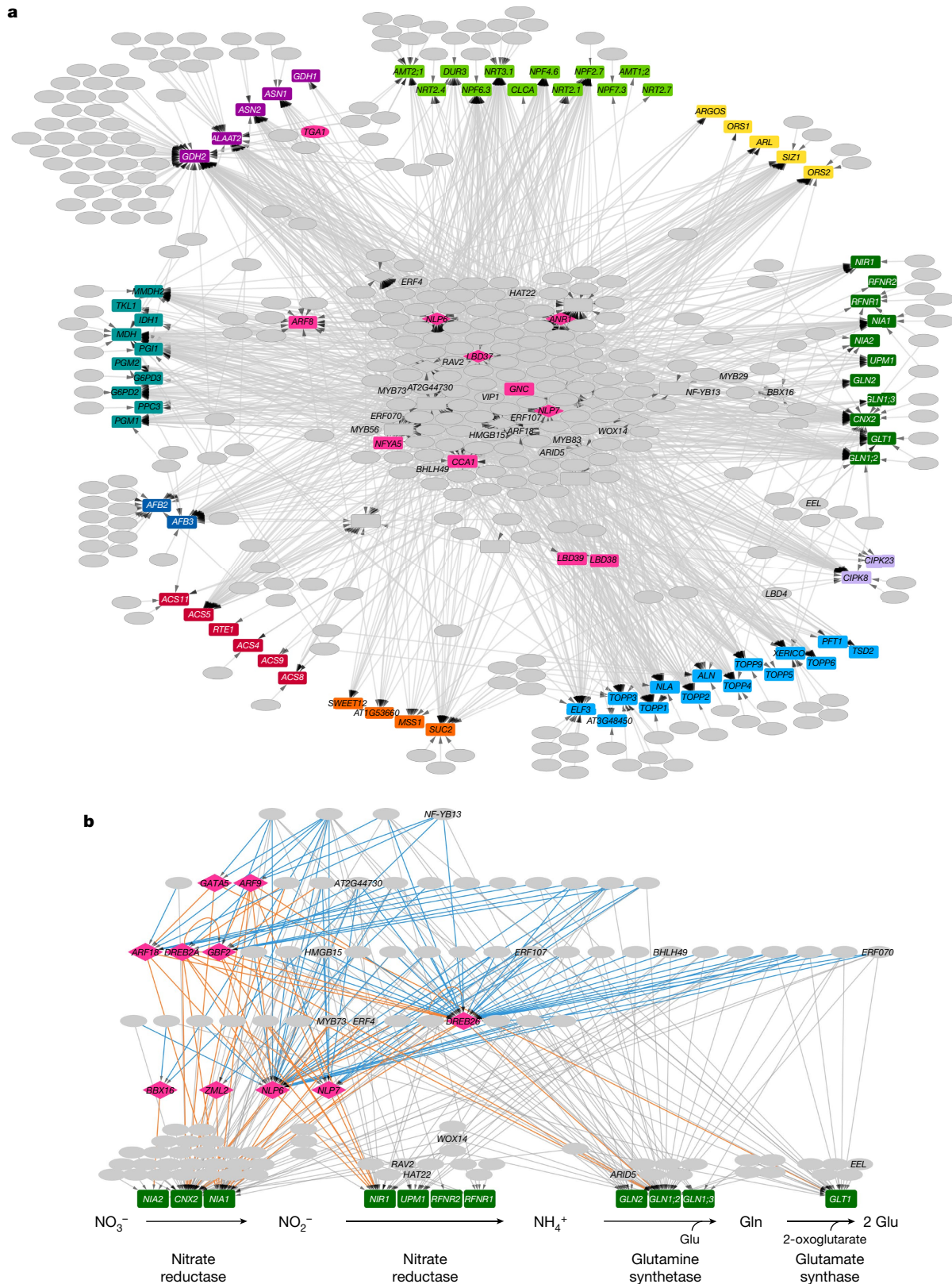


Fig. 1 | Combinatorial interactions between transcription factors and promoters of genes associated with nitrogen metabolism, signalling and nitrogen-associated processes. a, Interaction network for nitrogen-associated metabolism. See Extended Data Fig. 1 for the full diagram, including gene names. Rectangles, promoters; ovals, transcription factors; and diamonds, genes represented as both promoters and transcription factors. Nitrogen-associated biological processes are indicated by promoter colour. A grey line indicates an interaction between transcription factor and promoter. Light green, nitrogen transporter; yellow, organ growth;

dark green, nitrate assimilation; light purple, nitrogen signalling; light blue, nitrogen-linked; orange, carbon metabolism; red, ethylene; dark blue, auxin; teal, carbon transporter; dark purple, amino acid metabolism; and pink, transcription factors linked to nitrogen. **b**, Transcription factor-promoter interactions that are associated with nitrate assimilation are hierarchical. Edges participating in hierarchical regulation going into the transcription factors (diamonds) are blue, and outgoing edges from the transcription factors are orange. The NLP7 and NLP6 regulators are in the first tier of transcription-factor binding to assimilation enzymes.

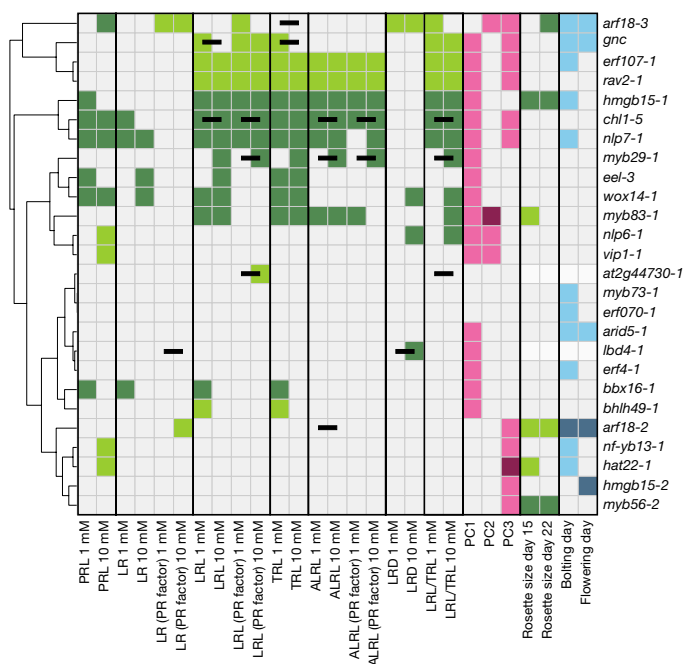


Fig. 2 | Phenotypes associated with transcription-factor mutant alleles. Mutant alleles are listed in rows and measured traits in columns. Statistically significant differences relative to wild type (Col-0) are shown with a coloured cell within the heat map ($P < 0.05$ as determined using a two-way ANOVA, exact n and P values for the analysis can be found in Supplementary Table 10). Trait categories are indicated with a dark-edged vertical line. Moving from left to right this comprises primary root length, lateral root number, total lateral root length, total root length, average lateral root length, lateral root density, ratio of total lateral root length to total root length, principal component analysis, rosette size and bolting and flowering analysis. Root traits were measured from 9-day-old plants grown on 1 mM KNO_3 or 10 mM KNO_3 . PRL, primary root length; LR, number of lateral roots; LRL, total lateral root length; total root length (TRL), PRL + LRL; average lateral root length (ALRL), LRL divided by LR; lateral root density (LRD), LR divided by PRL; LRL/TRL, LRL divided by TRL. 'PR factor' indicates that PRL was considered as a factor in the ANOVA model; PC1, principal component 1; PC2, principal component 2; PC3, principal component 3. Dark green, phenotype is larger than Col-0; light green, phenotype is smaller than Col-0; horizontal black bar, genotype-by-condition interaction. Genotype-specific (light pink) and genotype-by-condition-specific (dark pink) effects are shown, when considering variation across all root traits in a principal component analysis in PC1, PC2 and PC3. Light blue, early bolting and flowering; dark blue, late bolting and flowering. Mutants are hierarchically clustered using the Manhattan distance metric.

mutant of *NPF6.3*—displayed changes in its RSA that were dependent on genotype and on genotype-by-nitrate conditions (Figs. 2, 3c). Similarly, *nlp7-1* and *hmgbl5-1* plants displayed larger root systems, with genotype-dependent changes in their RSA (Figs. 2, 3d, e). *bbx16-1* plants had larger root systems under limiting nitrogen conditions (Figs. 2, 3f). Conversely, the *myb29-1* mutant had increased lateral root length, lateral root density and total root length under sufficient nitrate, in a manner that was dependent on genotype-by-nitrate conditions (Figs. 2, 3g). By contrast, the *erf107-1* and *rav1-2* plants showed a genotype-dependent decrease in the size of traits related to their lateral roots, in both nitrate conditions (Figs. 2, 3h, i). The *gnc* mutant showed decreases in lateral root length that were dependent on nitrate conditions and on genotype-by-nitrate condition (Fig. 2). The phenotype of *gnc* plants differed from that of *erf107-1* and *rav2-1* plants, in that these latter two mutants did not show any dependence on nitrate conditions. The composite principal component traits provided additional insights into perturbations in root growth that could not be discerned by looking at individual traits (Extended Data Fig. 4, Supplementary Table 11). In these experiments, we determined genes that control

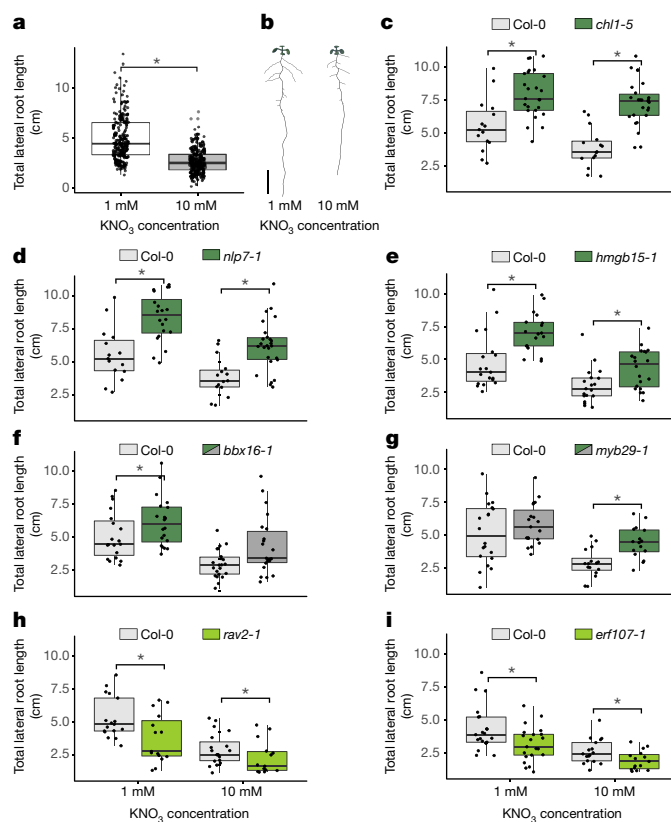


Fig. 3 | Total lateral root length phenotypes that are dependent on genotype and nitrate condition. **a**, Col-0 LRL is significantly longer at 1 mM KNO₃ compared to 10 mM KNO₃. **b**, Average Col-0 root growth. Scale bar, 1 cm. **c**, **d**, The *chl1-5* and *nlp7-1* mutant alleles were included as a nitrate transporter (*chl1-5*, **c**) and master transcriptional regulator (*nlp7-1*, **d**). Both mutants have a genotype-dependent influence on LRL at 1 and 10 mM KNO₃, with an LRL that is longer than that of wild type. *chl1-5* also has a genotype-by-treatment influence on LRL. **e**, The *hmgb15-1* allele shows a genotype-dependent influence on LRL relative to wild type, which is similar to *nlp7-1* and *chl1-5* relative to wild type. **f**, The *bbx16-1* allele has an influence on LRL that is dependent on nitrate condition, with a longer LRL only at 1 mM KNO₃. **g**, The *myb29-1* allele has an influence on LRL that is dependent on nitrate condition, with a longer LRL only at 10 mM KNO₃. **h**, **i**, The *rav2-1* (**h**) and *erf107-1* (**i**) alleles are both genotype-dependent at both 1 mM and 10 mM KNO₃, with shorter LRLs. **P* < 0.05, two-way ANOVA; exact *n* and *P* values for the analysis can be found in Supplementary Table 10. Box plots are centred at the data median and mark from the 25th to the 75th percentile. Individual measurements are plotted as black dots.

nitrogen-associated root length, lateral root development, and lateral root development that is dependent on primary root length, and then overlaid these on the YNM along with genes that regulate primary root length (Supplementary Table 12) and lateral root initiation²⁹ (Extended Data Fig. 5).

Given that perturbed RSA was observed in these mutants, we next determined whether the altered nitrogen status of the mutants affected shoot development and the transition from vegetative to reproductive growth (see Methods). Mutant alleles of thirteen genes showed a difference in either rosette size and/or bolting and flowering time (Supplementary Tables 9, 10, Supplementary Data 1, 2). Plants with the *arf18-2* allele had a smaller rosette with an increased number of days to flowering, whereas *arf18-3* plants showed the opposite phenotype. A change in rosette size was coupled with a change in the time to bolting or flowering for four mutants. *arf18-2*, *arf18-3* and *hmgbl5-1* showed the most significant changes in both root and shoot system architecture. A significant reduction in both ^{15}N in *rav2-1* plants and in the C:N ratio in *nlp7-1* plants was observed (Extended Data Fig. 6). Classical plant physiology experiments have also associated changes

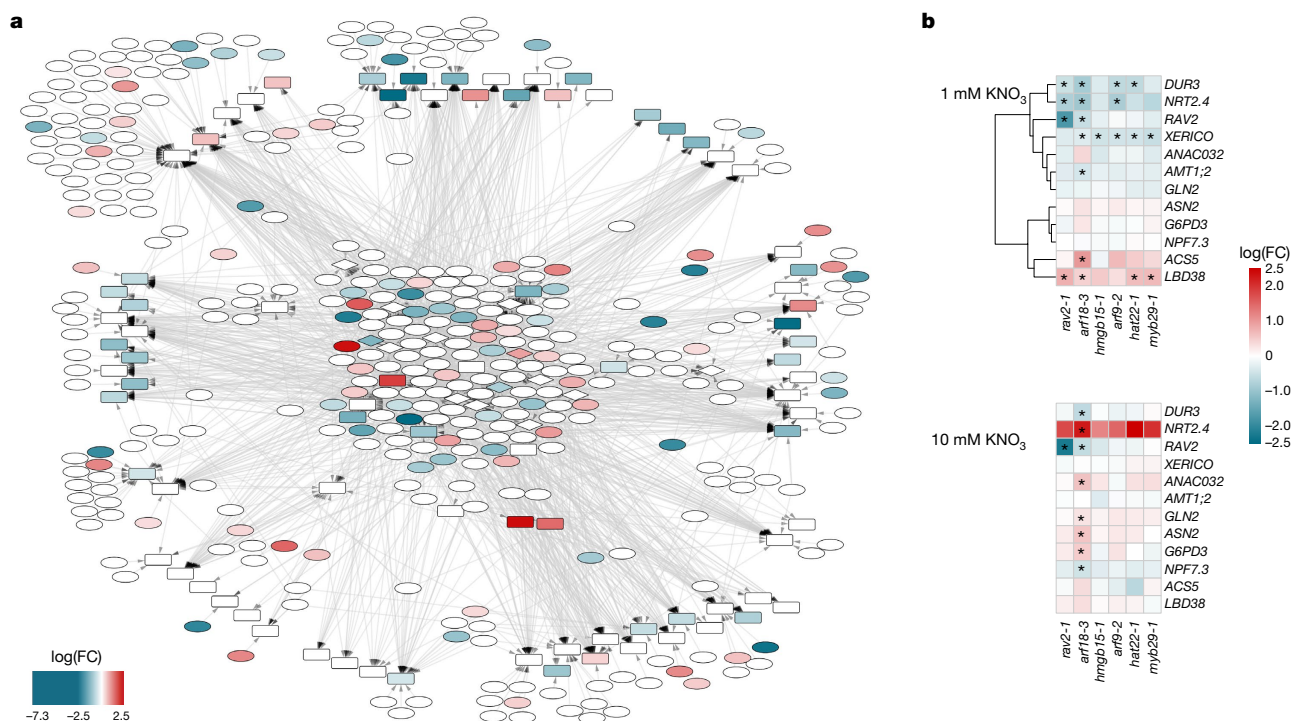


Fig. 4 | The nitrate-responsive transcriptional regulatory network.

a, The network is enriched for genes that are differentially expressed in the root grown on 1 mM KNO₃ or 10 mM KNO₃. Nodes that are significantly differentially expressed are coloured according to their log(fold change) (log(FC)), from -2.5 to 2.5 (Supplementary Table 14a, b). Node shape is the same as Fig. 1. **b**, Heat map showing the expression of specific YNM

target genes: *DUR3*, *NRT2.4*, *RAV2*, *XERICO*, *ANAC032*, *AMT1;2*, *GLN2*, *ASN2*, *G6PD3*, *NPF7.3*, *ACS5* and *LBD38* in 1 mM KNO₃ and 10 mM KNO₃. Each cell represents the log(fold change) relative to the control, as determined using a two-sided test with limmaVoom. *Corrected $P < 0.05$, (Supplementary Table 15). Four biological replicates were sampled per genotype per condition.

in nitrogen status with perturbation of chlorophyll levels. *nlp7-1* and *gnc* mutants showed significant reduction in their total chlorophyll content, whereas *lbd4-1* had increased chlorophyll content (Extended Data Fig. 7). Changes in shoot growth in the mutants were significantly correlated with the number of targets each transcription factor had in the YNM (Spearman rank correlation, $P < 0.05$), as well as with the number of biological processes that these transcription factors putatively regulated ($P < 0.05$, Supplementary Table 13). Thus, network connectivity is predictive of the influence of a given transcription factor on shoot growth.

Changes in nitrogen availability are accompanied by changes in transcription^{5,9,12,30}. Furthermore, the changes in development of transcription-factor mutants under conditions of both limiting and sufficient nitrogen are probably coordinated by perturbations in the underlying transcriptional regulatory network. To link mutant phenotypes with transcriptional changes, whole-genome expression was measured in a subset of mutant genotypes (see Methods, Supplementary Tables 14, 15). To provide further support that the YNM reflects the transcriptional regulation of nitrogen-dependent processes in the root, we tested for enrichment of nitrogen-status genes. Genes displaying differential expression in wild-type roots in 1 mM relative to 10 mM KNO₃ were significantly enriched in the YNM ($P = 3.94 \times 10^{-9}$) (Fig. 4a). Thus, the YNM captures transcriptional regulation of root nitrogen status.

At the level of individual transcription factors, *ARF9* and *ARF18* alleles showed differential expression of nitrogen-related genes. *ARF9* regulates the expression of two direct targets as predicted by the YNM (*XERICO* and *DUR3*) as well as *NRT2.4*, *NPF7.3*, *GLN2* and *ASN2*. *ARF18* regulated expression of three direct targets as predicted by the YNM (*NRT2.4*, *ANAC032* and *XERICO*) as well as *ACS5*, *DUR3*, *G6PD3* and *AMT1;2* (Fig. 4b). *HMG15* regulated the expression of one predicted direct target, *XERICO* (Fig. 4b). *LBD38* is misregulated

in the mutants of *ARF18*, *MYB29*, *RAV2* and *HAT22*; misregulation of *NRT2.4* was found in the mutants of *ARF18*, *HAT22* and *RAV2* (Fig. 4b).

A common mode of regulation in metabolism is metabolite feedback. To test whether feedback is present within the YNM, we curated gene-expression datasets of nitrate transporters and a transceptor, metabolic-enzyme mutants and genotype-by-nitrogen-dependent changes in mutants of previously described transcriptional regulators of nitrogen metabolism (Supplementary Table 16, see Methods). Upon perturbation of nitrogen transport, sensing and metabolism, genes in the YNM were significantly enriched for differential expression (Fig. 5a). Thus, a perturbation in nitrate uptake, reduction and the glutamine oxoglutarate aminotransferase cycle results in transcriptional perturbation of enzymes involved in nitrogen metabolism, and their upstream regulators. Genetic perturbation of nitrogen metabolism via the nitrogen-regulatory transcription factors also perturbs more genes in the YNM than expected by chance (Fig. 5a). Clustering analysis revealed targets of this metabolic feedback (Extended Data Figs. 8–10). A core set of enzymes involved in nitrogen metabolism—representing nearly every step of nitrate uptake, assimilation and conversion to glutamine and glutamate—were perturbed in most of the metabolic-mutant backgrounds queried. These perturbed genes include *NPF6.3*, *NRT3.1*, *NIA1*, *NIR1*, *G6PD2*, *G6PD3*, *RFNR1*, *RFNR2*, *ASN1* and the transcription factor *RAV2*, found in this study (Fig. 5b). Another cluster includes known nitrogen-associated genes *TGA1*, *NLP7*, *CIPK8*, *NRT2.1* and *GDH2* (Fig. 5c). *ANR1* is found in a cluster of transcription factors identified in this study, *ERF107*, *ARF18* and *BBX16*, which are perturbed in the mutant of *NLP7* and the double mutant of *TGA1/TGA4* (Fig. 5d). Similar transcriptional-regulation feedback on several of the transcription factors characterized in this study (*RAV2*, *ERF107*, *ARF18* and *BBX16*), in addition to previously established nitrogen-status regulators (*LBD38*, *LBD39*, *TGA1*, *NLP7*

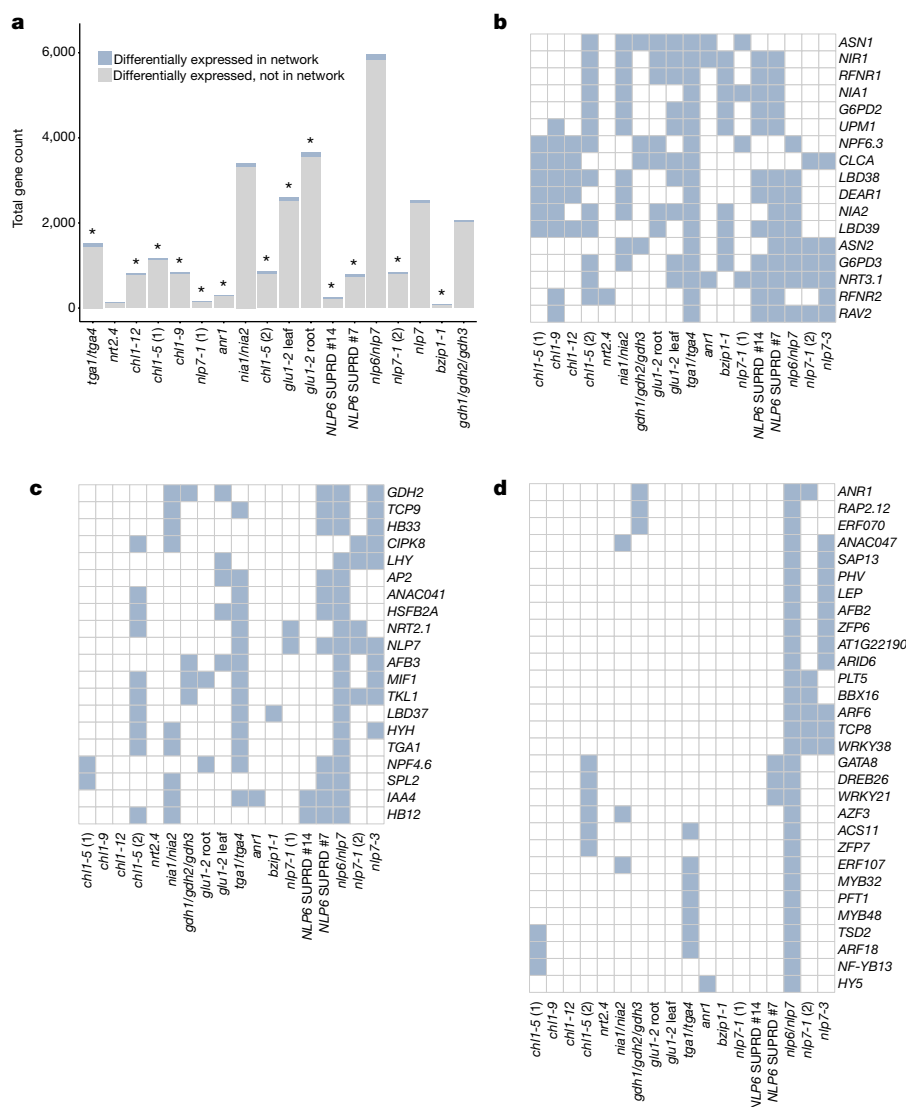


Fig. 5 | Transcriptional feedback upon genetic perturbation of nitrogen metabolism or regulation. a, Bar graph showing differentially expressed genes within the network in different mutant backgrounds. The y axis is the number of differentially expressed genes based on genotype (metabolism mutants) or genotype-by-nitrate condition (transcription-factor mutants). An asterisk indicates significance at $P < 0.01$ for enrichment in the network using a two-sided Fisher's exact test (see Methods). $n = 18$ expression datasets. SUPRD #7 and SUPRD #14 refer to dominant-repression mutant lines of the *NLP6* gene. **b**, A core set of nitrogen metabolism genes and regulators that are robust

targets of transcriptional feedback. Clusters were determined using k -means clustering. Blue, gene significantly differentially expressed; white, gene not significantly differentially expressed using a two-sided test with limma (false discovery rate < 0.05 , see Methods). **c**, **d**, Distinct clusters of transcription factors and metabolic enzymes that contain transcription factors found in this study and are targets of feedback by transcriptional regulators of nitrogen metabolism. Each study (see 'Sources for mutant alleles' in Methods) was analysed individually to test the effect of nitrate in the different mutants. For details of the studies from which mutants are derived, see 'Sources for mutant alleles' in Methods.

and *ANR1*), further emphasizes the importance of these transcription factors as central nitrogen regulators.

The YNM indicates the interconnected regulation of nitrogen metabolism: the more important a transcription factor is in regulating growth, the more likely it is to bind to promoters of genes in multiple nitrogen-related categories. The 21 transcription factors we describe here regulate diverse aspects of RSA and shoot development that contribute to how growth is regulated in different nitrogen environments. Transcriptional feedback within the YNM revealed a core set of enzymes involved in nitrogen metabolism, and their regulators. The mechanisms underlying this feedback remain to be determined and may include signalling, metabolite and/or allosteric feedback, or the action of the NPF6.3 transceptor. The identification of these genetically regulated gene expression modules places the genes found in this study within the existing nitrogen-regulatory framework. The transcription factors we identify—in addition to the 'core' set of enzymes involved in

nitrogen metabolism—will assist in breeding efforts to generate plants that use nitrogen more efficiently.

Online content

Any methods, additional references, Nature Research reporting summaries, source data, statements of data availability and associated accession codes are available at <https://doi.org/10.1038/s41586-018-0656-3>.

Received: 11 December 2017; Accepted: 22 August 2018;

Published online 24 October 2018.

1. Tilman, D., Cassman, K. G., Matson, P. A., Naylor, R. & Polasky, S. Agricultural sustainability and intensive production practices. *Nature* **418**, 671–677 (2002).
2. Sinha, E., Michalak, A. M. & Balaji, V. Eutrophication will increase during the 21st century as a result of precipitation changes. *Science* **357**, 405–408 (2017).
3. Zhang, H. & Forde, B. G. Regulation of *Arabidopsis* root development by nitrate availability. *J. Exp. Bot.* **51**, 51–59 (2000).

4. Castro Marín, I. et al. Nitrate regulates floral induction in *Arabidopsis*, acting independently of light, gibberellin and autonomous pathways. *Planta* **233**, 539–552 (2011).
5. Scheible, W.-R. et al. Genome-wide reprogramming of primary and secondary metabolism, protein synthesis, cellular growth processes, and the regulatory infrastructure of *Arabidopsis* in response to nitrogen. *Plant Physiol.* **136**, 2483–2499 (2004).
6. Liu, K. H. et al. Discovery of nitrate–CPK–NLP signalling in central nutrient-growth networks. *Nature* **545**, 311–316 (2017).
7. Krouk, G. et al. A framework integrating plant growth with hormones and nutrients. *Trends Plant Sci.* **16**, 178–182 (2011).
8. Zhang, H. & Forde, B. G. An *Arabidopsis* MADS box gene that controls nutrient-induced changes in root architecture. *Science* **279**, 407–409 (1998).
9. Gifford, M. L., Dean, A., Gutierrez, R. A., Coruzzi, G. M. & Birnbaum, K. D. Cell-specific nitrogen responses mediate developmental plasticity. *Proc. Natl Acad. Sci. USA* **105**, 803–808 (2008).
10. Rubin, G., Tohge, T., Matsuda, F., Saito, K. & Scheible, W. R. Members of the LBD family of transcription factors repress anthocyanin synthesis and affect additional nitrogen responses in *Arabidopsis*. *Plant Cell* **21**, 3567–3584 (2009).
11. Castangs, L. et al. The nodule inception-like protein 7 modulates nitrate sensing and metabolism in *Arabidopsis*. *Plant J.* **57**, 426–435 (2009).
12. Krouk, G., Mirowski, P., LeCun, Y., Shasha, D. E. & Coruzzi, G. M. Predictive network modeling of the high-resolution dynamic plant transcriptome in response to nitrate. *Genome Biol.* **11**, R123 (2010).
13. Konishi, M. & Yanagisawa, S. *Arabidopsis* NIN-like transcription factors have a central role in nitrate signalling. *Nat. Commun.* **4**, 1617 (2013).
14. Vidal, E. A., Álvarez, J. M. & Gutiérrez, R. A. Nitrate regulation of *AFB3* and *NAC4* gene expression in *Arabidopsis* roots depends on NRT1.1 nitrate transport function. *Plant Signal. Behav.* **9**, e28501 (2014).
15. Alvarez, J. M. et al. Systems approach identifies TGA1 and TGA4 transcription factors as important regulatory components of the nitrate response of *Arabidopsis thaliana* roots. *Plant J.* **80**, 1–13 (2014).
16. Guan, P. et al. Nitrate foraging by *Arabidopsis* roots is mediated by the transcription factor TCP20 through the systemic signaling pathway. *Proc. Natl Acad. Sci. USA* **111**, 15267–15272 (2014).
17. Medici, A. et al. AtNIGT1/HRS1 integrates nitrate and phosphate signals at the *Arabidopsis* root tip. *Nat. Commun.* **6**, 6274 (2015).
18. Xu, N. et al. The *Arabidopsis* NRG2 protein mediates nitrate signaling and interacts with and regulates key nitrate regulators. *Plant Cell* **28**, 485–504 (2016).
19. Obertello, M., Krouk, G., Katari, M. S., Runko, S. J. & Coruzzi, G. M. Modeling the global effect of the basic-leucine zipper transcription factor 1 (bZIP1) on nitrogen and light regulation in *Arabidopsis*. *BMC Syst. Biol.* **4**, 111 (2010).
20. Araus, V. et al. Members of BTB gene family of scaffold proteins suppress nitrate uptake and nitrogen use efficiency. *Plant Physiol.* **171**, 1523–1532 (2016).
21. Gaudinier, A. et al. Enhanced Y1H assays for *Arabidopsis*. *Nat. Methods* **8**, 1053–1055 (2011).
22. Reece-Hoyes, J. S. et al. Enhanced yeast one-hybrid assays for high-throughput gene-centered regulatory network mapping. *Nat. Methods* **8**, 1059–1064 (2011).
23. Marchive, C. et al. Nuclear retention of the transcription factor NLP7 orchestrates the early response to nitrate in plants. *Nat. Commun.* **4**, 1713 (2013).
24. Ristova, D. et al. Combinatorial interaction network of transcriptomic and phenotypic responses to nitrogen and hormones in the *Arabidopsis thaliana* root. *Sci. Signal.* **9**, rs13 (2016).
25. Tsay, Y. F., Schroeder, J. I., Feldmann, K. A. & Crawford, N. M. The herbicide sensitivity gene *CHL1* of *Arabidopsis* encodes a nitrate-inducible nitrate transporter. *Cell* **72**, 705–713 (1993).
26. Bi, Y.-M. et al. Genetic analysis of *Arabidopsis* GATA transcription factor gene family reveals a nitrate-inducible member important for chlorophyll synthesis and glucose sensitivity. *Plant J.* **44**, 680–692 (2005).
27. Little, D. Y. et al. The putative high-affinity nitrate transporter NRT2.1 represses lateral root initiation in response to nutritional cues. *Proc. Natl Acad. Sci. USA* **102**, 13693–13698 (2005).
28. Remans, T. et al. The *Arabidopsis* NRT1.1 transporter participates in the signaling pathway triggering root colonization of nitrate-rich patches. *Proc. Natl Acad. Sci. USA* **103**, 19206–19211 (2006).
29. De Smet, I. et al. Receptor-like kinase ACR4 restricts formative cell divisions in the *Arabidopsis* root. *Science* **322**, 594–597 (2008).
30. Wang, R., Guegler, K., LaBrie, S. T. & Crawford, N. M. Genomic analysis of a nutrient response in *Arabidopsis* reveals diverse expression patterns and novel metabolic and potential regulatory genes induced by nitrate. *Plant Cell* **12**, 1491–1509 (2000).

Acknowledgements We thank N. M. Crawford for *chl1-5* seeds, P. J. Etchells for *wox14-1* and *lbd4-1* seeds, and E. E. Sparks and P. N. Benfey for *erf107-1*, *abf4-2*, *eel-1*, *vip1-1* and *erf070* seeds. Some seed stocks were obtained from the *Arabidopsis* Biological Resource Center (ABRC) at Ohio State University. We thank E. A. Ainsworth and S. B. Gray for help with chlorophyll and protein assays, K. Kajala for help with RNA-seq libraries and E. M. McGinnis for help with root measurements. We thank K. Dehesh for discussions. This research was funded by DuPont Pioneer. A.G. was also supported by the Elsie Taylor Stocking Memorial Fellowship, the Katherine Esau Graduate Summer Fellowship and the University of California, Davis Dissertation Year Fellowship. J.R.-M. was supported by a UC-MEXUS CONACYT PhD Fellowship. D.J.K., M.T. and S.M.B. acknowledge funding from NSF-MCB-1330337. S.M.B. was partially funded by an HHMI Faculty Scholar Fellowship.

Reviewer information *Nature* thanks M. Bennett, C. Hodgman and the other anonymous reviewer(s) for their contribution to the peer review of this work.

Author contributions S.M.B., B.S. and D.W. conceived the project. A.G., L.Z., J.F., S.A. and M.T. cloned promoters. A.G. and S.M.B. designed experiments and A.G., D.J.K. and S.M.B. contributed to data analysis experimental design. A.G., J.F., A.-M.B., M.T. and B.L. performed enhanced yeast one-hybrid screens. A.G. genotyped plants. A.G., A.-M.B. and M.T. performed plant phenotyping. A.G., J.R.-M., A.O. and C.L.-M. performed bioinformatics. A.G. performed transcription factor–target correlation analysis. C.L.-M. and A.O. performed NeCorr analysis. J.R.-M. performed network analysis (enrichment tests), analysis of RNA sequencing data, clustering and network-metabolic analysis. A.G., S.M.B., D.E.R., D.J.K., B.S., D.W. and M.J.F. provided discussion, experimental design and analysis suggestions. S.M.B. and A.G. wrote the manuscript.

Competing interests The authors declare no competing interests.

Additional information

Extended data is available for this paper at <https://doi.org/10.1038/s41586-018-0656-3>.

Supplementary information is available for this paper at <https://doi.org/10.1038/s41586-018-0656-3>.

Reprints and permissions information is available at <http://www.nature.com/reprints>.

Correspondence and requests for materials should be addressed to S.M.B.

Publisher's note: Springer Nature remains neutral with regard to jurisdictional claims in published maps and institutional affiliations.

METHODS

No statistical methods were used to predetermine sample size. Seeds were randomized within each experiment and investigators were blinded to allocation during experiments and outcome assessment.

Promoter cloning, yeast transformation and yeast one-hybrid assays. Gene promoters were cloned to 2 kb or until the nearest upstream gene or synthesized by Life Technologies (Supplementary Table 2a). In the case of cloning, promoters were amplified from Col-0 genomic DNA using Phusion Taq polymerase (NEB). Promoters were recombined into 5' TOPO (Invitrogen), fully sequenced and then recombined into pMW2 and pMW3³¹ using LR clonase II (Invitrogen). pMW2 and pMW3 constructs were sequence-confirmed. They were transformed into the yeast strain YM4271 as previously described³². If constructs were resistant to transformation, they were transformed into the Y1H-S2 strain²². Yeast colonies were screened for autoactivation and construct presence. Promoter strains were mated against transcription-factor strains as previously described^{21,22}.

Transcription-factor cloning and yeast transformation. Transcription factors were cloned from root RNA extracted using the RNeasy Kit (Qiagen) (Supplementary Table 2b). Coding sequences were amplified using Phusion Taq polymerase (NEB). Transcription factors were recombined into D-TOPO (Invitrogen), fully sequenced and then recombined into pDEST-AD2μ using LR clonase II (Invitrogen). They were transformed into the yeast strain Yα1867 as previously described^{21,22}.

Network construction. Networks were made using Cytoscape v.3.2.0³³. All cytoscape network files can be found at <https://github.com/agaudinier/Gaudinier2018>.

Figure construction. Figures were made using Cytoscape, and ggplot2³⁴ v.3.0.0 in R. Figures were compiled using Inkscape (<http://www.inkscape.org>).

Plant material and growth conditions. Transfer DNA (tDNA) mutant lines were obtained through TAIR (<http://www.arabidopsis.org>) or collaborators. Seeds sorted between 250–300 μm were surface-sterilized using dichloroisocyanuric acid solution (0.9% (w/v) dichloroisocyanuric acid solution (10% water, 90% ethanol), then rinsed twice in 95% ethanol, and then dried completely). For the root mutant phenotyping experiment (Supplementary Table 2c), sets of four tDNA lines and a Col-0 control were plated in a random block design on a minimum of twelve 1-mM KNO₃ and twelve 10-mM KNO₃ medium plates, and stratified at 4 °C for two nights. Medium components: 1 or 10 mM KNO₃, 4 mM MgSO₄, 2 mM KH₂PO₄, 1 mM CaCl₂, 10 mM KCl, 36 mg/l FeEDTA, 0.146 g/l 2-morpholinoethane sulfonic acid, 1.43 mg/l H₂BO₃, 0.905 mg/l MnCl₂·4H₂O, 0.055 mg/l ZnCl₂, 0.025 mg/l CuCl₂·2H₂O, 0.0125 Na₂MoO₄·2H₂O, 1% sucrose, 0.75% phytagel, pH 5.7.

For the shoot phenotyping experiment, sorted seeds were stratified at 4 °C for two nights and sown on Sunshine Mix soil in flats containing 18 pots. Seventeen genotypes, plus Col-0, were randomized in a partial random block design for 8 or 9 biological replicates per experiment for a total of three experiments. Plants were watered twice a week, switching between a modified Hoagland's solution and deionized water. Modified Hoagland's solution components [16×]: 1.6 g/l KNO₃, 0.55 g/l KH₂PO₄, 3.85 g/l MgSO₄, 3.57 g/l KCl, 2.35 g/l CaCl₂, 1.34 g/l Sprint 330, 2.97 mg/l H₃BO₃, 3.17 mg/l MnCl₂·4H₂O, 4.6 mg/l ZnSO₄·7H₂O, 0.4 mg/l CuSO₄·5H₂O, 0.39 mg/l H₂MoO₄·H₂O, pH 5.5.

For the RNA-sequencing (RNA-seq) experiment to characterize gene expression in each mutant background, 200–300 seeds per plate were sown on Petri plates with medium containing 1 mM or 10 mM KNO₃ and nylon mesh, and stratified for two nights at 4 °C. Two plates of seedlings per genotype were grown and combined for each biological replicate. Four biological replicates were grown per genotype and treatment. Roots of 9-day-old seedlings were collected from 6–7 h after sunrise and immediately frozen in liquid N₂.

RNA-seq library preparation and pooling of technical replicates. RNA-seq libraries were prepared following the BRAD-Seq DGE protocol³⁵. Libraries were sequenced using the Illumina HiSeq 3000 in SR50 mode. Two technical replicate libraries were created from each RNA sample and after assessing sufficient reproducibility, counts across technical replicates were pooled together. Pooling was performed by summing the counts for the same gene across equivalent replicates. The merged file was subjected to the same quality processing. The number of mapped reads for each biological replicate and correlation of replicates are found in Supplementary Table 14c, d.

RNA-seq read processing and differential expression analysis. Before and after read processing, libraries were analysed with FastQC (<http://www.bioinformatics.babraham.ac.uk/projects/fastqc/>) to assess the quality of the sequences. We trimmed barcodes from raw reads using fastx-trimmer (http://hannonlab.cshl.edu/fastx_toolkit/index.html) with parameters: -f 9 -v Q 33. This was followed by adaptor trimming and quality filtering using reaper, from the Kraken Suite³⁶ with options: -geom no-bc -dust-suffix-late 10/ACTG -dust-suffix 10/ACTG -noqc -nnn-check 1/1 -qqq-check 33/10 -clean-length 30 -tri 20 -polya 5-bcq-late. Trimmed reads were mapped to the reference genome of *A. thaliana* (TAIR 10) using bowtie (-a -best -strata -n 1 -m 1 -p 4 -sam -tryhard) with subsequent

conversion to BAM format using samtools³⁷. HTSeq-count was used to obtain raw counts³⁸.

Differential gene expression analysis was done using limma³⁹ in R/Bioconductor⁴⁰, with empirical weights estimated for each observation using the voomWithQualityWeights function. Quantile normalization was used to account for different RNA inputs and library sizes. The linear model for each gene was specified as: log(counts per million) of a particular gene = mutant + treatment + mutant:treatment. Specific contrasts were constructed to compare each mutant to the control, and each genotype × treatment interaction. Differentially expressed genes were selected based on a false discovery rate < 0.05 (Supplementary Table 15).

Generation of the publically available gene expression profiling datasets for nitrogen-responsive genes. We compiled a comprehensive dataset of publically available gene-expression responses of wild-type plants in response to nitrogen availability in both the root and shoot (GEO accession GSE18984)^{9,10,12,15,19,41–45}, as well as profiling of nitrogen-status gene expression changes in specific root cell types⁹. Data from ATH1 affymetrix arrays were downloaded from the NCBI GEO database⁴⁶ and imported into R using the affy⁴⁷ package in Bioconductor. Arrays were normalized using the robust multi-array average (RMA) method. Gene expression was averaged across biological replicates, and then treatment datasets were expressed relative to their appropriate controls (Supplementary Table 5). Pearson and Spearman correlations were calculated in R for the treatment and cell-type-specific datasets for all transcription factor–target pairs (Supplementary Table 6).

Spearman rank correlation analysis of root and shoot phenotypes relative to network connectivity and related metrics. We prioritized transcription factors from the YNM with a Pearson or Spearman rank correlation greater than ±0.5 (for the nitrogen treatment dataset) or greater than ±0.8 (for the cell-type-specific dataset) with their target genes (Supplementary Table 6). Spearman rank correlations were calculated in R using rcorr() from the Hmisc package (<https://cran.r-project.org/package=Hmisc>) for the phenotype traits of transcription-factor mutants, relative to network connectivity and correlation with targets. Data and correlations can be found in Supplementary Table 13.

Generation of the publically available dataset for nitrogen-metabolism mutants and mutants of transcription factors associated with nitrogen metabolism. Affymetrix arrays were read using the affy package in Bioconductor. Agilent and Complete Arabidopsis Transcriptome Micro Array (CATMA) arrays were read with the read.maimages() function from limma; the source option was set to 'agilent' for the former and 'genepix' for the latter. After arrays were read, limma was used for downstream processing, normalization and differential expression analysis. In brief, Affymetrix arrays were normalized using the RMA method. Agilent and CATMA arrays were subjected to background correction and normalization using the functions backgroundCorrect() and normalizeBetweenArrays(). After normalization and filtering, differential expression was analysed using the standard limma approach.

NECorr. The starting hypothesis of NECorr is that an important interaction for a stimuli response is that of a regulator acting on one or several hub genes. Hence, hub genes will propagate the systemic cascade appropriate to the stimuli. Thenceforth the dynamics of the molecular network will evolve. This approach ranks transcription factors given several network metrics including betweenness centrality, degree distribution and as a function of their gene-expression similarity⁴⁸.

Hub calculation. The first step is a heuristic model, which merges molecular network topology and gene-expression data. NECorr-Hub is a linear model including five parameters: condition or tissue specificity of gene expression, co-expression of interactions across conditions, and the molecular network centralities betweenness, connectivity and transitivity. The rank given to each of these parameters was decided empirically.

Both genes of an interaction pair need to be co-expressed in most of the tissues and/or conditions, which shows that they can influence each other. Correlated gene expression was considered as the highest-ranking parameter, followed by gene-expression specificity in the studied tissue or condition. In addition, a high level of connectivity of the gene in the molecular network is required to generate a proper response. Connectivity can be defined in several manners: betweenness, degree connectivity and transitivity were chosen as the most meaningful centralities to define gene importance as a hub.

Based on the ranking, each parameter weight was estimated using the analytic hierarchy process (AHP)^{49,50}, a multiple-criteria decision analysis method. The AHP is applied through the R package pmr (<https://cran.r-project.org/package=pmr>). The importance of the five parameters is generated by pairwise comparisons. Hence, this leads to an adjacency matrix of pairwise weight importance. From this adjacency matrix, Eigen vectors are calculated to assign a weight to each parameter. The AHP method is applied as follows. Each gene is ranked for the five parameters above. Each ranked parameter is standardized in values between

0 and 1 (z-score), to obtain data with the same scale. For each tissue and/or condition, the parameter weights are applied as factors of a linear model that is used to prioritize hub genes.

For condition 1: $\text{Ranking}_{\text{condition 1}} = w_1 \times \text{IntSig} + w_2 \times \text{TS} + w_3 \times \text{BetC} + w_4 \times \text{Cot} + w_5 \times \text{Trs}$, in which IntSig represents the interaction significance (co-expression significance in the interaction involving the gene), TS represents tissue specificity (selectivity), BetC represents betweenness centrality, Cot represents connectivity centrality and Trs represents transitivity. The weights are defined as $w_1 = w_2 > w_3 > w_4 > w_5$.

To rank the interactions in the molecular network for a given condition, the average ranking of the two genes defining this edge is taken. When several conditions are evaluated, the gene ranking between conditions can be done by averaging each condition ranking.

NECorr-Hub parameter estimation. Molecular network topology centralities are obtained using the R package iGraph (<https://cran.r-project.org/package=igraph>). Co-expression analysis (or the significance of each interaction) was estimated using a Rcpp script to evaluate the Gini correlation coefficient related to each interaction. The Gini correlation coefficient was previously shown to be an effective method for detecting transcription-factor activity⁵¹. The co-expression significance for each gene is evaluated by averaging the magnitude of the correlation from all the interactions containing this particular gene using Fisher's method^{52,53}.

The genes with tissue and/or condition specificity (or selectivity) are detected using the intersection-union test (IUT) with a relaxed threshold (raw $P = 0.5$) (<https://cran.r-project.org/package=igraph>)⁵⁴. The tissue and/or condition-selective genes or tissue and/or condition-excluded genes are assigned for each specific tissue and/or condition within a set of samples. These genes attributed to a tissue and/or condition are fuzzy owing to the low selection threshold of the gene in IUT; a gene could therefore appear in a different tissue or condition as selective or excluded. Second, these selected genes are ranked for their tissue selectivity or exclusion using the tissue specificity index⁵⁵. We define both a positive and negative TSI:

$$\text{positive TSI} = \frac{\sum_{i=1}^N (1 - x_i/x_{\max})}{N - 1}$$

The negative tissue specific index measures the extent to which a gene is excluded from a tissue or condition:

$$\text{negative TSI} = \frac{\sum_{i=1}^N (x_i - x_{\min}/x_{\max})}{N - 1}$$

The results for TSI measurements are merged to obtain a ranking of all the tissue and/or condition-selective or -excluded genes defined from IUT test.

NeCorr rankings can be found in Supplementary Table 7.

Code. The NECorr source code is maintained in GitHub: <https://github.com/warelab/NECorr>.

Mutant line selection. The mutant lines acquired for this study represent most of the top-ranked and intermediate-ranked genes that were deemed interesting for having important binding targets (Supplementary Tables 10, 11).

Root phenotyping data collection and analysis. Traits measured included PRL, LR and LRL. Additionally, composite traits were considered, including total root length ($\text{TRL} = \text{PRL} + \text{LRL}$), average lateral root length ($\text{ALRL} = \text{LRL}/\text{LR}$), lateral root density ($\text{LRD} = \text{LR}/\text{PRL}$) and the percentage of LRL contributing to TRL (LRL/TRL) as well as the partitioning of variation across these mutants relative to wild type, using principal component analysis of all RSA traits⁵⁶ (Supplementary Data 1).

Plates were scanned using the V750 scanner. Primary roots and lateral roots of 9-day-old seedlings were traced using a Wacom Bamboo tablet in ImageJ. Data were log-transformed and analysed using ANOVA in R. Using a two-way ANOVA, three phenotypic categories were considered: genotype effects in both nitrogen conditions (genotype-dependent), genotype effects in only one condition (nitrogen-condition-dependent) or genotype by nitrogen condition-dependent effects ($P < 0.05$, Supplementary Data 2). The extent to which lateral root traits are uncoupled from PRL is not clear⁵⁷, thus an additional ANOVA model was used that included PRL as a factor—with the hypothesis that lateral root emergence or elongation may be dependent on PRL. As expected, composite traits extracted from the principal component analysis were significantly correlated with a number of RSA traits ($P < 0.05$, Extended Data Fig. 4, Supplementary Table 11). The scripts for analyses can be found at <https://github.com/agaudinier/Gaudinier2018>. All ANOVA tables can be found in Supplementary Data 2. A summary of the statistics can be found in Supplementary Table 13.

Principal component analysis. Mutant and wild-type controls were plotted in R using the `prcomp()` function. The loadings for each principal component (PC1–PC3) in the mutant and wild-type sets were analysed using ANOVA in R. The script for the analysis can be found at <https://github.com/agaudinier/Gaudinier2018>. All ANOVA tables can be found in Supplementary Data 2.

Shoot phenotyping data collection and analysis. Plants were photographed at 15 and 22 days old. ImageJ was used to analyse rosette size. Bolting and flowering days were recorded. Rosette-size data were log-transformed, and for bolting and flowering day a reciprocal transformation was used and analysed using a two-way ANOVA in R. All ANOVA tables can be found in Supplementary Data 2. A summary of the statistics can be found in Supplementary Table 13.

Chlorophyll extraction and analysis. Full rosette leaves were measured for their chlorophyll content index using the CCM-200 plus (Opti-Sciences). Chlorophyll measurements were done by collecting supernatants of discs from *nlp7-1*, *chl1-5* and Col-0 (control) leaves extracted in two extractions of 80% HEPES-buffered ethanol heated to 80 °C and one extraction of 50% HEPES-buffered ethanol. Absorbance for the supernatant was measured at 652 and at 665 nm. Total chlorophyll was calculated as $\text{chlorophyll} = 22.12 A_{650} + 2.71 A_{665}$, according to a previously published method⁵⁸.

Quantification of ¹⁵N and ¹³C abundance. Rosettes of 20-day-old plants were collected and dried at 60 °C for two days. Dried rosettes were homogenized. Samples of 0.7–3 mg were submitted to the Stable Isotope Facility at University of California at Davis for analysis of natural abundance levels of ¹⁵N and ¹³C using an elemental analyser with a continuous flow isotope ratio mass spectrometer.

YNM network analyses. *Genotype expression and expression dependent on genotype-by-nitrate condition.* To test for the presence of genes in the YNM that are significantly differentially expressed, a Fisher's exact test was used to test for enrichment in R, using the standard function `fisher.test()`. For this, we queried whether the overlap of YNM-predicted genes that overlap with differentially expressed genes was greater than differentially expressed genes that did not overlap with YNM genes; as a background, we used genes that were not differentially expressed. We performed this test for every contrast, which means that the groups of genes changed between each test but the absolute number of total genes remained the same.

To test for enrichment of various pathways, a list of CPK–NLP7-dependent genes⁶, a list of primary-root developmental genes (Supplementary Table 12) and lateral-root developmental genes²⁹, and a list of hormone-responsive genes⁵⁹ were queried. A Fisher's exact test was used to determine whether the proportions of genes from these datasets were enriched in the YNM. The background for the CPK–NLP7 test includes all genes in the *Arabidopsis* genome that are not part of the YNM. The background for the root development and hormone tests includes all genes on the ATH1 affymetrix microarray that are not part of the YNM.

Transcriptional feedback of nitrogen metabolism enzymes and regulators. To test whether any feedback is present within the YNM, we curated whole-genome expression datasets in mutants of nitrate transporters or a transporter, or metabolic enzymes (GEO accession GSE10786)^{44,60–63} (NPF6.3, the double mutant of NIA1/NIA2, GLU1, NRT2.4 and the triple mutant of GDH1/GDH2/GDH3 (Supplementary Table 16)). The expression of genes in mutants of previously described transcriptional regulators of nitrogen metabolism (ANR1, NLP6, NLP7, BZIP1 and the double mutants of TGA1/TGA4 and NLP6/NLP7) that show changes in gene expression dependent on genotype-by-nitrogen condition—relative to wild type—in a genotype-by-condition analysis was also considered (GEO accession GSE6824)^{13,15,19,23} (Supplementary Table 16).

Enrichment was calculated as above. We tested whether the overlap between differentially expressed genes within the YNM was greater than differentially expressed genes which did not overlap with genes in the YNM. Each microarray study was analysed independently.

Clustering analysis of transcriptional feedback on YNM. *k*-means clustering was performed using the presence or absence calls of significantly differentially expressed genes that were differentially expressed in at least one of the contrasts; if a gene predicted by the network was significantly differentially expressed, we assigned it a value of 1, and if it was not significantly differentially expressed we assigned it a value of 0. Genes with 0 across all contrasts were not considered for the analysis (not differentially expressed in any condition). In short, the algorithm used was to calculate the Euclidean distance of the binary matrix (dist function in R), then to obtain the principal components of this distance using a correlation matrix (`princomp` function in R with `cor = T`) and select the scores for the first two components. We then calculated the clusters based on these two first principal components, and a selected value for *k*.

The number of clusters (*k*) was selected by analytical and empirical analysis: the 'elbow method' looks at different values for *k* and their relationship with the within-cluster sum of squares, in which the optimal value is that at which the line starts to plateau. We then tested different values for *k* within a threshold given by the elbow method and selected that in which biologically relevant clusters were observed.

Identification of the dominant pattern in transcription-factor mutants of nitrogen-responsive genes in the root. Data in each mutant background was filtered for genes that were significantly differentially expressed owing to nitrogen treatment in wild-type plants (wild type 1 mM versus wild type 10 mM)

(Supplementary Table 18). The expression of each of these genes was obtained by taking the difference in log(FC) between the effect of nitrogen on each of the mutants (that is, *arf18-3* 1 mM versus *arf18-3* 10 mM) and the wild type (wild type 1 mM versus wild type 10 mM). Dominant patterns of expression were then identified using a previously published algorithm⁶⁴ (with parameters set as follows: minExpFilter = FALSE; minVarFilter = FALSE; fuzzyKmem = 1.04; alreadyLog2 = TRUE). The choice of number of clusters was set to kChoice = 7. Clustering of genes, the expression of which changes upon variation in nitrogen availability in the wild-type root, revealed that these mutants have similar perturbations in nitrogen-associated gene regulation (Extended Data Fig. 9).

Sources for mutant alleles. The sources for the mutant alleles displayed in Fig. 5 are as follows: *tga1/tga4* (ref. ¹⁵); *nrt2.4* (GEO accession GSE10786); *chl1-12*, *chl1-5* (1) and *chl1-9* (ref. ⁶⁰); *nlp7-1* (ref. ¹¹); *anr1* (GEO accession GSE6824); *nia1/nia2* (ref. ⁶¹); *chl1-5* (2) (ref. ⁴⁴); *glu1-2* leaf and *glu1-2* root (ref. ⁶²); *NLP6* SUPRD #7 and *NLP6* SUPRD #14 (ref. ¹⁵); *nlp7-1* (2), *nlp7-3* and *nlp6/nlp7* (ref. ²³); *bzip1-1* (ref. ¹⁹); and *gdh1/gdh2/gdh3* (ref. ⁶³).

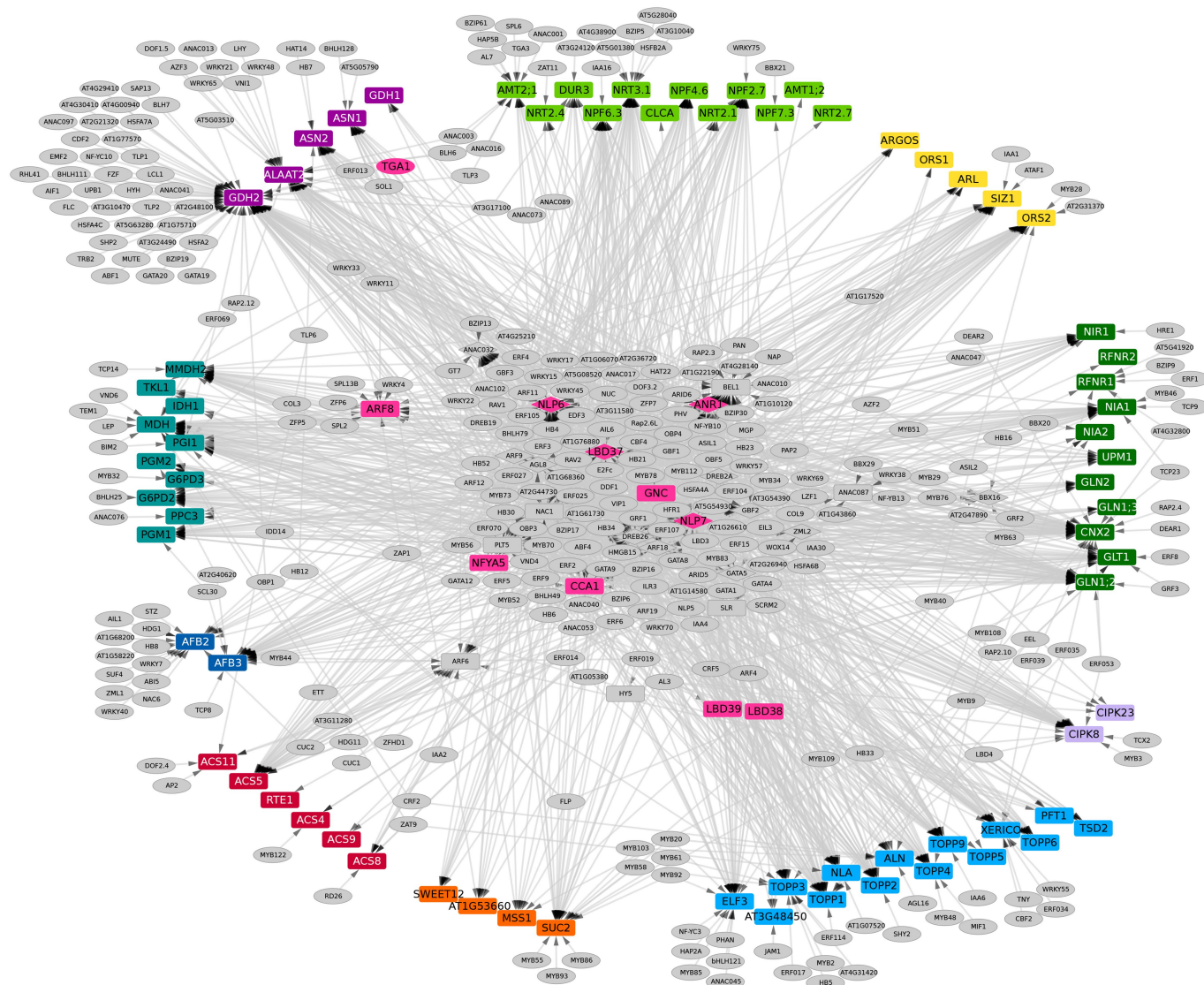
Code availability. Code for plant phenotyping analysis can be found at <https://github.com/agaudinier/Gaudinier2018>. Code for NeCorr analysis can be found at <https://github.com/warelab/NECorr>.

Reporting summary. Further information on research design is available in the Nature Research Reporting Summary linked to this paper.

Data availability

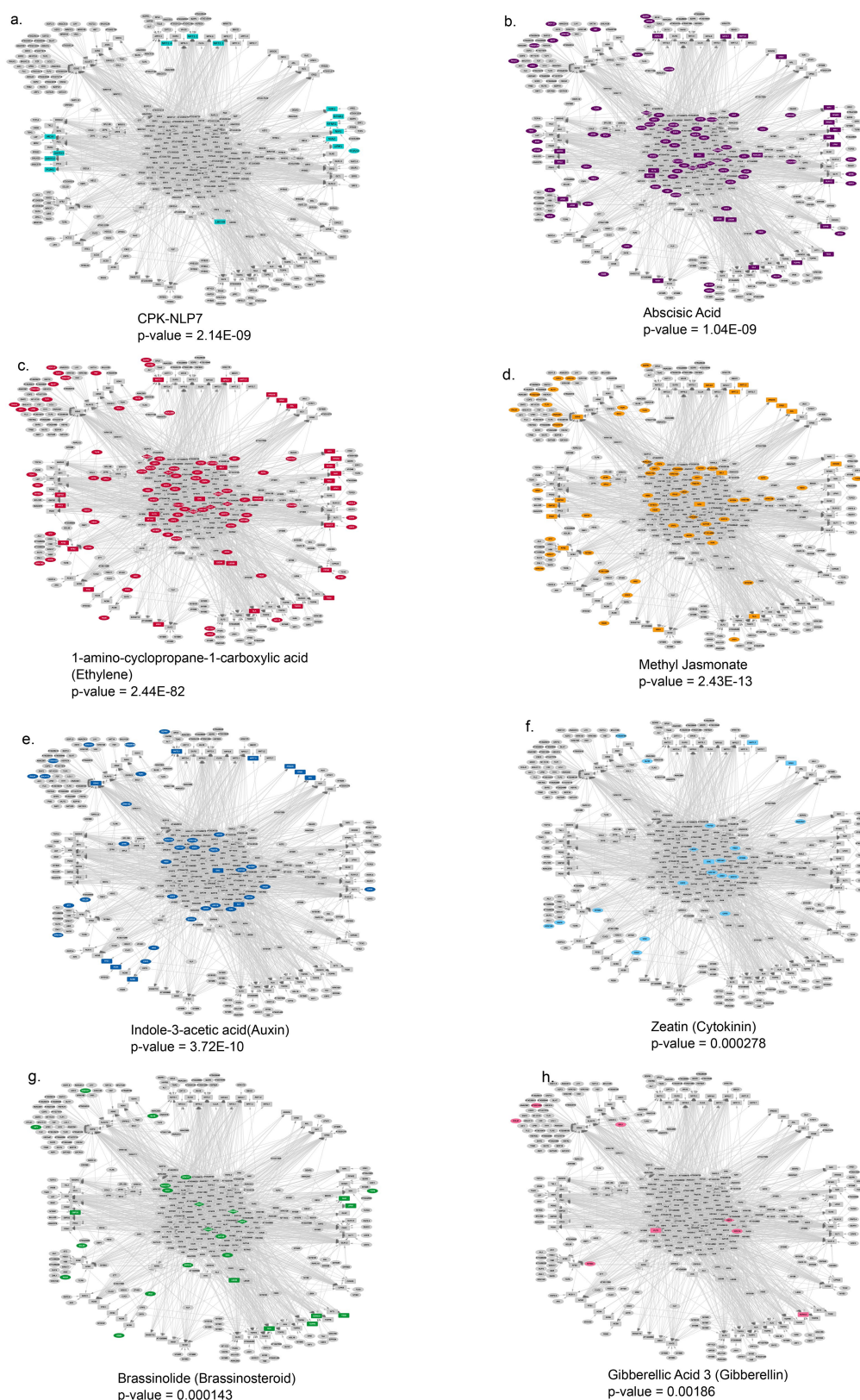
RNA sequencing data that support the findings of this study have been deposited in NCBI with the primary accession code GSE107988. Supplementary Tables, R code and Cytoscape files can be found at: <https://www.bradylab.org/resources/> or <https://github.com/agaudinier/Gaudinier2018>.

31. Deplancke, B., Vermeirssen, V., Arda, H. E., Martinez, N. J. & Walhout, A. J. Gateway-compatible yeast one-hybrid screens. *Cold Spring Harb. Protoc.* **2006**, <https://www.doi.org/10.1101/pdb.prot4590> (2006).
32. Deplancke, B., Dupuy, D., Vidal, M. & Walhout, A. J. A gateway-compatible yeast one-hybrid system. *Genome Res.* **14**, 2093–2101 (2004).
33. Shannon, P. et al. Cytoscape: a software environment for integrated models of biomolecular interaction networks. *Genome Res.* **13**, 2498–2504 (2003).
34. Wickham, H. *ggplot2: Elegant Graphics for Data Analysis* 2nd edn (Use R!) (Springer, Basel, 2016).
35. Townsley, B. T., Covington, M. F., Ichihashi, Y., Zumstein, K. & Sinha, N. R. BrAD-seq: breath adapter directional sequencing: a streamlined, ultra-simple and fast library preparation protocol for strand specific mRNA library construction. *Front. Plant Sci.* **6**, 366 (2015).
36. Davis, M. P., van Dongen, S., Abreu-Goodger, C., Bartonicek, N. & Enright, A. J. Kraken: a set of tools for quality control and analysis of high-throughput sequence data. *Methods* **63**, 41–49 (2013).
37. Li, H. et al. The Sequence Alignment/Map format and SAMtools. *Bioinformatics* **25**, 2078–2079 (2009).
38. Anders, S., Pyl, P. T. & Huber, W. HTSeq—a Python framework to work with high-throughput sequencing data. *Bioinformatics* **31**, 166–169 (2015).
39. Ritchie, M. E. et al. limma powers differential expression analyses for RNA-sequencing and microarray studies. *Nucleic Acids Res.* **43**, e47 (2015).
40. Huber, W. et al. Orchestrating high-throughput genomic analysis with Bioconductor. *Nat. Methods* **12**, 115–121 (2015).
41. Gutiérrez, R. A. et al. Qualitative network models and genome-wide expression data define carbon/nitrogen-responsive molecular machines in *Arabidopsis*. *Genome Biol.* **8**, R7 (2007).
42. Gutiérrez, R. A. et al. Systems approach identifies an organic nitrogen-responsive gene network that is regulated by the master clock control gene CCA1. *Proc. Natl Acad. Sci. USA* **105**, 4939–4944 (2008).
43. Patterson, K. et al. Distinct signalling pathways and transcriptome response signatures differentiate ammonium- and nitrate-supplied plants. *Plant Cell Environ.* **33**, 1486–1501 (2010).
44. Hu, H.-C., Wang, Y.-Y. & Tsay, Y.-F. AtCIPK8, a CBL-interacting protein kinase, regulates the low-affinity phase of the primary nitrate response. *Plant J.* **57**, 264–278 (2009).
45. Vidal, E. A., Moyano, T. C., Riveras, E., Contreras-López, O. & Gutiérrez, R. A. Systems approaches map regulatory networks downstream of the auxin receptor AFB3 in the nitrate response of *Arabidopsis thaliana* roots. *Proc. Natl Acad. Sci. USA* **110**, 12840–12845 (2013).
46. Edgar, R., Domrachev, M. & Lash, A. E. Gene Expression Omnibus: NCBI gene expression and hybridization array data repository. *Nucleic Acids Res.* **30**, 207–210 (2002).
47. Gautier, L., Cope, L., Bolstad, B. M. & Irizarry, R. A. affy—analysis of Affymetrix GeneChip data at the probe level. *Bioinformatics* **20**, 307–315 (2004).
48. Liseron-Monfils, C. V., Olson, A. & Ware, D. NECorr, a tool to rank gene importance in biological processes using molecular networks and transcriptome data. Preprint at <https://www.biorxiv.org/content/early/2018/05/21/326868> (2018).
49. Saaty, T. L. A scaling method for priorities in hierarchical structures. *J. Math. Psychol.* **15**, 234–281 (1977).
50. Saaty, T. L. Principles of the analytic hierarchy process. *Expert Judgment Expert Systems* **35**, 27–73 (1987).
51. Ma, C. & Wang, X. Application of the Gini correlation coefficient to infer regulatory relationships in transcriptome analysis. *Plant Physiol.* **160**, 192–203 (2012).
52. Poole, W., Gibbs, D. L., Shmulevich, I., Bernard, B. & Knijnenburg, T. A. Combining dependent *P*-values with an empirical adaptation of Brown's method. *Bioinformatics* **32**, i430–i436 (2016).
53. Fisher, R. A. Combining independent tests of significance. *Am. Stat.* **2**, 30 (1948).
54. Van Deun, K. et al. Testing the hypothesis of tissue selectivity: the intersection-union test and a Bayesian approach. *Bioinformatics* **25**, 2588–2594 (2009).
55. Yanai, I. et al. Genome-wide midrange transcription profiles reveal expression level relationships in human tissue specification. *Bioinformatics* **21**, 650–659 (2005).
56. Chitwood, D. H. & Topp, C. N. Revealing plant cryptotypes: defining meaningful phenotypes among infinite traits. *Curr. Opin. Plant Biol.* **24**, 54–60 (2015).
57. Gruber, B. D., Giehl, R. F., Friedel, S. & von Wirén, N. Plasticity of the *Arabidopsis* root system under nutrient deficiencies. *Plant Physiol.* **163**, 161–179 (2013).
58. Porra, R. J., Thompson, W. A. & Kriedemann, P. E. Determination of accurate extinction coefficients and simultaneous equations for assaying chlorophylls a and b extracted with four different solvents: verification of the concentration of chlorophyll standards by atomic absorption spectroscopy. *Biochim. Biophys. Acta Bioenerg.* **975**, 384–394 (1989).
59. Nemhauser, J. L., Hong, F. & Chory, J. Different plant hormones regulate similar processes through largely nonoverlapping transcriptional responses. *Cell* **126**, 467–475 (2006).
60. Bouguyon, E. et al. Multiple mechanisms of nitrate sensing by *Arabidopsis* nitrate transceptor NRT1.1. *Nat. Plants* **1**, 15015 (2015).
61. Gibbs, D. J. et al. Nitric oxide sensing in plants is mediated by proteolytic control of group VII ERF transcription factors. *Mol. Cell* **53**, 369–379 (2014).
62. Kissen, R. et al. Transcriptional profiling of an *Fd-GOGAT1/GLU1* mutant in *Arabidopsis thaliana* reveals a multiple stress response and extensive reprogramming of the transcriptome. *BMC Genomics* **11**, 190 (2010).
63. Fontaine, J.-X. et al. Characterization of a NADH-dependent glutamate dehydrogenase mutant of *Arabidopsis* demonstrates the key role of this enzyme in root carbon and nitrogen metabolism. *Plant Cell* **24**, 4044–4065 (2012).
64. Orlando, D. A., Brady, S. M., Koch, J. D., Dinnyen, J. R. & Benfey, P. N. Manipulating large-scale *Arabidopsis* microarray expression data: identifying dominant expression patterns and biological process enrichment. *Methods Mol. Biol.* **553**, 57–77 (2009).



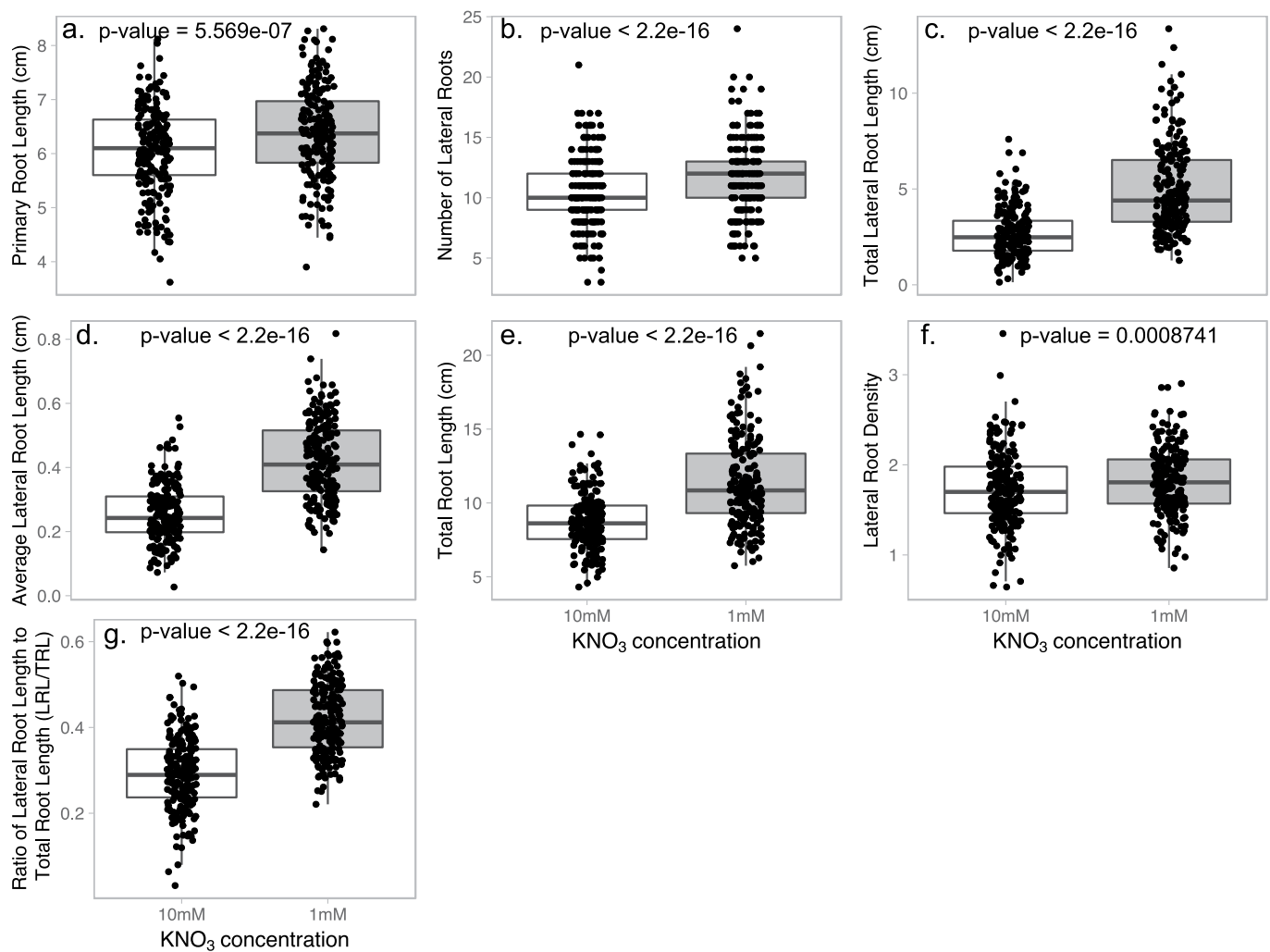
Extended Data Fig. 1 | Combinatorial interactions between transcription factors and promoters of genes associated with nitrogen metabolism, signalling and nitrogen-associated processes. Rectangles, promoters; ovals, transcription factors; diamonds, genes represented as both promoters and transcription factors. Nitrogen-associated biological processes are indicated by promoter colour. A grey line indicates

a transcription factor–promoter interaction. Light green, nitrogen transporter; yellow, organ growth; dark green, nitrate assimilation; light purple, nitrogen signalling; light blue, nitrogen-linked; orange, carbon metabolism; red, ethylene; dark blue, auxin; teal, carbon transporter; dark purple, amino acid metabolism; pink, transcription factors linked to nitrogen.



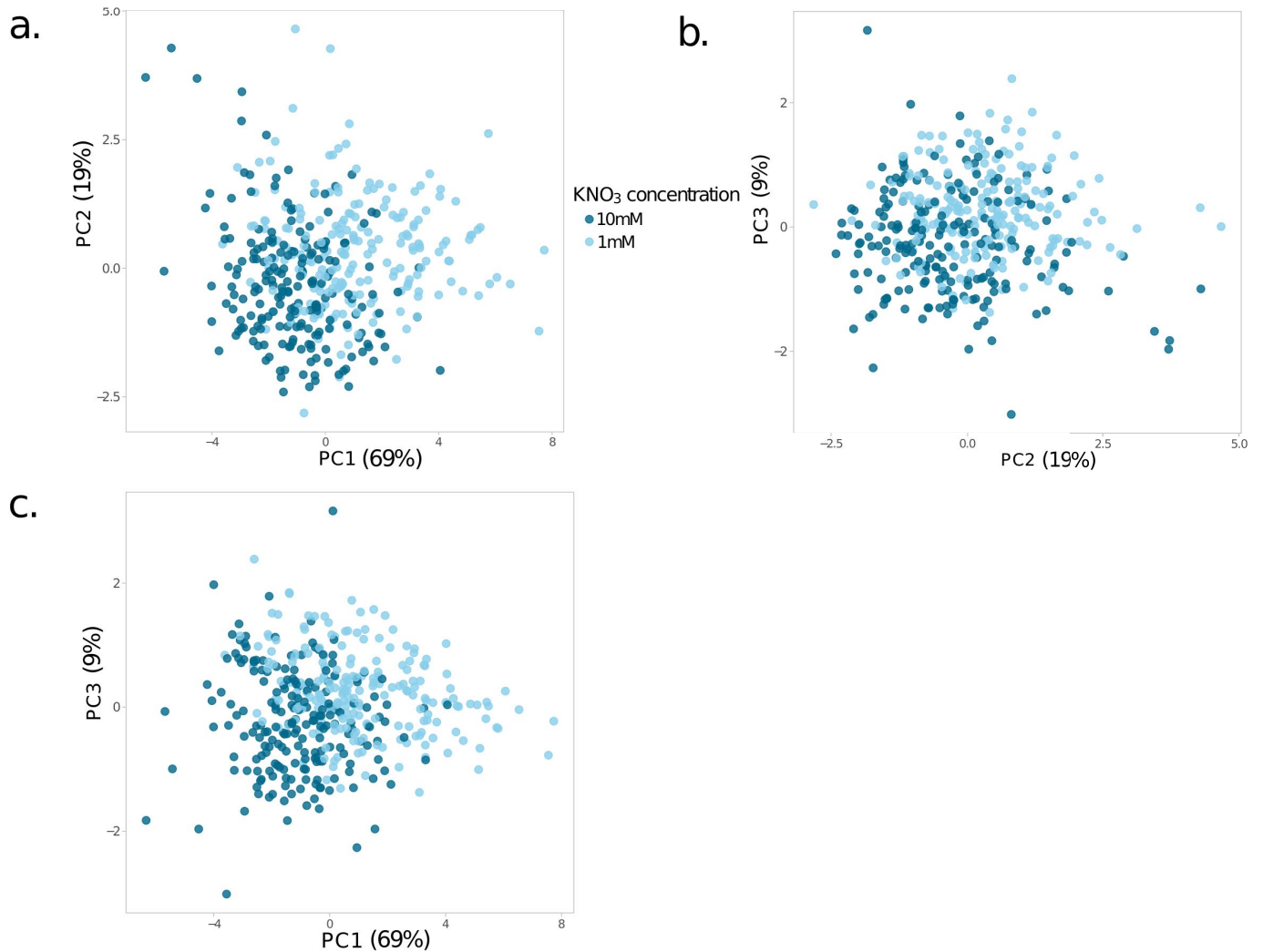
Extended Data Fig. 2 | Genes in the YNM regulated by hormone signalling. The YNM. Genes coloured in each panel are regulated by the CPK-NLP7 signalling cascade or indicated hormone. *P* value indicates significance for enrichment in the network using a two-sided Fisher's exact test. **a**, Genes regulated by the CPK-NLP7 signalling cascade (cyan). **b**, Genes regulated by abscisic acid (purple). **c**, Genes regulated by

ethylene (red). **d**, Genes regulated by methyl jasmonate (orange). **e**, Genes regulated by auxin (dark blue). **f**, Genes regulated by cytokinin (light blue). **g**, Genes regulated by brassinosteroid (green). **h**, Genes regulated by gibberellic acid (pink). Gene lists used for enrichment tests can be found in Supplementary Table 4.



Extended Data Fig. 3 | Wild-type root growth. RSA for wild-type (Col-0) nine-day-old seedlings in both limiting (1 mM) and sufficient (10 mM) KNO₃ conditions. **a–g.** Traits measured were primary root length (**a**), number of lateral roots (**b**), total lateral root length (**c**), average lateral root length (**d**), total root length (**e**), lateral root density (**f**) and the ratio of

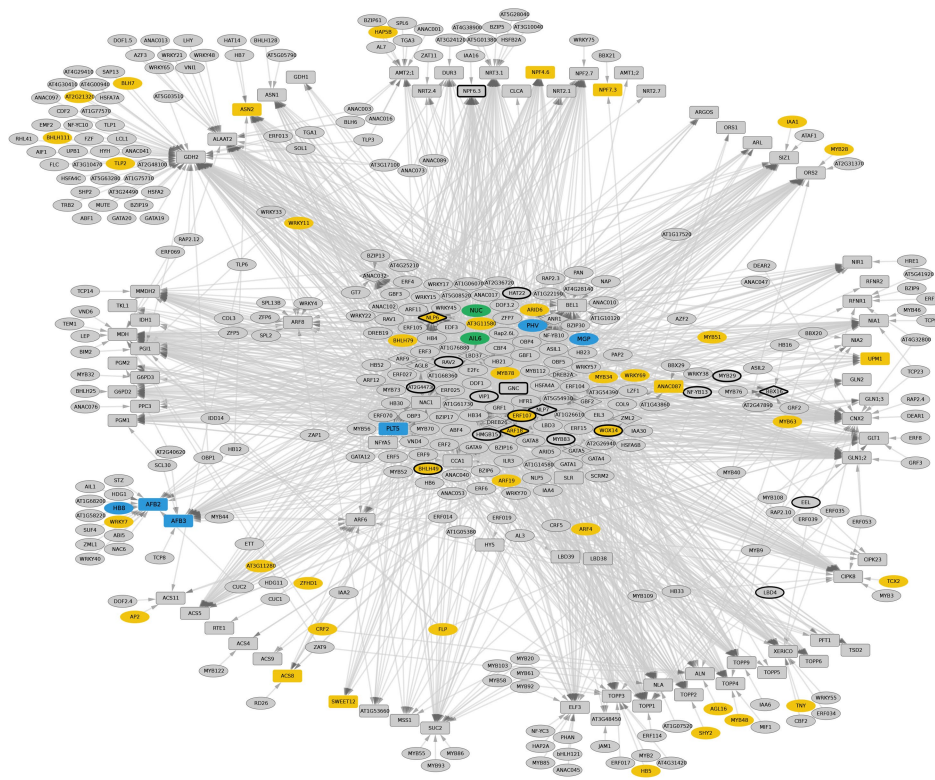
lateral root length contributing to the total root length (**g**). Box plots are centred at the data median and mark from the 25th to the 75th percentile. Individual measurements are plotted as black dots. $n = 209$ 1 mM KNO₃, $n = 201$ 10 mM KNO₃, P values were calculated using two-way ANOVAs.



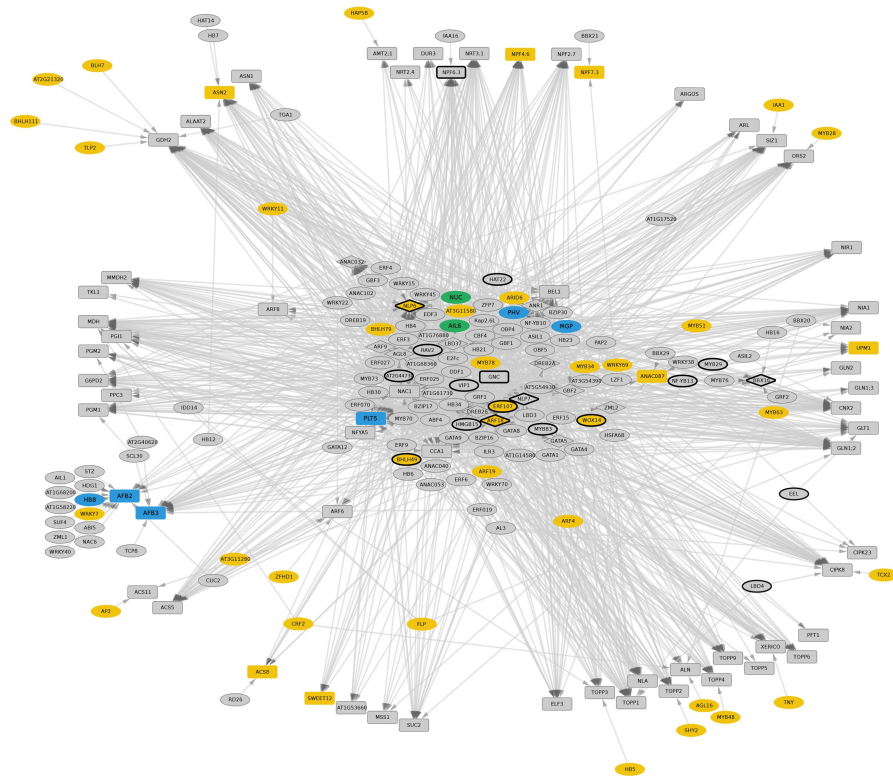
Extended Data Fig. 4 | Principal component analysis of all wild-type root traits. Dark blue, roots grown on 10 mM KNO₃; light blue, roots grown on 1 mM KNO₃. **a**, PC1 captures 69% of the variation and PC2

captures 19% of the variation. **b**, PC2 plotted with PC3 captures 9% of the variation. **c**, PC1 plotted with PC3 ($n = 209$ 1 mM KNO₃, $n = 201$ 10 mM KNO₃).

a.

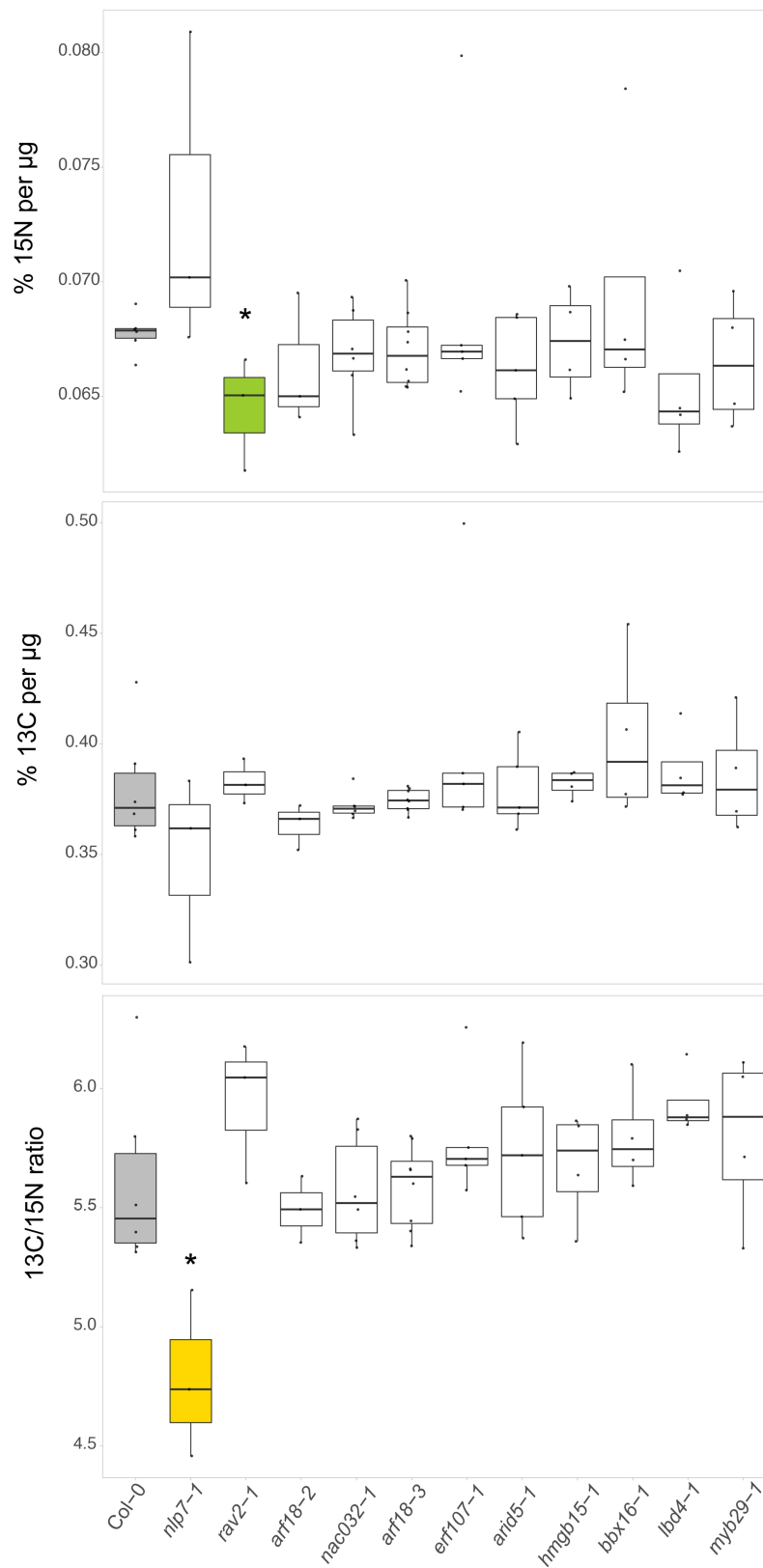


b.



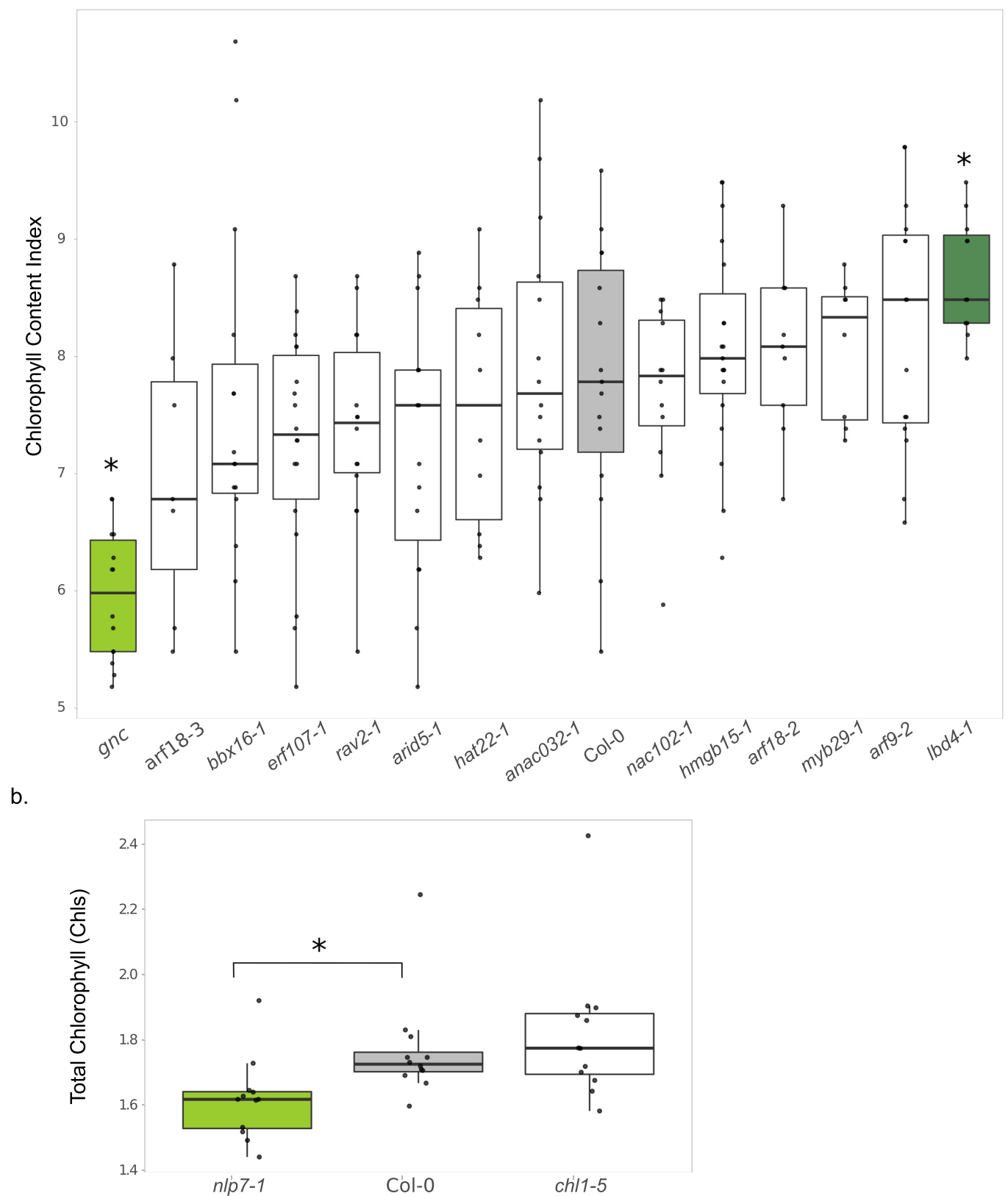
Extended Data Fig. 5 | YNM sub-network involved in nitrogen-associated influence on RSA. a. The YNM. Blue, genes associated with root length (Supplementary Table 10); yellow, genes associated with lateral root development²⁹; green, genes associated with root length and lateral

root development. Heavy black borders denote genes with a mutant root phenotype from this study. **b.** Sub-network of YNM with genes associated with RSA, and their first neighbour connections.



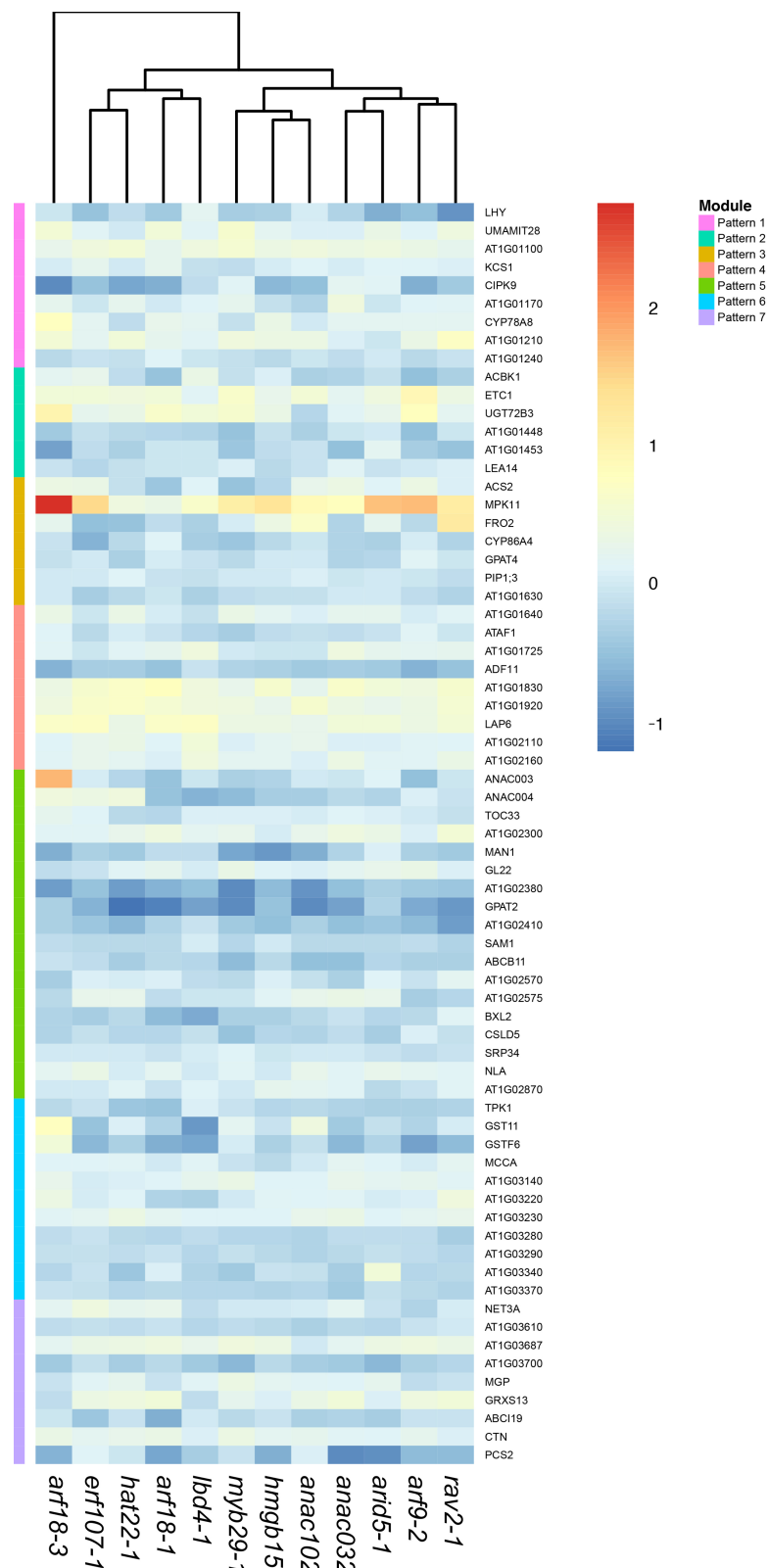
Extended Data Fig. 6 | Nitrogen, carbon and carbon:nitrogen ratio in transcription-factor mutants. **a**, Percentage of natural abundance of ^{15}N in total shoot tissue. **b**, Percentage of natural abundance of ^{13}C in total shoot tissue. **c**, Ratio of natural abundance of ^{13}C to ^{15}N . * $P < 0.05$ using

a two-way ANOVA; exact n and P values for the analysis can be found in Supplementary Table 10. Box plots are centred at the data median and mark from the 25th to the 75th percentile. Individual measurements are plotted as black dots.



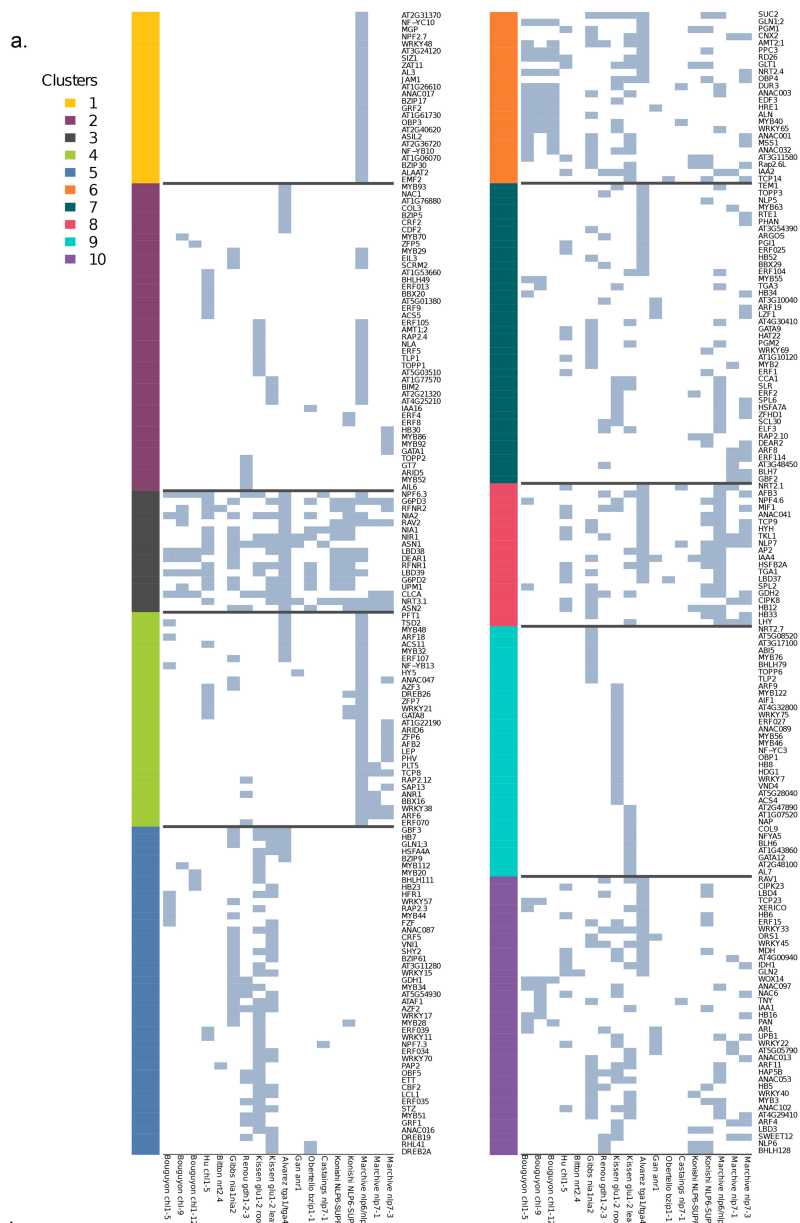
Extended Data Fig. 7 | Chlorophyll levels across transcription-factor mutants. **a.** Chlorophyll levels measured by chlorophyll content index. **b.** Total chlorophyll levels measured by ethanol extraction. * $P < 0.05$ using a two-way ANOVA; exact n and P values for the analysis can be found in

Supplementary Table 10. Box plots are centred at the data median and mark from the 25th to the 75th percentile. Individual measurements are plotted as black dots.



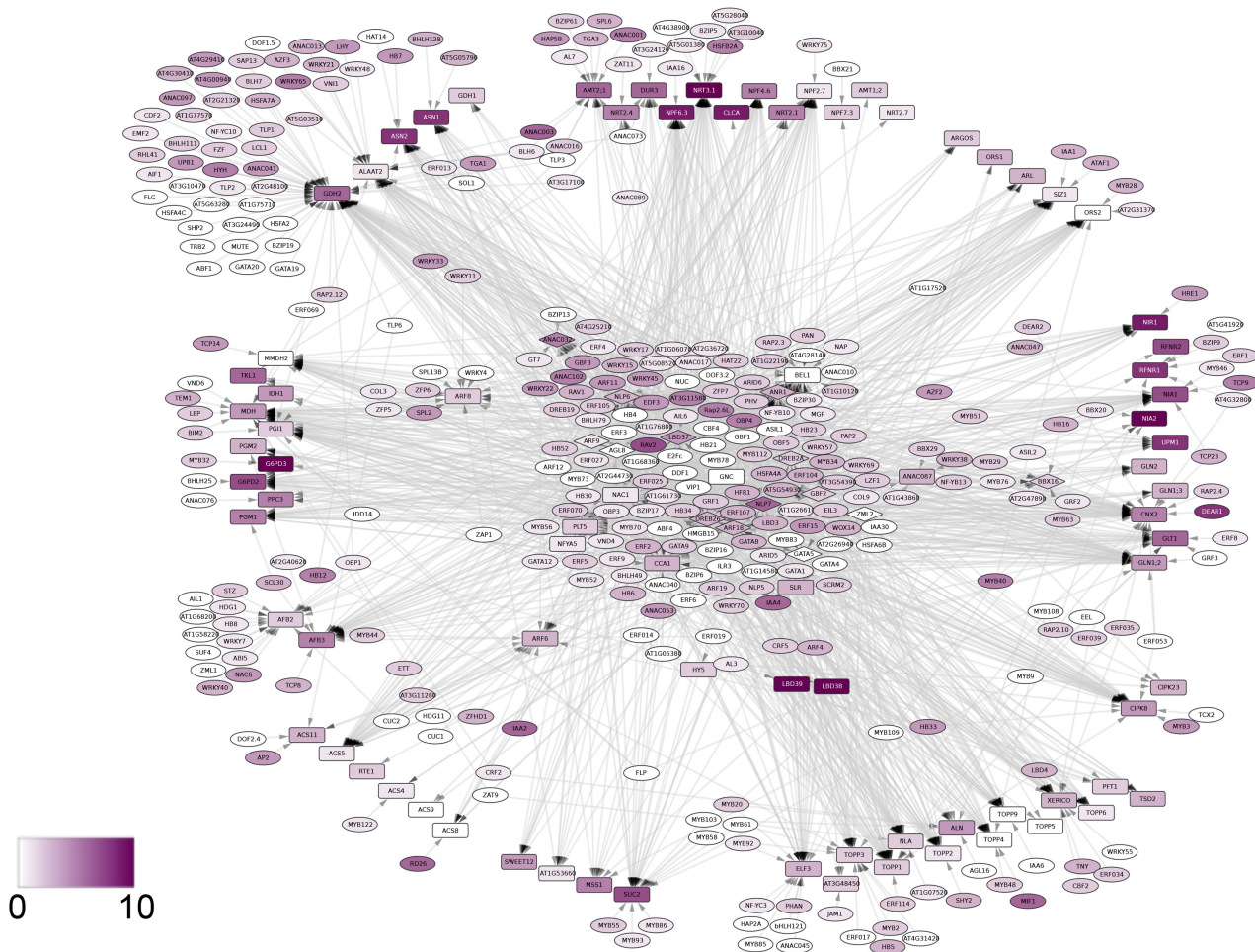
Extended Data Fig. 8 | Clustering of nitrogen-responsive genes in the root, in transcription-factor mutants. The expression in the root of genes responsive to nitrogen availability (Supplementary Table 15) was analysed in the mutant background of each transcription factor, and clustered using dominant pattern identification. Gene expression in each mutant

background was expressed as the \log_2 (fold change) of the expression of a given gene in 1 mM nitrate relative to 10 mM nitrate, and relative to its expression in wild type (\log_2 (fold change) in 1 mM nitrate relative to 10 mM nitrate). Colours on the y axis indicate each respective cluster or module. Gene names are indicated on the far right.



Extended Data Fig. 9 | Clusters of YNM genes in mutants of enzymes involved in nitrogen metabolism and their transcriptional regulators.
a, Clusters of genes significantly differentially expressed in the microarray

analysis of nitrogen-metabolism mutants and nitrogen transcriptional regulator mutants. **b**, Clusters overlaid on the YNM.



Extended Data Fig. 10 | Differentially expressed genes in the YNM in mutants of enzymes involved in nitrogen metabolism, and their transcriptional regulators. The YNM. Genes are coloured by the number

of mutant datasets in which they are found to be differentially expressed (white = 0, dark purple = 10).

The SWI/SNF complex is a mechanoregulated inhibitor of YAP and TAZ

Lei Chang^{1,6}, Luca Azzolin^{1,6}, Daniele Di Biagio^{1,6}, Francesca Zanconato¹, Giusy Battilana¹, Romy Lucon Xiccato¹, Mariaceleste Aragona¹, Stefano Giullitti¹, Tito Panciera¹, Alessandro Gandin², Gianluca Sigismondo³, Jeroen Krijgsvelde³, Matteo Fassan⁴, Giovanna Brusatin², Michelangelo Cordenonsi^{1,7*} & Stefano Piccolo^{1,5,7*}

Inactivation of ARID1A and other components of the nuclear SWI/SNF protein complex occurs at very high frequencies in a variety of human malignancies, suggesting a widespread role for the SWI/SNF complex in tumour suppression¹. However, the underlying mechanisms remain poorly understood. Here we show that ARID1A-containing SWI/SNF complex (ARID1A-SWI/SNF) operates as an inhibitor of the pro-oncogenic transcriptional coactivators YAP and TAZ². Using a combination of gain- and loss-of-function approaches in several cellular contexts, we show that YAP/TAZ are necessary to induce the effects of the inactivation of the SWI/SNF complex, such as cell proliferation, acquisition of stem cell-like traits and liver tumorigenesis. We found that YAP/TAZ form a complex with SWI/SNF; this interaction is mediated by ARID1A and is alternative to the association of YAP/TAZ with the DNA-binding platform TEAD. Cellular mechanotransduction regulates the association between ARID1A-SWI/SNF and YAP/TAZ. The inhibitory interaction of ARID1A-SWI/SNF and YAP/TAZ is predominant in cells that experience low mechanical signalling, in which loss of *ARID1A* rescues the association between YAP/TAZ and TEAD. At high mechanical stress, nuclear F-actin binds to ARID1A-SWI/SNF, thereby preventing the formation of the ARID1A-SWI/SNF-YAP/TAZ complex, in favour of an association between TEAD and YAP/TAZ. We propose that a dual requirement must be met to fully enable the YAP/TAZ responses: promotion of nuclear accumulation of YAP/TAZ, for example, by loss of Hippo signalling, and inhibition of ARID1A-SWI/SNF, which can occur either through genetic inactivation or because of increased cell mechanics. This study offers a molecular framework in which mechanical signals that emerge at the tissue level together with genetic lesions activate YAP/TAZ to induce cell plasticity and tumorigenesis.

Organs must have tissue-level checkpoints to preserve cell fates, repair wounds and avoid cancer. The highly related transcriptional regulators YAP and TAZ have recently emerged as a fundamental sensor through which cells read structural and architectural features of their tissue microenvironment using mechanotransduction³. Although YAP is sufficient to trigger several hallmarks of cancer, the normal microenvironment of adult tissues inhibits YAP/TAZ, such that emergence of a solid tumour must include the successful combination of YAP/TAZ activation and removal of YAP/TAZ inhibitors.

We set out to identify the nuclear factors that interact with YAP/TAZ using chromatin immunoprecipitation followed by mass spectrometry⁴, as the regulation of YAP/TAZ in the nuclear compartment has so far been largely overlooked in comparison to the available knowledge on YAP/TAZ regulation in the cytoplasm^{2,5}. The association of YAP/TAZ with several components of the SWI/SNF chromatin-remodelling complex attracted our attention (Extended Data Fig. 1a and Supplementary Table 1). The SWI/SNF complex contains a core ATPase involved in

nucleosome remodelling, either BRG1 or BRM, and other co-factors, such as ARID1A, the function of which is less well understood¹. YAP/TAZ associated with ARID1A, but not with ARID1B (Supplementary Table 1), which are known to define alternative SWI/SNF complexes¹. In several co-immunoprecipitation experimental set-ups, we found YAP in complex with ARID1A, BRG1, BRM and other components of the SWI/SNF complex (Fig. 1a–c and Extended Data Fig. 1b, c), also in the absence of chromatin (Extended Data Fig. 1f).

YAP associates with SWI/SNF through ARID1A. Indeed, depletion of *ARID1A*, but not of *ARID1B*, impaired the ability of YAP to be incorporated into BRG1- or BRM-containing SWI/SNF complexes (Fig. 1b and Extended Data Fig. 1c, g). Conversely, depletion of *BRM* (also known as *SMARCA2*) and *BRG1* (also known as *SMARCA4*) did not affect the association between endogenous ARID1A and YAP proteins (Fig. 1c). Purified recombinant YAP (or TAZ) and ARID1A proteins directly interact in vitro (Extended Data Fig. 1h) through physical association of their WW domain and PPxY motifs, respectively⁶ (Extended Data Fig. 1i–k).

We next assessed the functional relevance of SWI/SNF for YAP-dependent transcription. SWI/SNF inactivation caused induction of the YAP-TEAD luciferase reporter ($8 \times \text{GTIIC}$)⁷ through activation of endogenous YAP/TAZ (Fig. 1d) and also strongly enhanced the activity of co-transfected exogenous wild-type YAP (Extended Data Fig. 2a). By contrast, the WW-mutant YAP was insensitive to SWI/SNF depletion (Extended Data Fig. 2b). SWI/SNF inactivation by depletion of *ARID1A* (but not *ARID1B*) also induced the expression of several direct target genes of YAP/TAZ, in a manner that is rescued by concomitant YAP/TAZ depletion (Fig. 1e and Extended Data Fig. 2c, e). Of note, SWI/SNF depletion neither affects the subcellular localization of YAP/TAZ nor the phosphorylation level and stability of YAP (Extended Data Fig. 2f, g); therefore, SWI/SNF acted downstream of the classic modality of YAP/TAZ regulation that is dictated by Hippo kinases². Taken together, these findings indicate that SWI/SNF directly binds and inhibits nuclear YAP/TAZ, thus representing a new layer of YAP/TAZ regulation.

Our findings raised the possibility that YAP/TAZ regulation may contribute to SWI/SNF tumour-suppressive functions. There is indeed a remarkable overlap between the biological effects of YAP/TAZ activation and of SWI/SNF inactivation, including control of cell fate plasticity, gain of stemness properties and tumorigenesis^{1,8–10}. It is known that loss of SWI/SNF triggers the epithelial to mesenchymal transition and induces the gain of stem/progenitor-like properties in immortalized human mammary epithelial cells (HMECs)⁸. Notably, we found that activation of endogenous YAP/TAZ mediates the consequences of *BRG1* or *ARID1A* inactivation in these cells (Fig. 2a, b and Extended Data Fig. 3a–g). Therefore, SWI/SNF is a critical barrier that prevents the activation of endogenous YAP/TAZ; loss of control of this pathway in HMECs promotes YAP/TAZ-driven induction of stem/progenitor-like properties.

¹Department of Molecular Medicine, University of Padua, Padua, Italy. ²Department of Industrial Engineering and INSTM, University of Padua, Padua, Italy. ³German Cancer Research Center (DKFZ) and Heidelberg University, Heidelberg, Germany. ⁴Department of Medicine (DIMED), Surgical Pathology and Cytopathology Unit, Padua, Italy. ⁵IFOM, The FIRC Institute for Molecular Oncology, Padua, Italy. ⁶These authors contributed equally: Lei Chang, Luca Azzolin, Daniele Di Biagio. ⁷These authors jointly supervised this work: Michelangelo Cordenonsi, Stefano Piccolo. *e-mail: michelangelo.cordenonsi@unipd.it; piccolo@bio.unipd.it

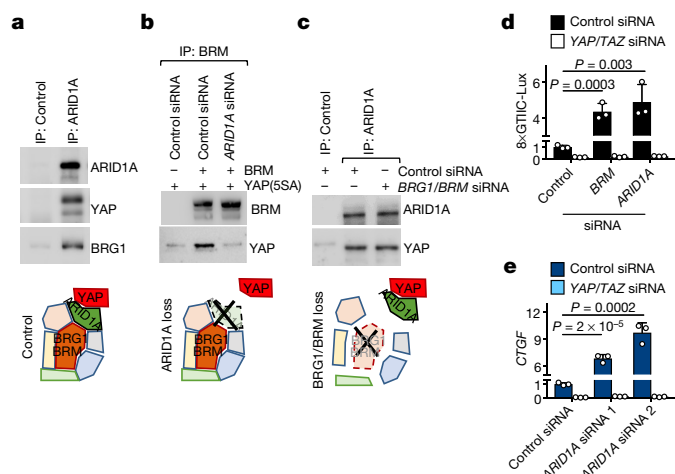


Fig. 1 | YAP interacts with SWI/SNF through ARID1A. **a–c**, Top, co-immunoprecipitation experiments. Bottom, schematics of the corresponding experimental results. See also Extended Data Fig. 1d, e. **a**, Endogenous ARID1A (top band) binds to endogenous YAP and BRG1 in co-immunoprecipitation experiments in MCF10AT cells. IP, immunoprecipitation. **b**, Binding of YAP to BRM requires ARID1A in HEK293T cells. **c**, Binding of YAP to ARID1A does not require BRG1 and BRM. **d**, Luciferase assay using the 8xGTIC-Lux reporter in HEK293 cells transfected with the indicated siRNAs. These inductions occurred without triggering epithelial to mesenchymal transition (Extended Data Fig. 2d). **d**, **e**, Data are mean + s.d. of $n = 3$ biologically independent samples; P values were determined by unpaired two-sided Student's t -test. Representative experiments are shown, which were repeated independently two (**a–c**) or three (**d**, **e**) times, all with similar results.

In *Drosophila* neuroblasts, the SWI/SNF complex acts as tumour suppressor, because it prevents cellular dedifferentiation back to a neural stem-cell (NSC) state¹¹. However, we found that the sole depletion

of *Brm* (also known as *Smarca2*) or *Arid1a* is insufficient to trigger a change of fate in cultures of fetal mouse hippocampal neurons (Extended Data Fig. 4a–c), possibly because mammalian neurons do not express the specific factors required for their dedifferentiation. We previously reported that fetal mouse hippocampal neurons are devoid of endogenous YAP expression and that expression of exogenous YAP is sufficient to convert these cells into NSC-like cells¹². Notably, inactivation of *Brm* or *Arid1a* by short hairpin RNA (shRNA), or genetic deletion of *Arid1a*, strongly potentiated the reprogramming of YAP-expressing neurons into NSCs (Fig. 2c and Extended Data Fig. 4b–e). Thus, YAP/TAZ are central for executing key biological responses downstream of SWI/SNF inactivation.

Next, we validated the role of ARID1A–SWI/SNF as a nuclear inhibitor of YAP/TAZ in vivo. Overactivation of YAP in the liver (for example, downstream of inactivation of the Hippo pathway by knocking out *Nf2*) leads to YAP-driven tumorigenesis but only after a long period of latency^{13,14}, suggesting that additional genetic or epigenetic events must be in place to induce the tumorigenic potential of YAP. We hypothesized that removal of the SWI/SNF complex might be one of these events. We used mice bearing tamoxifen-inducible Cre recombinase under the control of the hepatocyte-specific albumin promoter (*Alb^{creERT2}*) to induce genetic ablation of *Nf2* and *Arid1a* in adult hepatocytes (liver knockout (LKO)) (Extended Data Fig. 5a, b). YAP nuclear staining was clearly induced around the portal areas of *Nf2* LKO mice (Extended Data Fig. 5c). In spite of this, only a modest induction of transcriptional activity of YAP/TAZ and moderate phenotypic effects were observed (that is, ductular reactions with few proliferating cells) but no tumours developed up to four months after Cre activation (Fig. 2d, e and Extended Data Fig. 5d, e). Instead, at the same time point, all mice with combined knockout of *Nf2* and *Arid1a* exhibited liver overgrowth (Fig. 2d), with widespread areas of neoplasia, including full-blown cholangiocarcinomas and hepatocellular carcinomas (Fig. 2e). An extensive degree of proliferation was evident in tumours and across the remaining hepatocytes (Extended Data Fig. 5d), also including the hundreds-fold induction of the fetal/tumour marker

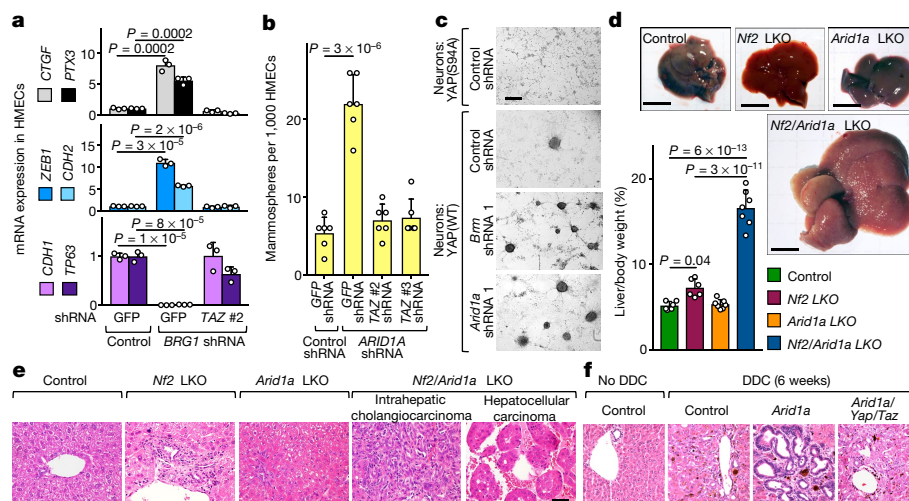


Fig. 2 | Loss of SWI/SNF promotes YAP/TAZ-driven biological effects. **a**, Depletion of BRG1 in HMECs causes changes in the expression of YAP/TAZ target genes (*CTGF* and *PTX3*) and the indicated markers for mesenchymal transition (*ZEB1* and *CDH2* (which encodes N-cadherin)) and epithelial differentiation (*CDH1* (which encodes E-cadherin) and *TP63* (which encodes Δ NP63)), in a TAZ-dependent manner. Data are mean + s.d. of $n = 3$ biologically independent samples. **b**, Mammosphere formation assay (which measures stem/progenitor-like properties) of HMECs transfected with the indicated shRNAs. Data are mean + s.d. of $n = 6$ biologically independent samples. **c**, Neurospheres emerging from neurons infected with inducible YAP-encoding vectors and the indicated shRNA-encoding lentiviral vectors. As a negative control, we used a transcriptionally inactive version of YAP (YAP(S94A)). Scale bar, 300 μ m. See also Extended Data Fig. 4b, c, d, Gross liver images and liver-to-body weight ratio from control

mice ($n = 6$ mice), and *Nf2* ($n = 6$ mice), *Arid1a* ($n = 7$ mice) and *Nf2/Arid1a* ($n = 7$ mice) liver knockout (LKO) mutant mice, four months after tamoxifen treatment. Scale bars, 1 cm. Data are mean + s.d. All animals were included. **e**, Liver sections from mice described in **d** were stained with haematoxylin and eosin. HCC, hepatocellular carcinomas; iCCA, intrahepatic cholangiocarcinomas. Scale bar, 100 μ m. **f**, Haematoxylin and eosin-stained liver sections from control ($n = 10$), *Arid1a* LKO ($n = 12$), and *Arid1a/Yap/Taz* LKO ($n = 15$) mice treated with tamoxifen and then fed a DDC diet, compared to control mice fed a normal diet ($n = 10$). Scale bar, 100 μ m. P values were determined by unpaired two-sided Student's t -test (**a**, **b**) and one-way analysis of variance (ANOVA) with Tukey's multiple comparisons test (**d**). **a–c**, **e**, **f**. Representative experiments are shown, which were repeated independently three (**a**, **b**) or four (**c**) times and of all mice (**e**, **f**), all with similar results.

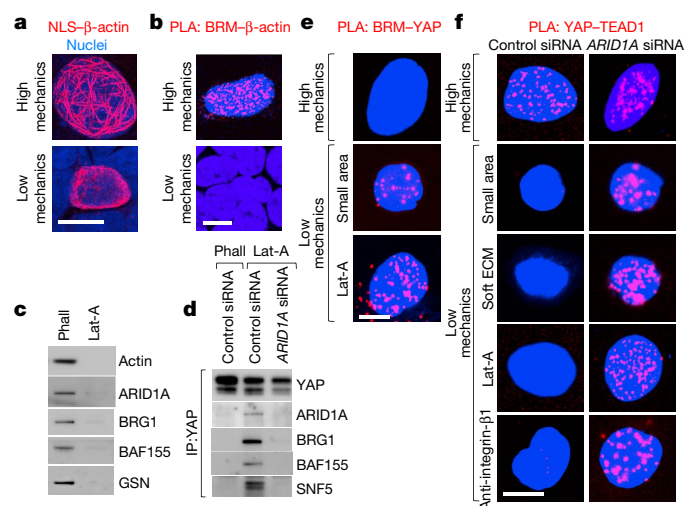


Fig. 3 | Mechanical regulation of the association of YAP/TAZ with the SWI/SNF complex or TEAD. **a**, Visualization of Flag-tagged NLS- β -actin filaments in nuclei of HEK293T cells using anti-Flag immunofluorescence. Scale bar, 10 μ m. No nuclear actin filaments were detected in cells transfected with a non-polymerizable variant of actin (see Extended Data Fig. 6a). **b**, Representative pictures of PLA detecting the interaction between endogenous BRM and Flag-tagged NLS- β -actin in the nucleus of HEK293T cells, which experienced high mechanical inputs (that is, spread cells; 94.7% PLA-positive) or confined on a small adhesive area (in a dense culture²²; 0% PLA-positive). See specificity controls using BRM and BRG1 siRNA (Extended Data Fig. 6b). **c**, Biotinylated phalloidin pull-down experiments using HEK293T cells, comparing phalloidin (Phall) and latrunculin A (Lat-A) treatment. See Methods and Extended Data Fig. 6d. Gelsolin serves as specificity control for purification of F-actin. **d**, In latrunculin-A-treated MCF10AT cells, endogenous YAP binds to SWI/SNF in an ARID1A-dependent manner. See also Extended Data Fig. 6f. ARID1A was loaded on a separate gel. **e**, Representative PLA images detecting the interaction between endogenous BRM and a version of YAP forced to enter the nucleus (NLS-YAP) in MCF10A cells. Cells were allowed to stretch over rigid ECM (high mechanics; 0% PLA-positive) or, for low mechanical experiments, allowed to adhere to a small area (100 μ m²; 11.25% PLA-positive) or treated with latrunculin A (18.75% PLA-positive). See also Extended Data Fig. 6g. **f**, Representative PLA images detecting the interaction between endogenous TEAD and NLS-YAP in MCF10A cells, stretched over a rigid ECM (see Methods) or experiencing low cell mechanics by adhesion to a small adhesive area, soft ECM or treatment with latrunculin A or anti-integrin- β 1 antibodies. The YAP-TEAD association (high mechanics; 46.3% PLA-positive) is lost under low mechanical conditions (low mechanics; 0% PLA-positive), but is rescued after depletion of ARID1A (PLA-positive: small, 44%; soft, 49.8%; latrunculin A, 48.5%; anti-integrin, 67%). See also Extended Data Fig. 6j. All panels show representative experiments that were repeated independently three times.

Afp. Notably, YAP/TAZ transcriptional activity was strongly induced in livers from *Nf2/Arid1a* LKO mice compared to livers from *Nf2* LKO mice (Extended Data Fig. 5e). The liver knockout of *Arid1a* alone was inconsequential; mice remained healthy with an ostensibly normal liver for the entire duration of our experiments (Fig. 2d, e and Extended Data Fig. 5d, e). This indicates that increasing YAP/TAZ nuclear levels after Hippo pathway inactivation is insufficient for their full activation due to their nuclear inhibition by ARID1A-SWI/SNF.

Chronic tissue damage is a fundamental driver of liver carcinogenesis, causing continuous rounds of injury and compensatory proliferation¹⁵. To assess the relevance of the ARID1A-YAP/TAZ association in this context, we fed *Arid1a* LKO mice a diet supplemented with the toxic compound 3,5-diethoxycarbonyl-1,4-dihydrocollidine (DDC) for six weeks. DDC induced the appearance of ductular reactions around the portal areas in wild-type livers (Fig. 2f). Notably, in all *Arid1a* LKO mice that were fed with a DDC diet, we found areas of cholangiocarcinomatous transformation, with clear signs of atypia, massive

proliferation of tumour cells and increased *Afp* expression (Fig. 2f and Extended Data Fig. 5f–h). By contrast, these lesions were absent from livers of DDC-treated *Arid1a/Yap/Taz* triple-mutant mice, which were similar to control DDC-treated mice (Fig. 2f and Extended Data Fig. 5f, g). Thus, inhibition of YAP/TAZ is an essential mediator of the tumour-suppressive function of SWI/SNF in vivo.

Data presented above indicate that the interaction between YAP/TAZ and ARID1A-SWI/SNF represents a modality to inhibit YAP/TAZ activity inside the nucleus. We next investigated how this interaction is regulated. Here we focused on modulation by mechanical inputs through the F-actin cytoskeleton. YAP/TAZ respond to changes in cell shape and physical forces that are transmitted by the tissue to ultimately influence the organization of the F-actin cytoskeleton³, including nuclear F-actin organization^{16,17}. We verified that the organization of nuclear F-actin changed markedly in cells that experienced low compared to high levels of mechanical signalling. By expressing β -actin fused to a nuclear localization sequence (NLS- β -actin)¹⁸ in HEK293T cells, we found that stretched cells (high mechanics) displayed a network of nuclear actin filaments that crossed the whole nucleoplasm (Fig. 3a), whereas a finer, almost exclusively perilaminar distribution was observed in cells confined to small adhesive areas (low mechanics) (Fig. 3a).

The SWI/SNF complex has previously been reported to associate with purified F-actin in vitro¹⁹, raising the possibility that it could be modulated by mechanical signals in cells. Notably, using in situ proximity-ligation assays (PLA, a method that enables the investigation of protein–protein interactions while preserving the structural integrity of the cells), we found an association between nuclear F-actin and endogenous SWI/SNF in nuclei of stretched cells, whereas at low mechanics (that is, on small adhesive areas) cells were almost devoid of signal (Fig. 3b). A form of β -actin²⁰ that is unable to polymerize (NLS- β -actin(R62D)) did not interact with SWI/SNF in stretched cells (Extended Data Fig. 6c), supporting the view that only polymerized actin can interact with SWI/SNF. In line with this hypothesis, purification of endogenous F-actin using biotinylated phalloidin on streptavidin beads leads to robust co-purification of the ARID1A-SWI/SNF complex (Fig. 3c), but not in cells treated with the F-actin inhibitor latrunculin A (Fig. 3c). Notably, by sequential salt extraction of nuclei (see Methods), ARID1A-SWI/SNF co-purified in the same fractions as F-actin when we used extracts in which F-actin was preserved with phalloidin (Extended Data Fig. 6e). By contrast, in the presence of latrunculin A, a substantial amount of ARID1A-SWI/SNF relocated to fractions that did not contain actin (Extended Data Fig. 6e), similar to the PLA protein–protein interactions in cells grown in conditions of high or low mechanical stress (Fig. 3b).

We then investigated whether nuclear F-actin might interfere with the interactions between ARID1A-SWI/SNF and YAP. As shown in Fig. 3d, no ARID1A-SWI/SNF–YAP associations could be detected in human mammary epithelial (MCF10A) cell extracts prepared under conditions preserving F-actin or when SWI/SNF was co-purified with endogenous YAP specifically in the absence of F-actin; however, this interaction was abolished by concomitant depletion of ARID1A (Fig. 3d), as expected if ARID1A is required for YAP/TAZ incorporation into this pool of SWI/SNF (see Fig. 1). These results were recapitulated in the nuclei of intact MCF10A cells by PLA: YAP interacts with endogenous BRM only in mechanically inhibited cells (Fig. 3e and Extended Data Fig. 6g).

Mechanistically, we found that the inhibitory association of YAP/TAZ with ARID1A-SWI/SNF is in fact alternative to the binding of YAP/TAZ to their DNA-binding platform, TEAD, which is necessary for YAP/TAZ-driven transcription²¹. We showed this first in co-immunoprecipitation experiments, showing that ARID1A associates with YAP, but not with TEAD proteins (Extended Data Fig. 6h). Then, we used PLA to monitor the dynamic of the YAP-TEAD1 interaction in nuclei of cells cultured under conditions of high compared to low mechanical signalling. As shown in Fig. 3f and Extended Data Fig. 6i, the YAP-TEAD association in MCF10A cell nuclei was severely inhibited

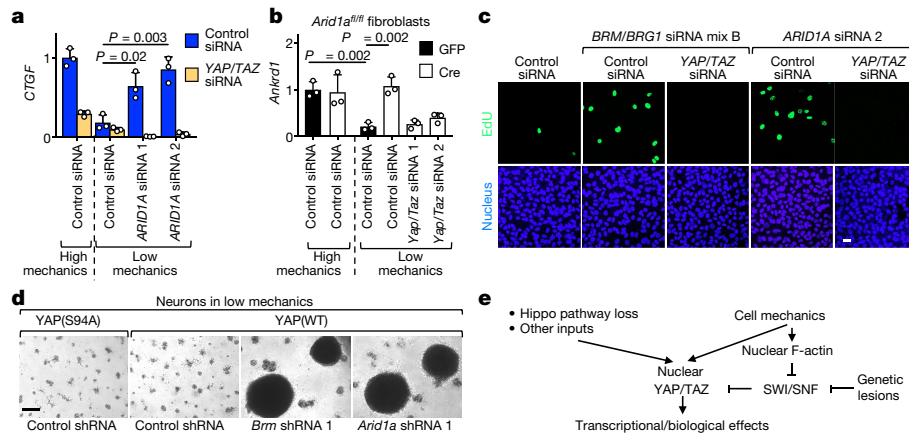


Fig. 4 | Loss of SWI/SNF rescues YAP/TAZ activities and biological effects in mechanically impaired cells. **a**, **b**, Under low mechanical conditions, ARID1A loss rescues expression of *CTGF* in MCF10A cells (**a**) and *Ankrd1* in *Arid1a*^{fl/fl} fibroblasts (**b**; Cre and GFP indicate cells transduced with Cre- or GFP-encoding adenoviral vectors, respectively) in a YAP/TAZ-dependent manner. ARID1A depletion had no effect on YAP/TAZ localization (Extended Data Fig. 7a). Data are mean \pm s.d. of $n = 3$ biologically independent samples. **c**, Cell proliferation (measured by EdU (5-ethynyl-2'-deoxyuridine) incorporation) in confluent MCF10A

at low mechanical regimes, when YAP/TAZ are associated with SWI/SNF; these conditions included inhibition of cellular mechanotransduction extracellularly (by culturing cells on small areas or soft extracellular matrix (ECM)), at the level of the integrin (with anti-integrin- $\beta 1$ blocking antibodies) or intracellularly (by using the Rho-inhibitor C3 or inhibiting F-actin with latrunculin A). Notably, under the same conditions, depletion of *ARID1A* was sufficient to restore the YAP-TEAD association (Fig. 3f). Taken together, the results suggest the following model: in mechanically impaired cells, YAP/TAZ are sequestered within the ARID1A-containing pool of SWI/SNF complexes, away from TEAD. Conversely, in mechanically challenged cells, nuclear F-actin structures engage with ARID1A-SWI/SNF and induce YAP/TAZ detachment from that pool of SWI/SNF and their binding to TEAD.

Following the above model, we next tested whether ARID1A-SWI/SNF inactivation could rescue YAP/TAZ activity in mechanically inhibited cells. In epithelial cells (MCF10A, HaCaT) that experienced low mechanical stimulation, or in which mechanotransduction was inhibited (either by attenuating ECM mechanics or inhibiting intracellular mechanotransduction), the expression of YAP/TAZ target genes was strongly downregulated, as expected⁷; however, in all conditions, YAP/TAZ activity could be restored after *ARID1A* depletion using short interfering RNA (siRNA). Moreover, such rescue of gene expression in mechanically impaired cells was YAP/TAZ-dependent (Fig. 4a and Extended Data Fig. 7b, c). Similar results were obtained in *Arid1a*^{fl/fl} mouse fibroblasts, in which the deletion of *Arid1a* was achieved by infection with an adenoviral vector encoding Cre (Fig. 4b and Extended Data Fig. 7d). Therefore, our data indicate that ARID1A functionally contributes to the mechanical inhibition of YAP/TAZ, and that YAP/TAZ are key mediators of the effect of ARID1A inactivation.

If raising cell mechanics attenuates the ARID1A-SWI/SNF-YAP/TAZ inhibitory axis through the F-actin cytoskeleton, then experimentally raising F-actin should be sufficient to overcome such inhibition. We tested this hypothesis through depletion of two F-actin severing proteins, ADF and Cofilin1, which act as cytoskeletal checkpoints of YAP/TAZ activation²²; loss of ADF/Cofilin1 potentially raised YAP/TAZ activity, to levels that could not be further modulated by ARID1A inactivation (Extended Data Fig. 7e). This is consistent with the results obtained in fibroblasts cultured on a stiff ECM (Fig. 4b, high mechanics) and with the notion that, at maximal mechanical signalling, the ARID1A-SWI/SNF-YAP/TAZ inhibitory axis is already disabled, making *ARID1A* depletion under these conditions essentially inconsequential.

cells transfected as indicated. Scale bar, 30 μ m. **d**, Representative images of neurospheres emerging from neurons plated on a soft ECM and infected with inducible YAP-encoding vectors and the indicated shRNA-encoding lentiviral vectors. Scale bar, 300 μ m. **e**, Model of the main conclusions. High mechanics, stiff ECM (**a**, **b**, **d**) or a sparse monolayer (**c**). Low mechanics, soft ECM (**a**, **b**, **d**) or a dense monolayer (**c**). *P* values were determined by unpaired two-sided Student's *t*-test. **a**–**d** Representative experiments are shown, which were repeated independently two (**c**), three (**a**, **b**) or four (**d**) times, all with similar results.

We next determined whether the loss of SWI/SNF induced reactivation of YAP/TAZ-driven biological responses in otherwise mechanically inhibited cells. YAP/TAZ inactivation by lowered cell mechanics is a main inducer of contact inhibition of proliferation (CIP) in a post-confluent epithelial sheet²². Indeed, contact inhibition of proliferation can be revoked (leading to S phase re-entry) through substantial Hippo-independent mechanical activation of YAP/TAZ, either by stretching the cell monolayer or remodelling the F-actin cytoskeleton^{22,23}. Phenocopying the effects of raised cell mechanics, SWI/SNF inactivation also triggered S phase re-entry in post-confluent epithelial sheets in a YAP/TAZ-dependent manner (Fig. 4c and Extended Data Fig. 8a).

Finally, we determined the role of cell mechanics in regulating YAP-driven changes in cell fate. For this, we used YAP-induced reprogramming of neurons into NSC-like cells¹², and hypothesized that such reprogramming should be disabled if cells are placed on a soft ECM, where the inhibitory function of ARID1A-SWI/SNF on YAP/TAZ is predominant. Indeed, only few neurospheres emerged from YAP-expressing wild-type neurons plated on a soft ECM compared to stiff ECM (Extended Data Fig. 8b); more relevantly, shRNA-mediated depletion of *Arid1a* or *Brm* rescued the ability of YAP to reprogram neurons into NSC-like cells on soft ECM (Fig. 4d and Extended Data Fig. 8c–e).

Our results shed light on the mechanisms of SWI/SNF tumour suppression, an aspect of cancer biology that has remained unclear. We found that SWI/SNF binds to and inhibits YAP/TAZ; this inhibitory function is restricted to the ARID1A-containing fraction of SWI/SNF complexes. YAP/TAZ are essential and sufficient for the unfolding of complex cellular phenotypes inherent to inactivation of ARID1A-SWI/SNF, occurring at exceedingly high frequency in human malignancies¹. Note that, in this scenario, pools of SWI/SNF that do not consist of ARID1A-SWI/SNF, such as those containing ARID1B (here shown to be irrelevant for YAP/TAZ regulation), remain in place to carry out other SWI/SNF functions, such as chromatin remodelling. In line with this, in living tissues and explanted cells, ARID1A appears to be a largely dispensable protein, for which a tumour-suppressive role becomes apparent under genetic or environmental conditions that lead to nuclear accumulation of YAP/TAZ. Of note, others before us have noted the interaction between SWI/SNF and TAZ, but concluded that SWI/SNF positively cooperated with TAZ-induced transcription of some targets²⁴. We have been unable to confirm the generality of those conclusions in our analyses, which included multiple redundant

reagents, cellular systems and in vivo genetic models and which all instead point to the opposite conclusion.

A second element of general interest concerns the mechanisms of YAP/TAZ mechanotransduction. Our results suggest the existence of a pathway that could be streamlined as follows: cell mechanics promotes the accumulation of nuclear F-actin, which binds the ARID1A–SWI/SNF pool, thus relieving YAP/TAZ from SWI/SNF inhibition. Biochemically, our data suggest that mechanical signals tune the ARID1A–SWI/SNF–YAP/TAZ inhibitory axis by controlling the levels and structural organization of the nuclear pool of F-actin. This nuclear pathway complements Hippo-independent and Hippo-regulated YAP/TAZ mechanotransduction that occurs in the cytoplasm^{3,22}.

Our data argue in favour of a paradigm in which, to fully unleash YAP/TAZ activity, at least two requirements need to be met: promotion of YAP/TAZ nuclear accumulation and SWI/SNF inhibition. Inactivation of the Hippo pathway alone is insufficient to fully enable YAP/TAZ activity in absence of concomitant inactivation of ARID1A. This indicates that the response to a number of signals that promote YAP/TAZ nuclear localization—including loss of Hippo signalling—would also concomitantly require a proficient mechanical environment to surpass the ARID1A–SWI/SNF barrier (Fig. 4e). It also suggests that nuclear levels of YAP/TAZ that are too low or transient to elicit any effect in normal cells may become above-threshold after genetic or mechanical inhibition of ARID1A–SWI/SNF. More generally, the data show how a genetic lesion, such as loss of *ARID1A* in tumour cells, may serve as means to increase cellular responsiveness to an epigenetic signal, such as mechanotransduction.

Online content

Any methods, additional references, Nature Research reporting summaries, source data, statements of data availability and associated accession codes are available at <https://doi.org/10.1038/s41586-018-0658-1>.

Received: 12 December 2017; Accepted: 7 September 2018;

Published online 31 October 2018.

- Kadoch, C. & Crabtree, G. R. Mammalian SWI/SNF chromatin remodeling complexes and cancer: mechanistic insights gained from human genomics. *Sci. Adv.* **1**, e1500447 (2015).
- Totaro, A., Panciera, T. & Piccolo, S. YAP/TAZ upstream signals and downstream responses. *Nat. Cell Biol.* **20**, 888–899 (2018).
- Panciera, T., Azzolin, L., Cordenonsi, M. & Piccolo, S. Mechanobiology of YAP and TAZ in physiology and disease. *Nat. Rev. Mol. Cell Biol.* **18**, 758–770 (2017).
- Rafiee, M. R., Girardot, C., Sigismondo, G. & Krijgsvel, J. Expanding the circuitry of pluripotency by selective isolation of chromatin-associated proteins. *Mol. Cell* **64**, 624–635 (2016).
- Ege, N. et al. Quantitative analysis reveals that actin and Src-family kinases regulate nuclear YAP1 and its export. *Cell Syst.* **6**, 692–708 (2018).
- Chen, H. I. & Sudol, M. The WW domain of Yes-associated protein binds a proline-rich ligand that differs from the consensus established for Src homology 3-binding modules. *Proc. Natl Acad. Sci. USA* **92**, 7819–7823 (1995).
- Dupont, S. et al. Role of YAP/TAZ in mechanotransduction. *Nature* **474**, 179–183 (2011).
- Wang, H. et al. BRCA1/FANCD2/BRG1-driven DNA repair stabilizes the differentiation state of human mammary epithelial cells. *Mol. Cell* **63**, 277–292 (2016).
- Cordenonsi, M. et al. The Hippo transducer TAZ confers cancer stem cell-related traits on breast cancer cells. *Cell* **147**, 759–772 (2011).
- Zanconato, F., Cordenonsi, M. & Piccolo, S. YAP/TAZ at the roots of cancer. *Cancer Cell* **29**, 783–803 (2016).
- Eroglu, E. et al. SWI/SNF complex prevents lineage reversion and induces temporal patterning in neural stem cells. *Cell* **156**, 1259–1273 (2014).

- Panciera, T. et al. Induction of expandable tissue-specific stem/progenitor cells through transient expression of YAP/TAZ. *Cell Stem Cell* **19**, 725–737 (2016).
- Zhang, N. et al. The Merlin/NF2 tumor suppressor functions through the YAP oncoprotein to regulate tissue homeostasis in mammals. *Dev. Cell* **19**, 27–38 (2010).
- Benhamouche, S. et al. Nf2/Merlin controls progenitor homeostasis and tumorigenesis in the liver. *Genes Dev.* **24**, 1718–1730 (2010).
- Bakiri, L. & Wagner, E. F. Mouse models for liver cancer. *Mol. Oncol.* **7**, 206–223 (2013).
- Plessner, M., Melak, M., Chinchilla, P., Baarlink, C. & Grosse, R. Nuclear F-actin formation and reorganization upon cell spreading. *J. Biol. Chem.* **290**, 11209–11216 (2015).
- Grosse, R. & Vartiainen, M. K. To be or not to be assembled: progressing into nuclear actin filaments. *Nat. Rev. Mol. Cell Biol.* **14**, 693–697 (2013).
- Baarlink, C., Wang, H. & Grosse, R. Nuclear actin network assembly by formins regulates the SRF coactivator MAL. *Science* **340**, 864–867 (2013).
- Rando, O. J., Zhao, K., Janmey, P. & Crabtree, G. R. Phosphatidylinositol-dependent actin filament binding by the SWI/SNF-like BAF chromatin remodeling complex. *Proc. Natl Acad. Sci. USA* **99**, 2824–2829 (2002).
- Miralles, F., Posern, G., Zaromytidou, A. I. & Treisman, R. Actin dynamics control SRF activity by regulation of its coactivator MAL. *Cell* **113**, 329–342 (2003).
- Zanconato, F. et al. Genome-wide association between YAP/TAZ/TEAD and AP-1 at enhancers drives oncogenic growth. *Nat. Cell Biol.* **17**, 1218–1227 (2015).
- Aragona, M. et al. A mechanical checkpoint controls multicellular growth through YAP/TAZ regulation by actin-processing factors. *Cell* **154**, 1047–1059 (2013).
- Benham-Pyle, B. W., Pruitt, B. L. & Nelson, W. J. Mechanical strain induces E-cadherin-dependent Yap1 and β -catenin activation to drive cell cycle entry. *Science* **348**, 1024–1027 (2015).
- Skibinski, A. et al. The Hippo transducer TAZ interacts with the SWI/SNF complex to regulate breast epithelial lineage commitment. *Cell Rep.* **6**, 1059–1072 (2014).

Acknowledgements We thank A. Fujimura for help with neuron preparation; G. Della Giustina for micropattern fabrication; V. Guzzardo for histology; C. Frasson and G. Basso for FACS; D. M. Livingston for HMECs and plasmids; D. J. Pan, M. Giovannini, Z. Wang, P. Chambon, and I. De Curtis and R. Brambilla for gifts of mice; R. Treisman for *ACTB* (encoding β -actin) cDNAs; L. Naldini for plasmids; S. Dupont for performing the initial experiments leading to biochemical identification of SWI/SNF and for the protocol to perform F-actin pull-down; Gianluca Greci and Mona Suryana (MBI-Singapore) and the MBI microfabrication facility team for the supply of quartz masks. This work is supported by AIRC Special Program Molecular Clinical Oncology ‘5 per mille’, by an AIRC PI-Grant, by a MIUR-FARE grant, and by Epigenetics Flagship project CNR-MIUR grants to S.P. This project has received funding from the European Research Council (ERC) under the European Union’s Horizon 2020 research and innovation programme (DENOOSTEM grant agreement No 670126 to S.P.).

Reviewer information Nature thanks M. Sudol, P. Wade and the other anonymous reviewer(s) for their contribution to the peer review of this work.

Author contributions L.C. carried out experiments in vitro, and L.A. carried out experiments on mice. Roles of other coauthors: D.D.B., molecular biology and IFs; D.D.B. and R.L.X., liver experiments; G.Ba. and F.Z., molecular biology and preparation of samples for ChIP–MS; L.C. and T.P., neuronal reprogramming; S.G., hydrogel preparation; G.S. and J.K. for mass spectroscopy; M.F., histology and histopathological evaluations; G.Br. and A.G., microfabrication. S.P. and M.C. conceived the initial hypothesis and experimental design, and planned, discussed and organized the work. L.C., L.A., F.Z., M.C. and S.P. wrote the manuscript.

Competing interests The authors declare no competing interests.

Additional information

Extended data is available for this paper at <https://doi.org/10.1038/s41586-018-0658-1>.

Supplementary information is available for this paper at <https://doi.org/10.1038/s41586-018-0658-1>.

Reprints and permissions information is available at <http://www.nature.com/reprints>.

Correspondence and requests for materials should be addressed to M.C. or S.P.

Publisher’s note: Springer Nature remains neutral with regard to jurisdictional claims in published maps and institutional affiliations.

METHODS

Reagents and plasmids. Latrunculin A, phalloidin, cerivastatin and tamoxifen were obtained from Sigma-Aldrich. Doxycycline was obtained from Calbiochem. Growth-factor-reduced Matrigel was obtained from Corning. C3 was obtained from Cytoskeleton Inc. Dasatinib was obtained from Selleckchem. Fasudil was obtained from Tocris. Anti-integrin- β 1 antibody (P5D2) was obtained from DSHB, University of Iowa. Cre- and GFP-expressing adenoviruses were obtained from the Gene Transfer Vector Core, University of Iowa.

HA-human YAP(5SA) (all five serines, which are phosphorylated by LATS1 and LATS2, were mutated to alanines in YAP), Flag-human YAP(WT), Flag-YAP(S94A) and Flag-human YAP(5SA) were cloned in pcDNA3.1 for transient expression, or in pBABE retroviral plasmids to establish stable cell lines. The pBABE-Puro empty vector was used as control for retroviral transduction. siRNA-insensitive Flag-YAP(WW1^{mut}), Flag-YAP(WW2^{mut}) and Flag-YAP(WW1/2^{mut}) were generated by PCR from the corresponding original cDNAs (a gift from M. Sudol, Addgene plasmids 19046, 19047 and 19048, respectively²⁵) and subcloned in pcDNA3.1 for transient expression. pCS2-Flag-mouse TAZ(WT) or pCS2-Flag-mouse TAZ(Δ WW) (deletion of residues 110–159) were as in a previous publication²⁶. pCS2-Flag-BRM was obtained by subcloning Flag-BRM from pBABEpuro-Flag-human BRM (a gift from R. Kingston, Addgene plasmid 1961²⁷) into pCS2. pCS2-Flag-BRG1 was obtained by subcloning Flag-BRG1 from pBABEpuro-Flag-human BRG1 (a gift from R. Kingston, Addgene plasmid 1959²⁷) into pCS2. pcDNA6-V5-ARID1A(WT) was a gift from I.-M. Shih (Addgene plasmid 39311²⁸). pcDNA6-V5-ARID1A(PPxA) (containing the PPAY¹⁴⁸/PPGY⁹¹⁵ to PPAA¹⁴⁸/PPGA⁹¹⁵ mutations) was generated as follows: the N-terminal cDNA fragment of ARID1A containing the Y148A/Y915A mutations was synthesized by GeneScript and swapped into pcDNA6-V5-ARID1A(WT) by using the NheI/HpaI restriction sites.

For doxycycline-inducible expression of YAP in MCF10A cells, cDNA of NLS-YAP was subcloned in pCW-MCS, obtained by substituting the sequence between NheI and BamHI of pCW57.1 (a gift from D. Root, Addgene 41393) with a new multiple cloning site (MCS).

For inducible expression of YAP in mouse neurons, FUW-tetO-YAP(WT) and FUW-tetO-YAP(S94A) (deposited as Addgene plasmids 84009 and #84010¹², respectively) were used in combination with FUDeltaGW-rtTA (a gift from K. Hochedlinger, Addgene 19780²⁹). Empty vector (FUW-tetO-MCS, Addgene 84008) was used as negative control.

The constructs for control shRNA, *Arid1a* shRNA and *Brm* shRNA expression in primary neurons were prepared by cloning the control shRNA (shCo), mouse *Arid1a* shRNA (shArid1a#2 and shArid1a#2), mouse *Brm* shRNA (shBrm#1 and shBrm#2) sequences (see 'RNA interference') into the pLKO.1-puro lentiviral vector (a gift from B. Weinberg, Addgene 8453³⁰) according to the manufacturer's protocol.

For stable shRNA infection of HMECs, we used pLKO.1-puro lentiviral vectors expressing control shRNA (see RNA interference), *BRG1* shRNA⁸ and *ARID1A* shRNA (from Sigma-Aldrich) in combination with pSUPER-RETRO-BLASTI vectors containing the GFP or TAZ RNA-interference sequences (as previously described⁹).

Plasmids encoding Flag-NLS- β -actin(WT) and Flag-NLS- β -actin(R62D) were generated by PCR from original cDNAs provided by R. Treisman²⁰ and cloned in pcDNA3.1.

For glutathione S-transferase (GST) pull-down experiments, full-length mouse TAZ and human YAP1 were cloned in pGEX4T1.

All constructs were confirmed by sequencing.

Micropatterns. The following procedure was used to make the adhesive micropatterns: a layer of photoresist (MICROPOSIT S1805 G2 Positive Photoresist, Dow) was spin-coated (3,000 r.p.m. for 30 s) on a glass substrate, functionalized with trimethoxysilylpropyl methacrylate, and cured at 120 °C for 1 min. The positive resist was patterned by ultraviolet-light (UV) exposure for 8 s in air by irradiation with a collimated UV lamp at 365 nm (UV365, Reinraumtechnik lanz) through a quartz chromium mask with the desired pattern (arrays of 10 μ m \times 10 μ m squares). The exposed areas, those around the squares, were removed by immersing the substrate in the developer solution MF 319 for 8 s. To polymerize non-adhesive polyacrylamide brushes outside of the squares, a drop of acrylamide solution (8% w/v in water with 0.225 w/v of ammonium persulfate and 1.5% v/v tetramethylethylenediamine) was put between the patterned glass and a blank coverslip and left to react for 30 min in air. The sandwich structure was detached by immersing it for 30 min in water; the functionalized pattern was then put in water overnight to completely remove unpolymerized acrylamide. The unexposed resist (the square areas) was stripped in acetone for 30 s and rinsed in water. Finally, after sterilization under UV light, the square areas were functionalized with fibronectin by putting a drop of protein solution (10 μ g ml⁻¹ in water) on top, leaving it to react for 1 h and then rinsing it in PBS.

Cell lines and treatments. HMECs were a gift from D. Livingston⁸ (DFCI) and were cultured in MEGM medium (Lonza). MCF10A and MCF10AT (also called MII) cells were a gift from F. Miller (Karmanos) and were cultured in DMEM/F12 (Gibco) with 5% horse serum, glutamine and antibiotics, freshly supplemented with insulin (Sigma-Aldrich), EGF (Peprotech), hydrocortisone (Sigma-Aldrich) and cholera toxin (Sigma-Aldrich). HEK293 or HEK293T cells were from ATCC and were cultured in DMEM (Gibco) supplemented with 10% fetal bovine serum (FBS), glutamine and antibiotics. HaCaT cells were a gift from N. Fusenig (DKFZ) and were cultured in DMEM (Gibco) supplemented with 10% FBS, glutamine and antibiotics. HEK293, HEK293T, MCF10A, MCF10AT and HaCaT were authenticated by DSMZ/Eurofins Genomics. All cell lines tested negative for mycoplasma contamination.

For experiments with NLS-YAP-transduced MCF10A cells, cells were treated with 0.5 μ g ml⁻¹ doxycycline in culture medium for the whole duration of the experiments.

For stiff versus soft ECM experiments, cells plated on standard fibronectin-coated tissue culture supports or on fibronectin-coated >40 KPa hydrogels (produced as described previously⁷) were considered as cultured on a 'stiff ECM' under the high mechanical conditions, as indicated in the figures. For experiments on soft ECM, 5,000–10,000 cells per cm² were seeded in a drop on top of 0.7-kPa fibronectin-coated hydrogels; after attachment, the wells containing the hydrogels were filled with the appropriate medium. Cells were collected for immunofluorescence or RNA extraction after 24 h. For experiments with cells experiencing small cell-ECM adhesion in ultra-confluent monolayers²², we plated 200,000 cells per cm² in the appropriate well (that is, plated at approximately 150% confluency). Cells were collected for immunofluorescence or RNA extraction after 48 h. For experiments with fibronectin-coated micropatterns, cells were seeded on fibronectin-coated micropatterns (100 μ m²; 'small area' in Fig. 3); after attachment, floating cells were removed and wells were filled with medium; cells were fixed 24 h later. These cells were compared to cells plated on an unpatterned/unconfined adhesive area (defined as stretched cells and labelled as 'high mechanics').

Latrunculin A was used at a final concentration of 0.5 μ M for the time indicated in the description of F-actin pull-down, sequential salt extraction and in situ proximity ligation assay

experiments. C3 was used at a final concentration of 0.5 μ g ml⁻¹ in culture medium for 24 h. Dasatinib was used at a final concentration of 0.1 μ M for 24 h. Fasudil was used at a final concentration of 10 μ M for 24 h. Anti-integrin- β 1 was used at a final concentration of 0.23 μ g ml⁻¹ for 24 h. Cerivastatin was used at a final concentration of 5 μ M for 24 h.

Primary fibroblasts (from biopsies of adult mouse ears) were cultured in DMEM (Gibco) supplemented with 20% FBS, glutamine and antibiotics. For the experiments depicted in Fig. 4b and Extended Data Fig. 7d, fibroblasts were transduced with adenoviral vectors and transfected with the indicated siRNAs (day 0), replated either on a soft or a stiff ECM (day 1), and then collected for RNA extraction 48 h later (day 3).

RNA interference. siRNA transfections were done with Lipofectamine RNAi-MAX (Thermo Fisher Scientific) in antibiotics-free medium according to the manufacturer's instructions. Sequences of siRNAs are provided in Supplementary Table 3.

Western blot. Cells were collected in lysis buffer (50 mM HEPES (pH 7.5), 100 mM NaCl, 50 mM KCl, 1% Triton X-100, 5% glycerol, 0.5% NP-40, 2 mM MgCl₂, 1 μ M DTT, and phosphatase and protease inhibitors) and lysed at 4 °C by sonication. Extracts were quantified using the Bradford method. Proteins were run on 4–12% NuPAGE-MOPS acrylamide gels (ThermoFisher) and transferred onto PVDF membranes by wet electrophoretic transfer. Blots were blocked with 0.5% non-fat dry milk and incubated overnight at 4 °C with primary antibodies. Secondary antibodies were incubated for 1 h at room temperature, and then blots were developed with chemiluminescent reagents. Images were acquired with Image Quant LAS 4000 1.2 (GE healthcare).

For western blot: anti-YAP/TAZ (sc-101199), anti-BAF53A (sc-137062 or sc47808), anti-BRG1 (sc-10768 or sc-17796), anti-lamin B (sc-6216), anti-SMARCC1 (also known as BAF155) (sc-137138 or sc-9746), anti-SNF5 (sc-166165), anti-vimentin (sc-7557-r), anti-gelsolin (sc-57509) and anti-TEAD4 (sc-101184) were from Santa Cruz; anti-ARID1A (HPA005456), anti-SNF5 (HPA018248), anti-TAZ (HPA007415) and anti- β -actin (A5316) were from Sigma-Aldrich; anti-YAP (ab52771), anti-histone H3 (ab1791) and anti-BRM (ab15597) were from Abcam; anti-GAPDH (MAB347) and anti-ARID1A (04-080) monoclonal antibodies were from Millipore. Anti-E-cadherin (610181) and anti-TEAD1 (610922) were from BD. Anti-phosphorylated YAP (S127) (CST 4911) was from Cell Signaling Technology.

Horseradish-peroxidase-conjugated anti-Flag (clone M2, A8592) was from Sigma-Aldrich, anti-HA (A190-107P) was from Bethyl and the anti-V5 antibody was from Abcam (ab27671).

Unless otherwise specified, loading controls for all blots were run on the same gel. **F-actin pull-down experiments.** For the experiments depicted in Fig. 3c, cells were plated in sparse conditions and treated for 4 h with latrunculin A (0.5 μ M) or biotinylated phalloidin (40 ng ml⁻¹). After treatment, cells were washed with prewarmed HBSS once and collected in 'actin lysis buffer' (20 mM HEPES (pH 7.5), 50 mM KCl, 0.1% Triton X-100, 5% glycerol, 0.1% NP-40, 5 mM MgCl₂, 1 μ M DTT, 10 μ M MG115, 10 μ M MG132, 1 mM ATP, 20 μ M phosphocreatine di(Tris) salt (P1937, Sigma-Aldrich), and phosphatase and protease inhibitors). All buffers were freshly prepared and prewarmed at room temperature. Cells were scraped and mechanically lysed by passing ten times through a 26G-needle syringe at room temperature. For latrunculin-A-treated cells, latrunculin A was also present in the buffers (1 μ M) used for collecting cells and pull-down experiments to avoid any F-actin re-assembly; for the biotinylated-phalloidin-treated cells, biotinylated phalloidin was also present in the buffers used for collecting cells and pull-down experiments (40 ng ml⁻¹). Extracts were cleared by centrifugation (10,000g in low-retention Eppendorf tubes) at room temperature and supernatants were immediately (we never froze supernatants) incubated at room temperature for 3 h with streptavidin-conjugated resin (Sigma-Aldrich) and biotinylated phalloidin (1 μ g ml⁻¹). Phalloidin-bound complexes were then washed with actin lysis buffer three times at room temperature, resuspended in SDS sample buffer, incubated at 95°C for 3 min, and subjected to SDS-PAGE and western blot analysis.

Sequential salt extraction. We have adapted a sequential salt-extraction assay for evaluating the chromatin-binding affinities of the SWI/SNF complex in HEK293T cells. All buffers were freshly prepared and prewarmed at room temperature before use and all procedures were carried out at room temperature. Nuclei were isolated from confluent HEK293T cells grown on 10-cm dishes by hypotonic lysis in 5 ml buffer 1 (20 mM HEPES (pH 7.5), 10 mM KCl, 0.1% NP-40, 5% glycerol, 5 mM MgCl₂, 1 μ M DTT, 10 μ M MG115, 10 μ M MG132, 1 mM ATP, 20 μ M phosphocreatine di(Tris) salt, and phosphatase and protease inhibitors) for 5 min. After centrifugation at 600g for 3 min, the supernatant was saved for western blot analysis, whereas the nuclear pellet was sequentially resuspended and centrifuged at 6,000g for 3 min in buffer 1 supplemented with increasing concentrations of NaCl (from 0 to 600 mM), as indicated in Extended Data Fig. 6e. The released proteins in each fraction were directly analysed by SDS-PAGE and western blot.

For latrunculin-A-treated cells (0.5 μ M, 4 h treatment), latrunculin A (1 μ M) was also present in all the buffers used for collecting cells and the salt-extraction assay, to avoid any F-actin re-assembly; for phalloidin-treated cells, phalloidin (50 μ M) was also present in all the buffers used for collecting cells and the salt-extraction assay.

Co-immunoprecipitation of endogenous proteins. For immunoprecipitation experiments of endogenous proteins shown in Fig. 1a, c and Extended Data Fig. 6h, cells were plated (day 0), transfected with the indicated siRNAs (day 1), collected two days after siRNA transfection (day 4) and lysed by sonication in lysis buffer (50 mM HEPES (pH 7.5), 100 mM NaCl, 50 mM KCl, 1% Triton X-100, 5% glycerol, 0.5% NP-40, 2 mM MgCl₂, 1 μ M DTT, and phosphatase and protease inhibitors). Extracts were cleared by centrifugation and incubated with anti-ARID1A antibody (sc-98441, Santa Cruz) or control anti-HA antibody (sc-805, Santa Cruz), immobilized on protein A-sepharose beads at 4°C for 3 h. Immunocomplexes were then washed with cold lysis buffer three times, resuspended in SDS sample buffer, incubated at 95°C for 3 min and subjected to SDS-PAGE and western blot analysis.

For the experiments depicted in Fig. 3d, cells were plated in sparse conditions, and treated and collected as described above for F-actin pull-down experiments. Extracts were cleared by centrifugation at room temperature and incubated with anti-YAP antibody (ab52771, Abcam) immobilized on protein A-Sepharose beads for 3 h at room temperature. Immunocomplexes were then washed with actin lysis buffer (see 'F-actin pull-down experiments') three times at room temperature, resuspended in SDS sample buffer, incubated at 95°C for 3 min, and subjected to SDS-PAGE and western blot analysis.

Co-immunoprecipitation of tagged proteins. Cells were collected and lysed by sonication in lysis buffer (50 mM HEPES (pH 7.5), 100 mM NaCl, 50 mM KCl, 1% Triton X-100, 5% glycerol, 0.5% NP-40, 2 mM MgCl₂, 1 μ M DTT, and phosphatase and protease inhibitors) and extracts were cleared by centrifugation at 4°C. Extracts were incubated for 3 h at 4°C with anti-Flag resin (Sigma-Aldrich). Immunocomplexes were then washed with cold lysis buffer three times, resuspended in SDS sample buffer, incubated at 95°C for 3 min, and subjected to SDS-PAGE and western blot analysis. Inputs were loaded based on Bradford assay measurements. In particular, for Fig. 1b, Extended Data Fig. 1c, g, i-k, we used lysates from HEK293T cells transfected with the indicated plasmids (concentrations of plasmids were as follows). For Fig. 1b: Flag-BRM, 83 ng cm⁻²; HA-YAP(5SA), 17 ng cm⁻². For Extended Data Fig. 1c: Flag-BRG1, 83 ng cm⁻²; HA-YAP(5SA), 17 ng cm⁻². For Extended Data Fig. 1g: HA-YAP(5SA), 17 ng cm⁻²; Flag-BRG1, 83 ng cm⁻². For Extended Data Fig. 1i: Flag-YAP(WT), 83 ng cm⁻²; Flag-YAP(WW1^{mut}), 83 ng cm⁻²; Flag-YAP(WW2^{mut}), 83 ng cm⁻²; Flag-YAP(WW1/2^{mut}), 83 ng cm⁻². For Extended Data Fig. 1j: Flag-TAZ(WT),

83 ng cm⁻²; Flag-TAZ(Δ WW), 83 ng cm⁻². For Extended Data Fig. 1k: Flag-YAP, 83 ng cm⁻²; V5-ARID1A(WT), 166 ng cm⁻²; V5-ARID1A(PPxA), 166 ng cm⁻². Lysates were collected 48 h after transfection. Where indicated, siRNAs were transfected 24 h before DNA transfection. For Extended Data Fig. 1b, we used lysates from empty vector-transduced MCF10A cells or MCF10A cells constitutively expressing Flag-YAP(5SA).

GST pull-down experiments. For the experiment in Extended Data Fig. 1h, V5-ARID1A was purified from transfected HEK293T cells. In brief, cells were transfected with pcDNA6-V5-ARID1A, collected and lysed by sonication in lysis buffer (50 mM HEPES (pH 7.5), 100 mM NaCl, 50 mM KCl, 1% Triton X-100, 5% glycerol, 0.5% NP-40, 2 mM MgCl₂, 1 μ M DTT, and phosphatase and protease inhibitors) and extracts were cleared by centrifugation at 4°C. Extracts were incubated for 3 h at 4°C with anti-V5 resin (Sigma-Aldrich). After washing three times with lysis buffer (2 min for each wash at room temperature), V5-ARID1A protein was eluted by incubation with V5 peptide (V7754, Sigma-Aldrich) in lysis buffer. V5 resin was eliminated by centrifugation. For the GST pull-down experiments, beads with purified proteins (GST-YAP or GST-TAZ, as indicated) were incubated with purified V5-ARID1A in lysis buffer for 3 h at 4°C. After three washes, GST pull-down proteins were analysed by western blot.

For the experiment in Extended Data Fig. 1f, beads with purified GST-YAP were incubated for 3 h at 4°C with the 0-mM NaCl fraction, which contained proteins released from DNase-treated nuclei of HEK293T cells. To prepare such extracts, nuclei of HEK293T cells were isolated from confluent HEK293T cells grown on 10-cm dishes by hypotonic lysis in 5 ml buffer 1 for 5 min. After centrifugation at 600g for 3 min, the supernatant was saved for western blot analysis, whereas the nuclear pellet was subjected to DNase treatment for 30 min at 37°C in buffer 1 supplemented with 1 mM CaCl₂. After centrifugation at 6,000g for 3 min, the supernatant was discarded and the DNase-treated nuclear pellet was sequentially resuspended and centrifuged at 6,000g for 3 min in buffer 1 supplemented with increasing concentrations of NaCl (from 0 to 600 mM). The 0-mM NaCl fraction was used for GST pull-down experiments. After three washes in buffer 1, GST pull-down proteins were then analysed by western blot.

Identification of native YAP/TAZ complexes by mass spectrometry. Live cells were cross-linked with 1% formaldehyde (Sigma-Aldrich) in culture medium for 10 min at room temperature before collection. Lysis was achieved by consecutive incubations in lysis buffer 1 (50 mM HEPES, pH 7.5, 10 mM NaCl, 1 mM EDTA, 10% glycerol, 0.5% NP-40 and 0.25% Triton X-100), lysis buffer 2 (10 mM Tris-HCl pH 8, 200 mM NaCl, 1 mM EDTA and 0.5 mM EGTA) and lysis buffer 3 (10 mM Tris-HCl pH 8, 200 mM NaCl, 1 mM EDTA, 0.5 mM EGTA, 0.1% sodium-deoxycholate and 0.5% N-lauroylsarcosine), followed by sonication with a Branson Sonifier 450D. Immunoprecipitation was performed by incubating cleared extracts (corresponding to 2×10^6 cells) with 20 μ g of antibody (anti-YAP: EP1674Y, Abcam; anti-TAZ: HPA007415, Sigma-Aldrich; pre-immune rabbit IgG: I5006, Sigma-Aldrich) and 100 μ l of Dynabeads-protein G (Invitrogen). After extensive washing, immunoprecipitates were eluted in 7.5% SDS, 200 mM DTT and de-crosslinked. After alkylation with iodoacetamide, proteins were purified with SP3 beads as previously described³¹ resuspended in 50 mM ammonium bicarbonate and digested with trypsin. Peptides were subjected to SP3 cleanup and they were eluted in 0.1% trifluoroacetic acid. Samples were analysed on an Orbitrap Fusion mass spectrometer (Thermo Fisher).

Quantitative real-time PCR (qPCR). Cells were collected using the RNeasy Mini Kit (Qiagen) for total RNA extraction, and contaminant DNA was removed by DNase treatment. Total RNA from fibroblasts (Fig. 4b and Extended Data Fig. 7d) and from livers (Extended Data Fig. 5e, g) was extracted using TriZOL (ThermoFisher) and NucleoSpin RNA (MACHERY-NAGEL, 740955.250), respectively. qPCR analyses were carried out on reverse-transcribed cDNAs with QuantStudio5 (applied Biosystems, ThermoFisher Scientific) and analysed with QuantStudio Design & Analysis software (version 1.4.3). Expression levels are always normalized to *GAPDH*. PCR oligonucleotide sequences are listed in Supplementary Table 2.

Proliferation assay (EdU staining). Cells were first transfected with indicated siRNAs under standard culture conditions. The day after, cells were replated in fibronectin-coated glass chamber slides. After 24 h, EdU (10 μ M) was added to the culture medium for 1 h. Cells were then fixed in 4% paraformaldehyde (PFA) for 10 min at room temperature. The EdU assays were performed according the manufacturer's instructions (Click-iT EdU Imaging Kits, Invitrogen). Images were obtained with a Leica TCS SP5 equipped with a CCD camera and analysed using Volocity software (PerkinElmer, version 5.5.1).

Immunofluorescence. Immunofluorescence on PFA-fixed cells and on PFA-fixed paraffin-embedded tissue slices was performed as previously described¹².

Primary antibodies were: anti-YAP/TAZ (sc-101199, Santa Cruz), anti-cytokeratin (wide spectrum screening, ZO622; Dako), anti-E-cadherin (610181, BD) and anti-Flag (F1804, Sigma-Aldrich). Secondary antibodies (1:200) were from Molecular Probes. Samples were counterstained with ProLong-DAPI

(Molecular Probes, Life Technologies) to label cell nuclei. Confocal images were obtained with a Leica TCS SP5 equipped with a CCD camera and analysed using Volocity software (PerkinElmer, version 5.5.1).

Immunohistochemical staining experiments were performed on PFA-fixed, paraffin-embedded tissue sections as previously described⁹. For immunohistochemistry: anti-Ki-67 polyclonal antibody (clone SP6; M3062) was from Spring Bioscience; anti-YAP (13584-I-AP) was from Proteintech.

In situ proximity ligation assay (PLA). In situ PLAs were performed with Duolink in situ reagents (Sigma-Aldrich).

For the experiments in Fig. 3b and Extended Data Fig. 6b, c, HEK293T cells were plated in standard cell culture dishes on day 1. Cells were transfected with the indicated DNA plasmids on day 2 (concentration of plasmids were as follows). Flag-NLS- β -actin(WT), 150 ng cm⁻²; Flag-NLS- β -actin(R62D), 150 ng cm⁻²; empty vector, 150 ng cm⁻². On day 3, cells were transfected with the indicated siRNAs. On day 4, cells were replated into fibronectin-coated glass chamber slides. Cells from each condition were plated in duplicate. After 24 h, cells were fixed in 4% PFA for 10 min at room temperature. With one of the duplicates, we performed anti-Flag (F-1804, Sigma-Aldrich) immunofluorescence in order to check the DNA transfection efficiency: the percentage of transfected cells was used for normalization. The other duplicate was subjected to PLA, following the manufacturer's instructions. Primary antibodies used in the PLA are: anti-Flag (F-1804, Sigma-Aldrich) and anti-BRM (ab15597, Abcam).

For the experiments in Fig. 3e, f and Extended Data Fig. 6g, i, j, NLS-YAP MCF10A cells were treated with doxycycline to induce NLS-YAP expression for the whole duration of the experiments. For Fig. 3e and Extended Data Fig. 6g, cells were either plated on small/micropatterned fibronectin-coated areas or treated for 24 h with latrunculin A (0.5 μ M) or dasatinib (0.1 μ M). For Fig. 3f and Extended Data Fig. 6i, j, cells were first transfected with siRNAs (control siRNA or *ARID1A* siRNA) and replated on small micropatterned/fibronectin-coated areas, soft (0.7 kPa) hydrogels, or treated for 24 h with latrunculin A (0.5 μ M), C3 (0.5 μ g ml⁻¹) or anti-integrin- β 1 (0.23 μ g ml⁻¹). Cells at 'high mechanics' were plated on unpatterned fibronectin-coated chamber slides. Cells were then fixed in 4% PFA for 10 min at room temperature. Samples were subjected to PLA, following the manufacturer's instructions. Primary antibodies used in the PLA are: anti-YAP (sc-101199, Santa Cruz) and anti-BRM (ab15597, Abcam) for Fig. 3e and Extended Data Fig. 6g; anti-YAP (ab52771, Abcam) and anti-TEAD1 (610922, BD Biosciences) for Fig. 3f and Extended Data Fig. 6i, j.

Images were acquired with a Leica TCS SP5 confocal microscope equipped with a CCD camera and analysed using Volocity software (PerkinElmer, version 5.5.1).

The percentages of PLA-positive cells reported in the legend of Fig. 3 have been determined by manual counting of at least 90 cells for each experimental condition.

Lenti- and retrovirus preparation. Lentiviral particles were prepared by transiently transfecting HEK293T (as previously described⁹) with lentiviral vectors (10 μ g per 60-cm² dish) together with packaging vectors pMD2-VSVG (2.5 μ g) and pPAX2 (7.5 μ g) using TransIT-LT1 (Mirus Bio) according to the manufacturer's instructions.

Retroviral particles were prepared by transiently transfecting HEK293GP (Takara) with retroviral vectors (15 μ g per 60-cm² dish) together with pMD2-Env (5 μ g per 60-cm² dish) using TransIT-LT1. Infections were carried out as previously described⁹.

Mammosphere assays. Confluent monolayers of HMECs were trypsinized, counted and plated as single-cell suspensions (with a density of 1,000 cells per cm²) on ultra-low attachment plates (Costar). Cells were cultured in DMEM/F12 supplemented with 1 \times B27 (Invitrogen), glutamine, antibiotics, 5 μ g ml⁻¹ insulin (Sigma-Aldrich), 20 ng ml⁻¹ EGF (Peprotech), 0.5 μ g ml⁻¹ hydrocortisone (Sigma-Aldrich), 52 μ g ml⁻¹ BPE (Thermo Fisher), 20 ng ml⁻¹ bFGF (Peprotech) and 4 μ g ml⁻¹ heparin. Mammospheres were counted after 10–14 days.

Luciferase assays. Luciferase assays were performed in HEK293 cells with the established YAP/TAZ-responsive luciferase reporter 8 \times GTIIC-Lux⁷.

8 \times GTIIC-Lux reporter (50 ng cm⁻²) was transfected together with CMV- β -gal (75 ng cm⁻²) to normalize for transfection efficiency using a CPRG (Roche) colorimetric assay. DNA transfections were done with TransIT-LT1 (Mirus Bio) according to the manufacturer's instructions. DNA content in all samples was kept uniform by adding a pBluescript plasmid at concentrations up to 250 ng cm⁻². For experiments using siRNA-depleted cells (Fig. 1d and Extended Data Fig. 2a, b), cells were plated at 15% confluence (day 0), transfected with the indicated siRNAs (day 1), changed to culture medium and transfected with plasmid DNA (concentrations of plasmids: for Extended Data Fig. 2a: empty vector was 2 ng cm⁻², Flag-YAP(WT) was 2 ng cm⁻²; for Extended Data Fig. 2b: Flag-YAP(WT) was 2 ng cm⁻², Flag-YAP(WW1^{mut}) was 21 ng cm⁻²) (day 2), and collected 48 h later (day 4).

Primary neuron isolation, infection and culturing. Preparation of neurons, transduction and culturing were performed as previously described¹². In brief,

neurons were isolated from hippocampi of embryonic day (E)18–E19 embryos of the indicated genotypes and plated on poly-L-lysine-coated wells (stiff conditions) or on top of a thick 0.5-cm Matrigel layer (soft conditions) in DMEM supplemented with 10% FBS, glutamine and antibiotics (day 1). After 24 h (day 2), the medium of the hippocampal preparation was changed to fresh DMEM:Neurobasal (1:1) supplemented with 5% FBS, 1 \times B27, glutamine and antibiotics. For reprogramming experiments, neurons were infected on the following day (day 3) with FUW-tetO-YAP(WT) and FUDeltaGW-rtTA viral supernatants. Negative controls were provided by neurons transduced with FUDeltaGW-rtTA in combination with FUW-tetO-YAP(S94A) or empty vector. After 24 h (day 4), medium was changed and cells were incubated in Neurobasal medium supplemented with 1 \times B27, glutamine, antibiotics, and 5 μ M Ara-C (cytosine β -D-arabinofuranoside, Sigma-Aldrich) for an additional seven days, at the end of which well-differentiated neurons were visible.

For the experiments in Extended Data Figs. 4e, 8b, neurons were switched to NSC medium and 2 μ g ml⁻¹ doxycycline for activating tetracycline-inducible gene expression. Sphere formation was evident upon YAP induction after 14 days on stiff ECM with doxycycline treatment.

For the experiments in Figs. 2c, 4d and Extended Data Figs. 4b, c, 8c, d, after Ara-C treatment, neurons were infected with pLKO.1-shRNA vectors. For the infection of a 10-cm² plate, we mixed 500 μ l of pLKO.1-shRNA produced in NSC medium (DMEM/F12 supplemented with 1 \times N2, 20 ng ml⁻¹ mouse EGF, 20 ng ml⁻¹ mouse bFGF, glutamine and antibiotics) and 1.5 ml of serum-free Neurobasal medium with 1 \times B27. After 24 h of infection, treated neurons were switched to NSC medium and 2 μ g ml⁻¹ doxycycline to activate tetracycline-inducible gene expression. After seven days, fresh doxycycline (final concentration of 2 μ g ml⁻¹) was added. Sphere formation was evident upon YAP induction after 14 days (stiff conditions) or 30–45 days (soft conditions) of doxycycline treatment.

Bright-field images were acquired with a Leica DM IRB microscope using LAS version 4.4 software.

Mice. Transgenic lines used in the experiments were provided by: D. Pan (*Nf2*^{fl/fl})¹³; Z. Wang (*Arid1a*^{fl/fl}), these mice have *loxP* sites flanking exon 8)³²; P. Chambon (*Alb*^{creERT2})³³; I. De Curtis and R. Brambilla (*Syn1*^{cre})³⁴. *Taz*^{fl/fl} and double *Yap*^{fl/fl} *Taz*^{fl/fl} conditional knockout mice were as previously described³⁵.

Animals were genotyped using standard procedures³⁶ and using the recommended set of primers. Animal experiments were performed adhering to our institutional and national guidelines as approved by OPBA (University of Padova) and the Ministry of Health of Italy. For experiments using mice, the limits for the end point 'body-condition scoring' were never exceeded.

For the experiment in Extended Data Fig. 4e, we used control (*Arid1a*^{fl/+}) and *Syn1*^{cre} *Arid1a*^{fl/+} mice. For this, we crossed *Syn1*^{cre} females (as transgene expression in male mice results in germline recombination³⁷) with *Arid1a*^{fl/fl} males. Littermate embryos derived from these crossings were collected at E18–E19 and kept separate for neurons derivation and following treatments (as described in 'Primary neuron isolation, infection and culturing'), genotypes were confirmed on embryonic tail biopsies and leftover brains. These animals were mixed strains.

Yap, *Taz*, *Arid1a* and *Nf2* conditional knockout mice were intercrossed with *Alb*^{creERT2} mice to obtain the different genotypes used for the experiments in Fig. 2 and Extended Data Fig. 5 (including controls). These animals were mixed strains. For the induction of recombination in the liver, mice of the indicated genotypes (two months old) received one intraperitoneal injection per day of 3 mg tamoxifen (Sigma-Aldrich) dissolved in corn oil (Sigma-Aldrich) during five consecutive days. For the experiments depicted in Fig. 2d, e and Extended Data Fig. 5c–e, mice were euthanized four months after tamoxifen treatment. For the DDC experiments (Fig. 2f and Extended Data Fig. 5f–h), two weeks after tamoxifen treatment, mice were fed with either normal diet (Mucedola) or the same diet containing 0.1% DDC (Sigma-Aldrich) for six weeks (DDC diet; Mucedola).

Statistics. The number of biological and technical replicates and the number of animals are indicated in figure legends, main text and Methods. All tested animals were included. Animal ages are specified in the text and Methods. Sample size was not predetermined. Randomization was not applicable for our experiments with cell lines. Mice were randomly allocated to experimental or treatment groups to ensure equal sex/age across genotypes. Investigators were not blinded for analyses relying on unbiased measurements of quantitative parameters, with exception of pathological examination of histological sections carried out by M.F. (a professional pathologist), who was blind to animal genotypes, sex/age or treatment. Data are mean \pm s.d. or mean \pm s.e.m. as indicated in the legends of the figures and extended data figures. Student's *t*-test, Mann–Whitney *U*-test and one-way ANOVA analyses were performed with GraphPad Prism 7.0d for Mac software.

Reporting summary. Further information on research design is available in the Nature Research Reporting Summary linked to this paper.

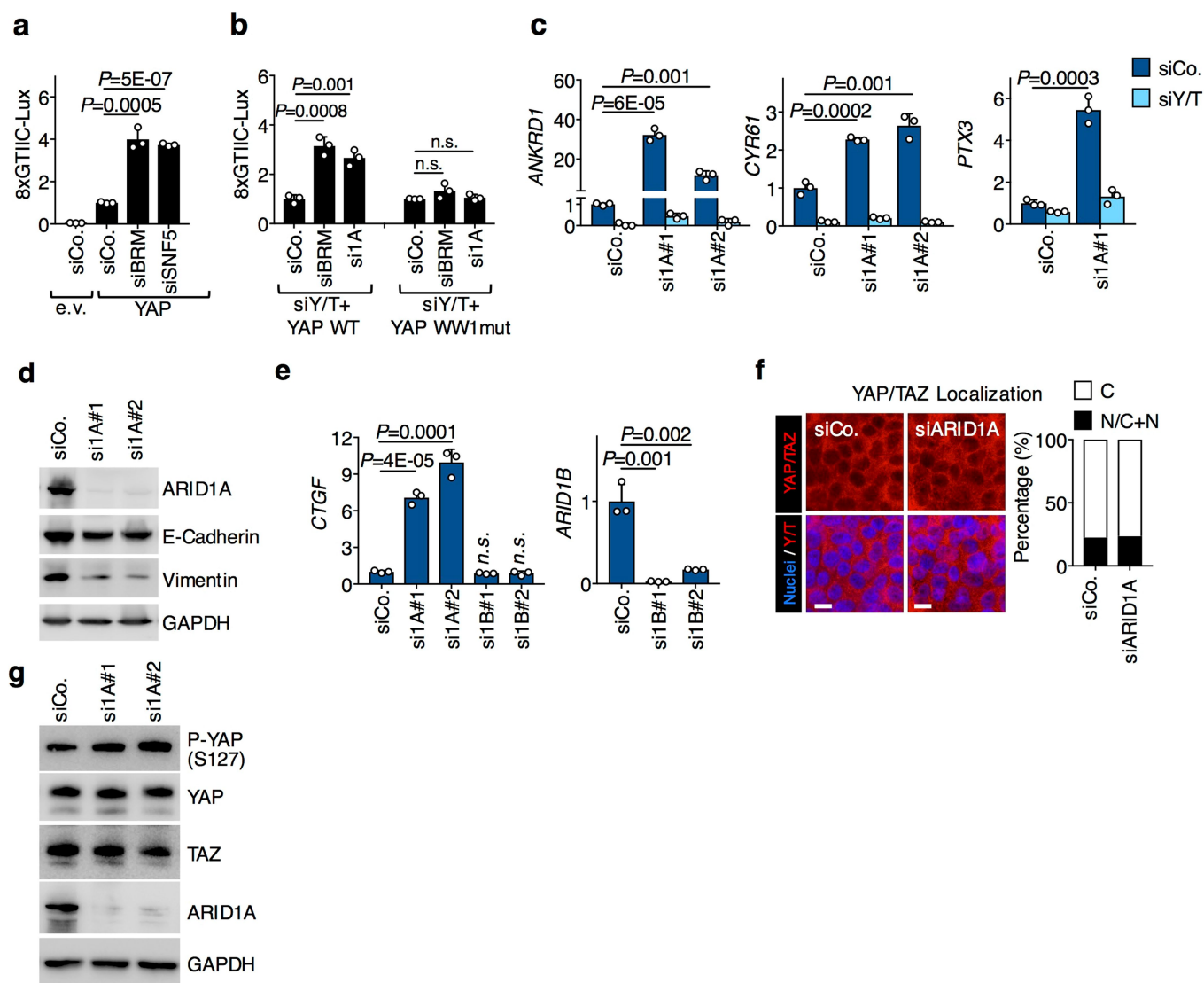
Data availability

Mass spectrometry data can be found in Supplementary Table 1. Source Data for Figs. 1, 2, 4 and Extended Data Figs. 2–5, 7, 8 can be found in the online version of the paper. Uncropped images of immunoblots can be found in Supplementary Fig. 1. All relevant data are included in the manuscript as Source Data or Supplementary Information; all other data are available from the corresponding authors upon reasonable request.

25. Komuro, A., Nagai, M., Navin, N. E. & Sudol, M. WW domain-containing protein YAP associates with ErbB-4 and acts as a co-transcriptional activator for the carboxyl-terminal fragment of ErbB-4 that translocates to the nucleus. *J. Biol. Chem.* **278**, 33334–33341 (2003).
26. Azzolin, L. et al. Role of TAZ as mediator of Wnt signaling. *Cell* **151**, 1443–1456 (2012).
27. Sif, S., Saurin, A. J., Imbalzano, A. N. & Kingston, R. E. Purification and characterization of mSin3A-containing Brg1 and hBrm chromatin remodeling complexes. *Genes Dev.* **15**, 603–618 (2001).
28. Guan, B. et al. Mutation and loss of expression of *ARID1A* in uterine low-grade endometrioid carcinoma. *Am. J. Surg. Pathol.* **35**, 625–632 (2011).
29. Maherali, N. et al. A high-efficiency system for the generation and study of human induced pluripotent stem cells. *Cell Stem Cell* **3**, 340–345 (2008).
30. Stewart, S. A. et al. Lentivirus-delivered stable gene silencing by RNAi in primary cells. *RNA* **9**, 493–501 (2003).
31. Hughes, C. S. et al. Ultrasensitive proteome analysis using paramagnetic bead technology. *Mol. Syst. Biol.* **10**, 757 (2014).
32. Gao, X. et al. ES cell pluripotency and germ-layer formation require the SWI/SNF chromatin remodeling component BAF250a. *Proc. Natl Acad. Sci. USA* **105**, 6656–6661 (2008).
33. Schuler, M., Dierich, A., Chambon, P. & Metzger, D. Efficient temporally controlled targeted somatic mutagenesis in hepatocytes of the mouse. *Genesis* **39**, 167–172 (2004).
34. Zhu, Y. et al. Ablation of NF1 function in neurons induces abnormal development of cerebral cortex and reactive gliosis in the brain. *Genes Dev.* **15**, 859–876 (2001).
35. Azzolin, L. et al. YAP/TAZ incorporation in the β -catenin destruction complex orchestrates the Wnt response. *Cell* **158**, 157–170 (2014).
36. Morsut, L. et al. Negative control of Smad activity by ectoderm/Tif1 γ patterns the mammalian embryo. *Development* **137**, 2571–2578 (2010).
37. Rempe, D. et al. Synapsin I Cre transgene expression in male mice produces germline recombination in progeny. *Genesis* **44**, 44–49 (2006).

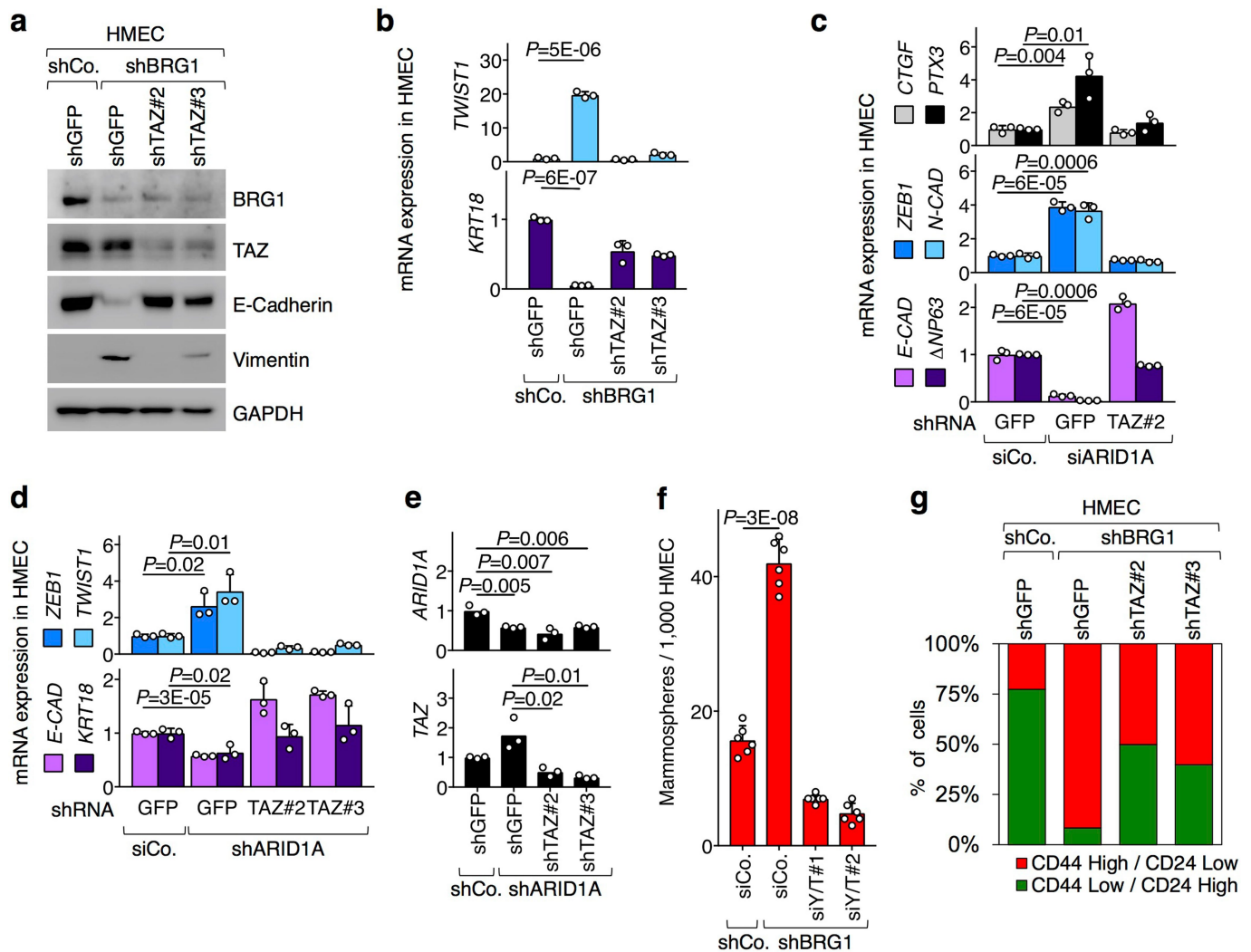
Extended Data Fig. 1 | Interaction between YAP and the SWI/SNF complex. **a**, Proteomic analyses of endogenous YAP/TAZ-binding partners reveal interactions with endogenous components of the SWI/SNF complex (green). Red, the used bait. R1 and R2 are the results from $n = 2$ biologically independent samples. See Supplementary Table 1. **b**, YAP(5SA) was immunoprecipitated from lysates of MCF10A cells stably expressing Flag-tagged YAP(5SA) using an anti-Flag antibody, and co-precipitating endogenous components of the SWI/SNF complex were detected by western blot. As a negative control, immunoprecipitation (IP) was repeated with cells transfected with empty vector. GAPDH serves as a loading control for inputs (right). **c**, HEK293T cells were transfected with independent siRNAs against the indicated genes (*ARID1A* in lanes 5 and 6; *BAF53A* in lanes 7 and 8; *SNF5* in lanes 9 and 10) and control siRNAs ((siCo) lanes 1–4) and with plasmids encoding HA–YAP(5SA) (all lanes) and Flag–BRG1 (lanes 3–10), as indicated. Cell lysates were subjected to anti-Flag immunoprecipitation and co-precipitating proteins were checked by western blot. *ARID1A* depletion impairs the interaction between YAP and BRG1, but it had no effect on the association of BRG1 with BAF53A (lanes 5 and 6). Depletion of *BAF53A* (lanes 7 and 8) or *SNF5* (lanes 9 and 10) had no effect on the interaction between YAP and BRG1. *ARID1A* blot, top band represents the full-length *ARID1A*. Input *ARID1A* was from a separate gel. **d**, Western blots of the inputs of the immunoprecipitation experiment shown in Fig. 1b. HEK293T cells were transfected with control (Co.) siRNA or siRNA against *ARID1A* and with plasmids encoding HA–YAP(5SA) and Flag–BRM, as indicated. **e**, Western blots of the inputs of the immunoprecipitation experiment shown in Fig. 1c. HEK293T cells were transfected with control siRNAs or with a siRNA mix against *BRG1* and *BRM*. **f**, DNase-treated nucleus preparations from HEK293T cells were subjected to sequential salt extraction and fractions were analysed by western blot (left, lanes 1–4). The unsonicated, chromatin-free 0-mM NaCl fraction was incubated

with GST–YAP or GST protein (negative control), immobilized on a glutathione resin, and proteins that were pulled down were analysed by western blot (right, lanes 5 and 6). **g**, HEK293T cells were transfected with siRNAs against the indicated genes and with plasmids encoding HA–YAP(5SA) and Flag–BRG1, as indicated. Cell lysates were subjected to anti-Flag immunoprecipitation and co-precipitating proteins were checked by western blot. **h**, Western blot of recombinant V5–*ARID1A* pulled down by GST–YAP or GST–TAZ, immobilized on a glutathione resin. GST protein was used as a negative control. Input, a fraction of V5–*ARID1A* used for the pull-down experiments. **i**, HEK293T cells were transfected with plasmids encoding empty vector (e.v.) or Flag–YAP(WT) or WW-domain mutants, as indicated. Cell lysates were subjected to anti-Flag immunoprecipitation and western blot analysis of endogenous *ARID1A*. GAPDH serves as a loading control in inputs. **j**, Flag–TAZ was immunoprecipitated from lysates of HEK293T cells transfected with Flag-tagged TAZ(WT) or TAZ(Δ WW) using an anti-Flag antibody, and co-precipitating endogenous *ARID1A* was detected by western blot only with TAZ(WT). As a negative control, immunoprecipitation was repeated using HEK293T cells transfected with empty vector. **k**, HEK293T cells were transfected with plasmids encoding Flag–YAP(WT) (all lanes) and either V5–*ARID1A*(WT) or V5–*ARID1A*(PPxA) mutant, as indicated. Cell lysates were subjected to anti-Flag immunoprecipitation and western blot analysis of V5–*ARID1A*. We notice that other SWI/SNF components (such as BRG1 or SNF5) also carry PPxY motifs; although these components are by themselves not essential for the association with YAP/TAZ, the presence of a second WW motif in YAP (although not in TAZ) raises the possibility of stronger, cooperative associations between YAP and other elements of the SWI/SNF complex. **b**, **c**, **f**–**k** Panels display representative experiments, repeated independently two (**c**, **f**–**k**) or three (**b**) times, all with similar results.



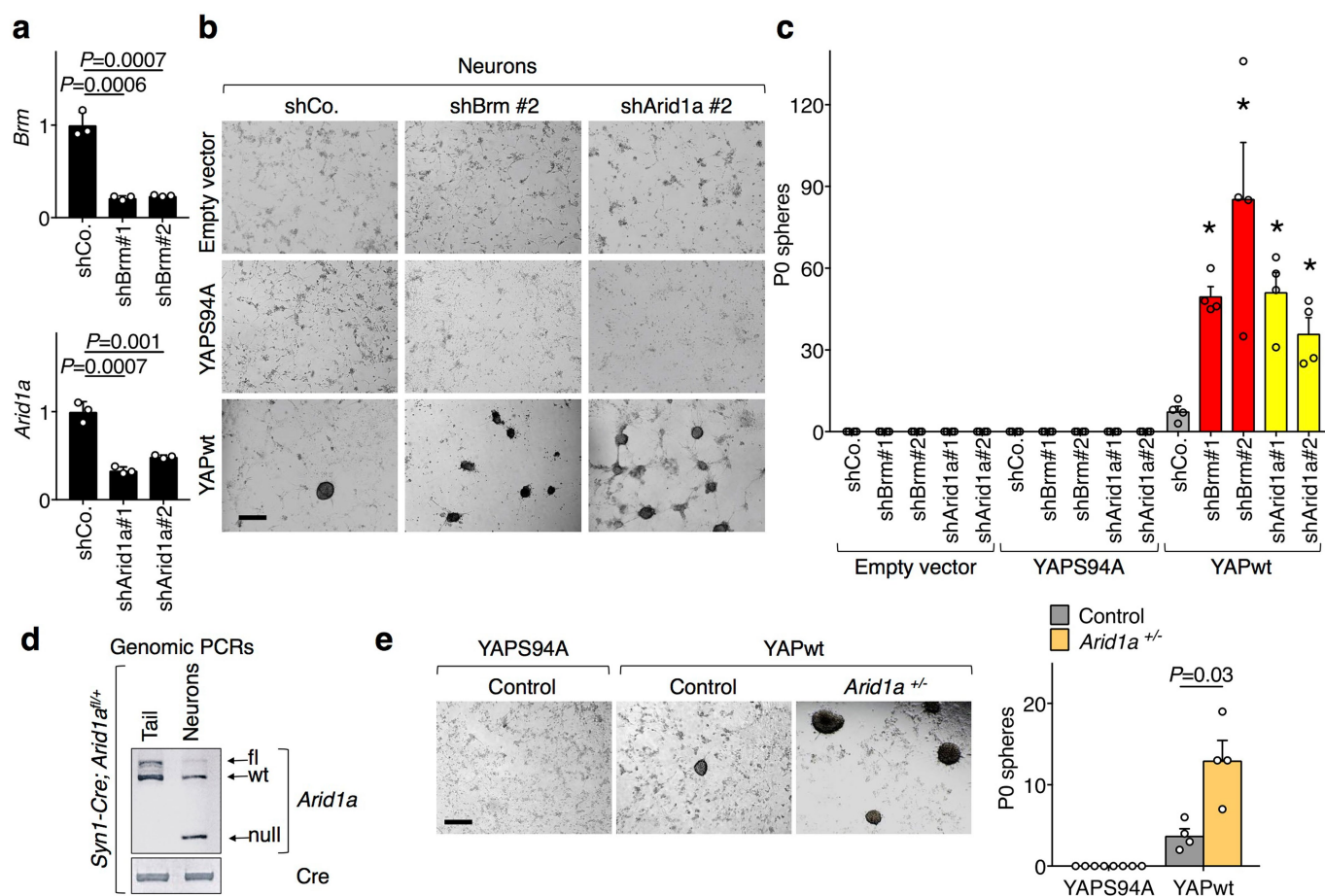
Extended Data Fig. 2 | Effect of ARID1A depletion on YAP/TAZ levels, localization and activity. a, Results of luciferase assays with the 8xGTIIC-Lux reporter in HEK293 cells transfected with empty or YAP-expressing vectors and the indicated siRNAs. Data are normalized to control siRNA- and empty vector-transfected cells and are presented as mean + s.d. of $n = 3$ biologically independent samples. **b**, Results of luciferase assays with the 8xGTIIC-Lux reporter in HEK293 cells reconstituted with either YAP(WT) or YAP(WW1^{mut}) and transfected with the indicated siRNAs. Data are normalized to control siRNA-transfected cells and are presented as mean + s.d. of $n = 3$ biologically independent samples. **c**, qPCR analyses of the YAP/TAZ targets *ANKRD1*, *CYR61* and *PTX3* in MCF10A cells transfected as indicated. Data are mean + s.d. of $n = 3$ biologically independent samples. **d**, Western blot

analysis of ARID1A, E-cadherin and vimentin from lysates of MCF10A cells transfected with the indicated siRNAs. **e**, qPCR analyses of *CTGF* (left) and *ARID1B* (right) expression in MCF10A cells transfected as indicated. Data are mean + s.d. of $n = 3$ biologically independent samples. **f**, Representative confocal images (left) and quantifications (right; >100 cells per condition) of YAP/TAZ localization in MCF10A cells transfected with the indicated siRNAs. **g**, Western blot analysis of YAP, TAZ and YAP phosphorylated at the key Hippo/LATS target site (p-YAP S127) in lysates of MCF10A cells transfected with the indicated siRNAs. P values were determined by unpaired two-sided Student's t -test; n.s., not significant. All panels display representative experiments, repeated independently two (d, e, g) or three (a–c, f) times with similar results.



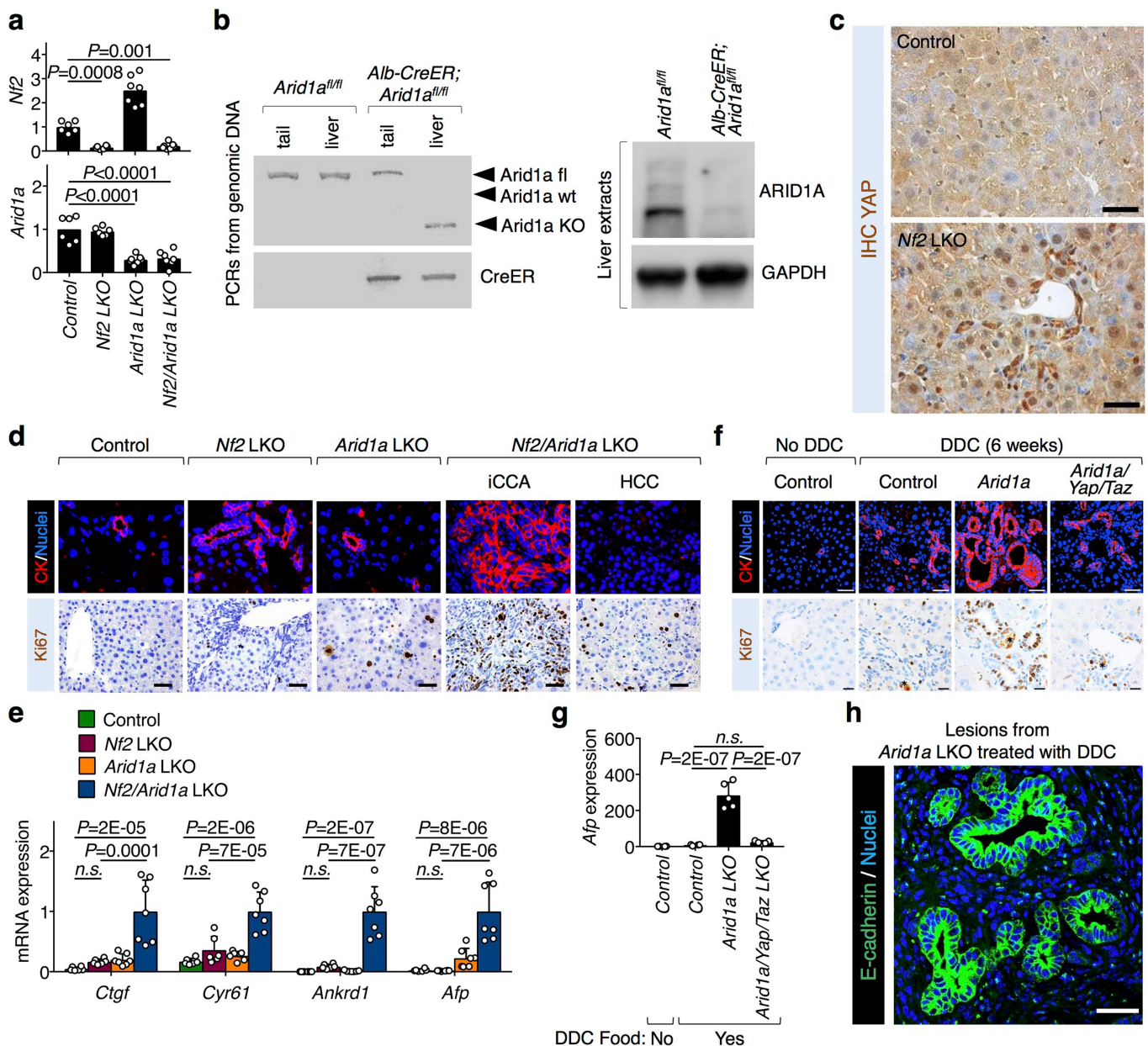
Extended Data Fig. 3 | YAP and TAZ are required for the biological effects of SWI/SNF depletion in HMECs. **a, b**, HMECs were transduced with the indicated shRNA-encoding vectors and collected for protein extraction (**a**) or RNA extraction (**b**). **a**, Western blot of BRG1, TAZ and epithelial (ECAD) and mesenchymal (vimentin) markers. **b**, qPCR analyses of mesenchymal (*TWIST1*) and epithelial (*KRT18*) markers. Data are mean + s.d. of $n = 3$ biologically independent samples. Continuation of Fig. 2a. **c–e**, HMECs were transduced with the indicated shRNA-encoding vectors and/or transfected with the indicated siRNAs and collected for RNA extraction. qPCR analyses of the indicated genes are shown. Data are mean + s.d. of $n = 3$ biologically independent samples.

f, Mammospheres formed by HMECs transduced with the indicated shRNAs and transfected with indicated siRNAs. Data are mean + s.d. of $n = 6$ biologically independent samples. **g**, HMECs were transduced with the indicated shRNA-encoding vectors and analysed for their CD44 and CD24 immunophenotype. Quantification of the percentage of cells that displayed either a CD44^{high}CD24^{low} (stem-like mesenchymal cells) or CD44^{low}CD24^{high} (differentiated epithelial cells) profile⁸. *P* values were determined by unpaired two-sided Student's *t*-test. All panels display representative experiments, repeated independently three times with similar results.



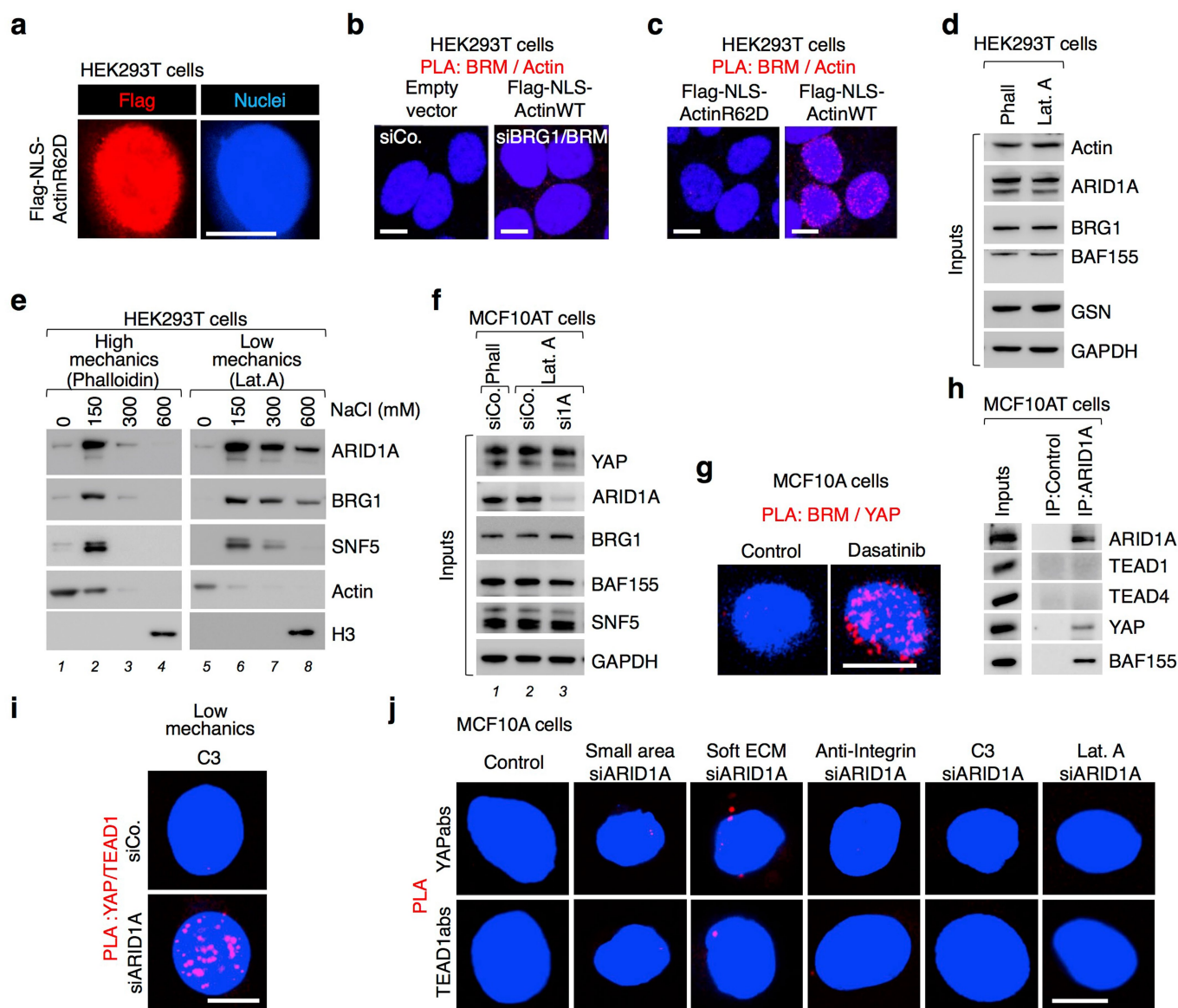
Extended Data Fig. 4 | SWI/SNF depletion potentiates YAP-induced reprogramming of neurons into NSCs. a, Efficiency of *Brm* and *Arid1a* downregulation in neurons transduced with the indicated shRNA-encoding vectors, as measured by qPCR. Data are mean + s.d. of $n = 3$ biologically independent samples. A representative experiment repeated twice with similar results is shown. **b**, **c**, Related to Fig. 2c. Neurons were infected with doxycycline-inducible YAP-encoding vectors or empty vector and the indicated shRNA-encoding lentiviral vectors. **b**, Representative images of the cultures after 14 days in NSC medium with doxycycline. Scale bar, 300 μm . **c**, Quantification of the emerging (P0) neurospheres. Data are mean + s.e.m. of four independent experiments; $*P = 0.03$ for comparisons between YAP(WT)-expressing neurons transduced with control shRNA (shCo.) and *Brm* shRNAs (shBrm) or between YAP(WT)-expressing neurons transduced with control shRNA and *Arid1a* shRNAs. **d**, **e**, Effect of *Arid1a* depletion on YAP-induced

reprogramming of neurons. **d**, *Syn1^{Cre}* drives *Arid1a* knockout specifically in neurons as shown by genotyping. Genomic DNA from neurons was compared to genomic DNA from the tail of the same *Syn1^{Cre}Arid1a^{fl/+}* mouse. PCR bands are shown for the indicated alleles. **e**, Control (*Arid1a^{+/+}*) and *Arid1a^{+/-}* (from *Syn1^{Cre}Arid1a^{fl/+}* mice) neurons were infected with inducible YAP-encoding vectors. Left, Representative images of P0 neurospheres that emerged from these cultures after doxycycline treatment in NSC medium. Scale bar, 300 μm . Right, quantification of P0 neurospheres that emerged from these cultures after doxycycline treatment in NSC medium. Data are mean + s.e.m. of four independent experiments. YAPS94A serves as negative control. **e** complements Fig. 2c and Extended Data Fig. 4b, c, which show comparable results between shRNA and genetic attenuation of *Arid1a*. P values were determined by unpaired two-sided Student's t -test (**a**) and by two-sided Mann-Whitney U -test (**c**, **e**).



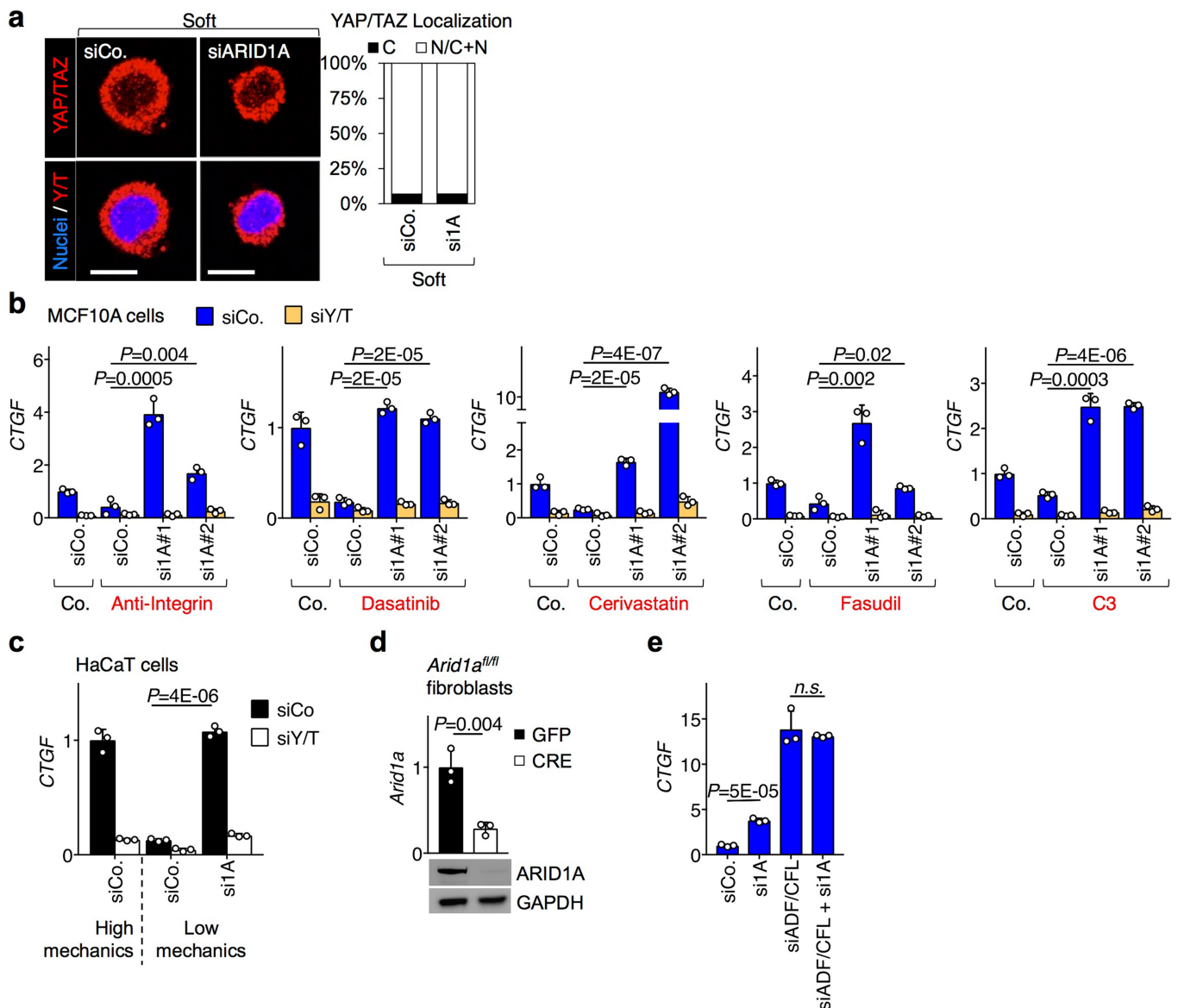
Extended Data Fig. 5 | Effect of ARID1A depletion in hepatocytes on tumour formation. **a**, qPCR analysis of *Nf2* and *Arid1a* expression in the livers of control ($n = 6$ mice), and *Nf2* ($n = 6$ mice), *Arid1a* ($n = 7$ mice) and *Nf2/Arid1a* ($n = 7$ mice) liver mutant (LKO) mice, four months after tamoxifen treatment. All animals were included. Mean and data for individual mice are shown. **b**, Livers of control (*Arid1a*^{fl/fl}) and *Arid1a* LKO (*Alb^{CreERT2}Arid1a*^{fl/fl}) mice were collected two weeks after tamoxifen treatment, and genomic DNA and proteins were extracted using standard procedures. Representative results are shown, experiments were repeated on four mice for each genotype. Left, PCR analysis of the indicated alleles. Right, Western blots of GAPDH (loading control) and ARID1A. **c**, YAP immunohistochemistry (IHC) staining in control and *Nf2* mutant livers. Scale bars, 40 μ m. Representative images of experiments that were independently replicated using three mice for each genotype, with similar results. **d**, Continuation of Fig. 2e. Representative cytokeratin (CK; top) and Ki-67 (bottom) stainings of sections of livers of the indicated genotypes (same genotypes as in Fig. 1d, e and Extended Data Fig. 5a). Note intrahepatic cholangiocarcinomas (iCCA; CK⁺Ki-67⁺) and hepatocellular carcinomas (HCC; Ki-67⁺CK⁻) were found only in livers from *Nf2/Arid1a* LKO mice. Scale bars, 100 μ m. Representative images are shown, experiments independently replicated for all of the mice of each genotype described in a, with similar results. **e**, qPCR analysis of selected genes of livers of mice with the indicated genotypes. All animals were included. Data are normalized to *Nf2/Arid1a* LKO mice. Data are

mean + s.d. for same number of mice per genotype as in a. **f**, Continuation of Fig. 2f. Control, *Arid1a* LKO and *Arid1a/Yap/Taz* LKO mice were treated with tamoxifen and were then fed a DDC-containing diet for six weeks. CK (top; scale bars, 40 μ m) and Ki-67 (bottom; scale bars, 20 μ m) stainings of liver sections from the indicated mice. Note the presence of early cholangiocarcinoma lesions (CK⁺Ki-67⁺) in the *Arid1a* LKO mice and their absence upon concomitant YAP/TAZ loss (that is, in the *Arid1a/Yap/Taz* LKO mice). Asterisks indicate porphyrin deposits, which are typically present in the liver of mice treated with DDC. Representative images are shown, experiments were independently replicated for all of the mice of each genotype (same number of mice as in Fig. 2f), with similar results. **g**, Representative qPCR analysis of *Afp* expression in the livers of control ($n = 4$), *Arid1a* LKO ($n = 5$), *Arid1a/Yap/Taz* LKO ($n = 5$) mice treated with tamoxifen and then DDC. Data are normalized to livers of mice not treated with DDC ($n = 4$). Data are mean + s.d. of the indicated number of mice. This experiment was independently repeated three times with similar results, analysing, in total, at least 10 mice for each genotype. **h**, Representative E-cadherin staining showing that CCA lesions retain an epithelial morphology in sections of the liver of the indicated genotype. Scale bar, 30 μ m. Experiments were independently repeated on three DDC-treated *Arid1a* LKO mice, with similar results. P values were determined by one-way ANOVA with Dunnett's multiple comparisons test (a) or with Tukey's multiple comparisons test (e, g).



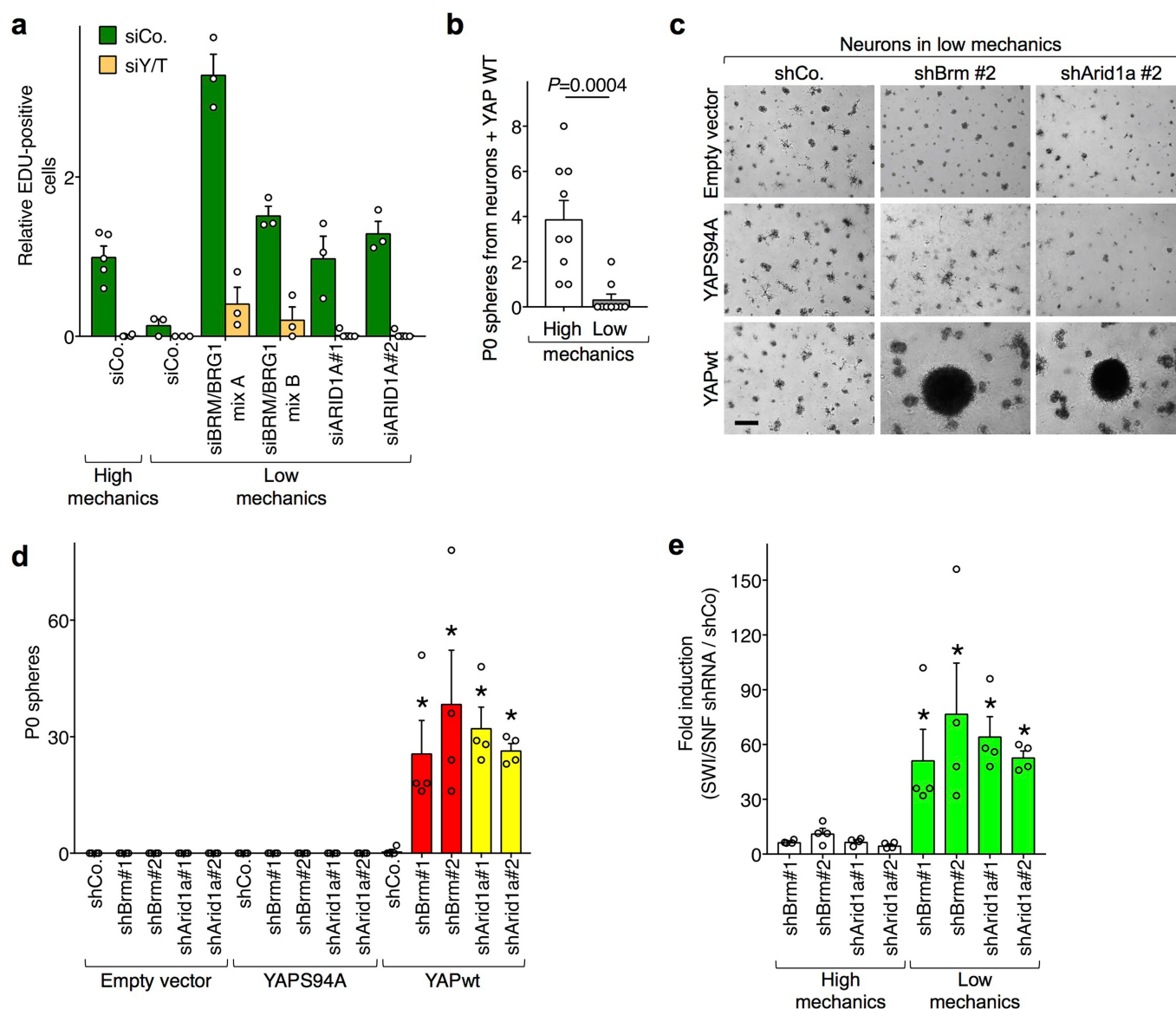
Extended Data Fig. 6 | Interaction of SWI/SNF with F-actin and YAP is mutually exclusive. **a**, Related to Fig. 3a. HEK293T cells were transfected with Flag-NLS- β -actin(R62D). Representative anti-Flag immunofluorescence images to visualize transfected Flag-NLS- β -actin. Nuclei were counterstained with DAPI. Scale bar, 10 μ m. **b**, **c**, Related to the PLAs shown in Fig. 3b. **b**, Negative controls for the PLA of Fig. 3b: in the absence of one of the two partners, no dots can be seen. **c**, In HEK293T cells, by PLA, endogenous BRM interacts with Flag-tagged NLS- β -actin(WT), but not with Flag-tagged NLS- β -actin(R62D), indicating that the association is specific to filamentous, and not monomeric, β -actin. **d**, Western blots of the inputs of the experiment shown in Fig. 3c. **e**, Sequential salt extraction of HEK293T cells treated with either phalloidin (Phall) or latrunculin A (Lat. A). Western blots of the indicated proteins are shown. H3 was loaded on a different blot. **f**, Western blots of the inputs of the experiment shown in Fig. 3d. MCF10AT cells were transfected with control siRNAs (siCo., lanes 1 and 2) or siRNAs against *ARID1A* (si1A; lane 3) and treated with phalloidin (lane 1) or latrunculin

A (lanes 2 and 3), as indicated. **g**, Continuation of Fig. 3e. A PLA was carried out to detect the interaction between endogenous BRM and NLS-YAP in MCF10A cells. Control untreated cells, 0% PLA-positive cells; cells treated with the Src inhibitor dasatinib (that is, a low-mechanics condition in addition to those shown in Figs. 3e), 14.5% PLA-positive cells. **h**, Co-immunoprecipitation and western blot analysis of MCF10AT lysates showing endogenous ARID1A bound to endogenous YAP but not to TEAD1 and TEAD4. As a specificity control, immunoprecipitation with unrelated rabbit IgG was repeated using the same lysates. **i**, **j**, Related to Fig. 3f. **i**, Representative PLA images detecting the interaction between endogenous TEAD and NLS-YAP in MCF10A cells. The YAP-TEAD1 association is lost in C3-treated cells (that is, in cells with attenuated mechanotransduction (low mechanics) upon C3-mediated inhibition of RhoGTPases), but rescued after depletion of ARID1A (PLA-positive cells: 43.4%). **j**, Specificity controls of single antibodies for the PLA shown in **i** and in Fig. 3f. **a-c**, **e**, **g-j** are representative experiments, repeated independently two (**e**, **h**) or three (**a-c**, **g**, **i**, **j**) times, with similar results.



Extended Data Fig. 7 | Loss of SWI/SNF restores YAP/TAZ transcriptional activity in mechanically inhibited cells. **a**, Representative confocal images (left) and quantification (right; >100 cells per conditions) of YAP/TAZ localization in MCF10A cells transfected with the indicated siRNAs and replated on a soft ECM. **b**, MCF10A cells were transfected with the indicated siRNAs, and left untreated (control) or treated with anti-integrin- $\beta 1$ antibodies, the Rho-inhibitors C3 and cerivastatin, the Src-inhibitor dasatinib or the ROCK inhibitor fasudil. qPCR analyses of *CTGF* expression (mean + s.d. of $n = 3$ biologically independent samples). Anti-integrin- $\beta 1$ and fasudil were part of the same experiment and thus share the same control repeated in their corresponding graphs. **c**, HaCaT cells were transfected with the indicated siRNAs and replated to obtain

either sparse (high mechanics) or dense monolayers (low mechanics). qPCR analyses of *CTGF* expression. Data are mean + s.d. of $n = 3$ biologically independent samples. **d**, Efficiency of *Arid1a* downregulation in *Arid1a*^{fl/fl} fibroblasts after transduction with Adeno-Cre, measured by qPCR (data are normalized to adeno-GFP-transduced cells and presented as mean + s.d. of $n = 3$ biologically independent samples) and western blot (in which GAPDH was used as a loading control). **e**, MCF10A cells were transfected with the indicated siRNAs and replated at very high density (see Methods). qPCR analyses of *CTGF* expression. Data are mean + s.d. of $n = 3$ biologically independent samples. All panels display representative experiments, repeated independently three times with similar results. *P* values were determined by unpaired two-sided Student's *t*-test.



Extended Data Fig. 8 | Loss of SWI/SNF enables YAP-induced biological effects in mechanically inhibited cells. **a**, MCF10A cells were transfected with the indicated siRNAs, and replated to obtain dense monolayers (low mechanics). After 24 h, cells were incubated for 1 h with a pulse of EdU to label cells undergoing DNA duplication. Cells were fixed and processed for EdU staining. Quantification of proliferation was measured as the relative number of EdU⁺ cells. Data are normalized to sparse cells (high mechanics) transfected with control siRNA. Data are mean + s.e.m. of at least $n = 3$ biologically independent samples. Statistics for rescue experiments at low mechanics: control siRNA ($n = 3$) versus siBRM/BRG1 mix A ($n = 3$), $P = 0.0003$; control siRNA versus siBRM/BRG1 mix B ($n = 3$), $P = 0.0005$; control siRNA versus siARID1A#1 ($n = 3$), $P = 0.04$; control siRNA versus siARID1A#2 ($n = 3$), $P = 0.002$. A representative experiment is shown, experiments were repeated independently twice with similar results. **b**, Neurons were plated on a stiff or soft ECM and infected with inducible YAP-encoding vectors. Quantification of neurospheres emerging from these cultures after doxycycline treatment in NSC medium. Data are mean + s.e.m. of all biological independent samples of three experiments, $n = 9$. **c**, **d**, Related

to Fig. 4d. Neurons were plated on a soft ECM and infected with inducible YAP-encoding vectors or empty vector and the indicated shRNA-encoding lentiviral vectors. **c**, **d**, Representative images (**c**) and quantification (**d**) of neurospheres (P0) emerging after doxycycline treatment. Scale bar, 300 μ m. Data are mean + s.e.m. of four independent experiments. $*P = 0.03$, control shRNA (shCo) versus *Brm* shRNA (shBrm#1 or shBrm#2) in neurons transduced with YAP(WT); $P = 0.03$, control shRNA versus *Arid1a* shRNA (shArid1a#1 or shArid1a#2) in neurons transduced with YAP(WT). **e**, Fold change in expression in neurospheres emerging from cultures of YAP-induced neurons transduced with the indicated shRNAs against *Brm* or *Arid1a*, and plated either on a stiff (high mechanics) or soft (low mechanics) ECM, with respect to the corresponding control shRNA-expressing cultures. Data are mean + s.e.m. of four independent experiments. $*P = 0.03$, for comparisons between *Brm* or *Arid1a* shRNA under high mechanical conditions and the corresponding samples under low mechanical conditions. P values were determined by unpaired two-sided Student's t -test (**a**) and by two-sided Mann-Whitney U -test (**b**, **d**, **e**).

Cryo-EM reveals two distinct serotonin-bound conformations of full-length 5-HT_{3A} receptor

Sandip Basak¹, Yvonne Gicheru¹, Shanlin Rao², Mark S. P. Sansom² & Sudha Chakrapani^{1,3*}

The 5-HT_{3A} serotonin receptor¹, a cationic pentameric ligand-gated ion channel (pLGIC), is the clinical target for management of nausea and vomiting associated with radiation and chemotherapies². Upon binding, serotonin induces a global conformational change that encompasses the ligand-binding extracellular domain (ECD), the transmembrane domain (TMD) and the intracellular domain (ICD), the molecular details of which are unclear. Here we present two serotonin-bound structures of the full-length 5-HT_{3A} receptor in distinct conformations at 3.32 Å and 3.89 Å resolution that reveal the mechanism underlying channel activation. In comparison to the apo 5-HT_{3A} receptor, serotonin-bound states underwent a large twisting motion in the ECD and TMD, leading to the opening of a 165 Å permeation pathway. Notably, this motion results in the creation of lateral portals for ion permeation at the interface of the TMD and ICD. Combined with molecular dynamics simulations, these structures provide novel insights into conformational coupling across domains and functional modulation.

Recent high-resolution pLGIC structures have highlighted several fundamentals of the gating mechanism^{3–7}. However, there is a lack of

information on conformational coupling between the different domains and, particularly, how the ICD modulates the overall channel function. The ICD has a role in localization to the plasma membrane⁸ and regulates single-channel conductance, rectification and gating^{9,10}. We recently reported the structure of the full-length mouse 5-HT_{3A} receptor (Extended Data Table 1a) in the unliganded (apo) state¹¹, solved by single-particle cryo-electron microscopy (cryo-EM), which revealed key features of the resting conformation. In the present study, we determined structures of the 5-HT_{3A} receptor in the presence of 100 μM serotonin by cryo-EM to gain insights into the mechanism of activation by serotonin. High-resolution data collection and processing revealed two distinct populations of the receptor with final 3D reconstructions to overall resolutions of 3.32 Å and 3.89 Å, which we will refer to as state 1 and state 2, respectively (Extended Data Figs. 1, 2, Extended Data Table 1b). The map for both states contained density for the entire ECD, TMD and a large region of the ICD (Extended Data Fig. 3), and the overall 3D architectures were similar to the apo structure¹¹.

The apo, state 1 and state 2 structures reveal distinct conformations of the pore (Fig. 1a, b). The apo pore is constricted at multiple

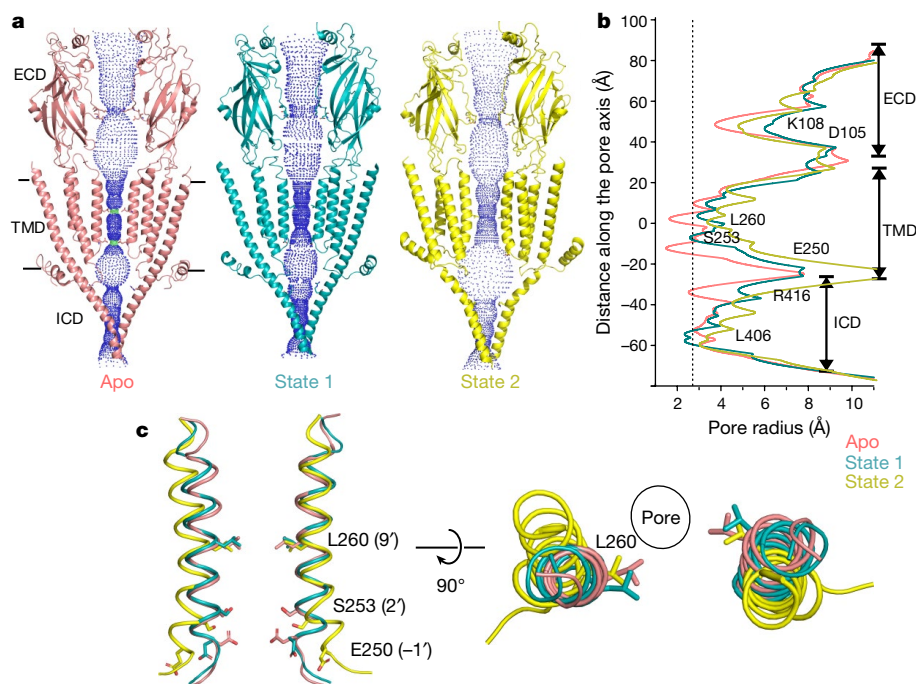


Fig. 1 | Ion permeation pathway. **a**, The profile of the ion permeation pathway for the full-length 5-HT_{3A} receptor in the apo state (salmon red) and in the two serotonin-bound conformations, state 1 (teal) and state 2 (yellow). The same colour scheme is used to represent the three states in all subsequent figures. For clarity, the cartoon representation is shown only for two subunits. Green and blue spheres define radii of 1.8–3.3 Å and

>3.3 Å, respectively. The position at which the pore is constricted below 2.76 Å in the apo state is shown as sticks. **b**, The pore radius is plotted as a function of distance along the pore axis. The dashed line indicates the approximate radius of a hydrated Na⁺ ion¹². **c**, Side (left) and top (right) views of the pore-lining M2 helices showing superposition of the apo, state 1 and state 2 structures.

¹Department of Physiology and Biophysics, Case Western Reserve University, Cleveland, OH, USA. ²Department of Biochemistry, University of Oxford, Oxford, UK. ³Department of Neuroscience, School of Medicine, Case Western Reserve University, Cleveland, OH, USA. *e-mail: sudha.chakrapani@case.edu

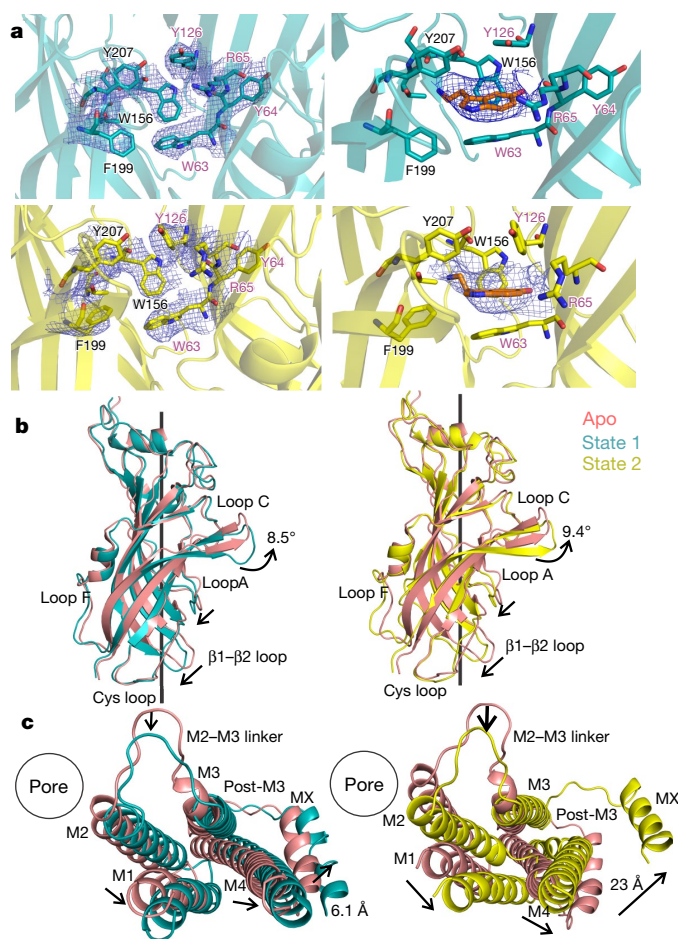


Fig. 2 | The serotonin-binding site and global conformational differences between the apo and serotonin-bound states. **a**, Top, the state 1 map around the side chains of residues at the subunit interface that constitute the serotonin-binding site (top left, contoured at 10σ); the density map for serotonin in state 1 (top right, contoured at 7.5σ). Bottom, the state 2 density map for the same residues (bottom left, 9σ) and serotonin (bottom right, 7.5σ). **b**, A comparison of the ECDs of the apo structure with state 1 (left) and state 2 (right) when aligned with respect to the TMD. Arrows indicate the direction of displacements between the two structures. **c**, A view of the TMDs of the (-) subunit from the extracellular end when aligned with respect to the ECDs of the (+) subunit for state 1 and apo (left), and for state 2 and apo (right).

locations along the permeation pathway (Lys108 and Asp105 in the ECD, Leu260 (L9') and Glu250 (E-1') in the TMD, and Arg416 in the ICD) to radii below approximately 2.76 \AA (the radius of a hydrated Na^+ ion)¹², reflecting its non-conductive conformation. The numbering in parentheses refers to the residue positions within the pore-lining M2 helices. Whereas Leu260 in the middle of the M2 helix forms part of the activation gate¹³, Glu250 at the intracellular end forms the selectivity filter¹⁴. Compared to the apo pore, state 1 exhibits an expansion of the pore at each of these constriction points. The radius at Leu260 is approximately 3.0 \AA and the pore within M2 is narrowest at Ser253 (S2') (approximately 2.7 \AA), suggesting that these locations may impede permeation of hydrated Na^+ ion. State 2 has the widest pore among the three structures, with an internal radius larger than 3.2 \AA , notably at positions below Leu260 and extending all the way into the ICD, indicating a potentially conductive conformation. In comparison to the apo structure, the M2 helices are rotated clockwise by 7.5° in state 1 and by 13° in state 2, and positioned outward (Fig. 1c) with the Leu260 side chains rotated away from the pore axis. Additionally, in state 2, the helix is bent at Ser253 and tilted 25° away from the pore axis at the level of Glu250, thereby creating a wider vestibule at the intracellular end of M2.

State 1 and state 2 reveal a distinct density for serotonin at the neurotransmitter-binding site located at the interface of two adjacent subunits (Fig. 2a, right). Residues from loops A, B and C on the principal (+) subunit and loops D, E and F from the complementary (-) subunit^{15,16} form a cage-like enclosure for serotonin (Fig. 2a, left). In state 1 and state 2, loop C is in a closed position in comparison to the outward or 'open' orientation of loop C in the apo state (Fig. 2b), consistent with agonist-bound conformations of the acetylcholine-binding protein¹⁷. Several interactions between serotonin and binding-site residues (Trp156, Arg65 and Trp63) have previously been proposed^{16,18,19}; these residues are within 4 \AA of serotonin in state 1 and state 2.

A comparison with the apo structure reveals a global twisting of the ECD and TMD in the serotonin-bound states (Extended Data Fig. 4a). There is an overall counter-clockwise rotation of the ECD around the pore axis, leading to major repositioning of individual interfacial loops (Fig. 2b, Extended Data Fig. 4b), similar to other pLGICs^{5,20}. As a result, buried areas between adjacent subunits are reduced in state 1 ($3,096\text{ \AA}^2$) and state 2 ($2,533\text{ \AA}^2$) compared to the apo state ($3,161\text{ \AA}^2$). This change is also reflected in decreasing inter-subunit interactions at the ECD-TMD and TMD-ICD interfaces from the apo state to state 1, and from state 1 to state 2 (Extended Data Fig. 5). At the level of the TMD, serotonin induces a clockwise rotation with an expansion of the transmembrane helices away from the pore axis (Extended Data Fig. 4a (bottom), c). An outward displacement of M2 is accompanied by a marked outward movement of the M2-M3 loop away from the inter-subunit interface (Fig. 2c), which reduces its interactions with the pre-M1 region and the $\beta 8$ - $\beta 9$ loop in the neighbouring subunit relative to the apo state (Extended Data Fig. 5a).

The most notable difference among the three structures is the conformation of the ICD, which is comprised largely of the M3-M4 linker. In state 1 and the apo state, the membrane-associated (MA) helix²¹ appears as a straight helix extending into M4. In state 2, the MA-M4 helix is bent (20° with respect to the MA helix) in the vicinity of Gly430, and appears as two separate helices that are tilted away from the pore axis³ (Fig. 3a, Extended Data Fig. 6), thereby enlarging the central cavity at the TMD-ICD interface (Fig. 1a). Gly430 may introduce greater flexibility at the hinge point between the MA and M4 helices. In the apo state, the ion-exit pathways are occluded at two different levels: the post-M3 loop obstructs the lateral portals lined by MA-M4 helices (Extended Data Fig. 5b), and the MA helices form a tight bundle that sterically occludes ion permeation along the pore axis (Fig. 1b, Extended Data Fig. 6). Whereas there are small conformational changes in these regions in state 1 relative to the apo state, there are much larger differences in state 2; the post-M3 loop extends away from the MA-M4 helix, creating lateral portals with openings of dimensions $16.0 \times 11.4\text{ \AA}$ (Fig. 3b, c). These portals are large enough to accommodate hydrated Na^+ ions and may serve as exit pathways for permeant ions (Fig. 3b), consistent with the early hypotheses made on the basis of studies on the nicotinic acetylcholine receptor (nAChR)²¹ and the 5-HT_{3A} receptor²². The MX helix in the apo state and state 1 lies parallel to the putative membrane-water interface. In state 2, it is displaced upward from the interface and, consequently, pulls the post-M3 loop away from the lateral portal. Additionally, the outward movement of the MA helix disrupts the tight packing of the helical bundle structure, thereby widening the pore in this region.

The electrostatic-potential maps show that, whereas the ion permeation pathway in the ECD and the TMD is lined with predominantly electronegative side chains (Fig. 3c), the ICD is lined with clusters of positively charged residues on the MA helix. In state 2, the entrances to the lateral portals are lined with three key arginine residues (Arg416, Arg420 and Arg424) from the MA helix (Extended Data Fig. 6a), which are reported to be responsible for the unusually low single-channel conductance of the 5-HT_{3A} receptor (0.4 – 0.6 pS)²³ through mechanisms involving steric occlusion and electrostatic repulsion²². As expected, mutations to the Arg side chain markedly increase single-channel conductance (up to 40-fold)⁹. Previous studies have demonstrated that both the length and the sequence of the M3-M4 linker have substantial

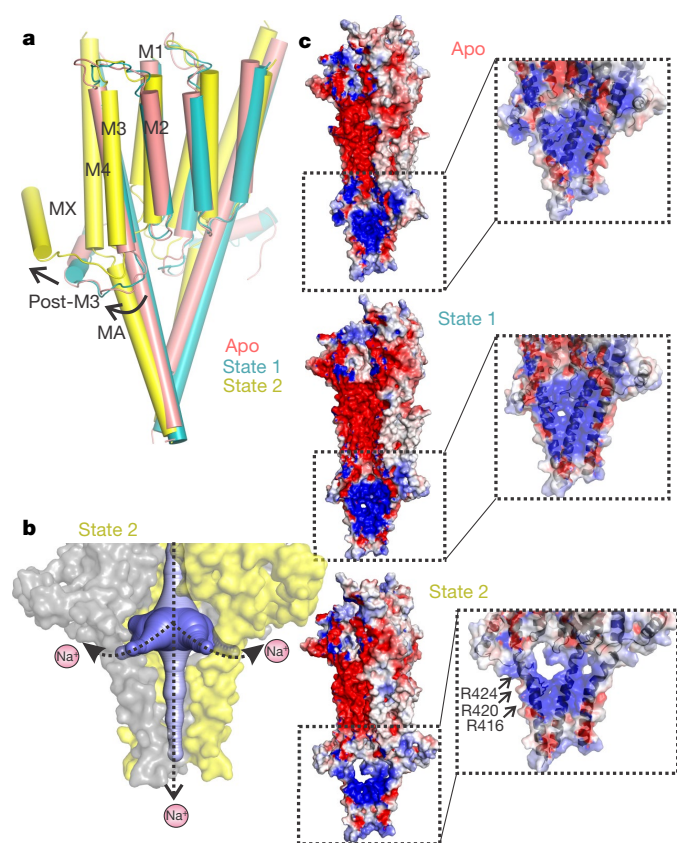


Fig. 3 | Opening of the lateral portal for ion exit. a, An alignment of apo, state 1 and state 2 structures. The TMD and ICD are shown for two adjacent subunits. The arrows show the direction of relative movements of the helices. **b**, The solvent-accessible vestibule in the ICD of state 2 was calculated with a minimum cavity radius of 2.8 Å. One of the subunits in the surface representation is removed for clarity. The plausible ion-exit pathways are indicated by dotted arrows. **c**, The solvent-accessible electrostatic potential map generated using the APBS tool. The inset shows a zoomed-in view of the ICD to highlight the progressive opening of the lateral portal from the apo structure to state 2. Residues Arg416, Arg420 and Arg424 (shown in stick representation) are implicated in regulating the single channel conductance of the 5-HT_{3A} receptor.

effects on channel function^{10,24}, and several positions in the MA helix regulate single-channel conductance^{22,25}, inward rectification¹⁰, gating and desensitization^{10,26,27}. Collectively, and in the light of the structures presented here, these studies underscore the role of the ICD in many aspects of channel function.

To assess the conductance in the apo state, state 1 and state 2, we performed molecular dynamics simulations with the structures inserted into a phospholipid bilayer (Fig. 4). An analysis of simulated water density along the pore axis suggests that the apo structure is closed to water, with two hydrophobic constrictions that are de-wetted: one is at about -60 Å in the ICD, lined by hydrophobic residues Leu402, Leu406 and Ile409 on the MA helix, and the other is at about 0 Å around Leu260 in M2. In simulations performed with a transmembrane potential, no permeation events were observed for Na⁺ ions in this conformation. In state 1, similar energetic barriers for water were present along the pore. However, a small number of Na⁺ ions were observed to traverse the channel when a transmembrane potential difference was added to the simulation. State 2, on the other hand, did not present a barrier for water within the TMD, and Na⁺ permeation events were observed throughout the simulations. However, the hydrophobic region at -60 Å was almost entirely de-wetted, and Na⁺ ions failed to permeate this region. Instead, the ions exited the ICD through the lateral portals, consistent with predictions that these regions serve as exit pathways for ions^{21,22} (Supplementary Video 1).

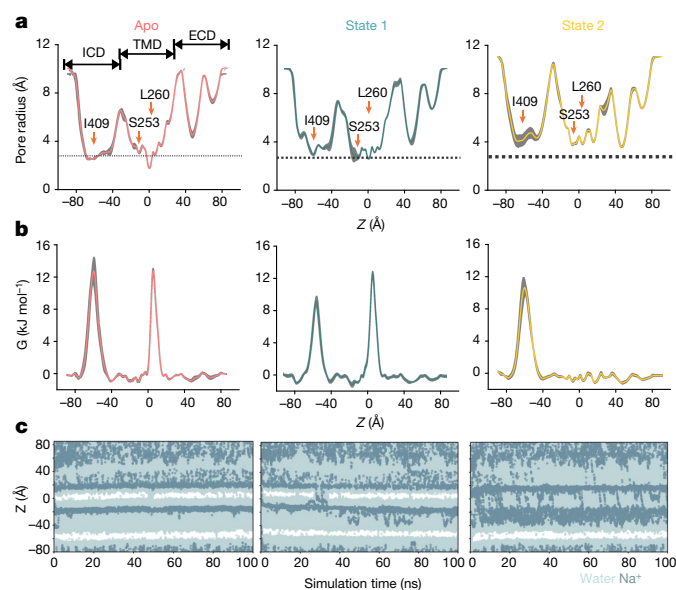


Fig. 4 | Molecular dynamics simulations of apo, state 1 and state 2 structures. a, b, Each structure was subjected to three 50-ns equilibrium simulations, with the replicates initiated from separately assembled protein-membrane systems. Radius and energy profiles were calculated for each simulation (using the final 40 ns of the trajectory, with a sampling interval of 0.5 ns) and averaged across replicates. For each structure, the mean profile and the one-standard-deviation range between calculations ($n = 3$) is shown as grey band. **a**, Mean radius along the central pore axis. The dashed line indicates the approximate radius of a hydrated Na⁺ ion. **b**, Corresponding free-energy profiles of a water molecule along the central pore axis. **c**, Trajectories of water and Na⁺ ion coordinates within 5 Å of the channel axis inside the pore over 100 ns with a 0.2-V transmembrane potential difference, with the cytoplasmic side having a negative potential. White stretches indicate regions devoid of water and ions. The energetic barriers due to the ring of Leu260 and Ile409 are at $z \sim 0$ Å and $z \sim -60$ Å, respectively. One of three independent 100-ns replicates is shown for each structure.

Overall, these findings reveal that the apo state is non-conductive, whereas state 2 represents a conductive conformation. Brief and infrequent permeation events observed for state 1 suggest that it has low conductance. Closer examination of state 1 shows that the pore is de-wetted when the Leu260 side chains point inwards (as seen in the apo state) and the pore is hydrated when the side chains point away (Extended Data Fig. 7). Of note, Glu250 side chains also underwent considerable shifts in conformation that led to changes in the local pore radius, which was sometimes reduced to approximately 2.4 Å when the Glu side chains were pointing inwards (Extended Data Fig. 8). Therefore, on the basis of these analyses we conclude that, although state 1 is mostly non-conductive, side-chain fluctuations may allow a small conductance in this state.

A comparison with representative pLGIC conformational states shows that in the resting conformation the hydrophobic extracellular half of M2 forms the activation gate—with 9' being the narrowest region—and in the desensitized conformation, the intracellular end is constricted (Extended Data Fig. 9). However, notable differences in the extent of constrictions may reflect the inherent differences in gating kinetics, origin or perhaps the nature of biochemical modification involved in determining these structures. Leu260 (9') is conserved across pLGICs, and our finding of the key role of this residue in pore constriction and hydration is consistent with its role in gating and desensitization^{28–30}. At the intracellular end, Ser253 (2') lines the narrowest region in state 1, and the S253T mutation results in serotonin-induced currents (10 μM) with unusually slow kinetics of decay (Fig. 5a, b). The narrow pore at this position is also consistent with Cd²⁺-coordination studies³¹. Glu250 (-1') is positioned at

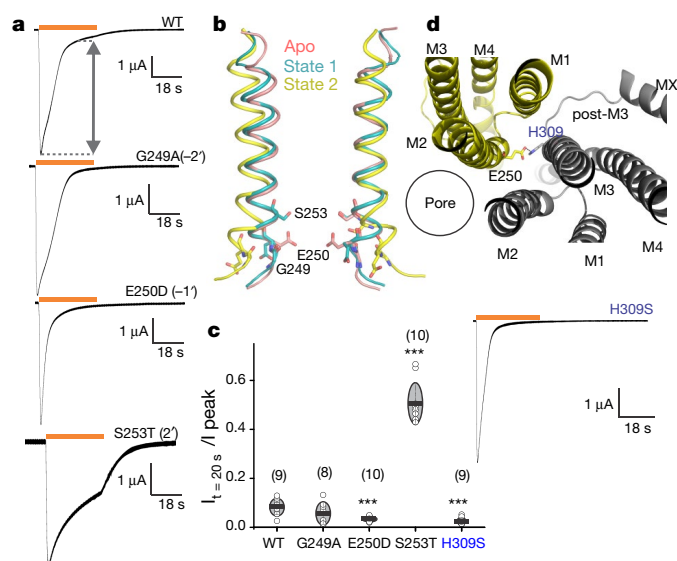


Fig. 5 | Functional characterization of mutations in pore-lining residues. **a**, Two-electrode voltage-clamp (TEVC) recording (at -60 mV) of wild-type (WT) 5-HT_{3A} receptor and G249A, E250D and S253T mutants, expressed in oocytes. Currents were elicited in response to 10 μ M serotonin (duration of serotonin application is shown as an orange line). **b**, The mutated residues in M2 (ribbons) are shown as sticks on two subunits. **c**, A plot of the ratio of current measured at $t = 20$ s over the peak current amplitude. The number of individual oocyte recordings is indicated in parenthesis. Data are shown as mean \pm s.d. ***, statistically significant. E250D, $P = 0.0003$; S253T, $P = 9.6 \times 10^{-11}$; H309S, $P = 0.0002$. Two-sample t -test for mutants and wild type at 95% confidence level. **d**, Top, interaction between Glu250 and His309 from two adjacent subunits as seen from the extracellular side (top). TEVC recording of current induced by 10 μ M serotonin for the H309S mutant (bottom).

the narrowest region in the nAChR structure captured in a desensitized conformation⁴, and the side chain shows extensive fluctuations in the simulations of state 1. A charge-preserving mutation at this position (E250D) led to enhanced desensitization (Fig. 5a, c). In state 2, Glu250 appears to potentially interact with His309 in M3 from the adjacent subunit (Fig. 5d), and the H309S mutant also shows rapidly desensitizing currents (Fig. 5c, d, bottom). There was no notable change in the desensitization of G249A, consistent with findings that the M1–M2 linker has relatively minimal effect on desensitization²⁷. Overall, these results are in agreement with the idea that the intracellular end of M2 has an important role in ion selectivity and gating.

Together, the apo and serotonin-bound 5-HT_{3A} receptor structures provide many insights into the activation mechanism. Serotonin induces a global twisting in the ECD, TMD and ICD, leading to reduced inter-subunit interactions and larger solvent-exposed surfaces. The state 2 conformation features large displacements in the ICD that widen the central cavity and open ion-exit pathways at the lateral portals and along the pore axis. The overall pore conformation suggests that state 2 is likely to represent a conductive, open state. We cannot unequivocally assign a functional state to the state 1 conformation, and it is unclear whether it corresponds to a pre-open, non-conducting intermediate or a desensitized state. Further studies are needed to further evaluate this conformation and determine the significance of potential intermediate states in channel gating.

Online content

Any methods, additional references, Nature Research reporting summaries, source data, statements of data availability and associated accession codes are available at <https://doi.org/10.1038/s41586-018-0660-7>.

Received: 21 May 2018; Accepted: 30 August 2018;
Published online 31 October 2018.

- Maricq, A. V., Peterson, A. S., Brake, A. J., Myers, R. M. & Julius, D. Primary structure and functional expression of the 5-HT₃ receptor, a serotonin-gated ion channel. *Science* **254**, 432–437 (1991).
- Machu, T. K. Therapeutics of 5-HT₃ receptor antagonists: current uses and future directions. *Pharmacol. Ther.* **130**, 338–347 (2011).
- Unwin, N. Refined structure of the nicotinic acetylcholine receptor at 4 Å resolution. *J. Mol. Biol.* **346**, 967–989 (2005).
- Morales-Perez, C. L., Novelli, C. M. & Hibbs, R. E. X-ray structure of the human $\alpha 4\beta 2$ nicotinic receptor. *Nature* **538**, 411–415 (2016).
- Du, J., Lu, W., Wu, S., Cheng, Y. & Gouaux, E. Glycine receptor mechanism elucidated by electron cryo-microscopy. *Nature* **526**, 224–229 (2015).
- Hassaine, G. et al. X-ray structure of the mouse serotonin 5-HT₃ receptor. *Nature* **512**, 276–281 (2014).
- Miller, P. S. & Aricescu, A. R. Crystal structure of a human GABA_A receptor. *Nature* **512**, 270–275 (2014).
- Connolly, C. N. Trafficking of 5-HT₃ and GABA_A receptors. *Mol. Membr. Biol.* **25**, 293–301 (2008).
- Peters, J. A. et al. The 5-hydroxytryptamine type 3 (5-HT₃) receptor reveals a novel determinant of single-channel conductance. *Biochem. Soc. Trans.* **32**, 547–552 (2004).
- Baptista-Hon, D. T., Deeb, T. Z., Lambert, J. J., Peters, J. A. & Hales, T. G. The minimum M3–M4 loop length of neurotransmitter-activated pentameric receptors is critical for the structural integrity of cytoplasmic portals. *J. Biol. Chem.* **288**, 21558–21568 (2013).
- Basak, S. et al. Cryo-EM structure of 5-HT_{3A} receptor in its resting conformation. *Nat. Commun.* **9**, 514 (2018).
- Marcus, Y. Ionic radii in aqueous solution. *Chem. Rev.* **88**, 1475–1498 (1988).
- Panicker, S., Cruz, H., Arrabit, C. & Slesinger, P. A. Evidence for a centrally located gate in the pore of a serotonin-gated ion channel. *J. Neurosci.* **22**, 1629–1639 (2002).
- Thompson, A. J. & Lummis, S. C. A single ring of charged amino acids at one end of the pore can control ion selectivity in the 5-HT₃ receptor. *Br. J. Pharmacol.* **140**, 359–365 (2003).
- Brejck, K. et al. Crystal structure of an ACh-binding protein reveals the ligand-binding domain of nicotinic receptors. *Nature* **411**, 269–276 (2001).
- Kesters, D. et al. Structural basis of ligand recognition in 5-HT₃ receptors. *EMBO Rep.* **14**, 49–56 (2013).
- Hansen, S. B. et al. Structures of *Aplysia* AChBP complexes with nicotinic agonists and antagonists reveal distinctive binding interfaces and conformations. *EMBO J.* **24**, 3635–3646 (2005).
- Beene, D. L. et al. Cation- π interactions in ligand recognition by serotonergic (5-HT_{3A}) and nicotinic acetylcholine receptors: the anomalous binding properties of nicotine. *Biochemistry* **41**, 10262–10269 (2002).
- Yuan, S., Filippek, S. & Vogel, H. A gating mechanism of the serotonin 5-HT₃ receptor. *Structure* **24**, 816–825 (2016).
- Sauguet, L. et al. Crystal structures of a pentameric ligand-gated ion channel provide a mechanism for activation. *Proc. Natl Acad. Sci. USA* **111**, 966–971 (2014).
- Miyazawa, A., Fujiyoshi, Y., Stowell, M. & Unwin, N. Nicotinic acetylcholine receptor at 4.6 Å resolution: transverse tunnels in the channel wall. *J. Mol. Biol.* **288**, 765–786 (1999).
- Kelley, S. P., Dunlop, J. I., Kirkness, E. F., Lambert, J. J. & Peters, J. A. A cytoplasmic region determines single-channel conductance in 5-HT₃ receptors. *Nature* **424**, 321–324 (2003).
- Hussy, N., Lukas, W. & Jones, K. A. Functional properties of a cloned 5-hydroxytryptamine ionotropic receptor subunit: comparison with native mouse receptors. *J. Physiol.* **481**, 311–323 (1994).
- McKinnon, N. K., Bali, M. & Akabas, M. H. Length and amino acid sequence of peptides substituted for the 5-HT_{3A} receptor M3M4 loop may affect channel expression and desensitization. *PLoS ONE* **7**, e35563 (2012).
- Hales, T. G. et al. Common determinants of single channel conductance within the large cytoplasmic loop of 5-hydroxytryptamine type 3 and $\alpha 4\beta 2$ nicotinic acetylcholine receptors. *J. Biol. Chem.* **281**, 8062–8071 (2006).
- Hu, X. Q., Sun, H., Peoples, R. W., Hong, R. & Zhang, L. An interaction involving an arginine residue in the cytoplasmic domain of the 5-HT_{3A} receptor contributes to receptor desensitization mechanism. *J. Biol. Chem.* **281**, 21781–21788 (2006).
- Papke, D. & Grosman, C. The role of intracellular linkers in gating and desensitization of human pentameric ligand-gated ion channels. *J. Neurosci.* **34**, 7238–7252 (2014).
- Yakel, J. L., Lagrutta, A., Adelman, J. P. & North, R. A. Single amino acid substitution affects desensitization of the 5-hydroxytryptamine type 3 receptor expressed in *Xenopus* oocytes. *Proc. Natl Acad. Sci. USA* **90**, 5030–5033 (1993).
- Revah, F. et al. Mutations in the channel domain alter desensitization of a neuronal nicotinic receptor. *Nature* **353**, 846–849 (1991).
- Basak, S., Schmandt, N., Gicheru, Y. & Chakrapani, S. Crystal structure and dynamics of a lipid-induced potential desensitized-state of a pentameric ligand-gated channel. *eLife* **6**, e23886 (2017).
- Panicker, S., Cruz, H., Arrabit, C., Suen, K. F. & Slesinger, P. A. Minimal structural rearrangement of the cytoplasmic pore during activation of the 5-HT_{3A} receptor. *J. Biol. Chem.* **279**, 28149–28158 (2004).

Acknowledgements This research was supported in part by the National Cancer Institute's National Cryo-EM Facility at the Frederick National Laboratory for Cancer Research, and we thank them for the imaging time. We thank the Cleveland Center for Membrane and Structural Biology for the access to cryo-EM instrumentation, D. Major for assistance with hybridoma

and cell culture at Department of Ophthalmology and Visual Sciences (NIH Core Grant P30EY11373), W. Boron for *Xenopus* oocytes and access to the oocyte rig, and G. Klesse and S. Tucker for the Channel Annotation Package methodology. This work was supported by an NIH grant (1R01GM108921), a cryo-EM supplement (3R01GM108921-03S1) to S.C. and an AHA postdoctoral Fellowship to S.B. (17POST33671152).

Reviewer information *Nature* thanks S. M. Sine, A. I. Sobolevsky and the other anonymous reviewer(s) for their contribution to the peer review of this work.

Author contributions S.B. and S.C. conceived the project and designed experimental procedures. S.B. carried out cryo-EM sample preparation, screening, data analysis and structure determination. Y.G. performed electrophysiological recordings. S.R. performed the molecular dynamics simulations under the supervision of M.S.P.S. S.C. supervised the execution of

the experiments, data analysis and interpretation. S.B., Y.G. and S.C. drafted the manuscript. All authors reviewed the final manuscript.

Competing interests The authors declare no competing interests.

Additional information

Extended data is available for this paper at <https://doi.org/10.1038/s41586-018-0660-7>.

Supplementary information is available for this paper at <https://doi.org/10.1038/s41586-018-0660-7>.

Reprints and permissions information is available at <http://www.nature.com/reprints>.

Correspondence and requests for materials should be addressed to S.C.

Publisher's note: Springer Nature remains neutral with regard to jurisdictional claims in published maps and institutional affiliations.

METHODS

No statistical methods were used to predetermine sample size. The experiments were not randomized. The investigators were not blinded to allocation during experiments and outcome assessment.

Cloning and functional measurements in oocytes. The gene encoding the mouse 5-HT_{3A} receptor (purchased from GenScript) was inserted into the pTLN vector for *Xenopus laevis* oocyte expression and confirmed by DNA sequencing. DNA linearization was carried out by incubation with the *MluI* restriction enzyme overnight at 37 °C. mRNA synthesis was done using the mMessage mMachine kit (Ambion) as per the manufacturer's instructions. The eluted mRNA was purified with RNeasy (Qiagen), and injected (3–10 ng) into *Xenopus laevis* oocytes (stages V–VI). As a control to verify that no endogenous currents were present, oocytes were injected with the same volume of water. The oocytes used in this study were kindly provided by W. F. Boron. Female *Xenopus laevis* were purchased from Nasco. All animal experimental procedures were approved by Institutional Animal Care and Use Committee (IACUC) of Case Western Reserve University. Oocytes were maintained at 18 °C in OR3 medium (GIBCO-BRL Leibovitz medium containing glutamate, 500 units each of penicillin and streptomycin, pH adjusted to 7.5, osmolality adjusted to 197 mOsm). Two-electrode voltage-clamp experiments were performed at room temperature 2–5 days after injection on a Warner Instruments Oocyte Clamp OC-725. The currents were sampled and digitized at 500 Hz with a Digidata 1332A and analysed by Clampfit 10.2 (Molecular Devices). Oocytes were clamped at a holding potential of –60 mV, and currents were recorded in response to serotonin application. Solutions were changed using a syringe pump perfusion system flowing at a rate of 6 ml/min. The electrophysiological solutions contained 96 mM NaCl, 2 mM KCl, 1.8 mM CaCl₂, 1 mM MgCl₂, and 5 mM HEPES (pH 7.4, osmolality adjusted to 195 mOsm). All chemical reagents were purchased from Sigma-Aldrich. For wild type and mutants, the current decay was assessed by the ratio of the current measured at time = 20 s (from the start of ligand application) over peak current amplitude.

Cloning and transfection. Codon-optimized mouse *Htr3a* gene (NCBI Reference Sequence: NM_001099644.1) was purchased from GenScript and subcloned into pFastBac1 vector. The pFastBac1 vector includes four strep-tags (WSHPQFEK) at the N terminus, followed by a linker sequence (GGGSGGGSGGG) and a TEV-cleavage sequence (ENLYFQG). The construct also includes a C-terminal 1D4-tag³². *Spodoptera frugiperda* cells (Sf9, Invitrogen) were cultured in ESF921 medium (Expression Systems) in the absence of antibiotics and incubated at 28 °C without CO₂ exchange. Sub-confluent cells were transfected with recombinant bacmid DNA using Cellfectin II transfection reagent (Invitrogen) per manufacturer instructions. The cell culture supernatants were collected and centrifuged at 1,000g for 5 min to remove cell debris to obtain progeny 1 (P1) recombinant baculovirus 72 h post-transfection. P2 viruses were obtained through consecutive rounds of Sf9 cells infection with P1 viruses. The supernatants (P2) were used to infect Sf9 cells, thereby generating P3 viruses. These viruses (P3) were used for recombinant protein production.

Expression and purification of recombinant protein. Recombinant protein production was performed by infection of approximately 2.5×10^6 per ml Sf9 cells with P3 recombinant viruses. After 72 h post-infection, the cell medium was collected and centrifuged at 8,000g for 20 min at 4 °C to separate the supernatant from the pellet. The cell pellet was then resuspended in 20 mM Tris-HCl, pH 7.5, 36.5 mM sucrose, and 1% protease inhibitor cocktail. Cells were disrupted by sonication on ice and non-lysed cells were removed by centrifugation (3,000g for 15 min). The membrane fraction was separated by ultracentrifugation (167,000g for 1 h) and solubilized with 1% C₁₂E₉ in a buffer containing 500 mM NaCl, 50 mM Tris pH 7.4, 10% glycerol and 0.5% protease inhibitor by rotating for 2 h at 4 °C. Non-solubilized material was removed by ultracentrifugation (167,000g for 15 min). The supernatant was collected and bound with 1D4 beads pre-equilibrated with 150 mM NaCl, 20 mM HEPES pH 8.0 and 0.01% C₁₂E₉ for 2 h at 4 °C. The beads were then washed with 100 column volumes of 150 mM NaCl, 20 mM HEPES pH 8.0, and 0.01% C₁₂E₉ (buffer A). The protein was then eluted with buffer A supplemented with 3 mg/ml 1D4 peptide (TETSQVAPA). Eluted protein was then concentrated and deglycosylated with PNGase F (NEB) by incubating 5 units of the enzyme per 1 µg of the protein for 2 h at 37 °C under gentle agitation. Deglycosylated protein was then applied to a Superose 6 column (GE healthcare) equilibrated with buffer A. The peak fractions around 13.9 ml were pooled and concentrated to 2–3 mg/ml using 50-kDa MWCO Millipore filters (Amicon) and used subsequently for cryo-EM studies.

Sample preparation and cryo-EM data acquisition. Functional characterization shows that serotonin-induced 5-HT_{3A} receptor currents saturate at 30 µM and beyond^{11,33,34}. Therefore, the 5-HT_{3A} receptor protein (~2.5 mg/ml) was filtered and first incubated with 100 µM serotonin for 30 min. After which, 3 mM fluorinated Fos-choline-8 (Anatrache) was added and the sample was incubated until blotting³⁵. The sample was blotted twice with 3.5 µl sample each time onto Cu 300 mesh Quantifoil 1.2/1.3 grids (Quantifoil Micro Tools), and immediately after the second blot, the grid was plunge frozen into liquid ethane using a Vitrobot (FEI).

The grids were imaged using a 300 kV FEI Titan Krios microscope equipped with a Gatan K2-Summit direct detector camera. Movies containing 40 frames were collected at 130,000× magnification (set on microscope) in super-resolution mode with a physical pixel size of 0.532 Å/pixel, dose rate of 3.754 electrons/pixel/s, and a total exposure time of 12 s. Defocus values of the images ranged from –1.0 to –2.5 µm (input range setting for data collection) as per the automated imaging software Latitude S (Gatan).

Image processing. Beam-induced motion was corrected using MotionCor³⁶ with a B-factor of 150 pixels². Super-resolution images were binned (2×2) in Fourier space, making a final pixel size of 1.064 Å. All subsequent data processing was conducted in RELION 2.1³⁷. The defocus values of the motion-corrected micrographs were estimated using Gctf software³⁸. Approximately, 3,000 particles were manually picked from the 2,810 micrographs and sorted into two-dimensional (2D) classes. The best of these classes were then used as templates for automated particle picking. A loose auto-picking threshold was selected to ensure no good particles were missed at this stage. This resulted in ~749,970 auto-picked particles that were subjected to 2D classification to remove suboptimal particles. An initial 3D model was generated from the apo-5-HT_{3A} receptor cryo-EM structure (RCSB Protein Data Bank code (PDB ID): 6BE1) and low-pass filtered to 60 Å using EMAN2³⁹. Multiple rounds of 3D auto-refinements and 3D classifications generated 5 good classes. Among them two classes (containing total of 115,992 particles) belonged to state 1 and the other three classes (containing a total of 25,547 particles) represented the state 2 conformation. Subsequent 3D re-classifications, auto-refinement, imposing C₅ symmetry, and post-processing yielded state 1 and state 2 5-HT_{3A} receptor structures with final total particles of 103,698 and 18,839, respectively. In the post-processing step in RELION, a soft mask was calculated and applied to the two half-maps before the Fourier shell coefficient (FSC) was calculated. The B-factor estimation and map sharpening were performed in the post-processing step. An overall resolution of state 1 and state 2 was calculated to 3.32 Å and 3.89 Å, respectively (based on the gold-standard FSC = 0.143 criterion). Local resolutions were estimated using the RESMAP software⁴⁰.

5-HT_{3A} receptor model building. The map for state 1 and state 2 contained density for the entire ECD, TMD and a large region of the ICD. The final refined models comprised of residues Thr8–Ile332 and Leu397–Ser461. The missing region (333–396) is of the unstructured MX loop that links the amphipathic MX helix⁶ and the MA helix²¹. The apo-5-HT_{3A} receptor cryo-EM structure (PDB ID: 6BE1) was used as an initial model and aligned to the 5-HT_{3A} receptor cryo-EM map calculated with RELION 2.1. Cryo-EM map was converted to the mtz format using mapmask and sfall tools in CCP4i software⁴¹. The mtz map was then used for manual model building in COOT⁴². After initial model building, the state 1 and state 2 models were refined against their respective EM-derived maps using the phenix.real_space_refinement tool from the PHENIX software package⁴³, using rigid body, local grid, NCS, and gradient minimization. The models were then subjected to additional rounds of manual model fitting and refinement, resulting in good final models to map cross-correlation (Extended Data Table 1). Stereochemical properties of the model were evaluated by Molprobit⁴⁴.

Protein surface area and interfaces were analysed by using PDBePISA server (<http://www.ebi.ac.uk/pdbe/pisa/>). To compare the apo, state 1 and state 2 structures, all ligands, ions and water molecules were removed from the PDB files. Additional residues in the apo-5-HT_{3A} receptor structure were also removed before analysis so that surface area comparisons were made between identical construct lengths. Electrostatic surface potential calculations were carried out using the APBS tools plug-in PyMOL⁴⁵. The pore profile was calculated using the HOLE program⁴⁶. All the tunnels were calculated using Caver3.0 PyMOL plug-in with minimal tunnel radius of 2.8 Å⁴⁷. Figures were prepared using PyMOL v.2.0.4 (Schrödinger, LLC).

Molecular dynamics simulations. Each simulation cell (of approximate dimensions 13.5×13.5×19.5 nm³) contains the full-length receptor structure embedded in a phospholipid (POPC, 1-palmitoyl-2-oleoyl-sn-glycero-3-phosphocholine) bilayer, with an aqueous solution of Na⁺ and Cl[−] ions on either side. The protein-bilayer systems were assembled and equilibrated following a previously established protocol⁴⁸. The TIP4P water model⁴⁹ was used. Simulations were performed with GROMACS version 5.1^{50,51}, using the OPLS all-atom protein force field with united-atom lipids⁵², and at an integration time-step of 2 fs. A Verlet cut-off scheme was applied, and long-range electrostatic interactions were measured using the Particle Mesh Ewald method⁵³. The temperature and pressure were maintained at 37 °C and 1 bar, respectively, using the velocity-rescale thermostat⁵⁴ in combination with a semi-isotropic Parrinello and Rahman barostat⁵⁵, with coupling constants of $\tau_T = 0.1$ ps and $\tau_P = 1$ ps. Bonds were constrained through the LINCS algorithm⁵⁶, and an additional harmonic restraint at a force constant of 1,000 kJ mol^{−1} nm^{−2} was placed on the protein backbone atoms to preserve the original conformational state of the cryo-EM structure.

For water free-energy estimation, three 50 ns simulation replicates were each initiated from an independently assembled receptor–membrane system, containing

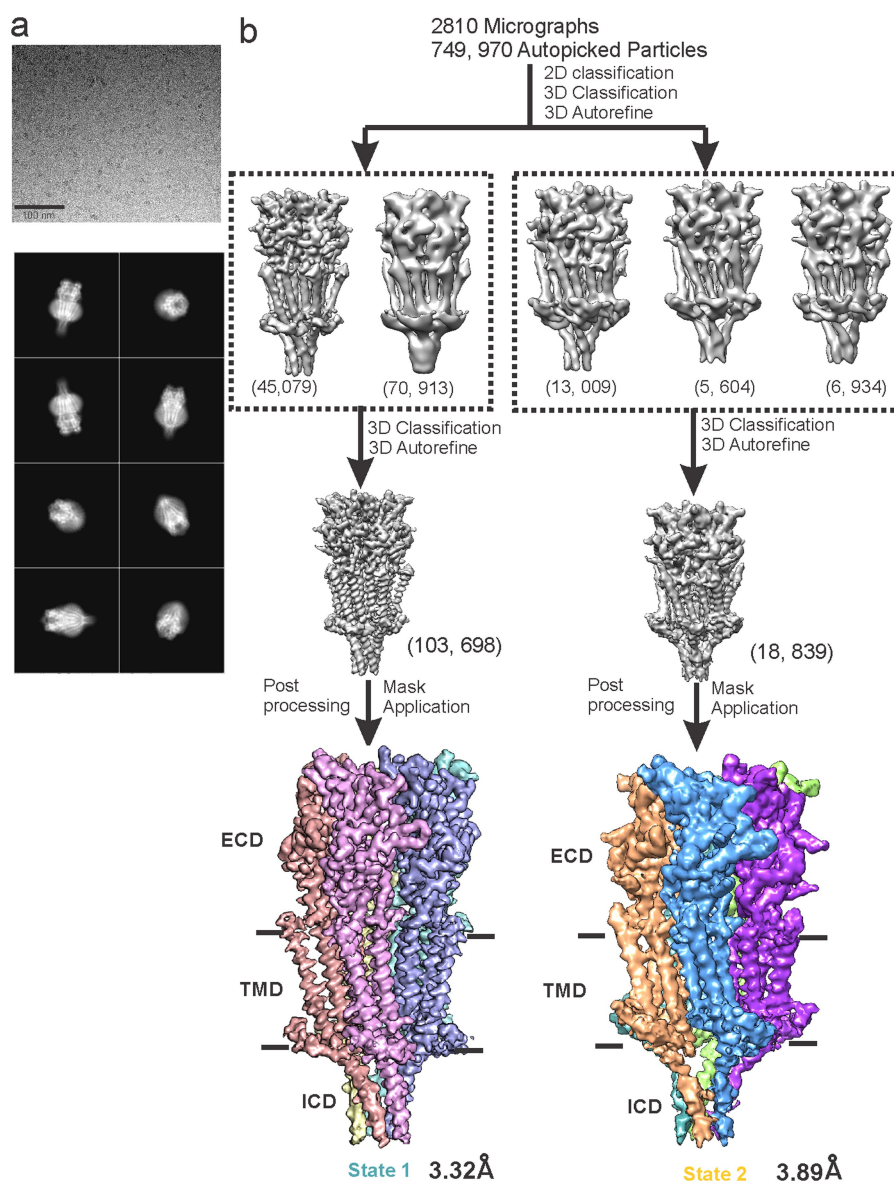
NaCl at an approximate concentration of 0.15 M. Using the Channel Annotation Package (www.channotation.org), the equilibrium density of water molecules at successive positions along the central pore axis was measured, and free-energy profiles were derived through an inverse Boltzmann calculation-based method⁵⁷. For monitoring ion permeation events, a separate set of simulations, each of 100 ns duration and with 0.7 M NaCl included in the simulation cell, were conducted in the presence of a 0.2 V transmembrane potential difference. This was applied by imposing an external, uniform electric field across the simulation cell along the membrane normal direction. The field strength was of magnitude 0.05 V nm^{-1} , with the cytoplasmic side having either negative or positive potential in different simulation runs.

Reporting summary. Further information on research design is available in the Nature Research Reporting Summary linked to this paper.

Data availability

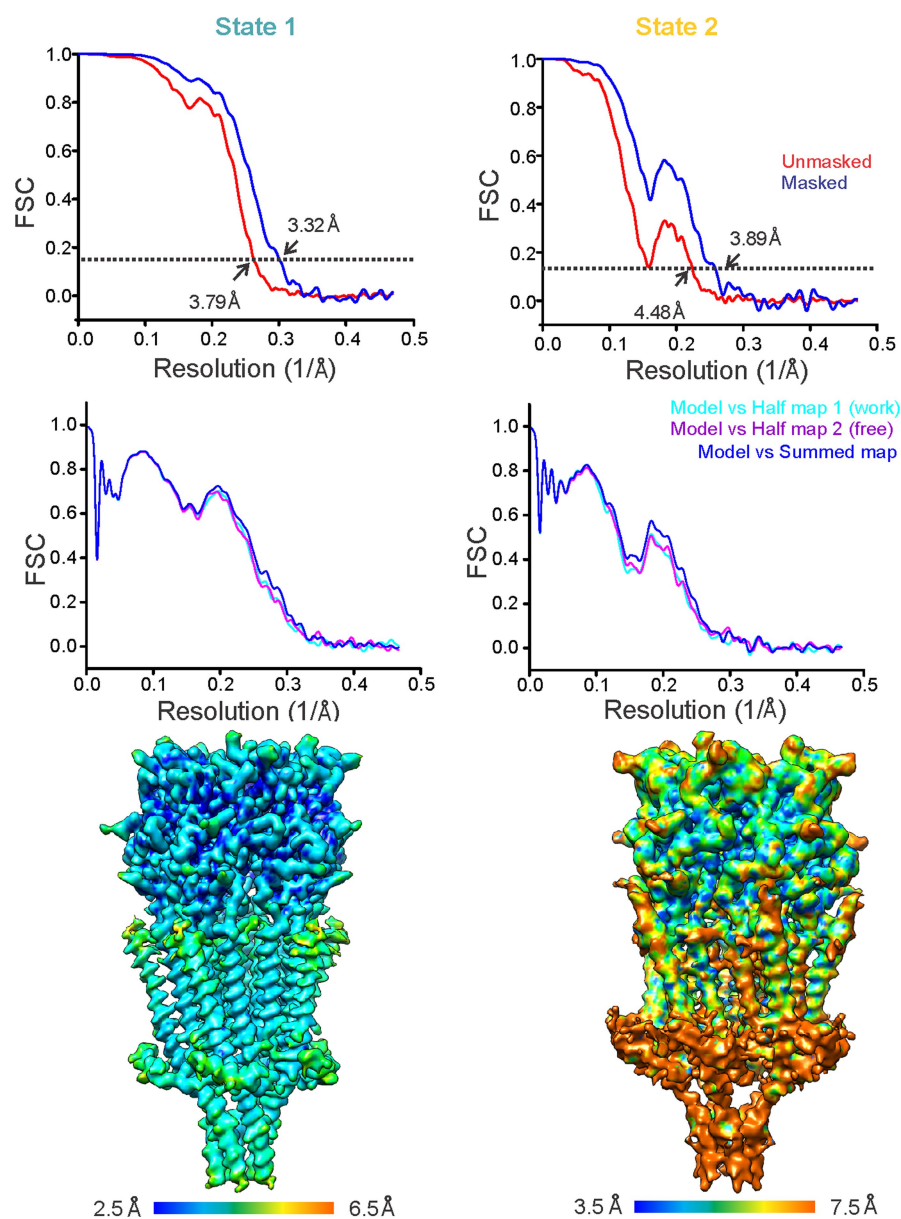
Coordinates of the 5-HT_{3A} receptor structures have been deposited at the PDB under accession codes 6DG7 (state 1) and 6DG8 (state 2). The cryo-EM map has been deposited in the Electron Microscopy Data Bank under accession code EMD-7882 (state 1) and EMD-7883 (state 2). All relevant data are available from the authors.

32. MacKenzie, D., Arendt, A., Hargrave, P., McDowell, J. H. & Molday, R. S. Localization of binding sites for carboxyl terminal specific anti-rhodopsin monoclonal antibodies using synthetic peptides. *Biochemistry* **23**, 6544–6549 (1984).
33. Stevens, R., Rusch, D., Solt, K., Raines, D. E. & Davies, P. A. Modulation of human 5-hydroxytryptamine type 3AB receptors by volatile anesthetics and *n*-alcohols. *J. Pharmacol. Exp. Ther.* **314**, 338–345 (2005).
34. Thompson, A. J. & Lummis, S. C. A single channel mutation alters agonist efficacy at 5-HT_{3A} and 5-HT_{3AB} receptors. *Br. J. Pharmacol.* **170**, 391–402 (2013).
35. Zhang, Z. & Chen, J. Atomic structure of the cystic fibrosis transmembrane conductance regulator. *Cell* **167**, 1586–1597 (2016).
36. Zheng, S. Q. et al. MotionCor2: anisotropic correction of beam-induced motion for improved cryo-electron microscopy. *Nat. Methods* **14**, 331–332 (2017).
37. Fernandez-Leiro, R. & Scheres, S. H. W. A pipeline approach to single-particle processing in RELION. *Acta Crystallogr. D* **73**, 496–502 (2017).
38. Mindell, J. A. & Grigorieff, N. Accurate determination of local defocus and specimen tilt in electron microscopy. *J. Struct. Biol.* **142**, 334–347 (2003).
39. Tang, G. et al. EMAN2: an extensible image processing suite for electron microscopy. *J. Struct. Biol.* **157**, 38–46 (2007).
40. Kucukelbir, A., Sigworth, F. J. & Tagare, H. D. Quantifying the local resolution of cryo-EM density maps. *Nat. Methods* **11**, 63–65 (2014).
41. Collaborative Computational Project. N. The CCP4 suite: programs for protein crystallography. *Acta Crystallogr. D* **50**, 760–763 (1994).
42. Emsley, P. & Cowtan, K. Coot: model-building tools for molecular graphics. *Acta Crystallogr. D* **60**, 2126–2132 (2004).
43. Adams, P. D. et al. PHENIX: building new software for automated crystallographic structure determination. *Acta Crystallogr. D* **58**, 1948–1954 (2002).
44. Chen, V. B. MolProbity: all-atom structure validation for macromolecular crystallography. *Acta Crystallogr. D* **66**, 12–21 (2010).
45. Baker, N. A., Sept, D., Joseph, S., Holst, M. J. & McCammon, J. A. Electrostatics of nanosystems: application to microtubules and the ribosome. *Proc. Natl Acad. Sci. USA* **98**, 10037–10041 (2001).
46. Smart, O. S., Neduvellil, J. G., Wang, X., Wallace, B. A. & Sansom, M. S. HOLE: a program for the analysis of the pore dimensions of ion channel structural models. *J. Mol. Graph.* **14**, 354–360, 376 (1996).
47. Chovancova, E. CAVER 3.0: a tool for the analysis of transport pathways in dynamic protein structures. *PLOS Comput. Biol.* **8**, e1002708 (2012).
48. Stansfeld, P. J. & Sansom, M. S. Molecular simulation approaches to membrane proteins. *Structure* **19**, 1562–1572 (2011).
49. Jorgensen, W. L., Chandrasekhar, J., Madura, J. D., Impey, R. W. & Klein, M. L. Comparison of simple potential functions for simulating liquid water. *J. Chem. Phys.* **79**, 926–935 (1983).
50. Berendsen, H. J. C., van der Spoel, D. & van Drunen, R. GROMACS: a message-passing parallel molecular dynamics implementation. *Comput. Phys. Commun.* **91**, 43–56 (1995).
51. Abraham, M. J., Murtola, T., Schulz, R., Pall, S. & Jeremy, C. GROMACS: high performance molecular simulations through multi-level parallelism from laptops to supercomputers. *SoftwareX* **1**, 19–25 (2015).
52. Jorgensen, W. L., Maxwell, D. S. & Tirado-Rives, J. Development and testing of the OPLS all-atom force field on conformational energetics and properties of organic liquids. *J. Am. Chem. Soc.* **118**, 11225–11236 (1996).
53. Darden, T., York, D. & Pedersen, L. Particle mesh Ewald: an *N*-log(*N*) method for Ewald sums in large systems. *J. Chem. Phys.* **98**, 10089–10092 (1993).
54. Bussi, G., Donadio, D. & Parrinello, M. Canonical sampling through velocity rescaling. *J. Chem. Phys.* **126**, 14101 (2007).
55. Parrinello, M. R. A. Polymorphic transitions in single crystals: a new molecular dynamics method. *J. Appl. Phys.* **52**, 7182–7190 (1981).
56. Hess, B., Bekker, H., Berendsen, H. J. C. & Fraaije, J. G. E. M. LINCS: a linear constraint solver for molecular simulations. *J. Comput. Chem.* **18**, 1463–1472 (1997).
57. Trick, J. L. et al. Functional annotation of ion channel structures by molecular simulation. *Structure* **24**, 2207–2216 (2016).
58. Cordes, F. S., Bright, J. N. & Sansom, M. S. Proline-induced distortions of transmembrane helices. *J. Mol. Biol.* **323**, 951–960 (2002).
59. Althoff, T., Hibbs, R. E., Banerjee, S. & Gouaux, E. X-ray structures of GluCl in apo states reveal a gating mechanism of Cys-loop receptors. *Nature* **512**, 333–337 (2014).
60. Hibbs, R. E. & Gouaux, E. Principles of activation and permeation in an anion-selective Cys-loop receptor. *Nature* **474**, 54–60 (2011).



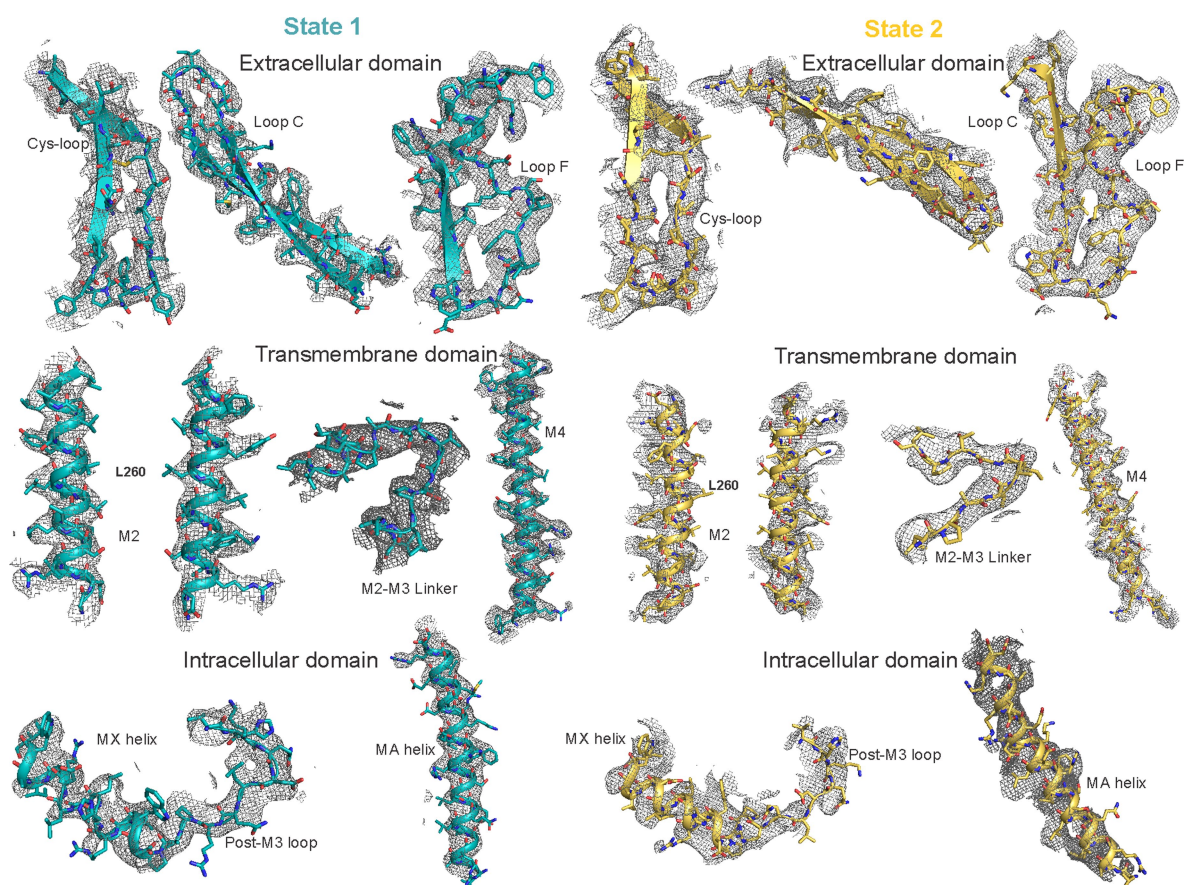
Extended Data Fig. 1 | Data processing workflow. **a**, A representative micrograph of 5-HT_{3A} receptor incubated with 100 μ M serotonin in vitreous ice (top). Selected 2D classes showing various orientations (bottom). **b**, A schematic of the steps followed in data processing leading to 3.32 Å and 3.89 Å reconstructions of state 1 and state 2, respectively.

Each subunit is shown in a different colour for clarity. Classes within the boxes represent two distinct conformations. Based on the number of particles for each state, it appears that state 1 is more populated than state 2 under our current conditions.



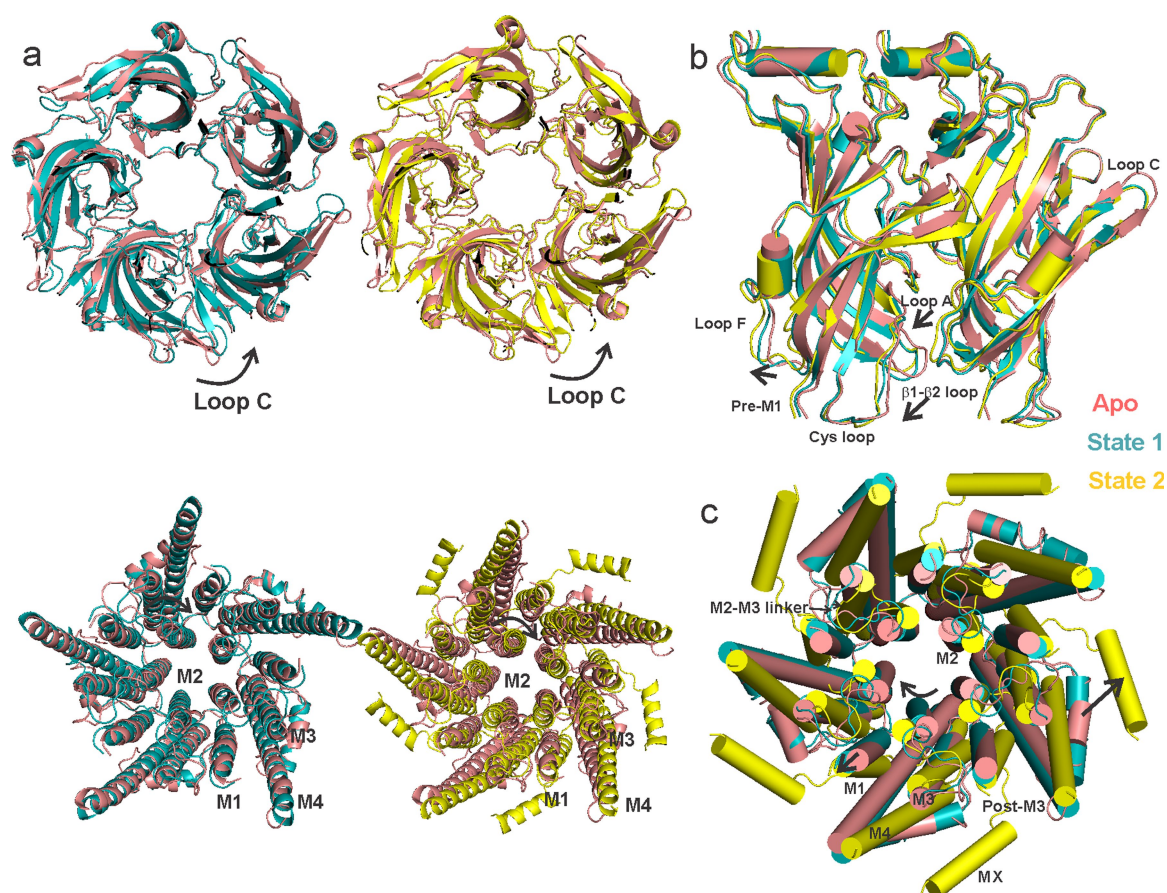
Extended Data Fig. 2 | Estimation of resolution and validation of the models. **a**, FSC curves before (red) and after (blue) the application of soft mask in RELION for state 1 (left) and state 2 (right). The dashed line represents FSC of 0.143. **b**, For cross validation, FSC curves of the refined model versus summed map (full dataset, blue), refined model versus half

map 1 (used during refinement, cyan), and refined model versus half map 2 (not used during refinement, purple) were calculated for state 1 (left) and state 2 (right). **c**, Local resolution of state 1 (left) and state 2 (right) reconstructions were estimated using the ResMap program⁴⁰.



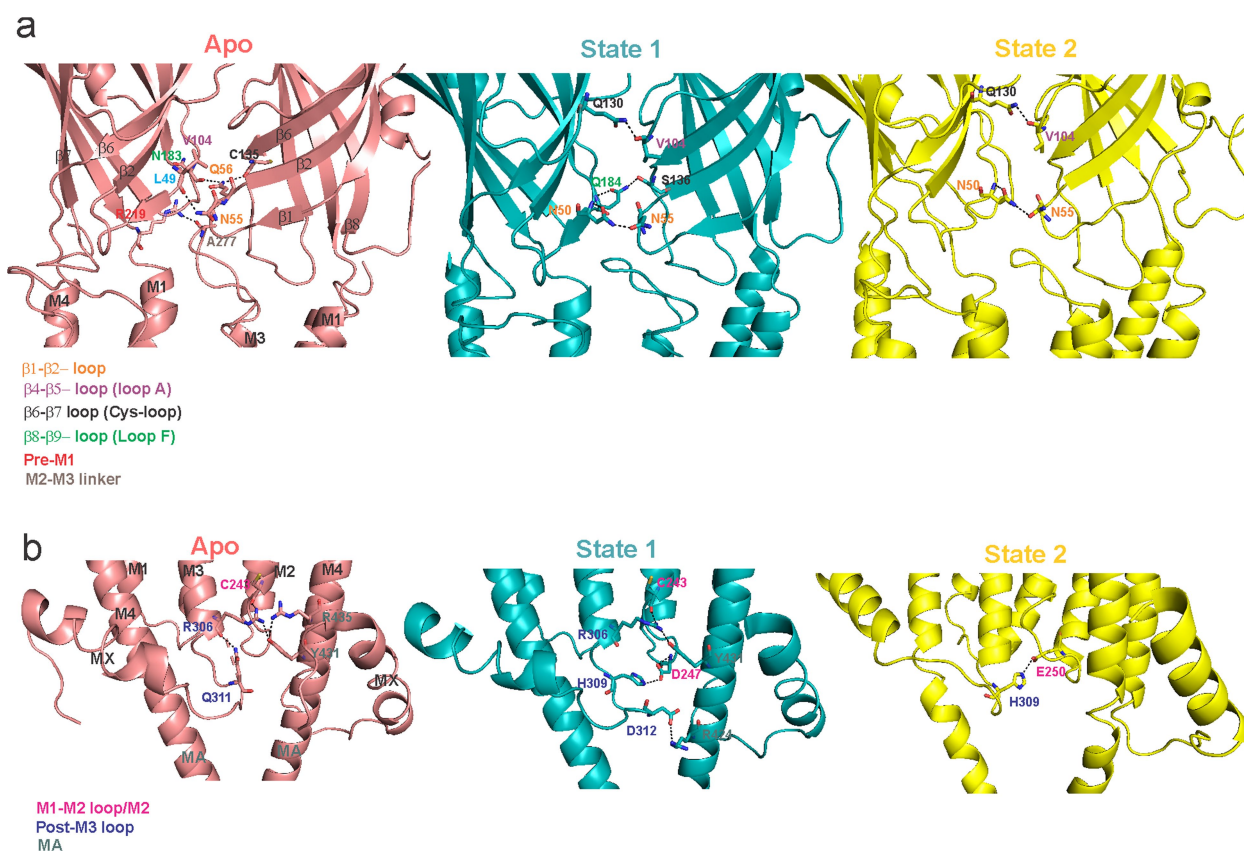
Extended Data Fig. 3 | Map correlation of state 1 and state 2. Various regions of the model (shown as a cartoon) and corresponding density map (mesh) around the residues are shown to validate the final model. Residues are depicted as sticks. The depicted regions in state 1 and the corresponding contour levels: Cys loop (7.0σ), loop C (8.0σ), loop F

(8.0σ), M2 (6.0σ), M2–M3 linker (7.0σ), M4 (6.5σ), MX helix (7.5σ) and MA helix (7.5σ). The depicted regions in state 2 and the corresponding contour levels: Cys loop (8.5σ), loop C (8.0σ), loop F (8.0σ), M2 (6.0σ), M2–M3 linker (7.0σ), M4 (7.0σ), MX helix (7.0σ) and MA helix (6.0σ).



Extended Data Fig. 4 | Serotonin-induced conformational changes in the ECD and TMD. **a**, A global alignment of the apo structure with state 1 (left) and state 2 (right). The top panel shows the ECD and the bottom panel shows the TMD, both viewed from the extracellular end. The arrows indicate the direction of rotation with respect to the apo state. State 1 and state 2 structures superimpose with the apo ECD with a root mean square deviation (r.m.s.d.) of 1.16 for state 1 and 1.41 for state 2 (residues 8–220).

State 1, and particularly state 2, diverge markedly in the TMD and ICD (r.m.s.d. of 1.1 for state 1 and 4.24 for state 2 for residues 221–462). **b**, A side-view of the ECDs upon aligning state 1 and state 2 to the apo state. **c**, A top view of the TMDs when aligned with respect to the ECD. The arrows show relative displacements in different regions of state 1 and state 2 with respect to the apo structure.

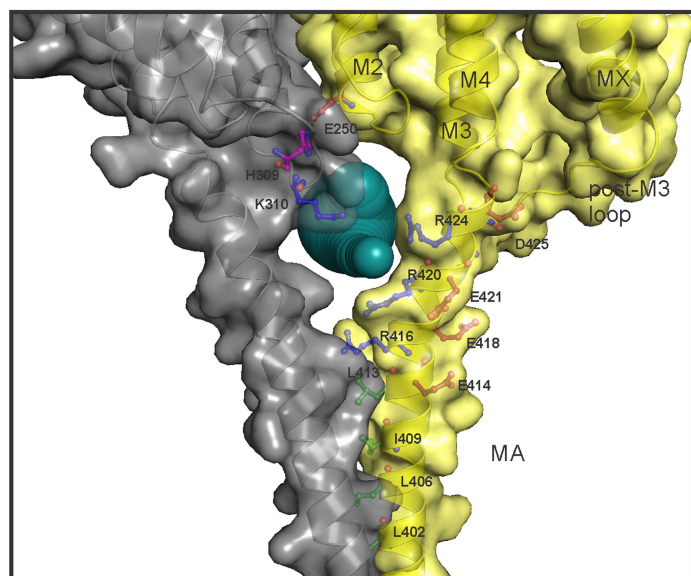


Extended Data Fig. 5 | Inter-subunit interaction at the ECD-TMD-ICD interface. **a**, Inter-subunit interactions at the ECD-TMD interface in the apo state, state 1 and state 2. **b**, Inter-subunit interactions at the TMD-ICD interface in the three states. The potential interactions were predicted as

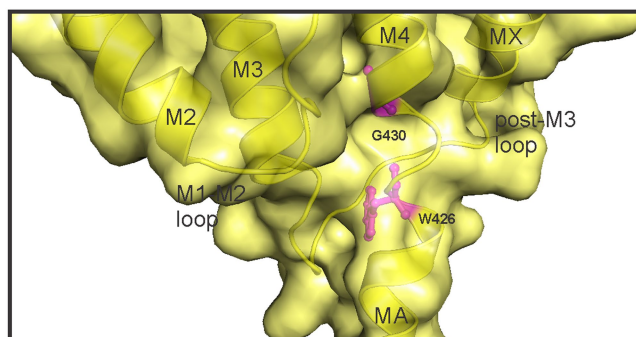
polar contacts in PyMOL. Interacting residues are shown as sticks. Residue labels are colour-coded based on their location. The apo state has the largest buried surface area ($31,610 \text{ \AA}^2$) which progressively decreases in state 1 ($30,960 \text{ \AA}^2$) and then state 2 ($25,340 \text{ \AA}^2$).

a

State 2

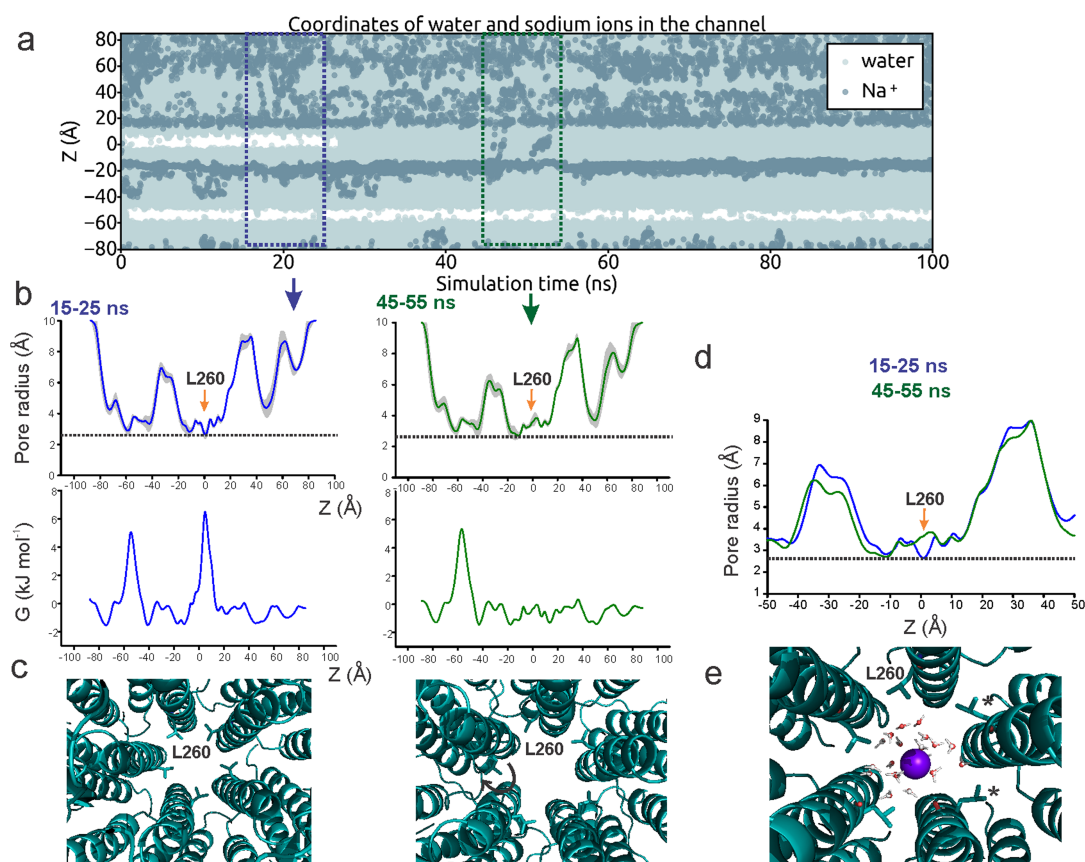


b



Extended Data Fig. 6 | The intracellular domain of state 2. **a**, A detailed view of the ICD with key residues shown in stick representation. Only two adjacent subunits are shown for clarity. The solvent-accessible vestibule in the ICD calculated using Caver3.0⁴⁷ with a minimum cavity radius of 2.8 Å is shown as dark-cyan spheres. The positively charged residues lining the portal are shown as blue sticks. The negatively charged residues in the vicinity are shown in red-brown. Residues that form the hydrophobic patch at the N-terminal end of the MA helix are shown as green sticks.

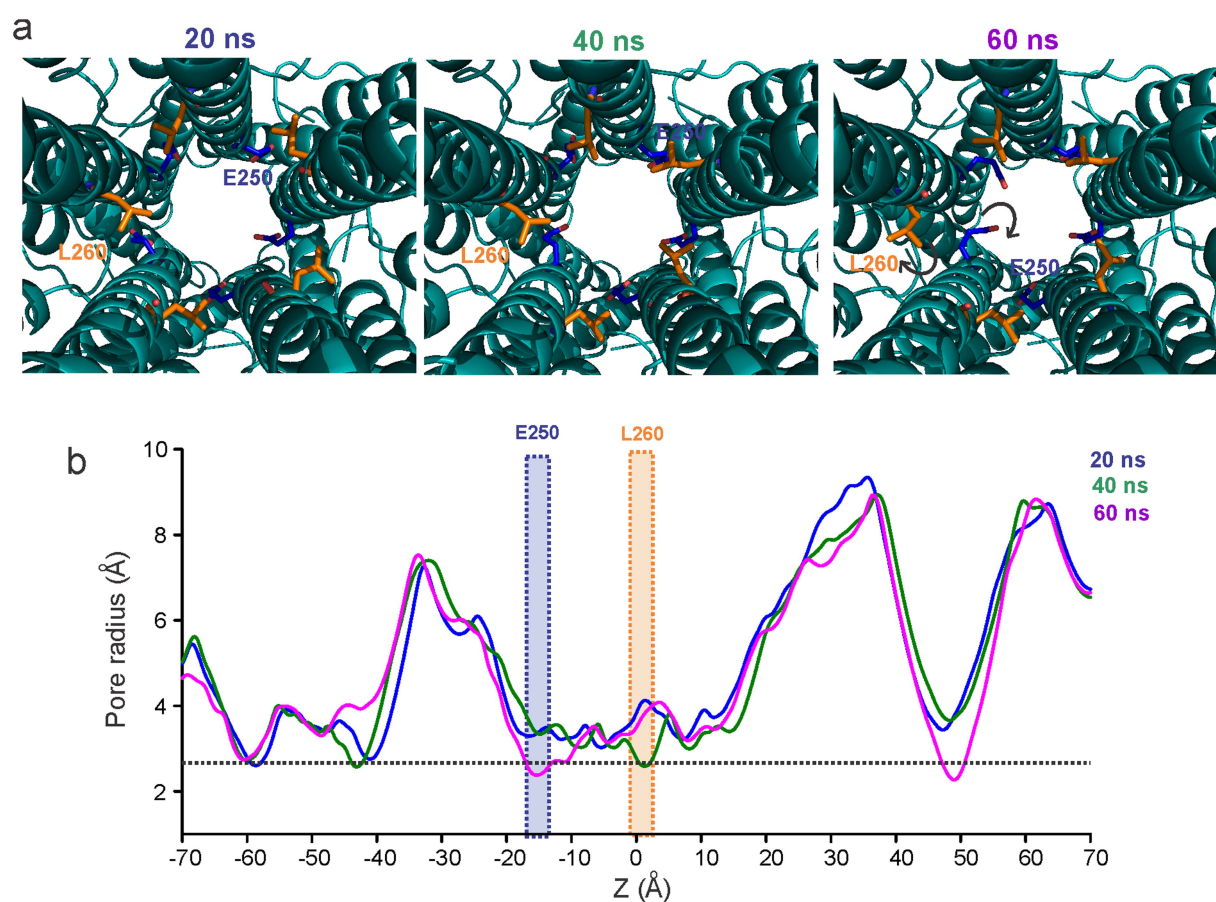
Residues His309 (post-M3 loop) and Glu250 (M2) are in a potential interaction and are shown in magenta. **b**, A zoomed view of the ICD to highlight the break in MA-M4 helices (highlighted in magenta) at Gly430. Glycine-mediated transmembrane-helix distortion at the *i*-3 position is well-studied⁵⁸, and Gly430 may have a dynamic role at the hinge point between MA and M4 helices. A similar bend in the MA-M4 helix was previously observed in the *Torpedo marmorata* nAChR structure even in the absence of glycine at the equivalent position³.



Extended Data Fig. 7 | Molecular dynamics simulations of state 1.

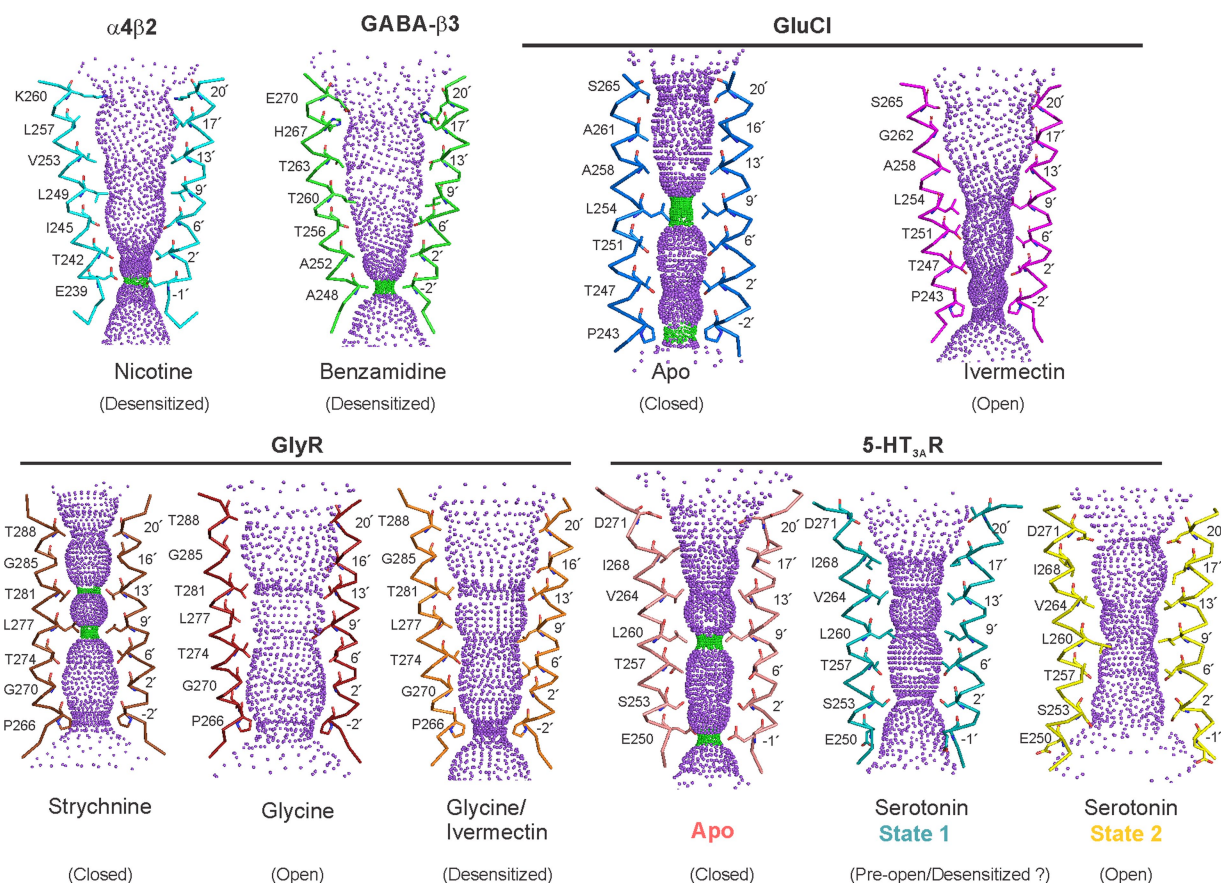
a, Trajectories of water and Na⁺ ion coordinates within 5 Å of the channel axis inside the pore over 100 ns with a 0.2-V transmembrane potential difference, with the cytoplasmic side having a positive potential. Stretches of white regions indicate areas devoid of water or ions. **b**, Time-averaged radii along the central pore axis of the state 1 structure during two 10-ns fractions of the simulation (within the boxed region of **a**) (top). The orange arrows indicate positions of Leu260. The dashed line indicates the approximate radius of a hydrated Na⁺ ion. Free-energy profile of a water molecule along the central pore axis during the 10-ns window (bottom).

The barrier at the Leu260 position disappears in the 45–55-ns time frame. **c**, Snapshots of pore conformation around Leu260 (shown in stick representation) during the corresponding time window. The widening of the pore radii and the disappearance of the barrier for water permeation is associated with the rotameric reorientation of the Leu260 side chain (indicated by the arrow). **d**, An overlay of the pore radii from the two time windows. Changes at position Leu260 are marked by the arrow. **e**, Snapshot of pore conformation around Leu260 as a Na⁺ ion (purple) is passing through, with two Leu260 side chains rotated away (indicated by *). Three independent simulations were run.



Extended Data Fig. 8 | Snapshots of the state 1 pore conformation from the molecular dynamics simulation. a, Side-chain orientations of Leu260 and Glu250 at different points during the simulation (indicated

in Extended Data Fig. 7). **b,** The corresponding pore radius profiles. The positions of Glu250 and Leu260 are highlighted.



Extended Data Fig. 9 | Comparison of pLGIC pore profiles. Pore profiles calculated using the HOLE program⁴⁶ for the M2 region of nAChR (PDB ID: 5KXI)⁴, GABA_A receptor $\beta 3$ homopentamer (PDB ID: 4COF)⁷, glutamate-gated chloride channel (GluCl) (apo structure, PDB ID: 4TNV⁵⁹; ivermectin-bound, PDB ID: 3RHW⁶⁰), glycine receptor (GlyR) (strychnine-bound, PDB ID: 3JAD; glycine-bound, PDB ID: 3JAE;

glycine- and ivermectin-bound, PDB ID: 3JAF)⁵ and 5-HT_{3A} receptor (apo structure, PDB ID: 6BE1¹¹; state 1, PDB ID: 6DG7; state 2, PDB ID: 6DG8). Only two M2 helices are shown as ribbon, for clarity. Pore-facing residues are shown as stick representation. Green and magenta spheres define radii of 1.8–3.3 Å and >3.3 Å, respectively.

Extended Data Table 1 | Sequence of mouse 5-HT_{3A} receptor used in the cryo-EM study and the data on cryo-EM and refinement

b

	State 1 (EMDB-7882) (PDB 6DG7)	State 2 (EMDB-7883) (PDB 6DG8)
Data collection and processing		
Magnification		130,000x
Voltage (kV)		300
Electron exposure (e-/Å ²)		40
Defocus range (μm)		-1.0 to -2.5
Pixel size (Å)		0.532
Symmetry imposed		C5
Initial particle images (no.)		749,970
Final particle images (no.)	103,698	18,839
Map resolution (Å)	3.32	3.89
FSC threshold	0.143	0.143
Refinement		
Initial model used (PDB code)	6BE1	6BE1
Model resolution (Å)	4.31	4.31
FSC threshold	0.143	0.143
Map sharpening B factor (Å ²)	-50	-50
Model composition		
Non-hydrogen atoms	16,720	16,715
Protein residues	16,175	16,175
Ligands	545	540
B factors (Å²)		
Protein	154.41	244.56
Ligand	133.45	169.20
R.m.s. deviations		
Bond lengths (Å)	0.004	0.004
Bond angles (°)	1.032	1.031
Validation		
MolProbity score	1.53 (94 th Percentile)	1.56 (94 th Percentile)
Clashscore	3.40 (97 th Percentile)	4.89 (94 th Percentile)
Poor rotamers (%)	1.27	0.55
Ramachandran plot		
Favored (%)	95.61	95.61
Allowed (%)	4.39	4.39
Disallowed (%)	0.00	0.00

a, The full-length mouse 5-HT_{3A} receptor sequence used in the cryo-EM study. Regions in the sequence highlighted in green, blue, grey and yellow represent strep-tag, linker, TEV cleavage site and 1D4-tag, respectively. Secondary structural elements as seen in state 1 are plotted above the sequence. Loops in grey are not seen in the final refined structure. All the important loops, sheets and helices are labelled. Glycosylation sites are marked as blue arrows. Key residues within the serotonergic binding sites are highlighted in brown. Cysteines present in the Cys loop are shown in cyan. Pore-facing residues in M2 are shown in green. Arg416 in the ICD is shown in red. **b**, Cryo-EM data collection, refinement and validation statistics.

Conformational transitions of the serotonin 5-HT₃ receptor

Lucie Polovinkin¹, Ghérici Hassaine², Jonathan Perot¹, Emmanuelle Neumann¹, Anders A. Jensen³, Solène N. Lefebvre⁴, Pierre-Jean Corringer⁴, Jacques Neyton^{1*}, Christophe Chipot^{5,6,7}, Francois Dehez^{5,6}, Guy Schoehn¹ & Hugues Nury^{1*}

The serotonin 5-HT₃ receptor is a pentameric ligand-gated ion channel (pLGIC). It belongs to a large family of receptors that function as allosteric signal transducers across the plasma membrane^{1,2}; upon binding of neurotransmitter molecules to extracellular sites, the receptors undergo complex conformational transitions that result in transient opening of a pore permeable to ions. 5-HT₃ receptors are therapeutic targets for emesis and nausea, irritable bowel syndrome and depression³. In spite of several reported pLGIC structures^{4–8}, no clear unifying view has emerged on the conformational transitions involved in channel gating. Here we report four cryo-electron microscopy structures of the full-length mouse 5-HT₃ receptor in complex with the anti-emetic drug tropisetron, with serotonin, and with serotonin and a positive allosteric modulator, at resolutions ranging from 3.2 Å to 4.5 Å. The tropisetron-bound structure resembles those obtained with an inhibitory nanobody⁵ or without ligand⁹. The other structures include an 'open' state and two ligand-bound states. We present computational insights into the dynamics of the structures, their pore hydration and free-energy profiles, and characterize movements at the gate level and cation accessibility in the pore. Together, these data deepen our understanding of the gating mechanism of pLGICs and capture ligand binding in unprecedented detail.

A decade after the structure of the *Torpedo marmorata* nicotinic acetylcholine receptor¹⁰ (nAChR), the set of known pLGIC structures is rapidly expanding and reflects the diversity of this protein family. The structures share a conserved architecture, in which subunits are arranged around a central five-fold pseudo-symmetry axis. Together they have clarified details of ligand binding, selectivity and allosteric modulation. They have also revealed a complex landscape of conformations, raising questions of how to relate structures to the wealth of data that established the existence of multiple agonist-bound pre-active intermediate states^{11–13}, of distinct open states¹⁴ and of multiple desensitized states¹⁵.

Mouse homomeric 5-HT_{3A} receptors, with their entire intracellular domain (ICD), were solubilized with the detergent C12E9 and purified. We first performed cryo-electron microscopy (cryo-EM) in the presence of the potent antagonist tropisetron, and obtained a 4.5 Å structure (Fig. 1b, Extended Data Figs. 1, 2, Extended Data Table 1), hereafter referred to as T. T is globally similar to the structure previously solved by X-ray crystallography⁵ (root mean square deviation (r.m.s.d.) of 0.6 Å), the pore of which was shown by molecular dynamics to be occluded¹⁶. Tropisetron fits in a peanut-shaped density present in the neurotransmitter pocket (Extended Data Fig. 3d–f). The ICD contains a region of about 60 residues, which is averaged out (also in the other reconstructions, see below) because of its intrinsic flexibility^{1,2}. T resembles the 4.5 Å cryo-EM structure of the apo 5-HT₃ receptor⁹ (r.m.s.d. of 1.15 Å), with small differences in the lipid-exposed helices M3, MX and M4.

We then sought to identify agonist-elicited conformations of the 5-HT₃ receptor, and performed cryo-EM imaging in the presence of serotonin. A first reconstruction presented heterogeneity in the membrane domain. Further focused 3D classification allowed two subsets of particles to be separated, which yielded reconstructions at 4.2 Å and 4.1 Å resolution, corresponding to two different conformations (Fig. 1b, Extended Data Fig. 4). The maps offer a variable level of information: most side chains in the extracellular domain are resolved, whereas some parts of the transmembrane domain (TMD) do not have side-chain information and some have limited information in the main chain position (Extended Data Figs. 4c, 5), reflecting the receptor dynamics. In the two refined structures, the extracellular domains (ECDs) have undergone an equivalent transition from the T state and serotonin could be modelled in the neurotransmitter site, whereas the TMDs differed markedly (Fig. 2, Extended Data Fig. 6). We call the first structure I1 for intermediate 1 and the second structure F for full, on the basis of the extent of movements compared to the inhibited state. I1 exhibits only limited displacements in the upper part of M1 and M2, and a rearrangement of the M2–M3 loop (Supplementary Video 1). F is characterized by a pronounced reorganization of the transmembrane helices, which can be described by a rigid-body movement of the four-helix bundle coupled to a rearrangement of M4 (and of M3 to a lesser extent) sliding along M1 and M2 (Supplementary Videos 2, 3). F also features a very dynamic ICD, beyond the intrinsically disordered region, in which model building was not possible even though the data showed incomplete densities for MX and M4 (Extended Data Fig. 4a–c).

Finally, we collected a dataset in the presence of serotonin and trans-3-(4-methoxyphenyl)-N-(pentan-3-yl)acrylamide (TMPPAA, a compound exhibiting agonist and positive allosteric modulator activity on the human receptor¹⁷), a combination that yields weakly desensitizing currents (Extended Data Fig. 1f). From this dataset, we reconstructed a 3.2 Å resolution structure (Extended Data Fig. 2d–g), which provides non-ambiguous side-chain information for nearly the entire receptor. The refined structure has an ECD conformation essentially equivalent to that of I1 and F. The membrane domain is similar to that of I1, albeit with a slightly more expanded top section and pore (Fig. 2). We call this structure I2 for intermediate 2.

Serotonin can be unambiguously positioned in the neurotransmitter site of I2. It fits tightly within its binding pocket (Extended Data Fig. 3a–c) in an orientation consistent with functional and binding studies¹. Surrounded by obligatory aromatic residues (F199 and Y207 on the principal side, Y126 and W63 on the complementary side), it is positioned to form a cation- π interaction with W156 and hydrogen bonds with the main chain of S155 and Y64. The C loop is positioned moderately inward relative to the inhibited conformations, its position locked by a salt bridge between D202 and R65. A hallmark of allosteric activation is the subunit–subunit rearrangement (Extended Data Fig. 3d), which affects the site volume and geometry.

¹CNRS, Université Grenoble Alpes, CEA, IBS, Grenoble, France. ²Theranyx, Marseille, France. ³Department of Drug Design and Pharmacology, Faculty of Health and Medical Sciences, University of Copenhagen, Copenhagen, Denmark. ⁴Channel Receptors Unit, CNRS UMR 3571, Institut Pasteur, Paris, France. ⁵Université de Lorraine, CNRS, LPCT, Nancy, France. ⁶Laboratoire International Associé CNRS and University of Illinois at Urbana-Champaign, Vandoeuvre-les-Nancy, France. ⁷Department of Physics, University of Illinois at Urbana-Champaign, Urbana, IL, USA. *e-mail: jacques.neyton@ibs.fr; hugues.nury@ibs.fr

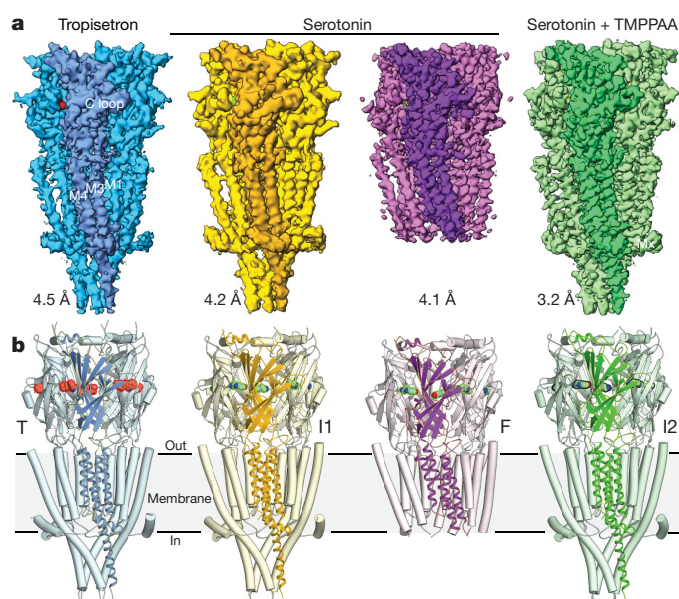


Fig. 1 | Three-dimensional reconstructions and structures of homomeric 5-HT_{3A} receptor. **a**, **b**, Reconstructions (**a**) and structures (**b**) for: the tropisetron dataset (protein in blue and ligand in red), the serotonin and Ca²⁺ dataset (I1 in yellow, F in purple and ligand in green), and the serotonin and TMPPAA dataset (I2 and ligand in green). Resolutions are shown according to the Fourier shell coefficient 0.143 criterion.

TMPPAA has previously been proposed to bind to an allosteric site in the TMD¹⁷, but there is no clearly interpretable density in our data to model the compound. We tested TMPPAA agonist activity on a set of around 45 single-point mutants of the human receptor, which collectively reveal that the drug binds between M4, M1 and M3 into an intra-subunit cavity skirted by lipids of the outer leaflet in the upper part of the TMD (Extended Data Fig. 7, Supplementary Table 1), where endogenous steroids bind to nAChRs¹⁸. More generally, several allosteric druggable sites have been identified in pLGICs, which bind diverse compounds including general anaesthetics such as propofol and flavourings such as citral or eucalyptol⁵. Allosteric sites in the 5-HT₃ receptor change in both shape and volume during transitions (Extended Data Figs. 3i, 7a).

At the ECD–TMD interface, a set of conserved residues that are essential for gating¹⁹ form a structural motif that is common to all pLGIC structures, the location of which may correlate with the state of the channel⁵. This motif consists of charged residues (E53, D145, E186 and R218) sandwiched between conserved aromatic residues: W187 at the top and the 142–FPF–144 motif of the Cys loop, plus Y223 at the bottom (Extended Data Fig. 8). The FPF motif itself penetrates the transmembrane domain similar to a wedge; its position differs in each conformation. When superimposing structures on a TMD subunit, the wedge lies close to M2 in the tropisetron-bound structure and moves towards M4–M1 in the I1, I2 and F structures (which is possible because the conserved P230 allows the upper M1 to kink or straighten). A marked downward concerted movement of the wedge and of the β 8– β 9 loop (containing E186 and W187) occurs in the F structure, pushing on the M2–M3 loop, and may be responsible for the marked reorganization of the TMD observed in that state.

pLGIC pores are lined with side chains of residues from the five M2 helices. In direct agreement with results from substituted cysteine accessibility mutagenesis¹ (SCAM), our structures show that in all conformations, positions –1', 2', 6', 9', 13', 16', 17' and 20' of the M2 α -helix are exposed to the pore lumen (Fig. 3a). Positions 12' and 15', which are also accessible in SCAM, are partly exposed to solvent on the rear of the M2 helices. Superimposition of a single M2 helix underscores its flexibility at both ends; superimposition of the five M2 helices highlights the crucial role of movements of the hydrophobic

side chain at the 9' position (Fig. 3b, c). Minimum pore diameter is often a key element in the assignment of experimental structures to physiological states. Pore profiles are compatible with closed hydrophobic gates (rings at positions 9', 13', 16' and 17') in the T and I1 structures, with an open channel in the F structure, whereas the I2 structure presents an intermediate profile. However, pore profiles are influenced by the resolution, symmetry and rotameric state of the side chains pointing into the pore lumen. Some positions, such as the key negative charge in –1' are often poorly resolved in density maps, and are known to adopt alternate conformations^{8,20}. Moreover, pore profiles are not informative about hydrophobicity, wetting or dynamics, which have key roles in permeability^{21,22}. We performed molecular dynamics simulations to better characterize permeation. In the microsecond-long trajectories starting from the inhibited X-ray structure or from I1, no water or ions cross the pore, and the hydrophobic 9', 13' and 16' rings establish a de-wetted hydrophobic gate that is tighter than in the starting structures (Fig. 3d, Extended Data Fig. 9). By sharp contrast, a simulation starting from F features an open pore that is accessible to ions and water throughout the trajectory (Supplementary Video 4). During the initial part of the simulations starting from I2, when the C_α atoms are positionally restrained, wetting and de-wetting events of the pore occur as if its conformation were on the open–closed verge (Extended Data Fig. 9). Wetting is linked to the presence of transiently hydrated grooves at the back of M2 helices, down to the polar residues Y11'–S12', affecting the electrostatic landscape inside the pore. Wetting also correlates with rotation of L9' out of the pore lumen. Once the geometric restraints are removed, the I2 pore relaxes to a closed conformation similar to that observed in the I1 trajectory. The absence of TMPPAA in the simulation may rationalize the closure. Potentials of mean force for the translocation of a K⁺ ion reveal an insurmountable 12 kcal mol^{–1} barrier in the case of I1 (representative of closed hydrophobic gate conformations), and an essentially flat free-energy landscape in the case of F (Fig. 3e).

We asked whether the structures could be assigned to physiological states. T and F are straightforward to assign, whereas I1 and I2 are less so. T typifies an inhibited state, with resting-like ECD stabilized by tropisetron, and a closed pore, resembling the apo state. F represents an open state, with an activated ECD with bound serotonin, an activated TMD and a wide open pore. Two assignments are possible for the closely related I1 and I2 conformations (Fig. 4a). In a first scheme, I1 exemplifies a serotonin-bound, pre-active closed state, in which the ECD and the ECD–TMD interface—but not the TMD—have undergone a transition. This is consistent with single-channel analysis of the 5-HT₃ receptor, which yields kinetic models in which opening can occur from a ligand-bound pre-active state¹⁴. In a second scheme, I1 represents a closed desensitized state that occurs downstream from the open state. In both schemes, I2 is best described as in a state close to I1 (that is, close to either pre-active or desensitized) wherein the slightly wider pore promotes wetting, which could enable ion passage or merely favour the switch to a fully open state, consistent with the TMPPAA-induced modulation.

A distinctive feature of the second scheme is that the activation gate, consisting of rings of hydrophobic residues in the upper pore, would open in the active state and close in the desensitized state. This implies a marked movement of the upper pore during desensitization, and no ion access from the extracellular compartment to the lower pore in the desensitized state. Functional experiments on anionic receptors indicate that they have distinct activation and desensitization gates, the latter being located at the cytoplasmic end of the pore²³. Moreover, structures of the GABA_A receptor β 3 homopentamer and of the α 4 β 2 nAChR, with pores constricted at positions –2' and –1', have been assigned to desensitized states^{6,8}. These receptors, however, were engineered close to the constriction, a feature that can alter desensitization in 5-HT₃ receptors²⁴.

To challenge the two schemes, we measured the movement of the gate region and the accessibility of the pore to organic cations. First, we

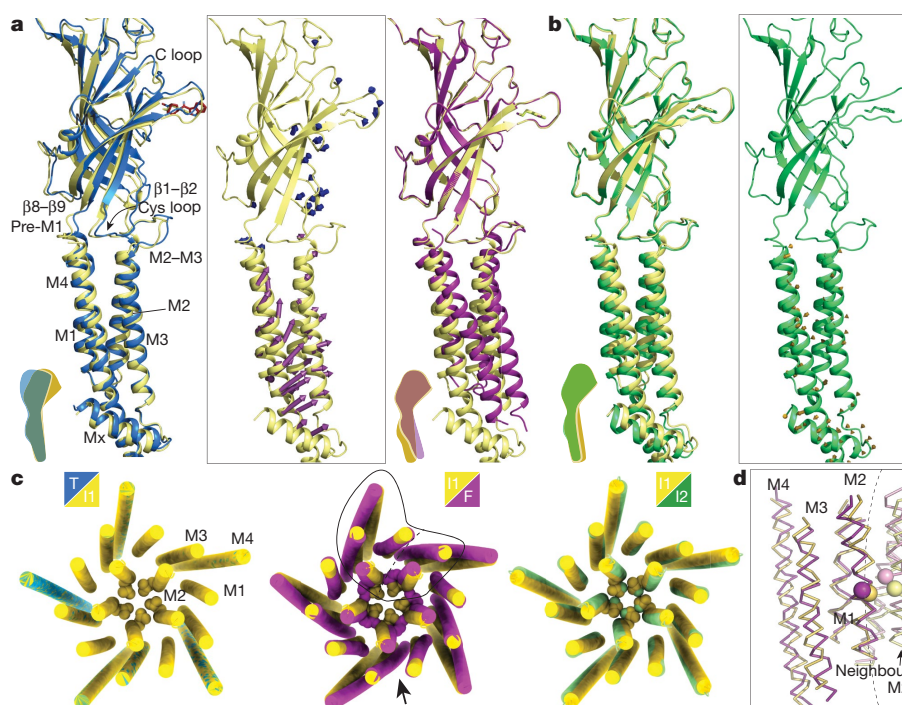


Fig. 2 | Transitions between the tropisetron-bound, the serotonin-bound, and the serotonin and TMPPA-bound states. **a**, View parallel to the membrane of one subunit of the serotonin-bound conformation I1 (yellow) overlaid with the tropisetron-bound conformation (blue, TMD superposition, left) or with the serotonin-bound conformation F (purple, ECD superposition, right). Inset, vectors indicate the local amplitude of movements, sampled on C_{α} atoms (T to I1 in blue, I1 to F in purple). **b**, Overlay of the I1 (yellow) and the serotonin and TMPPA-bound I2 (green) conformations (left); vector representations of the I1 to I2 transition (ECD superposition). **c**, Pairwise overlays of the

TMD illustrating transitions at the quaternary level. Structures were superimposed on the ECD pentamer. L9' (L260) residues are shown as spheres. The line and arrow on the middle overlay indicate the region depicted in **d** and the orientation of the view, respectively. **d**, Tertiary reorganization within a subunit TMD. Overlay in ribbon representation of I2 and F with L260 C_{α} as spheres (TMD superposition within a single subunit). Note the vertical shift of M3–M4 relative to M1–M2, distortions on the extracellular halves of M1–M2, and interface re-arrangement with the neighbouring subunit helices (on the right of the dotted line).

used voltage-clamp fluorometry (VCF) to probe the local conformational changes in the upper pore at the 19' position^{25,26} (Extended Data Fig. 10). We labelled S19'C mutants, expressed at the surface of *Xenopus*

laevis oocytes, with 5-carboxytetramethylrhodamine methanethiosulfonate (MTS-TAMRA). Transient stimulation with serotonin elicited simultaneous changes in current and fluorescence with parallel rise

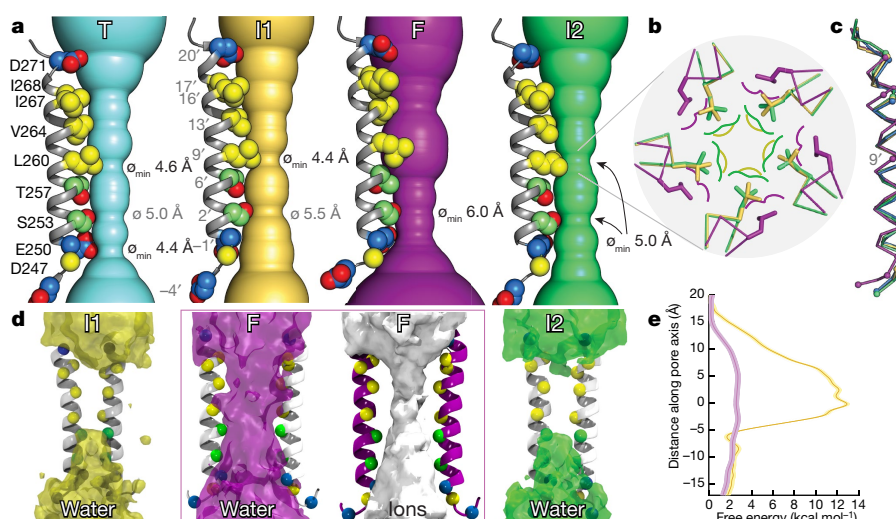


Fig. 3 | Geometry, wetting and energy landscape of the transmembrane pore. **a**, Static pore geometry; the accessible pathway through the pore is represented as a solid surface for each structure. Diameters (\varnothing) of the constriction zones are noted. One M2 helix is depicted as cartoon with pore-exposed side chains as spheres (polar in green, hydrophobic in yellow, charged in blue). The view is parallel to the plane of the membrane. **b**, Zoom on the hydrophobic gate constriction, formed at the level of L260 (sticks), which has a small movement backward in the I2 state and rotates

outwards in the F state. Coloured lines indicate molecular surfaces. The view is perpendicular to the membrane plane. **c**, Superposition of one M2 helix in the four conformations. **d**, Water densities of the pore region during the unrestrained part of simulations. Densities are depicted as transparent surfaces at the same contouring level. The density for K^+ ions is also included for the F trajectory featuring an open pore. **e**, Potentials of mean force of K^+ ions as a function of the position along the pore axis.

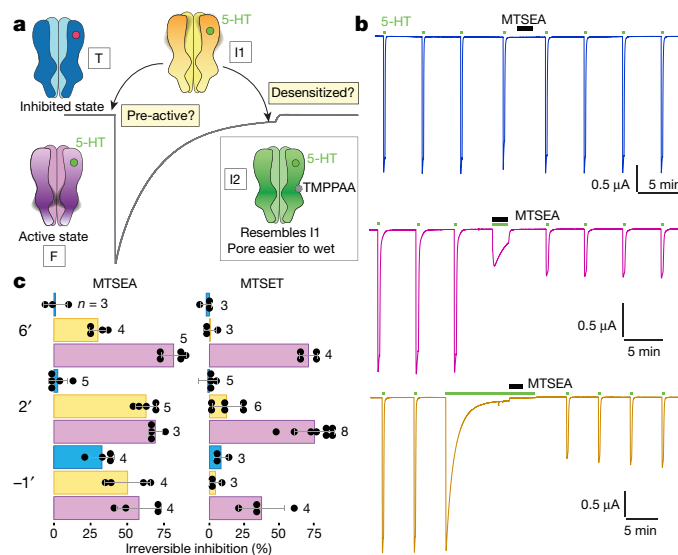


Fig. 4 | Putative molecular mechanisms of operation. **a**, T (blue) represents an inhibited state, stabilized by tropisetron (red circle). I1 (yellow) represents either a closed pre-active serotonin-bound (green circle) state or a desensitized state. F (purple) represents an open active state. The grey line illustrates the electrical response to serotonin recorded in an oocyte expressing 5-HT_{3A} receptors. **b**, Recordings of MTSEA (1 mM) modification on serotonin-evoked current in the S2'C mutant.

and decay, whereas prolonged (7-min) exposure to serotonin resulted in similar signals at the onset, followed by a slow decay for the current signal without a change in fluorescence. Both signals returned to baseline when serotonin was removed. The VCF results argue against the second scheme, because the probe environment changes upon activation but not during desensitization. Second, we performed SCAM in the resting (absence of ligand), open (during transient serotonin application) and desensitized (after prolonged serotonin application) states (Fig. 4b). MTSEA (2-aminoethyl methanethiosulfonate) and MTSET (2-(2-(trimethylammonium)ethyl) methanethiosulfonate) are organic cations that react with free cysteines through their methanethiosulfonate moiety. The aminoethyl head group of MTSEA is small, which enables it to access narrow spaces. MTSEA is, however, also known to cross membranes in its uncharged form. Application of 1 mM extracellular MTSEA in the resting state yielded no modification of currents in T6'C and S2'C mutants but inhibited currents (by 32%) in E1'C mutants (Fig. 4c). In the resting state, the compound can probably access position -1' from the internal compartment, but it is unable to access the 2' or 6' positions. Similar applications in the open state produced irreversible inhibitions at 6', 2' and -1' positions (82%, 69% and 58%, respectively). MTSEA can therefore reach 6' and 2' from the extracellular compartment in the open state, consistent with previous studies¹ and with the opening of the activation gate in F. Applications of extracellular MTSEA in the desensitized state also produced irreversible inhibitions at 6', 2' and -1' positions (30%, 63% and 50%, respectively). From these results, we infer that positions 6' and 2', located below the hydrophobic gate seen in T and I1, are accessible from the extracellular side in the desensitized state. No conclusions can be drawn for position -1', as its labelling in the resting state precludes further interpretation. The results suggest that the activation gate is open in the desensitized conformation(s). MTSET possesses a bulkier trimethylammonium headgroup and cannot cross membranes. We observed that MTSET labels cysteine mutants at 6', 2' and -1' positions when applied in the open state (71%, 75% and 46%, respectively). Application of MTSET in the desensitized state yielded a small variable inhibition at 2' (12 ± 10%) and none at 6', indicating that these positions are more accessible for MTSEA than for the bulkier MTSET. On the basis of these results, we favour the scheme in which I1 is assigned to a pre-active state. Nevertheless, desensitization is a complex process involving

MTSEA is applied in the resting (blue), the desensitized (orange), or active (purple) state. The protocol includes 10-s test serotonin applications before and after 2-min MTSEA modification. **c**, Changes in current after MTSEA (1 mM) or MTSET (1 mM) modification, for -1'C, S2'C and T6'C mutants, in the resting (blue), active (purple) or desensitized (yellow) state.

several distinct states¹⁵, and we cannot rule out the possibility that I1 represents a desensitized state.

The challenge of matching structures to states without ambiguity transcends the present study and pertains to the whole field of pLGIC structures^{2,27,28}. This challenge arises from diverse factors: limited resolution, putative influence of detergent, crystal packing and receptor engineering, and the possibility that ensembles of multiple related conformations are necessary to properly depict a physiological state. Bearing in mind the ambiguities on state assignment, we compared the 5-HT₃ transitions to those observed for the *Gloeobacter violaceus* receptor (GLIC)⁴, the worm glutamate-gated receptor (GluCl)²⁹ and the glycine α 1 receptor (GlyR)⁷. Common agonist-induced features emerge, such as a global twist, quaternary reorganization of the ECD, rearrangement of the interface between domains involving the conserved sandwich motif, and local movements of the upper TMD. Differences also appear: the extent of TMD reorganization seen in F, with M4 sliding on other helices, is not observed in the other receptors; the ECD reorganization is well-described as 'un-blooming'⁴ for GLIC and GluCl, but not for the 5-HT₃ and glycine receptors. The open pore of F is wider than that of GLIC and narrower than that of GlyR. Bacterial, animal anionic and animal cationic channels may have evolved distinct sets of conformations for a given physiological state, as they belong to separate branches of the pLGIC family. Our 5-HT₃ receptor structures highlight several transitions in the cationic branch. They also contribute to knowledge on other important aspects of pLGIC research that are only alluded to in this report, such as the role of M4 in gating, the pharmacology of allosteric sites and ICD dynamics. Further work with better resolution, structures of mutant receptors and structures of receptors in complex with other ligands will complement and increase mechanistic insights, but knowledge of this area may nevertheless remain incomplete until kinetic structural experiments come of age.

Online content

Any methods, additional references, Nature Research reporting summaries, source data, statements of data availability and associated accession codes are available at <https://doi.org/10.1038/s41586-018-0672-3>.

Received: 7 February 2018; Accepted: 7 September 2018;
Published online 31 October 2018.

1. Thompson, A. J., Lester, H. A. & Lummis, S. C. R. The structural basis of function in Cys-loop receptors. *Q. Rev. Biophys.* **43**, 449–499 (2010).
 2. Nemecek, A., Prevost, M. S., Menny, A. & Corringer, P.-J. Emerging molecular mechanisms of signal transduction in pentameric ligand-gated ion channels. *Neuron* **90**, 452–470 (2016).
 3. Sparling, B. A. & DiMauro, E. F. Progress in the discovery of small molecule modulators of the Cys-loop superfamily receptors. *Bioorg. Med. Chem. Lett.* **27**, 3207–3218 (2017).
 4. Sauguet, L. et al. Crystal structures of a pentameric ligand-gated ion channel provide a mechanism for activation. *Proc. Natl Acad. Sci. USA* **111**, 966–971 (2014).
 5. Hassaïne, G. et al. X-ray structure of the mouse serotonin 5-HT₃ receptor. *Nature* **512**, 276–281 (2014).
 6. Miller, P. S. & Aricescu, A. R. Crystal structure of a human GABA_A receptor. *Nature* **512**, 270–275 (2014).
 7. Du, J., Lü, W., Wu, S., Cheng, Y. & Gouaux, E. Glycine receptor mechanism elucidated by electron cryo-microscopy. *Nature* **526**, 224–229 (2015).
 8. Morales-Perez, C. L., Noviello, C. M. & Hibbs, R. E. X-ray structure of the human $\alpha 4\beta 2$ nicotinic receptor. *Nature* **538**, 411–415 (2016).
 9. Basak, S. et al. Cryo-EM structure of 5-HT_{3A} receptor in its resting conformation. *Nat. Commun.* **9**, 514 (2018).
 10. Unwin, N. Refined structure of the nicotinic acetylcholine receptor at 4 Å resolution. *J. Mol. Biol.* **346**, 967–989 (2005).
 11. Mukhtasimova, N., Lee, W., Wang, H. & Sine, S. Detection and trapping of intermediate states priming nicotinic receptor channel opening. *Nature* **459**, 451–454 (2009).
 12. Lape, R., Colquhoun, D. & Sivillotti, L. G. On the nature of partial agonism in the nicotinic receptor superfamily. *Nature* **454**, 722–727 (2008).
 13. Menny, A. et al. Identification of a pre-active conformation of a pentameric channel receptor. *eLife* **6**, e23955 (2017).
 14. Corradi, J., Gumilar, F. & Bouzat, C. Single-channel kinetic analysis for activation and desensitization of homomeric 5-HT_{3A} receptors. *Biophys. J.* **97**, 1335–1345 (2009).
 15. Sakmann, B., Patlak, J. & Neher, E. Single acetylcholine-activated channels show burst-kinetics in presence of desensitizing concentrations of agonist. *Nature* **286**, 71–73 (1980).
 16. Trick, J. L. et al. Functional annotation of ion channel structures by molecular simulation. *Structure* **6**, 2207–2216 (2016).
 17. Gasiorek, A. et al. Delineation of the functional properties and the mechanism of action of TMPPAA, an allosteric agonist and positive allosteric modulator of 5-HT₃ receptors. *Biochem. Pharmacol.* **110–111**, 92–108 (2016).
 18. Jin, X. & Steinbach, J. H. A portable site: a binding element for 17 β -estradiol can be placed on any subunit of a nicotinic $\alpha 4\beta 2$ receptor. *J. Neurosci.* **31**, 5045–5054 (2011).
 19. Mukhtasimova, N. & Sine, S. M. Nicotinic receptor transduction zone: invariant arginine couples to multiple electron-rich residues. *Biophys. J.* **104**, 355–367 (2013).
 20. Cymes, G. D. & Grosman, C. The unanticipated complexity of the selectivity-filter glutamates of nicotinic receptors. *Nat. Chem. Biol.* **8**, 975–981 (2012).
 21. Zhu, F. & Hummer, G. Drying transition in the hydrophobic gate of the GLIC channel blocks ion conduction. *Biophys. J.* **103**, 219–227 (2012).
 22. Aryal, P., Sansom, M. S. P. & Tucker, S. J. Hydrophobic gating in ion channels. *J. Mol. Biol.* **427**, 121–130 (2015).
 23. Gielen, M., Thomas, P. & Smart, T. G. The desensitization gate of inhibitory Cys-loop receptors. *Nat. Commun.* **6**, 6829 (2015).
 24. McKinnon, N. K., Bali, M. & Akabas, M. H. Length and amino acid sequence of peptides substituted for the 5-HT_{3A} receptor M3M4 loop may affect channel expression and desensitization. *PLoS ONE* **7**, e35563 (2012).
 25. Pless, S. A., Dibas, M. I., Lester, H. A. & Lynch, J. W. Conformational variability of the glycine receptor M2 domain in response to activation by different agonists. *J. Biol. Chem.* **282**, 36057–36067 (2007).
 26. Dahan, D. S. et al. A fluorophore attached to nicotinic acetylcholine receptor β M2 detects productive binding of agonist to the $\alpha\delta$ site. *Proc. Natl Acad. Sci. USA* **101**, 10195–10200 (2004).
 27. daCosta, C. J. B. & Baenziger, J. E. Gating of pentameric ligand-gated ion channels: structural insights and ambiguities. *Structure* **21**, 1271–1283 (2013).
 28. Gonzalez-Gutierrez, G., Wang, Y., Cymes, G. D., Tajkhorshid, E. & Grosman, C. Chasing the open-state structure of pentameric ligand-gated ion channels. *J. Gen. Physiol.* **149**, 1119–1138 (2017).
 29. Hibbs, R. E. & Gouaux, E. Principles of activation and permeation in an anion-selective Cys-loop receptor. *Nature* **474**, 54–60 (2011).
- Acknowledgements** We acknowledge access to the C-CINA and ESRF Krios microscopes, and thank M. Chami, L. Kovacic, H. Stahlberg, G. Effantin, E. Kandiah and M. Hons for support. We thank L. Estrozi, M. Bacia, G. Effantin and A. Desfosses for advice on cryo-EM; the Vivaudou and Moreau laboratories for providing high-quality oocytes and help with electrophysiology; members of the Nury laboratory, M. Gielen and E. Pebay-Peyroula for discussions. The work was funded by the Marie Curie CIG NeuroPenta and ERC Starting grant 637733 (to H.N.). It used the platforms of the Grenoble Instruct-ERIC Center (ISBG: UMS 3518 CNRS-CEA-UGA-EMBL) with support from FRISBI (ANR-10-INSB-05-02) and GRAL (ANR-10-LABX-49-01) within the Grenoble PSB. The electron microscopy facility is supported by the Rhône-Alpes Region, the FRM, the FEDER and the GIS-IBISA.
- Reviewer information** *Nature* thanks S. Sine, A. Sobolevsky and the other anonymous reviewer(s) for their contribution to the peer review of this work.
- Author contributions** L.P., J.P. and G.H. performed sample preparation. L.P., H.N., E.N. and G.S. optimized and collected microscopy data. L.P. and H.N. built the models. F.D. and C.C. conducted molecular dynamics simulations. J.N. performed electrophysiology experiments. S.N.L. and P.-J.C. performed VCF experiments. A.A.J. performed FLIPR experiments. All authors extensively discussed the data. H.N. and J.N. wrote the manuscript with inputs from all authors.
- Competing Interests** G.H. is employed by Theranym. The remaining authors declare no competing interests.
- Additional information**
Extended data is available for this paper at <https://doi.org/10.1038/s41586-018-0672-3>.
Supplementary information is available for this paper at <https://doi.org/10.1038/s41586-018-0672-3>.
Reprints and permissions information is available at <http://www.nature.com/reprints>.
Correspondence and requests for materials should be addressed to J.N. or H.N.
Publisher's note: Springer Nature remains neutral with regard to jurisdictional claims in published maps and institutional affiliations.

METHODS

No statistical methods were used to predetermine sample size. The experiments were not randomized. The investigators were not blinded to allocation during experiments and outcome assessment.

Protein expression. The wild-type mouse 5-HT_{3A} receptor was expressed in a stable, inducible cell line derived from HEK T-REx 293 cells (Thermo Fisher), as previously described^{5,30,31}. The cells were cultured in suspension in flasks in an orbital incubator (typical culture size, 5 l). The protein expression was induced when cells reached 2×10^6 cells/ml. Valproic acid was added one day later and cells were cultured for one more day. Cells were then pelleted by low-speed centrifugation, frozen and stored at -80°C .

Protein purification. In a typical purification batch, 20 g of cells were resuspended in buffer A (10 mM HEPES pH 7.4, 1 mM EDTA, antiprotease cocktail; 10 ml buffer per gram of cells) mechanically lysed (Ultraturrax T20, 6×30 s) and membranes were collected by ultracentrifugation (100,000g for 1 h). All steps were carried out at 4°C . Membranes were resuspended in buffer B (50 mM Tris pH 8, 500 mM NaCl, antiprotease cocktail, 25 ml buffer per gram of membrane) and the solution was supplemented with 0.15% of C12E9 for solubilisation using gentle stirring (1.5 h). The insoluble material was removed by ultracentrifugation (100,000g for 45 min). Solubilized proteins were purified by affinity chromatography using gravity flow Strep-Tactin resin (IBA, typically 25 ml resin), eluted in buffer C (50 mM Tris pH 7.5, 125 mM NaCl, 0.01% C12E9) and concentrated to ~ 0.5 mg/ml using Millipore 100-kDa cut-off filters. The purification tag was cleaved, and carbohydrates were digested by addition of 0.04 mg TEV protease and 0.1 mg PNGase F per 1 mg protein with gentle stirring overnight. The protein was further concentrated and then applied to a Superose 6 column (GE healthcare) equilibrated in buffer C.

Electron microscopy. The most homogeneous fractions of 5-HT₃ receptor following size-exclusion chromatography were concentrated to ~ 1.5 mg/ml (in the best cases, no concentration was required). The sample was mixed with lipids (0.01% phosphatidic acid, 0.01% cholesterol hemisuccinate, 0.01% brain phosphatidylcholine; Avanti Polar Lipids) and ligands: 2 mM tropisetron (Tocris), or 50 μM serotonin and 2 mM calcium (conditions known to promote fast desensitization^{32,33}); or 30 μM serotonin and 100 mM TMPPAA (Sigma-Aldrich). Samples were incubated for 10–30 min on ice. 3.5 μl were deposited on a glow-discharged (30 mA, 50 s) Quantifoil copper-rhodium 1.2/1.3 grid, blotted for 10 s at force 0 using a Mark IV Vitrobot and plunge-frozen in liquid ethane. Between four and ten grids were screened during each data collection, as ice thickness varied between grids. Optimization was performed on an in-house Polara electron microscope. Datasets were recorded on Titan Krios electron microscopes with K2 cameras at C-CINA (Basel) or at the ESRF (Grenoble). Details of data collections are shown in Extended Data Table 1.

Image processing. At the Basel Krios microscope, the data collection was monitored online and good images were selected using Focus³⁴; images were acquired in super-resolution mode and binned by Fourier-space cropping during the drift correction. At the ESRF Krios microscope, the counted mode was used. Drift was corrected with MotionCor2³⁵ and dose-weighted sums were used for subsequent processing, except for CTF correction, which was performed using GCTF³⁶ on non-dose-weighted sums. Picking was performed with Gautomatch (<http://www.mrc-lmb.cam.ac.uk/kzhang/Gautomatch/>) using average from 2D classes as templates. Subsequent steps were performed using Relion³⁷ on a GPU workstation. Typically, two rounds of 2D classifications with 20–30 classes were performed, followed by a round of 3D classification without imposing symmetry (3–6 classes) with a low-pass-filtered initial model of the receptor. Particles presenting five-fold symmetry were selected, submitted to 3D classifications (classifications and data processing are further described in Extended Data Figs. 2, 4) and the best sets of particles were subjected to 3D auto-refinement. In the post-processing step, a soft mask was calculated and applied to the two half maps before the Fourier shell coefficient (FSC) was calculated. Map sharpening (B -factor fixed at -100 \AA^2 for I1 and F, automatic estimation for T and I2) was also performed in the post-processing step. We tried the Phenix auto-sharpen program³⁸, which improved only the F map. The quality of the final reconstructions is shown in Extended Data Fig. 5.

Model refinement and structure analysis. Refinement was performed with the Phenix suite³⁹. Cycles of real-space refinement were performed using global minimization, rigid body fit and local rotamer fitting (and B -factor refinement in late stages), alternating with manual rebuilding in Coot⁴⁰. NCS and secondary structure restraints were enabled. The 4 models comprise residues 10–307 and 426–460. T, I1 and I2 also have MX and MA residues 308–330 and 399–426, which—owing to flexibility—could not be built in F. Tropisetron (numbered 902) was placed in the orthosteric side of T, and serotonin (numbered 901) was placed in the site of I1, F and I2. The densities for serotonin in I1 and F enable the ligand to be placed in several equivalent orientations, and we used the unambiguous density in I2 to choose the same ligand pose in these 3 structures. The stereochemical properties of the final models, analysed with the Molprobity server (<http://molprobity.biochem.duke.edu/>),

are reported in Extended Data Table 1. Pore profiles were plotted using HOLE⁴¹, r.m.s.d. values were calculated with 'superpose' in the CCP4 suite⁴². Figures were prepared with the PyMOL Molecular Graphics System (Schrodinger), Chimera⁴³ or CueMol.

Molecular dynamics. Molecular assays were built for the four conformational states of 5-HT₃ described in the manuscript. For F, I1 and I2, we used the reported cryo-EM structures, whereas for the inhibited conformation we used the crystal structure (RCSB Protein Data Bank code (PDB): 4PIR) because of its higher resolution. The co-crystallized nanobodies were removed and the protein was modelled without serotonin. The five serotonins present in F, I1 and I2 structures were kept in the models. For I2, because no obvious densities were observed for TMPPAA, it was not represented in the model. The intracellular domain of the F conformation (not resolved in the cryo-EM density) was not included in the model.

Using the CHARMM-GUI web interface^{44,45}, each structure was embedded in a fully hydrated palmitoyl-oleyl-phosphatidylcholine (POPC) bilayer consisting of around 240 lipid units and about 30,000 for F and 42,000 water molecules for T, I1 and I2. K^+Cl^- (150 mM) was explicitly added to each system, while ensuring their electric neutrality. The all-atom CHARMM36 force field⁴⁶ and revision thereof for lipids⁴⁷ were used to describe the system and CMAP corrections were introduced for the protein⁴⁸. For water, we used the TIP3P model⁴⁹. A subset of mass of the heavy atoms of lipids, protein and serotonin were transferred on the hydrogens atoms to which they are bound, to reach a hydrogen mass of 3.024 Da. Using such a mass repartitioning scheme, the equation of motions can be integrated with a time step of up to 4 fs without modifying the dynamics and thermodynamics of the system⁵⁰.

All simulations were carried out with the NAMD package v.2.12⁵¹. Simulations were performed in the isothermal-isobaric ensemble at $T = 300\text{K}$ and $P = 1$ atm with anisotropic scaling of the simulation cell⁵², long-range electrostatic interactions were treated with the particle-mesh Ewald method⁵³, and short-range electrostatics and Lennard-Jones interactions were smoothly truncated. The equations of motion were integrated with a time step of 4 and 8 fs for short- and long-range forces, respectively, using the Verlet r-RESPA multiple time-step propagator⁵⁴. Covalent bonds involving hydrogen atoms were constrained to their equilibrium length by means of the 'rattle/shake algorithm'^{55,56} and the 'settle' algorithm was used for water⁵⁷. For each system, a smooth equilibration along which the positions of the heavy atoms of the protein were restrained harmonically, was carried out for 60 ns. After releasing the restraints, the simulations were extended up to 1 μs . All analyses and molecular rendering were achieved with VMD⁵⁸. Pore radii were inferred using the program HOLE⁴¹.

The potentials of mean force underlying the translocation of a potassium ion in the I1 and F conformations of the 5-HT₃ receptor were determined using a multiple-walker version⁵⁹ of the adaptive biasing force algorithm⁶⁰. For the I1 conformation, the reaction coordinate model was chosen as the Euclidian distance between the ion and the centre of mass of the protein, projected onto its longitudinal axis; that is, the z -direction of Cartesian space. In the case of the F conformation, a two-dimensional free-energy landscape was generated, exploring ion diffusion in the pore not only longitudinally by means of the aforementioned projected Euclidian distance, but also radially. The potential of mean force along the pore was recovered by integration of the marginal law in the radial direction. The reaction pathway was broken down into 14 and 12 windows for the I1 and F conformations, respectively. The free-energy landscapes were explored by four walkers, syncing gradients every 500 molecular-dynamics steps. The total simulation time for the I1 and F conformations amounted to 2.16 and 3.04 μs , respectively, wherein the last 0.8 μs was used to estimate the error bars associated with the potentials of mean force, based on an independent mapping of the free-energy landscape by the walkers.

Electrophysiology. Electrical recordings were obtained by two-electrode voltage-clamp (TEVC) on *Xenopus* oocytes expressing either wild-type or mutated homomeric mouse 5-HT_{3A} receptors. Mutants were obtained using the QuickChange Lightning (Stratagene) site-directed mutagenesis kit and oligonucleotides (Supplementary Table 2) to introduce point mutations into the pcDNA5/TO-m5-HT_{3A} plasmid. All the mutations were verified by sequencing.

Oocytes were prepared as previously reported⁶¹ using procedures that conformed to European regulations for animal handling and experiments, and were approved by governmental services (authorization no. D 38 185 10 001 for the animal facility delivered by the Prefect of Isère) and the Institutional Ethics Committee (ethics approval N° 12-040 granted to C. Moreau by the Ethics Committee of Commissariat à l'Energie Atomique et aux Energies Alternatives). Difolliculated oocytes were injected with 30 nl plasmid DNA (1–10 ng/ μl) coding for the desired 5-HT_{3A} subunit (subcloned into pcDNA5 vector). Microinjected oocytes were incubated for 1 to 5 days at 19°C in Barth's solution (in mM: 1 KCl, 0.82 MgSO₄, 88 NaCl, 2.4 NaHCO₃, 0.41 CaCl₂, 16 HEPES, pH 7.4) supplemented with 100 U ml⁻¹ penicillin and streptomycin.

Whole-cell TEVC recordings were obtained using an OC-725C Oocyte Clamp amplifier (Warner Instruments) at a constant holding potential of -50 mV.

Macroscopic currents were filtered at 1 kHz, digitized at 2 kHz with a Digidata 1440 analogue-to-digital interface and analysed with Clampfit (Molecular Devices). During the recordings, oocytes were constantly perfused with a 0 Ca-ND96 solution (containing in mM: 91 NaCl, 2 KCl, 1 MgCl₂, 5 HEPES, 1 EGTA, pH 7.4) at a rate of 1.3 ml/min, which allowed the application of serotonin and other compounds in a time range of seconds (20-fold concentration change of applied compounds in 5 s). Throughout this study, electrophysiological responses were induced by 10 μ M serotonin (a saturating dose for all tested constructions, not shown) and peaked in less than 3 s. In all constructions tested, 10-min applications of serotonin induced almost complete desensitization (to less than 3% of the peak current with $t_{1/2}$ in the min range). Full recovery of desensitization was observed after washing serotonin for 10 min. Ca²⁺ ions are permeant through 5-HT₃ receptors⁶². Calcium was therefore carefully removed from the recording perfusion solution to avoid contamination of the serotonin-induced responses by endogenous oocyte current secondarily activated by Ca²⁺ ions entering the oocyte through the serotonin receptors.

MTSEA (2-aminoethyl methanethiosulfonate bromide) and MTSET (2-trimethylammonium-ethyl methanethiosulfonate bromide) were purchased from Interchim and prepared immediately before perfusion from stock solutions in water stored at -20°C . The effect of MTS compounds on pore cysteine-mutants was studied using the following protocol: (i) checking stability of the response with a train of three to five applications of 10 μ M serotonin for 10 s, every 5 min (I_{pre}); (ii) applying MTS compounds for 2 min at 1 mM, either in the absence of 5-HT (to probe cysteine accessibility in the resting state), simultaneously with 10 μ M 5-HT (to probe the open state) or simultaneously with 10 μ M 5-HT after a 10 min pre-application of 5-HT alone allowing for complete desensitization; (iii) following the effect of MTS compounds during a second set of five applications of 5-HT for 10 s every 5 min (I_{post}). Irreversible effects of MTS compounds were quantified by measuring I_{post} 25 min after removal of the MTS compound. The percentage of inhibition or potentiation was calculated as $(I_{\text{pre}} - I_{\text{post}})/I_{\text{pre}} \times 100$. MTS compounds (applied at 1 mM simultaneously with 10 μ M serotonin) have no detectable effect on wild-type receptors (not shown).

Voltage-clamp fluorometry. VCF recordings were performed on *Xenopus* oocytes provided by Ecocyte Bioscience that were injected with 50 ng/ μ l plasmid DNA encoding for the mouse 5-HT_{3A} receptor S19'C mutant, after 2 to 6 days of expression in Barth solution at 17°C . They were labelled with MTS-TAMRA (Toronto Chemicals) for 5 min at 17°C in ND96 buffer without CaCl₂ containing 10 μ M 5-hydroxytryptamine (5-HT), then rinsed and stored at 17°C for up to 4 h before recording in ND96. Recording were made in a TEVC setup as described¹³, adapted for fluorescence recording. In brief, recordings were made with a VCF dedicated chamber with only a fraction of the oocyte perfused and illuminated by a LED (cooled PE-4000). Light was collected using a fluorescence microscope (Zeiss Axiovert135) equipped with a 40 \times objective (Plan Neofluar), a TRITC filter set and a photomultiplier tube (Hamamatsu Photonics). Recordings were made at -60 mV clamp, 500-Hz sampling rate with a 550-nm excitation wavelength. Data were filtered, corrected for baseline and photobleaching where necessary, and analysed using pClamp and Axograph. Dose–response curves were fitted using Prism to the Hill equation: $I/I_{\text{max}} = 1/(1 + (\text{EC}_{50}/[5\text{-HT}])^n)$ in which I is the response at a given [5-HT] (serotonin concentration), I_{max} is the maximal response, EC_{50} is half maximal effective concentration and n is the Hill coefficient. Serotonin dose–response relations were shifted to the left with half-responses for fluorescence and current at 40 and 240 nM, respectively (the EC_{50} of the wild-type receptor is 800 nM).

Fluorescence imaging plate reader membrane potential blue assay. The agonist properties of 5-HT and TMPPAA (Sigma-Aldrich) were characterized at human wild-type or mutant 5-HT_{3A} receptors transiently expressed in tsA201 cells in the fluorescence imaging plate reader (FLIPR) membrane potential blue (FMP; fluorescence-based membrane potential) assay. The generation of some of the human 5-HT_{3A} mutants have previously been described⁶³. Other mutants were constructed by introduction of point mutations into the h5-HT_{3A}-pCIneo plasmid using Quikchange II XL site-directed mutagenesis (Stratagene) and oligonucleotides (TAG Copenhagen). The absence of unwanted mutations in all cDNAs created by PCR was verified by sequencing (Eurofins MWG Operon). The cells were cultured in Dulbecco's Modified Eagle Medium supplemented with penicillin (100 U/ml), streptomycin (100 mg/ml) and 10% fetal bovine serum in a humidified atmosphere of 5% CO₂ and 95% air at 37°C . Cells (1.2×10^6) were split into a 6-cm tissue culture plate, transfected the following day with 4 μ g cDNA (wild-type or mutant h5-HT_{3A}-pCIneo) using Polyfect (Qiagen) as transfection reagent, and split into poly-D-lysine-coated black 96-well plates (8×10^4 cells per well) with clear bottom (BD Biosciences) the following day. After 20–24 h following transfection, the medium was aspirated, and the cells were washed with 100 μ l Krebs buffer (140 mM NaCl, 4.7 mM KCl, 2.5 mM CaCl₂, 1.2 mM MgCl₂, 11 mM HEPES, 10 mM D-glucose, pH 7.4). Then 100 μ l Krebs buffer supplemented with 0.5 mg/ml FMP assay dye (Molecular Devices) was added to each well, and the 96-well

plate was assayed at 37°C in a FLEXStation3 Benchtop Multi-Mode Microplate Reader (Molecular Devices) measuring emission (in fluorescence units (FU)) at 565 nm caused by excitation at 530 nm before and up to 90 s after addition of 33.3 μ l assay buffer supplemented with agonist (5-HT or TMPPAA). The experiments were performed in duplicate at least three times for each agonist at all receptors. Concentration–response curves for the agonists were constructed based on the difference in the fluorescence units (rFU) between the maximal fluorescence recording made before and after addition of the agonists at different concentrations. The curves were generated by non-weighted least-squares fits using the program KaleidaGraph (Synergy Software).

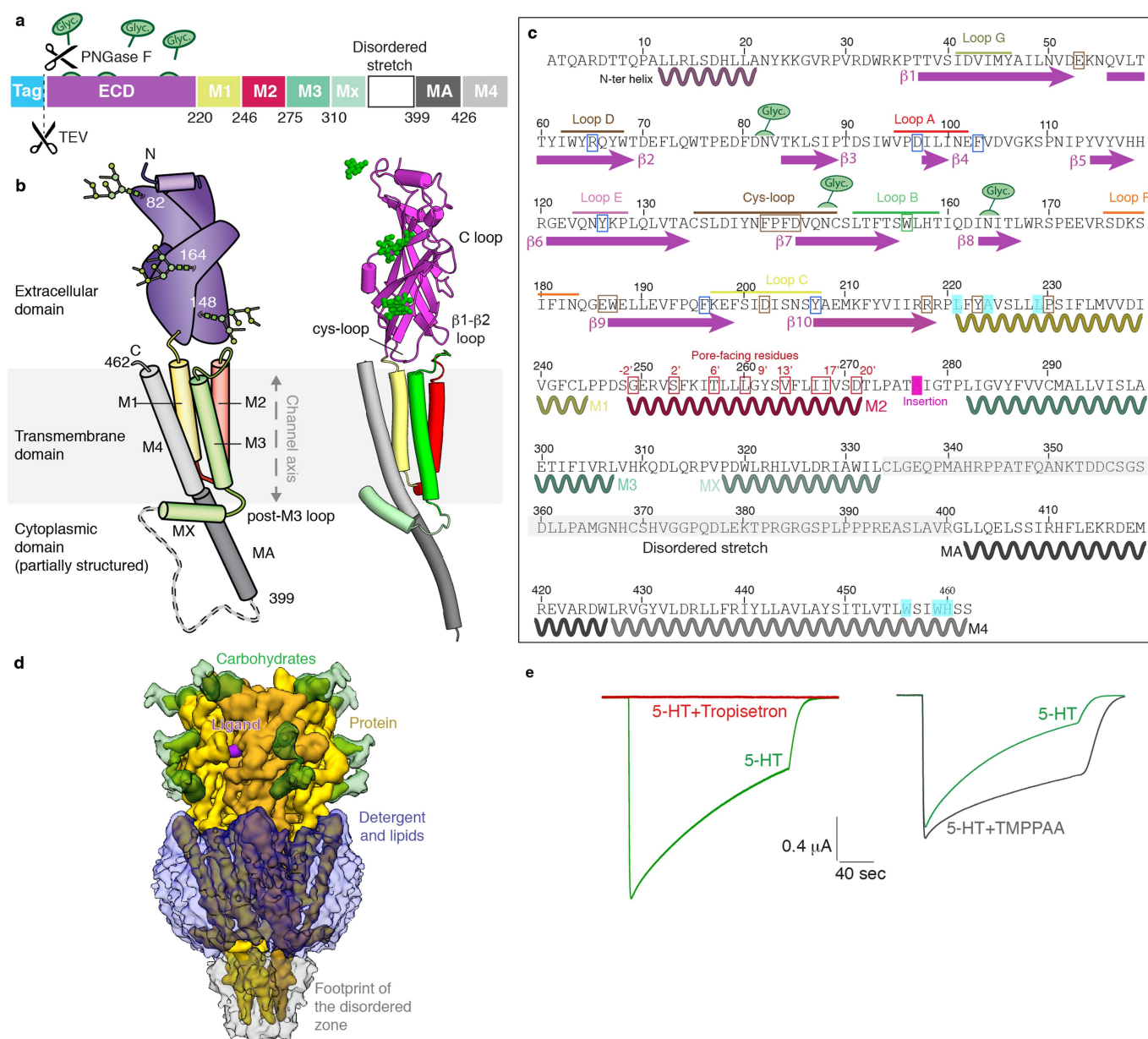
Reporting summary. Further information on research design is available in the Nature Research Reporting Summary linked to this paper.

Data availability

Atomic coordinates of the four conformations have been deposited in the Protein Data Bank with accession numbers 6HIN, 6HIO, 6HIQ and 6HIS for conformations F, I1, I2 and T, respectively. The cryo-EM density maps have been deposited in the Electron Microscopy Data Bank with accession numbers EMD-0225, EMD-0226, EMD-0227 and EMD-0228 for conformations F, I1, I2 and T, respectively.

- Hassaine, G. et al. Large scale expression and purification of the mouse 5-HT₃ receptor. *BBA Biomembranes* **1828**, 2544–2552 (2013).
- Hassaine, G. et al. Expression, biochemistry, and stabilization with camel antibodies of membrane proteins: case study of the mouse 5-HT₃ receptor. *Methods Mol. Biol.* **1635**, 139–168 (2017).
- Yakel, J. L., Lagrutta, A., Adelman, J. P. & North, R. A. Single amino acid substitution affects desensitization of the 5-hydroxytryptamine type 3 receptor expressed in *Xenopus* oocytes. *Proc. Natl Acad. Sci. USA* **90**, 5030–5033 (1993).
- Hu, X.-Q. & Lovinger, D. M. Role of aspartate 298 in mouse 5-HT_{3A} receptor gating and modulation by extracellular Ca²⁺. *J. Physiol. (Lond.)* **568**, 381–396 (2005).
- Biyani, N. et al. Focus: The interface between data collection and data processing in cryo-EM. *J. Struct. Biol.* **198**, 124–133 (2017).
- Zheng, S. Q. et al. MotionCor2: anisotropic correction of beam-induced motion for improved cryo-electron microscopy. *Nat. Methods* **14**, 331–332 (2017).
- Zhang, K. Gctf: Real-time CTF determination and correction. *J. Struct. Biol.* **193**, 1–12 (2016).
- Scheres, S. H. W. RELION: implementation of a Bayesian approach to cryo-EM structure determination. *J. Struct. Biol.* **180**, 519–530 (2012).
- Terwilliger, T. C., Sobolev, O. V., Afonine, P. V. & Adams, P. D. Automated map sharpening by maximization of detail and connectivity. *Acta Crystallogr. D* **74**, 545–559 (2018).
- Adams, P. D. et al. PHENIX: a comprehensive Python-based system for macromolecular structure solution. *Acta Crystallogr. D* **66**, 213–221 (2010).
- Emsley, P., Lohkamp, B., Scott, W. G. & Cowtan, K. Features and development of Coot. *Acta Crystallogr. D* **66**, 486–501 (2010).
- Smart, O. S., Neduvellil, J. G., Wang, X., Wallace, B. A. & Sansom, M. S. HOLE: a program for the analysis of the pore dimensions of ion channel structural models. *J. Mol. Graph.* **14**, 354–360 (1996).
- Winn, M. D. et al. Overview of the CCP4 suite and current developments. *Acta Crystallogr. D* **67**, 235–242 (2011).
- Pettersen, E. F. et al. UCSF Chimera—a visualization system for exploratory research and analysis. *J. Comput. Chem.* **25**, 1605–1612 (2004).
- Jo, S., Kim, T., Iyer, V. G. & Im, W. CHARMM-GUI: a web-based graphical user interface for CHARMM. *J. Comput. Chem.* **29**, 1859–1865 (2008).
- Wu, E. L. et al. CHARMM-GUI Membrane Builder toward realistic biological membrane simulations. *J. Comput. Chem.* **35**, 1997–2004 (2014).
- Mackereel, A. D. et al. All-atom empirical potential for molecular modeling and dynamics studies of proteins. *J. Phys. Chem. B* **102**, 3586–3616 (1998).
- Klauda, J. B. et al. Update of the CHARMM all-atom additive force field for lipids: validation on six lipid types. *J. Phys. Chem. B* **114**, 7830–7843 (2010).
- Best, R. B. et al. Optimization of the additive CHARMM all-atom protein force field targeting improved sampling of the backbone ϕ , ψ and side-chain χ 1 and χ 2 dihedral angles. *J. Chem. Theory Comput.* **8**, 3257–3273 (2012).
- Jorgensen, W. L., Chandrasekhar, J., Madura, J. D., Impey, R. W. & Klein, M. L. Comparison of simple potential functions for simulating liquid water. *J. Chem. Phys.* **79**, 926–935 (1983).
- Hopkins, C. W., Le Grand, S., Walker, R. C. & Roitberg, A. E. Long-time-step molecular dynamics through hydrogen mass repartitioning. *J. Chem. Theory Comput.* **11**, 1864–1874 (2015).
- Phillips, J. C. et al. Scalable molecular dynamics with NAMD. *J. Comput. Chem.* **26**, 1781–1802 (2005).
- Feller, S. E., Zhang, Y., Pastor, R. W. & Brooks, B. R. Constant pressure molecular dynamics simulation: the Langevin piston method. *J. Chem. Phys.* **103**, 4613–4621 (1995).
- Darden, T., York, D. & Pedersen, L. Particle mesh Ewald: an N -log(N) method for Ewald sums in large systems. *J. Chem. Phys.* **98**, 10089–10092 (1993).
- Tuckerman, M., Berne, B. J. & Martyna, G. J. Reversible multiple time scale molecular dynamics. *J. Chem. Phys.* **97**, 1990–2001 (1992).
- Ryckaert, J.-P., Ciccotti, G. & Berendsen, H. J. C. Numerical integration of the cartesian equations of motion of a system with constraints: molecular dynamics of n -alkanes. *J. Comput. Phys.* **23**, 327–341 (1977).
- Andersen, H. C. Rattle: A 'velocity' version of the shake algorithm for molecular dynamics calculations. *J. Comput. Phys.* **52**, 24–34 (1983).

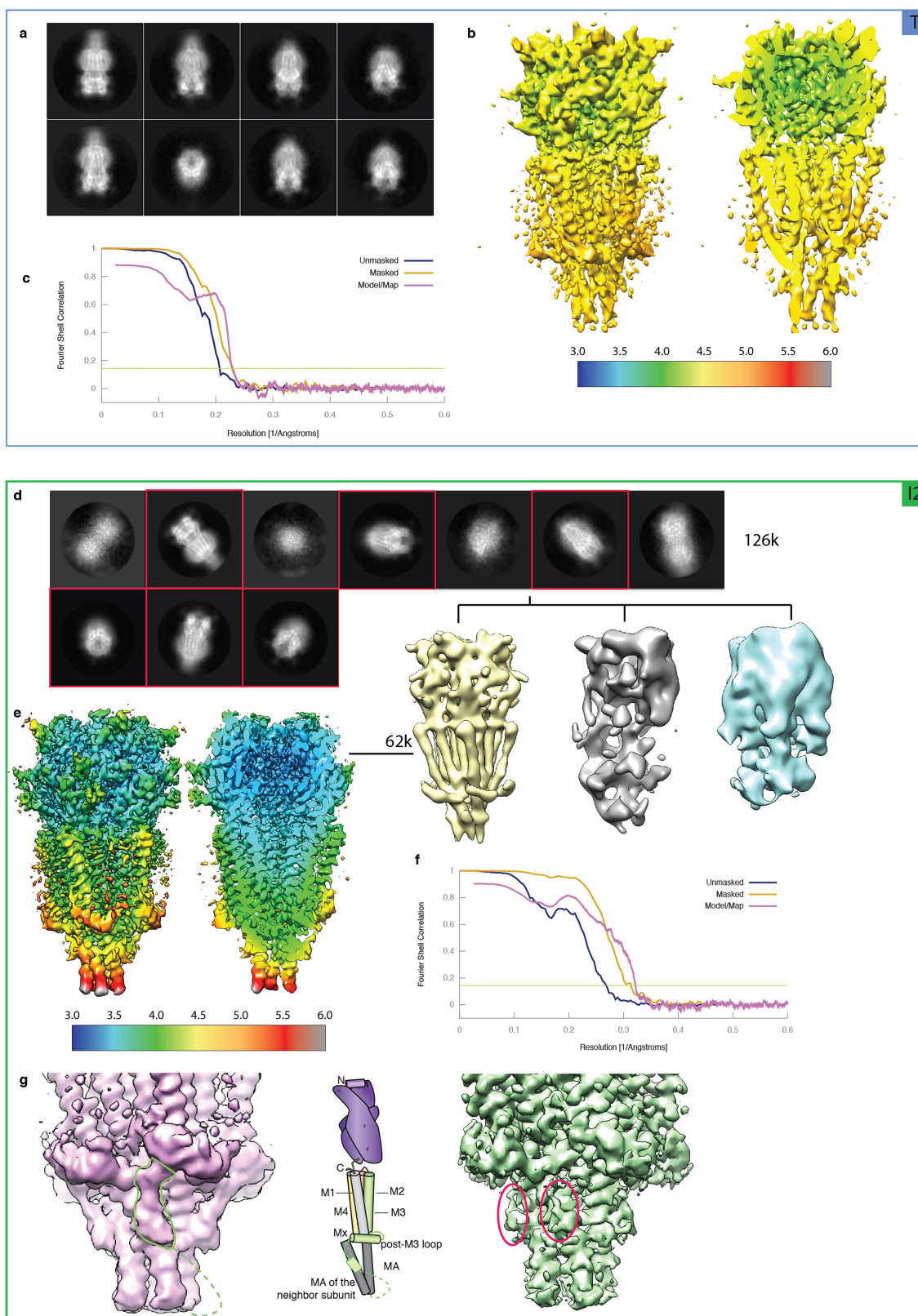
57. Miyamoto, S. & Kollman, P. A. Settle: an analytical version of the SHAKE and RATTLE algorithm for rigid water models. *J. Comput. Chem.* **13**, 952–962 (1992).
58. Humphrey, W., Dalke, A. & Schulten, K. VMD: visual molecular dynamics. *J. Mol. Graph.* **14**, 33–38 (1996).
59. Comer, J., Phillips, J. C., Schulten, K. & Chipot, C. Multiple-replica strategies for free-energy calculations in NAMD: multiple-walker adaptive biasing force and walker selection rules. *J. Chem. Theory Comput.* **10**, 5276–5285 (2014).
60. Comer, J. et al. The adaptive biasing force method: everything you always wanted to know but were afraid to ask. *J. Phys. Chem. B* **119**, 1129–1151 (2015).
61. Moreau, C. J., Niescierowicz, K., Caro, L. N., Revilloud, J. & Vivaudou, M. Ion channel reporter for monitoring the activity of engineered GPCRs. *Methods Enzymol.* **556**, 425–454 (2015).
62. Yang, J. Ion permeation through 5-hydroxytryptamine-gated channels in neuroblastoma N18 cells. *J. Gen. Physiol.* **96**, 1177–1198 (1990).
63. Trattnig, S. M. et al. Discovery of a novel allosteric modulator of 5-HT₃ receptors: inhibition and potentiation of Cys-loop receptor signaling through a conserved transmembrane intersubunit site. *J. Biol. Chem.* **287**, 25241–25254 (2012).
64. Suryanarayanan, A. et al. The loop C region of the murine 5-HT_{3A} receptor contributes to the differential actions of 5-hydroxytryptamine and *m*-chlorophenylbiguanide. *Biochemistry* **44**, 9140–9149 (2005).
65. Yan, D., Schulte, M. K., Bloom, K. E. & White, M. M. Structural features of the ligand-binding domain of the serotonin 5HT₃ receptor. *J. Biol. Chem.* **274**, 5537–5541 (1999).
66. Ruepp, M.-D., Wei, H., Leuenberger, M., Lochner, M. & Thompson, A. J. The binding orientations of structurally-related ligands can differ; a cautionary note. *Neuropharmacology* **119**, 48–61 (2017).
67. Kesters, D. et al. Structural basis of ligand recognition in 5-HT₃ receptors. *EMBO Rep.* **14**, 49–56 (2013).
68. Hibbs, R. E. et al. Structural determinants for interaction of partial agonists with acetylcholine binding protein and neuronal $\alpha 7$ nicotinic acetylcholine receptor. *EMBO J.* **28**, 3040–3051 (2009).
69. Spurny, R. et al. Pentameric ligand-gated ion channel ELIC is activated by GABA and modulated by benzodiazepines. *Proc. Natl Acad. Sci. USA* **109**, E3028–E3034 (2012).
70. Delbart, F. et al. An allosteric binding site of the $\alpha 7$ nicotinic acetylcholine receptor revealed in a humanized acetylcholine-binding protein. *J. Biol. Chem.* **293**, 2534–2545 (2018).
71. Steward, L. J. et al. Importance of phenylalanine 107 in Agonist recognition by the 5-hydroxytryptamine_{3A} receptor. *Mol. Pharmacol.* **57**, 1249–1255 (2000).
72. Purohit, P. & Auerbach, A. Acetylcholine receptor gating at extracellular transmembrane domain interface: the ‘pre-M1’ linker. *J. Gen. Physiol.* **130**, 559–568 (2007).
73. Lee, W. Y. & Sine, S. M. Principal pathway coupling agonist binding to channel gating in nicotinic receptors. *Nature* **438**, 243–247 (2005).
74. Hu, X.-Q., Zhang, L., Stewart, R. R. & Weight, F. F. Arginine 222 in the pre-transmembrane domain 1 of 5-HT_{3A} receptors links agonist binding to channel gating. *J. Biol. Chem.* **278**, 46583–46589 (2003).



Extended Data Fig. 1 | 5-HT₃ receptor topology and sequence.

a, Schematic of the full-length 5-HT₃ receptor. The colour code is the same for all panels. Scissors indicate the enzymatic treatments used during purification: purification tag removal using TEV protease, and partial removal of carbohydrates using PNGase F. **b**, Topology scheme and structure of one subunit of the 5-HT₃ receptor. **c**, Sequence and numbering of the mouse 5-HT_{3A} receptor used in the present study. Secondary structures and important loops are indicated. Neurotransmitter site binding loops are highlighted. Important residues discussed in the study are boxed (pore-facing residues in red, sandwich motif in brown and neurotransmitter site in blue). Cyan highlights residues important for TMPPAA potency. Glycosylation sites are depicted in green. The mouse receptor used for this study is a variant compared to the consensus

sequence as it contains an alanine insertion in the M2–M3 loop, which is highlighted by the pink box. Notably, this insertion is present in the consensus human receptor sequence. This panel is adapted from ref. ⁵. **d**, A typical unmasked reconstruction, with different density levels overlaid depicting the protein itself (yellow), ligands (purple), linked glycans (green), the detergent-lipid belt (transparent purple) and the footprint of the disordered zone (transparent grey). **e**, Currents induced in *Xenopus* oocytes expressing the mouse 5-HT_{3A} receptor by a 3-min application of 10 μM serotonin (green traces), co-application of 10 μM serotonin and 100 nM tropsisetron (following a 5-min pre-application of tropsisetron, red trace), co-application of 10 μM serotonin and 10 μM of TMPPAA (following a 5-min pre-application of TMPPAA, black trace). Current traces are representative of 3 independently repeated experiments.

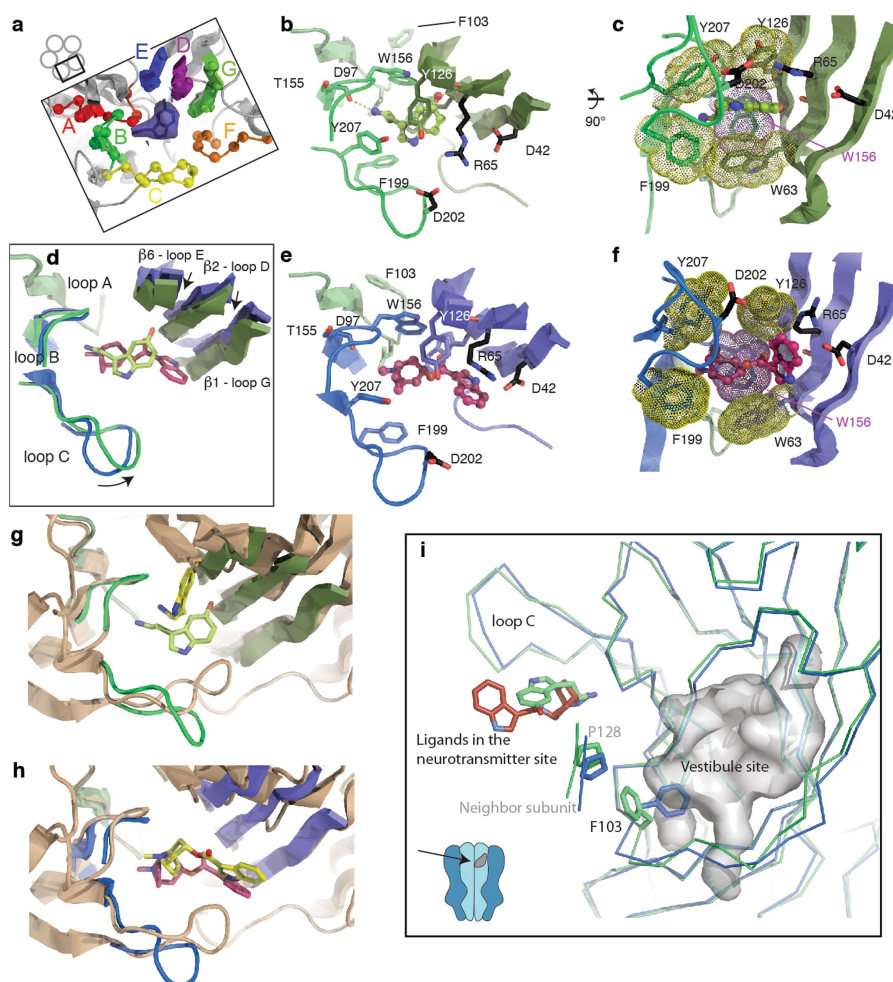


Extended Data Fig. 2 | See next page for caption.

Extended Data Fig. 2 | Electron microscopy and 3D reconstructions for the tropisetron dataset (T), and for the serotonin + TMPPAA dataset (I2).

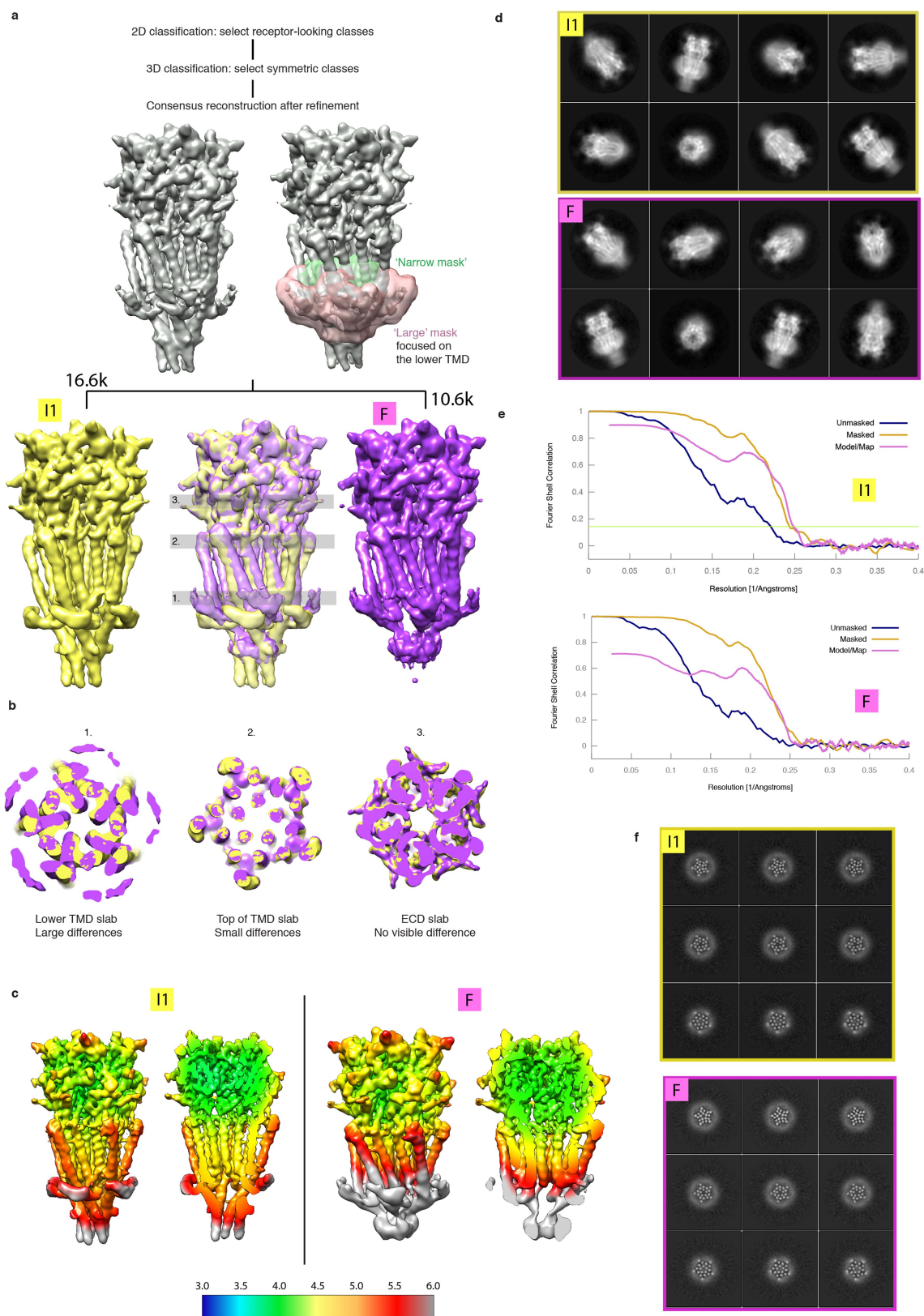
a, Tropisetron dataset (T). Selection of 2D class averages from the set of particles used for refinement of the tropisetron reconstruction. **b**, Three-dimensional reconstruction from the tropisetron dataset, filtered and coloured according to RELION local resolution. A global and a cut-through side view are shown. **c**, FSC curves for the density map before and after RELION post-processing, and between the model and the final map. **d**, Serotonin + TMPPAA dataset (I2). Selection of good 2D classes after one round of classification yields a set of 126,000 particles. One round of 3D classification with no symmetry imposed yields one class with pentameric symmetry, amounting to 62,000 particles. **e**, Unmasked unsharpened refined 3D reconstruction, filtered and coloured according to RELION local resolution. The colour range for resolution is similar to the equivalent representations for the other datasets in Extended Data

Fig. 4c, allowing direct comparison. **f**, FSC curves for the density map before and after RELION post-processing, and between the model and the final map. **g**, Left, a non-sharpened map filtered at 3.9 Å resolution, obtained with a subset of 55,000 particles from the I2 dataset, selected after further 3D classification focused on the ICD. The hypothetical trajectory of the polypeptide chain after MX is bordered by a green line. No full connectivity can be visualized and the model was not built. The chain appears to descend abruptly after MX, and may interact with MA of the neighbouring subunit at the level of H411, where there is a clear density. Then it must link to the beginning of MA, but maps show no information how it may do so. The schematic representation highlights that this putative trajectory contacts MA on the neighbouring subunit close to residue H411. Right, the corresponding sharpened and masked reconstruction, showing that model building is not possible. The density of the disordered stretch closed to H411 is highlighted by the pink ellipses.



Extended Data Fig. 3 | Serotonin and tropisetron bound in the orthosteric site; the vestibule allosteric site. a, Organization of one of the five equivalent binding sites at the subunit interfaces in the ECD. Binding loops A–C are located on the principal subunit, and binding elements D–G are on the complementary subunit. The density around serotonin in the I2 reconstruction is shown as a transparent blue surface. **b, c**, Serotonin (ball-and-stick) in the orthosteric site in the I2 structure. Aromatic residues (dotted surfaces in **c**), hydrogen bonds with main chain atoms (dashed lines) and charged residues within salt-bridge distances (D202 on the principal side, R65 on the complementary side) are noted in two orthogonal views. Of note, mutants D202A⁶⁴ and R65A⁶⁵ exhibit impaired serotonin binding with increases of around 140-fold and 50-fold, respectively, in K_i (the equilibrium inhibitor constant) during competition assay for [³H]-granisetron binding. **d**, Superimposition of tropisetron-bound T (blue) and serotonin-bound I2 (green) structures, highlighting loop C motion and quaternary reorganization with arrows (principal subunit superposition in this panel and in **g** and **h**; note complementary subunit β -strand shift). Serotonin (light green) and tropisetron (magenta) are represented as sticks. **e, f**, Tropisetron bound to the orthosteric site in the T structure. The bicyclic tropane moiety is sandwiched between W156 of loop B and Y207 of loop C, whereas the indole lies close to R65, W63 in loop D, D42 and I44 in loop G, and R169 in loop F. Functional exploration of the binding mode of tropisetron consistently showed that, among others, single mutations to cysteine of the aromatic residues W156, Y207 or W63 abolished binding⁶⁶. To fit tropisetron, the side chain of R65

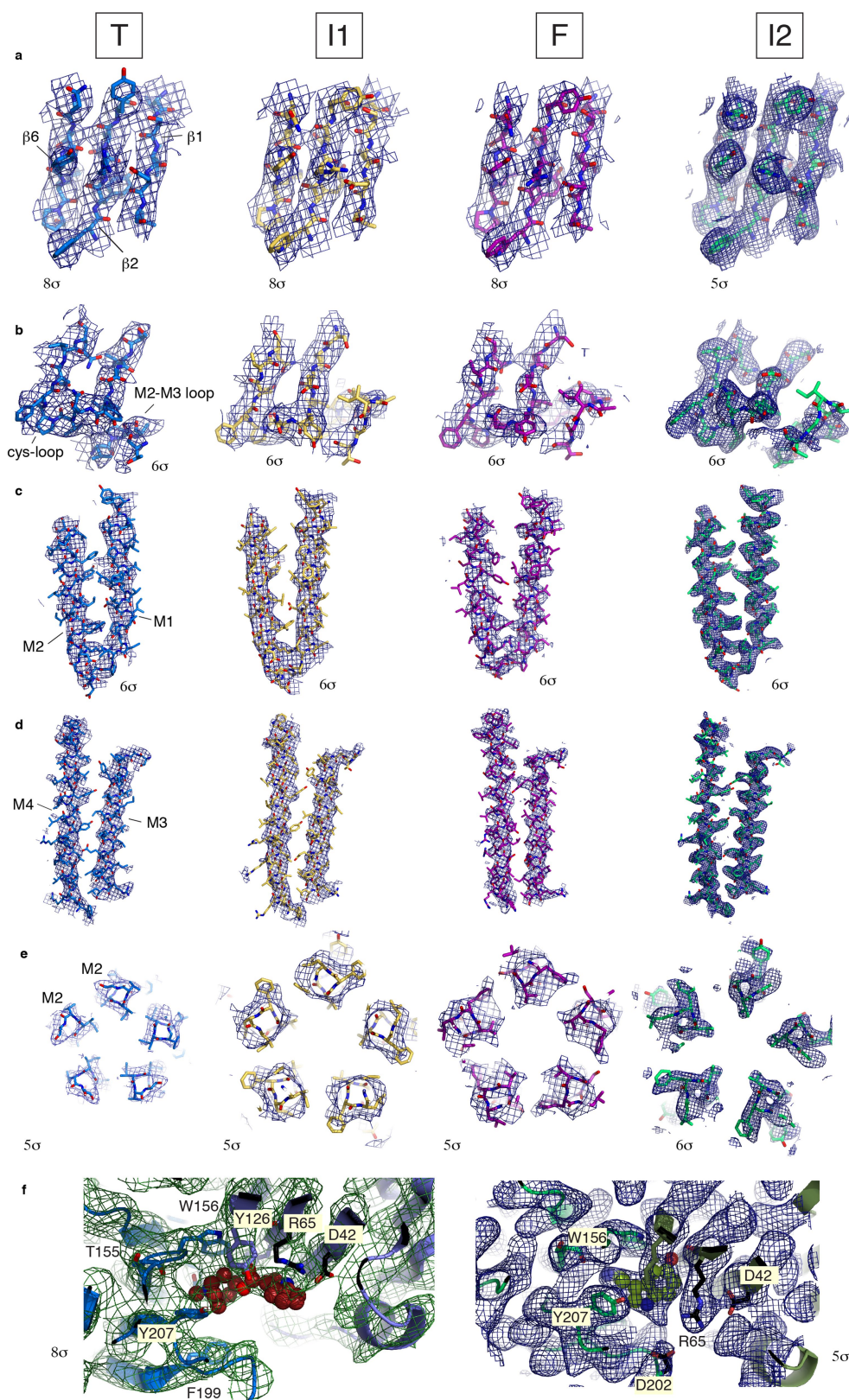
is pushed upward and in turn displaces the side chains of Y67 and W168, compared to the empty orthosteric site of the X-ray structure. Densities for these side chains are not well-resolved. The density for tropisetron is shown in Extended Data Fig. 5f. **g**, Superposition of the I2 structure with the crystal structure of a mutant acetylcholine binding protein (AChBP, wheat cartoon) in complex with serotonin⁶⁷ (yellow sticks) shows distinct binding modes. **h**, Superposition of the T structure with the crystal structure of AChBP (wheat cartoon) in complex with tropisetron (yellow sticks) shows a similar orientation of ligands but different interactions with the protein at loop C, D, E, F and G (not shown for clarity), consistent with the 3 orders of magnitude difference (0.7 versus 479 nM⁶⁸) in K_d (dissociation constant). **i**, Overlay of the T and I2 structures (in blue and green, respectively) superimposed on a subunit ECD, showing the motion of F103 out of the vestibule site. The protein depicted as ribbon is viewed from inside the vestibule, and the intra-subunit cavity (in the I2 conformation) is represented as a grey surface. Acetate in GLIC, flurazepam in the bacterial homologue ELIC⁶⁹ or a drug fragment in α 7-AChBP⁷⁰ bind to this cavity. A putative rationale for the strong effect of F103 mutants on serotonin EC₅₀⁷¹, despite its absence of participation in the binding site, comes from the observation of its concerted motion with that of strands from the neighbouring subunit (around P128 and around P110; for clarity, the latter is not represented here). Therefore, the motion of F103 may participate in subunit–subunit quaternary reorganization, exemplifying the allosteric coupling between sites.



Extended Data Fig. 4 | See next page for caption.

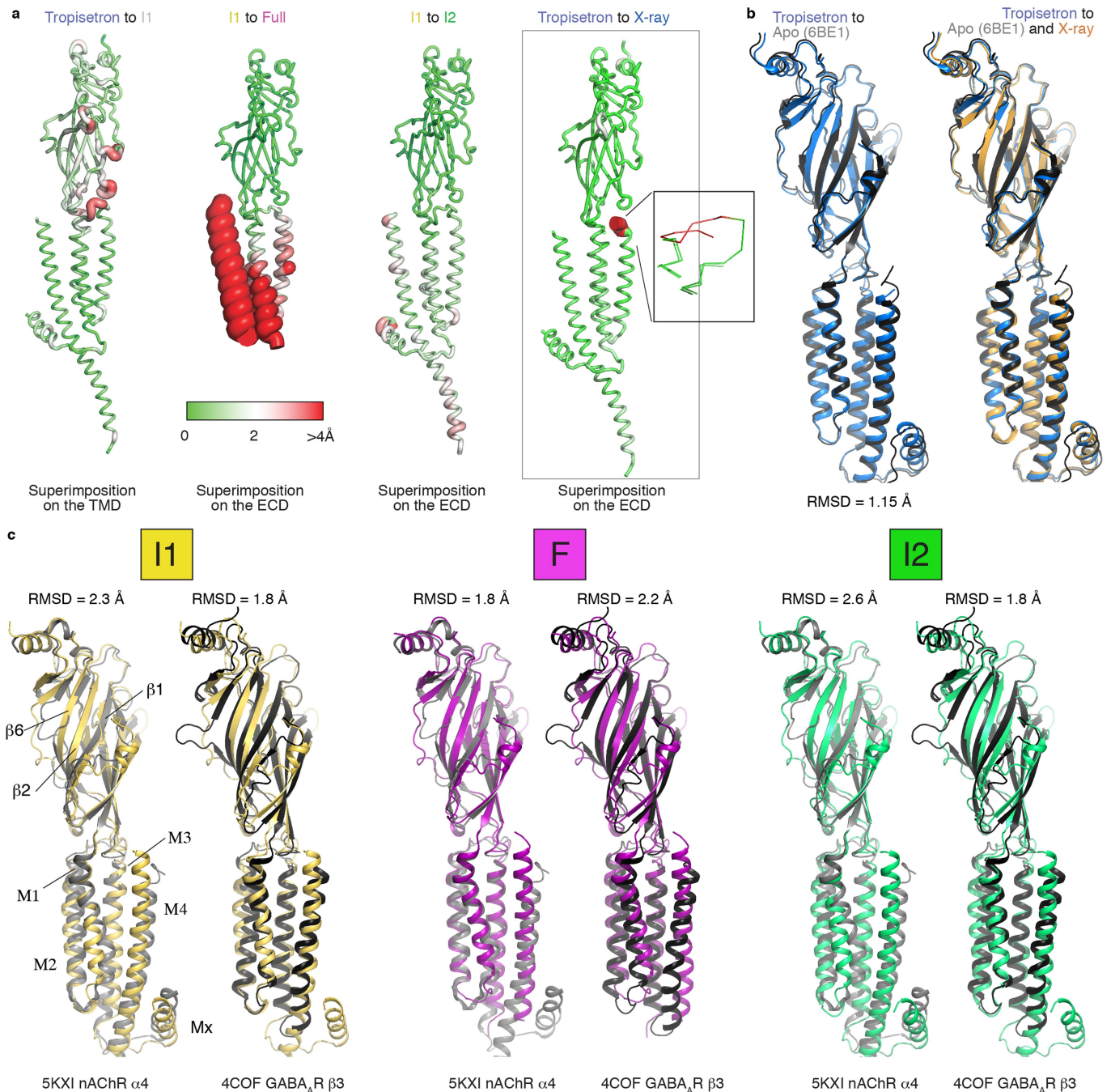
Extended Data Fig. 4 | Electron microscopy, classifications and 3D reconstructions for the serotonin dataset. **a**, Schematic of the data processing, with classical rounds of 2D and 3D classification yielding a consensus reconstruction seen parallel to the membrane plane (grey) where helices look like tubes of elliptic sections, indicating heterogeneity. Extensive classification trials, without alignment, with masks of various size covering the lower part of the TMD (shown in green and red) enable two conformations to be distinguished (yellow corresponding to the I1 structure, and purple corresponding to the F structure), representing the extreme positions of the helices in the consensus reconstruction. An overlay of the two reconstructions depicts the good superimposition

of the ECD and the clear difference in the lower TMD. Grey rectangles indicate the positions of the slabs represented in **b**. All reconstructions shown are unmasked outputs of RELION 3D refinements. **b**, Slabs, viewed perpendicular to the membrane plane, from the intracellular side showing the overlay of the I1 and the F reconstructions. **c**, Reconstructions filtered and coloured according to RELION local resolution. A global and a cut-through side view are shown. **d**, Selection of 2D class averages from the set of particles used for refinement of the I1 and F reconstructions. **e**, FSC curves showing the unmasked and masked FSCs (before and after post-processing in RELION), and the model-to-map FSC. **f**, Selection of 'slice' views of the TMD of the final unmasked unsharpened reconstructions.



Extended Data Fig. 5 | Quality of the density maps in representative regions of the four 5-HT₃ receptor reconstructions. Densities in mesh representations overlaid with structures for the T (blue), I1 (yellow), F (purple) and I2 (green) reconstructions and structures, left to right, respectively, in each panel. Views **a–e** are approximately the same as those in extended data figure 4 of a previous publication of $\alpha 1$ GlyR⁷. **a**, Representative densities of the β -sheets in the ECD. **b**, Densities of the Cys loop and the M2–M3 loop. **c**, Densities of helices M1 and M2.

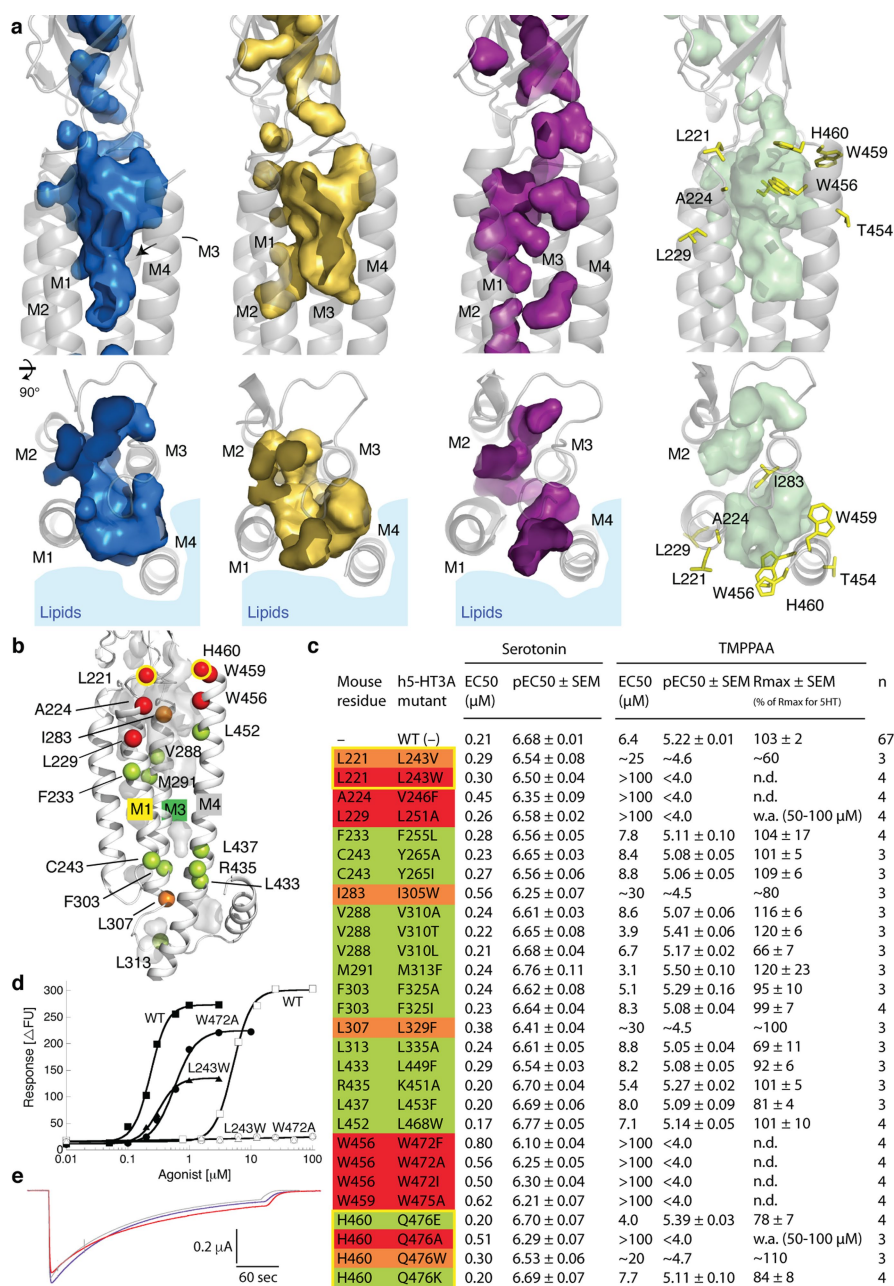
d, Densities of M3 and M4. **e**, Densities of M2 at the level of L9' (L260). **f**, Densities around the ligands tropisetron (in T) and serotonin (in I2). The 3.2 Å resolution of I2 permits unambiguous orientation of serotonin, and side chains of residues around the ligands are seen in densities. For tropisetron, given the limited 4.5 Å global resolution, the orientation of the ligand and the positions of surrounding side chain are less certain. The views are the same as in Extended Data Fig. 3b, e.



Extended Data Fig. 6 | Structural superpositions with the nAChR α4β2, the GABA_A receptor β3 subunit and the apo 5-HT₃ receptor structures.

a, Putty representations of pairwise deviations for the 5-HT₃ receptor conformations. The selection used for superimposition, and the two conformations used, are noted for each image. The colour code and tube thickness code are the same for all images. In the T versus X-ray image, the red zone corresponds to a loop that was not modelled in the X-ray structure. **b**, Superimposition of a 5-HT₃ receptor subunit in the inhibited T state (blue) and of a 5-HT₃ receptor subunit in the apo state (grey, PDB: 6BE1). Structures are globally similar with differences in the lipid-exposed helices M3, MX and M4, hypothetically a consequence of the different additives used—a lipid mixture in this study versus fluorinated fos-choline 8 for the apo structure. Superposition of the T structure (blue), the apo

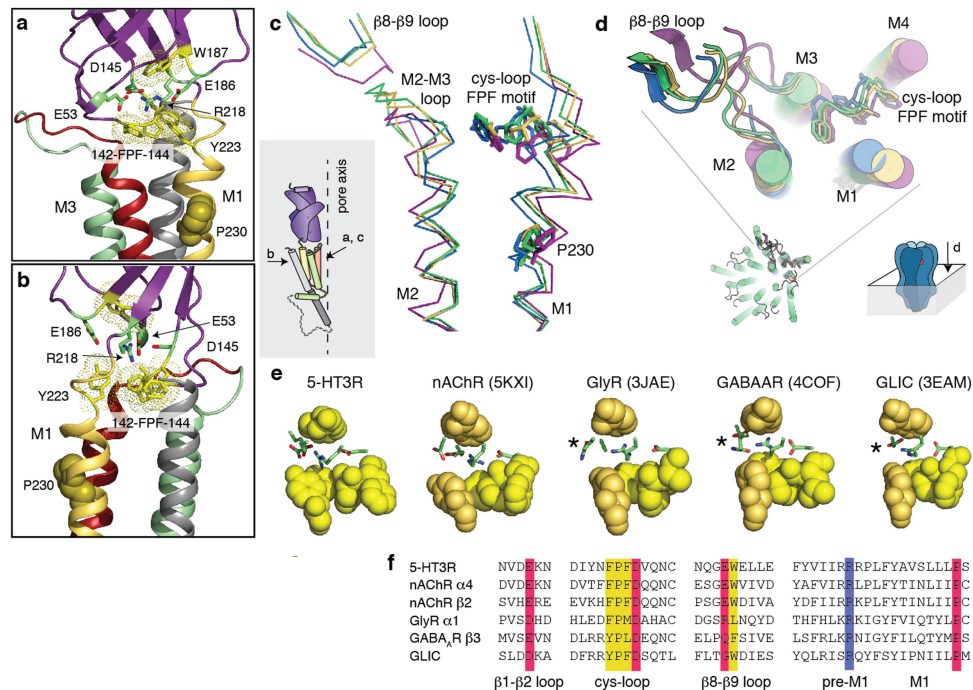
structure (grey) and the X-ray structure (orange). **c**, Superposition of a 5-HT₃ receptor subunit in the I1, I2 and F conformations with a nAChR α4 subunit (PDB: 5KXI, chain A) or a GABA_A receptor β3 subunit (PDB: 4COF). C_α r.m.s.d. is noted. Comparison of superpositions with r.m.s.d. below 2 Å shows that in the case of F and nAChR α4 (middle, purple and grey), the domain-to-domain orientation is very similar and the extracellular halves of helices M1, M2, M3 superimpose very well, whereas clear deviations are present in their intracellular halves and at the level of M4 (r.m.s.d. without M4 drops to 1.6 Å). In the case of I1 and GABA_A β3 (left, yellow and black), or I2 and GABA_A β3 (right, green and black), differences are more distributed; deviations of the ECD indicate different domain-to-domain orientations, and in the TMD M1 and M3 superimpose quite well but M2 and M4 clearly differ.



Extended Data Fig. 7 | TMPPAA binds to an allosteric site in the TMD.

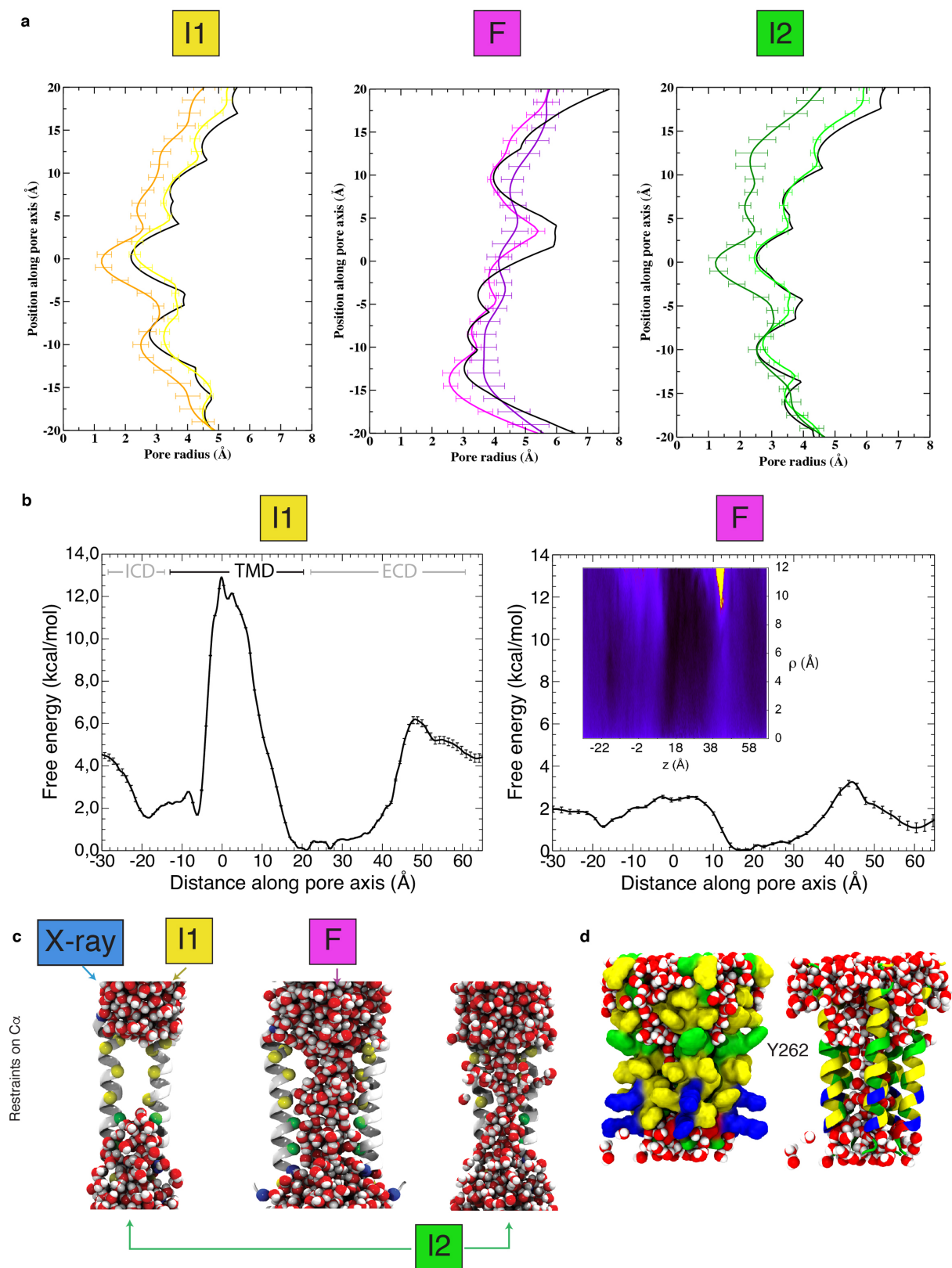
a, Cavities in surface mode for the T (blue), I1 (yellow), F (purple) and I2 (green) states. Note the re-arrangement of the cavities between states. The protein is depicted in cartoon, with sticks in the right panels for residues in which mutations impair the effect of TMPPAA. Noisy densities are found in the I2 reconstruction, in or close to the cavities, but they do not permit ligand modelling and could correspond to parts of a lipid or detergent molecule. **b**, Side view of the transmembrane domain of I2 with mutated positions depicted as green spheres (for residues for which mutations had negligible effect on TMPPAA potency), orange spheres (for residues for which mutations reduced TMPPAA potency substantially) or red spheres (for mutations that completely or almost completely eliminated TMPPAA activity at concentrations up to 100 μM). Yellow circles indicate residues for which different mutations produced different effects. **c**, Functional properties exhibited by serotonin and TMPPAA as agonists at 5-HT_{3A} receptors expressed in tsA201 cells in an FMP assay. The human 5-HT_{3A} receptor was used for these experiments, since TMPPAA evokes a more robust agonist response through this receptor than through mouse

5-HT_{3A} in this assay¹⁷. The colour code is similar to that in **b**. n.d., not determinable, w.a., weak activity. A complete table of data for all tested mutant receptors is shown in Supplementary Table 1. **d**, Concentration-response curves for serotonin (closed symbols) and TMPPAA (open symbols) tested as agonists at wild-type, W472A and L243W human 5-HT_{3A} receptors expressed in tsA201 cells, using the FMP assay. Data are from a single representative experiment determined in the same 96-well plate and are given as mean based on duplicate determinations. The experiment was repeated independently with similar results 3 times for the W472A and L243W receptors and 66 times for the wild-type receptor (*n* for wild-type and all mutant receptors are given in **c**). **e**, Loss of TMPPAA potency at the mouse W456A mutant receptor. Currents evoked by 10 μM serotonin (blue curve) or 10 μM serotonin plus 100 μM TMPPAA (red curve) are equivalent. The grey trace, obtained in an oocyte expressing wild-type receptors (response to 10 μM serotonin, normalized for the peak amplitude), shows that desensitization in wild-type and W456A mutant receptors is similar. Current traces are representative of 3 independently repeated experiments.



Extended Data Fig. 8 | Structural motif and reorganization at the ECD-TMD interface. **a, b**, Key interacting charged residues R218 (pre-M1, key in gating^{72–74}), E53 (loop β1–β2), E186 (loop β8–β9, conserved only in cationic eukaryotic receptors) and D145 (Cys loop)—represented as purple sticks—are sandwiched between conserved essential aromatic residues (FPF motif of the Cys loop, W187 of β8–β9 and Y223 of M1), represented as yellow sticks and dots. Lower in the membrane, the strictly conserved P230—represented as spheres—enables M1 to kink. This structural organization is common to all pLGICs of known structure. Orientations of the views are indicated on the topology scheme. **c, d**, Side and top views depicting the concerted relative positions of the Cys-loop FPF ‘wedge’, represented as sticks, of transmembrane helices and of the

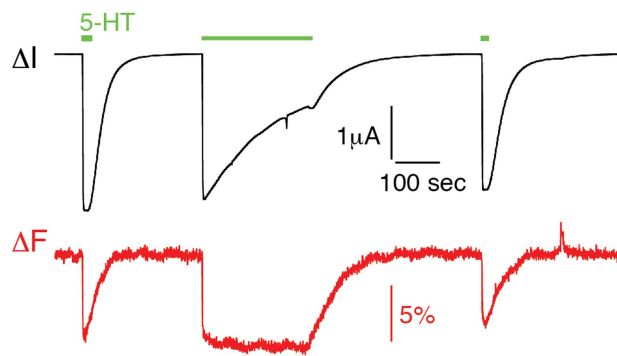
β8–β9 loop. Compared to the inhibited structure, the wedge moves towards and pushes on M1 and also moves towards M4 in I1, I2 and F. F presents the biggest re-organization in this zone: M1, the M2–M3 loop and M3 follow the motion of the FPF motif, and M2 moves away from the pore axis (that is, to the back in the view in **c** and to the top in **d**). **e**, Conservation of the ‘sandwich’ structural motif in representative pLGIC structures. The aromatic top and bottom layers are represented as spheres (yellow, Cys loop; orange, β8–β9 loop and pre-M1 residue) whereas the central layer of charges is depicted as sticks. Note that in anionic receptors and GLIC, the charge of β8–β9 is absent (noted with a star). **f**, Sequence alignment of the motif residues in representative pLGIC structures.



Extended Data Fig. 9 | See next page for caption.

Extended Data Fig. 9 | Geometry of the pore during the molecular dynamics simulations. **a**, HOLE transmembrane pore profiles for the trajectories starting from I1, F and I2. In each graph, the profile from the cryo-EM structure is represented in black, the average profile during the restrained part of the simulation (30–60 ns, mean \pm s.d. of $n = 30$ snapshots taken every ns) in the lighter colour and the average profile during the unrestrained part (60–1,000 ns, mean \pm s.d. of $n = 940$ snapshots taken every ns) in the darker colour. The y -axis origin corresponds to L260/9' whereas S253/2's is located at about -12 \AA . **b**, Complete potentials of mean force of K^+ ions as a function of position along the pore axis. The inset represents the 2D free-energy landscape as a function of the position along the pore axis and the radial direction, orthogonal to it. The represented free-energy profile is the

mean of 135,000,000 values distributed along 2.16 \mu s of the I1 trajectory (190,000,000 values distributed along 3.04 \mu s of the F trajectory); the standard deviation corresponds in both cases to 50,000,000 values from four independent walkers, distributed along the last 0.8 \mu s of the trajectory. **c**, Representative snapshots of the pore wetting during the initial restrained part (30–60 ns) of the simulations. A dewetted pore is observed for the T and I1 trajectories, a fully wetted one for the F trajectory, whereas wetting and dewetting occur in the I2 trajectory. C_α atoms of pore-exposed residues are represented as spheres. **d**, Snapshot of the I2 trajectory showing the wetting of grooves at the back of M2 (shown as molecular surface on the left, as cartoon on the right), concomitant with wetting of the pore.



Extended Data Fig. 10 | Local motions in the pore probed by VCF. Representative serotonin-evoked simultaneous current and fluorescence recordings from oocytes expressing S19'C mutant receptors labelled with MTS-TAMRA. Similar traces were obtained in 3 independent experiments.

Extended Data Table 1 | Statistics of 3D reconstructions and model refinement

	Tropisetron	Serotonin		Serotonin and TMPPAA
Data collection and processing				
Microscope	Krios@CCINA	Krios@CCINA		Krios@ESRF
Magnification	130,000	130,000		130,000
Voltage (kV)	300	300		300
Electron exposure (e-/Å ²)	~80	~60		~50
Defocus range (μm)	0.5-2.5	0.8-2.5		0.8-2.5
Pixel size (Å)	0.52	0.52		1.067
Symmetry imposed	C5	C5		C5
Number of images	~1500	~2000		~3000
Particles picked	160k	456k		250k
Symmetric-looking particles	133k	145k		62k
Particles refined	43,558	16,660	10,667	62,032
Refinement	T	I1	F	I2
Initial model used	4PIR	4PIR	4PIR	4PIR
Resolution (Å)	4.5	4.2	4.1	3.2
FSCthreshold	0.143	0.143	0.143	0.143
Map sharpening B-factor (Å ²)	-247	-100	-100	-127
Model composition				
Non-hydrogen protein atoms	15,645	15,670	13,805	15,670
Protein residues	1,935	1,925	1,675	1,925
Ligands	585	415	415	415
B-factor (Å ²)				
protein	127	130	83	78
ligand	113	102	73	53
R.M.Sdeviations				
Bond lengths (Å)	0.008	0.009	0.009	0.006
Bond angles (°)	1.5	1.1	1.2	1.0
Validation				
Molprobability score	2.0	1.45	1.35	1.18
Clashscore	14.1	8.3	6.4	3.9
Poor rotamers (%)	0.3	0.2	0.3	0.3
Ramachandran plot				
Favored (%)	95.1	98.0	98.5	98.4
Allowed (%)	4.9	2.0	1.5	1.6
Disallowed (%)	0.0	0.0	0.0	0.0

CAREERS

FELLOWSHIPS Design a winning proposal tailored to you **p.283**

ONLINE Career resources from our community at nature.com/careers

SOCIAL Follow us on Twitter at twitter.com/naturejobs

EFSA



EFSA chief scientist Marta Hugas is seeking more than 200 scientists to conduct high-quality, regulatory-driven research.

GOVERNMENT

Perks of agency science

European Commission scientists enjoy work–life balance and dynamic career paths.

BY QUIRIN SCHIERMEIER

David Krasa had never worked in one position for much more than three years before he became a research-programme officer at the European Research Council (ERC) in 2009. After the German scientist earned his PhD in geophysics from the Ludwig Maximilian University of Munich in Germany, he gained research experience as a postdoc at the University of Hawaii at Manoa and the University of Edinburgh, UK. For Krasa, seeing the world was part of the joy of studying rocks and minerals.

But when he and his wife had their first child in 2006, he wanted something secure. “I love science,” he says. “But job security and work–life balance become more and more important

when you start a family.”

Krasa had thought that research management, which involves organizing calls for proposals and coordinating administrative support for funded research projects, was a good option for permanent employment that would keep him in touch with science. In December 2008, he accepted a position as a research-programme officer for Earth sciences and solid-state physics at the ERC, which was set up two years earlier as the European Union’s premier funding agency for basic research.

Krasa now oversees the review process for ERC grants in the physical sciences and mathematics. His role includes organizing and moderating panel meetings of independent reviewers and following up with principal investigators on the progress of their research.

He no longer does bench work, but he interacts with scientists who do. Many proposals are far removed from Krasa’s own scientific background, so he must quickly learn their content and position their ideas within a broader framework. “I’m dealing with brilliant people whom I might never have met otherwise,” he says.

At the Brussels headquarters of the European Commission (EC), the executive arm of the EU, hundreds of officials administer the multi-billion-euro EU research programmes (including the ERC, which now represents almost 20% of the EU’s overall research budget). Scientists also work in the EC’s Joint Research Centre (JRC), a science and knowledge service based in Belgium, Germany, Italy, Spain and the Netherlands. The JRC generates and collates policy-relevant information for the EC and for ►

► regulatory authorities in all member states.

Fixed-term research positions and permanent jobs with a predominantly scientific profile are also available at specialized EU agencies, including the European Food Safety Authority (EFSA) in Parma, Italy, and the European Medicines Agency (EMA) in London, which will relocate to Amsterdam next year.

Scientists at EU institutions and agencies cannot choose which topics they work on. But the research they are assigned might profoundly influence rules and regulations that affect millions of citizens.

Officials and permanent research staff with the EC must have EU citizenship. Postdoctoral fellowships at the JRC are also open to citizens of 16 associated non-EU countries, including Switzerland, Norway, Turkey and Ukraine. Eligibility for traineeships is more flexible, but applicants from other countries must apply for special approval on the basis of their nationality.

The future of UK applicants for EU jobs depends on pending negotiations following Brexit. British EU officials and temporary agents — including researchers — have a right to request an exception to the requirement of EU citizenship. The EC has promised to grant exceptions generously and transparently.

COMPETITIVE APPLICATION

John Magan is deputy head of the photonics unit in the EC's Directorate-General for Communications Networks, Content and Technology (DG CONNECT) in Brussels. A physicist by training, Magan joined the EC as a programme officer in 1993 after his former employer, the German chemicals company Hoechst, closed down its laser-research department. "I wanted to help build a better Europe," he says.

EU-funded research in photonics operates under heavier application pressure than it did 25 years ago, he says. His unit now oversees an annual budget of €100 million (US\$114 million) to develop laser and sensor technologies for medicine and industry. Programme officers are not experts in everything; Magan must read the literature and consult with independent experts to identify cutting-edge research topics for inclusion in the EC's thematic work programmes, which are redefined every two years.

A senior programme officer might administer more than 12 large research collaborations at once, requiring almost a generalist's knowledge, says Magan. His own expertise ranges from optical- and fibre-laser systems for industrial purposes to medical sensors and silicon chips with various applications. "You lose out on doing actual research," he says. "But I like my job better than bench research where I might work, day in, day out, on just one narrow project."

Still, a research programme manager's job is not without frustrations. "We can only fund about 1 in 10 to 1 in 20 proposed projects," he says. "It really disappoints me that so many good ideas don't get funded."

The EC also employs some 2,000 researchers in the JRC across 6 units in 5 countries (see

TOUGH COMPETITION

Winning the job

The recruitment of trainees, postdocs and temporary research staff at the European Commission's Joint Research Centre and EU agencies is organized by the individual agencies. Job opportunities for specific positions are generally posted online.

The European Medicines Agency advertises its vacancies through its Jobs@EMA portal. Job opportunities at the European Food Safety Authority (EFSA) are posted on the agency's online recruitment platform. Unsolicited job applications are not considered. Under the European Food Risk Assessment Fellowship Programme, early- to mid-career scientists from national-risk-assessment authorities can apply for a 12-month EFSA fellowship.

The selection process for permanent positions is lengthy and arduous. Recruitment is centrally organized through

the European Personnel Selection Office (EPSO). Candidates should have EU citizenship and speak at least two official EU languages. To compete for EU jobs, candidates must create an EPSO profile and enter all relevant information that outlines their background and motivation.

Those who are invited to the next stage of the competition will sit through a series of cognitive tests that measure their verbal, numerical and abstract-reasoning abilities. EPSO provides sample tests to help candidates prepare.

Vacancies for research profiles are typically filled through specialist competitions in which candidates undergo further oral and written tests in their fields of expertise. Some EU member states offer training for candidates in different stages of the selection process. [A.S.](#)

'Winning the job'). Doing science in an EU context is quite different from academic or industrial settings. "When we interview job candidates, we make sure they understand where they are applying," says physicist Elisabetta Vignati, head of the JRC's Air and Climate Unit in Ispra, Italy. "People who are mainly interested in basic research are better off at a university. But for researchers who are open to looking at science from a policy-relevant angle, the JRC might well be the right place."

The JRC does not carry out blue-sky research, but it supplies a constant feed of scientific information to support EU policies — including energy, health and the environment — in all phases of implementation. Vignati's unit, for example, produces models for local authorities to design action plans in line with EU climate and air-quality regulations. This involves lab science, such as on chemical properties and atmospheric fluxes of pollutants, as well as monitoring activities in the field. JRC researchers are encouraged to publish their results in peer-reviewed journals, but they are under less pressure to publish prolifically than their academic peers.

The knowledge hub's mandate means that scientists with the JRC institutes in Brussels; Geel, also in Belgium; Ispra, Italy; Karlsruhe, Germany; Petten, the Netherlands; and Seville, Spain, must continuously liaise with policymakers and authorities. "Our scientists must know EU legislation, and they must understand how policy making works," says Vignati. "And they must also learn that talking with politicians is very different

from talking to scientists."

JRC research might have a direct impact on EU policies. For example, the EC in 2015 reduced the target for the use of transport bio-fuels in the EU, after JRC researchers warned that indirect land-use changes might negate greenhouse-gas savings from biofuels.

Few EC researchers work on the same subject for years on end. Michele Vespe, a migration researcher at the JRC Knowledge Centre on Migration and Demography in Ispra, developed radar remote-sensing technology for oil-spill detection and maritime surveillance before he switched to analysing big data and alternative data sources on migration.

Likewise, Ispra-based chemical engineer Bernd Gawlik switched his research focus from waste and soil to wastewater treatment and manure management when sustainability became increasingly popular in the EU. "I know of no other place in science where you can work as flexibly and interdisciplinarily as at the JRC," he says. "As a chemist, you might collaborate with economists, social scientists or artificial-intelligence researchers."

EU-employed scientists need not worry too much about funding. But they are not free to do what they like, and they must follow strict internal procedures concerning workflows, reporting and transparency, Gawlik says. They are encouraged to explore their ideas — but before starting something new, they must obtain approval from management, which could take months. In addition, EU officials must weigh their words carefully, especially when making public claims that might contradict political mainstream thinking. And when conflicts arise between the EC and EU member states, the JRC might be asked to produce scientific evidence under extreme time

"Here, I can work for the benefit of many thousands of patients instead of just a few."

pressure. “When we are asked for urgent advice, we work around the clock for days,” says Gawlik.

AGENCY SCIENCE

At EU regulatory agencies, scientists are tasked with rigorously testing potentially opposing claims concerning health and the environmental risks of drugs, chemicals and foodstuffs. The EMA, for example, evaluates applications for marketing authorizations of medicines and monitors the safety of approved drugs across their life cycles. “Our role is to ensure safe, effective and quality medicines for patients, who may need new treatment options,” says Pavel Balabanov, a Bulgarian neurologist who joined the EMA in 2008 after six years of clinical experience. “I really liked working with patients. But here, I can work for the benefit of many thousands of patients instead of just a few.”

Regulatory-driven research requires an interest in research methods (including statistics), project-management skills and a solid understanding of the regulatory framework in which the agency operates, says Marta Hugas, EFSA chief scientist.

The agency provides the EC, the European Parliament and EU member states with scientific advice on health risks related to human and animal food. EFSA scientists must handle and communicate uncertainty and sustain an evidence-based position in public debate over controversial issues such as the safety of genetically modified crops, says Hugas. The agency currently employs about 200 biologists, chemists, toxicologists, plant researchers, nutrition researchers and veterinary scientists who are in steady consultation — and who often become coauthors of meta-analysis and review articles — with leading experts in their fields. It plans to hire up to 100 scientists over the next few years. “We are looking for rigorous researchers at any career level who are interested in risk assessment for the public good,” says Hugas.

A traineeship at an EU agency raises young scientists’ employability, Hugas adds. Chemist Alessia Amodio, now an EFSA trainee, wanted something new after two years of postdoctoral research in nanotechnology at the University of Tor Vergata in Rome and the University of Melbourne in Australia. She enjoys the variety of tasks in regulatory-driven science, but hasn’t yet decided whether she prefers ‘desk’ science over bench research. She hopes that her experience in both worlds will open doors to whatever career path she might choose.

“I’ve been through many challenges and I’ve learned many new things,” she says. “I’m not scared at all about what might come next.” ■

Quirin Schiermeier is Nature’s Germany correspondent in Munich.

COLUMN

Forge your own path

Propose a fellowship that can propel you into your ideal career, say **Crystal M. Botham** and **Tanya M. Evans**.

Looking to win a US graduate or postdoctoral research fellowship? Don’t focus only on your current research: you’ll need a proposal that outlines your specific goals for career development and training.

Most US fellowships, such as the National Institutes of Health’s National Research Service Awards, support research-related and professional activities. These might include taking extra courses or giving a talk that will enhance the award recipient’s training experience and improve their potential for success. But the most common mistake we see applicants make in our coaching sessions (and that we made ourselves) is to focus only on their research. That’s just one component of a winning application.

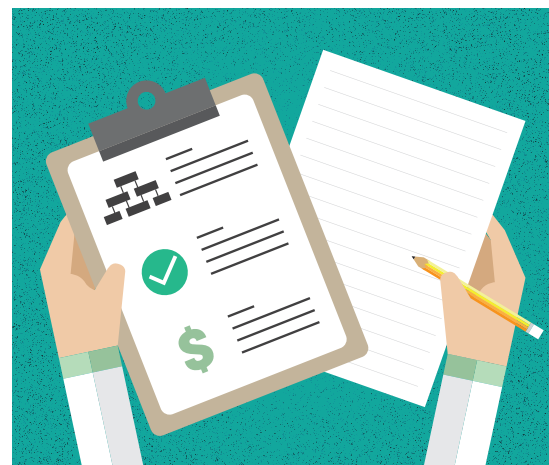
We encourage graduate students and postdocs to design a path that will complement their previous training and help to propel them towards their next career stage. We’ve developed an outline for incorporating training goals into fellowship proposals. Here are the basics:

- Write down what type of scientist you want to become. Are you aiming for an academic career at a research-intensive institution, a career with a focus on teaching, or do you see a non-academic path in science? Which research area most intrigues you? What approaches and methods excite you? It is also helpful to list the publications, grants and presentations that could emerge from this training opportunity.

- Describe experiences or outcomes that show your potential. Emphasize the evidence for your high potential by noting the publications, awards and research you have that illustrate creativity or technical skills. We know from experience that it is easy to be discouraged at this point, but your history, which defines who you are today, is not everything.

- Highlight career growth and development areas that need attention. We have noticed that trainees who are able to delineate gaps in training, or in the experience they need to move on to their next career stage, are highly successful at documenting the need for and value of the proposed training. We recommend describing 3–5 training goals, such as obtaining specific technical training, gaining laboratory management skills or establishing new collaborations.

- Design a thorough training plan. Anchor this plan around your goals to address specific areas for growth. You can include campus-seminar series, visits to a collaborator’s lab to learn a technical skill, oral or poster presentations



at scientific conferences, courses on specific research topics or professional-development skills such as management or scientific writing, mentoring or teaching. Throughout the proposal, you must make a compelling case that your future success depends on your getting this and career-development and research training. Explicitly state, for instance, that you need the proposed technical skill to complete one of your specific aims and future research goals.

We’ve found that discussing specific goals is crucial for successful fellowship applications. For example, we coached a postdoc on revising a proposal that reviewers had described as having a “cookie-cutter training plan”. It listed proposed activities without linking them to the postdoc’s background and trajectory.

In the revision, the applicant described how the plan addressed their specific training goals: to cultivate a certain technical skill, for example, the postdoc would complete specific coursework and work in a collaborator’s lab for three months. The proposal was funded.

Remember, too, that the exercise of completing this application is useful; even if you don’t win the grant this time, the experience that you gain will make you a stronger contender for the next one. Perhaps even more importantly, you will be armed with a clear plan for reaching your career goals and research milestones.

Crystal M. Botham directs the Stanford Biosciences Grant Writing Academy at Stanford University in California. **Tanya M. Evans** is a neuroscientist at the University of Virginia in Charlottesville.

REMEMBRANCE

Saving time.

BY MELANIE REES

“A long time ago, war was simple,” I tell the computer.

“No war is simple,” replies Patti.

“Simpler,” I clarify. My jittery fingers type the longitude, latitude and precise date. “And I guess the definition of ‘a long time ago’ is meaningless now.”

“It doesn’t change the job, however you look at it,” says Patti with mannered pitch and tone too nice to be real. I’m sure Perpetual Analytics researched phonetics to ensure the time-travel interface sounded that benevolent.

I transmit the weapons sequence to the drone. “Guildford’s Portal opening.”

“Confirmed.”

Across the other side of the laboratory, in its clear bubble insulated from all else, the drone hovers above the shimmering shards of energy.

“Engaging.” I press the button and it vanishes from sight.

White beaches, shrubby cliffs, tracks and trenches flicker onto my computer screen.

I turn down the volume, blocking out the bombardment of enemy gunfire. One of those bullets might’ve been the one that hit my great-grandfather.

Across the beaches, men and boys scramble. And fall. From the height of the drone’s camera, I could convince myself they’re ants.

But ants don’t bleed like that.

Beyond them, the target is clear. The drone zooms in on the frightened faces of the Central Forces.

“I am saving tens of thousands of lives by killing others.” Saying it aloud helps convince me.

“You are not killing,” Patti chimes, as if talking about the weather. “You are pressing a button.”

Was that scripted or Patti’s own reasoning breaking through?

Sure, I’m not killing. But, this war was over. A fair, untainted battle. The outcome already decided more than a century ago.

“My analysis suggests this moral win so early on could prevent the Second World War and the Holocaust. Potential lives saved are no longer just thousands on the beaches but millions.”

There it is; the computer’s pep talk.

I inhale and press the button. The small missile shoots from the drone. Fire engulfs the opposing troops until the drone’s images vanish.



I sit at my computer terminal. Confusion wracks my brain for a second. “What happened?”

“The drone annihilated the enemy on Gallipoli.” Patti projects images of my last mission. “You saved thousands of lives, including your great-grandfather’s.”

I can’t help but notice the way Patti emphasizes that the drone *killed* lives, but I *saved* lives.

“In the original timeline your great-grandfather died on the beaches.”

“Really?” Just last ANZAC Day dawn service, I was telling my young boy, Mickey, how brave my great-grandfather was as he ran into the enemy’s trenches, and how the Unknown Soldier burned them all.

Was that me?

“Do you fight like that? Is it scary?” my son had asked.

“Not exactly. My fighting is safe.” It’s the best reply I can muster, but it doesn’t feel honest somehow.

“We just need some minor adjustments.” Patti brings me back to reality. “My analysis has selected specific individuals to target,” it says as if about to recite a shopping list. “This time we may be able to prevent the Holocaust.”

Names, dates, coordinates. Data filter across my screen. Not data. People. My stomach churns.

“I showed your medal at show and tell. The teacher said you’re a hero,” Mickey had said the other day.

Hero? The word grinds in my guts. If I stopped a world war this way, how much of a hero would I really be?

I rest my head in my hands, and spot a note with date and coordinates in my handwriting. I set the program.

“Guildford’s Portal engaging.”

The drone hovers and vanishes. Images

of a messy laboratory stream onto my screen. Strewn across a desk are pages and pages of calculations. Alongside an old-fashioned desktop, a guttural snore erupts from underneath a tangled mess of grey hair.

“Is this the right time?” asks Patti.

I recognize those calculations. “Yes. We are at the right place.” The drone hums and projects a compilation of video footage onto the old man’s laboratory wall.

Sir Guildford grunts and raises his head a fraction. “What the heck,” he mutters still half-dazed.

Watching the blood and fire of men up close rips my heart from my chest. All those histories written and rewritten. All those men falling, who never should’ve fallen. I pray Sir Guildford is as affected as I am.

He looks at his computer calculations and then at the advanced drone.

“It is for the best,” says my drone to the old man.

“Why is the drone talking?” asks Patti.

“I think I programmed it in another past. Doesn’t it sound benevolent?”

“Step aside,” says the drone.

I press a few buttons and the small missile whirrs as it aims at his work desk.

Sir Guildford backs away from his chair, glances at the drone, and then runs from the room.

I guess I’ll never remember this, my great-grandfather will die young, my son may never call me a hero, but at least I can feel like one if just for this small moment in time.

I press the ignition button and fire engulfs the room.

I stand on the white beach with Mickey perched on my shoulders. Dawn bathes the crowd of people in a warm orange glow.

“Is this where your great-grandfather died?” Mickey asks.

“Yes.”

A memory niggles in my head. The thought grows heavy, but the weight of it dissipates as the bugle breaks the silence.

An official speaker recites the ode into the microphone. Silence falls across the beach.

“... At the going down of the sun and in the morning, we will remember them,” he finishes.

That must be all I was trying to recollect. I will remember them. ■

Melanie Rees is an Australian speculative fiction writer and ecological scientist. For more information on her stories, visit Twitter @FlexiRees or www.flexirees.wordpress.com.

ILLUSTRATION BY JACEY